Small Molecule Activation Studies Involving Thiolate-Ligated Manganese(II) Complexes and Biologically-Relevant Oxidants

Michael K. Coggins

A dissertation submitted in partial fulfillment of the requirements for the degree of

Doctor of Philosophy

University of Washington

2012

Reading Committee:

Julia Kovacs, Chair

James Mayer

Daniel Gamelin

Program authorized to offer degree:

Chemistry

University of Washington

Abstract

Small Molecule Activation Studies Involving Thiolate-Ligated Manganese(II) Complexes and Biologically-Relevant Oxidants

Michael K. Coggins

Chair of the Supervisory Committee:

Professor Julie A. Kovacs

Department of Chemistry

This dissertation focuses upon the synthesis, characterization, and reactivity of thiolate-ligated manganese complexes. Chapter 1 provides a brief introduction to the importance of manganese ions in biology, as well as the unique properties promoted by thiolate ligands. Chapter 2 discusses the synthesis and characterization of a library of structurally-analogous manganese(II) complexes used for further studies. Chapters 3-5 discuss the reactivity of the complexes discussed in Chapter 2 with various biologically-relevant oxidants, such as dioxygen, superoxide, and peroxides. Finally, Chapter 6 discusses the synthesis, characterization, and reactivity of model complexes for the manganese lipoxygenase metalloenzyme family. The results described throughout this dissertation provide many rare and unique insights into the role played by manganese in biology, as well as how various reaction intermediate species formed from manganese complexes may have relevance to reactions catalyzed in biology.

Table of Contents

Page

List of Figures

Figure Number Page

List of Schemes

Scheme Number Page

List of Tables

Table Number Page

Glossary

Common Abbreviations:

Å: Angström

Cat: catalase

CmOOH: cumene hydroperoxide

Co: cobalt

CV: cyclic voltammetry

DCM: dichloromethane

deg: degrees

$\Delta G^{\ddagger}$: free energy of activation

$\Delta H^{\ddagger}$: activation enthalpy

$\Delta S^{\ddagger}$: activation entropy

DFT: density functional theory

EPR: electron paramagnetic resonance

ESI-MS: electrospray-ionization mass spectrometry

EtCN: propionitile

Fe: iron

FT-IR: Fourier transform infrared

GC/MS: gas chromatography/mass spectrometry

LO: lipoxygenase

μ_{eff}: effective magnetic moment

MeCN: acetonitrile

Mn: manganese

NMR: nuclear magnetic resonance

OEC: oxygen-evolving complex

rR: resonance Raman

tBuOOH: *tert*-butyl hydroperoxide

SOD: superoxide dismutase

TFA: trifluoroacetic acid

UV/Vis: ultraviolet/visible

XANES: X-ray absorption near-edge spectroscopy

XAS: X-ray absorption spectroscopy

Compound Numbering Scheme (by Chapter)

Chapter 2

1: $[Mn^{II}(S^{Me2}N_4(tren))](PF_6)$

2: $[Mn^{II}(S^{Me2}N_4(6\text{-H-DPEN}))(MeOH)](BPh_4)\cdot MeOH$

3: $[Mn^{II}(S^{Me2}N_4(6\text{-H-DPPN}))]_2(BF_4)_2$

4: $[Mn^{II}(S^{Me2}N_4(6\text{-MeDPEN}))](BF_4)$

5: $[Mn^{II}(S^{Me2}N_4(6\text{-MeDPPN}))](BPh_4)\bullet MeCN$

6:$[(Mn^{II}(S^{Me2}N_4(4\text{-OMe-3,5-Me-DPEN})))(Mn^{II}(S^{Me2}N_4(4\text{-OMe-3,4-Me-DPEN}))(Cl))](BF_4)\cdot Et_2O$

8: $[Mn^{II}(S^{Me2}N_4(2\text{-QuinoEN}))](PF_6)\bullet Et_2O$

9: $[Mn^{II}(S^{Me2}N_4(2\text{-QuinoPN}))](PF_6)\bullet MeCN\bullet Et_2O$

10: $[Mn^{II}(O^{Me2}N_4(tren))]_2(PF_6)_2\cdot MeCN$

11: $[Mn^{II}(N^{Et2}N_4(tren))]_2(\mu\text{-}SO_4)(BPh_4)_2$

12: $[Mn^{II}((HO^{Me2})_2N_4(tren))(MeOH)](BPh_4)_2\cdot MeOH$

13: $[Mn^{II}(HO^{Me2}N_4(6\text{-Me-DPEN})(MeCN))](BPh_4)_2$

14: $[Mn^{II}(HO^{Me2}N_4(6\text{-Me-DPEN})(CHO_2))](BPh_4)\cdot MeCN\cdot Et_2O$

15: $[Mn^{II}(O^{Me2}N_4(6\text{-Me-DPPN}))](BPh_4)$

16: $[Fe^{II}(S^{Me2}N_4(tren))](PF_6)$

17: $[Fe^{II}(S^{Me2}N_4(6\text{-H-DPEN}))(MeOH)](PF_6)$

18: $[Fe^{II}(S^{Me2}N_4(6\text{-H-DPPN}))](PF_6)$

19: $[Fe^{II}(S^{Me2}N_4(6\text{-Me-DPEN}))](PF_6)$

20: $[Fe^{II}(S^{Me2}N_4(6\text{-Me-DPPN}))](PF_6)$

21: $[Fe^{II}(S^{Me2}N_4(2\text{-QuinoEN}))](PF_6)\cdot MeOH$

22: $[Zn^{II}(S^{Me2}N_4(tren))](PF_6)$

23: $[Zn^{II}(S^{Me2}N_4(6\text{-Me-DPEN}))](BPh_4)$

24: $[Zn^{II}(S^{Me2}N_4(6\text{-Me-DPPN}))](BPh_4)\cdot MeCN$

Chapter 3

1: $[Mn^{II}(S^{Me2}N_4(tren))](PF_6)$

2: $[Mn^{II}(S^{Me2}N_4(6\text{-H-DPEN}))(MeOH)](PF_6)\cdot MeOH$

3: $[Mn^{II}(S^{Me2}N_4(6\text{-H-DPPN}))]_2(BF_4)_2$

4: $[Mn^{II}(S^{Me2}N_4(6\text{-Me-DPEN}))](BF_4)$

5: $[Mn^{II}(S^{Me2}N_4(6\text{-Me-DPPN}))](BPh_4)$

6:$[(Mn^{II}(S^{Me2}N_4(4\text{-OMe-3,5-Me-DPEN})))(Mn^{II}(S^{Me2}N_4(4\text{-OMe-3,4-Me-DPEN}))(Cl))](BF_4)\cdot Et_2O$

7: $[Mn^{II}(S^{Me2}N_4(2\text{-QuinoEN}))](BPh_4)\cdot MeCN$

8: $[Mn^{II}(S^{Me2}N_4(2\text{-QuinoPN}))](PF_6)$

9: $[Mn^{II}(O^{Me2}N_4(tren))]_2(PF_6)_2\cdot MeCN$

10: $[Mn^{II}(HO^{Me2}N_4(6\text{-Me-DPEN})(CHO_2))](BPh_4)\cdot MeCN\cdot Et_2O$

11: $[Mn^{II}(O^{Me2}N_4(6\text{-Me-DPPN}))](BPh_4)$

12: $[Mn^{III}(S^{Me2}N_4(tren))]_2(\mu\text{-}O)(PF_6)_2$

13: $[Mn^{III}(S^{Me2}N_4(6\text{-H-DPEN}))]_2(\mu\text{-}O)(PF_6)_2\cdot(MeCN)_2$

14: $[Mn^{III}(S^{Me2}N_4(6\text{-H-DPPN}))]_2(\mu\text{-}O)(PF_6)_2\cdot(MeCN)_2$

15: $[Mn^{III}(S^{Me2}N_4(6\text{-Me-DPEN}))]_2(\mu\text{-}O)(BF_4)_2\cdot(MeOH)_2$

16: $[Mn^{III}(S^{Me2}N_4(6\text{-Me-DPPN}))]_2(\mu\text{-}O)(BPh_4)_2$

17: $[Mn^{III}(S^{Me2}N_4(4\text{-MeO-3,5-Me-DPEN}))]_2(\mu\text{-}O)(PF_6)_2\cdot(MeCN)_2$

18: $[Mn^{III}(S^{Me2}N_4(2\text{-QuinoEN}))]_2(\mu\text{-}O)(PF_6)_2\cdot(CH_2Cl_2)$

19: $[Mn^{III}(S^{Me2}N_4(2\text{-QuinoPN}))]_2(\mu\text{-}O)(BPh_4)_2\cdot(MeCN)$

20: $[Mn^{III}(O^{Me2}N_4(tren))]_2(\mu\text{-}OH)(PF_6)_3\cdot MeCN$

21: $[Mn^{III}(O^{Me2}N_4(6\text{-Me-DPEN}))]_2(\mu\text{-}O)(BF_6)_2\cdot(MeCN)_2$

22: $[Mn^{III}(O^{Me2}N_4(6\text{-Me-DPEN}))]_2(\mu\text{-}O)(BPh_4)_2$

23: $[Mn^{IV}(N_4(6\text{-Me-DPEN}))]_2(\mu\text{-}O)_2(BPh_4)_2$

24: $[Fe^{II}(S^{Me2}N_4(tren))](PF_6)$

25: $[Fe^{II}(S^{Me2}N_4(6\text{-H-DPEN}))(MeOH)](PF_6)$

26: $[Fe^{II}(S^{Me2}N_4(6\text{-H-DPPN}))](PF_6)$

27: $[Fe^{II}(S^{Me2}N_4(6\text{-Me-DPEN}))](PF_6)$

28: $[Fe^{II}(S^{Me2}N_4(2\text{-QuinoEN}))](PF_6)\cdot MeOH$

29: $[Fe^{III}(S^{Me2}N_4(tren))]_2(\mu\text{-}O)(PF_6)_2\cdot MeCN$

30: $[Fe^{III}(S^{Me2}N_4(6\text{-H-DPEN}))]_2(\mu\text{-}O)(PF_6)_2\cdot MeCN$

31: $[Fe^{III}(S^{Me2}N_4(6\text{-H-DPPN}))]_2(\mu\text{-}O)(PF_6)_2\cdot MeCN$

32: $[Fe^{III}(S^{Me2}N_4(6\text{-Me-DPEN}))]_2(\mu\text{-}O)(BF_4)_2\cdot CH_2Cl_2$

33: $[Fe^{III}(S^{Me2}N_4(2\text{-QuinoEN}))]_2(\mu\text{-}O)(BF_4)_2\cdot 2MeCN$

Chapter 4

1: $[Mn^{II}(S^{Me2}N_4(6\text{-Me-DPEN}))](BF_4)$

2: $[Mn^{II}(S^{Me2}N_4(2\text{-QuinoEN}))](BPh_4)\cdot MeCN$

3: $[Mn^{III}(S^{Me2}N_4(6\text{-Me-DPEN}))]_2(\mu\text{-}O)(BF_4)_2\cdot(MeOH)_2$

4: $[Mn^{III}(S^{Me2}N_4(2\text{-QuinoEN}))]_2(\mu\text{-}O)(PF_6)_2\cdot(CH_2Cl_2)$

5: $[Mn^{III}(S^{Me2}N_4(6\text{-Me-DPEN}))]_2(\mu\text{-}O_2)(BPh_4)_2\cdot 2CH_3CH_2CN$

6: $[Mn^{III}(S^{Me2}N_4(2\text{-QuinoEN}))]_2(\mu\text{-}O_2)(BPh_4)_2\cdot CH_3CH_2CN$

Chapter 5

1: $[Mn^{II}(S^{Me2}N_4(6\text{-Me-DPEN}))](BF_4)$

2: $[Mn^{II}(S^{Me2}N_4(2\text{-QuinoEN}))](BPh_4)\cdot MeCN$

3: $[Mn^{II}(S^{Me2}N_4(6\text{-Me-DPPN}))](BPh_4)$

4: $[Mn^{II}(S^{Me2}N_4(2\text{-QuinoPN}))](PF_6)$

5: $[Mn^{II}(S^{Me2}N_4(tren))](PF_6)$

6: $[Mn^{II}(S^{Me2}N_4(6\text{-H-DPEN}))(MeOH)](PF_6)\cdot MeOH$

7: $[Mn^{II}(S^{Me2}N_4(6\text{-H-DPPN}))]_2(BF_4)_2$

8: [(Mn^{II}($S^{Me2}N_4$(4-OMe-3,5-Me-DPEN)))(Mn^{II}($S^{Me2}N_4$(4-OMe-3,4-Me-DPEN))(Cl))(BF_4)·Et_2O

9: [Mn^{II}($HO^{Me2}N_4$(6-Me-DPEN)(CHO_2))](BPh_4)·MeCN·Et_2O

10: [Mn^{II}($O^{Me2}N_4$(6-Me-DPPN))](BPh_4)

1·OO^{t}Bu: [Mn^{III}($S^{Me2}N_4$(6-Me-DPEN))(OO^{t}Bu)](BPh_4)

2·OO^{t}Bu: [Mn^{III}($S^{Me2}N_4$(2-QuinoEN))(OO^{t}Bu)](BPh_4)

3·OO^{t}Bu: [Mn^{III}($S^{Me2}N_4$(6-Me-DPPN))(OO^{t}Bu)](BPh_4)·Et_2O

4·OO^{t}Bu: [Mn^{III}($S^{Me2}N_4$(2-QuinoPN))(OO^{t}Bu)](PF_6)·pentane

5·OO^{t}Bu: [Mn^{III}($O^{Me2}N_4$(6-Me-DPEN))(OO^{t}Bu)](BPh_4)

1·OOCm: [Mn^{III}($S^{Me2}N_4$(6-Me-DPEN))(OOCm)](BPh_4)

2·OOCm: [Mn^{III}($S^{Me2}N_4$(2-QuinoEN))(OOCm)](BPh_4)

Chapter 6

1: [Mn^{II}($S^{Me2}N_4$(tren))](PF_6)

2: [Mn^{III}($S^{Me2}N_4$(tren))]$_2$(μ-O)(PF_6)$_2$

3: [Mn^{III}($S^{Me2}N_4$(tren))(OH)](PF_6)·H_2O

4: [Mn^{III}($S^{Me2}N_4$(tren))(OCH_3)](PF_6)

5: [Mn^{III}($S^{Me2}N_4$(tren))(OPh)](PF_6)·MeCN·Et_2O

6: [Mn^{III}($S^{Me2}N_4$(tren))(OPh-^{p}NO_2)](PF_6)·MeCN

7: [Mn^{III}($S^{Me2}N_4$(2-QuinoPN))(OCH_3)](PF_6)

8: [Mn^{II}($O^{Me2}N_4$(tren))]$_2$(PF_6)$_2$

9: [Mn^{III}($O^{Me2}N_4$(tren))]$_2$(μ-OH)(PF_6)$_2$

10: [Fe^{II}($O^{Me2}N_4$(tren))(H_2O)](OTf)

11: [Fe^{III}($O^{Me2}N_4$(tren))]$_2$(μ-O)(OTf)$_2$·MeOH

12: [Fe^{III}($O^{Me2}N_4$(tren))]$_2$(μ-OH)(OTf)$_3$

13: [Fe^{II}($O^{Me2}N_4$(6-Me-DPEN))](PF_6)

14: [Fe^{III}($O^{Me2}N_4$(6-Me-DPEN))]$_2$(μ-OH)$_2$(PF_6)$_2$

Acknowledgements

My graduate school experience over the past four years has been shaped by an incredible number of wonderful and talented individuals. First and foremost, I have to thank Professor Julie Kovacs for being such a supportive and enthusiastic advisor. I will always be indebted to her for both her mentorship and her seemingly unlimited willingness to advocate in the best interests of her students. The Kovacs group as a whole has been great to me, both academically and personally. Professor Santiago Toledo, a senior-level student in the group when I first joined in 2008, was the person who "showed me the ropes" and helped me acclimate to the lab. Much of my own graduate research was really an extension of work Santiago began during his tenure in the group, for which I certainly believe he deserves a special acknowledgement. I have tried to be the same type of senior-level graduate mentor for the younger members of the group that Santiago was for me – very supportive and enthusiastic, yet still brutally honest and always fully transparent. The current Kovacs group (Ben Leipzig, Audra Johansen, Julian Rees, and Helen Ferreira) is very strong and I'm excited to see each of them continue to have successful graduate school experiences. Nothing less than great should be expected when you have a Boo Bear on your side.

I would also like to acknowledge my other exam committee members, Professors Jim Mayer, Daniel Gamelin, Gojko Lalic, and Ron Stenkamp. Aside from simply being members of my second year, general, and final exam committees, each of these individuals has given me a lot of valuable advice and support over the past few years. I understand and appreciate how hectic life is as a professor, especially when you run large research groups and travel often to give research talks, so the time each of these guys have taken out to discuss science with me or give advice regarding future endeavors is much appreciated. My interactions specifically with Jim helped to spark my interest in his particular field of work, proton-coupled electron transfer reactions, and has led to my decision to pursue research in that field as a postdoc. In mentioning Jim, I have to thank two of his former graduate students, Dr. (and no doubt future Professor) Jeff Warren and Dr. Tristan Tronic, both of whom have also given me a ton of advice, suggestions, and encouragement.

My initial interest in chemistry began when I joined the lab of Professor John Dawson at the University of South Carolina. Before then I was planning to only major in biology with hopes of attending medical school. In retrospect, I honestly couldn't have cared any less about chemistry at the time. Due to the incredible mentorship I received from John and his senior-level graduate student, Dr. Robert Osborne (Dr. Bob), over the three years I was in the Dawson group, I became so enthusiastic about my research projects that I decided I would rather pursue an advanced degree in chemistry rather than in medicine. This was one of the best decisions I have ever made, and it attests to the power and influence of good teaching. John has continued to advocate for my interests since I left his group in 2007, I am extremely grateful for both his efforts and enthusiasm. Robert and I also became very close friends during my time in John's lab, as some of my fondest memories from college are of him and me getting a few Spatens or Franziskaners after a day in the lab or watching football games in the fall with a few other friends. I will always have a ton of love for both Robert and his wife, Caroline, and thank them tremendously for their friendship.

Almost all of my work in graduate school has been largely contributed to by a number of collaborators, many of which have actually trained me in various techniques and allowed me to use their equipment to conduct experiments with my own compounds. Professor Tom Spiro, Dr. Mohammed Ibrahim, and Dr. Gurusamy Balakrishnan (UW) have allowed me to use their equipment to conduct resonance Raman experiments, as well as shown me how to work-up and manipulate data from these experiments. Professor Ed Solomon and Yeonju Kwak (Stanford U) have also allowed me to use their equipment for resonance Raman experiments. Dr. Stefan Ochsenbein (UW), a former postdoc in the Gamelin group, taught me how to conduct both EPR and SQUID experiments. Professor Stefan Stoll and Ellen Hayes (UW) have also help tremendously in more recent EPR experiments. Professor Elena Rybak-Akimova and Xianru Sun (Tufts U) have been fantastic collaborators and provided some critical stopped-flow kinetics data. Dr. Simon George (LBNL) sacrificed a considerable amount of beam time at SSRL so that I could conduct some XAS experiments. Finally, Professor Serena DeBeer and Dr. Vlad Martin-Diaconescu (MPI) provided us with some great computational data. I am extremely grateful to each of these individuals for all they have done to contribute to my graduate work.

Nothing has been reinforced to me during my graduate experience more so than the importance of family. When I decided to attend UW for graduate school, I knew being away from all of my family in South Carolina would be difficult, but I vastly underestimated how difficult. I thank them all for everything they do; mom, Chuck, Tori, Tara, Izzy, Nanny, Pop, Uncle Bug, Kathy, and Nathan. Often throughout my life they have had more confidence in me than I have had in myself, and it is because of the immense amount of love and support they have unwaveringly shown that I've been able to accomplish what I have. This is especially true regarding my mom, who hass always been my biggest fan, a source of comfort, and my best friend. To me, she represents everything that is good about a person and has always been my role model.

Finally, I want to end this acknowledgement section my writing about the greatest thing to happen to me during my time in graduate school, which was meeting Kate. Kate and I met for the first time on the second day of our graduate school orientation, went on our first date later than week, and have been essentially inseparable since. Having her as such an integral part of my life has made each and every day even more worthwhile, and there is nothing I look forward to more than spending my nights at home with her and our two golden retrievers, Brodie and Zoe (who are, of course, the greatest four-legged creatures ever). Along with them, I have also been blessed with getting to spend time with Kate's family - Brad, Mary, Jessi, Rachel, Brynn, and yes, Maggie and Royce, too - each of whom I have nothing but love and respect for. I am ever so grateful for the love and support I've received from Kate and her family, as they have contributed more to my success in graduate school than they may ever know.

Dedication

This dissertation is dedicated to the two most important women in my life – Kate and my mom.

Chapter 1

An Introduction to Manganese Metalloenzymes and Metal-Thiolate Bonds

1.1 Bioinorganic Chemistry – Understanding the Roles of Transition Metal Ions in Biology

As we further recognize the complexity of biological systems, our need for understanding the roles played by transition metal ions in these systems increases. The ability of transition metals to facilitate biological processes has undoubtedly resulted in Nature having evolved to require these elements for proper function. Towards uncovering the roles of transition metals in biological function, bioinorganic chemistry has developed into a large and thriving field. Bioinorganic chemistry is a unique area of chemistry because it requires expertise from a wide variety of other disciplines, such as coordination chemistry, molecular spectroscopy, enzymology, and molecular biology. These areas work synergistically to answer some of the most basic questions concerning structure-function relationships pertaining to metal ions in biology. For the true bioinorganic chemist, these relationships ultimately link to an understanding of, and appreciation for, the inorganic components of each individual system.

A primary functional advantage afforded to biological systems by transition metal ions is a large amount of structural diversity. Unlike organic moieties, transition metal ions are capable of forming complexes with a wide variety of coordination numbers and geometries. One only needs to quickly survey an undergraduate inorganic textbook or recent edition of the journal *Inorganic Chemistry* to realize the incredible number of unique coordination compounds which can be formed with these elements. This general property results, at least in part, from the large ranges of ion sizes and accessible oxidation states possible for transition metals. Because of the structural variation displayed by transition metal complexes, these elements are often critical in

maintaining the three-dimensional conformations of biological macromolecules and providing noncovalent intermolecular interactions for stabilizing macromolecular assemblies.

A further advantage of utilizing transition metal ions in biological systems is the ability of these elements to promote a wide variety of chemical reactions. Transition metals are Lewis acids; therefore they can influence Lewis acid/base chemistry by modulating the relative nucleophilicity or electrophilicity of coordinated ligands. Electron transfer reactions are also frequently mediated by transition metal ions since these elements can participate in multielectron redox chemistry. The Lewis acidity and redox potential of a transition metal can each be subtly modulated, or "tuned', by responding to changes in the primary and secondary coordination spheres of the metal complex. This results in direct correlations between the structural and reactive properties of a transition metal within a particular environment. Understanding the interplay between structure and reactivity, as well as how this interplay ultimately impacts particular biological processes, is a fundamental area of interest in bioinorganic chemistry.

1.2 Manganese Coordination Chemistry and Relevance to Metalloenzymes

Manganese is the third most abundant transition metal in the Earth's crust (~0.020 $mol \cdot kg^{-1}$) and is an essential element in living systems.[1-3] It is therefore unsurprising that Mn ions are often incorporated within metalloenzyme active sites to promote various biochemical transformations. The aqueous chemistry of Mn is well-established and oxidation states of II, III, and IV are known to be accessible under typical biological conditions.[4-6] Low-valent Mn(II) is considered the most common oxidation state for Mn in biology and is universally found to be high-spin (d^5, S = 5/2).[7-8] Given that complexes containing S = 5/2 metal ions lack ligand field stabilization energy, Mn(II) sites in biology are typically kinetically labile, thus they are able to

promote relatively rapid ligand exchange reactions.[7-8] Mn ions in biological systems also tend to show a preference for hard donor ligands (oxygen, nitrogen) over softer donor ligands (sulfur).[9-11] This may be most evident by the fact that all structurally-characterized Mn metalloenzymes contain at least one oxygen donor ligand, while there are no known examples sulfur-ligated Mn metalloenzymes. To further illustrate the functional diversity displayed by Mn-containing metalloenzymes, the following subsections will seek to briefly describe some of the more well-precedented examples within this group.

1.2.1 Manganese Superoxide Dismutase

The superoxide dismutases (SODs) are a group of metalloenzymes that disproportionate the deleterious superoxide radical ($O_2^{-\bullet}$) to molecular oxygen (O_2) and hydrogen peroxide (H_2O_2) (equation 1.1). The SOD family of enzymes is diverse with respect to metal ion cofactor specificity, as there are mononuclear members, including MnSOD, FeSOD, and NiSOD, as well as binuclear Cu/ZnSODs.[12-15] MnSODs and FeSODs are, however, closely related based upon similar amino acid sequences.[16-18] There even exists a small number of SODs which are catalytically-active with either Mn or Fe ((Mn,Fe)SODs) and are referred to as cambialistic metalloenzymes.[19-21] X-ray crystal structures of various MnSODs originating from both prokaryotic and eukaryotic organisms have been obtained and display a high degree of structural homology.[22-26] All structurally characterized active sites reveal a single Mn ion residing within a trigonal bipyramidal coordination environment comprised of two histidine imidazoles and an

$$2O_2^{-} + 2H^{+} \rightarrow H_2O_2 + O_2 \qquad (1.1)$$

aspartate carboxylate in the equatorial plane (xy-plane), while a third histidine imidazole residue and hydroxide ligand are found in the axial positions (z-axis) (Scheme 1.1). The primary

coordination spheres of MnSODs are somewhat akin to the 2-His-1-carboxylate facial triad motif frequently observed in the active sites of non-heme iron enzymes, such as Fe(II)-dependent catechol dioxygenases (*vide infra*).

Scheme 1.1 Active site representation of the reduced MnSOD.

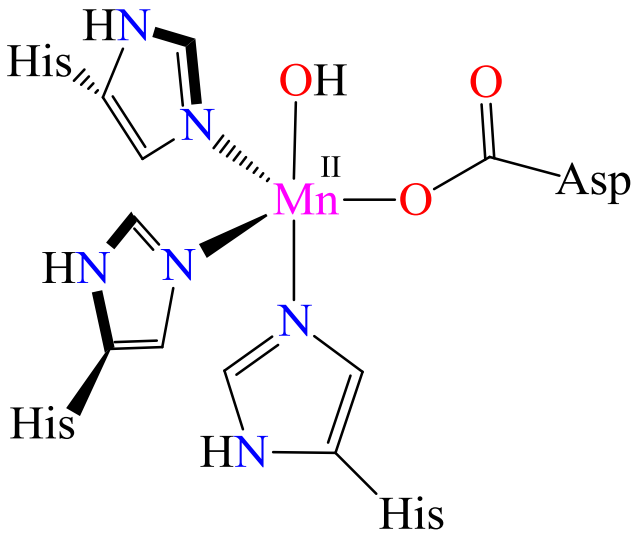

MnSODs are redox-active metalloenzymes, as they cycle between the Mn(II) and Mn(III) oxidation states via a ping-pong mechanism during the proton-dependent disproportionation of superoxide (equations 1.2 and 1.3).[27] Most mechanistic proposals for superoxide disproportionation by MnSODs invoke transient Mn(III)-peroxo or –hydroperoxo intermediates in each respective catalytic cycle. Although a putative peroxo/hydroperoxo intermediate has yet to be observed under normal catalytic conditions, a product-inhibited "dead-end" species has

$$O_2^- + \text{Mn(III)SOD} \rightarrow O_2 + \text{Mn(II)SOD} \qquad (1.2)$$

$$O_2^- + 2H^+ + \text{Mn(II)SOD} \rightarrow H_2O_2 + \text{Mn(III)SOD} \qquad (1.3)$$

been observed by electronic absorption spectroscopy under high concentrations of superoxide and is believed to contain a Mn(III)-hydroperoxo.[28-29] FeSODs are also believed to promote superoxide disproportionation through a similar catalytic mechanism involving Fe(III)-peroxo or –hydroperoxo intermediates.[30-33] Understanding why many of these enzymes are catalytically-active only with either Mn or Fe, despite the striking similarities in active site structures, is an ongoing area of active research which highlights the importance of subtle electronic differences between the two metal ions.

1.2.2 Manganese Lipoxygenase

Lipoxygenases (LOs) are a group of mononuclear metalloenzymes that promote the stereo- and regiospecific oxidation of *cis*,*cis*-1,4-pentadiene-containing fatty acids to the corresponding alkyl hydroperoxides.[34] Most of our current understanding regarding the properties of LOs has come by way of FeLOs, which have been characterized from both mammalian and plant sources.[35-37] A MnLO from the fungus *Gaeumannomyces graminis* has been discovered and was found to promote the oxidation of linoleic and linolenic acids in a fashion similar to FeLOs.[38-39] Although this MnLO has yet to be structurally characterized, it is believed that the MnLO active site is structurally similar to that of the analogous mammalian FeLOs. Mammalian FeLOs exclusively contain a six-coordinate Fe(III) ion ligated by two histidine imidazoles, the carboxylate oxygen of the C-terminus, and a hydroxide ligand within the equatorial plane, while a third histidine imidazole and either an asparagine amide oxygen or fourth histidine imidazole are located in the axial positions (Scheme 1.2).[40]

Scheme 1.2 Active site representation of the iron rabbit 15-lipoxygenase.

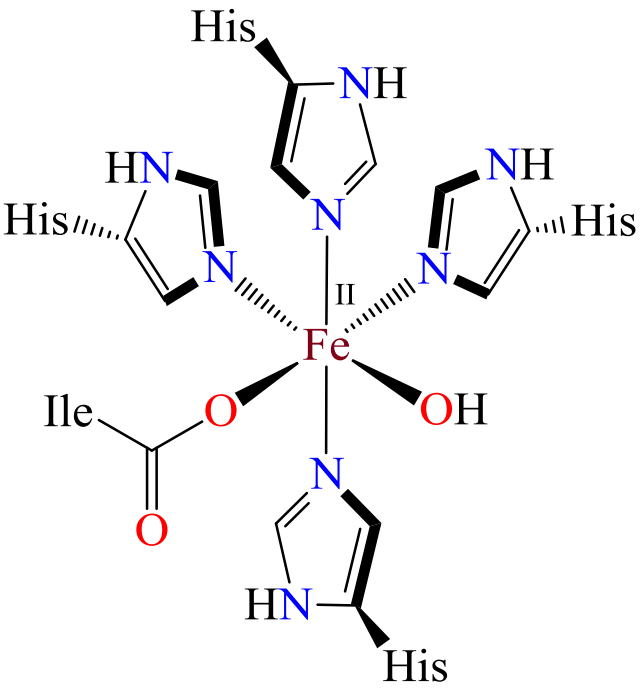

The proposed mechanism for fatty acid peroxidation by FeLOs involves substrate activation by the Fe(III)-OH active site (Scheme 1.3). A key step in this transformation is believed to involve an initial oxidation of the substrate through a proton-coupled electron transfer (this step is referred to by some as an electron-proton transfer and by others as a hydrogen atom transfer) forming an Fe(II)-OH_2 species and alkyl radical.[41-46] The alkyl radical is subsequently trapped by O_2 to form an alkylperoxy radical, which is capable of abstracting a hydrogen atom from the Fe(II)-OH_2 to reform the active state of the enzyme and the alkyl hydroperoxide product. Unlike many metalloenzymes which require the formation of a high-valent transition metal oxidant to active strong C-H bonds, LOs are capable of performing such reaction through a relatively low-valent transition metal center. Mechanistic studies suggest MnLO reacts with fatty acid substrates in a similar fashion to FeLOs and provides yet another parallel between the properties of Mn and Fe cofactors in biology.[45-46]

Scheme 1.3 Proposed mechanism for fatty acid peroxidation by FeLO enzymes.

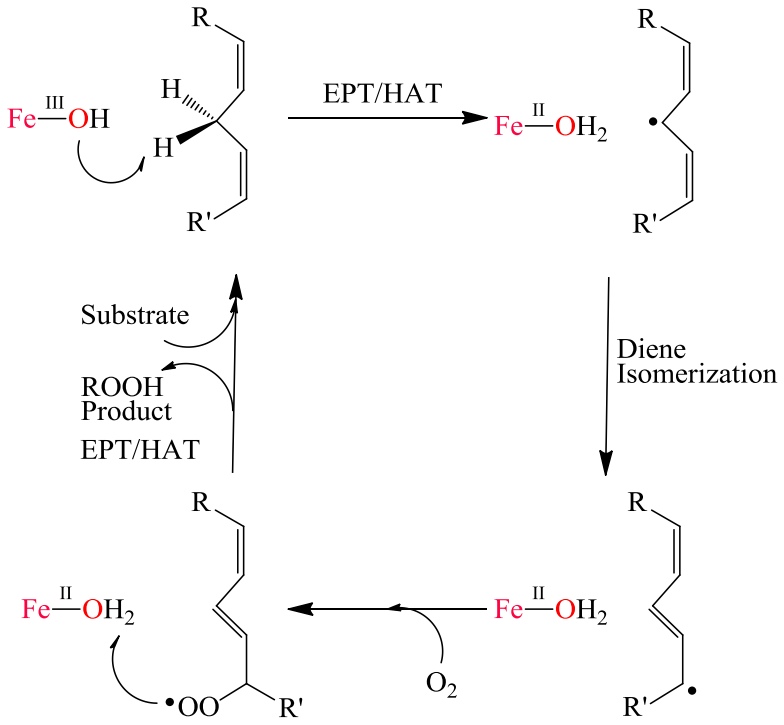

1.2.3 Manganese(II)-Dependent Extradiol-Cleaving Catechol Dioxygenase

The catechol dioxygenases are yet another family of metalloenzymes which are most understood by way of the Fe-containing members, although some Mn-dependent examples have been discovered. As a group, these metalloenzymes are responsible for the oxidative degradation of aromatic molecules through either intradiol or extradiol cleavage pathways.[47-48] Structurally characterized active sites of Fe(II)-dependent extradiol-cleaving dioxygenases include 2,3-dihydroxybiphenyl 1,2-dioxygenase from *Pseudomonas* sp. strain LB400 and catechol 2,3-dioxygenase from *Pseudomonas putida* mt-2; both are structurally similar to one other and contain the archetypical 2-His-1-carboxylate facial triad frequently observed for Fe-containing and O_2-dependent dioxygenases.[49-51] These active sites contain an Fe(II) cofactor within a trigonal bipyramidal coordination environment comprised of a histidine imidazole and

two water/hydroxide ligands within the equatorial plane, while a glutamate carboxylate and second histidine imidazole are found in the axial positions (Scheme 1.4). Sequence comparisons between the Fe(II)- and Mn(II)-dependent members isolated from *Bacillus brevis*, *Arthrobacter* sp. strain Mn-1, and *Arthrobacter globiformis* suggest a large amount of structural homology between the two different cofactor-dependent classes.[52-54] Although the wild-type Mn(II)-dependent enzymes have yet been characterized by X-ray crystallography, an X-ray structure has been described for a Mn(II)-reconstituted form of the Fe(II)-dependent 2,3-dioxygenase from *Arthrobacter globiformis*.[55] A unified reaction mechanism for catechol dioxygenation by both Fe(II)- and Mn(II)-dependent extradiol dioxygenases is provided in Scheme 1.5 and notably involves M(II)-superoxo and M(II)-alkylperoxo intermediates.

Scheme 1.4 Active site representations of Mn(II)-containing 2,3-dioxygenase from *Arthrobacter globiformis* (left) and Fe(II)-dependent extradiol-cleaving dioxygenase from *Psuedomonas putida* mt-2 (right).

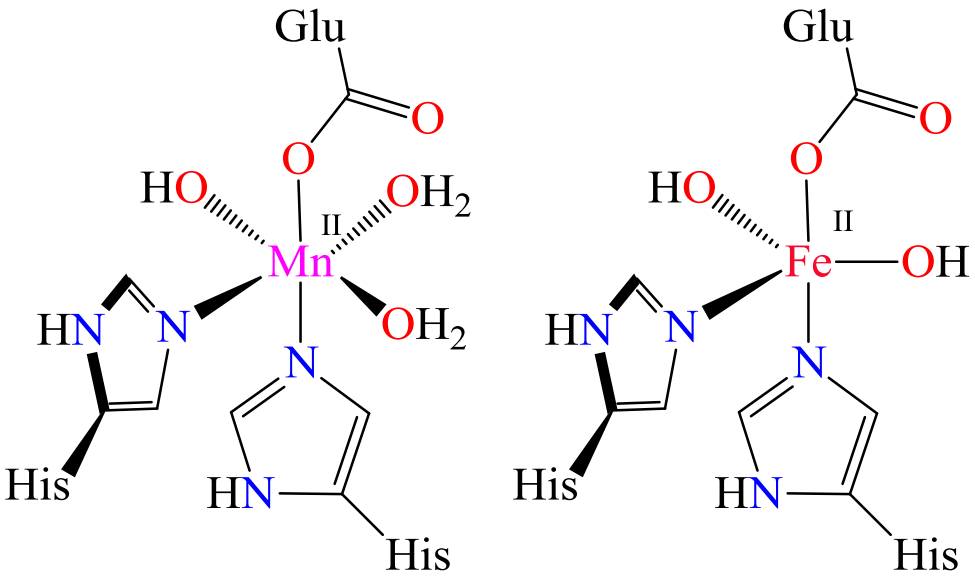

Scheme 1.5 Proposed reaction mechanism for the extradiol cleavage of catechol by Mn(II)- and Fe(II)-dependent catechol dioxygenases. Secondary sphere amino acid residues involved in proton removal/delivery during the reaction are arbitrarily labeled "B".

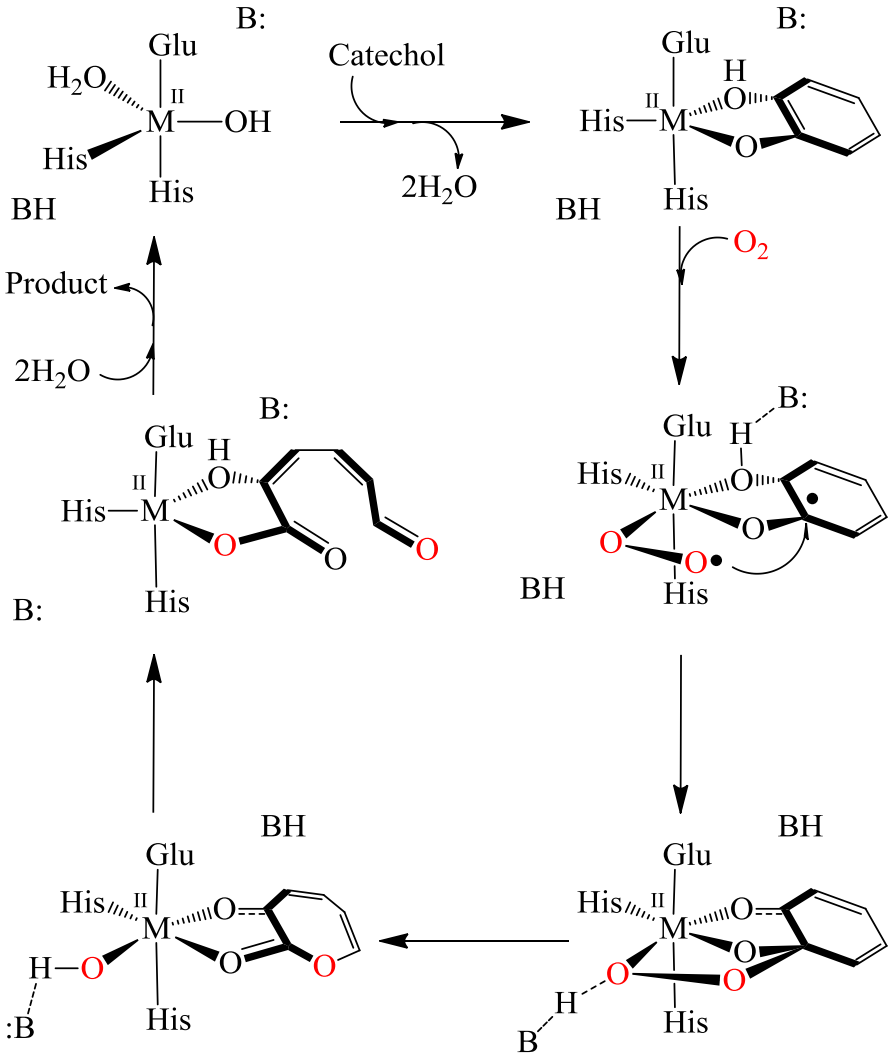

1.2.4 Manganese Catalase

Catalases are a group of metalloenzymes which are responsible for the metabolism of hydrogen peroxide via disproportionation to water and molecular oxygen (equation 1.4).[56]

$$2H_2O_2 \rightarrow 2H_2O + O_2 \quad (1.4)$$

Although most catalases are heme-containing Fe metalloenzymes, there are examples of binuclear Mn-containing catalases (MnCat) that have been isolated exclusively from bacteria.[57-59] Two structurally characterized MnCats have been obtained from *Lactobacillus planatarum* ATCC 14431 AND *Thermus thermophiles* HB-8, both of which been shown to contain a binuclear Mn active site with three potentially bridging ligands (the identity of two of these ligands as either aquo, hydroxo, or oxo are thus far undetermined) (Scheme 1.6).[60-61] Mechanistic investigations into the catalytic activity of MnCats have come primarily through small molecule model studies and often invoke the participation of various Mn-hydroperoxo and $Mn_2(\mu\text{-}O_2)$ intermediates (Scheme 1.7).[56,62]

1.2.5 Oxygen-Evolving Complex of Photosystem II

The oxygen-evolving complex (OEC) of photosystem II is a tetranuclear manganese cluster responsible for the light-driven oxidation of water to dioxygen (equation 1.5).[63] Properties

$$2H_2O + 4h\nu \rightarrow O_2 + 4e^- + 4H^+ \qquad (1.5)$$

of the OEC have been heavily investigated by members of the bioinorganic community and those interested in renewable energy production. A 1.9 Å resolution X-ray crystal structure of the OEC reveals a cubane cluster containing three oxo-bridged Mn ions and a Ca ion at the four corners of the cube, as well as a "dangling" oxo-bridged Mn ion found on the exterior of the cube (Scheme 1.8).[64] Although not intimately involved with the structural properties of the OEC Mn_4CaO_5 cluster, a key redox-active tyrosine residue has been identified near the OEC and serves to mediate electron transfer between the OEC and strongly oxidizing $P680^{\bullet+}$.[63,65] It is

Scheme 1.6 Active site representation of MnCat from *Thermus thermophiles* (x = 0, 1, or 2).

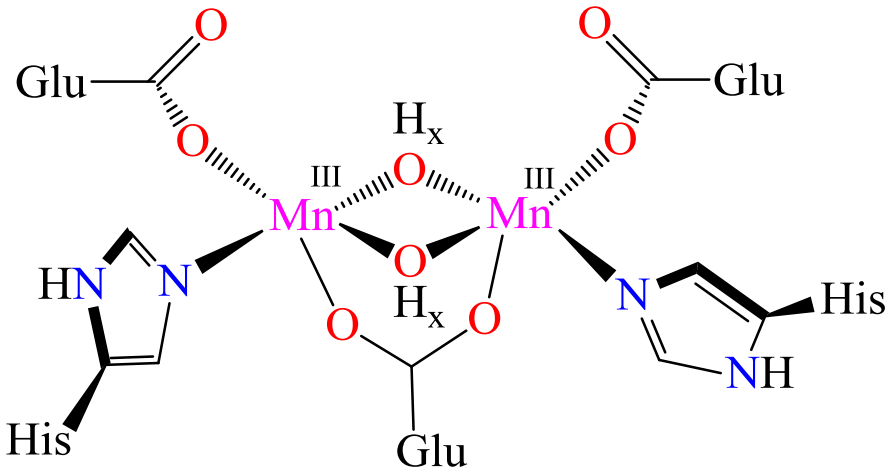

Scheme 1.7 Proposed reaction mechanism for hydrogen peroxide disproportionation by MnCat. Secondary sphere amino acid residues involved in proton removal/delivery during the reaction are arbitrarily labeled "B".

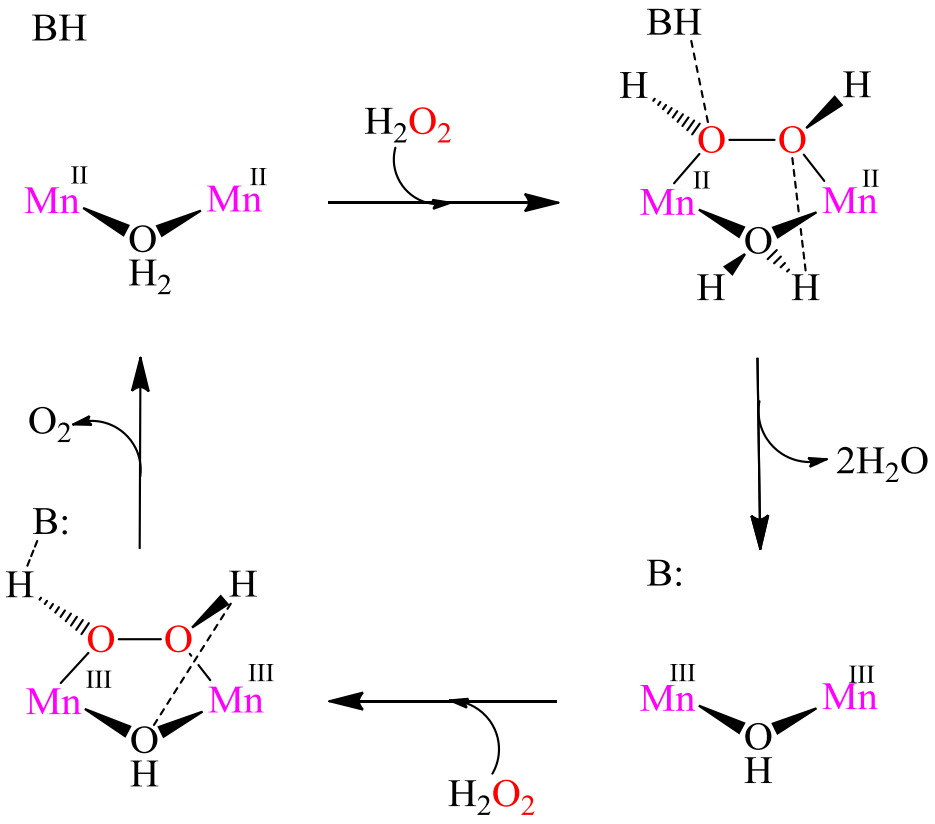

widely accepted that the mechanism of water oxidation involves four sequential steps collectively referred to as the Kok S-state cycle (Scheme 1.9).[66] The exact nature of each individual transformation during the Kok cycle is still debated; however there is an agreement that molecular oxygen is eventually produced through coupling of two oxo or hydroxo ligands located within the OEC.[67] It is also believed that many high-valent Mn-oxo intermediates are formed during the Kok cycle, possibly including a Mn(V)-oxo, giving the OEC access to some of the highest Mn oxidation states that occur in Nature.

Scheme 1.8 Active site representation of the OEC of photosystem II.

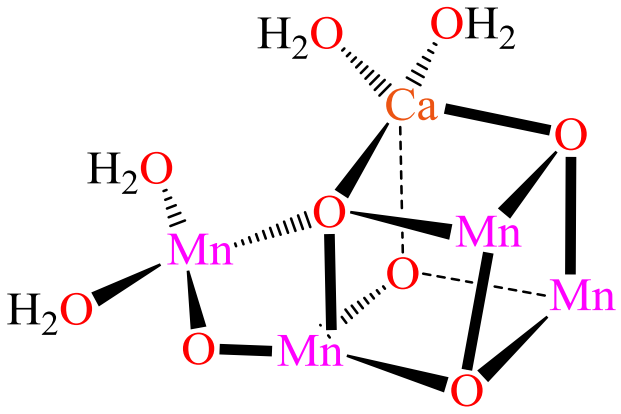

Scheme 1.9 Kok S-state cycle describing the steps involved in the OEC water oxidation cycle.

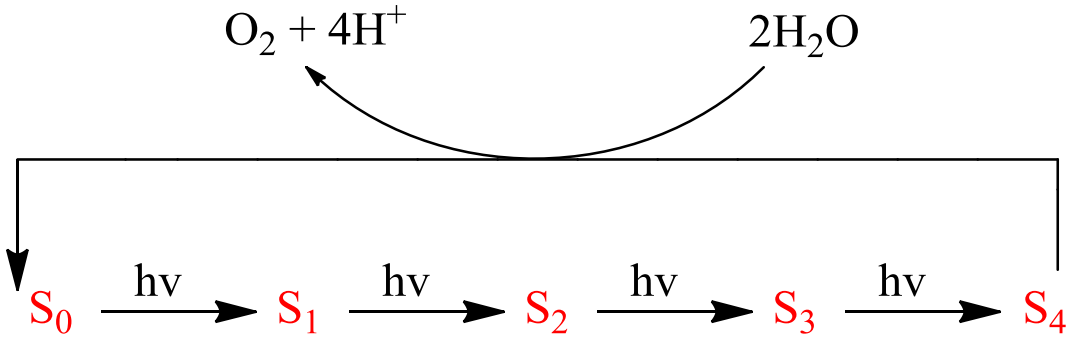

1.2.6 Unifying Features of Mn-Containing Metalloenzyme Reactions

Sections 1.2.1-1.2.5 have briefly described the active site structures and reactivity of some Mn metalloenzymes. Although this list certainly does not encompass every known type of Mn-containing metalloenzyme, it does serve to exemplify the large amount of structural and reactive diversity exhibited within this class of enzymes. Despite differences in active site nuclearities, Mn coordination environments, and reactive properties, there are significant unifying characteristics which can be noted from these examples. Each involves a reaction with either dioxygen or a reduced derivative of dioxygen (O_2^-, H_2O_2, H_2O). As a consequence, the catalytic cycles of each enzyme are believed to involve Mn-peroxo/hydroperoxo/alkylperoxo or Mn-oxo/hydroxo intermediates. Another common feature among this group of metalloenzymes is that, with the exception of Mn(II)-dependent extradiol-cleaving catechol dioxygenases, each is redox-active and involves Mn oxidation states ranging from II-V.

Finally, there are many structural and functional parallels between various Mn- and Fe-containing metalloenzymes, with the cambialistic (Mn,Fe)SODs providing the best illustration of this observation. Similarities between Mn and Fe with regards to atomic size, coordination chemistry, and accessible oxidation states offer at least a general explanation for why many metalloenzyme families contain both Mn and Fe members. It is not completely understood, however, which properties of each metal lead to one being specifically incorporated in a particular metalloenzyme over another. The electronic, structural, and reactive characteristics of each metal ion within specific coordination environments are fundamental properties which must be understood in order to help explain these cofactor specificities.

1.3 Metal-Thiolate Bonds in Bioinorganic Chemistry

As was previously mentioned, there are no examples of naturally-occurring Mn metalloenzymes which contain a coordinated sulfur ligand. This contrasts with Fe-containing metalloenzymes, as some of the most thoroughly explored Fe metalloenzymes contain thiolate ligands. The cytochrome P450 family of enzymes are heme-containing and cysteinate-ligated enzymes which promote a wide variety of organic oxidation reactions.[68] Single cysteine residues are also found in the active site of the non-heme iron enzymes superoxide reductase, which promotes the proton-dependent reduction of superoxide to hydrogen peroxide in anaerobic organisms, as well as peptide deformylase, a hydrolytic metalloenzyme that cleaves the N-terminus formyl group of eubacterial proteins during protein synthesis.[69-70] The binuclear hydrogenases (Fe-Fe and Ni-Fe) contain bridging cysteine thiolates and promote dihydrogen reduction.[71] Iron-sulfur clusters (Fe_4S_4) are often found in enzymes which promote multi-electron redox reactions, such as sulfite reductase, an enzyme responsible for sulfite reduction, and CO dehydrogenase, which converts CO to CO_2.[72-73]

Thiolate ligands are recognized as having significant contributions to the structural and reactive properties of metalloenzymes. These effects typically result specifically from highly covalent metal-thiolate bonds, in contrast to the more ionic bonding interactions between metal ions and nitrogen or oxygen donor ligands in biological systems.[74-75] Highly covalent metal-thiolate bonds can reduce the Lewis acidity of a metal ion and therefore stabilize coordinatively unsaturated metal centers, thus maintaining an available coordination site for exogenous ligand binding.[76-77] Electron transfer reactions are also facilitated by thiolate ligation due to a decrease in metal ion oxidation potential.[78-79] Thiolate ligands are also known to have a considerable *trans* effect, which can labilize ligands even if the metal ion may classified as substitution inert

(Co(III)-containing nitrile hydratase).[78] The degree of metal-thiolate bond covalency can also be tuned in response to changes in the metal and ligand environments, therefore thiolates serve as "electronic buffers" to help modulate redox potentials.[79] Possibly the most significant property of thiolate ligands with regards to reactivity is that these ligands have been shown to lower activation barriers for cleavage of strong C-H, O-O, N-O, and C≡N bonds.[80-85] Finally, metal-thiolate bonds often result in rich spectroscopic properties that reflect their highly covalent nature.[86-87]

1.4 Concluding Remarks

Manganese ions directly participate in some of the most fundamental biochemical transformations known in Nature. The versatility of this particular metal ion is evident from the large variety of structural and functional roles it serves in these transformations. It is also evident that there are many comparisons which can be made between metalloenzymes that utilize Mn and Fe cofactors, which is underlined by similarities between these two metal ions. The presence of a large and diverse class of thiolate-ligated Fe metalloenzymes, while no naturally-occurring Mn metalloenzymes contain metal-thiolate bonds, is one point of distinction between the two groups of cofactor-specific enzymes. This has inspired our group to investigate the properties of biomimetic Mn coordination complexes containing thiolate ligands.

The following chapters will discuss work performed towards further understanding how thiolate ligands may influence the structural and reactive properties of biomimetic Mn complexes. At times, these results will be compared with those from a set of analogous Fe complexes, highlighting differences promoted solely by the identity of the metal ion. The reactivity of these synthetic complexes with various biological oxidants has been explored in

order to further understand how Mn may activate small molecules in metalloenzyme systems. Chapter 2 of this thesis focuses upon the synthesis and characterization of a library of Mn(II) and Fe(II) complexes for an understanding of how ligand structure may influence the properties of analogous metal complexes. Chapter 3 discusses a reactivity survey of this Mn(II) and Fe(II) complexes library with various biological oxidants, highlighting novel reaction products and implications regarding differences between Mn and Fe oxidation chemistry. Chapters 4 and 5 discuss more thorough investigations into reactions with dioxygen and alkyl hydroperoxides, respectively. These chapters include mechanistic studies and the isolation and characterization of reaction intermediates of biological significance. Chapter 6 involves more of a focus upon the influence of thiolate ligands upon the properties and reactivity of Mn complexes, including MnLO and FeLO model complexes.

1.5 Notes to Chapter 1

1) Emsley, J. *The Elements*, Clarendon Press: Oxford, 1989.

2) Cox, P. A. *The Elements on Earth*, Oxford University Press: New York, 1995.

3) Fraústo da Silva, J. J. R.; Williams, R. J. P. *The Biological Chemistry of the Elements*, Clarendon Press: Oxford, 1991.

4) Spiro, T. G.; Stigliani, W. M. *The Chemistry of the Environment*, University Science Books: North America, 2012.

5) Stumm, W.; Morgan, J. J. *Aquatic Chemistry*, Wiley-Interscience: New York, 1996.

6) Myers, C. R.; Nealson, K. H. *Geochim. Cosmochim. Acta*. **1998**, *52*, 2927-2932.

7) Emerson, S.; Kalhorn, S.; Jacobs, L.; Tebo, B. M.; Nealson, K. H.; Rossen, R. A. *Geochim. Cosmochim. Acta*. **1982**, *46*, 1073-1079.

8) Sigel, A.; Sigel, H. *Metal Ions in Biological Systems: Volume 37, Manganese and Its Role in Biological Processes*, Marcel Dekker, Inc.: New York, 1999.

9) Cotton, F. A.; Wilkinson, G. *Advanced Inorganic Chemistry*, Interscience: New York, 1972.

10) Shriver, D. F.; Atkins, P. W.; Langford, C. H. *Inorganic Chemistry*, Freeman Publishing: New York, 1990.

11) Thorp, H. H.; Pecoraro, V. L. *Mechanisitic Bioinorganic Chemistry*, American Chemical Society: Washington, DC, 1995.

12) Miller, A.-F.; Sorkin, D. L. *Comments Mol. Cell. Biophys.* **1997**, *9*, 1-48.

13) Miller, A.-F. *Handbook of Metalloproteins*, Messerschmidt, A.; Huber, R.; Poulous, T.; Wieghardt, K., Eds; John Wiley & Sons: Chichester, 2001.

14) Packer, L. *Methods in Enzymology: Superoxide Dismutase*, Elsevier Ltd: Oxford, 2004.

15) Jackson, T. A.; Brunold, T. C. *Acc. Chem. Res.* **2004**, *37*, 461-470.

16) Parker, M. W.; Blake, C. C. F.; Barra, D.; Bossa, F.; Schinina, M. E.; Bannister, W. H.; Bannister, J. V. *Protein Eng.* **1987**, *1*, 393-397.

17) Parker, M. W.; Blake, C. C. F. *FEBS Lett.* **1988**, *229*, 377-382.

18) Hunter, T.; Ikeburkuro, K.; Bannister, W. H.; Bannister, J. V.; Hunter, G. J. *Biochemistry.* **1997**, *36*, 4925-4933.

19) Martin, M. E.; Byers, B. R.; Olson, M. O.; Salin, M. L.; Arceneaux, J. E.; Tolbert, C. J. *J. Biol. Chem.* **1986**, *261*, 9361-9367.

20) Sugio, S.; Hiraoka, B. Y.; Yamakura, F. *Eur. J. Biochem.* **2000**, *267*, 3487-3495.

21) Tabares, L. C.; Bittel, C.; Carrillo, N.; Bortolotti, A.; Cortez, N. *J. Bacteriol.* **2003**, *185*, 3223-3227.

22) Steinman, H. M.; Weinstein, L; Brenowitz, M. *J. Biol. Chem.* **1994**, *269*, 28629-28634.

23) Edwards, R. A.; Baker, H. M.; Whittaker, M. M.; Whittaker, J. W.; Jameson, G. B.; Baker, E. N. *J. Biol. Chem.* **1998**, *3*, 161-171.

24) Whittaker, M. M.; Ekberg, C. A.; Edwards, R. A.; Baker, E. N.; Jameson, G. B.; Whittaker, J. W. *J. Phys. Chem. B.* **1998**, *102*, 4668-4677.

25) Whittaker, M. M.; Whittaker, J. W. *J. Biol Chem.* **1998**, *273*, 22188-22193.

26) Whittaker, M. M.; Whittaker, J. W. *Biochemistry*. **1997**, *36*, 8923-8931.

27) Miller, A.-F. *Coordination Chemistry in the Biosphere and Geosphere*. Que Jr., L.; Tolman, W. Eds., Pergamon: New York, 2003.

28) Bull, C.; Niederhoffer, E. C.; Yoshida, T.; Fee, J. A. *J. Am. Chem. Soc.* **1991**, *113*, 2762-2763.

29) Hearn, A. S.; Tu, C. K.; Nick, H. S.; Silverman, D. N. *J. Biol. Chem.* **1999**, *113*, 24457-24460.

30) Jackson, T. A.; Yikilmaz, E.; Miller, A.-F.; Brunold, T. C. *J. Am. Chem. Soc.* **2003**, *125*, 8348-8363.

31) Bull, C.; Fee, J. A. *J. Am. Chem. Soc.* **1985**, *107*, 3295-3304.

32) Miller, A.-F.; Padmakumar, K.; Sorkin, D. L.; Karapetian, A.; Vance, C. K. *J. Inorg. Biochem.* **2003**, *93*, 71-83.

33) Han, W. G.; Lovell, T.; Noodleman, L. *Inorg. Chem.* **2002**, *41*, 205-218.

34) Nelson, M. J.; Seitz, S. *Active Oxygen in Biochemistry*. Chapman and Hall: Glasgow, 1995.

35) Skrzypczak-Jankun, E.; Amzel, L. M.; Kroa, B. A.; Funk, M. O., Jr. *Proteins: Struct., Funct., Genet.* **1997**, *29*, 15-31.

36) Minor, W.; Steczko, J.; Stec, B.; Otwinowski, Z.; Bolin, J. T.; Walter, R.; Axelrod, B. *Biochemistry* **1996**, *35*, 10687-10701.

37) Boyington, J. C.; Gaffney, B. J.; Amzel, L. M. *Science* **1993**, *260*, 1482-1486.

38) Su, C.; Oliw, E. *J. Biol. Chem.* **1998**, *273*, 13072-13079.

39) Hamberg, M.; Su, C.; Oliw, E. *J. Biol. Chem.* **1998**, *273*, 13080-13088.

40) Gillmore, S. A.; Villaseñor, A.; Fletterick, R.; Sigal, E.; Browner, M. F. *Nat. Struct. Biol.* **1997**, *4*, 1003-1009.

41) Que, L., Jr.; Ho, R. Y. N. *Chem. Rev.* **1996**, *96*, 2607-2624.

42) Jonsson, T.; Glickman, M. H.; Sun, S. J.; Klinman, J. P. *J. Am. Chem. Soc.* **1996**, *118*, 10319-10320.

43) Glickman, M. H.; Wiseman, J. S.; Klinman, J. P. *J. Am. Chem. Soc.* **1994**, *116*, 793-794.

44) Hwang, C.-C.; Grissom, C. B. *J. Am. Chem. Soc.* **1994**, *116*, 795-796.

45) Lewis, E. R.; Johansen, E.; Holman, T. R. *J. Am. Chem. Soc.* **1999**, *121*, 1395-1396.

46) Glickman, M. H.; Klinman, J. P. *Biochemistry* **1995**, *34*, 14077-14092.

47) Gibson, D. T. *Microbial Degradation of Organic Molecules*, Marcel Dekker: New York, 1984.

48) Lipscomb, J. D.; Orville, A. M. *Metal Ions Biol. Syst.* **1992**, *28*, 243-298.

49) Han, S.; Eltis, L. D.; Timmis, K. N.; Muchmore, S. W.; Bolin, J. T. *Science* **1995**, *270*, 976-980.

50) Senda, T.; Sugiyama, K.; Narita, H.; Yamamoto, T.; Kimbara, K.; Fukuda, M.; Sato, M.; Yano, K.; Mitsui, Y. *J. Mol. Biol.* **1996**, *255*, 735-752.

51) Kita, A.; Kita, S.-I.; Fujisawa, I.; Inaka, K.; Ishida, T.; Horiike, K.; Nozaki, M.; Miki, K. *Structure* **1999**, *7*, 25-34.

52) Que, L., Jr.; Widom, J.; Crawford, R. L. *J. Biol. Chem.* **1981**, *256*, 10941-10944.

53) Boldt, Y. R.; Sadowsky, M. J.; Ellis, L. B. M.; Que, L., Jr.; Wackett, L. P. *J. Bacteriol.* **1995**, *177*, 1225-1232.

54) Whiting, A. K.; Boldt, Y. R.; Hendrich, M. P.; Wackett, L. P.; Que, L., Jr. *Biochemistry* **1996**, *35*, 160-170.

55) Emerson, J. P.; Kovaleva, E. G.; Farquhar, E. R.; Lipscomb, J. D.; Que, L., Jr. *Proc. Natl. Acad. Sci. U.S.A.* **2008**, *105*, 7347-7352.

56) Wu, A. J.; Penner-Hahn, J. E.; Pecoraro, V. L. *Chem. Rev.* **2004**, *104*, 903-938.

57) Johnston, M. A.; Delwiche, E. A. *J. Bacteriol.* **1962**, *83*, 936-938.

58) Johnston, M. A.; Delwiche, E. A. *J. Bacteriol.* **1965**, *90*, 352-356.

59) Delwiche, E. A. *J. Bacteriol.* **1961**, *81*, 416-418.

60) Kono, Y.; Fridovich, I. *J. Biol. Chem.* **1983**, *258*, 6015-6059.

61) Khangulov, S. V.; Barynin, V. V.; Antonyuk-Barynina, S. V. *Biochem. Biophys. Acta* **1990**, *1020*, 25-33.

62) Barynin, V. V.; Hempstead, P. D.; Vagin, A. A.; Antonyuk, S. V.; Melik-Adamyan, W. R.; Lamzin, V. S.; Harrison, P. M.; Artymiuk, P. J. *J. Inorg. Biochem.* **1997**, *67*, 196.

63) McEvoy, J. P.; Brudvig, G. W. *Chem. Rev.* **2006**, *106*, 4455-4483.

64) Umena, Y.; Kawakami, K.; Shen, J.-R.; Kamiya, N. *Nature* **2011**, *473*, 55-60.

65) Warren, J. J.; Tronic, T. A.; Mayer, J. M. *Chem. Rev.* **2010**, *110*, 6961-7001.

66) Nugent, J. H. A.; Ball, R. J.; Evans, M. C. W. *Biochem. Biophys. Acta Bioenerg.* **2004**, *1655*, 217-221.

67) Betley, T. A.; Wu, Q.; Voorhis, T. V.; Nocera, D. G. *Inorg. Chem.* **2008**, *47*, 1849-1861.

68) Sono, M.; Roach, M. P.; Coulter, E. D.; Dawson, J. H. *Chem. Rev.* **1996**, *96*, 2841-2887.

69) Kovacs, J. A. *Chem. Rev.* **2004**, *104*, 825-848.

70) Meinnel, T.; Blanquet, S.; Dardel, F. *J. Mol. Biol.* **1996**, *262*, 375-.386.

71) Fontecilla-Camps, J. C.; Volbeda, A.; Cavazza, C.; Nicolet, Y. *Chem. Rev.* **2007**, *107*, 4273-4303.

72) Venkateswara Rao, P.; Holm, R. H. *Chem. Rev.* **2004**, *104*, 527-559.

73) Holm, R. H.; Kennepohl, P.; Solomon, E. I. *Chem. Rev.* **1996**, *96*, 2239-2314.

74) Solomon, E. I.; Gorelsky, S. I.; Dey, A. *J. Comput. Chem.* **2006**, *27*, 1415-1428.

75) Solomon, E. I.; Brunold, T. C.; Davis, M. I.; Kemsley, J. N.; Lee, S.-K.; Lehnert, N.; Neese, F.; Skulan, A. J.; Yang, Y.-S.; Zhou, J. *Chem. Rev.* **2000**, *100*, 235-349.

76) Brines, L. M.; Villar-Acevedo, G.; Kitagawa, T.; Swartz, R. D.; Lugo-Mas, P.; Kaminsky, W.; Benedict, J. B.; Kovacs, J. A. *Inorg. Chim. Acta* **2008**, *361*, 1070-1078.

77) Brines, L. M.; Shearer, J.; Fender, J. K.; Schweitzer, D.; Shoner, S. C.; Barnhart, D.; Kaminsky, W.; Lovell, S.; Kovacs, J. A. *Inorg. Chem.* **2007**, *46*, 9267-9277.

78) Kovacs, J. A.; Brines, L. M. *Acc. Chem. Res.* **2007**, *40*, 501-509.

79) Kitagawa, T.; Dey, A.; Lugo-Mas, P.; Benedict, J.; Kaminsky, W.; Solomon, E. I.; Kovacs, J. A. *J. Am. Chem. Soc.* **2006**, *128*, 14448-14449.

80) Lugo-Mas, P.; Dey, A.; Xu, L.; Davin, S. D.; Benedict, J.; Kaminsky, W.; Hodgson, K. O.; Hedman, B.; Solomon, E. I.; Kovacs, J. A. *J. Am. Chem. Soc.* **2006**, *128*, 11211-11221.

81) Villar-Acevedo, G.; Nam, E.; Fitch, S.; Benedict, J.; Freudenthal, J.; Kaminsky, W.; Kovacs, J. A. *J. Am. Chem. Soc.* **2011**, *133*, 1419-1427.

82) Sun, N.; Dey, A.; Villar-Acevedo, G.; Kovacs, J. A.; Darensbourg, M. Y.; Hodgson, K. O.; Hedman, B.; Solomon, E. I. *Inorg. Chem.* **2011**, *50*, 427-436.

83) Swartz, R. D.; Coggins, M. K.; Kaminsky, W.; Kovacs, J. A. *J. Am. Chem. Soc.* **2011**, *133*, 3954-3963.

84) Theisen, R. M.; Shearer, J.; Kaminsky, W.; Kovacs, J. A. *Inorg. Chem.* **2004**, *43*, 7682-7690 .

85) Nam, E.; Alokolaro, P. E.; Swartz, R. D.; Gleaves, M. C.; Pikul, J.; Kovacs, J. A. *Inorg. Chem.* **2011**, *50*, 1592-1602.

86) Neidig, M. L.; Wecksler, A. T.; Schenk, G.; Holman, T. R.; Solomon, E. I. *J. Am. Chem. Soc.* **2007**, *129*, 7531-7537.

87) Gorelsky, S. I.; Basumallick, L.; Vura-Weis, J.; Sarangi, R.; Hodgson, K. O.; Hedman, B.; Fujisawa, K.; Solomon, E. I. *Inorg. Chem.* **2005**, *44*, 4947-4960.

Chapter 2

Synthesis and Characterization of Thiolate-Ligated Manganese(II) Complexes and Comparisons to Analogous Thiolate-Ligated Iron(II) Complexes

2.1 Introduction

Nature utilizes manganese ions to promote a wide variety of transformations. Some of the most fundamental biochemical reactions, including the cleavage and formation of O-O bonds, involve manganese metalloenzymes.[1-4] The active sites of these enzymes exhibit tremendous variations with respect to Mn ion nuclearity, oxidation state, and coordination environments. For example, the reduced state of manganese superoxide dismutase contains a single Mn cofactor ligated within a trigonal bipyramidal coordination environment comprised of three histidine imidazoles, one aspartate carboxylate, and a hydroxide/water ligand.[5] Manganese catalase has a dimanganese active site which contains two bridging oxo, hydroxo, or water ligands and a bridging glutamate carboxylate.[3] The oxygen-evolving complex of photosystem II contains three Mn ions and a Ca ion in a cubane-type cluster with oxo-bridging ligands, as well as a fourth Mn ion bridged by two oxo ligands on the exterior of the cluster.[6-7] Despite the structural differences exhibited by these Mn metalloenzyme active sites, a unifying characteristic shared by these enzymes is that they each promote chemical reactions involving O_2 or reduced O_2 derivatives (O_2^-, H_2O_2, H_2O). These reactions are proposed to result in the formation of highly reactive Mn-superoxo, -peroxo, and/or -oxo intermediate species.[8] In order to fully understand the functional advantages afforded by Mn cofactors in these, and other, metalloenzyme systems, understanding the basic coordination chemistry of Mn within biologically relevant structural environments in needed.

Metalloenzymes which rely upon Fe cofactors for catalysis conduct very similar transformations to those performed by Mn metalloenzymes. In particular, cysteinate-ligated Fe metalloenzymes are known to also form metastable O_2-derived intermediates during reactions with various biological oxidants.[9-13] The ability of the heme-containing Fe dioxygenase cytochrome P450 to active O_2 is heavily influenced by the presence of a cysteine residue located *trans* to the site of O_2 binding.[14] The cytochrome P450s are also widely believed to form Fe-superoxo, -peroxo, -hydroperoxo, and –oxo intermediates upon reacting with O_2.[15] The ability of superoxide reductase, a non-heme Fe metalloenzyme, to reduce O_2^- to H_2O_2 has been intimately linked the presence of a thiolate ligand *trans* to an open coordination site.[16] Studies involving synthetic transition metal complexes have shown that thiolates can help to reduce the Lewis acidity of a metal ion and maintain an open coordination site at the metal, both of which help to promote chemical reactions.[17-19] Thiolate ligands are also known to result in unique spectral features for transition metal complexes, such as intense, low-energy absorption bands and unusual Hamiltonian parameters, which are inherently reflective of the highly covalent nature of metal-thiolate bonds.[20-23] Thiolate ligands thus have a considerable impact upon the structural and electronic properties of transition metals in both biology and small molecule complexes.

Given that biological and synthetic systems containing transition metal-thiolate bonds are known to have such unique structural and electronic properties, as well as the broad significance of Mn metalloenzymes in biology, we sought to construct a library of synthetic thiolate-ligated Mn(II) complexes. This chapter describes the synthesis and characterization of a new library of such complexes so that we may evaluate the effect thiolate ligation has upon low-valent Mn coordination compounds, as well as to have a set of structurally-analogous complexes for further reactivity studies to be conducted. Alkoxide-ligated analogues of some complexes have also

been prepared and are described, providing yet another benchmark for evaluating the influence specifically of the thiolate ligand. The thiolate-ligated Mn(II) library of complexes are also compared to the analogous Fe(II) complexes in order to highlight subtle structural or electronic differences between the two metal ions. Notably, we have observed unique similarities in electrochemical properties between some of the Mn(II) and Fe(II) complexes constructed with the same ligands. This chapter concludes by detailing experimental attempts towards rationalizing these observations through the influence of thiolate ligation.

2.2 Experimental Section

2.2.1 General Considerations

All manipulations were performed using Schlenk techniques or under an N_2 atmosphere in a glovebox. Reagents and solvents were purchased from commercial vendors, were of highest available purity, and were used without further purification unless otherwise noted. MeOH (Na), MeCN (CaH_2), and CH_2Cl_2 (CaH_2) were dried and distilled prior to use. Et_2O was rigorously degassed and purified using solvent purification columns housed in a custom stainless steel cabinet and dispensed by a stainless steel schlenk-line (GlassContour). ^1H NMR spectra were recorded on a Bruker AV 300 FT NMR spectrometer at ambient temperature and were referenced to residual deuterated solvent. Chemical shifts are listed in parts per million (ppm). UV/vis spectra were recorded on a Varian Cary 50 spectrophotometer equipped with a fiber optic cable connected to a "dip" ATR probe (C-technologies). A custom-built two-neck solution sample holder equipped with a threaded glass connector was sized specifically to fit the "dip" probe. Electrospray-ionization mass spectra were obtained on a Bruker Esquire Liquid Chromatograph-Ion Trap mass spectrometer. EPR spectra were recorded on a Bruker E580 CW-

EPR spectrometer operating at X-band frequency between 4 and 8 K with an Oxford helium cryostat. Magnetic moments (solid state) were obtained by zero-field cooling experiments from 5 to 300 K with polycrystalline samples in gel-caps using a Quantum Design MPMS S5 SQUID magnetometer. Pascal's constants were used to correct for diamagnetic contributions to the experimental magnetic moment. Solution magnetic moments were calculated by the Evans method, with temperature correction made as described by Van Geet.[24-25] Cyclic voltammograms were recorded in MeCN (100 mM $^{n}Bu_4N(PF_6)$ supporting electrolyte) on a PAR 263A potentiostat with a glassy carbon working electrode, platinum auxillary electrode, and a $Ag^{+}/AgNO_3$ reference electrode. X-ray crystallography data were recorded on a Bruker APEX II single crystal X-ray diffractometer with Mo Kα radiation or a Bruker SMART Apex CCD diffractometer with Mo Kα radiation. Complexes **16**-**22** were synthesized as previously reported.[26-27] Elemental analyses were performed by Atlantic Microlabs, Norcross, GA. Complex **1** has previously been reported, however a revised protocol and higher resolution X-ray crystal structure have been obtained during these studies for this complex and are described herein.[26]

2.2.2 Synthetic Protocols for Ligands L_2-L_9 and Complexes 1-24

2.2.2.1 Synthesis of 1-(tert-butyloxycarbonyl)ethyldiamine (NNBoc). To a stirred solution of 1,2-diaminoethane (2.8 mL, 41.9 mmol) in CH_2Cl_2 (25 mL), a 100 mL solution of di-*tert*-butyl dicarbonate (1.52 g, 6.9 mmol) was added *via* an addition funnel at room temperature over 2.5 to 3 h. The resulting solution was allowed to stir for a total of 24 h. A white insoluble precipitate was removed by filtration, and the resulting clear CH_2Cl_2 solution was washed with saturated Na_2CO_3 (2 x 100 mL), brine (2 x 100 mL), and finally dried over Na_2SO_4. Solvent removal *in vacuo* afforded the title compound as a clear viscous oil in 65 % yield (0.73 g, 4.5 mmol). ^{1}H

NMR (300 MHz, $CDCl_3$): δ 3.16 (m, 2H), 2.79 (t, 2H), 1.44 (s, 9H). ESI-MS: Expected *m/z* for $C_7H_{16}N_2O_2$ = 160.069, found *m/z* = 161.1.

2.2.2.2 Synthesis of 1-(tert-butyloxycarbonyl)propyldiamine (NPNBoc). To a stirred solution of 1,3-diaminopropane (3.10 g, 41.9 mmol) in CH_2Cl_2 (25 mL), a 100 mL solution of di-*tert*-butyl dicarbonate (1.52 g, 6.9 mmol) was added *via* an addition funnel at room temperature over 2.5 to 3 h. The resulting solution was allowed to stir for a total of 24 h. A white insoluble precipitate was removed by filtration, and the resulting clear CH_2Cl_2 solution was washed with saturated Na_2CO_3 (2 x 100 mL), brine (2 x 100 mL), and finally dried over Na_2SO_4. Solvent removal *in vacuo* afforded the title compound as a viscous clear oil in 63 % yield (0.76 g, 4.3 mmol). ^{1}H NMR (300 MHz, $CDCl_3$): δ 3.21 (q, 2H), 2.75 (t, 2H), 1.60 (t, 2H), 1.43 (s, 9H). ESI-MS: Expected *m/z* for $C_8H_{18}N_2O_2$ = 174.241, found *m/z* = 175.3.

2.2.2.3 Synthesis of 2-(chloromethyl)-6-methylpyridine hydrochloride. A solution of 6-methyl-2-(hydroxymethyl)pyridine hydrochloride (5.00 g, 40.6 mmol) in CH_2Cl_2 (10 mL) was cooled in an ice water bath to 0 ˚C under an inert atmosphere. Thionyl chloride (24.15 g, 244.1 mmol) was slowly added to the solution over a period of 1 h. The resulting mixture was allowed to slowly warm to room temperature overnight, followed by evaporation of all volatiles to result in a pink solid. The pink solid was redissolved in warm EtOH (30 mL) and slowly layered with cool Et_2O (80 mL) to cause the rapid precipitation of the title compound as a white solid. The product was isolated *via* filtration and dried under vacuum overnight to result in 99 % yield (7.13 g, 40.2 mmol). ^{1}H NMR (300 MHz, $CDCl_3$): δ 8.27 (t, 1H), 7.89 (d, 1H), 7.60 (d, 1H), 3.50 (s, 2H), 3.05 (s, 3H).

2.2.2.4 Synthesis of N-(tert-butyloxycarbonyl)-N',N'-[bis(2-pyridilmethyl)ethane-1,2-diamine] (6-H-DPENBoc). NNBoc (1.20 g, 7.5 mmol) was dissolved in 5 M NaOH (15 mL) and added to a stirring solution of 2-picolyl chloride hydrochloride (2.70 g, 12.7 mmol) that was also dissolved in 5 M NaOH (15 mL). The solution was allowed to stir at room temperature for 4 days. Water (25 mL) was then added to the reaction mixture, followed by the extraction of crude organics with CH_2Cl_2 (3 x 50 mL). The combined organics were washed with brine (3 x 100 mL), dried over Na_2SO_4, and dried under vacuum to afford an orange residue. The residue was chromatographed on silica gel using a 95:5 acetone:MeOH eluent mixture. Concentration of all fractions containing the desired product resulted in isolation of the title compound as an orange oil in 65 % yield (1.67 g, 4.9 mmol). ^{1}H NMR (300 MHz, $CDCl_3$): δ 8.54 (d, 2H), 7.63 (t, 2H), 7.41 (d, 2H), 7.14 (t, 2H), 5.79 (bs, 1H), 3.86 (s, 4H), 3.21 (m, 2H), 2.70 (t, 2H), 1.44 (s, 9H). ESI-MS: Expected *m/z* for $C_{19}H_{26}N_4O_2$ = 342.4, found *m/z* = 343.1.

2.2.2.5 Synthesis of N,N-bis(2-pyridilmethyl)ethane-1,2-diamine (6-H-DPEN, L_2). 6-H-DPENBoc (5.06 g, 14.8 mmol) was dissolved in CH_2Cl_2 (10 mL) at room temperature and added to a 25 mL pear-shaped flask charged with a stirbar. Slow addition of trifluoroacetic acid (16.80 g, 149 mmol) to the stirring solution resulted in a brown mixture that was allowed to continue stirring overnight. Evaporation of all volatiles resulted in a viscous brown oil that was mixed with 5 M NaOH (20 mL) and extracted with CH_2Cl_2 (3 x 20 mL). The combined organics were washed with brine (3 x 50 mL) and dried over Na_2SO_4. Removal of all volatiles *in vacuo* afforded the title compound as a pale orange oil in 85 % yield (3.04 g, 12.6 mmol). ^{1}H NMR (300 MHz, $CDCl_3$): δ 8.45 (d, 2H), 7.56 (t, 2H), 7.40 (d, 2H), 7.06 (t, 2H), 2.71 (t, 2H), 2.58 (t, 2H). ESI-MS: Expected *m/z* for $C_{14}H_{18}N_4$ = 242.3, found *m/z* = 242.2.

2.2.2.6 Synthesis of N-(tert-butyloxycarbonyl)-N',N'-[bis(2-pyridilmethyl)propane-1,3-diamine] (6-H-DPPNBoc). NPNBoc (1.30 g, 7.5 mmol) was dissolved in 5 M NaOH (15 mL) and added to a stirring solution of 2-picolyl chloride hydrochloride (2.21 g, 13.5 mmol) that was also dissolved in 5 M NaOH (15 mL). The solution was allowed to stir at room temperature for 4 days. Water (25 mL) was then added to the reaction mixture, followed by the extraction of crude organics with CH_2Cl_2 (3 x 50 mL). The combined organics were washed with brine (3 x 100 mL), dried over Na_2SO_4, and dried under vacuum to afford an orange residue. The residue was chromatographed on silica gel using a 93:7 acetone:MeOH eluent mixture. Concentration of all fractions containing the desired product resulted in isolation of the title compound as an orange oil in 67 % yield (1.67 g, 4.9 mmol). ^{1}H NMR (300 MHz, $CDCl_3$): δ 8.53 (d, 2H), 7.60 (t, 2H), 7.40 (t, 2H), 7.12 (t, 2H), 6.30 (bs, 1H), 3.74 (s, 4H), 3.17 (m, 2H), 2.58 (t, 2H), 1.69 (m, 2 H), 1.42 (s, 9H). ESI-MS: Expected *m/z* for $C_{20}H_{28}N_4O_2$ = 356.4, found *m/z* = 357.3.

2.2.2.7 Synthesis of N,N-bis(2-pyridilmethyl)propane-1,3-diamine (6-H-DPPN, L_3). 6-H-DPPNBoc (5.20 g, 14.8 mmol) was dissolved in CH_2Cl_2 (10 mL) at room temperature and added to a 25 mL pear-shaped flask charged with a stirbar. Slow addition of trifluoroacetic acid (16.80 g, 149 mmol) to the stirring solution resulted in a brown mixture that was allowed to continue stirring overnight. Evaporation of all volatiles resulted in a viscous brown oil that was mixed with 5 M NaOH (20 mL) and extracted with CH_2Cl_2 (3 x 20 mL). The combined organics were washed with brine (3 x 50 mL) and dried over Na_2SO_4. Removal of all volatiles *in vacuo* afforded the title compound as a pale orange oil in 87 % yield (3.13 g, 12.6 mmol). ^{1}H NMR (300 MHz, $CDCl_3$): δ 8.54 (d, 2H), 7.65 (t, 2H), 7.46 (d, 2H), 7.10 (t, 2H), 3.80 (s, 4H), 2.77 (t, 2H), 2.61 (t, 2H). ESI-MS: Expected *m/z* for $C_{15}H_{20}N_4$ = 256.3, found *m/z* = 257.2.

2.2.2.8 Synthesis of N-(tert-butyloxycarbonyl)-N',N'-[bis(6-methyl-2-pyridilmethyl)ethane-1,2-diamine] (6-Me-DPENBoc). Following the procedure outlined for the synthesis of 6-H-DPENBoc, NNBoc (1.20 g, 7.5 mmol) was reacted with 2-(chloromethyl)-6-methylpyridine hydrochloride (2.27 g, 12.7 mmol) to afford an orange residue that was chromatographed on silica gel using a 92:8 acetone:MeOH eluent mixture. The title compound was obtained as an orange oil in 63 % yield (1.75 g, 4.7 mmol). ^{1}H NMR (300 MHz, $CDCl_3$): δ 7.51 (t, 2H), 7.21 (d, 2H), 7.00 (d, 2H), 3.81 (s, 4H), 3.20 (m, 2H), 2.68 (t, 2H), 2.55 (s, 6H), 1.44 (s, 9H). ESI-MS: Expected *m/z* for $C_{21}H_{30}N_4O_2$ = 370.5, found *m/z* = 371.5.

2.2.2.9 Synthesis of N,N-bis(6-methyl-2-pyridilmethyl)ethane-1,2-diamine (6-Me-DPEN, L_4). Following the procedure outlined for the synthesis of 6-H-DPEN, 6-Me-DPENBoc (5.50 g, 14.8 mmol) was reacted with trifluoroacetic acid (17.00 g, 149.1 mmol) to afford the title compound as a pale orange oil in 89% yield (3.57 g, 13.2 mmol). ^{1}H NMR (300 MHz, $CDCl_3$): δ 7.54 (t, 2H), 7.33 (d, 2H), 7.00 (d, 2H), 3.81 (s, 4H), 2.77 (t, 2H), 2.64 (t, 2H), 2.53 (s, 6H). ESI-MS: Expected *m/z* for $C_{16}H_{22}N_4$ = 270.2, found *m/z* = 271.3.

2.2.2.10 Synthesis of N-[tert-butyloxycarbonyl]-N'-N'-[bis(6-methyl-2-pyridilmethyl)]propane-1,3-diamine] (6-Me-DPPNBoc). Following the procedure outlined for the synthesis fo 6-H-DPPNBoc, NPNBoc (1.30 g, 7.5 mmol) was reacted with 2-(chloromethyl)-6-methylpyridine hydrochloride (2.40 g, 13.5 mmol) to afford a crude product that was chromatographed on silica gel using a 94:6 acetone:MeOH eluent mixture. The title compound was obtained as an orange oil in 66 % yield (1.89 g, 4.9 mmol). ^{1}H NMR (300 MHz, $CDCl_3$): δ 7.52 (t, 2H), 7.30 (d, 2H), 7.00 (d, 2H), 3.74 (s, 4H), 3.13 (m, 2H), 2.58 (t, 2H), 2.53 (s, 6H), 1.67 (q, 2H), 1.41 (s, 9H). ESI-MS: Expected *m/z* for $C_{22}H_{32}N_4O_2$ = 384.5, found *m/z* = 385.6.

2.2.2.11 Synthesis of N,N-bis(6-methyl-2-pyridilmethyl)propane-1,3-diamine (6-Me-DPPN, L_5). Following the procedure outlined for the synthesis of 6-H-DPPN, 6-MeDPPNBoc (5.20 g, 13.5 mmol) was reacted with trifluoroacetic acid (17.00 g, 149.1 mmol) to afford the title compound as a pale orange oil in 88% yield (3.38 g, 11.9 mmol). ^{1}H NMR (300 MHz, $CDCl_3$): δ 7.54 (t, 2H), 7.35 (d, 2H), 7.00 (d, 2H), 3.77 (s, 4H), 2.71 (t, 2H), 2.59 (t, 2H), 2.52 (s, 6H), 1.69 (q, 2H). ESI-MS: Expected *m/z* for $C_{17}H_{24}N_4$ = 284.2, found *m/z* = 285.3.

2.2.2.12 Synthesis of N-(tert-butyloxycarbonyl)-N',N'-[bis(4-methoxy-3,5-dimethyl-2-pyridilmethyl)ethane-1,2-diamine] (4-MeO-3,5-Me-DPENBoc). Following the procedure outlined for the synthesis of 6-H-DPENBoc, NNBoc (1.20 g, 7.5 mmol) was reacted with 2-(chloromethyl)-4-methoxy-3,5-dimethylpyridine hydrochloride (3.33 g, 15.0 mmol) to afford an curde orange oil that was chromatographed on silica gel using a 95:5 acetone:MeOH eluent mixture. The title compound was obtained as an orange oil in 61 % yield (2.11 g, 4.6 mmol). ^{1}H NMR (300 MHz, $CDCl_3$): δ 8.56 (d, 2H), 7.65 (t, 2H), 7.40 (d, 2H), 7.14 (t, 2H), 5.80 (bs, 1H), 5.42 (s, 6H), 5.32 (s, 3H), 3.86 (s, 4H), 3.21 (m, 2H), 2.70 (t, 2H), 1.44 (s, 9H). ESI-MS: Expected *m/z* for $C_{25}H_{32}N_4O_4$ = 459.2, found *m/z* = 450.2.

2.2.2.13 Synthesis of N,N-bis(4-MeO-3,5-Me-2-pyridilmethyl)ethane-1,2-diamine (4-MeO-3,5-Me-DPEN, L_6). Following the procedure outlined for the synthesis of 6-H-DPEN, 4-Me-3,5-Me-DPENBoc (2.11 g, 4.6 mmol) was reacted with trifluoroacetic acid (16.80 g, 149 mmol) to afforded the title compound as a pale orange oil in 61 % yield (1.00 g, 2.8 mmol). ^{1}H NMR (300 MHz, $CDCl_3$): δ 8.45 (d, 2H), 7.56 (t, 2H), 7.40 (d, 2H), 7.12 (t, 2H), 5.40 (s, 6H), 5.29 (s, 3H), 2.71 (t, 2H), 2.58 (t, 2H). ESI-MS: Expected *m/z* for $C_{19}H_{30}N_4O_2$ = 358.1, found *m/z* = 359.2.

2.2.2.14 Synthesis of N-(tert-butyloxycarbonyl)-N',N'-[bis(4-methoxy-3,5-dimethyl-2-pyridilmethyl)propane-1,3-diamine] (4-MeO-3,5-Me-DPPNBoc). Following the procedure outlined for the synthesis of 6-H-DPPNBoc, NPNBoc (1.30 g, 7.5 mmol) was reacted with 2-(chloromethyl)-4-methoxy-3,5-dimethylpyridine hydrochloride (3.33 g, 15.0 mmol) to afford an curde orange oil that was chromatographed on silica gel using a 95:5 acetone:MeOH eluent mixture. The title compound was obtained as an orange oil in 62 % yield (2.13 g, 4.6 mmol). ^{1}H NMR (300 MHz, $CDCl_3$): δ 8.61 (d, 2H), 7.55 (t, 2H), 7.39 (d, 2H), 7.14 (t, 2H), 5.61 (bs, 1H), 5.42 (s, 6H), 5.29 (s, 3H), 3.81 (s, 4H), 3.39 (t, 2H), 3.12 (quintet, 2H), 2.71 (t, 2H), 1.44 (s, 9H). ESI-MS: Expected *m/z* for $C_{26}H_{34}N_4O_4$ = 463.4, found *m/z* = 464.1.

2.2.2.14 Synthesis of N,N-bis(4-methoxy-3,5-dimethyl-2-pyridilmethyl)propane-1,3-diamine (4-MeO-3,5-Me-H-DPPN, L_7). Following the procedure outlined for the synthesis of 6-H-DPEN, 4-Me-3,5-Me-DPPNBoc (2.13 g, 4.6 mmol) was reacted with trifluoroacetic acid (16.80 g, 149 mmol) to afforded the title compound as a pale orange oil in 30 % yield (0.689 g, 1.4 mmol). ^{1}H NMR (300 MHz, $CDCl_3$): δ 8.45 (d, 2H), 7.56 (t, 2H), 7.40 (d, 2H), 7.12 (t, 2H), 5.40 (s, 6H), 5.29 (s, 3H), 3.10 (quintet, 2H) 2.71 (t, 2H), 2.58 (t, 2H). ESI-MS: Expected *m/z* for $C_{20}H_{32}N_4O_2$ = 363.2, found *m/z* = 364.2.

2.2.2.14 Synthesis of N-(tert-butyloxycarbonyl)-N'-N'-[bis(2-quinolinemethyl)]ethane-1,2-diamine (QuinoENBoc). Following the procedure outlined for the synthesis of 6-H-DPENBoc, NNBoc (1.20 g, 7.5 mmol) was reacted with 2-(chloromethyl)quinoline hydrochloride (2.70 g, 12.7 mmol) to afford a crude product that waschromatographed on silica gel using a 92:8 acetone:MeOH eluent mixture. The title compound was afforded as an orange oil in 65 % yield (2.15 g, 4.9 mmol). ^{1}H NMR (300 MHz, $CDCl_3$): δ 8.17 (d, 2H), 8.07 (d, 2H), 7.76 (d, 2H), 7.69

(t, 2H), 7.53 (t, 2H), 7.50 (t, 2H), 6.58 (bs, 2H), 4.09 (s, 4H), 3.32 (m, 2H), 2.84 (m, 2H), 1.50 (s, 9H). ESI-MS: Expected *m/z* for $C_{27}H_{30}N_4O_2$ = 442.5, found *m/z* = 443.6.

2.2.2.15 Synthesis of N-N-[bis(2-quinolinemethyl)]ethane-1,2-diamine (2-QuinoEN, L_8). Following the procedure outlined for the synthesis of 6-H-DPEN, QuinoENBoc (2.10 g, 4.8 mmol) was reacted with trifluoroacetic acid (17.00 g, 149.1 mmol) to afford the title compound as a pale orange oil in 89 % yield (1.45 g, 4.2 mmol). ^{1}H NMR (300 MHz, $CDCl_3$): δ 8.08 (d, 4H), 7.78 (d, 2H), 7.70 (t, 2H), 7.60 (d, 2H), 7.50 (t, 2H), 4.09 (s, 4H), 2.91 (m, 2H), 2.87 (m, 2H). ESI-MS: Expected *m/z* for $C_{22}H_{22}N_4$ = 342.4, found *m/z* = 343.5.

2.2.2.16 Synthesis of N-(tert-butyloxycarbonyl)-N'-N'-[bis(2-quinolinemethyl)]propane-1,3-diamine (2-QuinoPNBoc). Following the procedure outlined for the synthesis of 6-H-DPPNBoc, NPNBoc (1.20 g, 6.9 mmol) was reacted with 2-(chloromethyl)quinoline hydrochloride (2.70 g, 12.7 mmol) to result in a crude oil that was chromatographed on silica gel using a 92:8 acetone:MeOH eluent mixture. The title compound was obtained as a dark orange solid in 64% yield (2.19 g, 4.8 mmol). ^{1}H NMR (300 MHz, $CDCl_3$): δ 8.09 (d, 4H), 7.76 (d, 2H), 7.66 (m, 4H), 7.48 (t, 2H), 5.79 (bs, 1H), 3.98 (s, 4H), 3.18 (m, 2H), 2.70 (t, 2H), 1.74 (m, 2H), 1.37 (s, 9H). ESI-MS: Expected *m/z* for $C_{28}H_{32}N_4O_2$ = 456.6, found *m/z* = 457.6.

2.2.2.17 Synthesis of N-N-[bis(2-quinolinemethyl)]propane-1,3-diamine (2-QuinoPN, L_9). Following the procedure outlined in the synthesis of 6-H-DPPN, 2-QuinoPNBoc (2.10 g, 4.6 mmol) was reacted with trifluoroacetic acid (17.00 g, 149.1 mmol) to afford the title compound as a pale orange solid in 91 % yield (1.63 g, 4.6 mmol). ^{1}H NMR (300 MHz, $CDCl_3$): δ 8.14 (d, 2H), 8.06 (d, 2H), 7.78 (d, 2H), 7.71 (d, 2H), 7.68 (m, 2H), 4.01 (s, 4H), 2.70 (m, 4H), 1.72 (q, 2H). ESI-MS: Expected *m/z* for $C_{23}H_{24}N_4$ = 356.5, found *m/z* = 357.5.

2.2.2.18 Synthesis of 3-chloro-3-methyl-2-butanone. 3-methyl-2-butanone (10.72 g, 124 mmol) was dissolved in CH_2Cl_2 (10 mL) in a 60 mL round-bottom flask and fitted with an addition funnel. The solution was stirred in a salt ice water bath and placed under a positive pressure of dinitrogen. Sulfuryl chloride (16.78 g, 124 mmol) was afforded as a clear liquid following distillation and added to the addition funnel immediately following distillation. The distilled sulfuryl chloride was added to the stirring solution 3-methyl-2-butanone dropwise in order to avoid an excess of HCl gas production. Following the complete addition of sulfuryl chloride (approx. 2.5 hours), the resulting solution was removed from the salt ice water bath and allowed to slowly warm to room temperature, where stirred was continued overnight to afford a brown solution. After removal of volatiles *via* rotary distillation, a crude yellow oil was obtained. Vacuum distillation of the resulting oil resulted in the desired product in 38% yield (5.700 g, 47.3 mmol). ^{1}H NMR (300 MHz, $CDCl_3$): 2.40 ppm (s, 3 H), 1.70 ppm (s, 6 H).

2.2.2.19 Synthesis of 3-methyl-3-mercapto-2-butanone. A 60 mL pear-shaped round-bottom flask was charged with a stirbar and $NaSH•H_2O$ (4.49 g, 47 mmol) in MeOH (10 mL), fitted with an addition funnel, and cooled on a salt ice water bath under a positive pressure of nitrogen. 3-chloro-3-methyl-2-butanone (5.70 g, 47 mmol) was placed in the addition funnel and added to the stirring solution dropwise over the course of 2 hours. Following complete addition of 3-chloro-3-methyl-2-butanone, the salt ice water bath was removed from the reaction, which was allowed to slowly warm to room temperature and continue to stir overnight. Sulfuric acid (20 mL) was added to the reaction mixture, which was then placed into a separation funnel and extracted with CH_2Cl_2 (3 x 20 mL). The combined organics were washed twice with water (30 mL) and twice with brine (30 mL). The combined organics are then dried over Na_2SO_4 and some volatiles removed *via* rotary distillation. The resulting mixture was then vacuum distilled to

afford to desired product as a clear liquid in 45% yield (2.52 g, 21.4 mmol). ^{1}H NMR (300 MHz, $CDCl_3$): 2.25 ppm (s, 3 H), 1.93 ppm (bs, 1H), 1.42 ppm (s, 6H).

2.2.2.20 Synthesis of [$Mn^{II}(S^{Me2}N_4$(tren))](PF_6) (1). Sodium methoxide (0.21 g, 4.0 mmol), 3-mercapto-3-methyl-2-butanone (0.47 g, 4.0 mmol), tris(2-aminoethyl)amine (L_1, 0.59 g, 4.0 mmol), manganese sulfate monohydrate (0.68 g, 4.0 mmol), and sodium hexafluorophosphate (0.67 g, 4.0 mmol) were each individually dissolved or slurried in MeOH (5 mL) under an inert atmosphere in a dry box. Each reagent was subsequently added to a Schlenk flask charged with a stir bar. After gently stirring the resulting reaction mixture at room temperature for two days, all volatiles were removed to afford a crude yellow solid. The crude product was redissolved in minimal MeCN and filtered through a fine fritted filter. The resulting MeCN solution was layered with an equal volume of Et_2O and allowed to crystallize at -30 °C to afford the title product as a white crystalline solid in 30 % yield (0.53 g, 1.2 mmol). Electronic absorption spectrum (MeCN): λ_{max} (nm) (ε ($M^{-1}cm^{-1}$)): 240 (2910). IR (Nujol): $\nu_{C=N}$ 1647 cm^{-1}. EPR spectrum (9:1 MeOH/EtOH glass, 5 K): g = 2.00. Redox potential (MeCN vs SCE, 298 K): $E_{1/2}$ = +270 ($Mn^{III/III}$), +705 ($Mn^{IV/III}$). Magnetic moment (solid state, 5-300 K): 6.01 μ_B; (solution, MeOH, 301 K): 5.90 μ_B. ESI-MS: Expected *m/z* for $[C_{11}H_{25}N_4SMn]^+$ = 300.1, found *m/z* = 299.1. Elemental Analysis for $C_{11}H_{25}N_4F_6PSMn$; Calculated: C, 29.67; H, 5.66; N, 12.58. Found: C, 30.01; H, 5.67; N, 11.41.

2.2.2.21 Synthesis of [$Mn^{II}(S^{Me2}N_4$(6-H-DPEN))(MeOH)](BPh_4)·MeOH (2). A procedure similar to that employed in the preparation of **1** was conducted with the following reagent amounts: sodium methoxide (0.10 g, 1.9 mmol), 3-mercapto-3-methyl-2-butanone (0.22 g, 1.9 mmol), L_2 (0.43, 1.8 mmol), manganese sulfate monohydrate (0.30 g, 1.8 mmol), and sodium tetraphenylborate (0.61 g, 1.8 mmol). Complex **2** was isolated as a white solid in 21 % yield

(0.28 g, 0.37 mmol). Electronic absorption spectrum (MeCN): λ_{max} (nm) (ε ($M^{-1}cm^{-1}$)): 283 (1690). IR (Nujol): $\nu_{C=N}$ 1600 cm^{-1}. EPR spectrum (9:1 MeOH/EtOH glass, 5 K): g = 1.99. Redox potential (MeCN vs SCE, 298 K): E_{pa} = +413 mV, E_{pc} = 0 mV. Magnetic moment (solid state, 5-300 K): 5.88 μ_B; (solution, MeOH, 301 K): 5.79 μ_B. ESI-MS: Expected *m/z* for $[C_{19}H_{25}N_4SMn]^+$ = 395.9, found *m*/*z* = 396.5.

2.2.2.22 Synthesis of $[Mn^{II}(S^{Me2}N_4(6\text{-H-DPPN}))]_2(BF_4)_2$ (3). A procedure similar to that employed in the preparation of **1** was conducted with the following reagent amounts: sodium methoxide (0.10 g, 1.9 mmol), 3-mercapto-3-methyl-2-butanone (0.22 g, 1.9 mmol), L_2 (0.44, 1.8 mmol), manganese sulfate monohydrate (0.30 g, 1.8 mmol), and sodium tetrafluoroborate (0.20 g, 1.8 mmol). Complex **2** was isolated as a white solid in 68 % yield (0.94 g, 1.2 mmol). Electronic absorption spectrum (MeCN): λ_{max} (nm) (ε ($M^{-1}cm^{-1}$)): 272 (1637). IR (Nujol): $\nu_{C=N}$ 1602 cm^{-1}. EPR spectrum (9:1 MeOH/EtOH glass, 5 K): g = 2.00. Redox potential (MeCN vs SCE, 298 K): E_{pa} = +397 mV, E_{pc} =+240 mV. Magnetic moment (per Mn, solid state, 5-300 K): 5.93 μ_B; (per Mn, solution, MeOH, 301 K): 5.70 μ_B. ESI-MS: Expected *m/z* for $[C_{20}H_{27}N_4SMn]^{2+}$ = 410.5, found *m*/*z* = 410.4.

2.2.2.23 Synthesis of $[Mn^{II}(S^{Me2}N_4(6\text{-MeDPEN}))](BF_4)$ (4). A procedure similar to that employed in the preparation of **1** was conducted with the following reagent amounts: sodium methoxide (0.20 g, 3.9 mmol), 3-mercapto-3-methyl-2-butanone (0.46 g, 3.9 mmol), L_4 (1.02, 3.8 mmol), manganese sulfate monohydrate (0630 g, 3.7 mmol), and sodium tetrafluoroborate (0.41 g, 3.7 mmol). Complex **4** was isolated as a yellow solid in 53 % yield (1.02 g, 2.0 mmol). Electronic absorption spectrum, λ_{max} (nm) (ε ($M^{-1}cm^{-1}$)) (MeCN): 317 (350); (EtCN): 317 (305); (MeOH): 297 (477); (CH_2Cl_2): 327 (350). IR (Nujol): $\nu_{C=N}$ 1605 cm^{-1}. EPR spectrum (9:1 MeOH/EtOH glass): g = 2.00. Redox potential (MeCN vs SCE, 298 K): $E_{1/2}(Mn^{III/II})$= +423

mV. Magnetic moment (solid state, 5-300 K): 5.83 μ_B; (solution, MeOH, 301 K): 5.89 μ_B. ESI-MS: Expected *m/z* for $[C_{21}H_{29}N_4SMn]^+$ = 424.4, found *m/z* = 424.3. Elemental Analysis for $C_{21}H_{29}BN_4F_4SMn$; Calculated: C, 49.33; H, 5.72; N, 10.96. Found: C, 48.36; H, 5.58; N, 10.72.

2.2.2.24 Synthesis of $[Mn^{II}(S^{Me2}N_4$(6-MeDPPN))$](BPh_4)$•MeCN (5). A procedure similar to that employed in the preparation of **1** was conducted with the following reagent amounts: sodium methoxide (0.11 g, 2.0 mmol), 3-mercapto-3-methyl-2-butanone (0.24 g, 2.0 mmol), L_5 (0.58, 2.0 mmol), manganese sulfate monohydrate (0.35 g, 2.0 mmol), and sodium tetraphenylborate (0.41 g, 3.7 mmol). Complex **5** was isolated as a yellow solid in 64 % yield (0.99 g, 1.3 mmol). Electronic absorption spectrum, λ_{max} (nm) (ε ($M^{-1}cm^{-1}$)) (MeCN): 282 (1655); (MeOH): 279 (770). IR(Nujol): $\nu_{C=N}$ 1651 cm^{-1}. EPR spectrum (MeOH/EtOH glass): g = 1.99. Redox potential (MeCN vs SCE, 298 K): E_{pa}= +580 mV, E_{pc} = +460 mV. Magnetic moment (solid state, 5-300 K): 5.57 μ_B; (solution, MeOH, 298 K): 5.78 μ_B. ESI-MS: Expected *m/z* for $[C_{22}H_{31}N_4SMn]^+$ = 438.5, found *m/z* = 438.2. Elemental Analysis for $C_{48}H_{54}BN_5SMn$; Calculated: C, 72.17; H, 6.81; N, 8.77. Found: C, 72.25; H, 6.41; N, 8.67.

2.2.2.25 Synthesis of $[(Mn^{II}(S^{Me2}N_4$(4-OMe-3,5-Me-DPEN))$(Mn^{II}(S^{Me2}N_4$(4-OMe-3,4-Me-DPEN))(Cl))$](BF_4)\cdot Et_2O$ (6). A procedure similar to that employed in the preparation of **1** was conducted with the following reagent amounts: sodium methoxide (0.12 g, 2.0 mmol), 3-mercapto-3-methyl-2-butanone (0.24 g, 2.0 mmol), L_6 (0.72, 2.0 mmol), manganese sulfate monohydrate (0.34 g, 2.0 mmol), and sodium tetrafluoroborate (0.22 g, 2.0 mmol). Complex **6** was isolated as an off white solid in 21 % yield (0.20 g, 0.42 mmol). ESI-MS: Expected *m/z* for $[C_{52}H_{78}N_8O_2S_2Mn_2]^{2+}$ = 510.6, found *m/z* = 511.5.

2.2.2.26 Synthesis of [$Mn^{II}(S^{Me2}N_4$(2-QuinoEN))](PF_6)•Et_2O (8). A procedure similar to that employed in the preparation of **1** was conducted with the following reagent amounts: sodium methoxide (0.11 g, 2.0 mmol), 3-mercapto-3-methyl-2-butanone (0.24 g, 2.0 mmol), L_8 (0.70, 2.0 mmol), manganese sulfate monohydrate (0.35 g, 2.0 mmol), and sodium hexafluorophosphate (0.41 g, 3.7 mmol). Complex **8** was isolated as a yellow solid in 60 % yield (0.78 g, 1.2 mmol). Electronic absorption spectrum, λ_{max} (nm) (ε ($M^{-1}cm^{-1}$)) (MeCN): 325 (3720). IR (Nujol): $\nu_{C=N}$ 1602 cm^{-1}. EPR spectrum (MeOH,EtOH glass): g = 1.99. Redox potential (MeCN vs SCE, 298 K): E_{pa}= +592 mV, E_{pc} = +312 mV. Magnetic moment (solid state, 5-300 K): 5.78 μ_B; (solution, MeOH, 298 K): 5.83 μ_B. ESI-MS: Expected *m/z* for $[C_{27}H_{29}N_4SMn]^+$ = 496.5, found *m/z* = 497.4. Elemental Analysis for $C_{27}H_{29}N_4F_6SPMn$; Calculated: C, 50.55%; H, 4.56%; N, 8.73%. Found: C, 51.17%; H, 5.00%; N, 8.51%.

2.2.2.27 Synthesis of [$Mn^{II}(S^{Me2}N_4$(2-QuinoPN))](PF_6)•MeCN•Et_2O (9). A procedure similar to that employed in the preparation of **1** was conducted with the following reagent amounts: sodium methoxide (0.11 g, 2.0 mmol), 3-mercapto-3-methyl-2-butanone (0.24 g, 2.0 mmol), L_9 (0.73, 2.0 mmol), manganese sulfate monohydrate (0.35 g, 2.0 mmol), and sodium hexafluorophosphate (0.41 g, 3.7 mmol). Complex **9** was isolated as a dark orange solid in 71 % yield (0.95 g, 1.5 mmol). Electronic absorption spectrum, λ_{max} (nm) (ε ($M^{-1}cm^{-1}$)) (MeCN): 320 (2570); (MeOH): 321 (1070). IR (Nujol): $\nu_{C=N}$ 1603 cm^{-1}. EPR spectrum (MeOH,EtOH glass): g = 1.99. Redox potential (MeCN vs SCE): E_{pa}= +525 mV. Magnetic moment (solid state, 5-300 K): 5.91 μ_B; (solution, MeOH, 298 K): 5.98 μ_B. ESI-MS: Expected *m/z* for $[C_{28}H_{31}N_4SMn]^+$ = 510.6, found *m/z* = 510.3. Elemental Analysis for $C_{28}H_{31}N_4F_6PSMn$; Calculated: C, 51.30; H, 4.77; N, 8.55. Found: C, 51.46; H, 5.00; N, 8.64.

2.2.2.28 Synthesis of $[Mn^{II}(O^{Me2}N_4(tren))]_2(PF_6)_2 \cdot MeCN$ (10). A procedure similar to that employed in the preparation of **1** was conducted with the following reagent amounts: sodium methoxide (0.14 g, 2.5 mmol), 3-hydroxy-3-methyl-2-butanone (0.30 g, 2.5 mmol), L_1 (0.37, 2.5 mmol), manganese sulfate monohydrate (0.42 g, 2.5 mmol), and sodium hexafluorophosphate (0.42 2.51.8 mmol). Complex **10** was isolated as a white solid in 97 % yield (1.6 g, 2.4 mmol). Electronic absorption spectrum (MeCN): λ_{max} (nm) (ε ($M^{-1}cm^{-1}$)): 281 (1410). IR (Nujol): $\nu_{C=N}$ 1599 cm^{-1}. EPR spectrum (9:1 MeOH/EtOH glass, 5 K): g = 2.00, 26.60. Redox potential (MeCN vs SCE, 298 K): E_{pa} = +391 mV, E_{pc} = +120 mV, -97 mV. Magnetic moment (per Mn, solution, MeOH, 301 K): 5.85 μ_B. ESI-MS: Expected *m/z* for $[C_{22}H_{50}N_8S_2Mn_2]^{2+}$ = 284.3, found *m/z* = 283.4. Elemental Analysis for $C_{24}H_{53}N_9F_{12}P_2O_2Mn_2$; Calculated: C, 32.05; H, 5.94; N, 14.01. Found: C, 31.70; H, 6.01; N, 14.11.

2.2.2.29 Synthesis of $[Mn^{II}(N^{Et2}N_4(tren))]_2(\mu\text{-}SO_4)(BPh_4)_2$ (11). A procedure similar to that employed in the preparation of **1** was conducted with the following reagent amounts: diethylaminoacetone (0.39 g, 3.0 mmol), L_1 (0.44, 3.0 mmol), manganese sulfate monohydrate (0.51 g, 3.0 mmol), and sodium tetraphenylborate (1.0 g, 3.0 mmol). Complex **11** was isolated as a dark yellow solid in 77 % yield (1.6 g, 1.2 mmol). Electronic absorption spectrum (MeCN): λ_{max} (nm) (ε ($M^{-1}cm^{-1}$)): 275 (2255). IR (Nujol): $\nu_{C=N}$ 1610 cm^{-1}. Redox potential (MeCN vs SCE, 298 K): E_{pa} = +573 mV, -21, E_{pc} = +447, +208 mV. Magnetic moment (per Mn, solution, MeOH, 301 K): 5.79 μ_B.

2.2.2.30 Synthesis of $[Mn^{II}((HO^{Me2})_2N_4(tren))(MeOH)](BPh_4)_2 \cdot MeOH$ (12). A procedure similar to that employed in the preparation of **1** was conducted with the following reagent amounts: sodium methoxide (0.067 g, 1.2 mmol), 3-hydroxy-3-methyl-2-butanone (0.26 g, 2.4 mmol), L_1 (0.18, 1.2 mmol), manganese sulfate monohydrate (0.21 g, 1.2 mmol), and sodium

tetraphenylborate (0.41 g, 1.2 mmol). Complex **12** was isolated as a white solid in 11 % yield (0.14 g, 0.13 mmol). Electronic absorption spectrum (MeCN): λ_{max} (nm) (ε ($M^{-1}cm^{-1}$)): 227 (1940). Magnetic moment (solution, MeOH, 301 K): 5.50 μ_B.

2.2.2.31 Synthesis of $[Mn^{II}(HO^{Me2}N_4(6\text{-Me-DPEN})(MeCN))](BPh_4)_2$ (13). A procedure similar to that employed in the preparation of **1** was conducted with the following reagent amounts: sodium methoxide (0.22 g, 4.0 mmol), 3-hydroxy-3-methyl-2-butanone (0.44 g, 14.0 mmol), L_4 (1.1, 4.0 mmol), manganese sulfate monohydrate (0.68 g, 4.0 mmol), and sodium tetraphenylborate (1.4 g, 4.0 mmol). Complex **13** was isolated as a white solid in 7 % yield (0.31 g, 0.28 mmol). ESI-MS: Expected *m/z* for $[C_{23}H_{33}N_5OMn_2]^{2+}$ = 250.1, found *m*/*z* = 251.2.

2.2.2.32 Synthesis of $[Mn^{II}(HO^{Me2}N_4(6\text{-Me-DPEN})(CHO_2))](BPh_4)\cdot MeCN\cdot Et_2O$ (14). A procedure similar to that employed in the preparation of **1** was conducted with the following reagent amounts: sodium methoxide (0.22 g, 4.0 mmol), 3-hydroxy-3-methyl-2-butanone (0.44 g, 14.0 mmol), L_4 (1.1, 4.0 mmol), manganese diformate (0.60 g, 4.0 mmol), and sodium tetraphenylborate (1.4 g, 4.0 mmol). Complex **14** was isolated as a white solid in 47 % yield (1.46 g, 1.9 mmol). Electronic absorption spectrum, λ_{max} (nm) (ε ($M^{-1}cm^{-1}$)) (MeCN): 315 (410). IR (Nujol): $\nu_{C=N}$ 1612 cm^{-1}. EPR spectrum (MeOH,EtOH glass): g = 1.98. Redox potential (MeCN vs SCE): E_{pa}= +589 mV, +43 mV, E_{pc} = +290 mV. Magnetic moment (solid state, 5-300 K): 5.84 μ_B; (solution, MeOH, 298 K): 5.93 μ_B. ESI-MS: Expected *m/z* for $[C_{19}H_{30}N_4OMn]^{2+}$ = 204.4, found *m*/*z* = 204.5.

2.2.2.33 Synthesis of $[Mn^{II}(O^{Me2}N_4(6\text{-Me-DPPN}))](BPh_4)$ (15). A procedure similar to that employed in the preparation of **1** was conducted with the following reagent amounts: sodium methoxide (0.056 g, 1.0 mmol), 3-hydroxy-3-methyl-2-butanone (0.11 g, 1.0 mmol), L_5 (0.29,

1.0 mmol), manganese sulfate monohydrate (0.17 g, 1.0 mmol), and sodium tetraphenylborate (0.34 g, 1.0 mmol). Complex **15** was isolated as a pale yellow solid in 81 % yield (0.34 g, 0.81 mmol). Electronic absorption spectrum, λ_{max} (nm) (ε ($M^{-1}cm^{-1}$)) (MeCN): 280 (1900). IR (Nujol): $\nu_{C=N}$ 1604 cm^{-1}. EPR spectrum (MeOH,EtOH glass): g = 2.00, 3.49, 5.51, 11.58. Redox potential (MeCN vs SCE): E_{pa}= +638 mV, E_{pc} = +502 mV. Magnetic moment (solution, MeOH, 298 K): 6.00 μ_B. ESI-MS: Expected *m/z* for $[C_{22}H_{31}N_4OMn]^+$ = 422.6, found *m*/*z* = 422.6. Elemental Analysis for $C_{48}H_{59}N_5OBMn$; Calculated: C, 74.49; H, 6.93; N, 7.55. Found: C, 77.24; H, 6.96; N, 7.31.

2.2.2.34 Synthesis of [$Zn^{II}(S^{Me2}N_4$(6-Me-DPEN))](BPh_4) (23). A procedure similar to that employed in the preparation of **1** was conducted with the following reagent amounts: sodium methoxide (0.056 g, 2.0 mmol), 3-mercapto-3-methyl-2-butanone (0.24 g, 2.0 mmol), L_4 (0.54, 2.0 mmol), zinc dichloride (0.27 g, 2.0 mmol), and sodium tetraphenylborate (0.69 g, 2.0 mmol). Complex **23** was isolated as a pale yellow solid in 95 % yield (1.4 g, 1.9 mmol). Electronic absorption spectrum, λ_{max} (nm) (ε ($M^{-1}cm^{-1}$)) (MeCN): 271 (1010). IR (Nujol): $\nu_{C=N}$ 1600 cm^{-1}. ^{1}H NMR (300 MHz, $CDCl_3$): δ 7.70 (m, 2H), 7.19 (m, 4H), 7.06 (t, 2H), 6.86 (s, 3H), 6.84 (d, 3H), 3.63 (s, 3H), 3.58 (s, 6H), 3.46 (d, 3H), 3.14 (m, 4H), 2.90 (t, 2H), 2.76 (t, 2H). ESI-MS: Expected *m/z* for $[C_{21}H_{29}N_4SZn]^+$ = 435.1, found *m*/*z* = 435.8.

2.2.2.35 Synthesis of [$Zn^{II}(S^{Me2}N_4$(6-Me-DPPN))](BPh_4)·MeCN (24). A procedure similar to that employed in the preparation of **1** was conducted with the following reagent amounts: sodium methoxide (0.056 g, 2.0 mmol), 3-mercapto-3-methyl-2-butanone (0.24 g, 2.0 mmol), L_5 (0.57, 2.0 mmol), zinc dichloride (0.27 g, 2.0 mmol), and sodium tetraphenylborate (0.69 g, 2.0 mmol). Complex **24** was isolated as a pale yellow solid in 91 % yield (1.4 g, 1.8 mmol). Electronic absorption spectrum, λ_{max} (nm) (ε ($M^{-1}cm^{-1}$)) (MeCN): 265 (990). ^{1}H NMR (300 MHz, $CDCl_3$):

δ 7.59 (t, 2H), 7.41 (d, 2H), 7.02 (d, 2H), 6.89 (m, 6H), 6.21 (s, 3 H), 3.83 (m, 4H), 2.80 (m, 2H), 2.45 (m, 2H), 2.52 (s, 6H). ESI-MS: Expected *m/z* for $[C_{22}H_{31}N_4SZn]^+$ = 449.2, found *m/z* = 449.4.

2.2.3 X-ray Crystallographic Structure Determination

A red crystal of **1** with dimensions 0.20 x 0.20 x 0.15 mm^3 was mounted on a glass capillary with oil. Data was collected at -173 ˚C. The crystal-to-detector distance was set to 40 mm and the exposure time was 10 seconds per degree for all sets of exposure. The scan width was 0.5˚. Data collection was 99.5% complete to 25.0˚ in ϑ. A total of 75,154 partial and complete reflections were collected covering the indices h = -12 to 12, k = -19 to 19, l = -26 to 26. 7,230 reflections were symmetry independent and the R_{int} = 0.0317 indicated that the data was good (0.07 average quality). Indexing and unit cell refinement indicated an orthorhombic P lattice with the space group P $2_12_12_1$ (No. 19).

A yellow crystal of **2** was cut to dimensions of 0.60 x 0.60 x 0.60 mm^3 and mounted on a glass capillary with oil. Data was collected at -143 ˚C. The crystal-to-detector distance was set to 30 mm and the exposure time was 15 seconds per degree for all sets of exposure. The scan width was 0.5˚. Data collection was 98.5% complete to 25.0˚ in ϑ. A total of 48,881 partial and complete reflections were collected covering the indices h = -13 to 13, k = -19 to 19, l = -19 to 19. 7,339 reflections were symmetry independent and the R_{int} = 0.039 indicated that the data was good (0.07 average quality). Indexing and unit cell refinement indicated a triclinic P lattice with the space group P -1 (No. 12).

A colorless prism of **3** with dimensions 0.15 x 0.06 x 0.02 mm^3 was mounted on a glass capillary with oil. Data was collected at -163 ˚C. The crystal-to-detector distance was set to 40

mm and the exposure time was 60 seconds per degree for all sets of exposure. The scan width was 0.5˚. Data collection was 98.6% complete to 25.0˚ in ϑ. A total of 11,372 partial and complete reflections were collected covering the indices h = -11 to 11, k = -13 to 14, l = -15 to 15. 4,497 reflections were symmetry independent and the R_{int} = 0.079 indicated that the data was problematic (0.07 average quality). Indexing and unit cell refinement indicated a triclinic P lattice with the space group P $\bar{1}$ (No. 2).

A red prism of **4** with dimensions 0.48 x 0.29 x 0.24 mm^3 was mounted on a glass capillary with oil. Data was collected at -143 ˚C. The crystal-to-detector distance was set to 40 mm and the exposure time was 60 seconds per degree for all sets of exposure. The scan width was 1.0˚. Data collection was 99.6% complete to 25.0˚ in ϑ. A total of 32,825 partial and complete reflections were collected covering the indices, h = -13 to 13, k = -19 to 19, l = -22 to 22. 5,980 reflections were symmetry independent and the R_{int} = 0.038 indicated that the data was above average quality (0.07 average quality). Indexing and unit cell refinement indicated an orthorhombic P lattice with the space group P $2_12_12_1$ (No. 19).

A yellow prism of **5** with dimensions 0.20 x 0.17 x 0.10 mm^3 was mounted on a glass capillary with oil. Data was collected at -163 ˚C. The crystal-to-detector distance was set to 40 mm and the exposure time was 20 seconds per degree for all sets of exposure. The scan width was 0.5˚. Data collection was 98.7% complete to 25.0˚ in ϑ. A total of 114,668 partial and complete reflections were collected covering the indices h = -17 to 17, k = -20 to 20, l = -22 to 22. 16,232 reflections were symmetry independent and the R_{int} = 0.0343 indicated that the data was above average quality (0.07 average quality). Indexing and unit cell refinement indicated a triclinic P lattice with the space group P $\bar{1}$ (No.2).

A black prism of **6** with dimensions 0.16 x 0.10 x 0.08 mm^3 was mounted on a glass capillary with oil. Data was collected at -173 ˚C. The crystal-to-detector distance was set to 40 mm and the exposure time was 10 seconds per degree for all sets of exposure. The scan width was 0.5˚. Data collection was 100% complete to 25.0˚ in ϑ. A total of 75,651 partial and complete reflections were collected covering the indices h = -13 to 13, k = -21 to 21, l = -31 to 31. 9,753 reflections were symmetry independent and the R_{int} = 0.063 indicated that the data was of average quality (0.07 average quality). Indexing and unit cell refinement indicated a monoclinic P lattice with the space group P $2_1/n$ (No.14).

A yellow block of **8** with dimensions 0.20 x 0.15 x 0.10 mm^3 was mounted on a glass capillary with oil. Data was collected at -173 ˚C. The crystal-to-detector distance was set to 40 mm and the exposure time was 10 seconds per degree for all sets of exposure. The scan width was 0.5˚. Data collection was 96.6% complete to 25.0˚ in ϑ. A total of 33,867 partial and complete reflections were collected covering the indices h = -15 to 15, k = -17 to 17, l = -21 to 21. 10,530 reflections were symmetry independent and the R_{int} = 0.0585 indicated that the data was above average quality (0.07 average quality). Indexing and unit cell refinement indicated a triclinic P lattice with the space group P $\bar{1}$ (No.2).

A yellow prism of **9** with dimensions 0.18 x 0.15 x 0.10 mm^3 was mounted on a glass capillary with oil. Data was collected at -163 ˚C. The crystal-to-detector distance was set to 40 mm and the exposure time was 20 seconds per degree for all sets of exposure. The scan width was 0.5˚. Data collection was 99.7% complete to 25.0˚ in ϑ. A total of 61,040 partial and complete reflections were collected covering the indices h = -18 to 17, k = -20 to 20, l = -21 to 22. 8,766 reflections were symmetry independent and the R_{int} = 0.0432 indicated that the data

was above average quality (0.07 average quality). Indexing and unit cell refinement indicated a monoclinic P lattice with the space group P $2_1/n$ (No.14).

A colorless plate of **10** with dimensions 0.10 x 0.10 x 0.01 mm^3 was mounted on a glass capillary with oil. Data was collected at -173 ˚C. The crystal-to-detector distance was set to 40 mm and the exposure time was 40 seconds per degree for all sets of exposure. The scan width was 0.5˚. Data collection was 100% complete to 25.0˚ in ϑ. A total of 35,368 partial and complete reflections were collected covering the indices h = -14 to 14, k = -17 to 17, l = -19 to 19. 5,204 reflections were symmetry independent and the R_{int} = 0.0224 indicated that the data was above average quality (0.07 average quality). Indexing and unit cell refinement indicated a monoclinic P lattice with the space group P $2_1/c$ (No.14).

A colorless needle of **11** with dimensions 0.20 x 0.10 x 0.05 mm^3 was mounted on a glass capillary with oil. Data was collected at -163 ˚C. The crystal-to-detector distance was set to 40 mm and the exposure time was 50 seconds per degree for all sets of exposure. The scan width was 0.5˚. Data collection was 100% complete to 25.0˚ in ϑ. A total of 90,468 partial and complete reflections were collected covering the indices h = -13 to 13, k = -34 to 34, l = -29 to 29. 13,593 reflections were symmetry independent and the R_{int} = 0.2453 indicated that the data was problematic (0.07 average quality). Indexing and unit cell refinement indicated a monoclinic P lattice with the space group P $2_1/c$ (No.4).

A black block of **12** with dimensions 0.10 x 0.05 x 0.05 mm^3 was mounted on a glass capillary with oil. Data was collected at -173 ˚C. The crystal-to-detector distance was set to 40 mm and the exposure time was 60 seconds per degree for all sets of exposure. The scan width was 0.5˚. Data collection was 97.8% complete to 25.0˚ in ϑ. A total of 47,447 partial and

complete reflections were collected covering the indices h = -15 to 16, k = -18 to 16, l = -18 to 24. 14,561 reflections were symmetry independent and the R_{int} = 0.0814 indicated that the data was above average quality (0.07 average quality). Indexing and unit cell refinement indicated a triclinic P lattice with the space group P $\bar{1}$ (No.2).

A colorless plate of **13** with dimensions 0.20 x 0.15 x 0.15 mm^3 was mounted on a glass capillary with oil. Data was collected at -173 ˚C. The crystal-to-detector distance was set to 40 mm and the exposure time was 10 seconds per degree for all sets of exposure. The scan width was 0.5˚. Data collection was 99.8% complete to 25.0˚ in ϑ. A total of 219,416 partial and complete reflections were collected covering the indices h = -17 to 17, k = -31 to 31, l = -31 to 31. 30,979 reflections were symmetry independent and the R_{int} = 0.0280 indicated that the data was above average quality (0.07 average quality). Indexing and unit cell refinement indicated a triclinic P lattice with the space group P $\bar{1}$ (No.2).

A black block of **14** with dimensions 0.40 x 0.35 x 0.20 mm^3 was mounted on a glass capillary with oil. Data was collected at -173 ˚C. The crystal-to-detector distance was set to 40 mm and the exposure time was 30 seconds per degree for all sets of exposure. The scan width was 0.5˚. Data collection was 99.6% complete to 25.0˚ in ϑ. A total of 135,220 partial and complete reflections were collected covering the indices h = -23 to 21, k = -25 to 25, l = -28 to 28. 33,770 reflections were symmetry independent and the R_{int} = 0.0371 indicated that the data was above average quality (0.07 average quality). Indexing and unit cell refinement indicated a triclinic P lattice with the space group P $\bar{1}$ (No.2).

A yellow needle of **15** with dimensions 0.15 x 0.05 x 0.05 mm^3 was mounted on a glass capillary with oil. Data was collected at -173 ˚C. The crystal-to-detector distance was set to 40

mm and the exposure time was 30 seconds per degree for all sets of exposure. The scan width was 0.5˚. Data collection was 97.0% complete to 25.0˚ in ϑ. A total of 31,192 partial and complete reflections were collected covering the indices h = -11 to 12, k = -17 to 17, l = -20 to 20. 9,121 reflections were symmetry independent and the R_{int} = 0.0455 indicated that the data was above average quality (0.07 average quality). Indexing and unit cell refinement indicated a triclinic P lattice with the space group P $\bar{1}$ (No.2).

A colorless plate of **23** with dimensions 0.15 x 0.10 x 0.10 mm^3 was mounted on a glass capillary with oil. Data was collected at -173 ˚C. The crystal-to-detector distance was set to 40 mm and the exposure time was 10 seconds per degree for all sets of exposure. The scan width was 0.5˚. Data collection was 98.8% complete to 25.0˚ in ϑ. A total of 32,726 partial and complete reflections were collected covering the indices h = -12 to 12, k = -16 to 16, l = -23 to 23. 9,223 reflections were symmetry independent and the R_{int} = 0.0468 indicated that the data was above average quality (0.07 average quality). Indexing and unit cell refinement indicated a triclinic P lattice with the space group P $\bar{1}$ (No.2).

A colorless plate of **24** with dimensions 0.40 x 0.30 x 0.20 mm^3 was mounted on a glass capillary with oil. Data was collected at -173 ˚C. The crystal-to-detector distance was set to 40 mm and the exposure time was 10 seconds per degree for all sets of exposure. The scan width was 0.5˚. Data collection was 98.4% complete to 25.0˚ in ϑ. A total of 65,334 partial and complete reflections were collected covering the indices h = -23 to 22, k = -15 to 15, l = -29 to 29. 10,464 reflections were symmetry independent and the R_{int} = 0.0524 indicated that the data was above average quality (0.07 average quality). Indexing and unit cell refinement indicated a monoclinic P lattice with the space group P $2_1/c$ (No.14).

All X-ray data sets were integrated and scaled using either hkl-SCALEPACK or SAINT, SADABS within the APEX2 software package by Bruker.[28] Solutions were made by direct methods (SHELXS, SIR97) to produce complete heavy atom phasing models.[29-30] Scattering factors are from Waasmair and Kirfel.[31] Structures were completed by difference Fourier synthesis with either SHELXL97 or SHELXTL 6.10. Hydrogen atoms were placed in geometrically idealized positions and constrained to ride on their parent atoms with C-H distances in the range of 0.95-1.00 Å. Isotropic thermal parameters Ueq were fixed such that they were 1.2Ueq of their parent aom Ueq for C-Hs and 1.5Ueq for methyl groups. All non-hydrogen atoms were refined anisotropically by full-matrix least-squares.

2.2.4 X-ray Absorption Data Collection and Fitting Procedures

Sulfur K-edge XAS data were measured at the Stanford Synchrotron Radiation Lightsource (SSRL) using the 20-pole 2.0 Tesla wiggler unfocused beamline 4-3. Operating conditions were 3 GeV and ~200 mA for the ring current. Samples were prepared by grounding each solid compound into a fine powder under an inert atmosphere in a glove box, followed by placing a the powder sample on sulfur-free Mylar tape as a thin film. Details of the experimental configuration for low-energy studies have been described previously.[32] Energy calibration was performed by setting the pre-edge peak of $Na_2S_2O_3$ at 2472 eV.[33] A total of four to five scans were measured for each sample to ensure reproducibility and detect possible photodecomposition. Raw data was normalized by fitting a flattened second-order polynomial to the post-edge region and normalizing to an edge jump of 1.0 at 2490 eV for the sulfur K-edges using the PySpline software package.[34] Intensities of the pre-edge features were quantified by fitting the normalized data with pseudo-Voigt line shapes with a fixed 1:1 ratio of Lorentzian to Gaussian contributions using the EDG_FIT program available in the EXAFSPAK software

package.[35] Fitted intensities were converted to percent S_{3p} character using the pre-edge feature of plastocyanin as a reference where 1.02 units of intensity are equal to 38% S_{3p} character.[36] Error resulting from background corrections, normalization, and fitting procedures can introduce 1 - 3 % error in the total pre-edge areas. The uncertainty of the pre-edge energy is ~0.1 eV.

2.2.5 Computational Details

Geometry optimization and single point energy calculations were performed using the Gaussian 03 software package with the spin-unrestricted B3LYP hybrid functional for all complexes.[37] The 6-311G(d) basis set was used for Fe, Mn, S, and N atoms, while the 6-21G(d) basis set was used for C and H atoms. The initial atomic coordinates for the geometry optimization calculations were obtained from the X-ray crystal structures. Single point calculations were performed using the 6-311G(d) basis set for all atoms. Molecular orbitals were plotted using the Gaussview v3.0 software. Fragmentation analyses were performed using the QMForge software program.[38]

2.3 Results and Discussion

2.3.1 Synthesis and Structural Characterization of Thiolate-Ligated Mn(II) Complexes

Our research group has worked extensively with a pentadentate ligand system based upon a *tris*(2-aminoethyl)amine framework.[39-41] A series of first-row transition metal complexes have been described using this ligand scaffold (L_1), including a rare example of a thiolate-ligated Mn(II) complex, $[Mn^{II}(S^{Me2}N_4(tren))](PF_6)$ (**1**) (Figure 2.1).[26] An important structural feature of the X-ray crystal structure of **1** is the presence of an available coordination site at the metal despite having been crystallized from coordinating solvents. Ligand L_1 served as inspiration for the design of an N-heterocyclic-containing set of ligand specifically containing either pyridine or

quinoline moieties. Pyridines are frequently used in the synthesis of biomimetic first-row transition metal complexes and permit facile ligand modifications by altering the pyridine substituents.[42-44] The synthetic strategy used to construct this series of ligands and respective Mn(II) complexes, as well as representations of each ligand, are provided in Schemes 2.1 and 2.2, respectively. The desired ligands outlined in Scheme 2.2 show variations with respect to both the alkyl backbone length (ethyl and propyl linkers) and the substituents of the N-heterocyclic moieties (pyridine, 6-methylpyridine, 4-methoxy-3,5-dimethylpyridine, and quinoline). Maintaining a single primary amine in L_2-L_9 was a key prerequisite for the desired thiolate-containing ligands, which were constructed via Mn(II)-templated Schiff-base condensations between the primary amine and 3-mercapto-3-methyl-2-butanone.

Synthetic attempts towards the desired mononuclear thiolate-ligated Mn(II) complexes using L_2-L_9 were each made in similar fashions by combining equimolar amounts of $MnSO_4 \cdot H_2O$, ligands L_2-L_9 (respectively), $NaOCH_3$, 3-methyl-3-mercapto-2-butanone, and either $NaBF_4$, $NaPF_6$, or $NaBPh_4$ in MeOH under an inert atmosphere (N_2). The desired complexes from reactions with L_2 ($[Mn^{II}(S^{Me2}N_4(6\text{-H-DPEN}))(MeOH)](PF_6) \cdot MeOH$ (**2**)), L_4 ($[Mn^{II}(S^{Me2}N_4(6\text{-Me-DPEN}))](BF_4)$ (**4**)), L_5 ($[Mn^{II}(S^{Me2}N_4(6\text{-Me-DPPN}))](BPh_4)$ (**5**)), L_8 ($[Mn^{II}(S^{Me2}N_4(2\text{-QuinoEN}))](BPh_4) \cdot MeCN$ (**8**)), and L_9 ($[Mn^{II}(S^{Me2}N_4(2\text{-QuinoPN}))](PF_6)$ (**9**)) were successfully obtained in 20-70 % yield under these conditions and verified through structural characterization via X-ray crystallography. Reactions with L_3 resulted in the formation of a dithiolate-bridged Mn(II) dimer, $([Mn^{II}(S^{Me2}N_4(6\text{-H-DPPN}))]_2(BF_4)_2$ (**3**), in 68 % yield, while reactions with L_6 yielded a monothiolate-bridged Mn(II) dimer, $([(Mn^{II}(S^{Me2}N_4(4\text{-OMe-3,5-Me-DPEN})))(Mn^{II}(S^{Me2}N_4(4\text{-OMe-3,4-Me-DPEN}))(Cl))](BF_4) \cdot Et_2O$ (**6**), in 7 % yield.

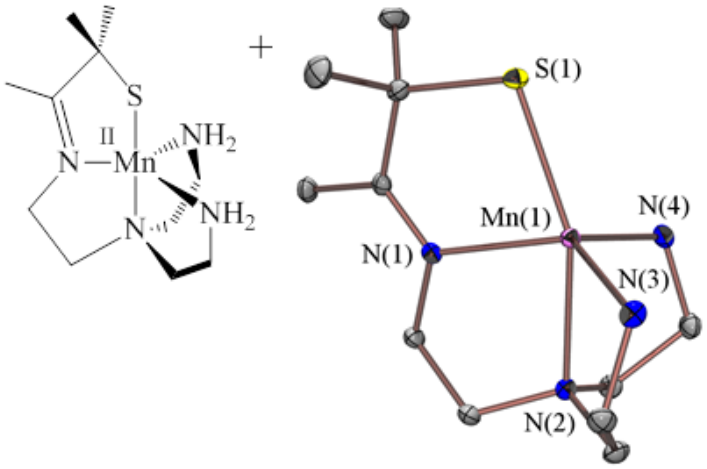

Figure 2.1 ORTEP diagram of $[Mn^{II}(S^{Me2}N_4(tren))]^+$ (**1**) with counterion and hydrogen atoms omitted for clarity.

Scheme 2.1 Synthetic strategy for the thiolate-ligated Mn(II) complexes in this study.

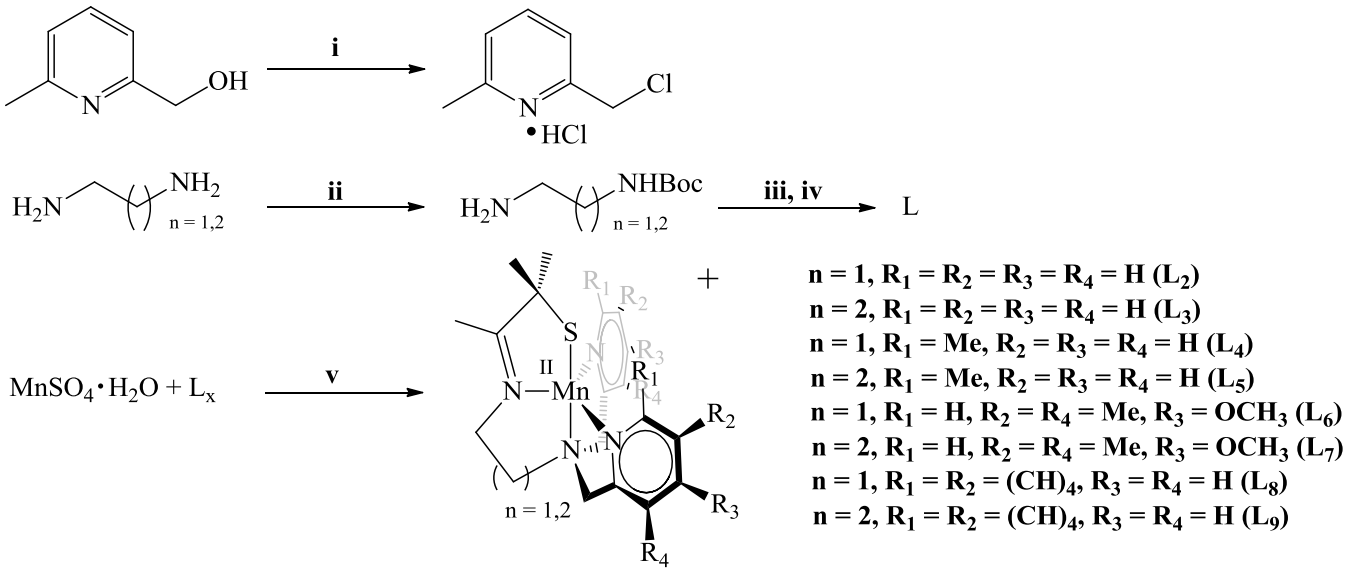

Reaction conditions: (i) 6.0 equivalents of $SOCl_2$, CH_2Cl_2, inert atmosphere (N_2), 0 °C → ambient temperature, 16 hrs. (ii) 0.17 equivalents of Boc_2O, CH_2Cl_2, inert atmosphere (N_2), ambient temperature, 24 hrs; (iii) 1.7-1.9 equivalents of 2-(chloromethyl)-pyridine hydrochloride (L_2 and L_3), 2-(chloromethyl)-6-methylpyridine hydrochloride (L_4 and L_5), 2-(chloromethyl)-4-methoxy-3,5-dimethylpyridine hydrochloride (L_6 and L_7), or 2-(chloromethyl)-quinoline hydrochloride (L_8 and L_9), 5 M NaOH (aq), room temperature, 3-5 days; (iv) 10-32 equivalents of trifluoroacetic acid, CH_2Cl_2, 12 hrs. (v) 1.0 equivalent of 3-methyl-3-mercapto-2-butanone, 1.0 equivalent of NaOMe, 1.0 equivalent of NaX (X= PF_6^-, BPh_4^-, or BF_4^-), MeOH, inert atmosphere (N_2), ambient temperature, 24-48 hrs.

Scheme 2.2 N-heterocyclic ligands synthesized for this study.

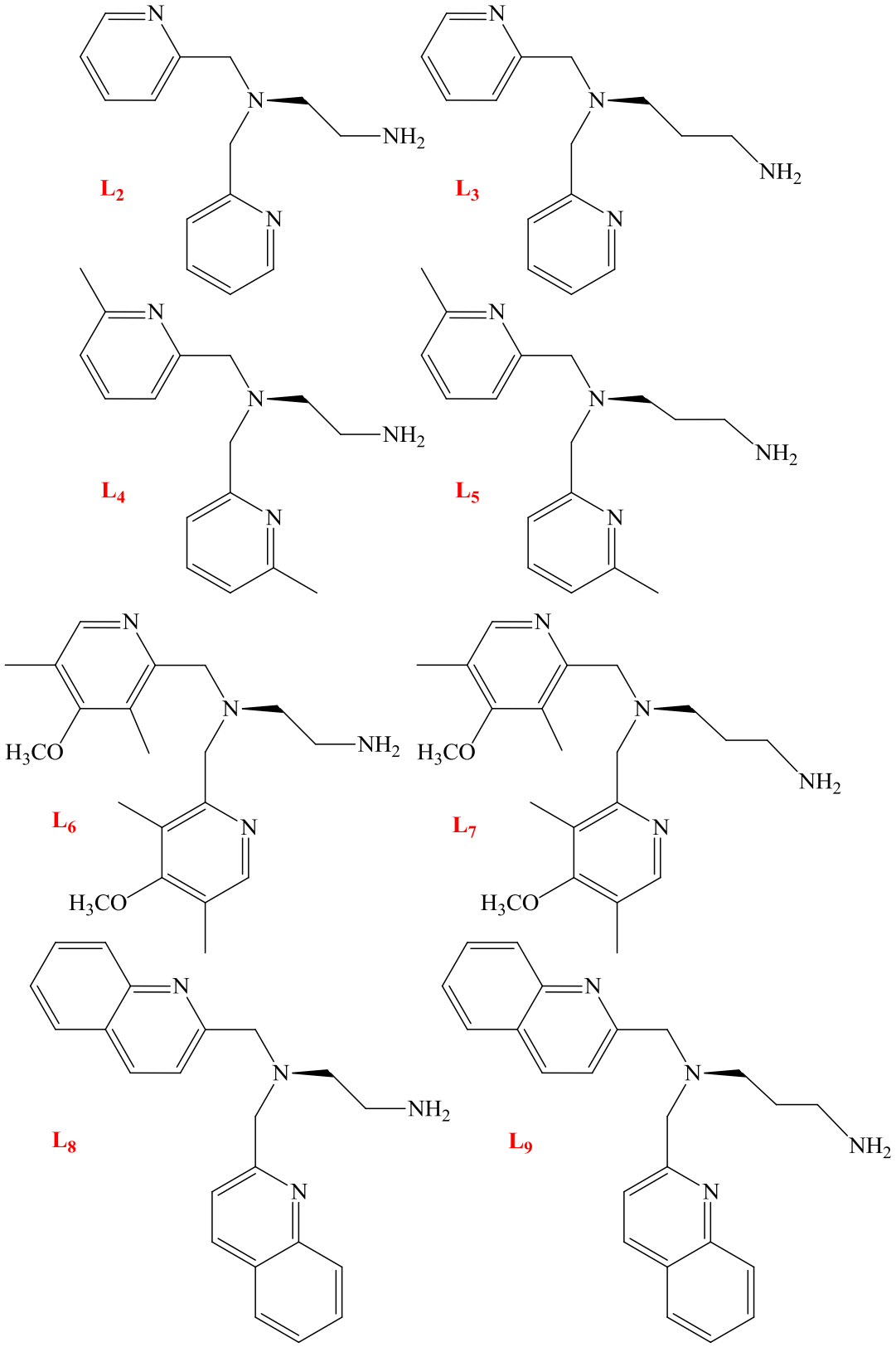

Attempts at obtaining a Mn-containing species from reactions with L_7 were unsuccessful. ORTEP diagrams of the X-ray crystal structures and molecular representations of complexes **2**, **4**, **5**, **8**, and **9** are provided in Figures 2.2 and 2.3, respectively; the ORTEP diagrams of complexes **3** and **6** are provided in Figure 2.4. Selected metrical parameters and crystal data for **1**, **2**, **4**, **5**, **8**, and **9** are provided in Tables 2.1 and 2.2, respectively.

As shown in the ORTEP diagrams of Figure 2.2, monocationic complexes **4**-**5** and **8**-**9** are five-coordinate despite being synthesized and crystallized in coordinating solvents (MeOH and MeCN). These observations are consistent with the X-ray crystal structure of five-coordinate **1**. The primary coordination sphere of each complex contains a thiolate sulfur (S(1)), imine nitrogen (N(1)), tertiary amine (N(2)), and two N-heterocyclic moieties (N(3) and N(4)). Complex **2**, on the other hand, was found to contain a methanol ligand bound in an available coordination site *trans* to the imine nitrogen (Figure 2.2). The presence of a single anionic counterion per Mn complex in the X-ray crystal structure of **2** supports the assignment of this exogenous ligand as methanol and not methoxide.

Close inspection of the metrical parameters (Table 1) for methanol-bound **2** reveals a fairly dramatic elongation of the Mn···N(2) separation (2.3595(16) Å) relative to these distances in **4**-**5** and **8**-**9** (2.2424(16) - 2.274(2) Å, Table 2.1). Considering the sum of the ionic radii for a high-spin Mn(II) ion and sp^3-hybridized nitrogen is 2.29 Å, the X-ray crystal structure of **2** is also best described as a five-coordinate complex.[45] Complex **2** is further distinguished from **4**-**5** and **8**-**9** in that the N-heterocyclic ligand moieties are unsubstituted and therefore impose less steric congestion upon the open coordination site than do the 6-methylpyridine or quinoline moieties (Figures 2.2 – 2.3). Solvent coordination to **2** is presumably more facile due to the absence of these bulkier substituents. Substitution of the pyridine 6-position has been shown in a

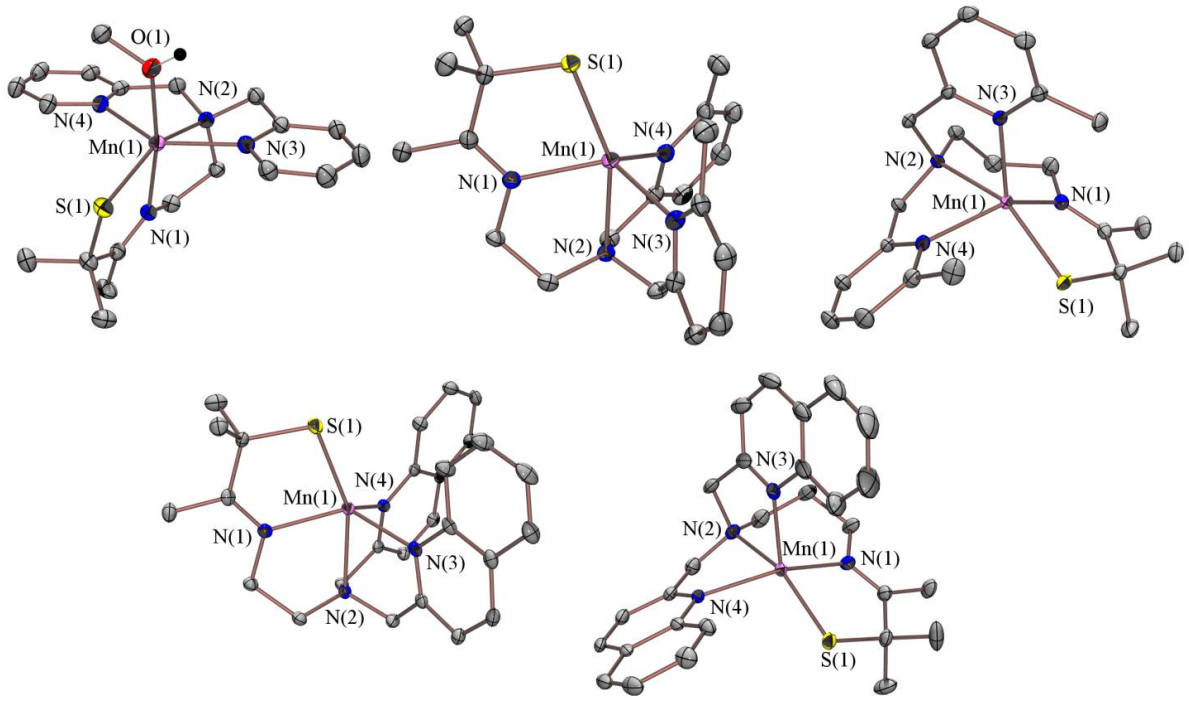

Figure 2.2 ORTEP diagrams (50 % probability) of $[Mn^{II}(S^{Me2}N_4(6\text{-H-DPEN}))(MeOH)]^+$ (**2**, top left), $[Mn^{II}(S^{Me2}N_4(6\text{-Me-DPEN}))]^+$ (**4**, top center), $[Mn^{II}(S^{Me2}N_4(6\text{-Me-DPPN}))]^+$ (**5**, top right), $[Mn^{II}(S^{Me2}N_4(2\text{-QuinoEN}))]^+$ (**8**, bottom left), and $[Mn^{II}(S^{Me2}N_4(2\text{-QuinoPN}))]^+$ (**9**, bottom right) with hydrogen atoms, counterions, and solvents of crystallization omitted for clarity.

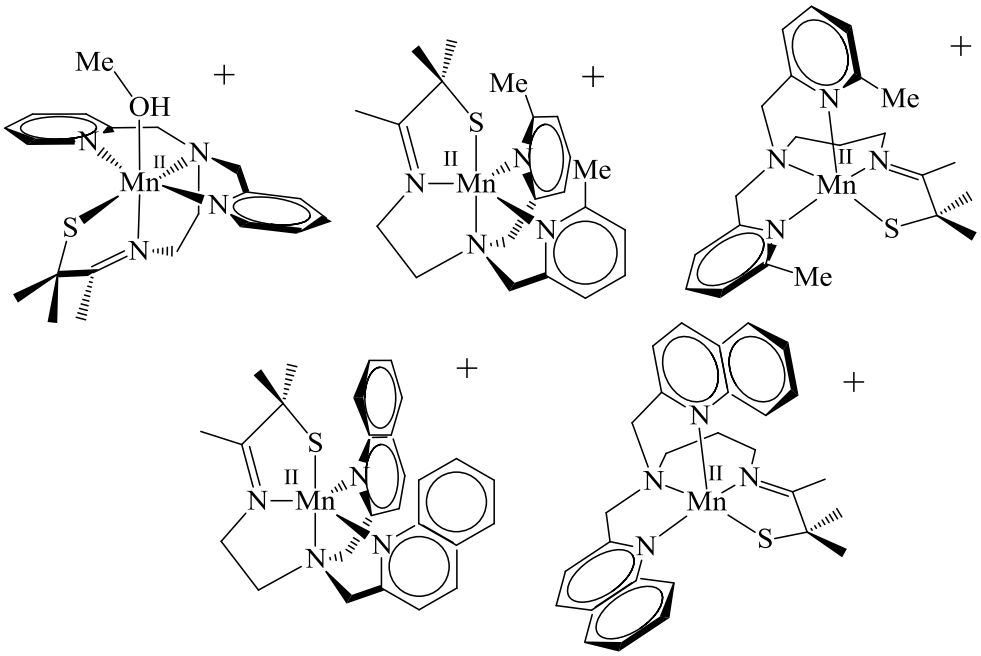

Figure 2.3 ChemDraw representations of $[Mn^{II}(S^{Me2}N_4(6\text{-H-DPEN}))(MeOH)]^+$ (**2**, top left), $[Mn^{II}(S^{Me2}N_4(6\text{-Me-DPEN}))]^+$ (**4**, top center), $[Mn^{II}(S^{Me2}N_4(6\text{-Me-DPPN}))]^+$ (**5**, top right), $[Mn^{II}(S^{Me2}N_4(2\text{-QuinoEN}))]^+$ (**8**, bottom left), and $[Mn^{II}(S^{Me2}N_4(2\text{-QuinoPN}))]^+$ (**9** bottom right).

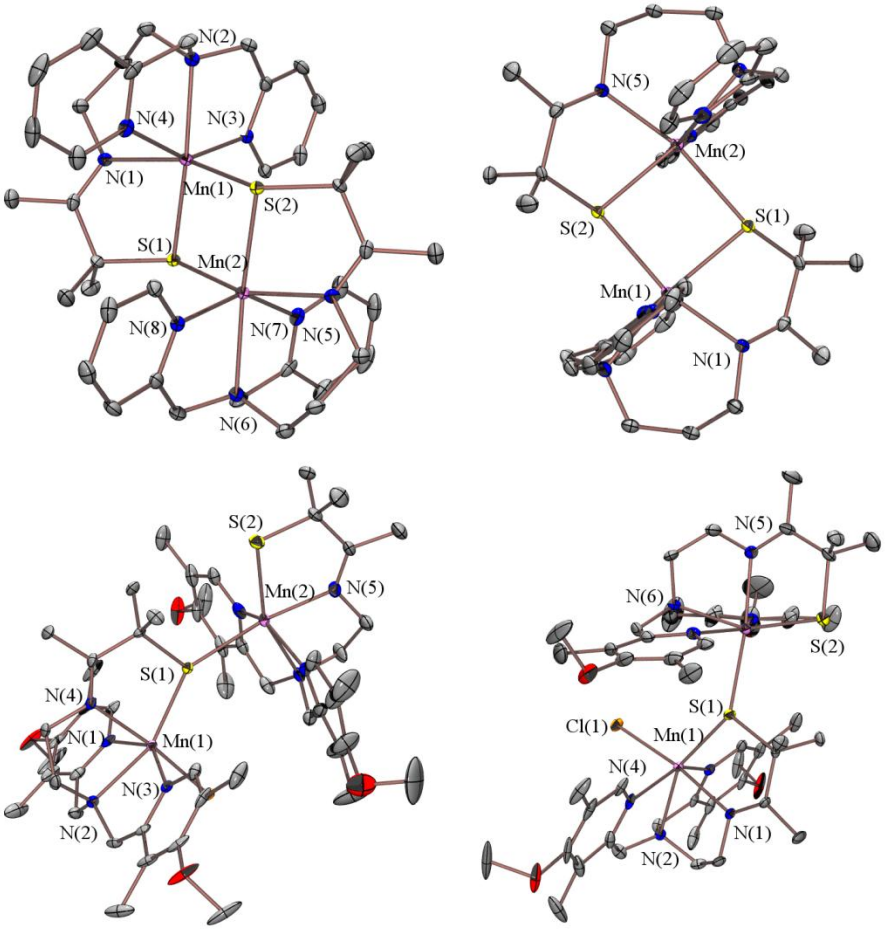

Figure 2.4 ORTEP diagrams (50 % probability) of $\{[Mn^{II}(S^{Me2}N_4(6\text{-H-DPPN}))]_2\}^{2+}$ (**3**, top) and $\{[(Mn^{II}(S^{Me2}N_4(4\text{-OMe-3,5-Me-DPEN})))(Mn^{II}(S^{Me2}N_4(4\text{-OMe-3,4-Me-DPEN}))(Cl))]\}^{+}$ (**6**, bottom) with hydrogen atoms, counterions, and solvent of crystallization omitted for clarity. Two alternate orientations of each dimer are provided. Selected distances (Å) and angles (degrees) for **3**: Mn(1)-S(1), 2.4854(10); Mn(1)-S(2), 2.6051(10); Mn(1)-N(1), 2.233(3); Mn(1)-N(2), 2.218(3); Mn(1)-N(3), 2.313(3); Mn(1)-N(4), 2.342(3); Mn(1)-S(1)-Mn(2), 88.47(3); S(1)-Mn(1)-S(2), 91.53(3). Selected distances (Å) and angles (degrees) for **6**: Mn(1)-S(1), 2.4555(18); Mn(2)-S(2), 2.4654(18); Mn(2)-S(1), 2.5880(18); Mn(1)-Cl(1), 2.429(2); Mn(1)-N(1), 2.319(5); Mn(1)-N(2), 2.277(5); Mn(1)-N(3), 2.282(6); Mn(1)-N(4), 2.258(5); Mn(2)-N(5), 2.329(6); Mn(2)-N(6), 2.268(6); Mn(2)-N(7), 2.279(6); Mn(2)-N(8), 2.224(6); S(1)-Mn(1)-Cl(1), 109.36(6); N(7)-Mn(2)-S(2), 106.81(19); N(8)-Mn(2)-S(2), 171.19(18); Mn(1)-S(1)-Mn(2), 144.12(7); S(1)-Mn(2)-S(2), 109.24(7). Crystal data for **3**: Formula, $C_{40}H_{54}B_2F_8Mn_2N_8S_2$; MW, 994.53; T, 110(2); unit cell[a], triclinic; space group, P-1; dimensions, a = 9.0113(3), b = 11.3892(3), c = 12.2008(4), α = 68.094(2)°, β = 83.307(2)°, γ = 73.183(2)°; Z, 1; V (Å^3), 11112.04(6); d(calc, g/cm^3), 1.485; R[b], 0.0494; R_w[c], 0.0867; GOF, 0.954. Crystal data for **6**: Formula, $C_{52.78}H_{81.55}BClF_4Mn_2N_8O_5S_2$; MW, 1204.39; T, 110(2); unit cell[a], orthorhombic; space group, P b c a; dimensions, a = 15.4385(7), b = 19.6551(9), c = 39.8775(18), α = 90°, β = 90°, γ = 90°; Z, 8; V (Å^3), 121006(10); d(calc, g/cm^3), 1.322; R[b], 0.1040; R_w[c], 0.2189; GOF, 1.122. [a]In all cases: Mo Kα(λ = 0.7170 Å) radiation. [b]$R = \Sigma||F_0| - |F_c||/ \Sigma|F_0|$. [c]$R_w = [\Sigma w(|F_0| - |F_c|)^2/ \Sigma wF_0^{1/2}$, where $w^{-1} = [\sigma_{count}^2 + (0.05F^2)^2]4F^2$.

Table 2.1 Selected bond distances (Å) and angles (degrees) for $[Mn^{II}(S^{Me2}N_4(tren))](PF_6)$ (**1**), $[Mn^{II}(S^{Me2}N_4(6\text{-H-DPEN}))(MeOH)](PF_6)\cdot MeOH$ (**2**), $[Mn^{II}(S^{Me2}N_4(6\text{-Me-DPEN}))](BF_4)$ (**4**), $[Mn^{II}(S^{Me2}N_4(6\text{-Me-DPPN}))](BPh_4)$ (**5**), $[Mn^{II}(S^{Me2}N_4(2\text{-QuinoEN}))](BPh_4)\cdot MeCN$ (**8**), and $[Mn^{II}(S^{Me2}N_4(2\text{-QuinoPN}))](PF_6)$ (**9**).

	1	**2**	**4**	**5**	**8**	**9**
Mn-S(1)	2.4033(3)	2.4597(6)	2.3710(6)	2.3742(3)	2.3835(9)	2.3626(5)
Mn-N(1)	2.1738(8)	2.2215(16)	2.186(2)	2.1909(10)	2.170(2)	2.2106(15)
Mn-N(2)	2.3193(8)	2.3595(16)	2.297(2)	2.2476(10)	2.274(2)	2.2424(16)
Mn-N(3)	2.1936(8)	2.2790(18)	2.222(2)	2.1830(10)	2.225(3)	2.1886(16)
Mn-N(4)	2.1956(9)	2.2463(17)	2.239(2)	2.2787(10)	2.200(3)	2.2689(14)
Mn-O(1)	N/A	2.183(1)	N/A	N/A	N/A	N/A
S(1)-Mn-N(1)	81.75(2)	78.77(4)	81.15(5)	82.03(3)	82.20(7)	82.66(4)
S(1)-Mn-N(2)	158.71(2)	155.39(4)	156.98(5)	154.06(3)	156.10(7)	155.06(4)
S(1)-Mn-N(3)	114.15(2)	108.79(5)	117.36(5)	127.47(3)	106.98(7)	124.91(5)
S(1)-Mn-N(4)	109.33(2)	108.23(4)	117.38(5)	93.97(3)	123.09(7)	100.31(4)
N(1)-Mn-N(3)	125.48(3)	84.76(6)	121.37(7)	114.15(4)	118.53(9)	104.28(6)
N(1)-Mn-N(4)	109.54(3)	104.19(6)	120.58(7)	140.58(4)	119.04(9)	152.29(6)
N(3)-Mn-N(4)	112.28(3)	142.93(6)	100.00(7)	99.40(4)	104.16(9)	99.55(5)
O(1)-Mn-S(1)	N/A	97.35(4)	N/A	N/A	N/A	N/A
O(1)-Mn-N(1)	N/A	171.07(6)	N/A	N/A	N/A	N/A
O(1)-Mn-N(2)	N/A	107.21(6)	N/A	N/A	N/A	N/A
O(1)-Mn-N(3)	N/A	88.95(6)	N/A	N/A	N/A	N/A
O(1)-Mn-N(4)	N/A	84.64(6)	N/A	N/A	N/A	N/A
τ	0.55	0.47	0.59	0.22	0.55	0.05

Table 2.2 Crystal data for $[Mn^{II}(S^{Me2}N_4(tren))](PF_6)$ (**1**), $[Mn^{II}(S^{Me2}N_4(6\text{-H-DPEN}))(MeOH)](PF_6)\cdot MeOH$ (**2**), $[Mn^{II}(S^{Me2}N_4(6\text{-Me-DPEN}))](BF_4)$ (**4**), $[Mn^{II}(S^{Me2}N_4(6\text{-Me-DPPN}))](BPh_4)$ (**5**), $[Mn^{II}(S^{Me2}N_4(2\text{-QuinoEN}))](BPh_4)\cdot MeCN$ (**8**), and $[Mn^{II}(S^{Me2}N_4(2\text{-QuinoPN}))](PF_6)$ (**9**).

	1	**2**	**4**	**5**	**8**	**9**
Formula	$C_{11}H_{25}F_6Mn_1N_4PS$	$C_{46}H_{57}BMnN_4O_3S$	$C_{21}H_{29}F_6MnN_4PS$	$C_{48}H_{54}BMnN_5S$	$C_{53}H_{52}BMnN_5S$	$C_{64}H_{78}F_{12}Mn_2N_{10}OP_2S_2$
MW	445.32	811.77	569.46	798.77	856.82	1467.30
T, K	100(2)	130(2)	130(2)	110(2)	100(2)	110(2)
Unit Cell[a]	Orthorhombic	Triclinic	Orthorhombic	Triclinic	Triclinic	Monoclinic
a, Å	8.1812(4)	9.8409(2)	10.2775(2)	11.4076(2)	11.6485(3)	13.8606(2)
b, Å	12.6974(6)	14.7102(3)	14.7368(3)	13.3193(2)	13.2436(4)	15.4379(2)
c, Å	18.1422(8)	14.9428(3)	16.0656(3)	14.7867(2)	15.8074(4)	16.6849(3)
α, deg	90	96.6399(7)	90	90.4060(10)	75.6490(10)	90
β, deg	90	94.6004(7)	90	105.2960(10)	75.6020(10)	108.2020(10)
γ, deg	90	97.0075(10)	90	101.1620(10)	69.4330(10)	90
V, $Å^3$	1884.61(15)	2122.80(7)	2433.25(8)	2122.11(6)	2176.54(10)	3391.56(9)
Z	4	2	4	2	2	2
d(calc), g/cm^3	1.569	1.270	1.2554	1.250	1.307	1.437
Sp. Group	$P\ 2_12_12_1$	P -1	$P\ 2_12_12_1$	P -1	$P\ \bar{1}$	$P\ 2_1/n$
R[b]	0.0209	0.0505	0.0364	0.0413	0.527	0.0390
R_w[c]	0.0474	0.1499	0.0941	0.1091	0.1146	0.0933
GOF	1.036	1.071	1.018	1.020	1.004	1.013

[a]In all cases: Mo Kα(λ = 0.7170 Å) radiation. [b]$R = \Sigma||F_0| - |F_c||/ \Sigma|F_0|$. [c]$R_w = [\Sigma w(|F_0| - |F_c|)^2/ \Sigma wF_0^{1/2}$, where $w^{-1} = [\sigma_{count}^2 + (0.05F^2)^2]4F^2$.

number of cases to have dramatic effects upon the structural and electronic properties of first-row transition metal complexes containing polydentate pyridine-containing ligands.[46-47] The steric congestion imposed by the pyridine methyl substituents upon the open coordination sites in **4** and **5**, and the extra aromatic rings in **8** and **9**, are clearly evident from the ball and stick and space-filling diagrams of alkyl amine-ligated **1** compared with **4**, **5**, **8**, and **9** (Figure 2.5).

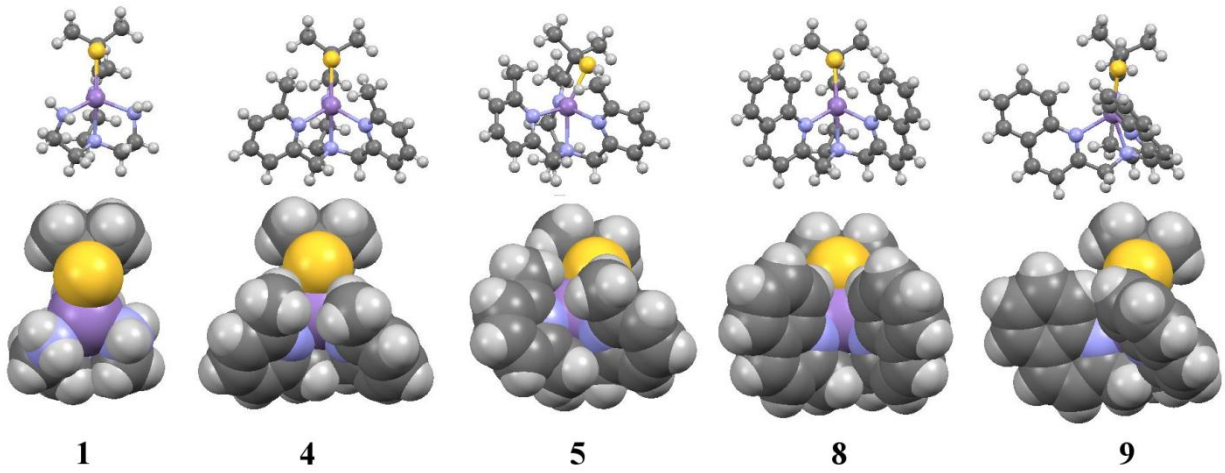

Figure 2.5 Ball and stick (top) and space-filling (bottom) diagrams of $[Mn^{II}(S^{Me2}N_4(tren))]^+$ (**1**), $[Mn^{II}(S^{Me2}N_4(6\text{-Me-DPEN}))]^+$ (**4**), $[Mn^{II}(S^{Me2}N_4(6\text{-Me-DPPN}))]^+$ (**5**), $[Mn^{II}(S^{Me2}N_4(2\text{-QuinoEN}))]^+$ (**8**), and $[Mn^{II}(S^{Me2}N_4(2\text{-QuinoPN}))]^+$ (**9**). All molecular representations are projected down the Mn-N(1) (Mn-imine) bond for consistency.

The coordination geometries of complexes **1**-**2**, **4**-**5**, and **8**-**9** are found to vary from distorted trigonal bipyramidal to square pyramidal (τ(**1**) = 0.55, τ(**2**) = 0.47, τ(**4**) = 0.59, τ(**5**) = 0.22, τ(**8**) = 0.55, and τ(**9**) = 0.05), with complexes containing an ethyl alkyl linker exhibiting trigonal bipyramidal geometries and those with a propyl alkyl linker being closer to square pyramidal (Table 2.1).[48] These observations indicate that increasing the alkyl spacer length by one methylene unit has a considerable impact upon the coordination geometry of these complexes. This effect has previously been observed when comparing the structures of five-coordinate *bis*-thiolate-ligated $[Fe^{III}(S_2{}^{Me2}N_3(Et,Pr))]^+$ and $[Fe^{III}(S_2{}^{Me2}N_3(Pr,Pr))]^+$, although the

addition of an extra methylene unit in the latter complex was found to promote a more trigonal bipyramidal geometry.[49]

The Mn-S(1) bond distances in N-heterocyclic-ligated **4**-**5** and **8**-**9** range from 2.3710(6) Å to 2.3835(9) Å (Table 2.1) and are very similar to the Mn-SR bonds in aromatic thiolate-ligated $[Mn^{II}_4(SPh)_{10}]$ and $[Mn^{II}\{HB\text{-}(3,5\text{-}Me_2pz)_3\}(SC_6F_5)]$ (Mn-SR = 2.38(1) Å (mean length) and 2.385(3) Å, respectively), but shorter than those in alkyl thiolate-ligated $[Mn^{II}(edt)_2]^{2-}$ and **1** (Mn-SR = 2.432(7) Å and 2.412(3) Å, respectively).[50-51] The π-accepting N-heterocyclic moieties found in **4**-**5** and **8**-**9** should increase the metal ion Lewis acidity relative to structurally analogous **1**, which could explain the shorter Mn-S(1) bonds in these complexes relative to that in **1**. Complex **2** also has a longer Mn-S(1) bond (2.4597(6) Å) compared to those in **4**-**5** and **8**-**9** (Table 2.1), which presumably is due to the coordination of methanol. Differences in spin state do not factor into considerations made for these metrical parameters, as all complexes discussed herein are high-spin (S = 5/2, *vide infra*).

In contrast to the mononuclear X-ray crystal structures obtained for **1**, **2**, **4**, **5**, **8**, and **9**, the ORTEP diagrams of **3** and **6** reveal dimeric Mn(II) complexes. These structures illustrate the propensity of alkyl thiolate ligands to form bonds with multiple metals and result in polynuclear complexes. This property is frequently exploited by Nature, as is evident by the presence of metal-sulfur clusters and other multinuclear metal-sulfur species in metalloenzyme active sites. For synthetic attempts towards obtaining mononuclear metal-thiolate complexes, this property is clearly a disadvantage and often requires the design of ligands which restrict the flexibility of the thiolate moiety. The gem-dimethyls found adjacent to the thiolate sulfur in each complex are rational parts of this ligand design, as the Kovacs group has previously proposed that these substituents can provide a suitable amount of steric congestion to prevent the dimerization of

thiolate-ligated first-row transition metal complexes.[26] The presence of bulky pyridine substituents in the 6 position, or replacement of the pyridine moieties with quinolines, appears to also help stabilize mononuclear complexes as is suggested by the X-ray crystal structures of **2**-**9** (Figures 2.2 -2.5).

Dimeric complex **3** contains two Mn(II) ions that are each ligated by two alkyl thiolate sulfurs (S(1) and S(2)), an imine nitrogen (N(1)), a tertiary amine (N(2), and two pyridine nitrogens (N(3) and N(4)) (Figure 2.4). Each half of **3** is equivalent regarding bond distances and angles, therefore only metrical parameters associated with Mn(1) are discussed. Both Mn-S distances in **3** (Mn(1)-S(1) = 2.4854(10) Å and Mn(1)-S(2) = 2.6051(10) Å) are longer than those observed in **1**, **2**, **4**, **5**, **8**, and **9**, which is likely explained by this complex existing a dimer instead of a monomer and each sulfur being bound to two metal ions. The Mn(1)-N(1), Mn(1)-N(3), and Mn(1)-N(4) distances are also longer than those in the respective mononuclear counterparts and can be rationalized through similar reasoning, although the Mn(1)-N(1) distance may be notably elongated as a result of the *trans* influence from the second thiolate ligand bound to each Mn ion (N(1)-Mn(1)-S(2) = 168.53(3)°). In contrast to these five Mn-L bonds, the Mn(1)-N(2) distance is shorter in **3** (2.218(3) Å) relative to the mononuclear Mn(II) complexes (2.2424(16)-2.359(16) Å).

Unlike the X-ray structure for **3**, complex **6** contains only single bridging thiolate sulfur (Figure 2.4). All three Mn-S distances (Mn(1)-S(1) = 2.4555(18) Å, Mn(2)-S(2) = 2.4654(18) Å, Mn(2)-S(1) = 2.5880(18) Å) are similar to those observed in **3**. This notably includes Mn(2)-S(2), in which S(2) does not bridge the two Mn ions. The *trans* influence of the bridging thiolate ligand is again evident from the elongated Mn(2)-N(5) distance (2.329(6) Å, S(1)-Mn(2)-N(5) = 172.59(15)°). The chloride ligand (Cl(1)) found in the X-ray structure of **6** is unexpected and can only be explained by chloride being present in the L_6 used during the synthesis of this

complex (chloride salts are involved in the ligand synthesis, Scheme 2.1). Derivatives of **6** without the chloride ligand were not obtained, although the X-ray structure for this complex does provide evidence that bulky substituents at the pyridine 6 position may be critical in obtaining a mononuclear and coordinatively unsaturated ligated Mn(II) complex with this type of ligand framework.

2.3.2 Magnetic, Spectroscopic, and Electrochemical Characterization of Thiolate-Ligated Mn(II) Complexes 1-6 and 8-9

With the exception of only a few synthetic compounds, Mn(II) exists with a sextet ground state (S = 5/2) in all ligand environments. Solid-state magnetic susceptibility measurements were made for **1**-**5** and **8**-**9** by SQUID magnetometry over a temperature range of 5-300 K and are consistent with this general observation. As shown in Figures 2.6-2.11, each complex displays Curie-Weiss behavior from 5–300 K (except for **2**, as data was only collected from 25-300 K) and all experimental data were fit to afford effective magnetic moments per Mn ion (μ_{eff}/Mn) of 5.88 B.M. (**2**), 5.93 B.M. (**3**), 5.83 B.M. (**4**), 5.57 B.M. (**5**), 5.78 B.M. (**8**), and 5.91 B.M. (**9**). Each of these values are close to the theoretical spin-only value of 5.92 B.M. for an S = 5/2 spin state. Solid-state magnetic susceptibility measurements for **1** have previously been reported to result in a μ_{eff} value of 6.01 B.M., supporting a high-spin state for this complex as well. Solution magnetic susceptibility measurements were made by the Evans method for each complex in ambient temperature d_4-MeOD solutions to afford μ_{eff} values of 5.90 B.M. (**1**), 5.79 B.M (**2**), 5.70 B.M. per Mn (**3**), 5.89 B.M. (**4**), 5.78 B.M. (**5**), 5.83 B.M. (**8**), and 5.98 B.M. (**9**); each measurement again supporting a high-spin state for these complexes in solution. All magnetic data is summarized in Table 2.3.

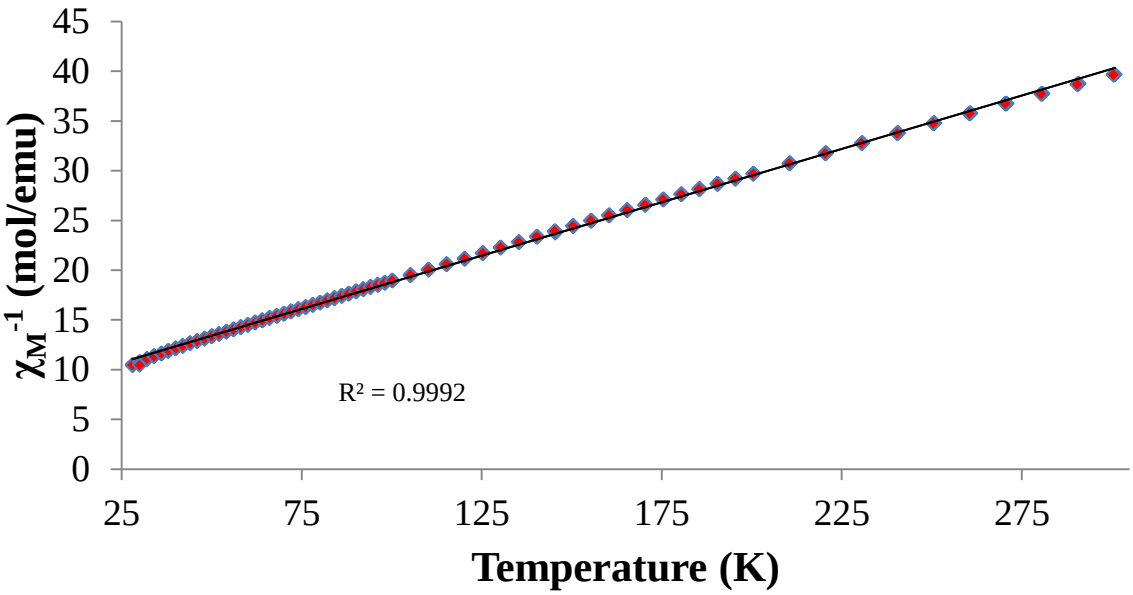

Figure 2.6 Inverse molar magnetic susceptibility (χ_M^{-1}) versus temperature (T) for $[Mn^{II}(S^{Me2}N_4(6\text{-H-DPEN}))(MeOH)](PF_6)\cdot MeOH$ (**2**).

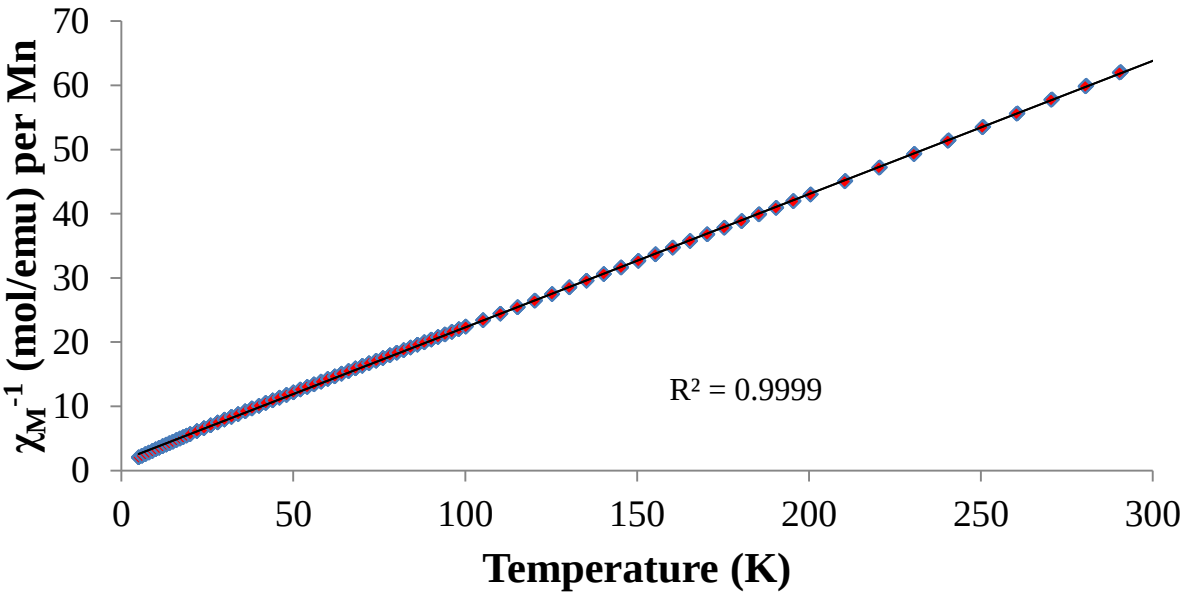

Figure 2.7 Inverse molar magnetic susceptibility (χ_M^{-1}) versus temperature (T) for $[Mn^{II}(S^{Me2}N_4(6\text{-H-DPPN}))]_2(BF_4)_2$ (**3**).

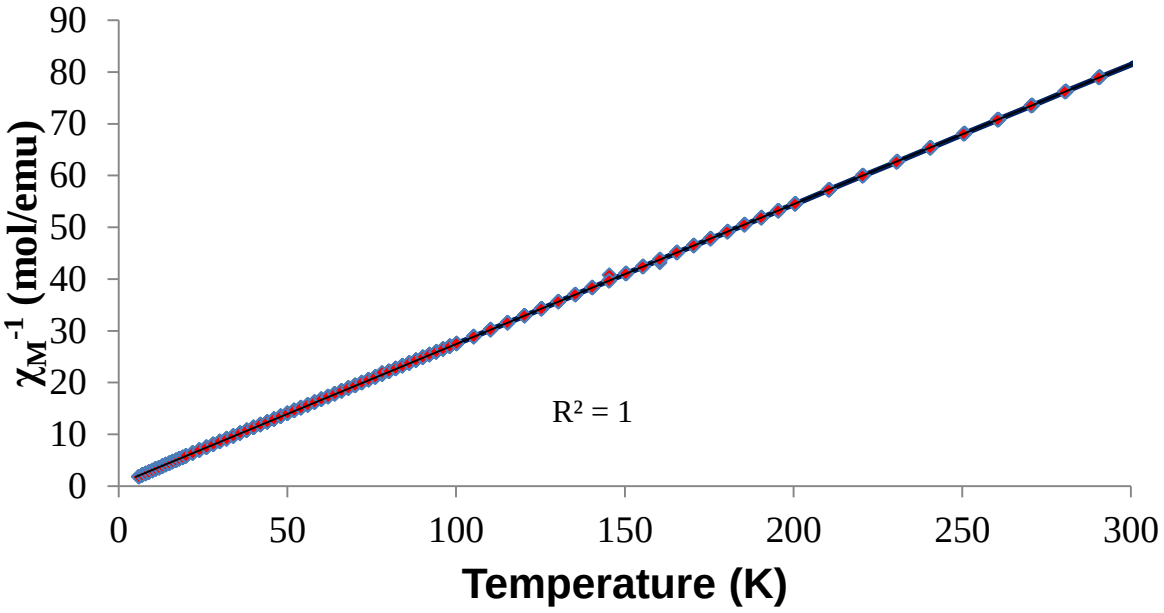

Figure 2.8 Inverse molar magnetic susceptibility (χ_M^{-1}) versus temperature (T) for [$Mn^{II}(S^{Me2}N_4$(6-Me-DPEN))](BF_4) (**4**).

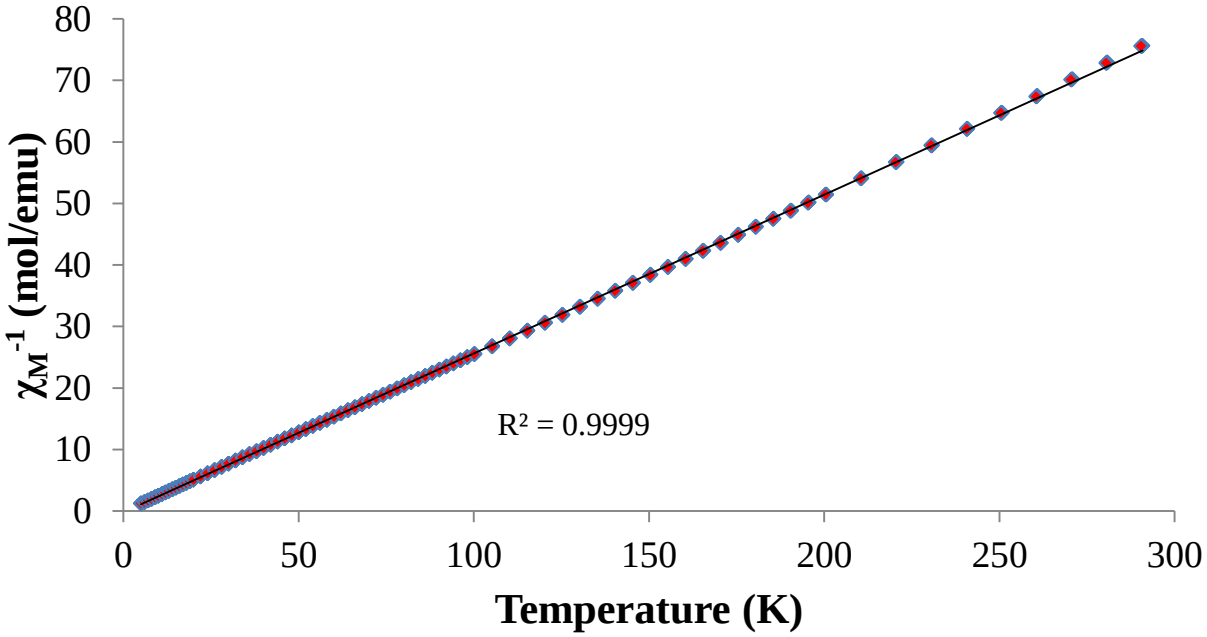

Figure 2.9 Inverse molar magnetic susceptibility (χ_M^{-1}) versus temperature (T) for [$Mn^{II}(S^{Me2}N_4$(6-Me-DPPN))](BPh_4) (**5**).

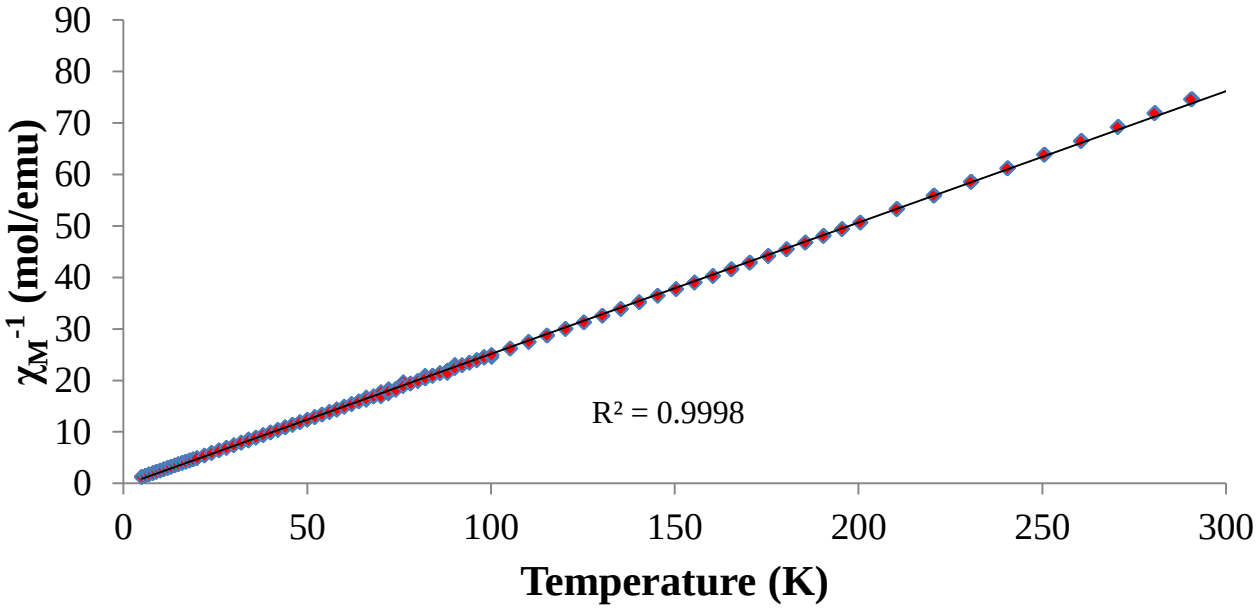

Figure 2.10 Inverse molar magnetic susceptibility (χ_M^{-1}) versus temperature (T) for $[Mn^{II}(S^{Me2}N_4(2\text{-QuinoEN}))](BPh_4)\cdot MeCN$ (**8**).

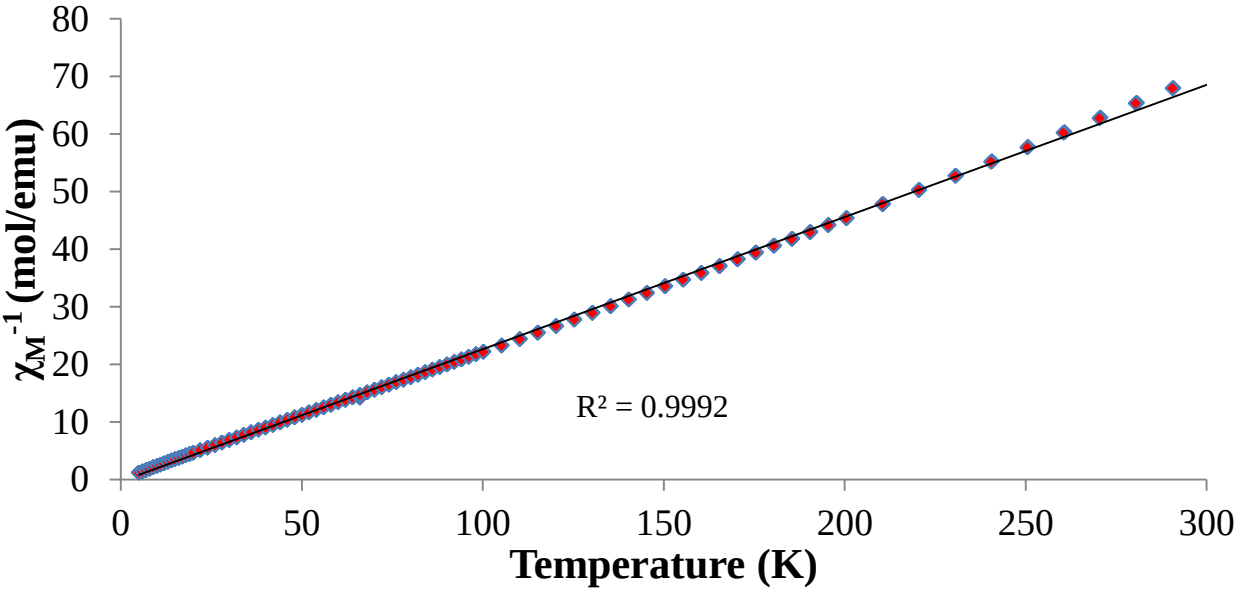

Figure 2.11 Inverse molar magnetic susceptibility (χ_M^{-1}) versus temperature (T) for $[Mn^{II}(S^{Me2}N_4(2\text{-QuinoPN}))](PF_6)$ (**9**).

The electronic absorption spectra (UV/Vis) for each complex were found to be featureless throughout the visible spectral region in a variety of solvents (MeCN, MeOH, and CH_2Cl_2). This is expected given that ligand field transitions are both Laporté and spin forbidden for an S = 5/2 spin system. The absence of intense S(π) → Mn(d) charge transfer bands in the visible region implies that these transitions likely occur at higher energy (UV region).[52] Ligand centered π→π* transitions involving the imine and N-heterocyclic moieties are expected to contribute to the absorbance features observed in the near UV spectral region of each complex (Appendix A.1-A.7, Table 2.3).

The X-band EPR spectra of complexes **2-5** and **8-9** were obtained from MeOH/EtOH (9/1) glasses at low temperatures (4-8 K) and are provided in Figure 2.12. All six spectra display

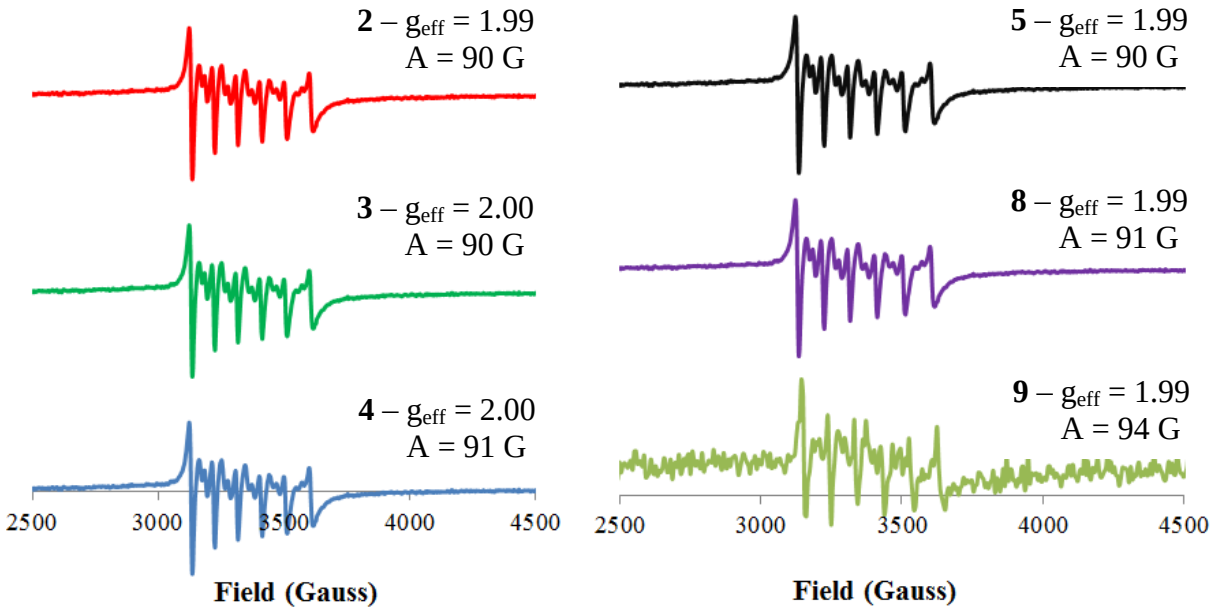

Figure 2.12 X-band (9.4 GHz) EPR spectra of $[Mn^{II}(S^{Me2}N_4(6\text{-H-DPEN}))(MeOH)](PF_6)\cdot MeOH$ (**2**, red, top left column), $[Mn^{II}(S^{Me2}N_4(6\text{-H-DPPN}))]_2(BF_4)_2$ (**3**, green, middle left column), $([Mn^{II}(S^{Me2}N_4(6\text{-Me-DPEN}))](BF_4)$ (**4**, green, bottom left column), $[Mn^{II}(S^{Me2}N_4(6\text{-Me-DPPN}))](BPh_4)$ (**5**, black, top right column), $[Mn^{II}(S^{Me2}N_4(2\text{-QuinoEN}))](BPh_4)\cdot MeCN$ (**8**, purple, middle right column), and $[Mn^{II}(S^{Me2}N_4(2\text{-QuinoPN}))](PF_6)$ (**9**, light green, bottom right column) in MeOH/EtOH glass between 4-8 K.

typical EPR features for high-spin Mn(II) ions; notably a lone transition with an effective g-value (g_{eff}) of approximately 2.00. Also characteristic of Mn EPR spectra are the presence of hyperfine splittings due to coupling between the unpaired electron spin (S = 5/2) and Mn nuclear spin (Mn^{55}; I = 5/2, 100% abundance), which ultimately results in six allowed $\Delta m_s = \pm 1$, $\Delta m_I = 0$ transitions for a mononuclear Mn(II) species (2nI + 1 transitions, where n is the number of nuclei and I is the nuclear spin). Forbidden transitions ($\Delta m_s > \pm 1$) that arise due to zero-field splitting are also observed between each of the main hyperfine lines (Figure 2.13). The hyperfine

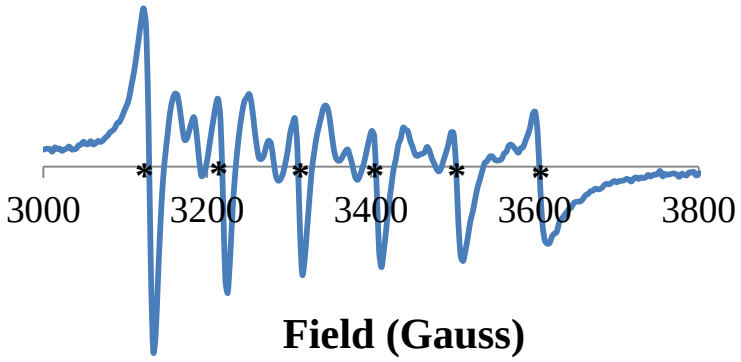

Figure 2.13 Representative X-band EPR spectrum of $[Mn^{II}(S^{Me2}N_4(2\text{-QuinoPN}))](PF_6)$ (**9**, light green trace, bottom right column) in MeOH/EtOH glass at 5 K displaying both the allowed main line features (designated with *) and forbidden transitions between each of the main lines.

coupling constant (A), or magnetic field difference between consecutive hyperfine features, is also unique for each nuclei and can be useful for determining the nuclearity of an EPR-active species. Typical A values for monomeric Mn(II) complexes range from 80-95 G, while dimeric Mn(II) complexes exhibit A values of 40-50 G. The g_{eff} and A values for **2**-**5** and **8**-**9** range from 1.99-2.00 and 90-94 G, respectively (Figure 2.12, Table 2.3), and are expected given that the X-ray crystal structures for these complexes revealed monomeric species (Figures 2.2-2.3). The

experimentally determined A value for **3** (90 G), however, is twice in magnitude what would be expected for a binuclear Mn(II) complex (Figure 2.4). Also inconsistent with a dimeric species in solution is the appearance of only six main hyperfine features in the respective X-band EPR spectrum, as a dimer would exhibit more than six lines (n = 2, 2nI + 1 transitions, *vide supra*). These experimental observations collectively suggest that **3** likely exists as a monomer in solution despite having been crystallized and characterized in the solid-state as a dimer. This would occur if, hypothetically, two Mn(II)-S bonds cleaved upon entering into solution, which is a reasonable scenario given the considerably elongated bridging Mn(II)-S bonds from the X-ray structure of **3** (Mn(1)-S(2) = Mn(2)-S(1) = 2.6051(10) Å, Figure 2.4). The X-band EPR spectrum of **1** was previously reported in MeOH/EtOH glass at 5 K and exhibited a g_{eff} = 2.00 and A = 90.

Complexes **1**-**5** and **8**-**9** were also characterized by X-band EPR experiments in neat MeCN, as this solvent served as the most suitable solvent for O_2 reactivity studies (Chapters 3-4, *vide infra*). Unfortunately, hyperfine structure was not observed in these signals (possibly due to poor glass formation), although the g_{eff} values ranged from 1.99-2.00. The energy of each spin level for a high-spin Mn(II) ion is described by the effective spin Hamiltonian provided in equation 2.1, where the first term is the Zeeman interaction, the second term is the electron-

$$\hat{H} = g\beta BS_z + AI_zS_z + (D/3)(3S_z^2 - S(S + 1)) + (E/2)(S_+^2 + S_-^2) \quad (2.1)$$

nuclear hyperfine interaction, and the last two terms describe the describe the zero-field interaction. The D and E parameters are known respectively as the axial and rhombic zero-field splitting (ZFS) parameters and collectively help define the ground state electronic structure of a paramagnetic species. In order to obtain the magnitude and sign of D, variable-temperature EPR

spectra of each complex in MeCN was collected from 5-100 K under nonsaturating experimental conditions. The normalized intensity of the $g_{eff} \approx 2.00$ signal in each spectrum was plotted as a function of temperature, from which a Boltzmann fit to the Curie law dependence for each signal affords the D parameters by equation 2.2.[53] In equation 2.2, C is the Curie constant, T is the temperature in kelvin, and *k* is the Boltzmann constant. A suitable fit to the variable-temperature data collected for complex **4** was obtained to afford D = 0.21 cm^{-1} (Figure 2.14). Fits to the experimental data for complexes **1**-**3**, **5**, and **8**-**9** were unsatisfactory for an accurate determination of D.

$$\text{Normalized Signal Intensity} = (C/T)[1 + \exp(-2D/kT)]^{-1} \quad (2.2)$$

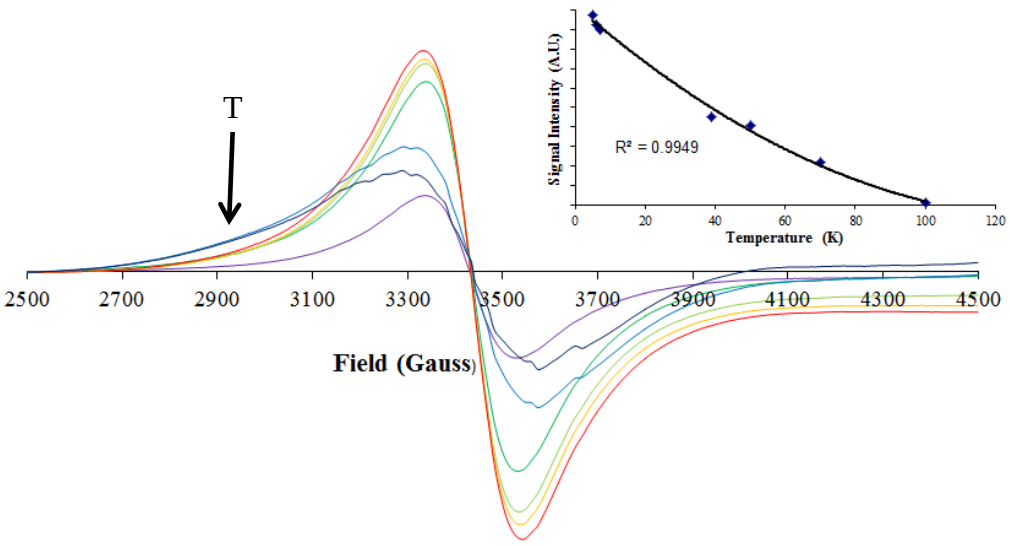

Figure 2.14 Variable-temperature X-band EPR spectra of $[Mn^{II}(S^{Me2}N_4(6\text{-Me-DPEN}))](BF_4)$ (**4**) in frozen MeCN from 5-100 K. A plot of normalized signal intensity versus temperature (K) is provided in the inset.

The electrochemical properties of complexes **2**-**5** and **8**-**9** were explored by cyclic voltammetry (CV) experiments in MeCN at room temperature (Figure 2.15). Under these

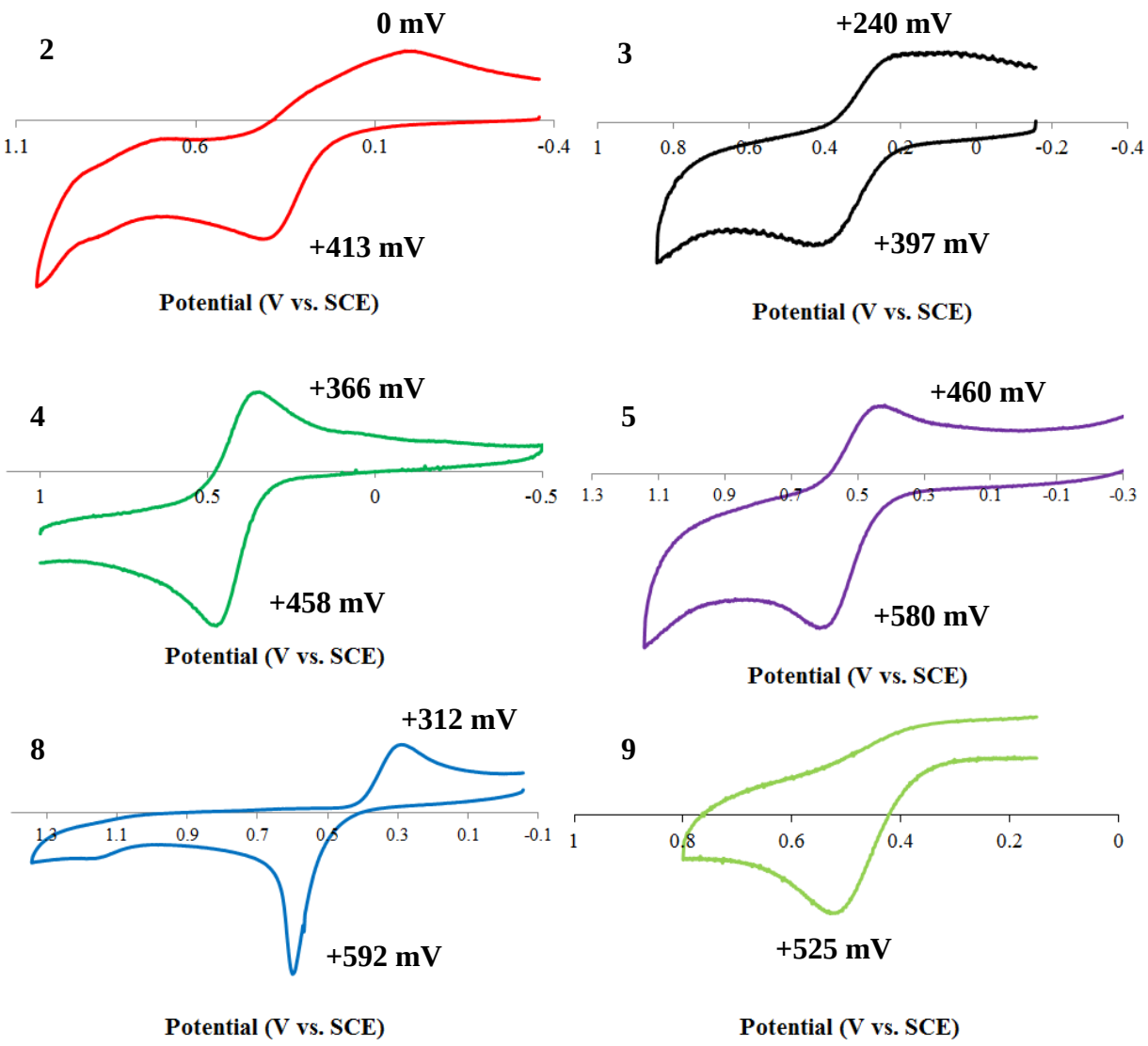

Figure 2.15 Cyclic voltammograms of $[Mn^{II}(S^{Me2}N_4(6\text{-H-DPEN}))(MeOH)](PF_6)\cdot MeOH$ (**2**, red trace, top left column), $[Mn^{II}(S^{Me2}N_4(6\text{-H-DPPN}))]_2(BF_4)_2$ (**3**, black trace, top right column), $([Mn^{II}(S^{Me2}N_4(6\text{-Me-DPEN}))](BF_4)$ (**4**, green trace, middle left column), $[Mn^{II}(S^{Me2}N_4(6\text{-Me-DPPN}))](BPh_4)$ (**5**, purple trace, middle right column), $[Mn^{II}(S^{Me2}N_4(2\text{-QuinoEN}))](BPh_4)\cdot MeCN$ (**8**, blue trace, bottom left column), and $[Mn^{II}(S^{Me2}N_4(2\text{-QuinoPN}))](PF_6)$ (**9**, light green trace, bottom right column) in MeCN vs. SCE. Each experiment was performed with a 0.1 M $^{n}Bu_4PF_6$ supporting electrolyte and with a scan rate of 150 $mV\cdot s^{-1}$ at room temperature. Anodic (E_{pa}) and catholic (E_{pc}) peak potentials are labeled in each voltammogram.

experimental conditions, **1** was previously reported to display a quasi-reversible $Mn^{III/II}$ couple (E_{pa} = +270 mV, E_{pc} = -10 mV versus the saturated calomel electrode, SCE) and reversible $Mn^{IV/III}$ couple ($E_{1/2}$ = +705 mV vs. SCE, ΔE = 110 mV).[26] Complexes **2-5** and **8** display either fully reversible or quasi-reversible $Mn^{III/II}$ couples at relatively moderate potentials (200-500 mV vs. SCE) at a scan rate of 150 $mV \cdot sec^{-1}$. Unlike **1**, these complexes do not display a wave at higher potentials that could potentially be attributed to a $Mn^{IV/III}$ redox couple. The cyclic voltammogram of **9** only contained a clearly discernible anodic wave, suggesting this complex in unstable upon oxidation. All electrochemical data are summarized along with the corresponding magnetic and spectroscopic data in Table 2.3.

Insights into how ligand structure may influence the redox properties of the Mn ions in **1-5** and **8-9** are suggested by a few noteworthy trends in the electrochemical data. The $Mn^{III/II}$ $E_{1/2}$ values for N-heterocyclic-containing **2-5** and **8** (+207 to +520 mV vs. SCE, Table 2.3) are all at higher potentials relative to that of alkyl amine-ligated **1** (+140 mV vs. SCE, Table 2.3), suggesting the N-heterocyclic moieties do promote a more electron-deficient Mn center. When comparing only the complexes containing N-heterocyclic ligand moieties, **2-5** and **8-9**, it is evident that the complexes without substituted pyridine rings (**2** and **3**) display $Mn^{III/II}$ couples at more negative potentials relative to complexes containing 6-methylpyridine (**4** and **5**) or quinoline (**8** and **9**) moieties (Figure 2.14, Table 2.3). This particular observation may result from the presence of a coordinated MeOH ligand in **2** (and possibly a solvent ligand bound to **3** if indeed it exists as a monomer in solution, *vide supra*), however there is no clear evidence to suggest that solvent ligands do not coordinate to the other complexes (**4**-**5**, **8**-**9**) in solution, as well. Finally, comparisons made between the N-heterocyclic complexes containing an ethyl backbone (**2**, **4**, and **8**) to those with a propyl backbone (**3**, **5**, and **9**) reveal that, for every set of

two complexes containing the same N-heterocycles (**2**/**3**, **4**/**5**, **8**/**9**), higher $Mn^{III/II}$ couples are found with the member of each pair containing a propyl alkyl linker (Figure 2.14, Table 2.3). It is worthwhile to note that these electrochemical values do not directly correlate with any particular set of metrical parameters, such as the lengths of the Mn-S(1) bonds (Table 2.1).

Table 2.3 Magnetic, spectroscopic, and electrochemical data for $[Mn^{II}(S^{Me2}N_4(tren))](PF_6)$ (**1**), $[Mn^{II}(S^{Me2}N_4(6\text{-H-DPEN}))(MeOH)](PF_6)\cdot MeOH$ (**2**), $[Mn^{II}(S^{Me2}N_4(6\text{-H-DPPN}))]_2(BF_4)_2$ (**3**), $[Mn^{II}(S^{Me2}N_4(6\text{-Me-DPEN}))](BF_4)$ (**4**), $[Mn^{II}(S^{Me2}N_4(6\text{-Me-DPPN}))](BPh_4)$ (**5**), $[Mn^{II}(S^{Me2}N_4(2\text{-QuinoEN}))](BPh_4)\cdot MeCN$ (**8**), and $[Mn^{II}(S^{Me2}N_4(2\text{-QuinoPN}))](PF_6)$ (**9**).

	1	**2**	**3**	**4**	**5**	**8**	**9**
μ_{eff} (solid)[a]	6.01	5.88	5.93	5.83	5.57	5.78	5.91
μ_{eff} (sol'n)[b]	5.90	5.79	5.70	5.89	5.78	5.83	5.98
λ_{max} (nm)[c]	232	283	272	317	282	325	320
$(\varepsilon, M^{-1}cm^{-1})$[c]	(2880)	(1690)	(1637)	(350)	(1655)	(3720)	(2570)
g_{eff} (A, G)[d]	2.00 (90)	1.99 (90)	2.00 (90)	2.00 (91)	1.99 (90)	1.99 (91)	1.99 (94)
$E_{1/2}$ (mV)[e]	+140	+207	+319	+412	+520	+452	N/A
E_{pa} (mV)[e]	+270	+413	+397	+458	+580	+592	+525
E_{pc} (mV)[e]	-10	0	+240	+366	+460	+312	N/A
ΔE (mV)[e]	280	413	157	92	120	280	N/A

[a]Measurements made by SQUID magnetometry. [b]Evans method measurements, d_4-MeOD, ambient temperature. [c]MeCN solution, ambient temperature. [d]X-band EPR measurements, MeOH/EtOH glass, 4-8 K. [e]MeCN, ambient temperature, 0.1 M $^nBu_4PF_6$ supporting electrolyte, referenced versus SCE, $Ag^+/AgNO_3$ reference electrode, Pt auxillary electrode, GC working electrode.

2.3.3 Synthesis and Structural Characterization of Alcohol-, Alkoxide- And Amine-Ligated Mn(II) Complexes – Comparisons to Thiolate-Ligated Mn(II) Complexes

In order to further understand the influence thiolate-ligation may have upon the structural, magnetic, or spectroscopic properties of the monomeric Mn(II) complexes discussed above, synthetic attempts were made towards analogues of these complexes in which the thiolate was replaced by either an alkoxide or amine moiety. The general synthetic strategy used for these derivatives is identical to that shown in Scheme 2.1, except that 3-mercapto-3-methyl-2-butanone was replaced by either 3-hydroxy-3-methyl-2-butanone (for the alkoxide-ligated analogues) or diethylaminoacetone (for the amine-ligated analogues). Derivatives of **1** were the

first to be explored; these synthetic attempts resulted in the isolation of a dialkoxide-bridged Mn(II) dimer, $[Mn^{II}(O^{Me2}N_4(tren))]_2(PF_6)_2 \cdot MeCN$ (**10**), and a sulfate-bridged Mn(II) dimer, $[Mn^{II}(N^{Et2}N_4(tren))]_2(\mu\text{-}SO_4)(BPh_4)_2$ (**11**). The ORTEP diagrams for **10** and **11** are provided in Figure 2.16, while selected metrical parameters and crystal data is compiled in Tables 2.4 and 2.5, respectively.

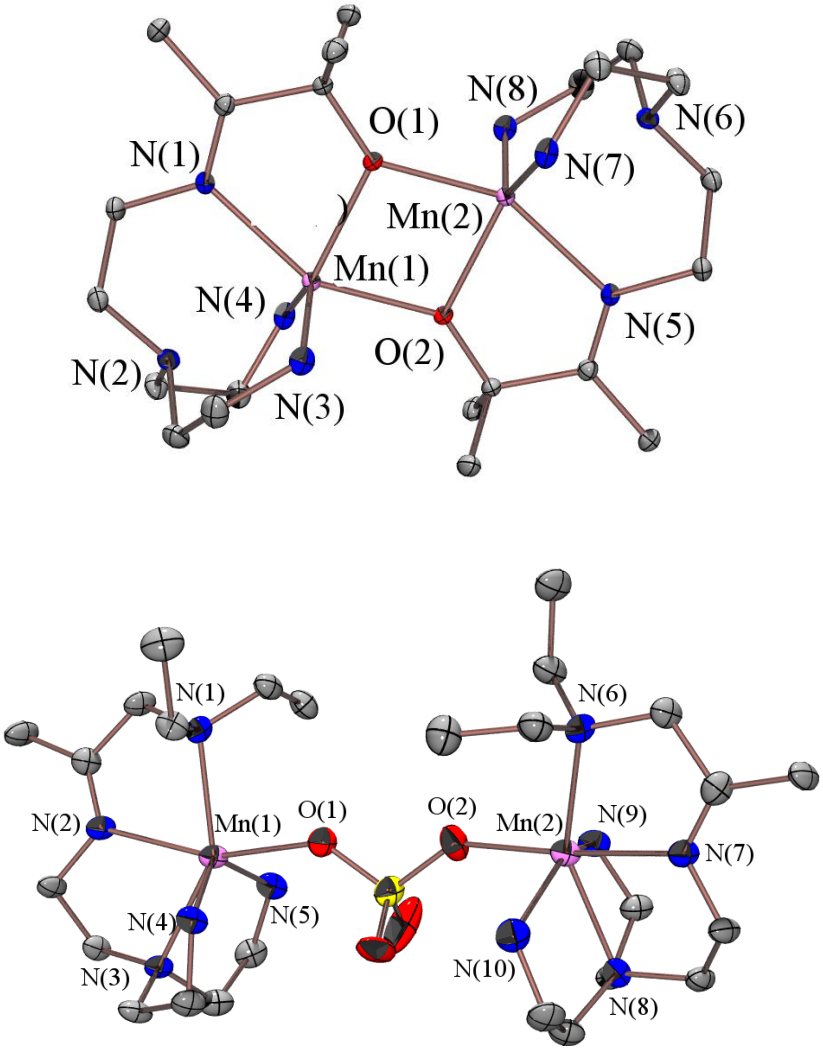

Figure 2.16 ORTEP diagram (50 % probability) of $\{[Mn^{II}(O^{Me2}N_4(tren))]_2\}^{2+}$ (**10**) (top) and $\{[Mn^{II}(N^{Et2}N_4(tren))]_2(\mu\text{-}SO_4)\}^{2+}$ (**11**) (bottom) with hydrogen atoms, counterions, and solvents of crystallization omitted for clarity. A ChemDraw representation of **10** is also provided with emphasis upon the Mn ions and coordinating atoms.

Dialkoxide-bridged **10** contains two Mn(II) ions that are each coordinated by two alkoxide oxygens (O(1) and O(2), an imine nitrogen (N(1), tertiary amine (N(2), and two primary amines (N(3) and N(4)). Sulfate-bridged **11** also contains two Mn(II) ions which are each coordinated by two tertiary amine nitrogens (N(1) and N(3) or N(6) and N(8)), an imine nitrogen (N(2) or N(3)), two primary amine nitrogens (N(4) and N(5) or N(9) and N(10)), and a sulfate oxygen (O(1) or O(2)). All metrical parameters associated with each the two Mn(II) ions in **10** are equivalent, therefore only the metrics relevant to Mn(1) are included in Table 2.4. Both complexes display longer Mn-imine, Mn-tertiary amine, and Mn-primary amine distances relative to those in **1**, presumably due to these complexes being dimers.

In order to prevent dimerization, the synthetic strategy in Scheme 2.1 was slightly modified by using two equivalents of 3-hydroxy-3-methyl-2-butanone and $NaOCH_3$ instead of one. The rationale behind these experiments was that dimerization could be prevented if Mn(II)-templated Schiff base condensations between two primary amines in *tris*(2-aminoethyl)amine (tren) and 3-hydroxy-3-methyl-2-butanone were achieved to yield a more sterically-congested dialkoxide-ligated Mn(II) species. Condensing two equivalents of 3-hydroxy-3-methyl-2-butanone with tren was successful; however a dialcohol product was isolated and characterized instead of the desired dialkoxide complex. The ORTEP diagram of $[Mn^{II}((HO^{Me2})_2N_4(tren))(MeOH)](BPh_4)_2 \cdot MeOH$ (**12**) is provided in Figure 2.17, while selected metrical parameters and crystal data are compiled in Table 2.4 and 2.5, respectively. As is seen in Figure 2.16, the Mn(II) ion in **12** is found in a distorted pentagonal bipyramidal coordination environment containing three alcohol oxygens (O(1), O(2), and O(3)), two imine nitrogens (N(1)

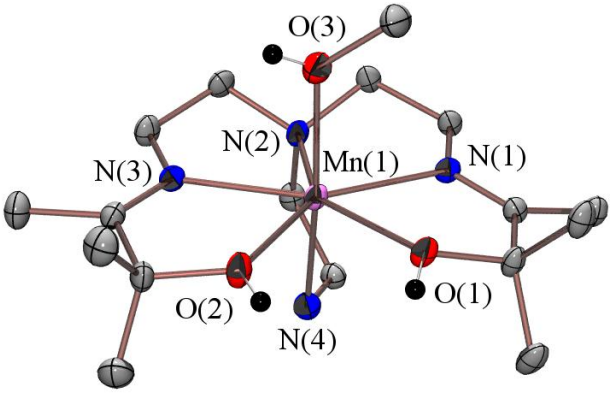

Figure 2.17 ORTEP diagram (50 % probability) of $[Mn^{II}((HO^{Me2})_2N_4(tren))(MeOH)]^{2+}$ (**12**) with most hydrogen atoms, counterions, and solvent of crystallization omitted for clarity. Alcohol protons are shown in black.

and N(3)), a tertiary amine (N(2)), and a primary amine (N(4)). The protons present on each of the coordinating oxygen atoms were visible in the crystallographic difference map and supported by the presence of two anionic counterions (BPh_4^-) for each complex.

Analogues of N-heterocyclic-containing **4** and **5** were also pursued. Similar to **12**, synthetic attempts toward an alkoxide-ligated analogue of **4** via the synthetic strategy in Scheme 2.1 resulted in the isolation of a mononuclear alcohol-ligated Mn(II) product, $[Mn^{II}(HO^{Me2}N_4(6\text{-}Me\text{-}DPEN)(MeCN))](BPh_4)_2$ (**13**). Reactions were also performed using $Mn(CHO_2)_2$ as a staring reagent, however an alcohol-ligated product, $[Mn^{II}(HO^{Me2}N_4(6\text{-}Me\text{-}DPEN)(CHO_2))](BPh_4)\cdot MeCN\cdot Et_2O$ (**14**), was again obtained from these reactions instead of the desired alkoxide complex. The only mononuclear alkoxide-ligated derivative of the thiolate complexes **1**-**5** or **8**-**9** that has been successfully isolated and characterized is an analogue of **5**, $[Mn^{II}(O^{Me2}N_4(6\text{-}Me\text{-}DPPN))](BPh_4)$ (**15**). The ORTEP diagrams of **13**-**15** are shown in Figure 2.18. Selected metrical parameters and crystal data for **13**-**15** are compiled in Tables 2.4 and 2.5,

respectively. The X-ray crystal structure of **14** was found to contain a hydrogen bonded tetramer of Mn(II) complexes within the asymmetric unit; an ORTEP diagram representing this hydrogen bonded network is provided in Figure 2.19.

Alcohol-ligated **13** and **14** are each six coordinate complexes with either MeCN (**13**) or formate (**14**) bound to the Mn(II) center *trans* to the imine nitrogen. It is surprising that the alcohol moieties in these complexes, as well as those in complex **12**, are protonated despite being synthesized in the presence of $NaOCH_3$. Assuming that coordination of these moieties to a Lewis acid (Mn(II)) would decrease the respective alcohol pK_a values, $NaOCH_3$ was anticipated to serve as a sufficient base for deprotonation. Reactions were also performed in which excess

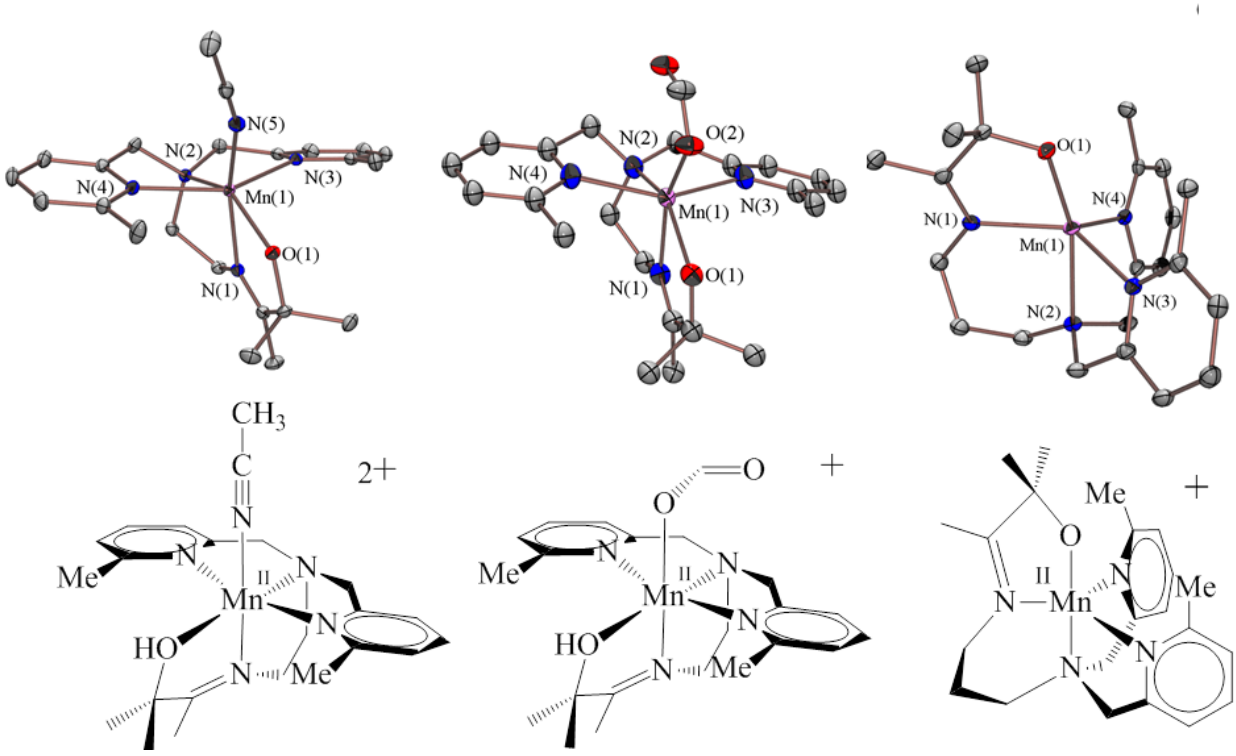

Figure 2.18 ORTEP diagram (50 % probability) of $[Mn^{II}(HO^{Me2}N_4(6\text{-Me-DPEN})(MeCN))]^{2+}$ (**13**), $[Mn^{II}(HO^{Me2}N_4(6\text{-Me-DPEN})(CHO_2))]^{+}$ (**14**), and $[Mn^{II}(O^{Me2}N_4(6\text{-Me-DPPN}))]^{+}$ (**15**) with hydrogen atoms, counterions, and solvents of crystallization omitted for clarity.

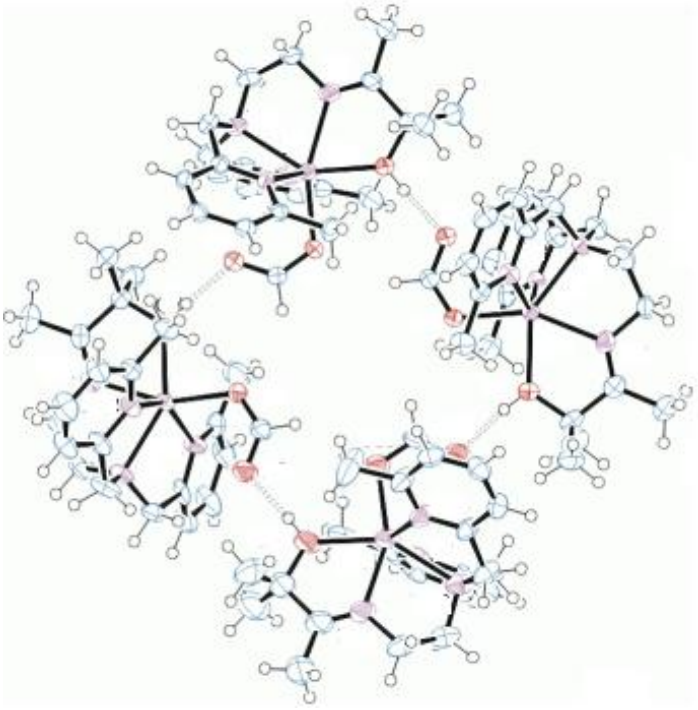

Figure 2.19 ORTEP diagram (50 % probability) of the asymmetric unit for **14**. Counterions and solvents of crystallization have been omitted for clarity.

amounts of $NaOCH_3$ (10-50 equivalents) were added to individual solutions containing **12-14**, followed by multiple recrystallizations in order to isolate the desired alkoxide complexes. These attempts resulted only in the formation of unidentified white precipitates. The precipitates isolated from these reactions were found to be completely insoluble in a wide range of organic solvents unless a proton source (MeOH, AcOH) was introduced to each reaction solution. NaOH was also used in attempt to deprotonate the alcohol moieties in these complexes, however these reactions also resulted in the formation of insoluble white precipitates.

Table 2.4 Selected bond distances (Å) and angles (degrees) for $[Mn^{II}(O^{Me2}N_4(tren))]_2(PF_6)_2\cdot MeCN$ (**10**), $[Mn^{II}(N^{Et2}N_4(tren))]_2(\mu\text{-}SO_4)(BPh_4)_2$ (**11**), $[Mn^{II}((HO^{Me2})_2N_4(tren))(MeOH)](BPh_4)_2\cdot MeOH$ (**12**), $[Mn^{II}(HO^{Me2}N_4(6\text{-Me-DPEN})(MeCN))](BPh_4)_2$ (**13**), $[Mn^{II}(HO^{Me2}N_4(6\text{-Me-DPEN})(CHO_2))](BPh_4)\cdot MeCN\cdot Et_2O$ (**14**), and $[Mn^{II}(O^{Me2}N_4(6\text{-Me-DPPN}))](BPh_4)$ (**15**).

	10	**11**	**12**	**13**	**14**	**15**
Mn-O(1)	2.1099(8)	2.093(5)	2.251(2)	2.203(10)	2.172(4)	1.9585(14)
Mn-O(2)	2.1312(8)	N/A	2.233(2)	N/A	2.118(3)	N/A
Mn-O(3)	N/A	N/A	2.205(2)	N/A	N/A	N/A
Mn-N(1)	2.2307(10)	2.325(5)	2.269(2)	2.2027(9)	2.248(3)	2.2184(19)
Mn-N(2)	2.5045(10)	2.216(5)	2.356(2)	2.2798(9)	2.329(3)	2.2962(17)
Mn-N(3)	2.2882(10)	2.334(5)	2.265(2)	2.3157(10)	2.267(3)	2.2293(18)
Mn-N(4)	2.2792(10)	2.267(5)	2.279(2)	2.2784(10)	2.275(3)	2.1931(18)
Mn-N(5)	N/A	2.294(5)	N/A	2.2254(10)	N/A	N/A
O(1)-Mn-N(1)	73.75(3)	99.74(19)	68.57(3)	69.95(3)	70.10(9)	77.95(6)
O(1)-Mn-N(2)	144.09(3)	172.3(2)	141.25(3)	147.53(3)	137.91(9)	162.39(7)
O(1)-Mn-N(3)	120.21(4)	110.97(19)	144.331(2)	105.39(3)	116.68(9)	118.62(6)
O(1)-Mn-N(4)	106.67(4)	82.1(2)	92.85(3)	108.30(4)	110.18(10)	105.96(6)
O(1)-Mn-O(2)	79.32(3)	N/A	78.48(3)	N/A	83.98(10)	N/A
N(1)-Mn-N(3)	95.04(4)	149.28(19)	147.07(8)	102.24(3)	100.76(12)	112.41(7)
N(1)-Mn-N(4)	104.38(4)	107.85(19)	88.16(8)	86.94(3)	119.04(9)	133.98(7)
N(3)-Mn-N(4)	132.54(4)	75.55(18)	88.16(9)	146.22(3)	104.16(9)	105.51(6)
O(2)-Mn-N(1)	151.48	N/A	144.47(3)	N/A	158.63(11)	N/A
O(2)-Mn-N(2)	136.25(3)	N/A	141.24(8)	N/A	126.62(11)	N/A
O(2)-Mn-N(3)	90.40(3)	N/A	60.08(8)	N/A	89.22(11)	N/A
O(2)-Mn-N(4)	92.06(3)	N/A	98.09(3)	N/A	85.98(11)	N/A
O(2)-Mn-N(5)	N/A	N/A	N/A	N/A	N/A	N/A
Mn(1)-O(1)-Mn(2)	100.68	N/A	N/A	N/A	N/A	N/A
τ	N/A	N/A	N/A	N/A	N/A	0.47

Table 2.5 Crystal data for $[Mn^{II}(O^{Me2}N_4(tren))]_2(PF_6)_2 \cdot MeCN$ (**10**), $[Mn^{II}(N^{Et2}N_4(tren))]_2(\mu\text{-}SO_4)(BPh_4)_2$ (**11**), $[Mn^{II}((HO^{Me2})_2N_4(tren))(MeOH)](BPh_4)_2 \cdot MeOH$ (**12**), $[Mn^{II}(HO^{Me2}N_4(6\text{-Me-}DPEN)(MeCN))](BPh_4)_2$ (**13**), $[Mn^{II}(HO^{Me2}N_4(6\text{-Me-}DPEN)(CHO_2))](BPh_4) \cdot MeCN \cdot Et_2O$ (**14**), and $[Mn^{II}(O^{Me2}N_4(6\text{-Me-}DPPN))](BPh_4)$ (**15**).

	10	**11**	**12**	**13**	**14**	**15**
Formula	$C_{26}H_{56}F_{12}Mn_2N_{10}O_2P$	$C_{76}H_{105}B_2Mn_2N_{11}O_4S$	$C_{135}H_{176}B_4Mn_2N_8O_{11}$	$C_{73}H_{76}B_2MnN_6O$	$C_{394}H_{451}B_8Mn_8N_{43}O_{25}$	$C_{46}H_{51}BMnN_4O$
MW	940.63	1400.27	2239.96	1129.96	6714.98	741.66
T, K	100(2)	110(2)	130(2)	100(2)	100(2)	100(2)
Unit Cell[a]	Monoclinic	Monoclinic	Triclinic	Triclinic	Triclinic	Triclinic
a, Å	10.7523(7)	11.0686(13)	12.2328(7)	12.7936(8)	19.2352(8)	9.6744(6)
b, Å	13.2427(9)	28.376(4)	14.1700(8)	23.6188(14)	20.8100(10)	13.1126(8)
c, Å	14.9055(10)	24.203(3)	18.0290(10)	23.6569(15)	23.8489(11)	15.6697(9)
α, deg	90	90	98.597(3)	60.919(3)	93.329(2)	86.880(4)
β, deg	105.278(3)	102.720(7)	100.582(3)	88.719(3)	102.293(2)	82.992(4)
γ, deg	90	90	92.814(3)	83.578(3)	99.785(2)	76.867(3)
V, $Å^3$	2047.4(2)	7415.0(16)	3028.0(3)	6203.8(7)	9147.6(7)	1920.6(2)
Z	2	4	1	4	1	2
d(calc), g/cm^3	1.526	1.254	1.228	1.210	1.3219	1.282
Sp. Group	P $2_1/c$	P $2_1/c$	P -1	P $\bar{1}$	P -1	P -1
R[b]	0.0239	0.0902	0.0622	0.0338	0.0682	0.0464
R_w[c]	0.0634	0.2172	0.1514	0.0939	0.2068	0.1072
GOF	1.019	1.055	0.975	1.019	1.067	1.016

[a]In all cases: Mo Kα(λ = 0.7170 Å) radiation. [b]$R = \Sigma||F_0| - |F_c||/ \Sigma|F_0|$. [c]$R_w = [\Sigma w(|F_0| - |F_c|)^2/ \Sigma wF_0^{1/2}$, where $w^{-1} = [\sigma_{count}^2 + (0.05F^2)^2]4F^2$.

Although only one mononuclear five-coordinate amine- or alkoxide-ligated analogue of the thiolate-ligated complexes discussed previously was successfully obtained and characterized (complex **15**), **10**-**15** do offer indirect insights into how thiolate ligation may influence the structural properties of this series of Mn(II) complexes. Replacing the thiolate ligand in **1** with an alkoxide ligand (**10**) results in the dimerization of the alkoxide-ligated complex, supporting the idea that thiolate ligands help to stabilize coordinatively unsaturated metal centers (Figures 2.2 and 2.15). This idea is further reinforced by comparing **1** with sulfate-bridged and amine-ligated **11**, although a difference in overall charge between these two complexes (+1 for **1**, +2 for **11**) likely promotes a more Lewis acidic metal center in **11** (Figures 2.2 and 2.15). Unlike the coordinatively unsaturated metal center in thiolate-ligated **4**, alcohol-ligated complexes **12** and

13 also each contain a sixth ligand. Comparisons between **4** and **12** are, however, again misleading due a difference in overall charge between the two complexes (+1 for **4**, +2 for **12**, Figures 2.2 – 2.17).

Thiolate-ligated **5** and alkoxide-ligated **15** are both mononuclear and monocationic five-coordinate Mn(II) complexes constructed with the same ligand scaffold (L_5, Scheme 2.2), therefore comparing the metrical parameters of these two complexes should provide the best insight into the structural influence of thiolate ligation (Tables 2.1 and 2.4). From the bond angles provided in Table 2.1, complex **5** is best described as having a distorted square pyramidal coordination geometry ($\tau = 0.22$). Complex **15**, on the other hand, is distorted more towards a trigonal bipyramidal coordination geometry ($\tau = 0.47$, Table 2.4). Three of the four Mn-N bond lengths in **5** (Mn-N(1), Mn-N(2), and Mn-N(4)) are also notably longer than the corresponding distances in **15** (Tables 2.1 and 2.4). The Mn-N(3) distance, which is longer in **15** than in **5**, is found within the equatorial plane of **15** and in the axial position in **5**. The observed differences in bond distances may result from variations in coordination geometry; however this could also be partially attributable to the longer Mn-S(1) distance in **5** (2.3742(3) Å) relative to the Mn-O(1) distance in **15** (1.9585(14) Å) (Tables 2.1 and 2.4). Regardless of the specific reasons for the metrical differences, complex **15** clearly demonstrates that the presence of a thiolate ligand does impact the structural properties of these Mn(II) complexes.

2.3.4 Magnetic, Spectroscopic, and Electrochemical Characterization of Alcohol-, Alkoxide- And Amine-Ligated Mn(II) Complexes 10-13 and 15

The magnetic, spectroscopic, and electrochemical properties of **10**-**12** and **14**-**15** were explored in order to provide further comparisons with the thiolate-ligated Mn(II) series **1**-**5** and

8-**9**. Solution magnetic susceptibility measurements were made for all five complexes by the Evans method in ambient temperature d_4-MeOD solutions to afford μ_{eff} values of 5.85 B.M. (**10**), 5.79 B.M. (**11**), 5.50 B.M. (**12**), 5.93 B.M. (**14**), and 6.00 B.M. (**15**), supporting a high-spin state (S = 5/2) in each case. Solid-state magnetic susceptibility measurements via SQUID magnetometry have only been made for **14**, which again yielded data to support a high-spin Mn(II) ion in this complex (μ_{eff} = 5.84 B.M., Figure 2.20).

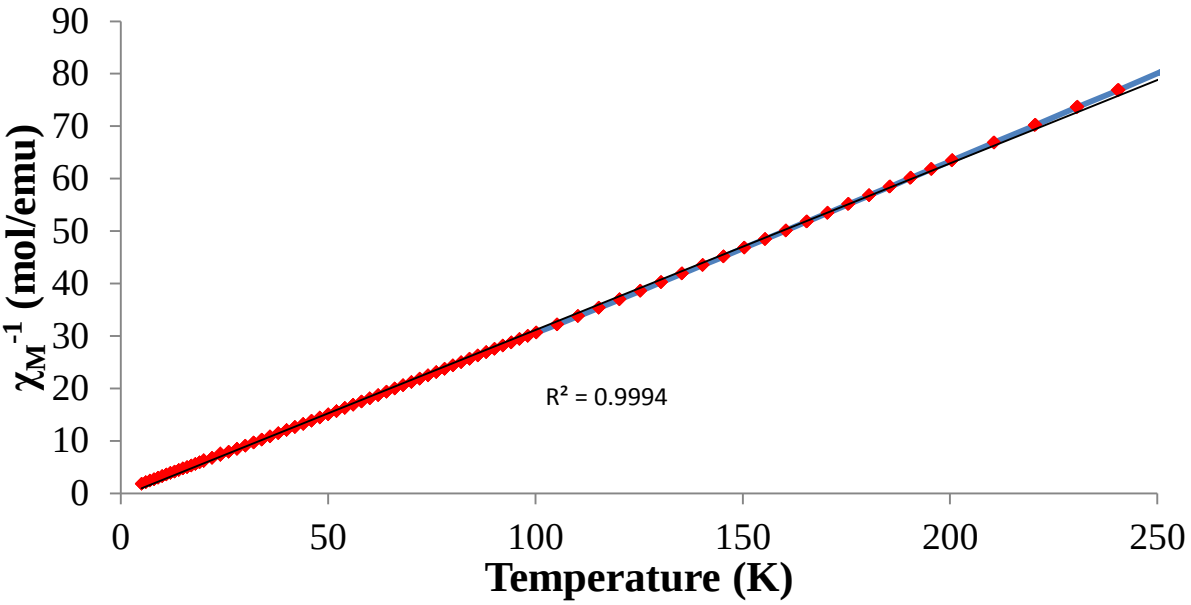

Figure 2.20 Inverse molar magnetic susceptibility (χ_M^{-1}) versus temperature (T) for $[Mn^{II}(HO^{Me2}N_4(6\text{-Me-DPEN}))(CHO_2)](BPh_4)\cdot MeCN$ (**14**).

The spectroscopic properties of **10**-**12** and **14**-**15** are also quite similar to those observed for the thiolate-ligated Mn(II) complexes, as the electronic absorption spectra of each complex exhibited featureless visible spectral regions (MeCN) and X-band EPR spectra displayed typical features for monomeric high-spin Mn(II) ions ($g_{eff} \approx 2.00$ and $A \approx 90$ G, Figure 2.20). Some of the X-band EPR spectra provided in Figure 2.20 do, however, contain unique low-field features

that were unobserved in the spectra for **2**-**5** and **8**-**9**. The spectra of **10** and **15** contain signals with g_{eff} values 2.00, as well as 26.6 (**10**) and 3.49, 5.51, and 11.58 (**15**) (Figure 2.21). These broad low-field resonances could arise due to significant zero-field splittings or the formation of polynuclear Mn clusters with variable coordination environments. A second noteworthy feature

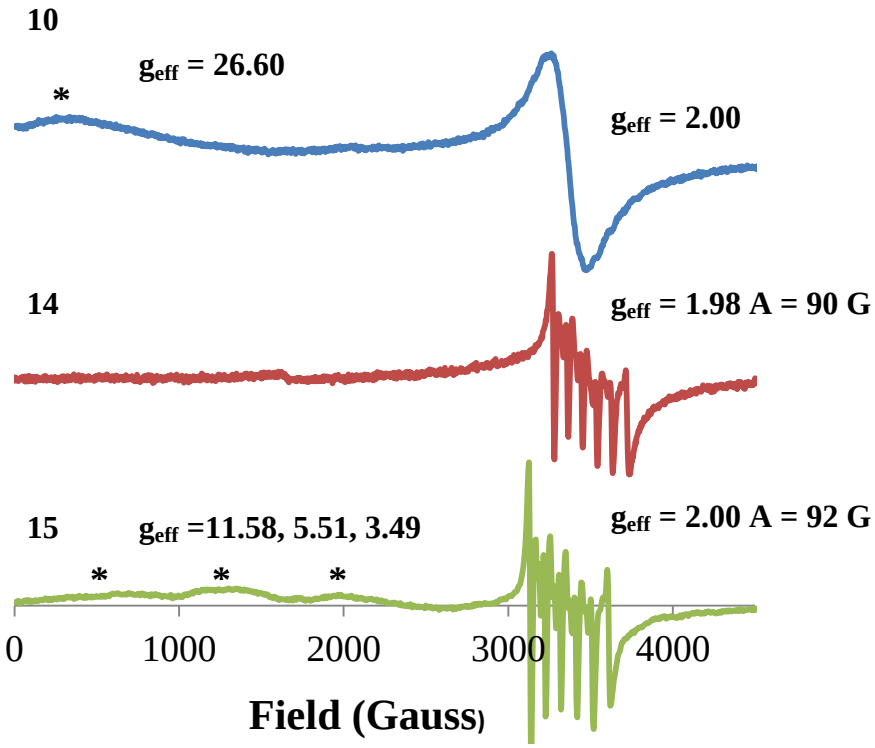

Figure 2.21 X-band (9.4 GHz) EPR spectra of $[Mn^{II}(O^{Me2}N_4(tren))]_2(PF_6)_2 \cdot MeCN$ (**10**, top blue trace), $[Mn^{II}(HO^{Me2}N_4(6\text{-Me-DPEN})(CHO_2))](BPh_4) \cdot MeCN \cdot Et_2O$ (**14**, middle red trace), and $[Mn^{II}(O^{Me2}N_4(6\text{-Me-DPPN}))](BPh_4)$ (**15**, bottom green trace). Low-field resonances discussed in the text are identified with an asterisk (*).

from the EPR spectrum of **10** is the absence of hyperfine structure in the main g_{eff} = 2.00 resonance. As was noted for the EPR spectra of **1**-**5** and **8**-**9** in frozen MeCN, the lack of observable hyperfine features could result simply from poor glass formation, however this would

also occur if the Mn(II) ions in the sample contained a wide distribution of different coordination environments.

The electrochemical properties of **10**-**11** and **14**-**15** were explored by cyclic voltammetry experiments in MeCN at room temperature (Figure 2.22). Cyclic voltammograms for **10** and 1**1** are difficult to interpret as there are multiple cathodic waves following a pronounced anodic wave (Figure 2.12). The onset of the primary anodic wave in each voltammogram (+391 mV vs. SCE for **10**, +573 mV vs. SCE for **11**) occurs at a higher potential than the anodic wave of

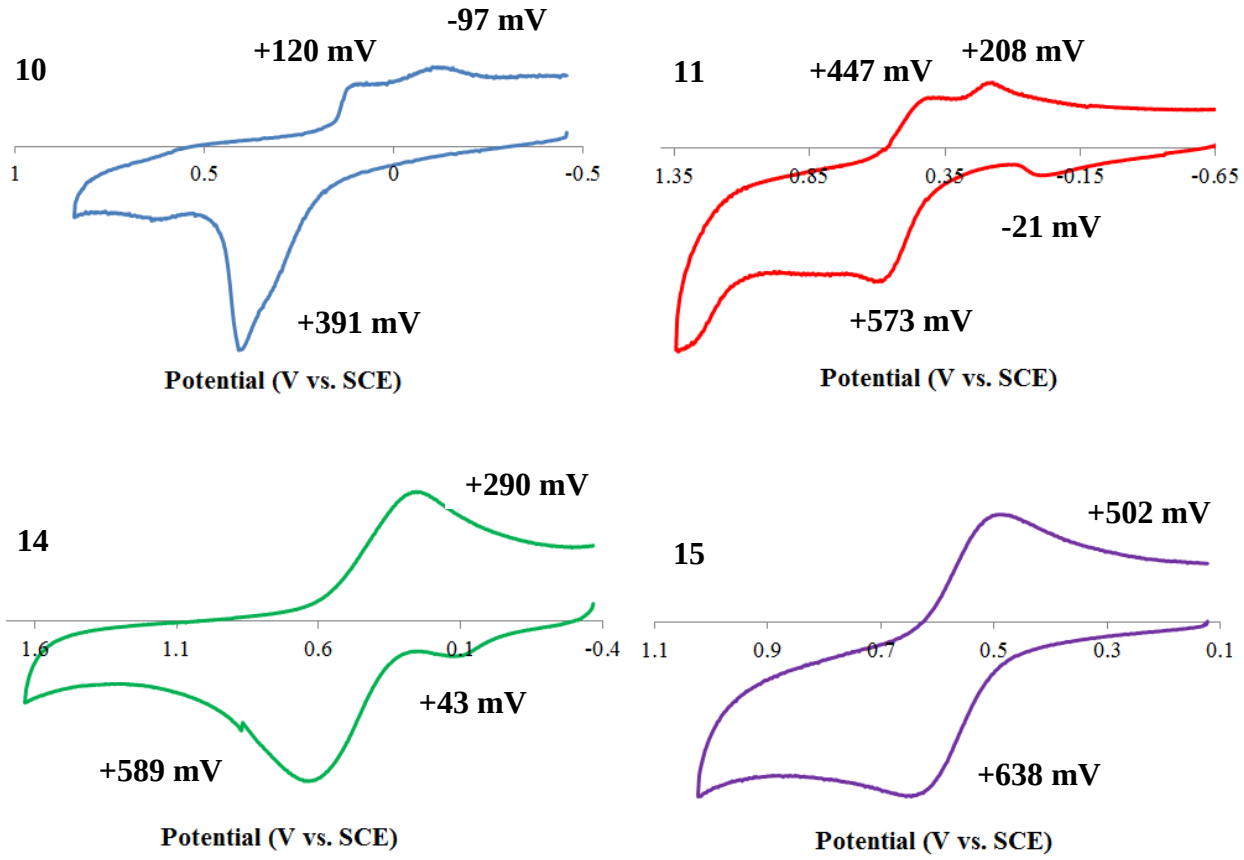

Figure 2.22 Cyclic voltammograms of $[Mn^{II}((O^{Me2})_2N_4(tren))]_2(PF_6)_2\cdot MeCN$ (**10**, blue trace, top left), $[Mn^{II}(N^{Et_2}N_4(tren))]_2(\mu\text{-}SO_4)(BPh_4)_2$ (**11**, red trace, top right), $[Mn^{II}(HO^{Me2}N_4(6\text{-Me-DPEN})(CHO_2))](BPh_4)\cdot MeCN\cdot Et_2O$ (**14**, green trace, bottom left), and $[Mn^{II}(O^{Me2}N_4(6\text{-Me-DPPN}))](BPh_4)$ (**15**, purple trace, bottom right). Each experiment was performed with a 0.1 M $^nBu_4PF_6$ supporting electrolyte and with a scan rate of 120-140 $mV\cdot s^{-1}$ at room temperature. Anodic (E_{pa}) and catholic (E_{pc}) peak potentials are labeled in each voltammogram.

thiolate-ligated **1** (+270 mV vs. SCE), which is consistent with the thiolate ligand lowering the potential for Mn(II) oxidation. Interpretation of the voltammograms for **14** and **15** is much clearer, as each contains only a single prominent anodic and cathodic wave (although **14** does exhibit an additional anodic wave with relatively low current density), therefore these waves are attributed to the $Mn^{III/II}$ couple for each complex ($E_{1/2}$ = +440 mV (**14**) and +570 mV (**15**), Figure 2.21). The $Mn^{III/II}$ couple for **15** is approximately 50 mV more positive than in thiolate-ligated **5** ($Mn^{III/II}$ $E_{1/2}$ = +520 mV vs SCE), again suggesting the thiolate ligand reduces the Mn(II) redox potentials. All magnetic, spectroscopic, and electrochemical data for **10**-**15** are compiled in Table 2.6.

Table 2.6 Magnetic, spectroscopic, and electrochemical data for $[Mn^{II}(O^{Me2}N_4(tren))]_2(PF_6)_2\cdot MeCN$ (**10**), $[Mn^{II}(N^{Et_2}N_4(tren))]_2(\mu\text{-}SO_4)(BPh_4)_2$ (**11**), $[Mn^{II}((HO^{Me2})_2N_4(tren))(MeOH)](BPh_4)_2\cdot MeOH$ (**12**), $[Mn^{II}(HO^{Me2}N_4(6\text{-Me-DPEN})(CHO_2))](BPh_4)\cdot MeCN\cdot Et_2O$ (**14**), and $[Mn^{II}(O^{Me2}N_4(6\text{-Me-DPPN}))](BPh_4)$ (**15**).

	10	**11**	**12**	**14**	**15**
μ_{eff} (solid)[a]	N/A	N/A	N/A	5.84	N/A
μ_{eff} (sol'n)[b]	5.85	5.79	5.50	5.93	6.00
λ_{max} (nm)[c]	281	275	277	315	280
(ε,$M^{-1}cm^{-1}$)[c]	(1410)	(2255)	(1940)	(410)	(1900)
g_{eff} (A, G)[d]	2.00 (N/A), 26.60	N/A	N/A	1.98 (90)	2.00 (92), 3.49, 5.51, 11.58
$E_{1/2}$ (mV)[e]	N/A	N/A	N/A	+440	+570
E_{pa} (mV)[e]	+391	+573, -21	N/A	+589, +43	+638
E_{pc} (mV)[e]	+120, -97	+447, +208	N/A	+290	+502
ΔE (mV)[e]	N/A	N/A	N/A	299	120

[a]Measurements made by SQUID magnetometry. [b]Evans method measurements, d_4-MeOD, ambient temperature. [c]MeCN solution, ambient temperature. [d]X-band EPR measurements, MeOH/EtOH glass, 4-8 K. [e]MeCN, ambient temperature, 0.1 M $^nBu_4PF_6$ supporting electrolyte, referenced versus SCE, $Ag^+/AgNO_3$ reference electrode, Pt auxillary electrode, GC working electrode.

2.3.5 Comparisons Between Thiolate-Ligated Mn(II) Complexes 1-5, 8-9 and Analogous Thiolate-Ligated Fe(II) Complexes

Part of the motivation for exploring the properties of thiolate-ligated **1**-**5** and **8**-**9** is to understand how these properties may differ from the analogous Fe(II) complexes. From a bioinorganic perspective, recognizing the fundamental differences between these two metal ions is key in understanding why particular metalloenzymes are specific for one cofactor over the other. Chapter 1 provided a general description of various metalloenzyme families, such as the superoxide dismutases, lipoxygenase, and catechol dioxygenases, which contain members that are specific for either Mn or Fe, as well as cambialistic metalloenzymes that are functional with either metal ion. A second and much narrower point of interest with these comparisons is to understand how thiolate ligands may influence the properties of Mn coordination complexes. Given the curious fact that there are no examples of naturally occurring metalloenzymes with sulfur-containing ligands coordinated directly to a Mn cofactor, exploring the coordination chemistry of thiolate-ligated Mn systems could possibly offer unique biologically-relevant insights specifically regarding the properties of Mn ions.

Towards obtaining a library of thiolate-ligated Fe(II) complexes for these comparisons, the synthetic strategy provided in Scheme 2.1 has been employed with $FeCl_2$ or $Fe(OAc)_2$ as starting reagents to yield Fe(II) complexes analogous to **1**-**5** and **8**-**9,** $[Fe^{II}(S^{Me2}N_4(tren))](PF_6)$ (**16**), $[Fe^{II}(S^{Me2}N_4(6\text{-H-DPEN}))(MeOH)](PF_6)$ (**17**), $[Fe^{II}(S^{Me2}N_4(6\text{-H-DPPN}))](PF_6)$ (**18**), $[Fe^{II}(S^{Me2}N_4(6\text{-Me-DPEN}))](PF_6)$ (**19**), $[Fe^{II}(S^{Me2}N_4(6\text{-Me-DPPN}))](PF_6)$ (**20**), and $[Fe^{II}(S^{Me2}N_4(2\text{-QuinoEN}))](PF_6)\cdot MeOH$ (**21**). ORTEP diagrams from the X-ray structures and molecular representations of **16**-**21** are provided in Figures 2.23-2.24 and 2.25, respectively, while selected metrical parameters are compiled in Table 2.7. The X-ray structure of **17** revealed

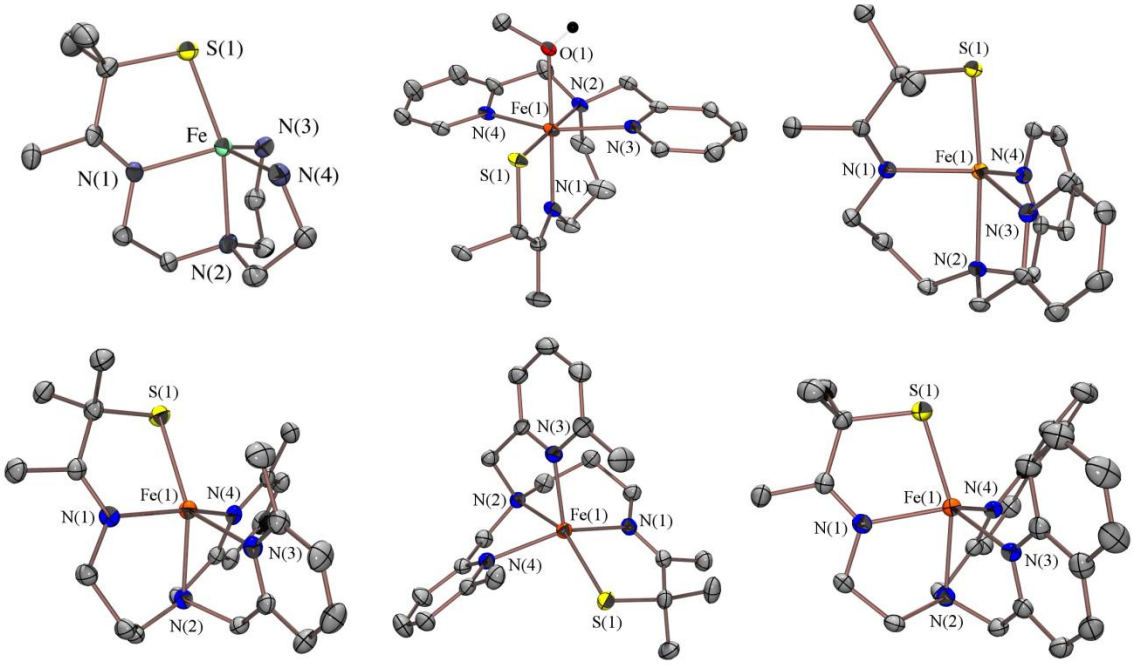

Figure 2.23 ORTEP diagrams (50 % probability) of $[Fe^{II}(S^{Me2}N_4(tren))]^+$ (**16**, top left), $[Fe^{II}(S^{Me2}N_4(6\text{-H-DPEN})(MeOH)]^+$ (**17**, top center), $[Fe^{II}(S^{Me2}N_4(6\text{-H-DPPN}))]^+$ (**18**, top right), $[Fe^{II}(S^{Me2}N_4(6\text{-Me-DPEN}))]^+$ (**19**, bottom left), $[Fe^{II}(S^{Me2}N_4(6\text{-Me-DPPN}))]^+$ (**20**, bottom middle) and $[Fe^{II}(S^{Me2}N_4(2\text{-QuinoEN}))]^+$ (**21**, bottom right) with hydrogen atoms, counterions, and solvents of crystallization omitted for clarity.

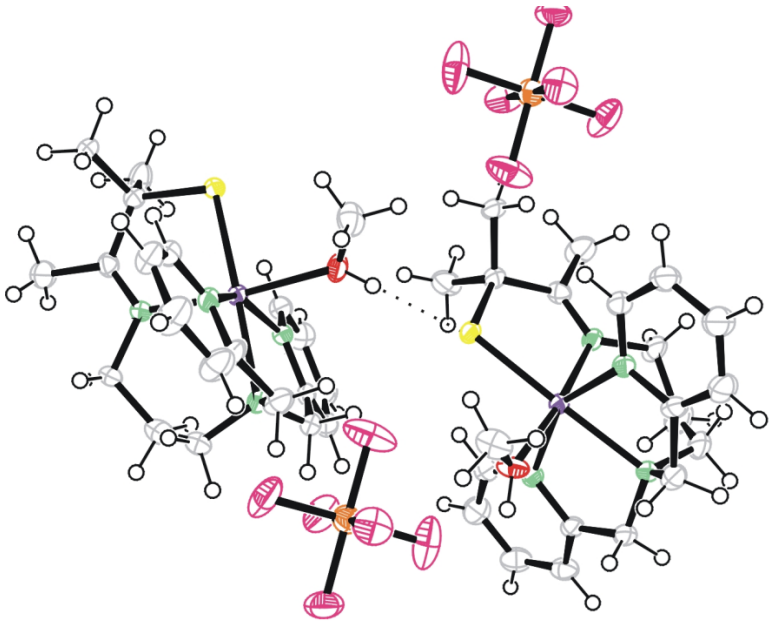

Figure 2.24 ORTEP diagram (50 % probability) of $[Fe^{II}(S^{Me2}N_4(6\text{-H-DPEN}))(MeOH)](PF_6)$ (**17**) illustrating an intermolecular hydrogen bond between neighboring complexes.

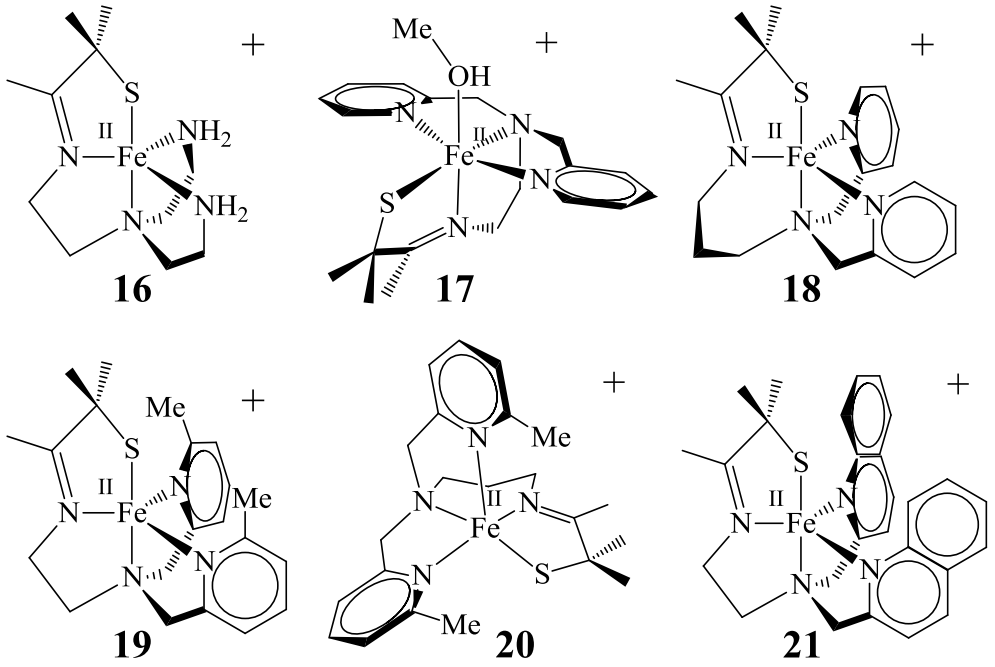

Figure 2.25 ChemDraw representations of $[Fe^{II}(S^{Me2}N_4(tren))]^+$ (**16**, top left), $[Fe^{II}(S^{Me2}N_4(6\text{-H-DPEN})(MeOH)]^+$ (**17**, top center), $[Fe^{II}(S^{Me2}N_4(6\text{-H-DPPN}))]^+$ (**18**, top right), $[Fe^{II}(S^{Me2}N_4(6\text{-Me-DPEN}))]^+$ (**19**, bottom left), $[Fe^{II}(S^{Me2}N_4(6\text{-Me-DPPN}))]^+$ (**20**, bottom middle) and $[Fe^{II}(S^{Me2}N_4(2\text{-QuinoEN}))]^+$ (**21**, bottom right).

Table 2.7 Selected bond distances (Å) and angles (degrees) for $[Fe^{II}(S^{Me2}N_4(tren))](PF_6)$ (**16**), $[Fe^{II}(S^{Me2}N_4(6\text{-H-DPEN}))(MeOH)](PF_6)$ (**17**), $[Fe^{II}(S^{Me2}N_4(6\text{-H-DPPN}))](PF_6)$ (**18**), $[Fe^{II}(S^{Me2}N_4(6\text{-Me-DPEN}))](PF_6)$ (**19**), $[Fe^{II}(S^{Me2}N_4(6\text{-Me-DPPN}))](PF_6)$ (**20**), and $[Fe^{II}(S^{Me2}N_4(2\text{-QuinoEN}))](PF_6)\cdot MeOH$ (**21**).

	16	**17**	**18**	**19**	**20**	**21**
Fe-S(1)	2.329(1)	2.3351(9)	2.3186(10)	2.326(1)	2.301(1)	2.3357(9)
Fe-N(1)	2.091(3)	2.169(3)	2.077(3)	2.132(4)	2.155(4)	2.111(2)
Fe-N(2)	2.268(3)	2.273(3)	2.299(3)	2.253(4)	2.206(4)	2.226(2)
Fe-N(3)	2.117(3)	2.152(3)	2.092(3)	2.165(4)	2.210(4)	2.152(2)
Fe-N(4)	2.131(3)	2.158(3)	2.094(3)	2.191(4)	2.133(4)	2.159(2)
Fe-O(1)	N/A	2.210(2)	N/A	N/A	N/A	N/A
S(1)-Fe-N(1)	84.02(8)	82.13(7)	84.00(8)	81.50(1)	83.78(7)	82.91(7)
S(1)-Fe-N(2)	163.02(7)	178.58(8)	174.86(8)	158.71(1)	149.70(7)	157.80(6)
S(1)-Fe-N(3)	107.86(9)	104.03(8)	106.18(9)	116.1(1)	94.04(7)	106.98(7)
S(1)-Fe-N(4)	108.81(8)	104.11(8)	105.73(8)	115.0(1)	129.45(7)	121.74(7)
N(1)-Fe-N(3)	110.29(12)	93.00(11)	114.29(12)	150.0(1)	150.42(9)	120.28(9)
N(1)-Fe-N(4)	124.95(12)	96.16(11)	126.22(12)	123.1(1)	105.34(10)	119.21(9)
N(3)-Fe-N(4)	115.20(12)	155.33(10)	113.12(12)	100.5(1)	98.78(9)	104.91(9)
O(1)-Fe-S(1)	N/A	91.94(8)	N/A	N/A	N/A	N/A
O(1)-Fe-N(1)	N/A	173.97(7)	N/A	N/A	N/A	N/A
O(1)-Fe-N(2)	N/A	89.26(11)	N/A	N/A	N/A	N/A
O(1)-Fe-N(3)	N/A	86.30(11)	N/A	N/A	N/A	N/A
O(1)-Fe-N(4)	N/A	87.38(11)	N/A	N/A	N/A	N/A
τ	0.63	N/A	0.81	0.59	0.01	0.60

intermolecular hydrogen bonding interactions between neighboring complexes, which is demonstrated by the ORTEP diagram found in Figure 2.24. The same ligands used to construct **16**-**21** are also found in **1**-**5** and **8** (Figures 2.1-2.4, 2.23-2.25), affording pairs of complexes that only differ by the identity of the metal ion (**1**/**16** (L_1), **2**/**17** (L_2), **3**/**18** (L_3), **4**/**19** (L_4), **5**/**20** (L_5), and **8**/**21** (L_8), Scheme 2.2). The coordination geometries of each pair are preserved except for **3** and **18**, as **3** was structurally characterized as a dithiolate-bridged Mn(II) dimer while **18** is a mononuclear trigonal bipyramidal Fe(II) complex (Tables 2.1 and 2.7). Metal-ligand bond distances for the Mn member of each pair are consistently found to be slightly longer than those in the analogous Fe(II) complex by 0.05-0.1 Å on average, which is likely explained by Fe(II) having a higher effective nuclear charge (smaller ionic radius) than Mn(II) (Tables 2.1 and 2.7). The same metrical trends noted within the Mn(II) series **1**-**5** and **8**-**9** (*vide supra*) are also present in the Fe(II) series, suggesting that alterations in ligand architecture influence the structural properties of each series in a similar fashion. Differences in spin state do not account for any of metrical trends within the Fe(II) series, as each Fe(II) complex has been characterized as high-spin (S = 2).

Comparing the electrochemical properties between the two series of complexes is of particular interest, as differences in $M^{III/II}$ redox potentials have been invoked to explain why particular superoxide dismutases are functional with either Mn or Fe cofactors. In contrast to what periodic trends in redox potential would suggest, Fe(II) is often found to be more reducing than Mn(II) in the same coordination environment. This can be illustrated by comparing the standard reduction potentials of each ion in acidic aqueous solution (equations 2.3 and 2.4).[54] The electrochemical properties of **16**-**21** have previously been explored by cyclic voltammetry experiments in ambient temperature MeCN solutions; the values from these experiments are

$$Mn^{III}(aq) + e^- \rightarrow Mn^{II}(aq) \quad E° = 1.542 \text{ V (NHE)} \quad (2.3)$$

$$Fe^{III}(aq) + e^- \rightarrow Fe^{II}(aq) \quad E° = 0.77 \text{ V (NHE)} \quad (2.4)$$

provided along with those for **1**-**5** and **8** in Table 2.8. To provide an even broader comparison to other pairs of monocationic, isostructural, and high-spin Mn and Fe systems, Table 2.8 also includes $E_{1/2}$ values for similar monocationic complexes which have been reported in the literature. It should be noted that direct comparisons are not made between **3** and **18** (both synthesized with L_3) since the X-ray structures of these two complexes are not complimentary.

Table 2.8 Electrochemical data ($E_{1/2}$ ($M^{III/II}$), mV vs. SCE) for pairs of monocationic and isostructural Mn(II) and Fe(II) complexes, including $[Mn^{II}(S^{Me2}N_4(tren))](PF_6)$ (**1**), $[Mn^{II}(S^{Me2}N_4(6\text{-H-DPEN}))(MeOH)](PF_6)\cdot MeOH$ (**2**), $[Mn^{II}(S^{Me2}N_4(6\text{-Me-DPEN}))](BF_4)$ (**4**), $[Mn^{II}(S^{Me2}N_4(6\text{-Me-DPPN}))](BPh_4)$ (**5**), $[Mn^{II}(S^{Me2}N_4(2\text{-QuinoEN}))](BPh_4)\cdot MeCN$ (**8**), $[Fe^{II}(S^{Me2}N_4(tren))](PF_6)$ (**16**), $[Fe^{II}(S^{Me2}N_4(6\text{-H-DPEN}))(MeOH)](PF_6)$ (**17**), $[Fe^{II}(S^{Me2}N_4(6\text{-Me-DPEN}))](PF_6)$ (**19**), $[Fe^{II}(S^{Me2}N_4(6\text{-Me-DPPN}))](PF_6)$ (**20**), and $[Fe^{II}(S^{Me2}N_4(2\text{-QuinoEN}))](PF_6)\cdot MeOH$ (**21**). The difference in $E_{1/2}$ values between each pair of complexes is provided in the far right column.

	Mn	**Fe**	**ΔE(Mn/Fe)**
$[M(S^{Me2}N_4(tren))]^+$	+140 (**1**)	-150 (**16**)	290
$[M(S^{Me2}N_4(6\text{-H-DPEN}))(MeOH)]^+$	+207 (**2**)	+41 (**17**)[d]	230
$[M(S^{Me2}N_4(6\text{-Me-DPEN}))]^+$	+412 (**4**)	+407 (**19**)	5
$[M(S^{Me2}N_4(6\text{-Me-DPPN}))]^+$	+520 (**5**)	+430 (**20**)	90
$[M(S^{Me2}N_4(2\text{-QuinoEN}))]^+$	+452 (**8**)	+401 (**21**)	51
$[M(PY5)(Cl)]^+$ [a, 55]	+970	+710	260
$[M(PY5)(OH)]^+$ [a, 55]	+600	+345	255
$[M(L_5{}^2)(Cl)]^+$ [b, 56]	+950	+570	380
$[M(L_5{}^3)(Cl)]^+$ [c, 56]	+1020	+640	380

[a]PY5 is 2,6-bis(bis(2-pyridyl)methoxymethane)pyridine. [b]$L_5{}^2$ is N-methyl-N,N',N'-tris(2-pyridylmethyl)ethane-1,2-diamine. [c]$L_5{}^3$is N-methyl-N,N',N'-tris(2-pyridylmethyl)propane-1,3-diamine. [d]Cyclic voltammogram is provided in Appendix A.8.

As can be seen from the values in Table 2.8, the $M^{III/II}$ redox couples are higher in each pair for the Mn member than the analogous Fe complex. The overall range of $E_{1/2}$ values for the thiolate-ligated complexes provided in Table 2.8 (-150 to +520 mV vs. SCE) is lower than that of the other chloride- or hydroxide-bound complexes (+345 to +1020 mV vs. SCE), which again

suggests that thiolate ligands effectively lower the redox potentials of metal ions. A striking observation from the ΔE(Mn/Fe) values is that some of the thiolate-ligated pairs have relatively little difference between their respective $E_{1/2}$ values. This is particularly noted by the 5 mV difference between the $E_{1/2}$ values for **4** and **19**, as these values are certainly within experimental error of one another. Other pairs of thiolate-ligated complexes, such as **5**/**20** (ΔE = 90 mV) and **8**/**21** (ΔE = 51 mV), also have $Mn^{III/II}$ redox couples within narrow ranges of one another.

The possibility of ligand redox non-innocence was considered since some sulfur-containing ligands, such as dithiolenes, are known to be redox active. Zn(II) has a full occupied 3d manifold (d^{10}) and is redox-inactive, therefore the electrochemical properties of the thiolate-containing ligands discussed in this chapter were explored by obtaining thiolate-ligated Zn(II) complexes analogous to **1**/**16**, **4**/**19**, and **5**/**20**. These complexes were synthesized via the synthetic strategy in Scheme 2.1 with $ZnCl_2$ as a reagent and subsequently characterized by X-ray crystallography. The ORTEP diagrams and molecular representations of $[Zn^{II}(S^{Me2}N_4(tren))](PF_6)$ (**22**), $[Zn^{II}(S^{Me2}N_4(6\text{-Me-DPEN}))](BPh_4)$ (**23**), and $[Zn^{II}(S^{Me2}N_4(6\text{-Me-DPPN}))](BPh4)\cdot MeCN$ (**24**) are provided in Figures 2.26 and 2.27, respectively. Selected metrical parameters and crystal data for **23** and **24** are provided in Tables 2.9 and Appendix A.9, respectively. Like the Mn(II) and Fe(II) analogues for each of these complexes, **22**-**24** were each found to contain five-coordinate complexes, further supporting the claim that thiolate ligands stabilize coordinatively unsaturated metal ions. Electrochemical experiments performed on thiolate-ligated **22**-**24** by cyclic voltammetry revealed these complexes are each redox inactive within window of +1.3 to -1.0 V vs. SCE in MeCN. These results strongly support the observed redox properties of the thiolate-ligated Mn(II) and Fe(II) discussed within this chapter as being completely metal-centered.

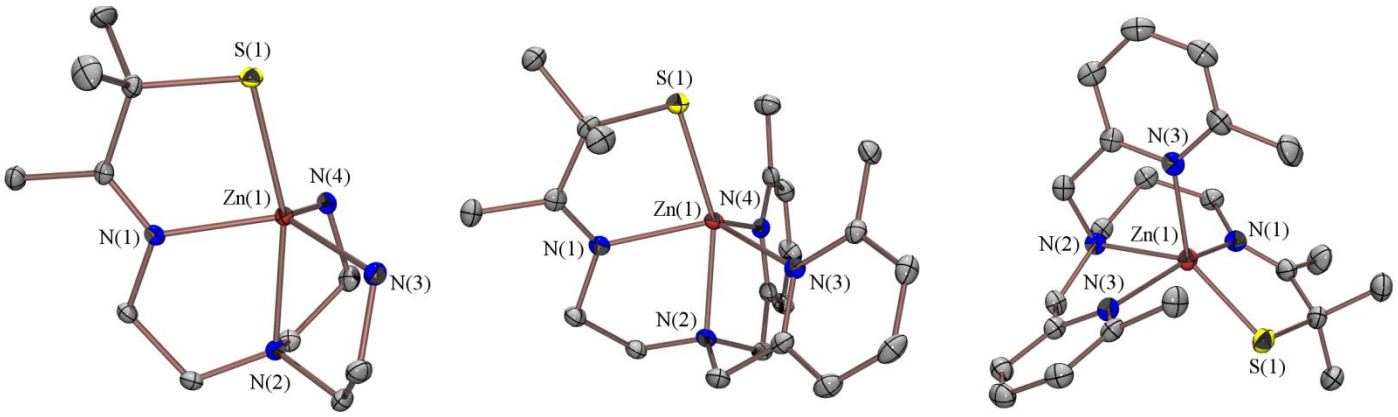

Figure 2.26 ORTEP diagrams (50 % probability) of $[Zn^{II}(S^{Me2}N_4(tren))]^+$ (**22**, left), $[Zn^{II}(S^{Me2}N_4(6\text{-Me-DPEN}))]^+$ (**23**, middle), and $[Zn^{II}(S^{Me2}N_4(6\text{-Me-DPPN}))]^+$ (**24**, right) with hydrogen atoms, counterions, and solvents of crystallization omitted for clarity.

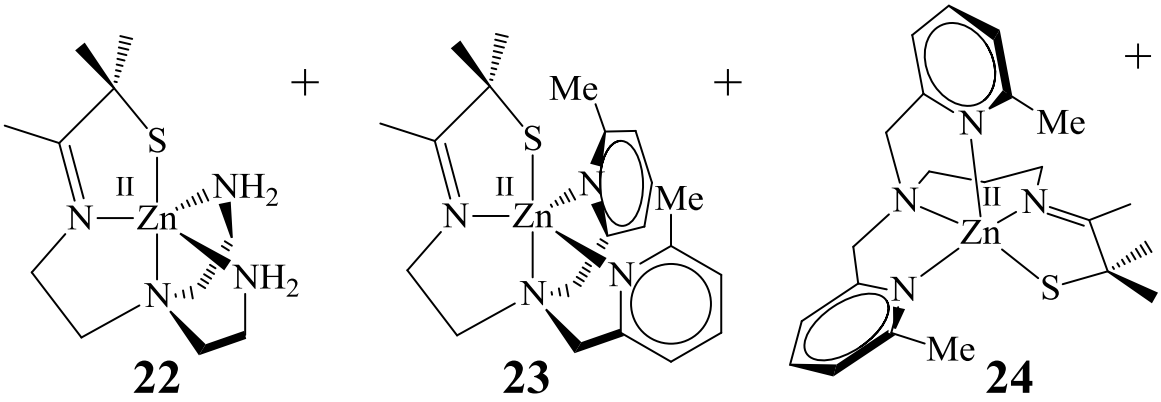

Figure 2.27 ChemDraw representations of $[Zn^{II}(S^{Me2}N_4(tren))]^+$ (**22**, left), $[Zn^{II}(S^{Me2}N_4(6\text{-Me-DPEN}))]^+$ (**23**, middle), and $[Zn^{II}(S^{Me2}N_4(6\text{-Me-DPPN}))]^+$ (**24**, right).

Table 2.9 Selected bond distances (Å) and angles (degrees) for $[Zn^{II}(S^{Me2}N_4(tren))](PF_6)$ (**22**), $[Zn^{II}(S^{Me2}N_4(6\text{-Me-DPEN}))](BPh_4)$ (**23**), and $[Zn^{II}(S^{Me2}N_4(6\text{-Me-DPPN}))](BPh_4)\cdot MeCN$ (**24**).

	22	**23**	**24**
Zn-S(1)	2.3220(6)	2.2892(7)	2.2419(7)
Zn-N(1)	2.074(1)	2.1496(19)	2.154(2)
Zn-N(2)	2.301(2)	2.2214(19)	2.130(2)
Zn-N(3)	2.083(2)	2.1156(19)	2.064(2)
Zn-N(4)	2.075(2)	2.1539(19)	2.322(2)
S(1)-Zn-N(1)	85.35(6)	83.21(5)	85.51(6)
S(1)-Zn-N(2)	163.88(5)	159.00(5)	140.42(6)
S(1)-Zn-N(3)	106.86(6)	113.46(6)	135.48(6)
S(1)-Zn-N(4)	108.74(6)	114.50(6)	93.96(5)
N(1)-Zn-N(3)	126.41(8)	119.25(7)	102.85(8)
N(1)-Zn-N(4)	110.83(8)	121.18(7)	157.61(8)
N(3)-Zn-N(4)	113.32(8)	104.43(7)	93.22(8)
τ	0.62	0.63	0.29

Given that isostructural Mn and Fe complexes typically exhibit large differences in $M^{III/II}$ couples (exemplified by the E° values from equations 2.3-2.4), we sought to further understand these observations by considering what further influence thiolate ligation may have on the electrochemical properties of these complexes. An intriguing correlation between the ΔE(Mn/Fe) values and differences in *trans*-axial bond angles (S(1)-M-N(2)) for the four pairs of complexes included in Table 2.8 was observed and is represented in Figure 2.26. The plot in Figure 2.28 reveals that there is a direct correlation between the difference in *trans*-axial angle and the difference in redox potential between members of each pair. This relationship further

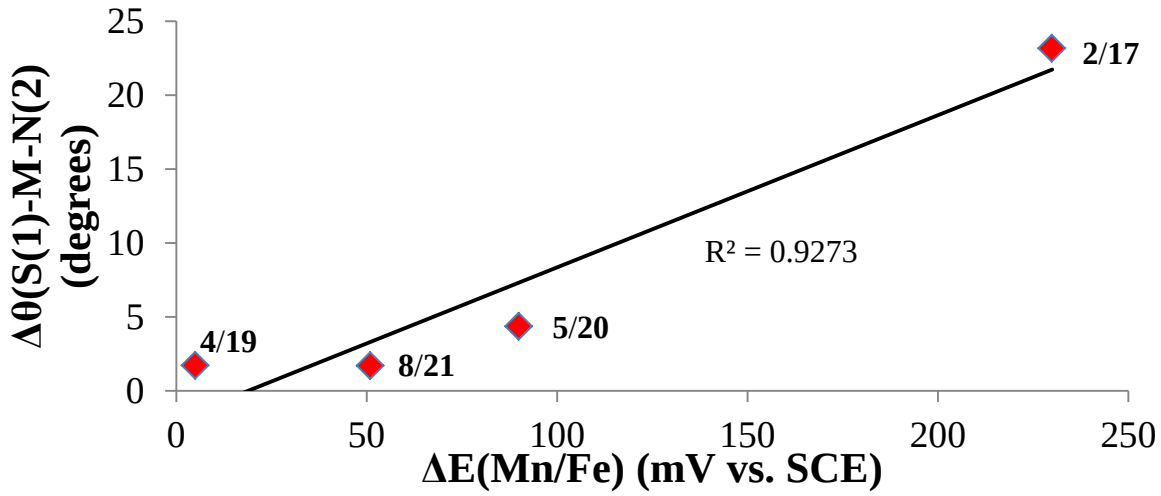

Figure 2.28 Plot of difference in *trans*-axial angle (Δθ(S(1)-M-N(2)) as a function of difference in $M^{III/II}$ redox couples (ΔE(Mn/Fe)).

suggests that orbital overlap between the sulfur and metal atoms may be intimately linked to the "electronic buffering" found in these complexes. Since the ability of thiolate ligands to influence the electronic properties of transition metal ions is correlated to the amount of covalency in the respective metal-thiolate bond, sulfur K-edge XAS experiments were conducted in order to quantify the amount of metal-sulfur covalency for each complex.

2.3.6 Characterization of Thiolate-Ligated Mn(II) and Fe(II) Complexes by Sulfur K-Edge X-Ray Absorption Spectroscopy

Ligand K-edge X-ray absorption spectroscopy (XAS) has been developed as a direct experimental probe of metal-ligand covalency. Sulfur K-edge spectra of thiolate-ligated transition metal complexes contain a low-energy (pre-edge) feature that corresponds to a sulfur 1s to metal 3d ($S_{1s} \rightarrow M_{3d}$) transition. The S 1s orbital is completely localized on the sulfur atom, thus this transition can only gain intensity if there is contribution from the S 3p orbital into the metal 3d orbitals. Pre-edge transition intensity is therefore the intensity of a purely dipole-allowed 1s → 3p transition weighed by the metal 3d and S 3p bond covalency. The intensity of this pre-edge transition is represented by equation 2.5, where $I(S_{1s} \rightarrow M_{3d})$ is the pre-edge

$$I(S_{1s} \rightarrow M_{3d}) = \alpha^2 I(S_{1s} \rightarrow S_{np}) \quad (2.5)$$

transition intensity, α is ligand coefficient in the acceptor orbital wavefunction, and $I(S_{1s} \rightarrow S_{np})$ represents the intensity of a purely ligand-based transition. Through equation 2.5, metal-thiolate bond covalency is found to be directly proportional to the intensity of the pre-edge transition (α^2).

The absorption and second derivative S K-edge XAS spectra for $[Mn^{II}(S^{Me2}N_4(6\text{-Me-DPEN}))](BF_4)$ (**4**) and $[Fe^{II}(S^{Me2}N_4(6\text{-Me-DPEN}))](PF_6)$ (**19**) are shown in Figures 2.29 and 2.30, while both spectra for $[Mn^{II}(S^{Me2}N_4(2\text{-QuinoEN}))](BPh_4)\cdot MeCN$ (**8**) and $[Fe^{II}(S^{Me2}N_4(2\text{-QuinoEN}))](PF_6)\cdot MeOH$ (**21**) are provided in Figures 2.31 and 2.32, each respectively. Fits to both the normalized absorption and second derivative spectra for each complex are provided in

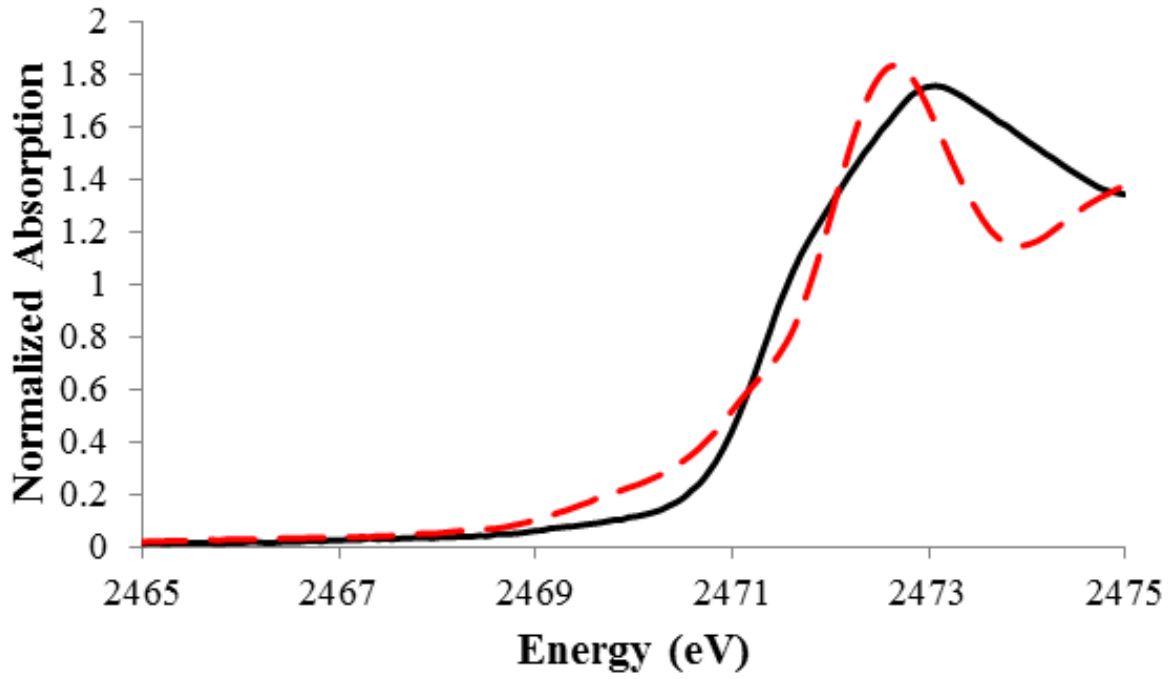

Figure 2.29 Normalized S K-edge XAS spectra of [$Mn^{II}(S^{Me2}N_4$(6-Me-DPEN))](BF_4) (**4**, solid black trace) and [$Fe^{II}(S^{Me2}N_4$(6-Me-DPEN))](PF_6) (**19**, dotted red trace).

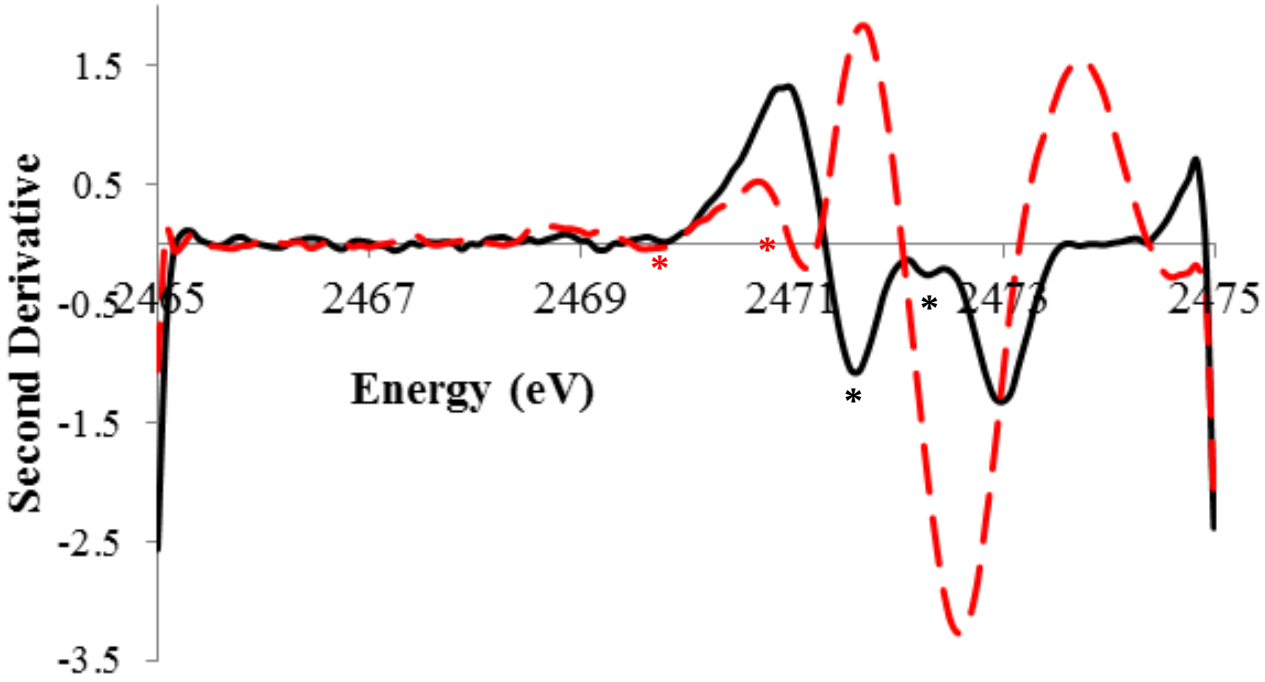

Figure 2.30 Second derivative of the S K-edge XAS spectra of [$Mn^{II}(S^{Me2}N_4$(6-Me-DPEN))](BF_4) (**4**, solid black trace) and [$Fe^{II}(S^{Me2}N_4$(6-Me-DPEN))](PF_6) (**19**, dotted red trace). Pre-edge transition maxima are labeled with an asterisk (*).

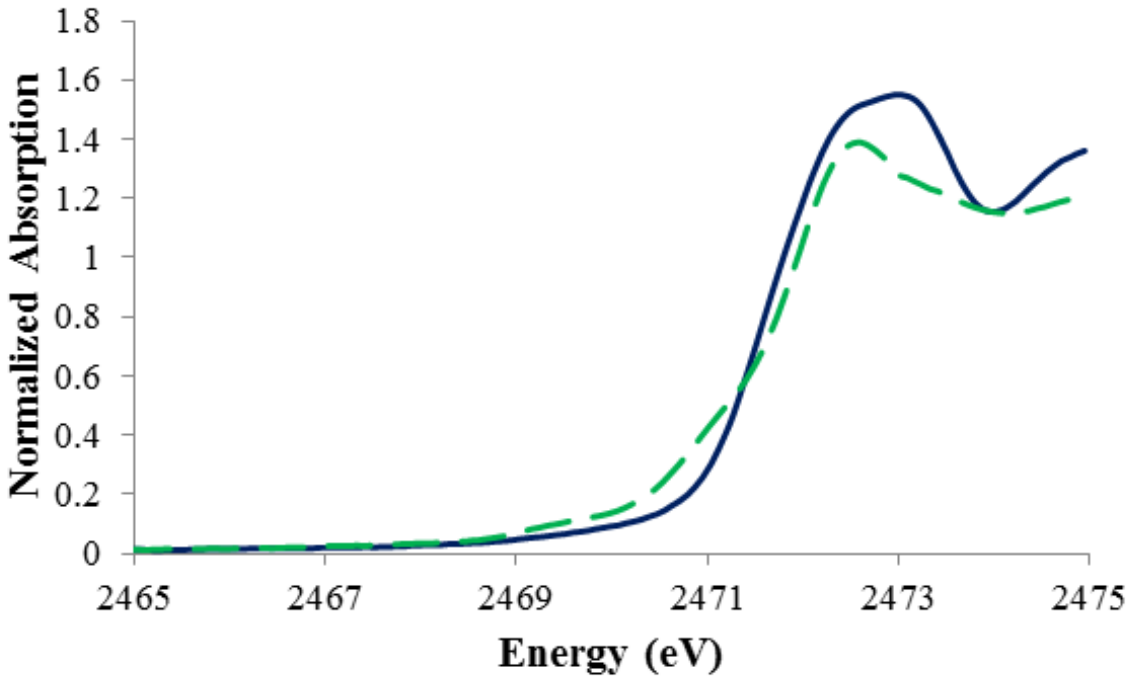

Figure 2.31 Normalized S K-edge XAS spectra of [$Mn^{II}(S^{Me2}N_4$(2-QuinoEN))](BPh_4)·MeCN (**8**, solid blue trace) and [$Fe^{II}(S^{Me2}N_4$(2-QuinoEN))](PF_6)·MeOH (**21**, dotted green trace).

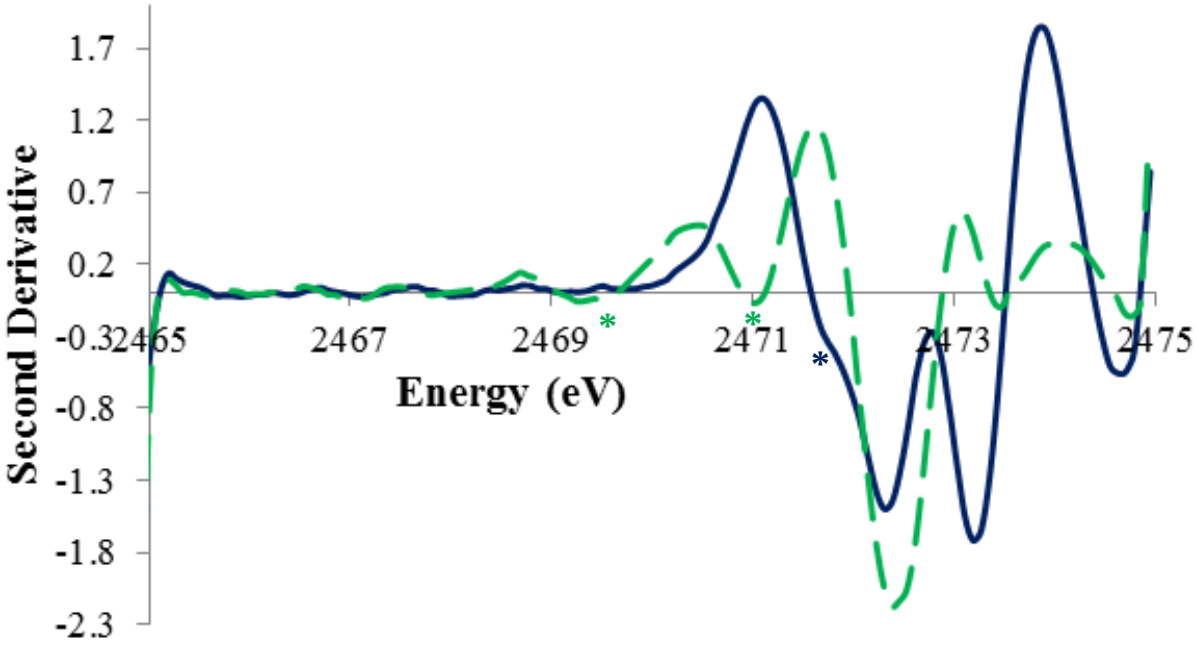

Figure 2.32 Second derivative of S K-edge XAS spectra of [$Mn^{II}(S^{Me2}N_4$(2-QuinoEN))](BPh_4)·MeCN (**8**, solid blue trace) and [$Fe^{II}(S^{Me2}N_4$(2-QuinoEN))](PF_6)·MeOH (**21**, dotted green trace). Pre-edge transition maxima are labeled with an asterisk (*).

Appendix A.10-A.17. Pre-edge transition energies, areas, and percent covalency values are compiled in Table 2.10.

Table 2.10 S K-edge XAS pre-edge transition energies (E, eV)[a], amplitudes, widths, areas, covalency (%), and calculated covalency[b] from DFT for $[Mn^{II}(S^{Me2}N_4(6\text{-Me-DPEN}))](BF_4)$ (**4**), $[Fe^{II}(S^{Me2}N_4(6\text{-Me-DPEN}))](PF_6)$ (**19**), $[Mn^{II}(S^{Me2}N_4(2\text{-QuinoEN}))](BPh_4)\cdot MeCN$ (**8**), and $[Fe^{II}(S^{Me2}N_4(2\text{-QuinoEN}))](PF_6)\cdot MeOH$ (**21**).

	E	Amp	Width	Area	Covalency	Calculated Covalency[b]
4	2471.6	0.407	0.486	0.396	14	13
	2472.2	0.136	0.373	0.101	4	6
19	2470.2	0.119	0.900	0.214	8	5
	2471.1	0.159	0.406	0.129	5	6
8	2471.7	0.216	0.487	0.210	8	12
21	2469.6	0.031	0.492	0.031	1	2
	2471.1	0.185	0.600	0.222	8	10

[a]Error in pre-edge energy is ±0.1 eV. [b]6-311G(d) basis set was used for Fe, Mn, S, and N atoms, while the 6-21G(d) basis set was used for C and H atoms.

The S K-edge XAS spectrum of **4** contains pre-edge transitions at 2471.6 eV and 2472.2 eV, which are higher in energy than the pre-edge transitions at 2470.2 eV and 2471.1 eV found for **19** (Table 2.9). This trend is also found when comparing **8** to **21**, as **8** displays a single pre-edge transition at 2471.7 eV while **21** has two transitions at 2469.6 eV and 2471.1 eV (Table 2.9). The higher energy features observed for the Mn(II) complex relative to the analogous Fe(II) species can be rationalized based upon periodic trends in effective nuclear charge, as the Fe(II) 3d orbitals will be lower in energy and close to that of the sulfur 1s orbital than those of Mn(II). Similar observations have been made by Solomon and coworkers by comparing the XANES regions of the S K-edge XAS spectra for various thiophenolate-ligated first-row transition metal complexes.[52]

The total percent S_{3p} character in each metal-sulfur bond is found to be 18 % (**4**), 13 % (**19**), 8 % (**8**), and 9 % (**21**). High-spin Mn(II) and Fe(II) have five and four electron holes, respectively, which are available to participate in a covalent bonding interaction with a thiolate

ligand. The total percent covalency is divided by the number of electron holes found in the 3d manifold of each metal in order to make fair comparisons between each pair of complexes containing the same ligand, affording normalized percent covalency values of 3.6 % (**4**), 3.3 % (**19**), 1.6 % (**8**), and 2.3 % (**21**). Geometry-optimized DFT calculations were performed with **4**, **19**, **8**, and **12** in order to obtain a calculated percent covalency value for each complex (selected metrical parameters from the geometry-optimized calculations are provided in Appendix A.18); the metrical parameters from these optimized structures compare well with the X-ray structures (Tables 2.1 and 2.6). DFT calculated values for the normalized percent covalency are similar in magnitude to the experimental values (Table 2.9). Qualitatively, a considerable degree of metal-sulfur covalency is apparent through visualization of the molecular orbitals generated from single point energy calculations with the optimized structures (Figure 2.33). Unfortunately, the two percent covalency values within each pair of complexes containing the same ligand are within experimental error of one another despite being differentiated by DFT calculations. A

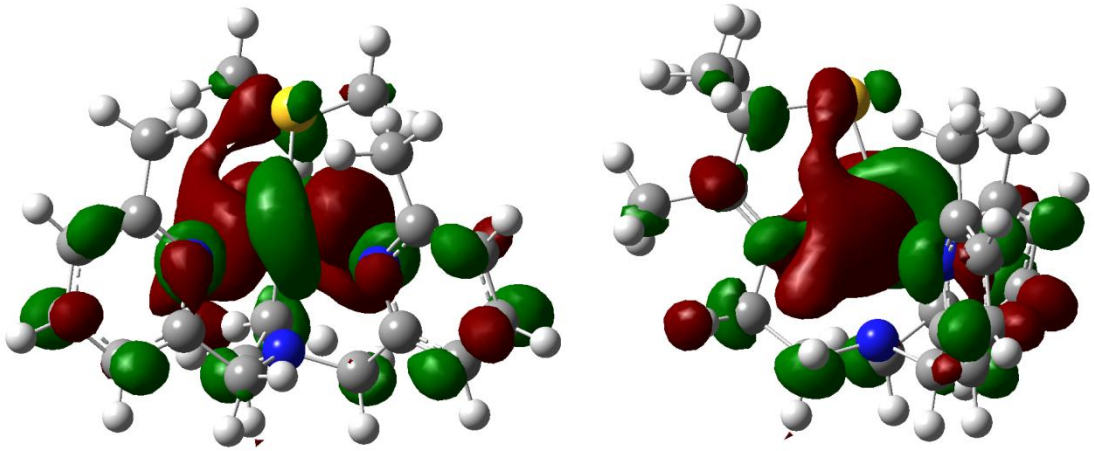

Figure 2.33 Alternate views of a DFT-generated molecular orbital (β-155) from **4** representing significant mixing between the Mn $3d_{x2-y2}$ (56 %) and S $3p_x$ (21 %) and $3p_y$ (15 %) orbitals.

considerable amount of uncertainty in these values will also arise due to the pre-edge energies being very close to the rising-edge energies (ranges from 2472.8 eV to 2473.3 eV), which has been noted to prevent an accurate determination of metal-sulfur covalency in other similar complexes.[52]

2.4 Conclusions

The predominant focus of this chapter has been the synthesis and characterization of thiolate-ligated Mn(II) complexes. The X-ray crystal structures of many of these complexes reveal coordinatively unsaturated Mn centers with distorted trigonal bipyramidal or square pyramidal coordination geometries. Subtle ligand modifications, such as substitution of coordinated pyridine moieties, result in considerable metal-ligand bond and coordination geometry changes. A few complexes were characterized by X-ray crystallography as containing thiolate-bridged Mn(II) dimers, illustrating the propensity of thiolate ligand to form multiple metal-sulfur bonds. Magnetic and spectroscopic data are consistent with each of these complexes as being high-spin (S = 5/2), while electrochemical characterization has resulted in the observation of fully reversible or quasi-reversible $Mn^{III/II}$ couples at relatively moderate potentials for most complexes. Many of these redox couples are lower than those of other mononuclear and monocationic Mn(II) complexes. Collectively, the characterization data obtained for these complexes supports previous observations that thiolate ligands help to stabilize coordinatively unsaturated transition metal centers and lowers redox potentials.

Alkoxide- and amine-ligated analogues of these thiolate-ligated Mn(II) complexes were also synthesized and characterized in order to gain indirect insight as to how thiolate ligation influences the properties of synthetic Mn(II) complexes. These attempts have afforded mixed

results, as dialkoxide-bridged Mn(II) dimers and alcohol-ligated Mn(II) monomers were obtained. The one alkoxide-ligated Mn(II) complex that was successfully obtained, which was mononuclear, monocationic, and coordinatively unsaturated, was found to have a higher $Mn^{III/II}$ couple relative to the thiolate-ligated analogue of this complex. This observation reinforces the idea that thiolate ligands help to reduce redox potentials. The lone amine-ligated analogue of a thiolate-ligated complex was structurally characterized as a sulfate-bridged dimer, suggesting that replacing an anionic thiolate with a neutral tertiary amine results in a more Lewis acidic metal center.

The thiolate-ligated Mn(II) complexes described were also compared to analogous thiolate-ligated Fe(II) complexes in order to understand fundamental differences between the two metals. The metal-ligand bond lengths for the Fe(II) complexes were each found to be shorter than the respective bond lengths found in the Mn(II) series, which is likely a result of the smaller ionic radius (and increased Lewis acidity) of high-spin Fe(II) compared to high-spin Mn(II). Most members of each set of complexes were found to be coordinatively unsaturated by the respective X-ray crystal structures. Likewise, each complex was found to be high-spin ($S = 5/2$ for Mn(II), $S = 2$ for Fe(II)). Differences between $M^{III/II}$ redox potentials between isostructural pairs of complexes were found to vary from a few 100 mV to being almost indistinguishable, suggesting the thiolate ligand may be acting a "redox buffer" and maintaining a relatively constant redox potential. Sulfur K-edge XAS experiments were pursued to determine if the metal-sulfur bond covalency changes considerably within each pair of complexes; unfortunately the experimental data did show a considerable difference between each pair within error.

2.5 Notes to Chapter 2

1) Miller, A.-F.; Sorkin, D. L. *Comments Mol. Cell. Biophys.* **1997**, *9*, 1-48.

2) Lipscomb, J. D.; Orville, A. M. *Metal Ions Biol. Syst.* **1992**, *28*, 243-298.

3) Wu, A. J.; Penner-Hahn, J. E.; Pecoraro, V. L. *Chem. Rev.* **2004**, *104*, 903-938.

4) McEvoy, J. P.; Brudvig, G. W. *Chem. Rev.* **2006**, *106*, 4455-4483.

5) Whittaker, M. M.; Whittaker, J. W. *J. Biol Chem.* **1998**, *273*, 22188-22193.

6) Barynin, V. V.; Hempstead, P. D.; Vagin, A. A.; Antonyuk, S. V.; Melik-Adamyan, W. R.; Lamzin, V. S.; Harrison, P. M.; Artymiuk, P. J. *J. Inorg. Biochem.* **1997**, *67*, 196.

7) Umena, Y.; Kawakami, K.; Shen, J.-R.; Kamiya, N. *Nature* **2011**, *473*, 55-60.

8) Pecoraro, V. L.; Baldwin, M. J.; Gelasco, A. *Chem. Rev.* **1994**, *94*, 807-826.

9) Sono, M.; Roach, M. P.; Coulter, E. D.; Dawson, J. H. *Chem. Rev.* **1996**, *96*, 2841-2887.

10) Kovacs, J. A. *Chem. Rev.* **2004**, *104*, 825-848.

11) Solomon, E. I.; Szilagyi, R. K.; DeBeer George, S.; Basumallick, L. *Chem. Rev.* **2004**, *104*, 419-458.

12) Solomon, E. I.; Brunold, T. C.; Davis, M. I.; Kemsley, J. N.; Lee, S.-K.; Lehnert, N.; Neese, F.; Skulan, A. J.; Yang, Y.-S.; Zhou, J. *Chem. Rev.* **2000**, *100*, 235-350.

13) Ibers, J. A.; Holm, R. H. *Science* **1980**, *208*, 223-235.

14) Meunier, B.; de Visser, S. P.; Shaik, S. *Chem. Rev.* **2004**, *104*, 3947-3980.

15) Ortiz de Montellano, P. R. *Acc. Chem. Res.* **1998**, *31*, 543-549.

16) Coelho, A. V.; Matias, P.; Fulop, V.; Thompson, A.; Gonzalez, A.; Carrondo, M. A. *J. Biol. Inorg. Chem.* **1997**, *2*, 680-689.

17) Shoner, S. C.; Barnhart, D.; Kovacs, J. A. *Inorg. Chem.* **1995**, *34*, 4517-4518.

18) Ellison, J. J.; Nienstedt, A.; Shoner, S. C.; Barnhart, D.; Cowen, J. A.; Kovacs, J. A. *J. Am. Chem. Soc.* **1998**, *120*, 5691-5700.

19) Shearer, J.; Nehring, J.; Lovell, S.; Kaminsky, W.; Kovacs, J. A. *Inorg. Chem.* **2001**, *40*, 5483-5484.

20) Kung, I.; Schweitzer, D.; Shearer, J.; Taylor, W. D.; Jackson, H. L.; Lovell, S.; Kovacs, J. A. *J. Am. Chem. Soc.* **2000**, *122*, 8299-8300.

21) Stasser, J.; Namuswe, F.; Kasper, G. D.; Jiang, Y.; Krest, C. M.; Green, M. T.; Penner-Hahn, J.; Goldberg, D. P. *Inorg. Chem.* **2010**, *49*, 9178-9190.

22) Solomon, E. I.; Gorelsky, S. I.; Dey, A. *J. Comp. Chem.* **2006**, *27*, 1415-1428.

23) Solomon, E. I.; Hadt, R. G. *Coord. Chem. Rev.* **2011**, *255*, 774-789.

24) Evans, D. A. *J. Am. Chem. Soc.* **1959**, 2005.

25) Van Geet, A. L. *Anal. Chem.* **1969**, *40*, 2227-2229.

26) Brines, L. M.; Shearer, J.; Fender, J. K.; Schweitzer, D.; Shoner, S. C.; Barnhart, D.; Kaminsky, W.; Kovacs, J. A. *Inorg. Chem.* **2007**, *46*, 9267-9277.

27) Toledo, S. Ph.D. thesis, University of Washington, Seattle, Washington, 2010.

28) (a) Altomare, A.; Burla, C.; Camalli, M.; Cascarano, L.; Giacovazzo, c.; Guagliardi, A.; Moliterni, A. G. G.; Polidori, G.; Spanga, R. *J. Appl. Cryst.* **1999**, *32*, 115-119. (b) Altomare, A.; Cascarano, G.; Giacovazzo, C.; Guagliardi, A. *J. Appl. Cryst.* **1993**, *26*, 343.

29) Sheldrick, G. M. SHELXL-97: Program for the Refinement of Crystal Structures **1997**, University of Gottingen, Germany.

30) Mackay, S.; Edwards, C.; Henderson, A.; Gilmore, C.; Stewart, N.; Shankland, K.; Donald, A.; MaXus: a Computer Program for the Solution and Refinement of Crystal Structures from Diffraction Data. University of Glasgow, Scotland, 1997.

31) Waasmaier, D.; Kirfel, A. *Acta Crystallogr. A* **1995**, *51*, 416.

32) Hedman, B.; Frank, P.; Gheller, S. F.; Roe, A. L.; Newton, W. E.; Hodgson, K. O. *J. Am. Chem. Soc.* **1988**, *110*, 3798-3805.

33) Ellis, P. J.; Freeman, H. C. *J. Synchrotron Radiat.* **1995**, *2*, 190-195.

34) Tenderholt, A. L. *PySpline*, Version 1.0; http://pyspline.sourceforge.net/.

35) George, G. N.; *EDG_FIT*; Stanford Synchrotron Radiation Laboratory, Stanford Linear Accelerator Center, Stanford University: Stanford, CA, 2000.

36) Shadle, S. E.; Penner-Hahn, J. E.; Schugar, H. J.; Hedman, B.; Hodgson, K. O.; Solomon, E. I. *J. Am. Chem. Soc.* **1993**, *115*, 767-776.

37) Frisch, M. J.; Trucks, G. W.; Schlegel, H. B.; Scuseria, G. E.; Robb, M. A.; Cheeseman, J. R.; Montgomery, J. A., Jr.; Vreven, T.; Kudin,K. N.; Burant, J. C.; Millam, J. M.; Lyengar, S. S.; Tomasi, J.; Barone, V.; Mennucci, B.; Cossi, M.; Scalmani, G.; Rega, N.; Petersson, G.A.; Nakatsuji, H.; Hada, M.; Ehara, M.; Toyota, K.; Fukuda, R.; Hasegawa,

J.; Ishida, M.; Nakajima, T.; Honda, Y.; Kitao, O.; Nakai,H.; Klene, M.; Li, X.; Knox, J. E.; Hratchian, H. P.; Cross, J. B.; Adamo, C.; Jaramillo, J.; Gomperts, R.; Stratmann, R. E.; Yazyev, O.; Austin, A. J.; Cammi, R.; Pomelli, C.; Ochterski, J. W.; Ayala, P. Y.; Morokuma, K.; Voth, G. A.; Salvador, P.; Dannenberg, J. J.; Zakrzewski, V. G.; Dapprich, S.; Daniels, A. D.; Strain, M. C.; Farkas, O.; Malick, D. K.; Rabuck, A. D.; Raghavachari, K.; Foresman, J. B.; Ortiz, J. V.; Cui, Q.; Baboul, A. G.; Clifford, S.; Cioslowski, J.; Stefanov, B. B.; Liu, G.; Liashenko, A.; Piskorz, P.; Komaromi, I.; Martin, R. L.; Fox, D. J.; Keith, T.; Al-Laham, M. A.; Peng, C. Y.; Nanayakkara, A.; Challacombe, M.; Gill, P. M. W.; Johnson, B.; Chen, W.; Wong, M. W.; Gonzalez, C.; Pople, J. A. Gaussian 03, revision C.01; Gaussian, Inc.: Wallingford, CT, 2004.

38) Tenderholt, A. L. *QMForge*, Version 2.1, http://qmforge.sourceforge.net.

39) Shearer, J.; Scarrow, R. C.; Kovacs, J. A. *J. Am. Chem. Soc.* **2002**, *124*, 11709-11717.

40) Shearer, J.; Fitch, S. B.; Kaminsky, W.; Benedict, J.; Scarrow, R. C.; Kovacs, J. A. *Proc. Natl. Acad. Sci. USA* **2003**, *100*, 3671-3676.

(41) Nam, E.; Alokolaro, P. E.; Swartz, R. D.; Gleaves, M. C.; Pikul, J.; Kovacs, J. A. *Inorg. Chem.* **2011**, *50*, 1592-1602.

(42) Costas, M.; Chen, K.; Que, Jr., L. *Coord. Chem. Rev.* **2000**, *200*, 517-544.

(43) Mirica, L. M.; Otterwaelder, X.; Stack, T. D. P. *Chem. Rev.* **2004**, *104*, 1013-1045.

(44) Lewis, E. A.; Tolman, W. B. *Chem. Rev.* **2004**, *104*, 1047-1076.

(45) Shannon, R. D. *Acta Crystallogr.* **1976**, *32*, 751-767.

(46) Costas, M.; Que, Jr., L. *Angew. Chem. Int. Ed.* **2002**, *41*, 2179-2182.

(47) Roelfes, G.; Lubben, M.; Chen, K.; Ho, R. Y. N.; Meetsma, A.; Genseberger, S.; Hermant, R. M.; Hage, R.; Mandal, S. K.; Young, Jr., V. G.; Zang, Y.; Kooijman, H.; Spek, A. L.; Que, Jr., L.; Feringa, B. L. *Inorg. Chem.* **1999**, *38*, 1929-1936.

48) Addison, A. W.; Rao, T. N.; Reedijk, J. *J. Chem. Soc., Dalton Trans.* **1984**, 1349-1356; τ is defined as (a - b)/60, where a = largest angle, b = second largest angle (τ = 1.0 for ideal trigonal bipyramidal; τ = 0.0 for ideal square pyramidal).

49) Schweitzer, D.; Shearer, J.; Rittenberg, D. K.; Shoner, S. C.; Ellison, J. J.; Loloee, R.; Lovell, s.; Barnhart, D.; Kovacs, J. A. *Inorg. Chem.* **2002**, *41*, 3128-3136.

50) Seela, J. L.; Knapp, M. J.; Kolack, K. S.; Chang, H.-R.; Huffman, J. C.; Hendrickson, D. N.; Christou, G. *Inorg. Chem.* **1998**, *37*, 516-525.

51) Coasta, T.; Dorfman, J. R.; Hagen, K. S.; Holm, R. H. *Inorg. Chem.* **2002**, *41*, 3128-3136.

52) Gorelsky, S. I.; Basumallick, L.; Vura-Weis, J.; Sarangi, R.; Hodgson, K. O.; Hedman, B.; Fujisawa, K.; Solomon, E. I. *Inorg. Chem.* **2005**, *44*, 4947-4960.

53) Brown, C. D.; Neidig, M. L.; Neibergall, M. B.; Lipscomb, J. D.; Solomon, E. I. *J. Am. Chem. Soc.* **2007**, *129*, 7427-7438.

54) Cotton, F. A.; Wilkinson, G. *Advanced Inorganic Chemistry*, Interscience: New York, 1972.

55) Goldsmith, C. R.; Stack, T. D P. *J. Am. Chem. Soc.* **2005**, *127*, 9904-9912.

56) Groni, S.; Hureau, C.; Guillot, R.; Blondin, G.; Blain, G.; Anxolabéhère-Mallart, E. *Inorg. Chem.* **2008**, *47*, 11783-11797.

Chapter 3

Reactivity of Thiolate-Ligated Mn(II) Complexes with Biological Oxidants

3.1 Introduction

Many biochemical transformations mediated by metalloenzymes involve the activation of small molecules. The activation of dioxygen (or reduced dioxygen derivatives) is particularly important regarding the function of many manganese metalloenzymes, such as the Mn superoxide dismutase, Mn catalase, and Mn(II)-dependent extradiol-cleaving catechol dioxygenases.[1-7] The formation of O-O bonds, or microscopic reverse of O-O bond activation, is also of high interest since this reaction occurs at the oxygen-evolving complex of photosystem II.[8-10] In order to further understand how Nature utilizes transition metal ions to promote these types of processes, the reactivity of synthetic Mn complexes with various biologically-relevant small molecules have been widely explored. These studies have been valuable in understanding the properties and reactivity of many Mn metalloenzymes, especially when biochemical data is inconclusive or missing all together. This is particular true with regards to observing reaction intermediates, as synthetic Mn complexes have provided the only known examples of Mn-peroxo and Mn-oxo species which are widely believed to participate in many enzymatic reactions.[11-14]

Synthetic complexes have also been helpful in understanding how thiolate ligands influence the structural, magnetic, spectroscopic, and reactive properties of transition metal ions in biological systems. Regarding the influence of these ligands on reactivity, electron transfer reactions are known to be facilitated by thiolate ligands due to a decrease in metal ion redox potentials.[15-17] It has also been demonstrated that thiolate ligands lower activation barriers for O_2

binding.[18-19] Furthermore, thiolate ligands have been shown to promote the activation of strong bonds, such as the C-H bonds in saturated hydrocarbons and the C≡N bond of nitriles.[20-22] Most of these properties have been established through studies involving thiolate-ligated Fe(II), Co(II), and Cu(I) complexes; despite the large number of Mn metalloenzymes that react with O_2 or reduced O_2 derivatives, small molecule activation reactions involving thiolate-ligated Mn(II) complexes have gone practically unexplored.

This chapter discusses the reactivity of each thiolate-ligated Mn(II) complex described in Chapter 2 with various biological oxidants, including O_2, O_2^-, and H_2O_2. Reactions between these complexes and non-biologically relevant oxygen-atom transfer reagents, such as iodosylbenzene (PhIO) and *meta*-chloroperbenzoic acid (*m*CPBA), and one electron chemical oxidants are also described. The reactivity of the alkoxide-ligated Mn(II) complexes and thiolate-ligated Fe(II) complexes from Chapter 2 have also been explored and are discussed herein. It is worthwhile to note that metastable intermediates have been observed from low temperature O_2 reactions with a few thiolate-ligated Mn(II) complexes included in this chapter; characterization of these intermediates are the topic of Chapter 4. Also omitted from this chapter are reactions involving alkyl hydroperoxides, as these studies are discussed in Chapter 5.

The labeling scheme used to reference each complex is slightly modified from that used in Chapter 2 and is provided here; $[Mn^{II}(S^{Me2}N_4(tren))](PF_6)$ (**1**), $[Mn^{II}(S^{Me2}N_4(6\text{-H-DPEN}))(MeOH)](PF_6)\cdot MeOH$ (**2**), $[Mn^{II}(S^{Me2}N_4(6\text{-H-DPPN}))]_2(BF_4)_2$ (**3**), $[Mn^{II}(S^{Me2}N_4(6\text{-Me-DPEN}))](BF_4)$ (**4**), $[Mn^{II}(S^{Me2}N_4(6\text{-Me-DPPN}))](BPh_4)$ (**5**), $[(Mn^{II}(S^{Me2}N_4(4\text{-OMe-3,5-Me-DPEN})))(Mn^{II}(S^{Me2}N_4(4\text{-OMe-3,4-Me-DPEN}))(Cl))](\mu\text{-}S^{Me2})(BF_4)\cdot Et_2O$ (**6**), $[Mn^{II}(S^{Me2}N_4(2\text{-QuinoEN}))](BPh_4)\cdot MeCN$ (**7**), $[Mn^{II}(S^{Me2}N_4(2\text{-QuinoPN}))](PF_6)$ (**8**), $[Mn^{II}(O^{Me2}N_4(tren))]_2(PF_6)_2\cdot MeCN$ (**9**), $[Mn^{II}(HO^{Me2}N_4(6\text{-Me-}$

DPEN)(CHO$_2$))](BPh$_4$)·MeCN·Et$_2$O (**10**), [Mn^{II}(O^{Me2}N$_4$(6-Me-DPPN))](BPh$_4$) (**11**), [Fe^{II}(S^{Me2}N$_4$(tren))](PF$_6$) (**24**), [Fe^{II}(S^{Me2}N$_4$(6-H-DPEN))(MeOH)](PF$_6$) (**25**), [Fe^{II}(S^{Me2}N$_4$(6-H-DPPN))](PF$_6$) (**26**), [Fe^{II}(S^{Me2}N$_4$(6-Me-DPEN))](PF$_6$) (**27**), and [Fe^{II}(S^{Me2}N$_4$(2-QuinoEN))](PF$_6$)·MeOH (**28**) (Schemes 3.1 and 3.2).

Scheme 3.1 ChemDraw representations of [Mn^{II}(S^{Me2}N$_4$(tren))]$^+$ (**1**), [Mn^{II}(S^{Me2}N$_4$(6-H-DPEN))(MeOH)]$^+$ (**2**), {[Mn^{II}(S^{Me2}N$_4$(6-H-DPPN))]$_2$}$^{2+}$ (**3**), [Mn^{II}(S^{Me2}N$_4$(6-Me-DPEN))]$^+$ (**4**), [Mn^{II}(S^{Me2}N$_4$(6-Me-DPPN))]$^+$ (**5**), and {[(Mn^{II}(S^{Me2}N$_4$(4-OMe-3,5-Me-DPEN)))(Mn^{II}(S^{Me2}N$_4$(4-OMe-3,4-Me-DPEN))(Cl))]}$^+$ (**6**), (revised numbering scheme).

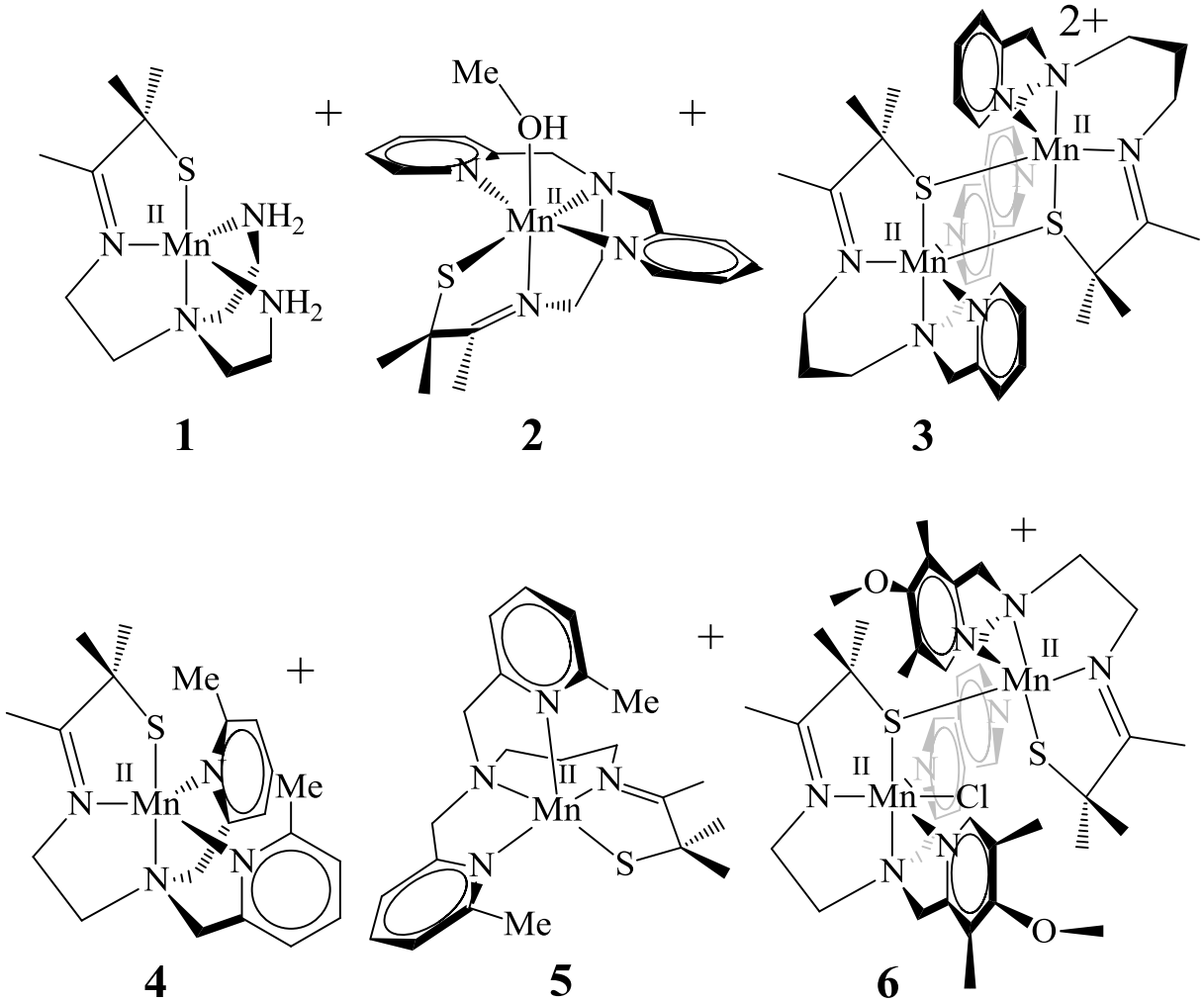

Scheme 3.2 ChemDraw representations of $[Mn^{II}(S^{Me2}N_4(2\text{-QuinoEN}))]^+$ (**7**), $[Mn^{II}(S^{Me2}N_4(2\text{-QuinoPN}))]^+$ (**8**), $\{[Mn^{II}(O^{Me2}N_4(tren))]_2\}^{2+}$(**9**), $[Mn^{II}(HO^{Me2}N_4(6\text{-Me-DPEN})(CHO_2))]^+$ (**10**), and $[Mn^{II}(O^{Me2}N_4(6\text{-Me-DPPN}))]^+$ (**11**) (revised numbering scheme).

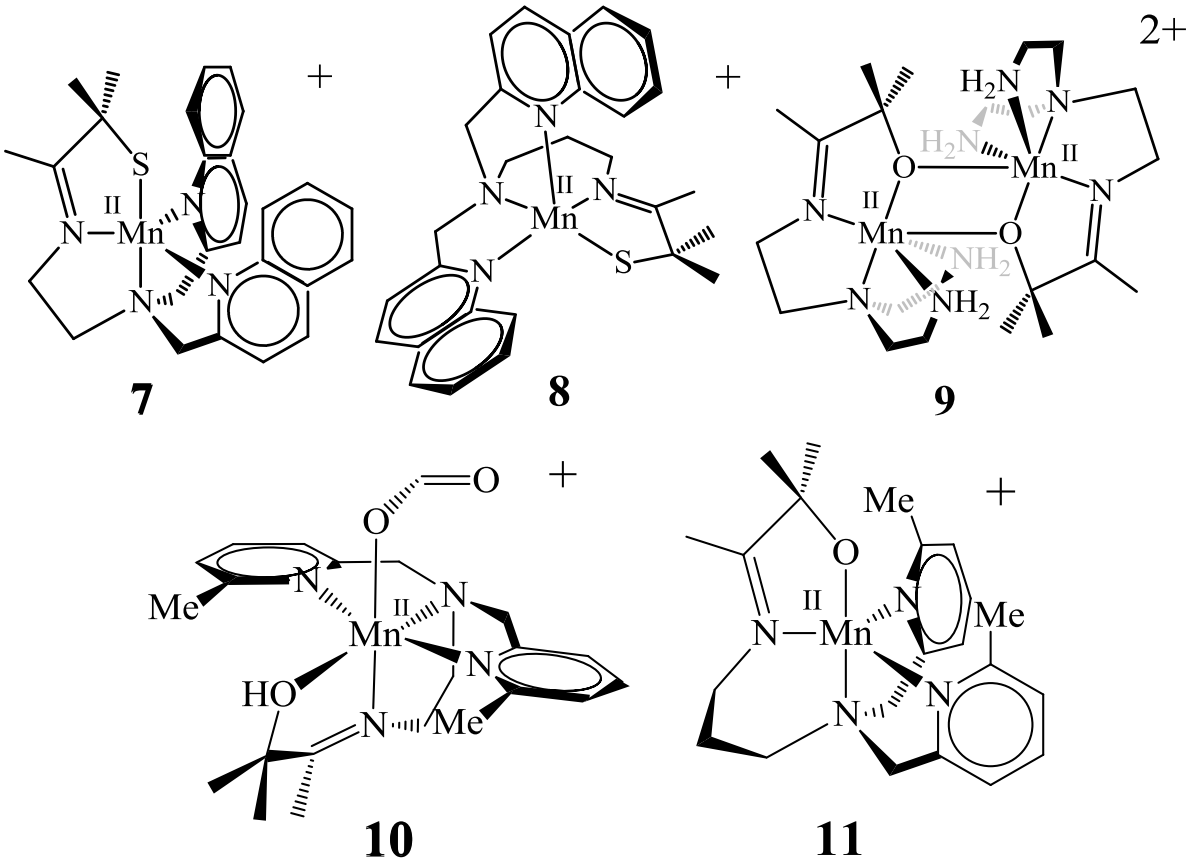

3.2 Experimental Section

3.2.1 General Considerations

All manipulations were performed using Schlenk techniques or under an N_2 atmosphere in a glovebox. Reagents and solvents were purchased from commercial vendors, were of highest available purity, and were used without further purification unless otherwise noted. MeOH (Na), MeCN (CaH_2), and CH_2Cl_2 (CaH_2) were dried and distilled prior to use. Et_2O was rigorously degassed and purified using solvent purification columns housed in a custom stainless steel

cabinet and dispensed by a stainless steel schlenk-line (GlassContour). ^{1}H NMR spectra were recorded on a Bruker AV 300 FT NMR spectrometer at ambient temperature and were referenced to residual deuterated solvent. Chemical shifts are listed in parts per million (ppm). UV/vis spectra were recorded on a Varian Cary 50 spectrophotometer equipped with a fiber optic cable connected to a "dip" ATR probe (C-technologies). A custom-built two-neck solution sample holder equipped with a threaded glass connector was sized specifically to fit the "dip" probe. Electrospray-ionization mass spectra were obtained on a Bruker Esquire Liquid Chromatograph-Ion Trap mass spectrometer. EPR spectra were recorded on a Bruker E580 CW-EPR spectrometer operating at X-band frequency between 4 and 8 K with an Oxford helium cryostat. Magnetic moments (solid state) were obtained by zero-field cooling experiments from 5 to 300 K with polycrystalline samples in gel-caps using a Quantum Design MPMS S5 SQUID magnetometer. Solid state magnetic susceptibility data were fit with the julX software program. Pascal's constants were used to correct for diamagnetic contributions to the experimental magnetic moment.[23] Solution magnetic moments were calculated by the Evans method and temperature corrections were made by the method described by Van Geet.[24-25] Cyclic voltammograms were recorded in MeCN (100 mM $^{n}Bu_4N(PF_6)$ supporting electrolyte) on a PAR 263A potentiostat with a glassy carbon working electrode, platinum auxillary electrode, and a $Ag^{+}/AgNO_3$ reference electrode. X-ray crystallography data were recorded on a Bruker APEX II single crystal X-ray diffractometer with Mo Kα radiation or a Bruker SMART Apex CCD diffractometer with Mo Kα radiation. Elemental analyses were performed by Atlantic Microlabs, Norcross, GA. Complexes **1-11** were synthesized as described in Chapter 2, while complexes **24-33** and tri(para-tolyl)aminium hexafluorophosphate were synthesized as

previously described.[26-27] All dioxygen reactions (with excess O_2) were performed with a pressurized O2 tank.

3.2.2 Synthetic Protocols for Complexes 12-21

3.2.2.1 Synthesis of $[Mn^{III}(S^{Me2}N_4(tren))]_2(\mu\text{-}O)(PF_6)_2$ (12). A solution of **1** (1.3 g, 3.0 mmol) was prepared in MeCN (5 mL) under an inert atmosphere in a dry box. Solid iodosylbenzene (0.70 g, 3.2 mmol) was added directly to the MeCN solution of **1**. The resulting mixture was allowed to stir at ambient temperature for approximately five minutes. After filtering all insoluble reaction components, the resulting solution was evaporated to dryness *in vacuo* to afford a dark purple solid. Recrystallization of the crude purple solid from MeCN at -30 °C afforded the title compound in 97 % yield (1.32 g, 0.16 mmol). Electronic absorption spectrum: λ_{max} (nm) (ε ($M^{-1}cm^{-1}$)) (MeCN): 535 (510). Redox potential (MeCN vs. SCE, 298 K): $E_{1/2}$ = +31 mV. IR (Nujol): $\nu_{C=N}$ 1628 cm^{-1}. Magnetic moment (solution, CD_2Cl_2, 298 K): 4.32 μ_B/Mn. ESI-MS: Expected *m/z* for $[C_{22}H_{50}N_8OS_2Mn_2]^{2+}$ = 315.2, found *m/z* = 316.2. Elemental Analysis for $C_{22}H_{50}N_8OF_{12}P_2S_2Mn_2$ Calculated: C, 29.15; H, 5.56; N, 12.36. Found: C, 28.19; H, 5.40; N, 12.28.

3.2.2.2 Synthesis of $[Mn^{III}(S^{Me2}N_4(6\text{-}H\text{-}DPEN))]_2(\mu\text{-}O)(PF_6)_2\cdot(MeCN)_2$ (13). A procedure similar to that employed in the preparation of **12** was conducted with the following reagent amounts; **2** (0.20 g, 0.35 mmol) and iodosylbenzene (0.08 g, 0.35 mmol). Complex **13** was obtained as a light purple solid in 95 % yield (0.19 g, 0.17 mmol). Electronic absorption spectrum: λ_{max} (nm) (ε ($M^{-1}cm^{-1}$)) (MeCN): 327 (4463), 332 (4470), 533 (286). Redox potential (MeCN vs. SCE, 298 K): $E_{1/2}$ = +295 mV. IR (Nujol): $\nu_{C=N}$ 1600 cm^{-1}. Magnetic moment (solid state, 300 K): 4.89 μ_B/Mn; (solution, MeOH, 298 K): 4.01 μ_B/Mn. ESI-MS: Expected *m/z* for $[C_{38}H_{50}N_8OS_2Mn_2]^{2+}$ = 404.3, found *m/z* = 404.3. Elemental Analysis for $C_{38}H_{50}N_8OF_{12}P_2S_2Mn_2$ Calculated: C, 41.54; H, 4.59; N, 10.20. Found: C, 41.31; H, 4.68; N, 10.36.

3.2.2.3 Synthesis of $[Mn^{III}(S^{Me2}N_4(6\text{-H-DPPN}))]_2(\mu\text{-O})(PF_6)_2\cdot(MeCN)_2$ (14). A procedure similar to that employed in the preparation of **13** was conducted with the following reagent amounts; **3** (0.43 g, 0.78 mmol). Complex **14** was obtained as a dark purple solid in 98 % yield (0.43 g, 0.38 mmol). Electronic absorption spectrum: λ_{max} (nm) (ε ($M^{-1}cm^{-1}$)) (MeCN): 363 (3300), 513 (1140). Redox potential (MeCN vs. SCE, 298 K): $E_{1/2}$ = +276 mV. IR (Nujol): $\nu_{C=N}$ 1601 cm^{-1}. Magnetic moment (solution, MeOH, 298 K): 4.44 μ_B/Mn. ESI-MS: Expected *m/z* for $[C_{40}H_{54}N_8OS_2Mn_2]^{2+}$ = 418.4, found *m/z* = 418.4. Elemental Analysis for $C_{40}H_{54}N_8OF_{12}P_2S_2Mn_2$ Calculated: C, 42.63; H, 4.83; N, 9.94. Found: C, 39.94; H, 4.70; N, 10.00.

3.2.2.4 Synthesis of $[Mn^{III}(S^{Me2}N_4(6\text{-Me-DPEN}))]_2(\mu\text{-O})(BF_4)_2\cdot(MeOH)_2$ (15). Complex **4** (0.500 g, 0.48 mmol) was dissolved in MeCN (5 mL) and allowed to stir while exposed to air for 30 minutes, during which time the solution turned from yellow to dark purple. The purple solution was then added dropwise into pentane (10 mL), causing the immediate precipitation of a purple solid. The solid material was isolated via filtration, redissolved in MeCN (2 mL), and carefully layered with Et_2O (10 mL). The mixture was allowed to diffuse together at room temperature overnight, resulting in dark purple crystals suitable for X-ray diffraction studies in 97% yield (0.49 g, 0.47 mmol). Electronic absorption spectrum (MeCN): λ_{max} (nm) (ε ($M^{-1}cm^{-1}$)): 325 (3690), 557 (520). IR (Nujol): $\nu_{C=N}$ 1602 cm^{-1}. Magnetic moment (solution, MeOH, 298 K): 3.11 μ_B/Mn. Redox potential (MeCN vs. SCE, 298 K): $E_{1/2}$ = +465 mV. ESI-MS: Expected *m/z* for $[C_{42}H_{58}N_8OS_2Mn_2]^{2+}$ = 432.5, found *m/z* = 432.6. Elemental Analysis for $C_{44}H_{66}B_2N_8O_3F_8S_2Mn_2$; Calculated: C, 47.93; H, 6.03; N, 10.16. Found: C, 46.18; H, 5.62; N, 10.34.

3.2.2.5 Synthesis of $[Mn^{III}(S^{Me2}N_4(6\text{-Me-DPPN}))]_2(\mu\text{-O})(BPh_4)_2$ (16). An 8 mL EtCN solution of **5** (0.200 g, 0.26 mmol) was prepared under an inert atmosphere in a dry box. The resulting yellow solution was removed from the dry box, cooled to -80 °C, and exposed to air overnight. During this period the solution was found to turn from yellow to dark brown. Cold Et_2O (-80 °C, 10 mL) was carefully layered on top of the EtCN solution, and the resulting mixture was maintained at -80 °C for a

few weeks to permit the formation of small crystals suitable for X-ray diffraction studies. Electronic absorption spectrum (MeCN): λ_{max} (nm) (ε ($M^{-1}cm^{-1}$)): 374 (750), 594 (190). ESI-MS: Expected *m/z* for $[C_{44}H_{62}N_8OS_2Mn_2]^{2+}$ = 446.5, found *m/z* = 446.3.

3.2.2.6 Synthesis of $[Mn^{III}(S^{Me2}N_4$(4-MeO-3,5-Me-DPEN))$]_2(\mu$-O)$(PF_6)_2\cdot(MeCN)_2$ (17). A procedure similar to that employed in the preparation of **13** was conducted with the following reagent amounts; **6** (0.12 g, 0.19 mmol). Complex **17** was obtained as a dark red solid in 98% yield (0.012 g, 0.0093 mmol). Electronic absorption spectrum: (MeCN): λ_{max} (nm) (ε ($M^{-1}cm^{-1}$)): 357 (6330), 419 (3250), 497 (br, 2720). IR (Nujol): $\nu_{C=N}$ 1617 cm^{-1}. Magnetic moment (solution, MeOH, 298 K): 4.29 μ_B/Mn. Redox potential (MeCN vs. SCE, 298 K): E_{pa} = +334 mV. ESI-MS: Expected *m/z* for $[C_{58}H_{64}N_8O_5S_2Mn_2]^{2+}$ = 563.6, found *m/z* = 564.0. Elemental Analysis for $C_{58}H_{64}N_8O_5F_{12}P_2S_2Mn_2$; Calculated: C, 39.70; H, 4.93; N, 7.41. Found: C, 38.54; H, 4.70; N, 7.55.

3.2.2.7 Synthesis of $[Mn^{III}(S^{Me2}N_4$(2-QuinoEN))$]_2(\mu$-O)$(PF_6)_2\cdot(CH_2Cl_2)$ (18). A procedure similar to that employed in the preparation of **15** was conducted with the following reagent amounts; **7** (0.50 g, 0.78 mmol). Complex **18** was obtained as a dark purple solid in 98% yield (0.50 g, 0.38 mmol). Electronic absorption spectrum: λ_{max} (nm) (ε ($M^{-1}cm^{-1}$)) (MeCN): 345 (3450), 562 (550); (MeOH): 332 (2000), 606 (240). IR (Nujol): $\nu_{C=N}$ 1603 cm^{-1}. Magnetic moment (solution, MeOH, 298 K): 4.40 μ_B/Mn. Redox potential (MeCN vs. SCE, 298 K): E_{pa} = +780 mV. ESI-MS: Expected *m/z* for $[C_{54}H_{58}N_8OS_2Mn_2]^{2+}$ = 504.5, found *m/z* = 504.4. Elemental Analysis for $C_{54}H_{58}N_8OF_{12}P_2S_2Mn_2$ Calculated: C, 49.93; H, 4.50; N, 8.63. Found: C, 50.93; H, 4.63; N, 8.77.

3.2.2.8 Synthesis of $[Mn^{III}(S^{Me2}N_4$(2-QuinoPN))$]_2(\mu$-O)$(BPh_4)_2\cdot$(MeCN) (19). A procedure similar to that described for the synthesis of **16** was employed with a 4 mL EtCN solution of the BPh_4^- salt of **8** (0.400 g, 0.482 mmol). Small gray crystals of **19** were obtained in extremely low yields from crystallization attempts. Electronic absorption spectrum (MeCN): λ_{max} (nm): 388, 573 (br). ESI-MS: Expected *m/z* for $[C_{56}H_{62}N_8OS_2Mn_2]^{2+}$ = 518.6, found *m/z* = 518.3.

3.2.2.9 Synthesis of $[Mn^{III}(O^{Me2}N_4(tren))]_2(\mu\text{-}OH)(PF_6)_3\cdot MeCN$ (20). A procedure similar to that employed in the preparation of **15** was conducted with the following reagent amounts; **9** (1.71 g, 2.0 mmol). Complex **20** was obtained as a black solid in 35% yield (0.31 g, 0.35 mmol). Electronic absorption spectrum (MeCN): λ_{max} (nm): 424 (600), 553 (570). IR (Nujol): $\nu_{O\text{-}H}$ 3312 cm^{-1}. Redox potential (MeCN vs. SCE, 298 K): E_{pa} = +767 mV, E_{pc} = +487 mV.

3.2.2.10 Synthesis of $[Mn^{III}(O^{Me2}N_4(6\text{-}Me\text{-}DPEN))]_2(\mu\text{-}O)(BF_6)_2\cdot(MeCN)_2$ (21). A procedure similar to that employed in the preparation of **15** was conducted with the following reagent amounts; **10** (1.72 g, 3.2 mmol). Complex **21** was obtained as a dark purple solid in 89% yield (1.54 g, 1.4 mmol). Electronic absorption spectrum (MeCN): λ_{max} (nm): 213 (390), 423 (90), 557 (125). ESI-MS: Expected *m/z* for $[C_{42}H_{58}N_8O_3Mn_2]^{2+}$ = 416.1, found *m/z* = 416.2.

3.2.3 Alternative Synthetic Protocol for Complexes 12-21 Using Iodosylbenzene

Addition of 1.1 equivalents of solid iodosylbenzene to a saturated MeCN solution (2-4 mL typical volume) containing either **2-4**, **6-7**, or **9-10** under an inert atmosphere and at room temperature resulted in the immediate formation of **13-15**, **17-18**, or **20-21**, respectively. After removing the remaining solids by filtration, the resulting MeCN solution was added dropwise into stirring pentane (10-12 mL) to precipitate the desired product. Isolation of the precipitated solid materials via filtration afforded products in yields close to, or identical to, those when using dioxygen as a reagent.

3.2.4 X-ray Crystallographic Structure Determination

A purple plate of **12** with dimensions 0.48 x 0.36 x 0.07 mm^3 was mounted on a glass capillary with oil. Data was collected at -143 ˚C. The crystal-to-detector distance was set to 43.5 mm and the exposure time was 60 seconds per degree for all sets of exposure. The scan

width was 1˚. Data collection was 99.0% complete to 25.0˚ in ϑ. A total of 74,378 partial and complete reflections were collected covering the indices h = -15 to 15, k = -20 to 20, l = -44 to 44. 7,279 reflections were symmetry independent and the R_{int} = 0.0971 indicated that the data was less than average quality (0.07 average quality). Indexing and unit cell refinement indicated an orthorhombic P lattice with the space group P b c a (No. 61). One of the two PF_6^- anions in each asymmetric unit was disordered about an F-P-F axis. Disorder was also observed on carbon 6 and modeled with a 61/39 % occupancy factor.

A purple plate of **13** with dimensions 0.59 x 0.40 x 0.40 mm^3 was mounted on a glass capillary with oil. Data was collected at -143 ˚C. The crystal-to-detector distance was set to 30 mm and the exposure time was 45 seconds per degree for all sets of exposure. The scan width was 1˚. Data collection was 99.3% complete to 25.0˚ in ϑ. A total of 78,553 partial and complete reflections were collected covering the indices h = -21 to 21, k = -26 to 26, l = -15 to 19. 910 reflections were symmetry independent and the R_{int} = 0.114 indicated that the data was less than average quality (0.07 average quality). Indexing and unit cell refinement indicated an orthorhombic P lattice with the space group P 2_12_12 (No. 18).

A black prism of **14** with dimensions 0.36 x 0.24 x 0.05 mm^3 was mounted on a glass capillary with oil. Data was collected at -143 ˚C. The crystal-to-detector distance was set to 30 mm and the exposure time was 60 seconds per degree for all sets of exposure. The scan width was 1˚. Data collection was 65.8% complete to 25.0˚ in ϑ. A total of 25,195 partial and complete reflections were collected covering the indices h = -104 to 8, k = -27 to 14, l = -23 to 23. 5,576 reflections were symmetry independent and the R_{int} = 0.1052 indicated that the data was less than average quality (0.07 average quality). Indexing and unit cell refinement indicated a monoclinic P lattice with the space group P $2_1/c$ (No. 14). One of the two PF_6^- anions in the

asymmetric unit was disordered (50 % occupancy) with a SO_4^{2-} anion (25 % occupancy). The two acetonitriles present were also disordered and therefore modeled with 50 % occupancy.

A black block of **15** with dimensions 0.30 x 0.20 x 0.15 mm^3 was mounted on a glass capillary with oil. Data was collected at -183 ˚C. The crystal-to-detector distance was set to 40 mm and the exposure time was 10 seconds per degree for all sets of exposure. The scan width was 0.5˚. Data collection was 98.7% complete to 25.0˚ in ϑ. A total of 21,006 partial and complete reflections were collected covering the indices h = -16 to 13, k = -23 to 24, l = -9 to 14. 5,905 reflections were symmetry independent and the R_{int} = 0.041 indicated that the data was good (0.07 average quality). Indexing and unit cell refinement indicated a monoclinic P lattice with the space group P 2_1/c (No. 14). A methanol molecule was present with half-site occupancy in each asymmetric unit.

A colorless plate of **16** with dimensions 0.30 x 0.20 x 0.15 mm^3 was mounted on a glass capillary with oil. Data was collected at -173 ˚C. The crystal-to-detector distance was set to 40 mm and the exposure time was 10 seconds per degree for all sets of exposure. The scan width was 0.5˚. Data collection was 99.7% complete to 25.0˚ in ϑ. A total of 123,964 partial and complete reflections were collected covering the indices h = -38 to 38, k = -15 to 15, l = -33 to 34. 10,165 reflections were symmetry independent and the R_{int} = 0.0732 indicated that the data was less than average quality (0.07 average quality). Indexing and unit cell refinement indicated a monoclinic C lattice with the space group C 2/c (No. 15).

A red plate of **17** with dimensions 0.50 x 0.30 x 0.10 mm^3 was mounted on a glass capillary with oil. Data was collected at -143 ˚C. The crystal-to-detector distance was set to 30 mm and the exposure time was 20 seconds per degree for all sets of exposure. The scan width

was 2˚. Data collection was 98.0% complete to 25.0˚ in ϑ. A total of 68,741 partial and complete reflections were collected covering the indices h = -21 to 21, k = -28 to 27, l = -19 to 18. 10,722 reflections were symmetry independent and the R_{int} = 0.1380 indicated that the data was less than average quality (0.07 average quality). Indexing and unit cell refinement indicated a monoclinic C lattice with the space group C c (No. 9).

A black block of **18** with dimensions 0.40 x 0.30 x 0.15 mm^3 was mounted on a glass capillary with oil. Data was collected at -163 ˚C. The crystal-to-detector distance was set to 40 mm and the exposure time was 10 seconds per degree for all sets of exposure. The scan width was 0.5˚. Data collection was 100% complete to 25.0˚ in ϑ. A total of 40,331 partial and complete reflections were collected covering the indices h = -27 to 27, k = -12 to 12, l = -29 to 29. 5,109 reflections were symmetry independent and the R_{int} = 0.0638 indicated that the data was good (0.07 average quality). Indexing and unit cell refinement indicated a monoclinc C lattice with the space group C 2/c (No. 15). Nearly total molecular disorder required the use of restraints on all thermal parameters.

A gray block of **19** with dimensions 0.10 x 0.10 x 0.05 mm^3 was mounted on a glass capillary with oil. Data was collected at -173 ˚C. The crystal-to-detector distance was set to 40 mm and the exposure time was 60 seconds per degree for all sets of exposure. The scan width was 0.5˚. Data collection was 49.5% complete to 25.0˚ in ϑ. A total of 69,414 partial and complete reflections were collected covering the indices h = -25 to 25, k = -49 to 48, l = -14 to 14. 9,478 reflections were symmetry independent and the R_{int} = 0.6592 indicated that the data was marginal (0.07 average quality). Indexing and unit cell refinement indicated a monoclinic P lattice with the space group P 2_1/c (No. 14).

A black plate of **20** with dimensions 0.17 x 0.15 x 0.05 mm^3 was mounted on a glass capillary with oil. Data was collected at -173 ˚C. The crystal-to-detector distance was set to 40 mm and the exposure time was 40 seconds per degree for all sets of exposure. The scan width was 0.5˚. Data collection was 98.0% complete to 25.0˚ in ϑ. A total of 8,083 partial and complete reflections were collected covering the indices h = -47 to 43, k = 0 to 15, l = 0 to 23. 8,083 reflections were symmetry independent and the R_{int} = 0.1316 indicated that the data was problematic (0.07 average quality). Indexing and unit cell refinement indicated a monoclinic C lattice with the space group C 2/c (No. 15). The raw data appeared twinned. A 180° twin operation (1.000 0 0) was found and resolved with CELL_NOW.[28] One of the three PF_6^- anions in the asymmetric unit was disordered, while a second was disordered with an acetonitrile molecule.

A black plate of **21** with dimensions 0.20 x 0.10 x 0.01 mm^3 was mounted on a glass capillary with oil. Data was collected at -173 ˚C. The crystal-to-detector distance was set to 40 mm and the exposure time was 10 seconds per degree for all sets of exposure. The scan width was 0.5˚. Data collection was 99.6% complete to 25.47˚ in ϑ. A total of 111,610 partial and complete reflections were collected covering the indices h = -29 to 29, k = -16 to 16, l = -30 to 30. 15,865 reflections were symmetry independent and the R_{int} = 0.0543 indicated that the data was good (0.07 average quality). Indexing and unit cell refinement indicated an monoclinic P lattice with the space group P 2_1/c (No. 14). The structure contains disordered diethyl ether and propionitrile molecules.

A black plate of **22** with dimensions 0.10 x 0.05 x 0.05 mm^3 was mounted on a glass capillary with oil. Data was collected at -173 ˚C. The crystal-to-detector distance was set to 40 mm and the exposure time was 50 seconds per degree for all sets of exposure. The scan width

was 0.5˚. Data collection was 99.3% complete to 25.0˚ in ϑ. A total of 54,712 partial and complete reflections were collected covering the indices h = -19 to 19, k = -16 to 16, l = -21 to 21. 7,069 reflections were symmetry independent and the R_{int} = 0.2384 indicated that the data was less than average quality (0.07 average quality). Indexing and unit cell refinement indicated an orthorhombic P lattice with the space group P $2_1/n$ (No. 14).

A yellow prism of **23** with dimensions 0.15 x 0.05 x 0.05 mm^3 was mounted on a glass capillary with oil. Data was collected at -173 ˚C. The crystal-to-detector distance was set to 40 mm and the exposure time was 20 seconds per degree for all sets of exposure. The scan width was 0.5˚. Data collection was 96.5% complete to 25.0˚ in ϑ. A total of 22,505 partial and complete reflections were collected covering the indices h = -16 to 16, k = -16 to 16, l = -18 to 18. 8,374 reflections were symmetry independent and the R_{int} = 0.0994 indicated that the data was less than average quality (0.07 average quality). Indexing and unit cell refinement indicated a monoclinic P lattice with the space group P $\bar{1}$ (No. 2). A fraction of a water molecule is disordered with a hydroxide dimer with an 85/15 ratio.

All X-ray data sets were integrated and scaled using either hkl-SCALEPACK or SAINT, SADABS within the APEX2 software package by Bruker.[29-30] Solutions were made by direct methods (SHELXS, SIR97) to produce complete heavy atom phasing models.[31] Scattering factors are from Waasmair and Kirfel.[32] Structures were completed by difference Fourier synthesis with either SHELXL97 or SHELXTL 6.10. Hydrogen atoms were placed in geometrically idealized positions and constrained to ride on their parent atoms with C-H distances in the range of 0.95-1.00 Å. Isotropic thermal parameters Ueq were fixed such that they were 1.2Ueq of their parent aom Ueq for C-Hs and 1.5Ueq for methyl groups. All non-hydrogen atoms were refined anisotropically by full-matrix least-squares.

3.3 Results and Discussion

3.3.1 Reactivity of Thiolate-Ligated Mn(II) Complexes 1-8 With Dioxygen, Superoxide, Hydrogen Peroxide, Iodosylbenzene, and *meta*-Chloroperbenzoic Acid

Reactions between complexes **1-8** and a wide variety of oxidants (O_2, KO_2, H_2O_2, iodosylbenzene (PhIO), *meta*-chloroperbenzoic acid (*m*CPBA)) were each performed in MeCN solution (1-2 mM Mn(II)) at room temperature and monitored by UV/Vis spectroscopy. Each of the five oxidants explored were found to rapidly react with the eight thiolate-ligated Mn(II) complexes under these experimental conditions. Reactions between each Mn(II) complex and oxidant combination were easily observed by color changes in the respective reaction solution from pale yellow (Mn(II)) to either dark purple or red, indicating the possible formation of an oxidized Mn species. Regardless of the oxidant used, reactions with complexes **1**-**4** and **6**-**7** resulted in the formation of robust oxo-bridged Mn(III,III) dimers (complexes **12**-**15** and **17**-**18**, respectively) which could be isolated in high yields (90-98 %). The final products from room temperature reactions involving complexes **5** and **8** in MeCN have yet to be determined, however the formation of oxo-bridged Mn(III,III) dimers (complexes **16** and **19**, respectively) from O_2 reactions under slightly different conditions (EtCN, 193 K) with these two complexes has been determined.

The oxo-bridged Mn(III,III) dimers **12**-**19** have each been structurally characterized by X-ray crystallography; ORTEP diagrams of $[Mn^{III}(S^{Me2}N_4(tren))]_2(\mu\text{-}O)(PF_6)_2$ (**12**), $[Mn^{III}(S^{Me2}N_4(6\text{-}H\text{-}DPEN))]_2(\mu\text{-}O)(PF_6)_2\cdot(MeCN)_2$ (**13**), $[Mn^{III}(S^{Me2}N_4(6\text{-}H\text{-}DPPN))]_2(\mu\text{-}O)(PF_6)_2\cdot(MeCN)_2$ (**14**), $[Mn^{III}(S^{Me2}N_4(6\text{-}Me\text{-}DPEN))]_2(\mu\text{-}O)(BF_4)_2\cdot(MeOH)_2$ (**15**), $[Mn^{III}(S^{Me2}N_4(6\text{-}Me\text{-}DPPN))]_2(\mu\text{-}O)(BPh_4)_2$ (**16**), $[Mn^{III}(S^{Me2}N_4(4\text{-}MeO\text{-}3,5\text{-}Me\text{-}DPEN))]_2(\mu\text{-}$

O)$(PF_6)_2$·$(MeCN)_2$ (**17**), $[Mn^{III}(S^{Me2}N_4(2\text{-QuinoEN}))]_2(\mu\text{-O})(PF_6)_2$·$CH_2Cl_2$ (**18**), and $[Mn^{III}(S^{Me2}N_4(2\text{-QuinoPN}))]_2(\mu\text{-O})(BPh_4)_2$·MeCN (**19**) are provided in Figures 3.1-3.3. Two orientations of each dimer are shown in each figure in order to fully illustrate the structural features of each complex. Selected metrical parameters and crystal data for **12**-**19** are provided in Tables 3.1 and 3.2, respectively.

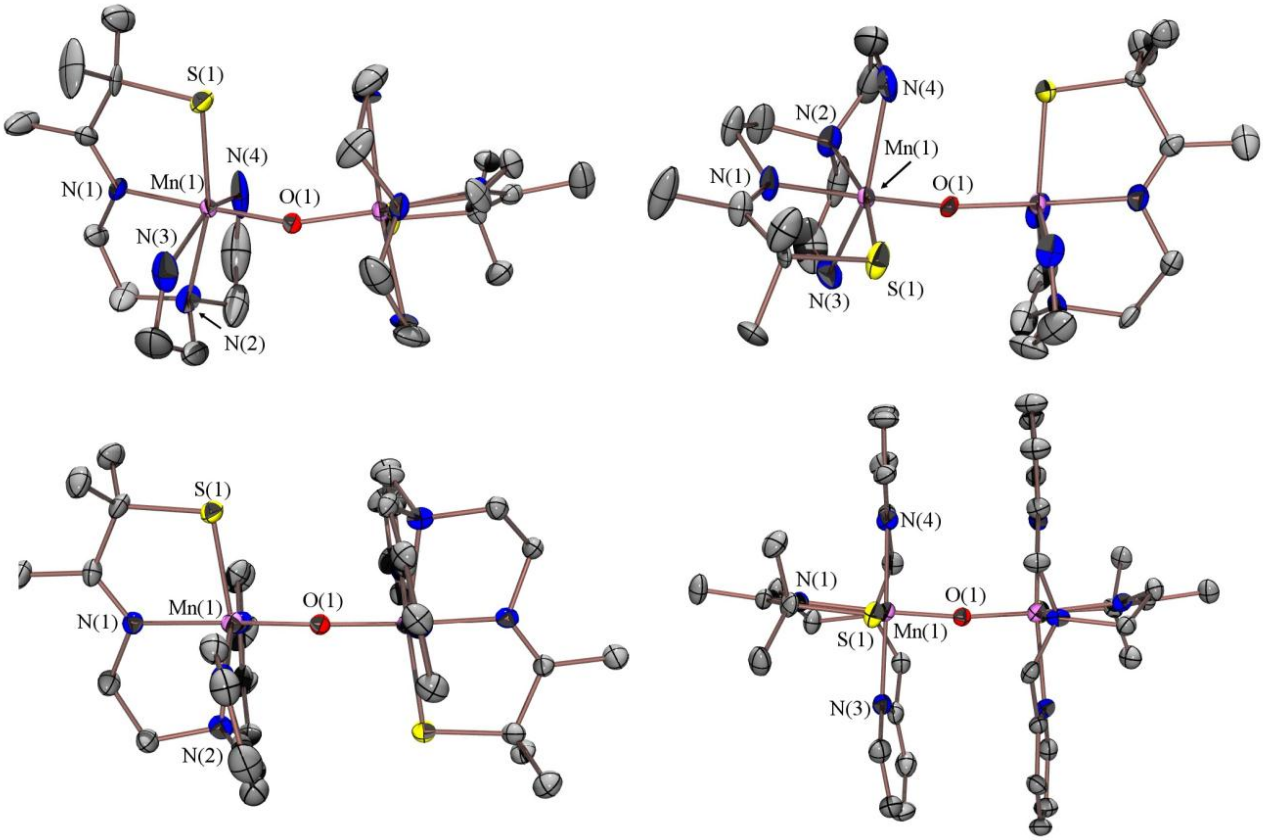

Figure 3.1 ORTEP diagrams (50 % probability) of $\{[Mn^{III}(S^{Me2}N_4(tren))]_2(\mu\text{-O})\}^{2+}$ (**12**, top) and $\{[Mn^{III}(S^{Me2}N_4(6\text{-H-DPEN}))]_2(\mu\text{-O})\}^{2+}$ (**13**, bottom) with hydrogen atoms, counterions, and solvents of crystallization omitted for clarity.

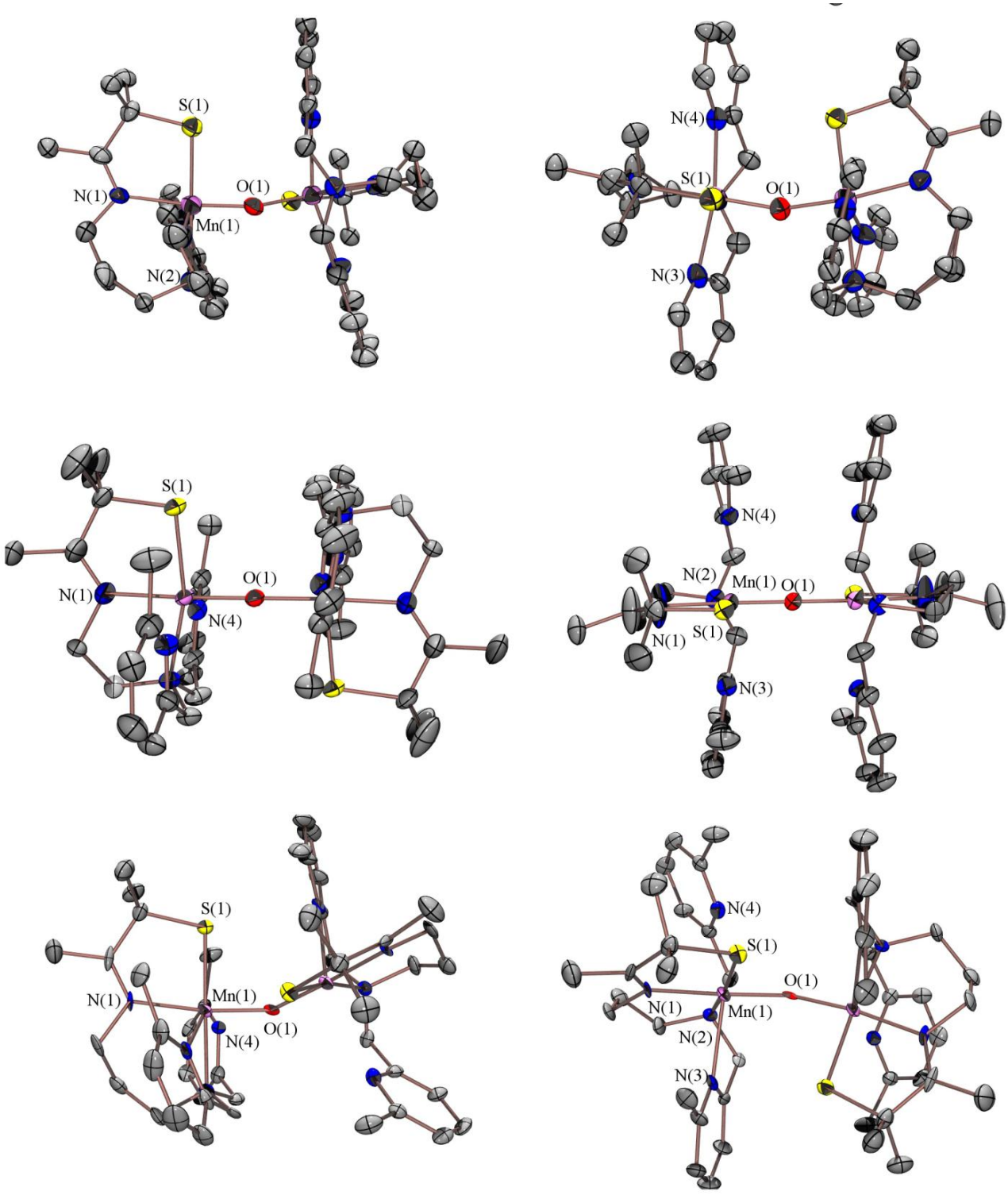

Figure 3.2 ORTEP diagrams (50 % probability) of $\{[Mn^{III}(S^{Me2}N_4(6\text{-H-DPPN}))]_2(\mu\text{-O})\}^{2+}$ (**14**, top), $\{[Mn^{III}(S^{Me2}N_4(6\text{-Me-DPEN}))]_2(\mu\text{-O})\}^{2+}$ (**15**, center), $\{[Mn^{III}(S^{Me2}N_4(6\text{-Me-DPPN}))]_2(\mu\text{-O})\}^{2+}$ (**16**, bottom) with hydrogen atoms, counterions, and solvents of crystallization omitted for clarity.

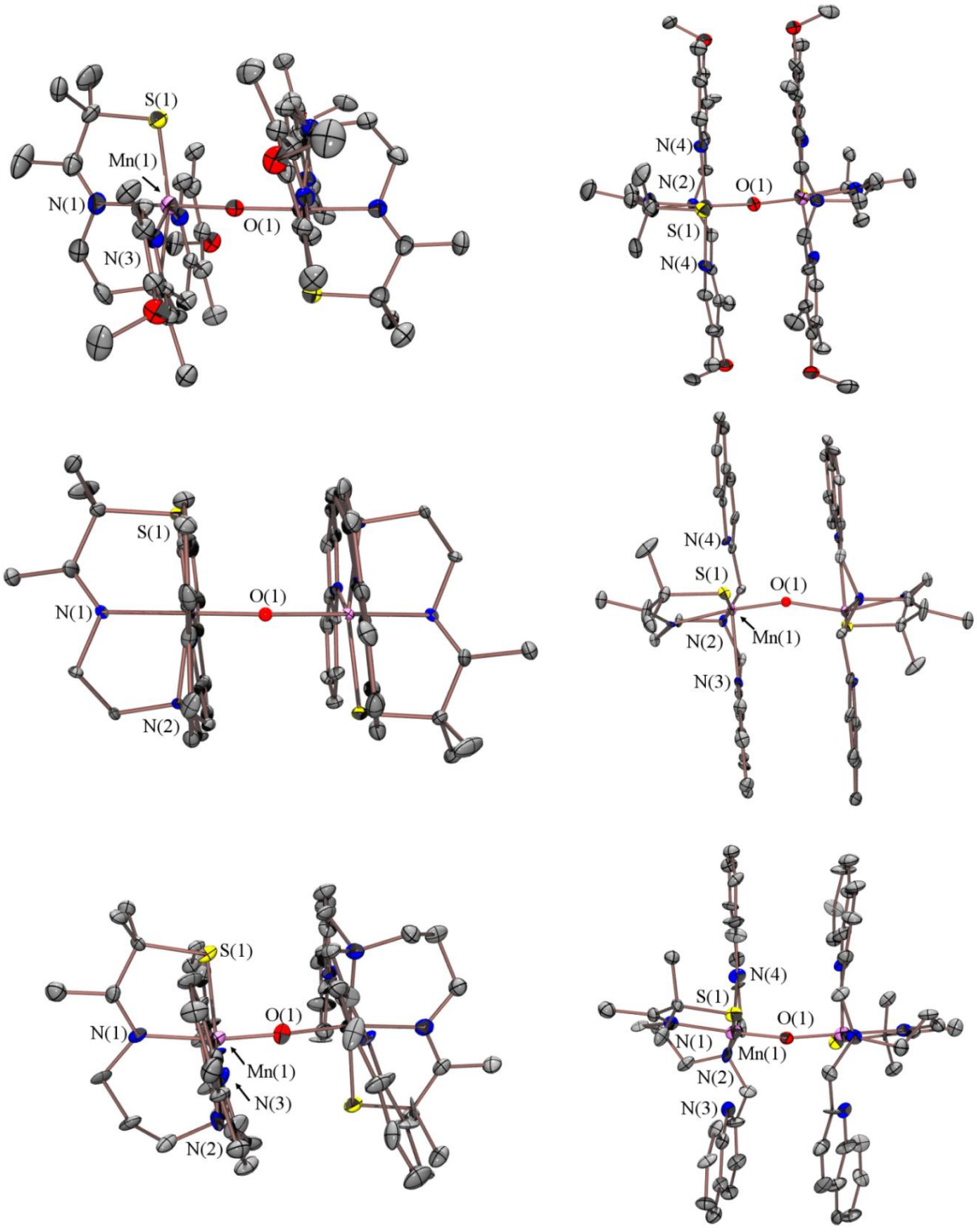

Figure 3.3 ORTEP diagrams (50 % probability) of $\{[Mn^{III}(S^{Me2}N_4(4\text{-MeO-3,5-Me-DPEN}))]_2(\mu\text{-}O)\}^{2+}$ (**17**, top), $\{[Mn^{III}(S^{Me2}N_4(2\text{-QuinoEN}))]_2(\mu\text{-}O)\}^{2+}$ (**18**, center), and $\{[Mn^{III}(S^{Me2}N_4(2\text{-QuinoPN}))]_2(\mu\text{-}O)\}^{2+}$ (**19**, bottom) with hydrogen atoms, counterions, and solvent of crystallization omitted for clarity.

Table 3.1 Selected bond distances (Å) and angles (degrees) for $[Mn^{III}(S^{Me2}N_4(tren))]_2(\mu\text{-}O)(PF_6)_2$ (**12**), $[Mn^{III}(S^{Me2}N_4(6\text{-}H\text{-}DPEN))]_2(\mu\text{-}O)(PF_6)_2\cdot(MeCN)_2$ (**13**), $[Mn^{III}(S^{Me2}N_4(6\text{-}H\text{-}DPPN))]_2(\mu\text{-}O)(PF_6)_2\cdot(MeCN)_2$ (**14**), $[Mn^{III}(S^{Me2}N_4(6\text{-}Me\text{-}DPEN))]_2(\mu\text{-}O)(BF_4)_2\cdot(MeOH)_2$ (**15**), $[Mn^{III}(S^{Me2}N_4(6\text{-}Me\text{-}DPPN))]_2(\mu\text{-}O)(BPh_4)_2$ (**16**), $[Mn^{III}(S^{Me2}N_4(4\text{-}MeO\text{-}3,5\text{-}Me\text{-}DPEN))]_2(\mu\text{-}O)(PF_6)_2\cdot(MeCN)_2$ (**17**), $[Mn^{III}(S^{Me2}N_4(2\text{-}QuinoEN))]_2(\mu\text{-}O)(PF_6)_2\cdot(CH_2Cl_2)$ (**18**), and $[Mn^{III}(S^{Me2}N_4(2\text{-}QuinoPN))]_2(\mu\text{-}O)(BPh_4)_2\cdot(MeCN)$ (**19**).

	12	**13**	**14**	**15**	**16**	**17**	**18**	**19**
Mn(1)-S(1)	2.286(2)	2.2968(15)	2.263(6)	2.2767(7)	2.2547(16)	2.271(6)	2.292(1)	2.290(8)
Mn(1)-N(1)	2.017(6)	2.011(4)	2.080(14)	1.999(3)	2.0660(16)	2.014(13)	2.010(3)	2.08(2)
Mn(1)-N(2)	2.172(7)	2.190(4)	2.258(14)	2.151(2)	2.2008(16)	2.164(13)	2.130(3)	2.18(2)
Mn(1)-N(3)	2.351(8)	2.243(5)	2.303(16)	2.581(2)	2.3524(16)	2.241(14)	2.543(3)	2.33(2)
Mn(1)-N(4)	2.280(6)	2.223(5)	2.224(15)	2.501(2)	2.796(16)	2.187(13)	2.370(3)	2.54(2)
Mn(1)-O(1)	1.783(5)	1.771(4)	1.801(9)	1.7602(4)	1.7941(6)	1.762(12)	1.7599(6)	1.753(17)
Mn(2)-S(2)	2.283(2)	2.3018(15)	2.264(5)	2.2767(7)	2.2547(16)	2.301(5)	2.292(1)	2.269(8)
Mn(2)-N(5)	2.023(6)	2.023(5)	2.060(13)	1.999(3)	2.0660(16)	2.008(14)	2.010(3)	2.12(2)
Mn(2)-N(6)	2.163(6)	2.181(4)	2.258(15)	2.151(2)	2.2008(16)	2.199(15)	2.130(3)	2.17(2)
Mn(2)-N(7)	2.315(6)	2.279(5)	2.310(17)	2.581(2)	2.3524(16)	2.274(12)	2.543(3)	2.36(2)
Mn(2)-N(8)	2.360(6)	2.229(5)	2.231(12)	2.501(2)	2.3524(16)	2.222(13)	2.370(3)	2.60(2)
Mn(2)-O(1)	1.799(5)	1.750(4)	1.797(9)	1.7602(4)	1.7941(6)	1.748(12)	1.7599(6)	1.852(17)
S(1)-Mn(1)-N(1)	83.1(2)	83.37(13)	83.2(5)	82.08(8)	82.43(5)	83.1(4)	82.60(8)	81.2(6)
S(1)-Mn(1)-N(2)	164.58(19)	164.23(14)	107.4(4)	164.17(7)	169.44(5)	166.1(4)	163.90(9)	171.5(7)
S(1)-Mn(1)-N(3)	104.6(2)	101.24(13)	105.2(5)	106.19(6)	117.65(5)	103.7(4)	101.40(8)	110.6(6)
S(1)-Mn(1)-N(4)	102.3(2)	106.60(13)	177.6(4)	106.84(6)	98.04(5)	105.8(5)	109.23(8)	101.4(6)
O(1)-Mn(1)-S(1)	96.65(17)	98.93(13)	90.3(3)	95.37(2)	98.9(1)	98.2(5)	99.20(3)	91.2(6)
O(1)-Mn(1)-N(1)	177.7(3)	176.47(18)	173.5(6)	177.21(9)	172.35(6)	177.1(5)	177.02(12)	172.4(9)
O(1)-Mn(1)-N(2)	98.9(2)	96.10(18)	98.5(4)	100.44(6)	100.44(6)	95.7(6)	95.8(4)	93.8(8)
O(1)-Mn(1)-N(3)	90.7(2)	88.18(17)	93.0(5)	92.79(5)	95.78(4)	92.0(5)	92.7(3)	92.0(7)
O(1)-Mn(1)-N(4)	92.6(2)	92.32(17)	89.6(5)	89.14(5)	90.25(6)	93.9(5)	102.7(4)	87.8(7)
S(2)-Mn(2)-N(5)	82.7(2)	82.66(13)	83.1(4)	82.08(8)	82.43(5)	82.9(6)	82.60(8)	81.1(7)
S(2)-Mn(2)-N(6)	164.71(17)	165.07(14)	107.0(4)	164.17(7)	169.44(5)	165.3(4)	165.9(4)	169.4(6)
S(2)-Mn(2)-N(7)	98.4(2)	102.85(12)	105.9(5)	106.19(6)	117.65(5)	103.5(4)	105.9(3)	112.2(6)
S(2)-Mn(2)-N(8)	107.47(18)	106.18(12)	179.1(5)	106.84(6)	98.04(5)	105.9(4)	103.1(3)	100.38(6)
O(1)-Mn(2)-S(2)	95.50(17)	99.34(13)	90.5(3)	95.37(2)	98.9(1)	98.7(5)	99.20(3)	90.3(6)
O(1)-Mn(2)-N(5)	175.9(2)	175.78(18)	173.4(5)	177.21(9)	172.35(6)	174.3(6)	177.02(12)	171.4(8)
O(1)-Mn(2)-N(6)	99.2(2)	95.22(18)	95.3(5)	100.44(6)	100.44(6)	96.0(6)	95.8(4)	112.2(6)
O(1)-Mn(2)-N(7)	93.7(2)	90.07(17)	93.3(5)	92.79(5)	95.78(6)	90.7(5)	92.7(3)	92.0(7)
Mn(1)···Mn(2)	3.521	3.515	3.540	3.520	3.433	3.508	3.512	3.590
Mn(1)-O(1)-Mn(2)	158.8(3)	173.0(2)	159.4(6)	180.0	146.15(11)	175.4(7)	172.3(2)	169.4(9)

Table 3.2 Crystal data for $[Mn^{III}(S^{Me2}N_4(tren))]_2(\mu\text{-}O)(PF_6)_2$ (**12**), $[Mn^{III}(S^{Me2}N_4(6\text{-}H\text{-}DPEN))]_2(\mu\text{-}O)(PF_6)_2\cdot(MeCN)_2$ (**13**), $[Mn^{III}(S^{Me2}N_4(6\text{-}H\text{-}DPPN))]_2(\mu\text{-}O)(PF_6)_2\cdot(MeCN)_2$ (**14**), $[Mn^{III}(S^{Me2}N_4(6\text{-}Me\text{-}DPEN))]_2(\mu\text{-}O)(BF_4)_2\cdot(MeOH)_2$ (**15**), $[Mn^{III}(S^{Me2}N_4(6\text{-}Me\text{-}DPPN))]_2(\mu\text{-}O)(BPh_4)_2$ (**16**), $[Mn^{III}(S^{Me2}N_4(4\text{-}MeO\text{-}3,5\text{-}Me\text{-}DPEN))]_2(\mu\text{-}O)(PF_6)_2\cdot(MeCN)_2$ (**17**), $[Mn^{III}(S^{Me2}N_4(2\text{-}QuinoEN))]_2(\mu\text{-}O)(PF_6)_2\cdot(CH_2Cl_2)$ (**18**), and $[Mn^{III}(S^{Me2}N_4(2\text{-}QuinoPN))]_2(\mu\text{-}O)(BPh_4)_2\cdot(MeCN)$ (**19**).

	12	**13**	**14**	**15**	**16**	**17**	**18**	**19**
Formula	$C_{24}H_{53}F_{12}Mn_2N_9P_2S_2$	$C_{158}H_{209}F_{48}Mn_8N_{35}O_4P_8S_8$	$C_{168}H_{228}F_{36}Mn_8N_{36}O_8P_6S_9$	$C_{43}H_{62}B_2F_8Mn_2N_8O_2S_2$	$C_{92}H_{102}B_2Mn_2N_8OS_2$	$C_{106}H_{156}F_{24}Mn_4P_4N_{19}O_{10}S_4$	$C_{55}H_{60}B_2Cl_2F_8Mn_2N_8OS_2$	$C_{106}H_{105}B_2Mn_2N_9OS_2$
MW	947.69	4,518.36	4,477.74	1,070.63	1,531.44	2,785.39	1,267.63	1,716.61
T, K	130(2)	130(2)	130(2)	90.0(5)	100(2)	130(2)	110(2)	100(2)
Unit Cell[a]	Orthorhombic	Orthorhombic	Monoclinic	Monoclinic	Monoclinic	Monoclinic	Monoclinic	Monoclinic
a, Å	12.5660(2)	17.7825(3)	10.0220(11)	12.1000(8)	29.031(5)	17.836(6)	22.609(5)	25.110(7)
b, Å	17.0110(4)	22.2270(4)	24.809(2)	18.4235(13)	11.517(5)	24.061(7)	10.503(5)	48.999(14)
c, Å	36.2170(6)	12.5151(7)	21.184(3)	10.9203(8)	25.531(5)	15.955(2)	24.302(5)	14.589(6)
α, deg	90	90	90	90	90	90	90	90
β, deg	90	90	92.476(4)	96.947(2)	106.070(5)	105.976(15)	106.332(5)	89.56(8)
γ, deg	90	90	90	90	90	90	90	90
V, $Å^3$	7,741.8(3)	4,946.6(3)	5,262.2(11)	2,416.5(3)	8,203(4)	6,583(3)	5,538(3)	17,949(10)
Z	8	1	1	2	4	2	4	4
d(calc), g/cm^3	1.626	1.517	1.413	1.471	1.240	1.405	1.520	0.635
Sp. Group	P b c a	P 2_12_12	P $2_1/c$	P $2_1/c$	C 2/c	C c	C 2/c	P $2_1/c$
R[b]	0.0971	0.1140	0.1140	0.0538	0.0890	0.0814	0.0447	0.1630
R_w[c]	0.1460	0.1133	0.2388	0.1499	0.1661	0.2175	0.1250	0.4681
GOF	1.014	0.969	0.995	1.02	0.917	0.864	1.023	1.044

[a]In all cases: Mo Kα(λ = 0.7170 Å) radiation. [b]$R = \Sigma||F_0| - |F_c||/ \Sigma|F_0|$. [c]$R_w = [\Sigma w(|F_0| - |F_c|)^2/ \Sigma wF_0^{1/2}$, where $w^{-1} = [\sigma_{count}^2 + (0.05F^2)^2]4F^2$.

UV/Vis titration experiments revealed that reactions with complexes **1**-**4** and **6**-**7** required the same amount of each type of oxidant (per Mn ion) to maximize the formation of each respective oxo-bridged Mn(III,III) dimer product (*vide infra*). These reactions were also found to result in nearly *quantitative* formation of the respective oxo-bridged dimer, as determined by using extinction coefficients obtained from crystalline samples of high analytical purity. Quantitative UV/Vis spectra (extinction coefficient versus wavelength) for dimers **12**-**15** and **17**-**18** are provided in Appendix A.19-A.24. In solution, oxo-bridged dimers **12**-**15** and **17**-**18** were found to be indefinitely stable, even if exposed to excess O_2 over extended periods of time. Collectively, these observations are significant because they demonstrate that the reactions between each Mn(II) complex and oxidant are metal-centered, as opposed to sulfur oxidation reactions that are often found to occur with thiolate-ligated transition metal complexes under oxidizing conditions. The reaction conditions and minimum reagent stoichiometries that were found necessary to provide maximum yields for oxo-bridged **12**-**15** and **17**-**18** from **1**-**4** and **6**-**7**, respectively, are illustrated in Scheme 3.3. The instability of dimers **16** and **19** precluded similar quantitative experiments to be performed with complexes **5** and **8**. A typical UV/Vis titration experiment between complex **4** and PhIO is provided in Figure 3.4; similar spectra were obtained from reactions with all combinations of Mn(II) complexes (**1**-**4**, **6**-**7**) and oxidants.

Experiments aimed towards observing reaction intermediates were conducted through low temperature reactions between complexes **1**-**8** and each oxidant at either 233 K (MeCN) or 193 K (EtCN) and monitored by UV/Vis spectroscopy. The metastable oxo-bridged Mn(III,III) dimers from O_2 reactions with **5** and **8** (yielding dimers **16** and **19**, respectively) were observed in EtCN at 193 K (*vide supra*). As shown in Figure 3.5, the addition of excess amounts of O_2 to

Scheme 3.3 Generic representation of the reaction conditions used for oxidation of thiolate-ligated **1**-**4** and **6**-**7** to oxo-bridged **12**-**15** and **17**-**18**.

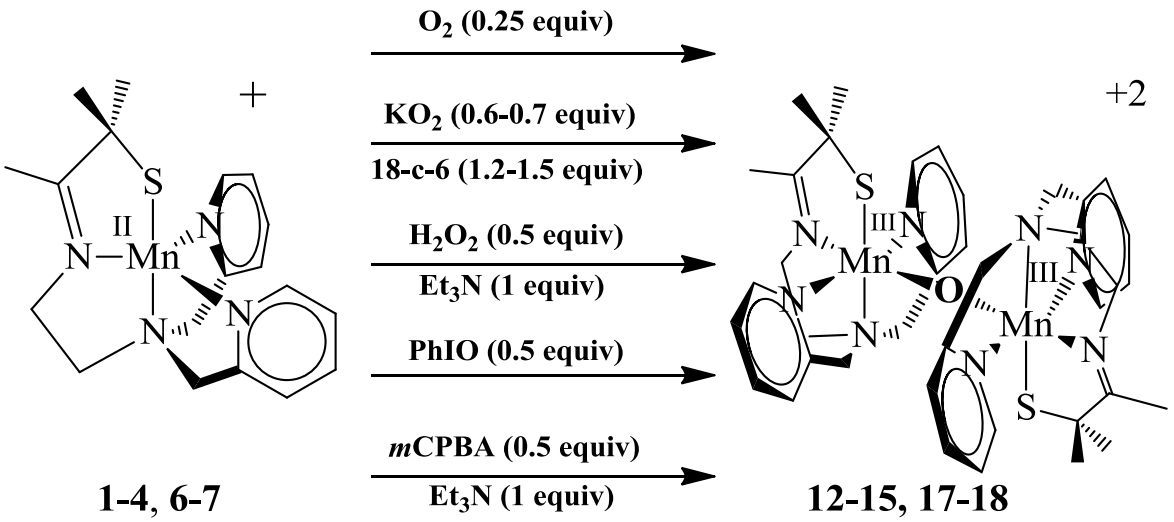

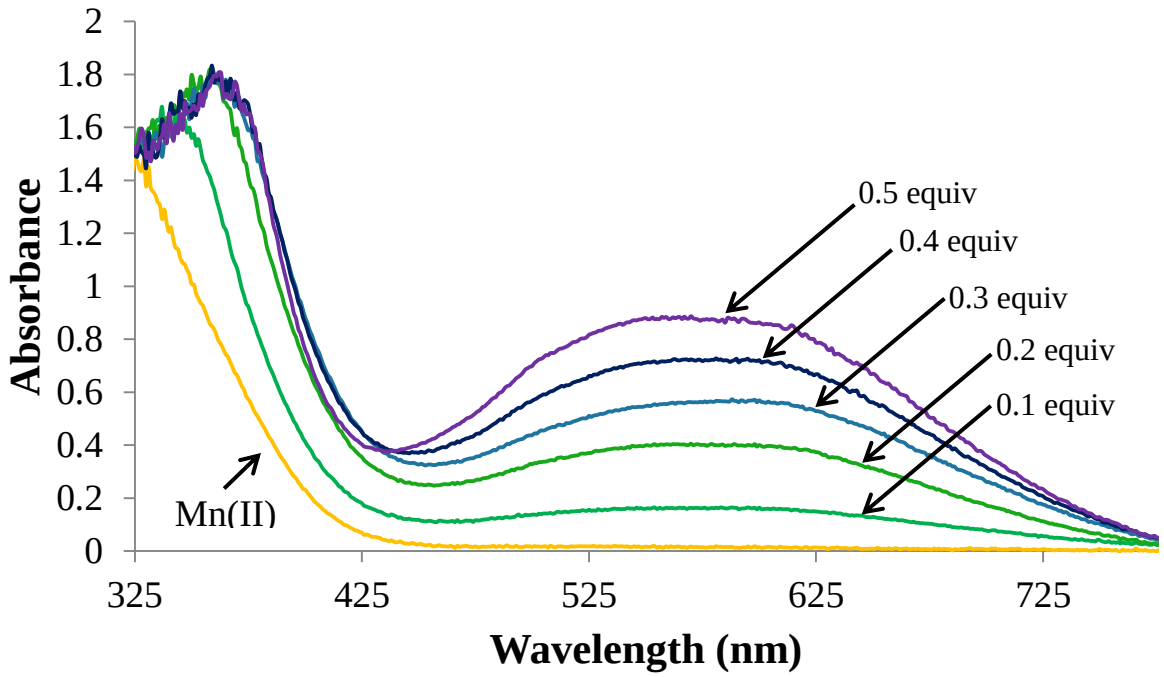

Figure 3.4 Anaerobic UV/Vis titration experiment displaying the reaction between $[Mn^{II}(S^{Me2}N_4(6\text{-Me-DPEN}))](BF_4)$ (**4**, 2.5 mM) and 0.1 equivalent aliquots of iodosylbenzene (PhIO) in MeCN at 293 K. Addition of PhIO beyond 0.5 equivalents did not elicit an observable change in the UV/Vis spectrum.

193 K EtCN solutions of **5** resulted in the formation of a new species characterized by an absorbance band with a λ_{max} of 610 nm. The final absorbance spectrum in Figure 3.5 is identical to that observed for the X-ray quality crystals of **16**. A similar comparison was made between spectra from reactions between **8** and O_2 and that from X-ray quality crystals of **19** (Figure 2.6). Similar spectra were observed from reactions between **5** and **8** with KO_2 or PhIO, respectively.

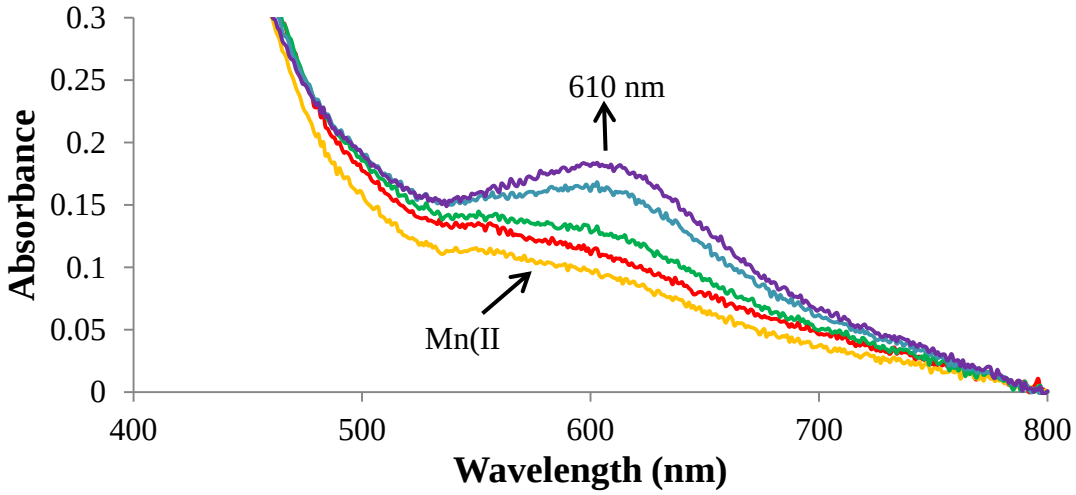

Figure 3.5 UV/Vis spectra displaying the reaction between $[Mn^{II}(S^{Me2}N_4(6\text{-Me-DPPN}))](BPh_4)$ (**5**, 1 mM) and excess O_2 in EtCN at 193 K. Traces were recorded in 2 minute intervals.

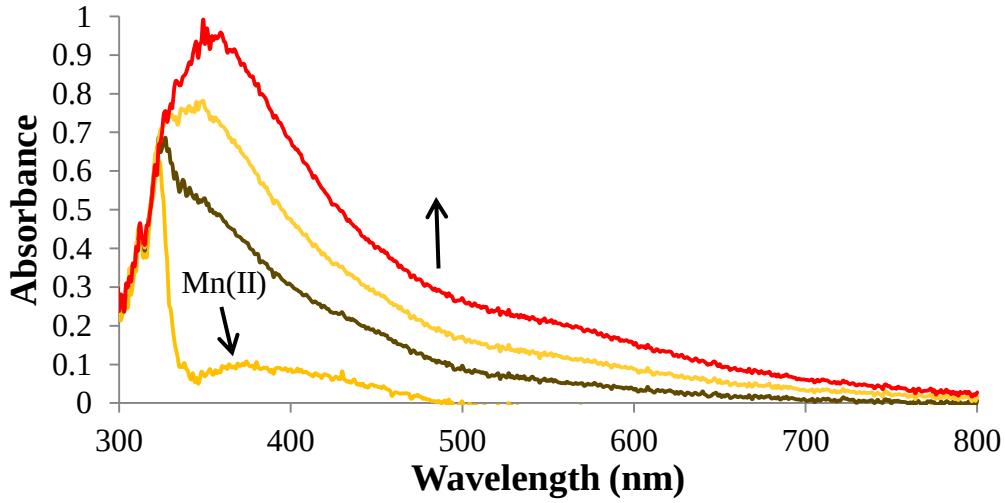

Figure 3.6 UV/Vis spectra displaying the reaction between $[Mn^{II}(S^{Me2}N_4(2\text{-QuinoPN}))](PF_6)$ (**8**, 1.7 mM) and excess O_2 in EtCN at 193 K. Traces were recorded in 5 minute intervals.

Intermediates observed from low temperature O_2 reactions with complexes **4** and **7** are discussed in Chapter 4. No intermediates have been observed from other combinations of Mn(II) complexes and the five oxidants discussed thus far. It is worthwhile to note that intermediates have, however, been observed from reactions between alkyl hydroperoxides and complexes **4**-**5** and **7**-**8**, which are discussed in Chapter 5.

In order to conclusively determine that the bridging oxo ligand in these Mn(III,III) dimers originated from each oxidant and not adventitious water in solution, reactions with ^{18}O-labeled oxidants ($^{18}O_2$, $K^{18}O_2$ (50 % enrichment), $H_2{}^{18}O_2$, $PhI^{18}O$) were performed with each Mn(II) complex and monitored by mass spectrometry (ESI-MS). The presence of ^{16}O or ^{18}O in each dicationic oxo-bridged dimer could be determined from peaks corresponding to a mass-to-charge ratio (*m*/*z*) of M/2 (where M is the dimer mass). This is illustrated by mass spectra obtained from reactions between complex **4** and $^{16}O_2$ or $^{18}O_2$, respectively, which are provided in Figure 3.7. These mass spectra each display a prominent ion peak with *m*/*z* ratios of 432.6 ($^{16}O_2$ reaction) and 433.3 ($^{18}O_2$ reaction), which are close to the calculated *m*/*z* ratios for ^{16}O- and ^{18}O-labeled **15** (432.5 and 433.5, respectively). Similar shifts in ion peak *m*/*z* ratios (~1 mass unit) were observed when comparing the ESI mass spectra of **12**-**14** and **16**-**17** formed from $^{16}O_2$ and $^{18}O_2$, as well. Likewise, experiments with $H_2{}^{18}O_2$ and $PhI^{18}O$ yielded identical results for complexes **1**-**4** and **6**-**7**. Experiments with 50%-labeled $K^{18}O_2$ afforded peaks corresponding to both the ^{16}O- and ^{18}O-labeled oxo-bridged dimers, as is illustrated by the mass spectrum obtained for a reaction between **4** and 50%-labeled $K^{18}O_2$ (Figure 3.8). These results collectively show that the oxo-bridging ligands in dimers **12**-**15** and **17**-**18** are derived from each respective oxidant and suggest that O-O bond activation processes are indeed occurring during reactions with O_2, O_2^-, and H_2O_2.

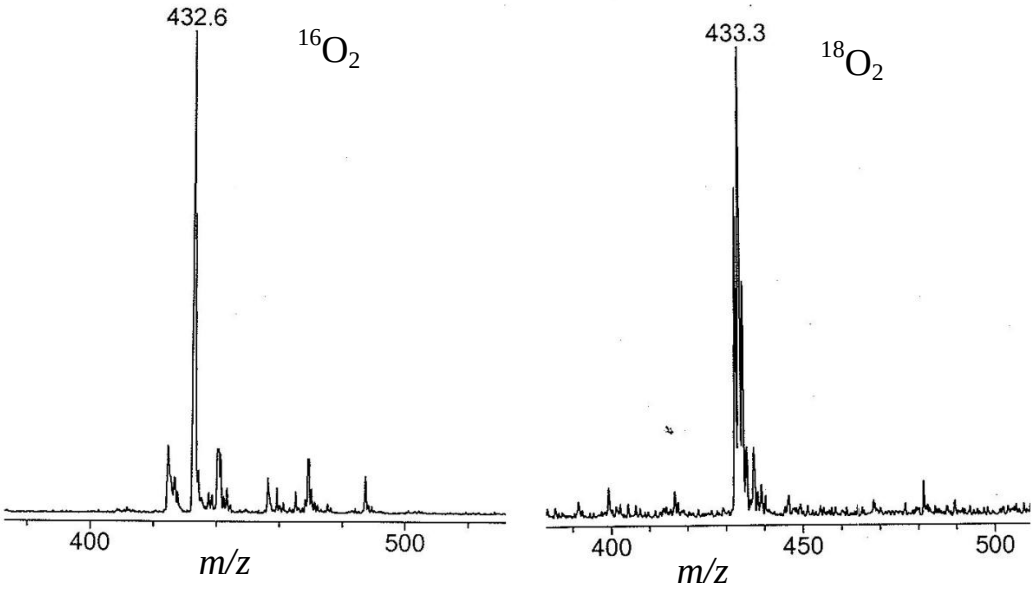

Figure 3.7 Electrospray ionization mass spectra (ESI-MS) from reactions between $[Mn^{II}(S^{Me2}N_4(6\text{-Me-DPEN}))](BF_4)$ (**4**) and $^{16}O_2$ (xs, left) and $^{18}O_2$ (xs, right) in MeCN at 293 K. Parent ion peaks are consistent with the proposed masses of ^{16}O- and ^{18}O-labeled $[Mn^{III}(S^{Me2}N_4(6\text{-Me-DPEN}))]_2(\mu\text{-}O)(BF_4)_2\cdot(MeOH)_2$ (**15**), respectively.

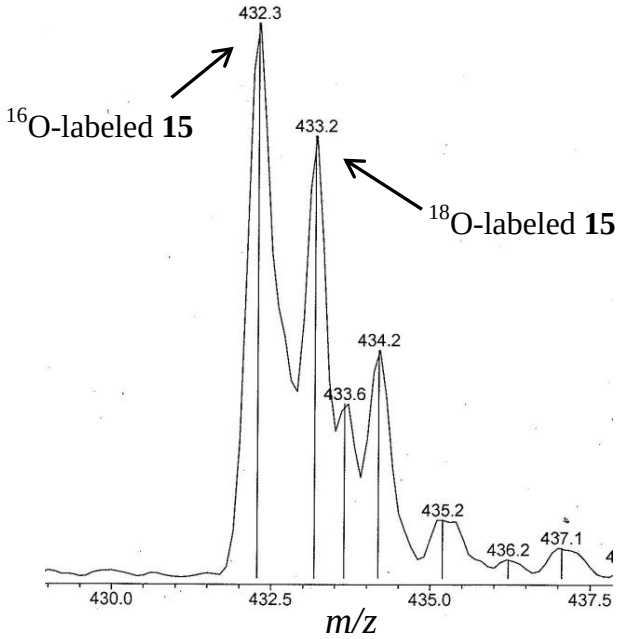

Figure 3.8 Electrospray ionization mass spectrum from a reaction between $[Mn^{II}(S^{Me2}N_4(6\text{-Me-DPEN}))](BF_4)$ (**4**) and 0.7 equivalents of $K^{18}O_2$ (50 % isotopic enrichment) solubilized by 1.0 equivalent of 18-crown-6 either in MeCN at 293 K.

Reactions with complexes **1-4** and **6-7** were also conducted at room temperature in MeCN where $H_2{}^{18}O$ was present prior to the addition of O_2. Given that high-valent Mn-oxo complexes have been shown to undergo rapid oxo ligand exchange reactions with water, these experiments served to provide indirect evidence for the presence of such a species during the O_2 reactions of these complexes (Scheme 3.4).[33] Reactions with 1,000 equivalents of $H_2{}^{18}O$ present in each solution prior to the addition of O_2 resulted in at least partial incorporation of the ^{18}O isotope into each respective oxo-bridged dimer, as was determined by ESI-MS (Scheme 3.5). The ^{18}O isotope was not incorporated if $H_2{}^{18}O$ was added to a MeCN solution containing only the oxo-bridged dimer product, suggesting the species capable of incorporating ^{18}O from a ligand exchange reaction forms prior to the oxo-bridged dimer.

Scheme 3.4 Oxo ligand exchange reaction with high-valent Mn-oxo complexes.

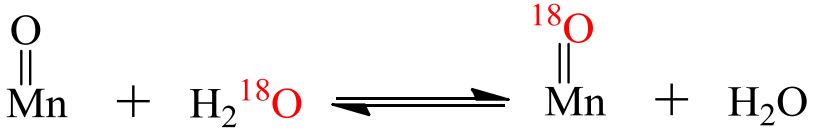

Scheme 3.5 Incorporation of ^{18}O into oxo-bridged **12-15** and **17-18** during O_2 reactions with complexes **1-4** and **6-7** (generic representation).

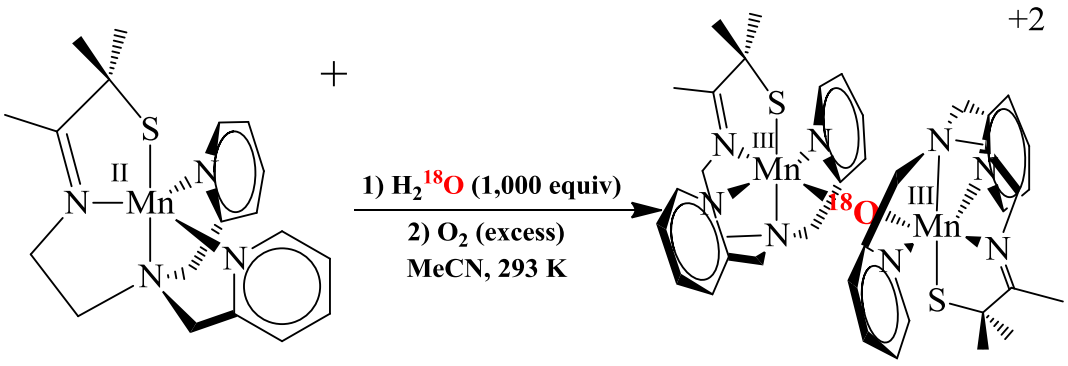

3.3.2 Outer-Sphere Oxidation of Thiolate-Ligated Mn(II) Complexes 1-8

Attempts to oxidize complexes **1-8** via outer-sphere electron transfer reactions were made using tri(para-tolyl)aminium hexafluorophosphate ($[N(C_7H_7)_3](PF_6)$) in anaerobic MeCN solutions at 273 K. These experiments served two purposes; first as control experiments to determine if the corresponding oxo-bridged Mn(III,III) dimers could form as a result of an initial outer-sphere oxidation, as well as to gain insight into how stable the +3 oxidation state is for these complexes. The $[N(C_7H_7)_3]^{\bullet+}$ radical cation has a formal one electron reduction potential, E°', of +780 mV (vs. SCE, MeCN, 293 K), which is at least a few hundred mV higher than the $Mn^{III/II}$ couples determined for **1-5** and **7-8** under these conditions (Chapter 2).[34] Titration of substoichiometric amounts of $[N(C_7H_7)_3](PF_6)$ into solutions containing each of these Mn(II) complexes elicited the appearance of visible region absorption features distinct from those of each respective oxo-bridged Mn(III,III) dimer. As is shown in Figure 3.9, the intensities of these new absorption features maximized following the complete addition of 1 equivalent of $[N(C_7H_7)_3](PF_6)$ per equivalent of Mn(II). Addition beyond 1 equivalent of $[N(C_7H_7)_3](PF_6)$ to

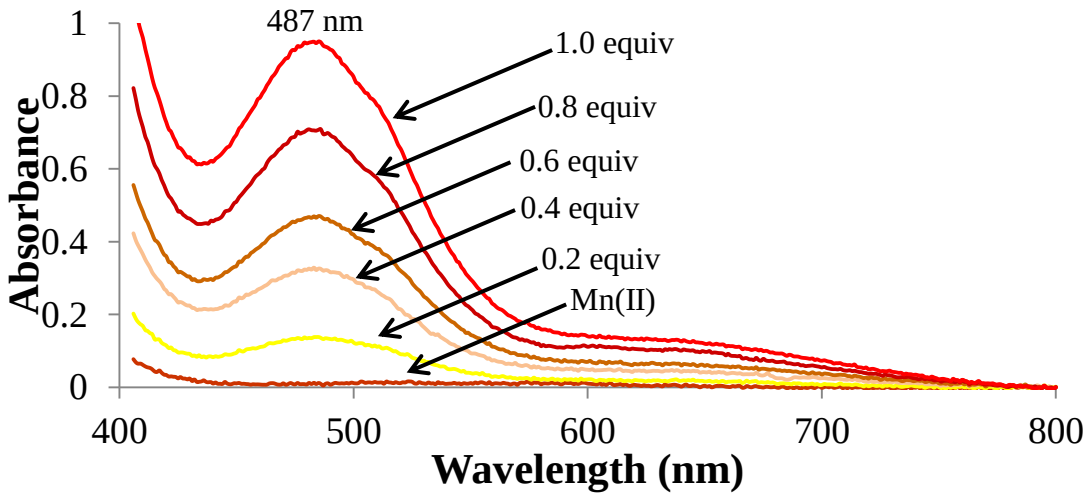

Figure 3.9 Anaerobic UV/Vis titration experiment displaying the reaction between $[Mn^{II}(S^{Me2}N_4(6\text{-Me-DPEN}))](BF_4)$ (**4**, 2 mM) and 0.2 equivalent aliquots of tri(para-tolyl)aminium hexafluorophosphate (200 mM stock solution in MeCN) in MeCN at 0 °C.

each solution resulted in the appearance of an absorbance band at 647 nm that is attributable to the $[N(C_7H_7)_3]^{\bullet+}$ radical cation. Similar titration experiments were also monitored by X-band EPR spectroscopy; these experiments revealed that the addition of $[N(C_7H_7)_3](PF_6)$ to MeCN solutions containing each Mn(II) complex resulted in the disappearance of the characteristic Mn(II) EPR signal centered at $g_{eff} \approx 2.00$ (Figure 3.10). The absence of an observable EPR signal

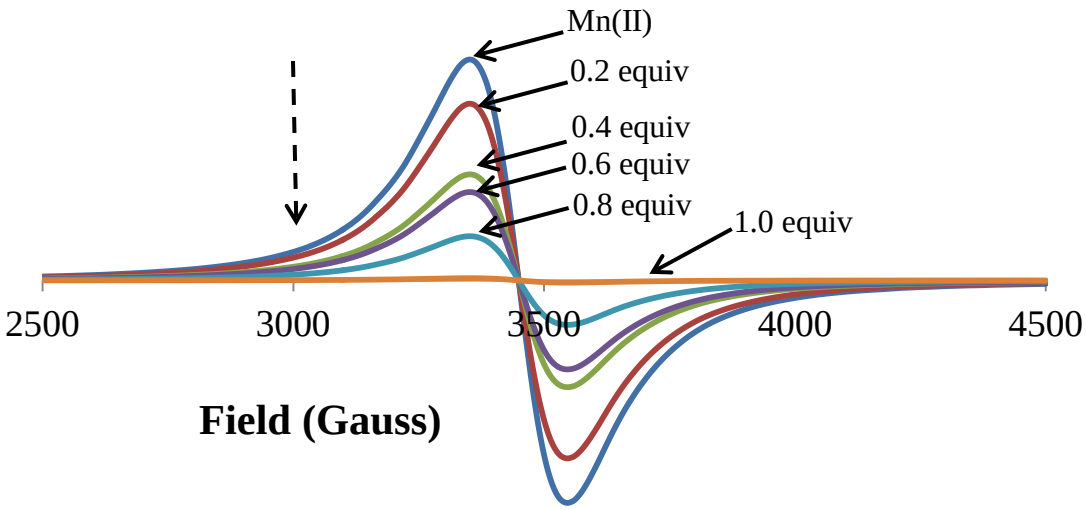

Figure 3.10 X-band EPR spectra obtained from the titration of tri(para-tolyl)aminium hexafluorophosphate (0.2 equiv aliquots) to $[Mn^{II}(S^{Me2}N_4(6\text{-Me-DPEN}))](BF_4)$ (**4**, 5 mM, MeCN, 7 K).

after the addition of 1 equivalent of $[N(C_7H_7)_3](PF_6)$ is consistent with the formation of a Mn(III) species in these reactions. Similar observations were made from experiments with complexes **1**-**3** and **5**-**8**. UV/Vis spectra for the one electron oxidized products for complexes **1**-**3** and **5**-**8** (tentatively assigned as the Mn(III) analogues of these complexes) are provided in the Appendix (A.25-A.31).

Reactions were also performed in which solutions of **1**-**4** and **6**-**7**, respectively, had been spiked with water (~1,000 equivalents) prior to the addition of $[N(C_7H_7)_3](PF_6)$. The absorbance

features of each respective oxo-bridged Mn(III,III) dimer were observed immediately upon addition of 1 equivalent of $[N(C_7H_7)_3](PF_6)$ in a single aliquot to solutions of each Mn(II) complex. The successful formation of dimers **12-15** and **17-18**, respectively, from these reactions was confirmed via ESI-MS. These experiments reveal that these oxo-bridged Mn(III,III) dimers can form from an initial outer-sphere oxidation of each Mn(II) complex, respectively. A working hypothesis to explain these observations is provided in Scheme 3.6. It should be further noted that attempts to structurally characterize these one electron oxidized products have been unsuccessful, as each oxidized species decays in solution, even at low temperatures, over a relatively short period of time (5-10 min).

Scheme 3.6 Formation of oxo-bridged Mn(III,III) dimers **12-15** and **17**-18 by an initial outer-sphere oxidation of the respective Mn(II) complexes **1-4** and **6-7** (MeCN, 293 K).

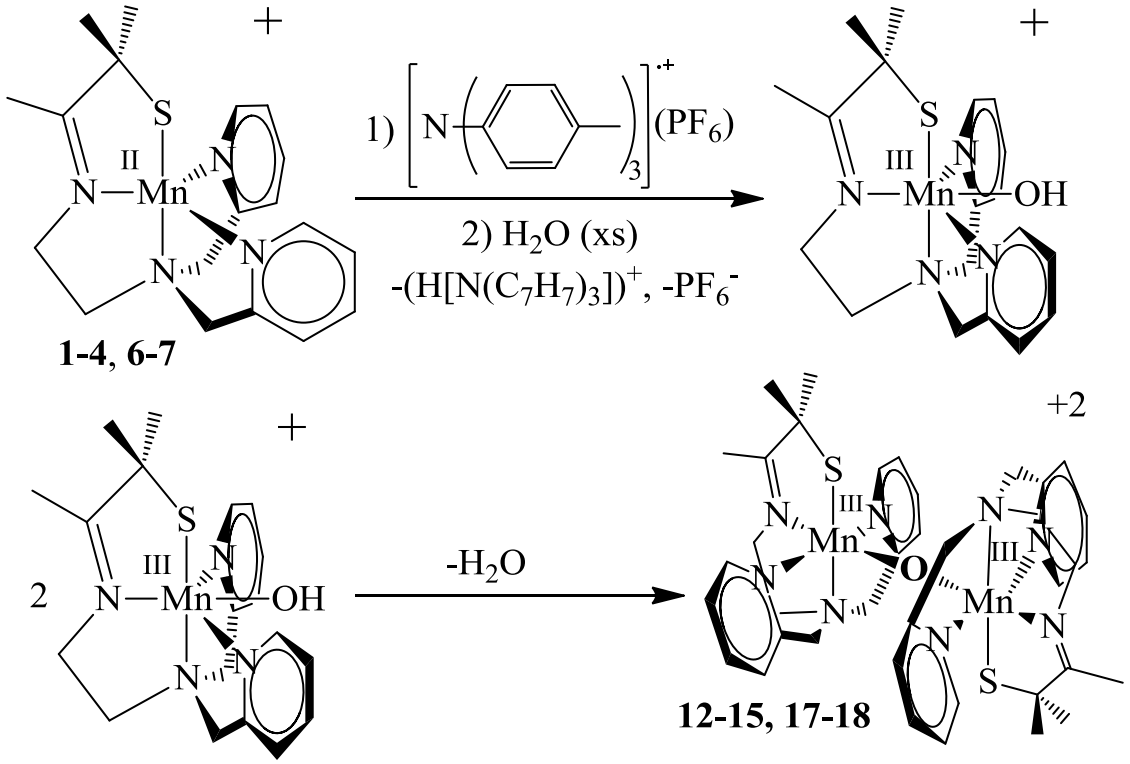

3.3.3 Structural and Magnetic Characterization of Oxo-Bridged Mn(III,III) Dimers 12-15 and 17-18.

Although many examples dimeric Mn complexes are known and have X-ray structures reported, very few are known to contain only a single and unsupported oxo-bridging ligand.[4] The ORTEP diagrams of $[Mn^{III}(S^{Me2}N_4(tren))]_2(\mu\text{-}O)(PF_6)_2$ (**12**), $[Mn^{III}(S^{Me2}N_4(6\text{-}H\text{-}DPEN))]_2(\mu\text{-}O)(PF_6)_2\cdot(MeCN)_2$ (**13**), $[Mn^{III}(S^{Me2}N_4(6\text{-}H\text{-}DPPN))]_2(\mu\text{-}O)(PF_6)_2\cdot(MeCN)_2$ (**14**), $[Mn^{III}(S^{Me2}N_4(6\text{-}Me\text{-}DPEN))]_2(\mu\text{-}O)(BF_4)_2\cdot(MeOH)_2$ (**15**), $[Mn^{III}(S^{Me2}N_4(6\text{-}Me\text{-}DPPN))]_2(\mu\text{-}O)(BPh_4)_2$ (**16**), $[Mn^{III}(S^{Me2}N_4(4\text{-}MeO\text{-}3,5\text{-}Me\text{-}DPEN))]_2(\mu\text{-}O)(PF_6)_2\cdot(MeCN)_2$ (**17**), $[Mn^{III}(S^{Me2}N_4(2\text{-}QuinoEN))]_2(\mu\text{-}O)(PF_6)_2\cdot(CH_2Cl_2)$ (**18**), and $[Mn^{III}(S^{Me2}N_4(2\text{-}QuinoPN))]_2(\mu\text{-}O)(BPh_4)_2\cdot(MeCN)$ (**19**) are provided in Figures 3.1-3.3 and selected metrical parameters are compiled in Table 3.1. The coordination environment of each Mn(III) ion in these dimers contains a thiolate sulfur (S(1)) *trans* to a tertiary amine (N(2), an oxo-bridging ligand (O(1)) *trans* to an imine nitrogen (N(1), and either two primary amines or two N-heterocyclic moieties (N(3) and N(4)) *trans* to one another. The oxo bridging ligands in dimers **12**-**13**, **15**, and **18**, respectively, are bound to each respective Mn(III) ion in coordination sites which were unoccupied in the corresponding monomeric Mn(II) complex (Scheme 3.1-3.2). This also may be true for dimers **14** and **17**, however the corresponding Mn(II) complexes were structurally characterized as thiolate-bridged dimers without available coordination sites in the solid state. The coordination sites observed for the oxo-bridging ligands in dimers **16** and **19**, respectively, are unexpected, however, given that the corresponding Mn(II) complexes each contain an single open coordination site *trans* to either a 6-methylpyridine (**5**) or quinoline (**8**) ligand moiety.

These observations suggest that the structures of these complexes in solution may differ considerably to those characterized in the solid state.

The +3 oxidation state of each Mn ions in these dimers is clearly evident from the Mn-S distances, which are each roughly 0.1 Å shorter than those observed in the respective *monomeric* Mn(II) complexes (Tables 2.1 and 3.1). These distances are comparable to those of five-coordinate Mn(III)-S(thiosalicylate) (2.2913(24) and 2.2752(25) Å), but are shorter than those of dinuclear $[Mn_2(edt)_4]^{2-}$ (Mn(III)-RS_b = 2.632(2) Å, Mn(III)-RS_t = 2.32 Å; RS_b = bridging, RS_t = terminal).[35-36] The Mn-N(imine) and Mn-N(tertiary amine) distances are also shorter in each dimer relative to the respective Mn(II) monomer, which would be expected based on an increase in effective nuclear charge upon oxidation of Mn(II) to Mn(III). The Mn(1)-O(1) and Mn(2)-O(1) distances for dimers **12**-**18** fall within a relatively narrow range of 1.748(12)-1.801(9) Å and agree well with those reported for other Mn(III,III) dimers containing a single, unsupported oxo bridge. Due to the low resolution of the X-ray structure for **19** (16 %), metrical parameters from this dimer are unreliable and therefore not considered.

In contrast to these observations, many of the Mn-N(primary amine), Mn-N(pyridine), or Mn-N(quinoline) distances are considerably elongated in the Mn(III,III) dimers compared to those of the respective Mn(II) monomers. Complexes containing Mn(III) ions are well-recognized as having elongated metal-ligand bond distances along one of the principle axes, which is often attributed to Jahn-Teller distortion.[37] However, these observed bond elongations are not consistent in relative magnitude for all complexes. For example, in comparing the Mn-N(pyridine) bond lengths for six-coordinate **2** to those of the corresponding oxo-bridged Mn(III,III) dimer, **13**, these distances are only found to increase by roughly 0.1 Å (Tables 2.1 and 3.1). Dimer **17**, which also lacks sterically-congestive substituents in the pyridine six-

position, has Mn-N(pyridine) distances of similar length to those in **13**. When comparing the Mn-N(6-methylpyridine) and Mn-N(quinoline) distances in **4** and **7**, two five-coordinate complexes with bulkier N-heterocyclic moieties, to those in the corresponding oxo-bridged dimers, **15** and **18**, respectively, these distances are found to increase by as much as ~0.3 Å. The largest Mn-N(pyridine) elongation is found in dimer **16**, where the Mn-N(3) distance increases by nearly 0.5 Å from that in the respective Mn(II) complex, **5** (Table 2.1 and 3.1). The presence of bulky N-heterocyclic moieties was found to have a considerable impact upon the structural properties of the thiolate-ligated Mn(II) complexes discussed in Chapter 2; these moieties appear to have a similar influence upon the structural properties of the oxo-bridged Mn(III,III) dimers discussed here.

Another set of metrical parameters which display a considerable amount of variation throughout this series of dimers are the Mn(1)-O(1)-Mn(2) bridging angles, which vary from 146.15(11)° to 180.0° (Table 3.1). The Mn(1)-O(1)-Mn(2) bridging angles found in dimers **12** (158.3(3)°), **14** (159.4(6)°), and **16** (146.15(11)°) are notably the most acute angles found for any unsupported oxo-bridged Mn(III,III) dimer reported.[38] Given that an acute bridging angle would prevent the formation of strong π-bonding interactions between the oxo bridge and Mn(III) ions, the instability of **16** (*vide supra*) may be at least partially attributable to this structural property. There also appears to be an inverse correlation between the Mn(1)-O(1)-Mn(2) bridging angles and both the average Mn-O bond lengths and dihedral angles formed between the Mn(1)-S(1)-O(1)-N(1)-N(2) and Mn(2)-S(2)-O(1)-N(5)-N(6) planes (the dihedral angle between these two planes is a quantitative measure of the relative orientation of each of the two dimer halves, 43.2° (**12**), 7.1° (**13**), 64.9° (**14**), 0° (**15**), 73.7° (**16**), 14.3° (**17**), and 16.0° (**18**)), respectively (Figure 3.11). Both observations can be rationalized if the most ideal overlap between the symmetry-

appropriate oxygen p orbitals and Mn d orbitals occurs when the Mn-O-Mn angle is close to linear, permitting the formation of stronger, shorter Mn-O bonds. It is also expected that dimers containing a fairly acute bridging angle should have a relatively basic oxo bridge (more p character in the hybridized valence orbitals of the oxo bridge), which has considerable implications regarding the reactive properties of each dimer (*vide infra*).

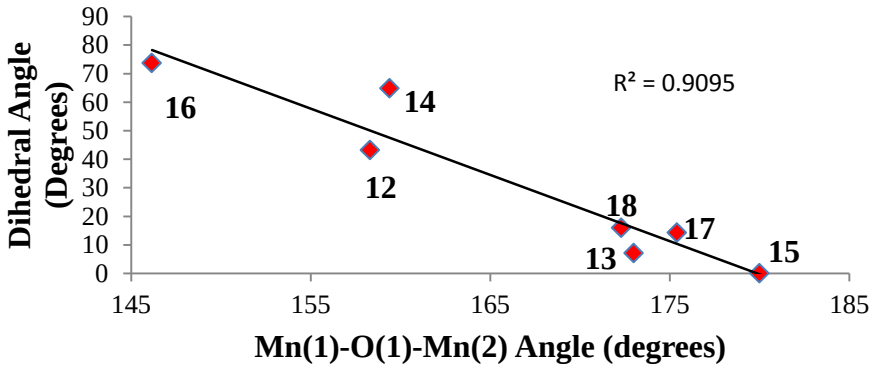

Figure 3.11 Plot of dihedral angle (degrees) versus Mn(1)-O(1)-Mn(2) angle (degrees).

The magnetic properties of dimers **12**-**15** and **17**-**18** were explored by both solution and solid state methods in order to determine how metrical differences associated with the Mn(1)-O(1)-Mn(2) bridging unit may influence these properties. Solution magnetic moments were determined by the Evans method in either CD_2Cl_2 (**12**) or d_4-MeOD (**13**-**15**, **17**-**18**) at room temperature, while solid state measurements were made by SQUID magnetometry for **13**-**15** and **17**-**18** with crystalline samples from 5-300 K. Solution effective magnetic moments per Mn(III) ion (μ_{eff}/Mn(III)) were determined to be 4.32 B.M. (**12**), 4.89 B.M. (**13**), 4.44 B.M. (**14**), 3.11 B.M. (**15**), 4.24 B.M. (**17**), and 4.40 B.M. (**18**). With the exception of **15**, data for **12**-**14** and **17**-**18** are each relatively close to the spin-only value of 4.87 for an S = 2 ion. Data from solid state magnetic susceptibility measurements were fit to the expressions provided in equations 3.1-3.4,

where H is the spin Hamiltonian, H_{ex} is the exchange Hamiltonian, H_{ZFS} accounts for zero-field splitting, H_{Zee} accounts for the Zeeman interaction, J_{ij} is the exchange coupling constant for spins "i" and "j", "ns" is the number of spins (2), D_i and E_i are the axial and rhombic zero-field splitting parameters (respectively), and g is the Landè factor.[23] All magnetic data were

$$H = H_{ex} + H_{ZFS} + H_{Zee} \qquad (3.1)$$

$$H_{ex} = -2\sum_{i=1}^{ns-1}\sum_{j=i+1}^{ns} J_{ij}\cdot S_i \cdot S_j \qquad (3.2)$$

$$H_{ZFS} = \sum_{i=1}^{ns} D_i[S_{z,i}^2 - \frac{1}{3S_i(S_i+1)} + \frac{E_i}{D_i}(S_{x,i}^2 - S_{y,i}^2)] \qquad (3.3)$$

$$H_{Zee} = \sum_{i-1}^{ns} g\beta S_i B \qquad (3.4)$$

fit with $S_i = S_j = 2$ and $g \approx 2.00$. Good fits were obtained for all data sets (except for **14**) with J values of -48.0 cm^{-1} (**13**), -125.6 cm^{-1} (**15**), -4.5 cm^{-1} (**17**), and -1.0 cm^{-1} (**18**). Although a satisfactory fit to the solid state magnetic data for **14** was not obtained, J was estimated for this dimer to be -15.7 cm^{-1} using the expression in equation 3.5.[24] In equation 3.5, J is the exchange

$$J = \frac{2}{5}T_N k \qquad (3.5)$$

coupling constant, T_N is the Néel temperature, and *k* is the Boltzmann constant. Fits to the solid state magnetic susceptibility data for dimers **13**-**15** and **17**-**18** are provided in Figures 3.12 and Appendix A.32-A.35, respectively. For further comparison, selected metrical parameters and magnetic data for all unsupported oxo-bridged Mn(III,III) dimers reported are compiled in Table 3.3 along with data for **12**-**18**.

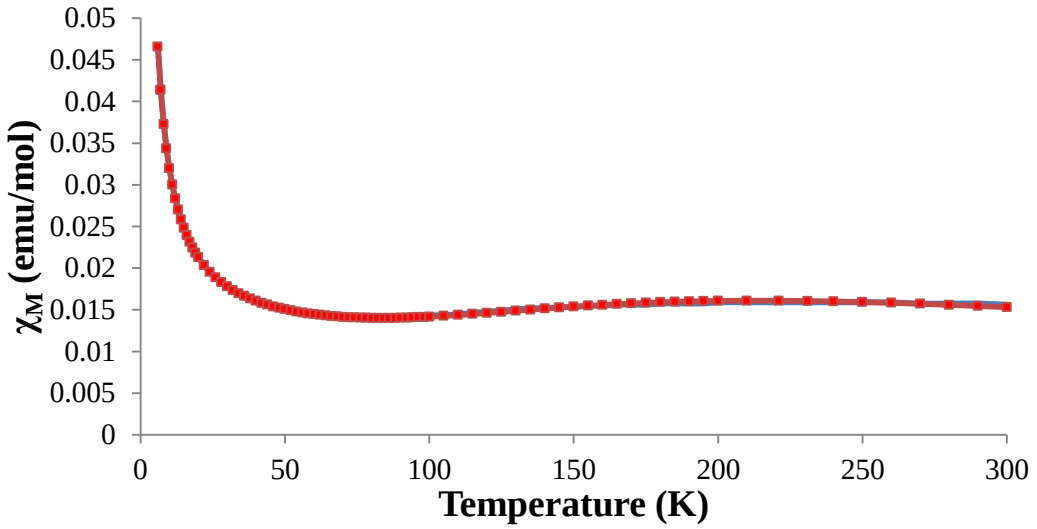

Figure 3.12 Molar magnetic susceptibility (χ_M) versus temperature (K) for [Mn^{II}($S^{Me2}N_4$(6-Me-DPEN))](BF_4) (**4**). Experimental data points are represented by red squares ( ) and the solid line represents the best fit to the experimental data.

Table 3.3 Selected Mn-O-Mn angles (deg), Mn(III)···Mn(III) distances (Å), magnetic exchange constants (cm^{-1}), and solution magnetic moments per Mn(III) ion (B.M./Mn(III)) for [Mn^{III}($S^{Me2}N_4$(tren))]$_2$(μ-O)(PF_6)$_2$ (**12**), [Mn^{III}($S^{Me2}N_4$(6-H-DPEN))]$_2$(μ-O)(PF_6)$_2$·(MeCN)$_2$ (**13**), [Mn^{III}($S^{Me2}N_4$(6-H-DPPN))]$_2$(μ-O)(PF_6)$_2$·(MeCN)$_2$ (**14**), [Mn^{III}($S^{Me2}N_4$(6-Me-DPEN))]$_2$(μ-O)(BF_4)$_2$·(MeOH)$_2$ (**15**), [Mn^{III}($S^{Me2}N_4$(6-Me-DPPN))]$_2$(μ-O)(BPh_4)$_2$ (**16**), [Mn^{III}($S^{Me2}N_4$(4-MeO-3,5-Me-DPEN))]$_2$(μ-O)(PF_6)$_2$·(MeCN)$_2$ (**17**), [Mn^{III}($S^{Me2}N_4$(2-QuinoEN))]$_2$(μ-O)(PF_6)$_2$·(CH_2Cl_2) (**18**), [Mn^{III}($S^{Me2}N_4$(2-QuinoPN))]$_2$(μ-O)(BPh_4)$_2$·(MeCN) (**19**), and other unsupported oxo-bridged Mn(III,III) dimers reported in the literature.

	Mn-O-Mn	Mn···Mn	J	μ_{eff} (sol'n)[a]
12	158.8(3)	3.521	N/A	4.32
13	173.0(2)	3.515	-48.0	4.89
14	159.4(6)	3.540	-15.7[b]	4.44
15	180.0	3.520	-125.6	3.11
16	146.15(11)	3.433	N/A	N/A
17	175.4(7)	3.508	-4.5	4.24
18	172.3(2)	3.512	-1.0	4.40
19	169.4(9)	3.590	N/A	N/A
[K{Mn(pc)py}$_2$)O][40]	178	3.42	N/A	N/A
$K_7[Mn_2O(CN)_{10}](CN)$[41]	180	3.446	N/A	N/A
[Mn_2O(5-NO_2-saldien)$_2$][42]	168.4(2)	3.490(2)	-120	N/A
[Mn_2O(bpmsed)$_2$](ClO_4)$_2$[43]	180	3.516(2)	-108	N/A
cis-Mn_2O(terpy)$_2$(CF_3CO_2)$_4$[44]	176.7(4)	3.493	N/A	N/A
trans-Mn_2O(terpy)$_2$(CF_3CO_2)$_4$[44]	178.0(2)	3.504	N/A	N/A
[Mn_2O(bpia)$_2Cl_2$](ClO_4)$_3$[45]	180	3.5326(9)	N/A	N/A
Mn_2O(HB(3,5-^{i}Pr_2-pz)$_2$[46]	179.9(7)	3.530(4)	N/A	N/A
[Mn_2O(2,6-BrMePy)]($Br)_4$[47]	174.7(3)	3.521	-249.0	N/A
[(Mn($PaPy_3$))$_2$(μ-O)](ClO_4)$_2$[48]	173.0(3)	3.5636(8)	-115.8	N/A

[a]Evans method, 293 K, CD_2Cl_2 or d_4-MeOD. [b]Estimated from Néel temperature.

As can be seen from Table 3.3, all unsupported oxo-bridged Mn(III,III) dimers which have been characterized by magnetic susceptibility measurements have been found to exhibit antiferromagnetic coupling between the two respective Mn(III) ions. With the exception of **15**, J values determined for the dimers discussed in this chapter are each much lower in magnitude than previously reported Mn(III,III) dimers containing a single oxo bridging ligand. The presence of a thiolate ligand in complexes **13-15** and **17-18** obviously distinguishes these complexes from other known dimers with this particular bridging motif, and thiolates have been shown to reduce the magnitude of magnetic coupling in multinuclear transition metal complexes.[18] Dimer **15** is unique within this series of thiolate-ligated Mn(III,III) dimers because it is the only example with a perfectly linear Mn-O-Mn bridging angle and it exhibits the largest magnitude of antiferromagnetic coupling between the two Mn ions. These observations would suggest that a linear Mn-O-Mn angle provides the best overlap between magnetic orbitals to allow for the most efficient antiferromagnetic superexchange pathways to be operative. However, a direct correlation between the magnitude of J and any particular set of metrical parameters is not evident (Table 3.3). A magnetostructural correlation to rationalize the magnetic coupling within unsupported oxo-bridged Mn(III,III) dimers has also yet to be clearly established.

3.3.4 Electrochemical Characterization of Oxo-Bridged Mn(III,III) Dimers 12-15, 18 and Reactivity with Outer-Sphere Oxidants

The electrochemical properties of oxo-bridged dimers **12-15** and **18** were evaluated by cyclic voltammetry experiments in MeCN at room temperature (Figure 3.13). Electrochemical data for each dimer has also been compiled in Table 3.4. Each thiolate-ligated dimer exhibits

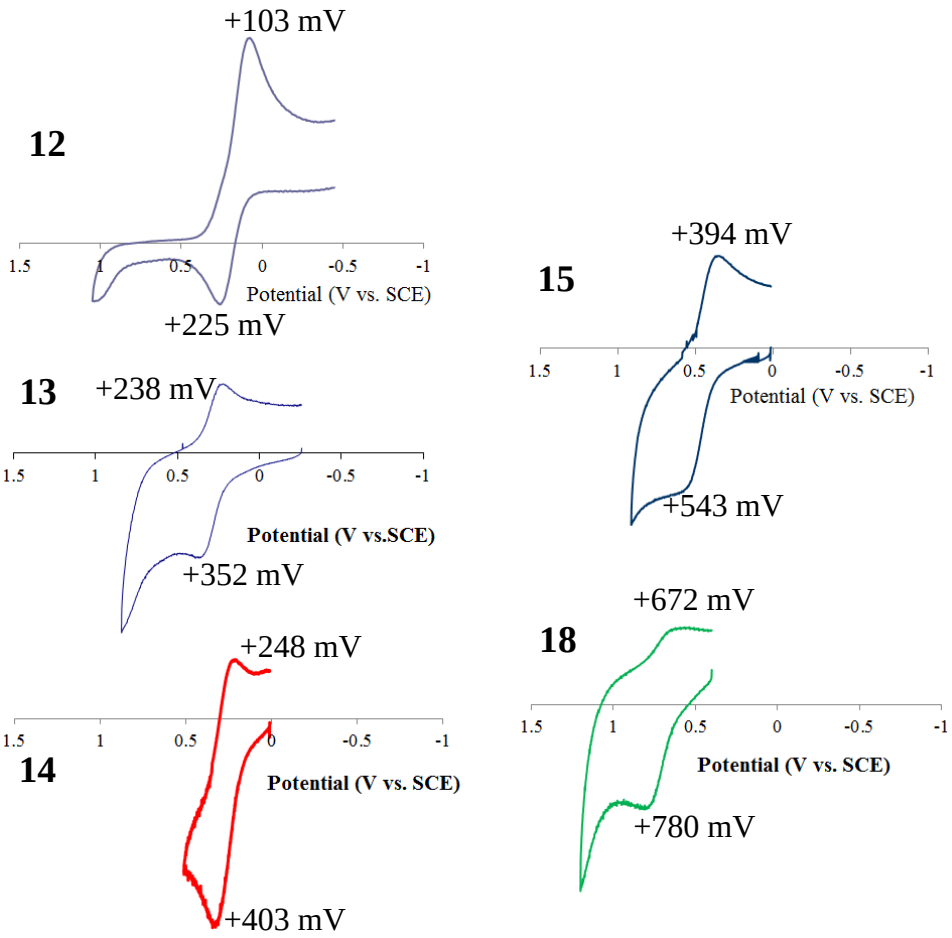

Figure 3.13 Cyclic voltammograms of $[Mn^{III}(S^{Me2}N_4(tren))]_2(\mu\text{-}O)(PF_6)_2$ (**12**, top left), $[Mn^{III}(S^{Me2}N_4(6\text{-}H\text{-}DPEN))]_2(\mu\text{-}O)(PF_6)_2\cdot(MeCN)_2$ (**13**, middle left), $[Mn^{III}(S^{Me2}N_4(6\text{-}H\text{-}DPPN))]_2(\mu\text{-}O)(PF_6)_2\cdot(MeCN)_2$ (**14**, bottom left), $[Mn^{III}(S^{Me2}N_4(6\text{-}Me\text{-}DPEN))]_2(\mu\text{-}O)(BF_4)_2\cdot(MeOH)_2$ (**15**, top right), and $[Mn^{III}(S^{Me2}N_4(2\text{-}QuinoEN))]_2(\mu\text{-}O)(PF_6)_2\cdot(CH_2Cl_2)$ (**18**, bottom right) in MeCN vs. SCE. Each experiment was performed with a 0.1 M $^nBu_4PF_6$ supporting electrolyte and with a scan rate of 120-150 $mV\cdot s^{-1}$ at room temperature. Anodic (E_{pa}) and catholic (E_{pc}) peak potentials are labeled in each voltammogram.

Table 3.4 Summary of electrochemical data for $[Mn^{III}(S^{Me2}N_4(tren))]_2(\mu\text{-}O)(PF_6)_2$ (**12**), $[Mn^{III}(S^{Me2}N_4(6\text{-}H\text{-}DPEN))]_2(\mu\text{-}O)(PF_6)_2\cdot(MeCN)_2$ (**13**), $[Mn^{III}(S^{Me2}N_4(6\text{-}H\text{-}DPPN))]_2(\mu\text{-}O)(PF_6)_2\cdot(MeCN)_2$ (**14**), $[Mn^{III}(S^{Me2}N_4(6\text{-}Me\text{-}DPEN))]_2(\mu\text{-}O)(BF_4)_2\cdot(MeOH)_2$ (**15**), $[Mn^{III}(S^{Me2}N_4(2\text{-}QuinoEN))]_2(\mu\text{-}O)(PF_6)_2\cdot(CH_2Cl_2)$ (**18**), and *cis*-$Mn_2O(terpy)_2(CF_3CO_2)_4$. All potentials are references against the saturated calomel electrode (SCE) in MeCN at 293 K.

	E_{pa} (mV)	E_{pc} (mV)	$E_{1/2}$ (mV)	ΔE (mV)
12	+225	+103	+164	122
13	+352	+238	+295	114
14	+403	+248	+326	155
15	+543	+394	+467	146
18	+780	+672	+726	108
cis-$Mn_2O(terpy)_2(CF_3CO_2)_4$	N/A	+208	N/A	N/A

a single quasi-reversible or reversible one electron redox process tentatively assigned as a $Mn^{(IV/III)/(III/III)}$ couple with $E_{1/2}$ values (vs. SCE) of +164 mV (**12**), +295 mV (**13**), +276 mV (**14**), +467 mV (**15**), +726 mV (**18**) (Figure 3.12 and Table 3.4). These values are each relatively close to the potential at which *cis*-$Mn_2O(terpy)_2(CF_3CO_2)_4$ is oxidized from Mn(III,III) to Mn(III,IV) (+208 mV vs. SCE, Table 3.4)).[44] Unlike these thiolate-ligated dimers, however, a cathodic wave was not observed for *cis*-$Mn_2O(terpy)_2(CF_3CO_2)_4$ due to disproportionation of the oxidized Mn(III,IV) intermediate.[44]

In order to further characterize the putative oxo-bridged Mn(IV,III) dimer products, reactions between **12**-**15** and **18** and $[N(C_7H_7)_3](PF_6)$ were each performed in MeCN at 233 K and monitored by UV/Vis spectroscopy. As is shown in Figure 3.14, titration of $[N(C_7H_7)_3](PF_6)$ into solutions of each dimer promoted the formation of new absorbance bands, indicating a

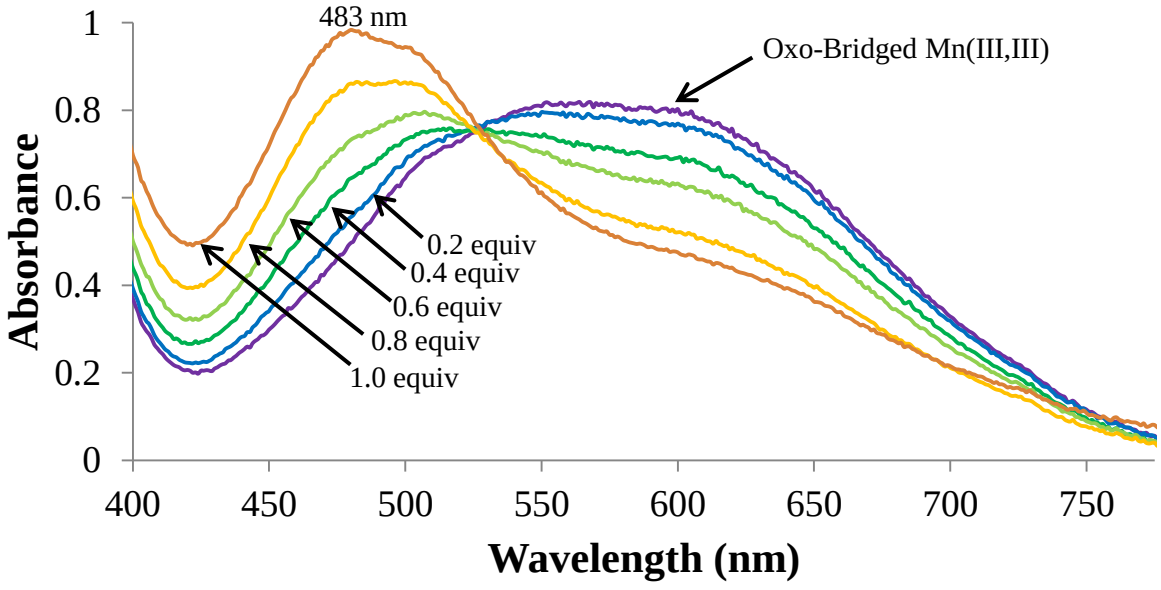

Figure 3.14 Anaerobic UV/Vis titration experiment displaying the reaction between $[Mn^{III}(S^{Me2}N_4(6\text{-Me-DPEN}))]_2(\mu\text{-O})(BF_4)_2\cdot(MeOH)_2$ (**15**, 0.17 mM) and 0.2 equivalent aliquots of tri(para-tolyl)aminium hexafluorophosphate (200 mM stock solution in MeCN) in MeCN at 233 K.

reaction had occurred. Only one equivalent of $[N(C_7H_7)_3](PF_6)$ per equivalent of each Mn(III,III) dimer was found to result in maximum formation of these new spectral features, consistent with a 1:1 stoichiometry between the oxidant and metal dimers. The spectral features of each oxo-bridged Mn(III,III) dimer could be restored by adding one equivalent of a one electron reducing agent to each respective reaction solution, suggesting each redox reaction is reversible. Interestingly, dimer **15** could be reformed by using KO_2 as a reducing agent (Figure 3.15). Further characterization of the one electron oxidized products from each Mn(III,III) dimer has thus far been unsuccessful, as the absorbance bands of each putative Mn(IV,III) species bleached over a time period of approximately 20 minutes.

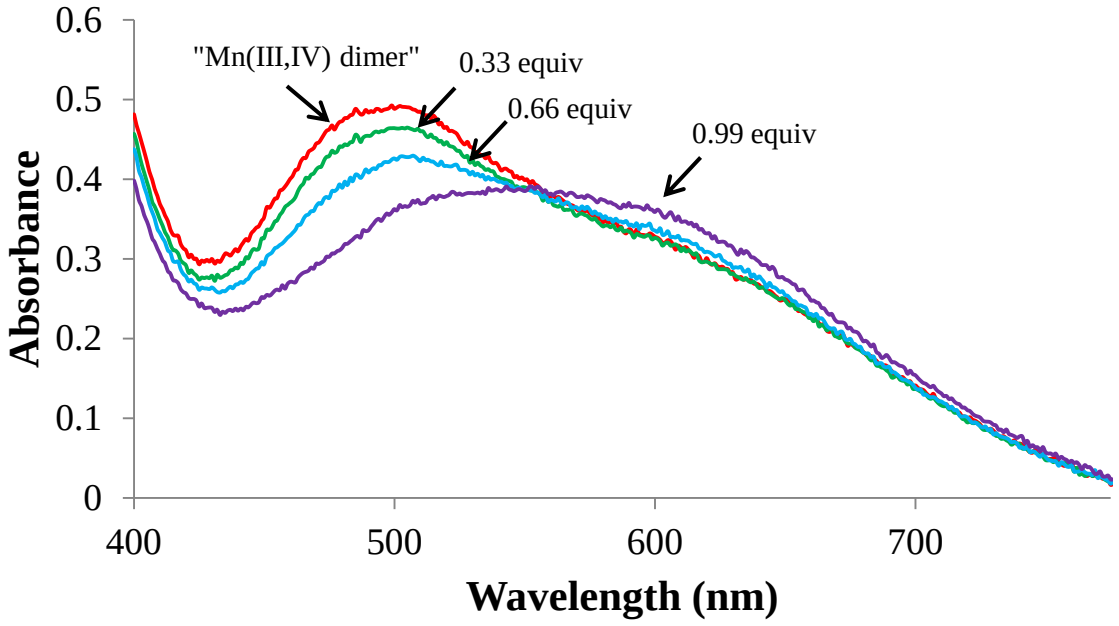

Figure 3.15 Anaerobic UV/Vis titration experiment displaying the reaction between the one electron oxidized product of **15** and 0.33 equivalent aliquots of KO_2 (15 mM stock solution in THF, solubilized with 18-crown-6 either, 23 mM) in MeCN at -40 °C. The final spectrum (purple trace) is identical to that of $[Mn^{III}(S^{Me2}N_4(6\text{-Me-DPEN}))]_2(\mu\text{-}O)(BF_4)_2\cdot(MeOH)_2$ (**15**).

3.3.5 Proton-Induced Oxo-Bridge Cleavage of Thiolate-Ligated Mn(III,III) Dimers 12-15 and 17-19

The presence of a thiolate ligand coordinated to each Mn(III) ion in dimers **12-15** and **17-19** suggested that the oxo-bridging ligands may be relatively basic, therefore reactions between each dimer and various weak acids were explored in dry MeCN solutions. Each dimer was indeed found to be unstable while in the presence of various weak acids; slight excess amounts of acetic acid (pK_a in MeCN = 23.5, 2-8 equivalents per dimer) were found to be sufficient in order to completely react with **12-15** and **17-18** as determined by UV/Vis spectroscopy and ESI-MS.[49] As is illustrated in Figure 3.16, addition of acetic acid in a single aliquot to 273 K

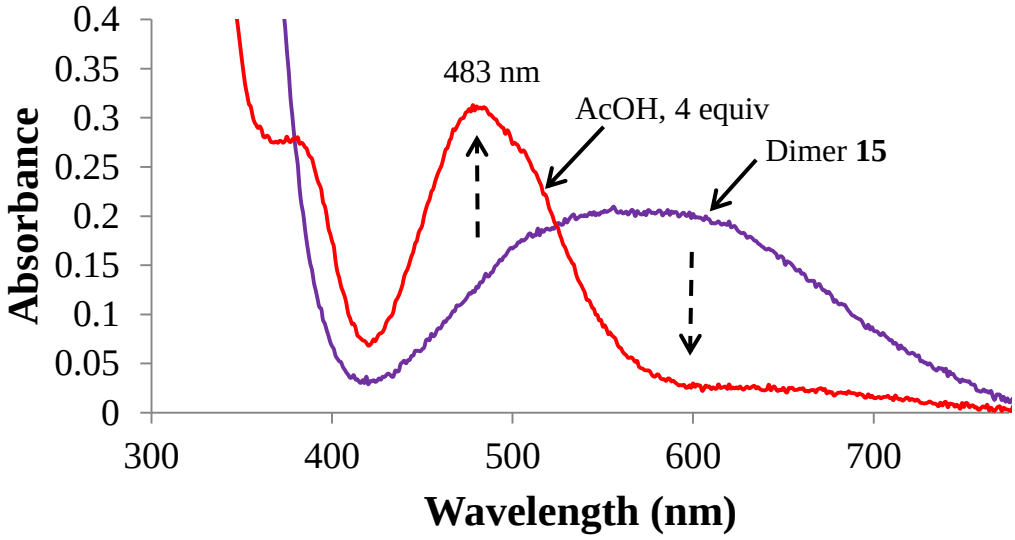

Figure 3.16 UV/Vis spectra representing the reaction between $[Mn^{III}(S^{Me2}N_4(6\text{-Me-DPEN}))]_2(\mu\text{-}O)(BF_4)_2\cdot(MeOH)_2$ (**15**, 1.1 mM, purple trace) and AcOH (4 equivalents, 10 mM stock solution in MeCN, red trace) in MeCN at 0 °C.

MeCN solutions of dimers **13-15** and **17-18** resulted in the formation of a species with an absorbance spectrum distinct from that of the respective oxo-bridged dimer. Disappearance of the absorption features for each oxo-bridged dimer coincided with the loss of an ESI-MS peak

corresponding to each dimer, which provides further evidence that a reaction between each dimer and acetic acid has occurred. The absorbance spectrum of the product from each reaction is nearly identical to that observed from the outer-sphere one electron oxidation of the respective Mn(II) complexes under similar reaction conditions (*vide supra*, Figure 3.9). These observations collectively suggest that at least one of the products formed from reactions between dimers **13-15** and **17-18** and acetic acid may be the corresponding mononuclear Mn(III)-OAc or Mn(III)-NCMe complexes. Attempts to structurally characterize these new species have thus far been unsuccessful due to the instability of each product in solution, even at low temperatures, which again parallels the observations made from the chemical oxidation experiments previously discussed. It is significant to note that no reaction was observed between any of these oxo-bridged dimers and either NaOAc or $(Et_4N)(OAc)$ in high excess amounts (up to 1,000 equivalents), suggesting that an acidic proton is required for each reaction to occur.

Given the instability of oxo-bridged **19** (*vide supra*), reactions between this dimer and various acids were explored at lower temperatures in EtCN (193 K). Unlike reactions with **13-15** and **17-18**, in which AcOH was the weakest acid capable of cleaving the oxo-bridge in each respective dimer, **19** was found to react with much weaker acids. Also unlike experiments with **13-15** and **17-18**, attempts to structurally characterize a product from these reactions were successful when MeOH was used as the acid. An ORTEP diagram of the reaction product formed between **19** and MeOH, $[Mn^{III}(S^{Me2}N_4(2\text{-QuinoPN}))(OCH_3)](PF_6)$ (**20**), is provided in Figure 3.17. Methoxide-bound **20** was isolated in high yields (95-98 %) and found to be extremely robust at ambient temperature in the solid state. Two notable metrical parameters from the X-ray structure obtained for **20** are the elongated Mn(III)-N(quinoline), or Mn(1)-N(3) and Mn(1)-N(4), distances, which were determined to be 2.411(2) Å and 2.483(2) Å,

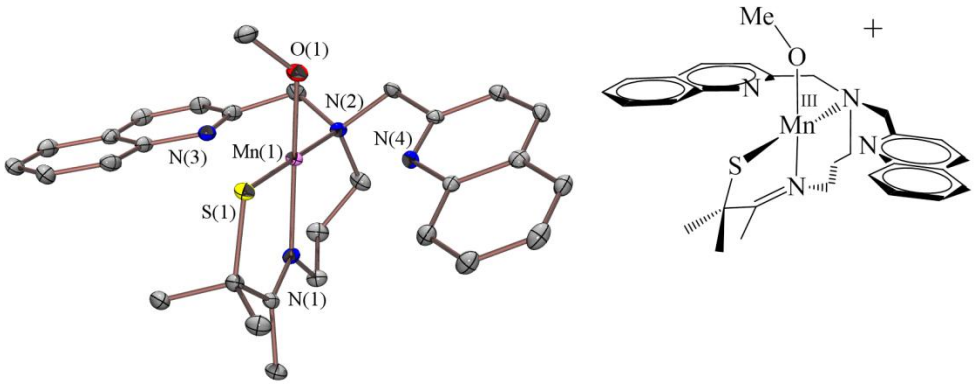

Figure 3.17 ORTEP diagram (50 % probability) of $[Mn^{III}(S^{Me2}N_4(2\text{-QuinoPN}))(OCH_3)]^+$ (**20**) with hydrogen atoms and counterion omitted for clarity. Selected bond distances (Å) and angles (deg) for **20**: Mn(1)-S(1), 2.2650(9); Mn(1)-N(1), 2.084(3); Mn(1)-N(2), 2.180(3); Mn(1)-N(3), 2.411(2); Mn(1)-N(4), 2.483(2); Mn(1)-O(1), 1.837(2); S(1)-Mn(1)-N(1), 83.00(7); S(1)-Mn(1)-N(2), 178.93(8); S(1)-Mn(1)-N(3), 106.29(6); S(1)-Mn(1)-N(4), 105.43(7); S(1)-Mn(1)-O(1), 91.41(7). Crystal data for **20**: Formula, $C_{29}H_{34}F_6MnN_4OPS$; MW, 686.57; T, 110(2); unit cell[a], triclinic; space group, P-1; dimensions, a = 7.4087(2), b = 12.1143(3), c = 16.4567(4), α = 89.3450(10)°, β = 85.8390(10)°, γ = 82.8680(10)°; Z, 2; V (Å^3), 1,461.71(6); d(calc, g/cm^3), 1.560; R[b], 0.0517; R_w[c], 0.1229; GOF, 1.003. [a]Mo Kα(λ = 0.7170 Å) radiation. [b]$R = \Sigma||F_0| - |F_c||/ \Sigma|F_0|$. [c]$R_w = [\Sigma w(|F_0| - |F_c|)^2/ \Sigma wF_0{}^{1/2}$, where $w^{-1} = [\sigma_{count}{}^2 + (0.05F^2)^2]4F^2$.

respectively. These distances are roughly 0.2 Å longer than those found in **8** and consistent with the elongated Mn-N(N-heterocyclic) bond distances observed from the X-ray structures of dimers **13**-**18**.

Dimer **12**, which contains aliphatic amines instead of N-heterocyclic ligand moieties, was found to undergo bridge-cleaving reactions with the weakest acids within this series of oxo-bridged dimers. The reactivity of **12** was surveyed with a relatively wide range of acids in MeCN at room temperature, including water, methanol, phenol, para-nitrophenol, and acetic acid; each acid elicited a distinct change in the absorbance spectrum of **12** to indicate the formation of a new species (Figures 3.18). The products from reactions between **12** and each acid have been identified and structurally characterized as the conjugate base-ligated

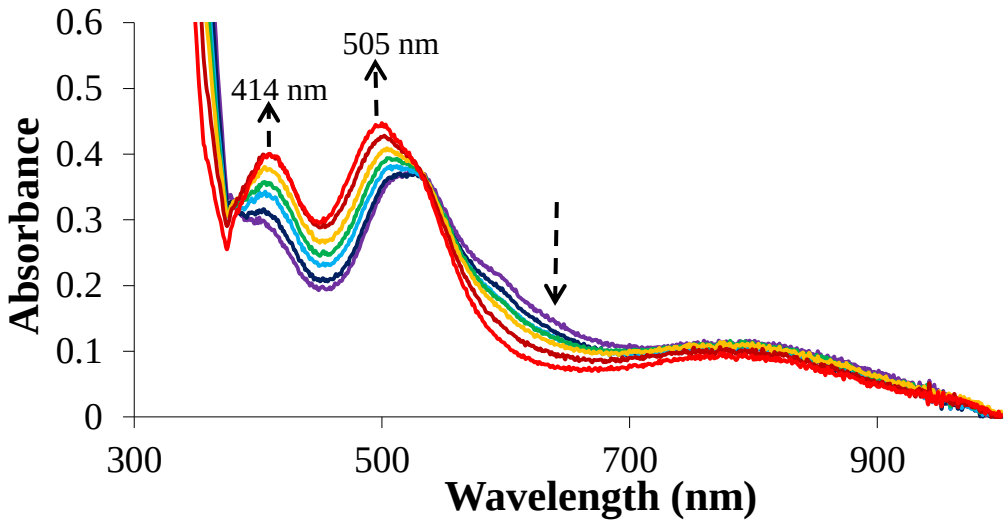

Figure 3.18 Anaerobic UV/Vis titration experiment displaying the reaction between $[Mn^{III}(S^{Me2}N_4(tren))]_2(\mu\text{-}O)(PF_6)_2$ (**12**, 1.3 mM) and H_2O (each trace represents a 5 equivalent aliquot from a 10 mM stock solution in MeCN) in MeCN at 293 K.

mononuclear Mn(III) complexes, again showing that weak acids can cleave the oxo-bridges in these dimers (*vide infra*, Chapter 6). The ability of acids as weak as water to successfully cleave the oxo-bridge in **12** likely reflects the increased basicity of the oxo ligand relative to those in **13**-**15** and **17**-**19**, which can be attributed to the coordination of an electron-donating thiolate and two aliphatic amines to each Mn(III) ion in this dimer, as well as the relatively acute Mn-O-Mn bridging angle. The properties of each mononuclear Mn(III) complex isolated from the bridge-cleaving reactions with **12**, as well as a more thorough description of each individual reaction, are described in Chapter 6. A general scheme illustrating the proton-assisted bridge-cleaving reactions observed between the Mn(III,III) dimers **12**-**15** and **17**-**19** and various weak acids (HA) is provided in Scheme 3.7.

Scheme 3.7 General scheme illustrating the proton-assisted bridge-cleaving reactions performed with oxo-bridged Mn(III,III) dimers **12**-**15** and **17**-**19**.

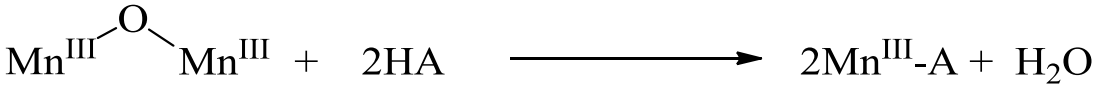

3.3.6 Reactivity of Alkoxide- or Alcohol-Ligated Mn(II) Complexes 9-11 With Dioxygen and Iodosylbenzene

In order to determine how the thiolate ligands in complexes **1**-**8** may influence reactions with various oxidants, the reactivity of alkoxide- or alcohol-ligated **9**-**11** was explored with O_2 and PhIO in MeCN at 293 K. Alkoxide-ligated **9** was found to undergo a relatively slow reaction (over hours) with each oxidant (excess O_2 or 0.5 equivalents of PhIO) as was indicated by a color change in each respective reaction solution from clear to dark brown. Reactions with both oxidants yielded the same final product, which has been structurally characterized by X-ray crystallography as a hydroxide-bridged Mn(III,III) dimer. An ORTEP diagram of this product, $[Mn^{III}(O^{Me2}N_4(tren))]_2(\mu\text{-}OH)(PF_6)_3 \cdot MeCN$ (**21**), is provided in Figure 3.19 along with selected metrical parameters and crystal data. Dimer **21** is one of only three known examples of an unsupported hydroxide-bridged Mn(III,III) dimer.[50-51] The Mn(1)-O(2)-Mn(2) bond angle of **21** (139.1(4)) is notably the most acute angle of these three examples.[50-51] The source of the hydroxide proton in **21** has thus far been unidentified. This dimer will be reintroduced and further discussed in Chapter 6.

Alcohol-ligated **10** also reacts with O_2 and PhIO each in a similar fashion to that observed for thiolate-ligated **1**-**8**, respectively, by yielding an unsupported oxo-bridged and alkoxide-ligated Mn(III,III) dimer. Two ORTEP diagrams of this product, $[Mn^{III}(O^{Me2}N_4(6\text{-Me-DPEN}))]_2(\mu\text{-}O)(BPh_4)_2$ (**22**), are provided in Figure 3.20 along with selected metrical parameters and crystal data. Dimer **22** is structurally analogous to **15** with the exception that **22** contains alkoxide ligand moieties while **15** contains thiolate moieties (Figure 3.1). The X-ray structures of **22** and **15** reveal that each dimer has a perfectly linear Mn-O-Mn angle (180°) and a 0° dihedral angle between the Mn(1)-S(1)-O(1)-N(1)-N(2) and Mn(2)-S(2)-O(1)-N(5)-N(6) planes.

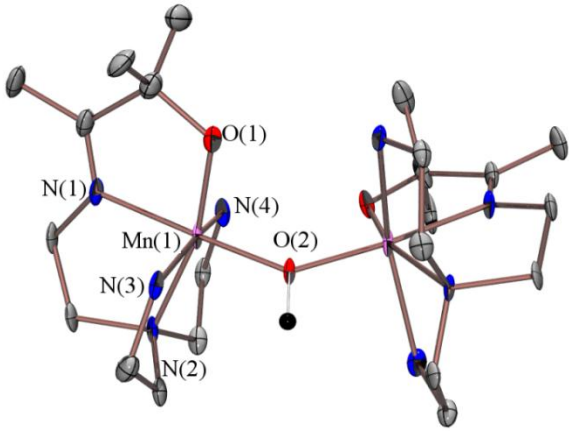

Figure 3.19 ORTEP diagram of $\{[Mn^{III}(O^{Me2}N_4(tren))]_2(\mu\text{-}OH)\}^{3+}$ (**21**) with some hydrogen atoms, counterion, and solvent of crystallization omitted for clarity. Selected bond distances (Å) and angles (deg) for **21**: Mn(1)-O(1), 1.856(7); Mn(2)-O(3), 1.827(7); Mn(1)-N(1), 1.993(8); Mn(1)-N(2), 2.100(8); Mn(1)-N(3), 2.310(9); Mn(1)-N(4), 2.312(8); Mn(1)-O(2), 1.755(6); Mn(2)-O(2), 1.843(6); O(1)-Mn(1)-N(1), 80.9(3); O(1)-Mn(1)-N(2), 162.9(3); O(1)-Mn(1)-N(3), 98.9(3); O(1)-Mn(1)-N(4), 104.9(3); O(1)-Mn(1)-O(2), 96.1(3), Mn(1)-O(2)-Mn(2), 139.1(4). Crystal data for **21**: Formula, $C_{46}H_{105}F_{36}Mn_4N_{17}O_6P_6$; MW, 2,082.05; T, 110(2); unit cell[a], monoclinic; space group, C 2/c; dimensions, a = 38.076(3), b = 12.3735(8), c = 18.5152(12), α = 90°, β = 112.438(4)°, γ = 90°; Z, 4; V (Å^3), 8,062.7(9); d(calc, g/cm^3), 1.715; R[b], 0.1231; R_w[c], 0.2681; GOF, 1.035. [a]Mo Kα(λ = 0.7170 Å) radiation. [b]$R = \Sigma||F_0| - |F_c||/ \Sigma|F_0|$. [c]$R_w = [\Sigma w(|F_0| - |F_c|)^2/ \Sigma wF_0{}^{1/2}$, where $w^{-1} = [\sigma_{count}{}^2 + (0.05F^2)^2]4F^2$.

All metal-ligand bonds involving the oxygen bridge, imines, tertiary amines, and pyridines are slightly shorter in **22** relative to **15** (Table 3.1, Figure 3.20), which likely results as a consequence of the Mn(III) ions in alkoxide-ligated **22** being more Lewis acidic than those found in thiolate-ligated **15**. Solutions of dimer **22** in MeCN were also found to be relatively stable while in the presence of a slight excess of AcOH (~10 equivalents), suggesting that replacement of the thiolate moieties with alkoxide moieties effectively decreases the relative pK_a of the oxygen bridge in **22**.

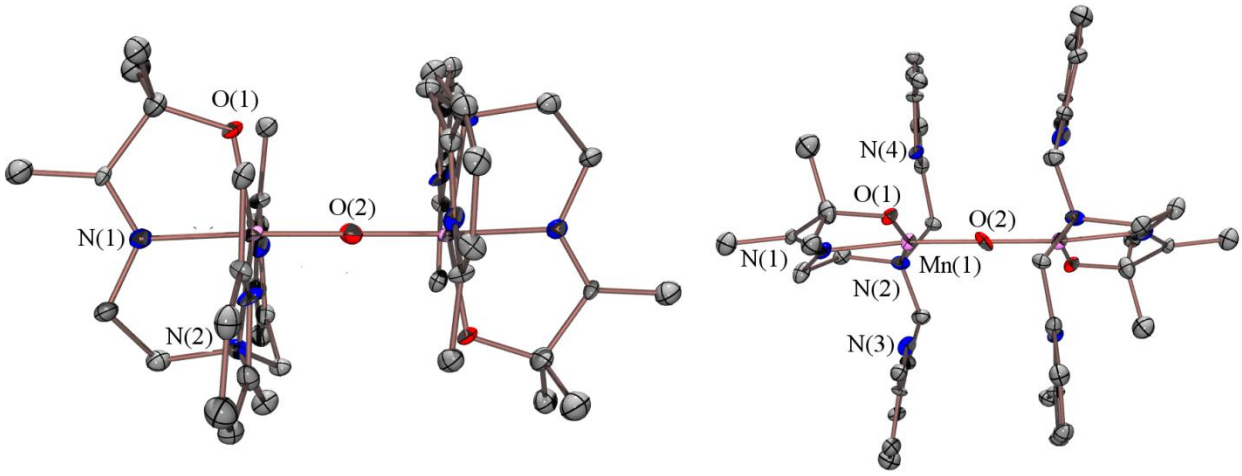

Figure 3.20 ORTEP diagram of $\{[Mn^{III}(S^{Me2}N_4(6\text{-Me-DPEN}))]_2(\mu\text{-O})\}^{2+}$ (**22**) with hydrogen atoms, counterions, and solvent of crystallization omitted for clarity. Selected bond distances (Å) and angles (deg) for **22**: Mn(1)-O(1), 1.895(8); Mn(1)-N(1), 1.993(11); Mn(1)-N(2), 2.139(11); Mn(1)-N(3), 2.479(11); Mn(1)-N(4), 2.430(11); Mn(1)-O(2), 1.7513(19); Mn(2)-O(2), 1.7513(19); O(1)-Mn(1)-N(1), 80.9(4); O(1)-Mn(1)-N(2), 174.4(3); O(1)-Mn(1)-N(3), 102.9(4); O(1)-Mn(1)-N(4), 108.5(4); O(1)-Mn(1)-O(2), 101.0(3), Mn(1)-O(2)-Mn(2), 180.00(9). Crystal data for **22**: Formula, $C_{390}H_{449}B_8Mn_8N_{41}O_{15}$; MW, 6,476.90; T, 110(2); unit cell[a], monoclinic; space group, P 2_1/c; dimensions, a = 24.4534(17), b = 14.0120(9), c = 25.0853(16), α = 90°, β = 91.857(4)°, γ = 90°; Z, 1; V (Å^3), 8,590.7(10); d(calc, g/cm^3), 1.252; R^b, 0.0459; $R_w{}^c$, 0.1089; GOF, 1.028. [a]Mo Kα(λ = 0.7170 Å) radiation. [b]$R = \Sigma||F_0| - |F_c||/ \Sigma|F_0|$. [c]$R_w = [\Sigma w(|F_0| - |F_c|)^2/ \Sigma wF_0{}^{1/2}$, where $w^{-1} = [\sigma_{count}{}^2 + (0.05F^2)^2]4F^2$.

Alkoxide-ligated **11** was also found to be highly reactive with both O_2 and PhIO in MeCN at room temperature, and again the final products from both reactions were the same. Unlike the other reaction products discussed thus far throughout this chapter, a *bis*(μ-oxo)-bridged Mn(IV,IV) dimer was identified and structurally characterized as a product from these reactions. An ORTEP diagram of this species, $[Mn^{IV}(N_4(6\text{-Me-DPEN}))]_2(\mu\text{-O})_2(BPh_4)_2$ (**23**), is provided along with selected metrical parameters and crystal data in Figure 3.21. As is seen in Figure 3.20, the Schiff base is missing from both polydentate ligands in this structure.

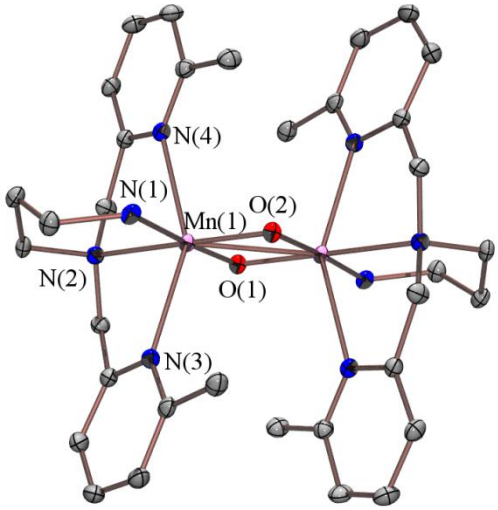

Figure 3.21 ORTEP diagram of $\{[Mn^{IV}(N_4(6\text{-Me-DPEN}))]_2(\mu\text{-}O)_2\}^{2+}$ (**23**) with hydrogen atoms and counterions omitted for clarity. Selected bond distances (Å) and angles (deg) for **23**: Mn(1)-O(1), 1.8324(15); Mn(1)-N(1), 1.96(3); Mn(1)-N(2), 2.133(6); Mn(1)-N(3), 2.3522(18) Mn(1)-N(4), 2.3251(18); Mn(1)-O(2), 1.8349(15); O(1)-Mn(1)-N(1), 89.10(13); O(1)-Mn(1)-N(2), 174.90(7); O(1)-Mn(1)-N(3), 106.39(6); O(1)-Mn(1)-N(4), 94.31(6); O(1)-Mn(1)-O(2), 85.98(7), Mn(1)-O(2)-Mn(2), 94.02(7). Crystal data for **22**: Formula, $C_{90}H_{108}B_2Mn_2N_8O_4$; MW, 1,497.34; T, 100(2); unit cell[a], monoclinic; space group, P 2_1/n; dimensions, a = 15.9472(16), b = 13.8380(14), c = 17.5219(17), α = 90°, β = 91.123(5)°, γ = 90°; Z, 2; V (Å^3), 3,865.9(7); d(calc, g/cm^3), 1.286; R^b, 0.0487; $R_w{}^c$, 0.1338; GOF, 1.050. [a]Mo Kα(λ = 0.7170 Å) radiation. [b]$R = \Sigma||F_0| - |F_c||/ \Sigma|F_0|$. [c]$R_w = [\Sigma w(|F_0| - |F_c|)^2/ \Sigma wF_0{}^{1/2}$, where $w^{-1} = [\sigma_{count}{}^2 + (0.05F^2)^2]4F^2$.

3.3.7 Structural Comparisons Between Oxo-Bridged Mn(III,III) Dimers 12-18 and Isostructural Fe(III,III) Dimers

Reactions between thiolate-ligated **1**-**8** and the various biologically-relevant oxidants discussed in this chapter parallel that previously described for the analogous thiolate-ligated Fe(II) complexes $[Fe^{II}(S^{Me2}N_4(tren))](PF_6)$ (**24**), $[Fe^{II}(S^{Me2}N_4(6\text{-H-DPEN}))(MeOH)](PF_6)$ (**25**), $[Fe^{II}(S^{Me2}N_4(6\text{-H-DPPN}))](PF_6)$ (**26**), $[Fe^{II}(S^{Me2}N_4(6\text{-Me-DPEN}))](PF_6)$ (**27**), and $[Fe^{II}(S^{Me2}N_4(2\text{-QuinoEN}))](PF_6)\cdot MeOH$ (**28**).[18,26] Reactions between each of these Fe(II) complexes and most of the oxidants discussed in this chapter (O_2, O_2^-, H_2O_2, PhIO, *m*CPBA) have been shown to result in high yields of the corresponding unsupported oxo-bridged Fe(III,III) dimers.[26] The ORTEP diagrams of these oxo-bridged ferric dimers,

$[Fe^{III}(S^{Me2}N_4(tren))]_2(\mu\text{-}O)(PF_6)_2$ (**29**), $[Fe^{III}(S^{Me2}N_4(6\text{-}H\text{-}DPEN))]_2(\mu\text{-}O)(PF_6)_2\cdot MeCN$ (**30**), $[Fe^{III}(S^{Me2}N_4(6\text{-}H\text{-}DPPN))]_2(\mu\text{-}O)(PF_6)_2\cdot MeCN$ (**31**), $[Fe^{III}(S^{Me2}N_4(6\text{-}Me\text{-}DPEN))]_2(\mu\text{-}O)(BF_4)_2\cdot CH_2Cl_2$ (**32**), and $[Fe^{III}(S^{Me2}N_4(2\text{-}QuinoEN))]_2(\mu\text{-}O)(BF_4)_2\cdot 2MeCN$ (**33**) are provided in Figures 3.22-3.24, while selected metrical parameters are compiled in Table 3.5.[18,26] Comparisons between isostructural pairs of oxo-bridged Mn(III,III) and Fe(III,III) dimers (comparison between pairs containing the same ligands) reveal that the geometrical orientations of each dimer are preserved between members of each pair (Tables 3.1 and 3.4). A notable difference in the M-S bonds between the Mn and Fe dimers is that, just as was noted in comparing the monomeric M(II) complexes from Chapter 2, each Fe(III)-S bond is approximately 0.1 Å shorter than the Mn(III)-S bonds. The M-N(pyridine) or M-N(quinoline) distances, however, are up to 0.4 longer in the Mn(III)-containing dimers compared to those in those containing Fe(III) ions. This difference is much less pronounced in comparing **12** and **29**, each of which contain aliphatic amines instead of bulkier pyridine or quinoline moieties, and again suggests that steric influences have a considerable effect upon the structures of these complexes.

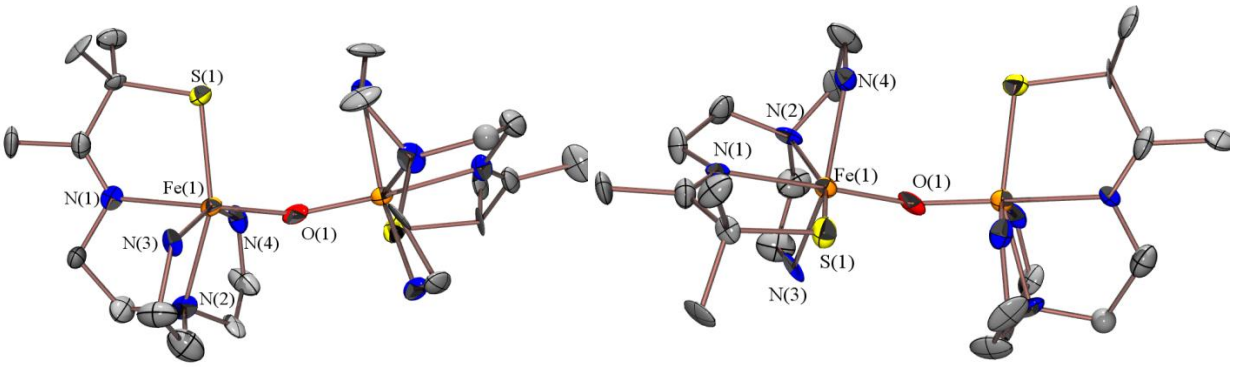

Figure 3.22 ORTEP diagrams (50 % probability) of $\{[Fe^{III}(S^{Me2}N_4(tren))]_2(\mu\text{-}O)\}^{2+}$ (**29**) with hydrogen atoms, counterions, and solvents of crystallization omitted for clarity.

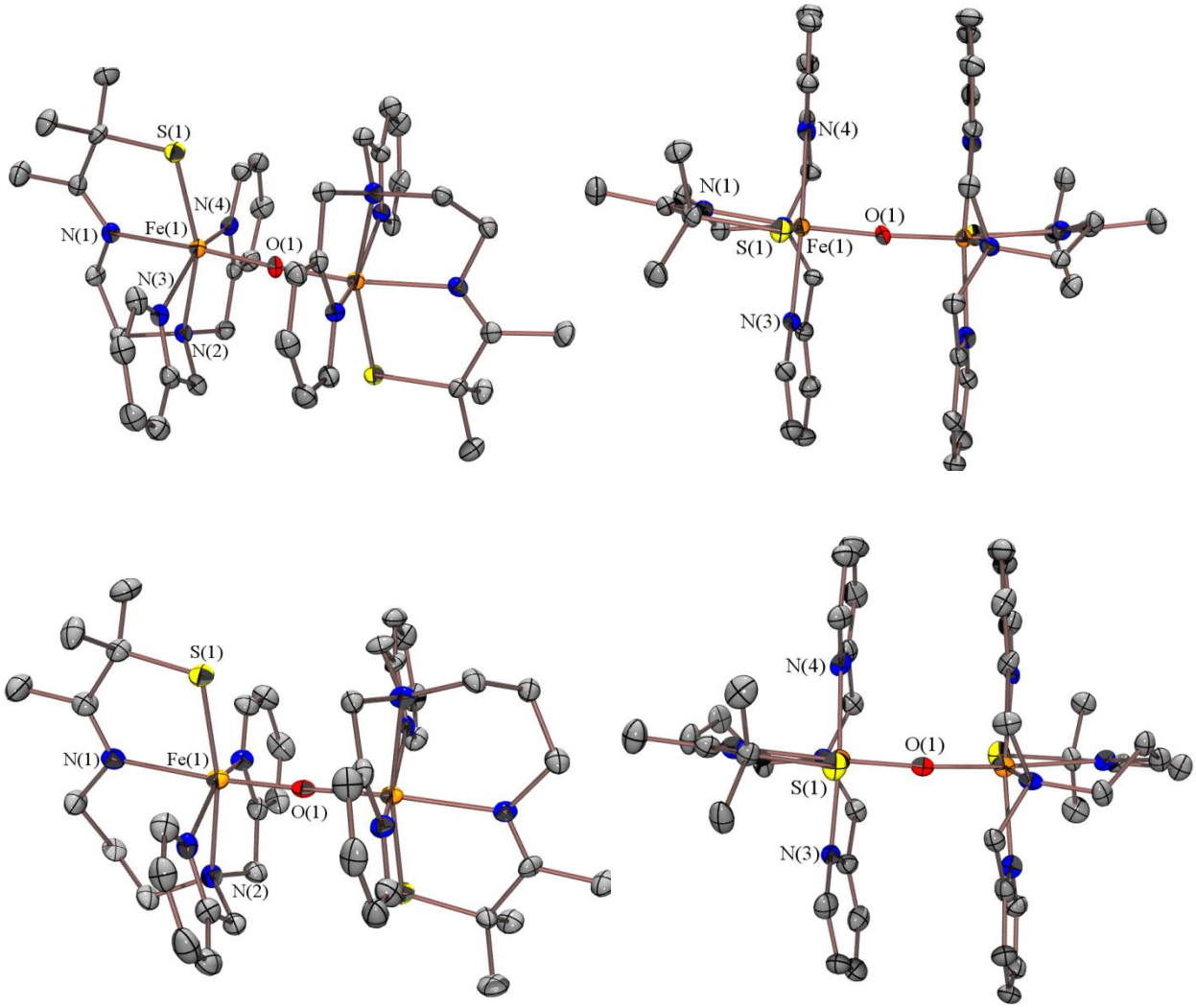

Figure 3.23 ORTEP diagrams (50 % probability) of $\{[Fe^{III}(S^{Me2}N_4(6\text{-H-DPEN}))]_2(\mu\text{-O})\}^{2+}$ (**30**, top) and $\{[Fe^{III}(S^{Me2}N_4(6\text{-H-DPPN}))]_2(\mu\text{-O})\}^{2+}$ (**31**, bottom) with hydrogen atoms, counterions, and solvents of crystallization omitted for clarity.

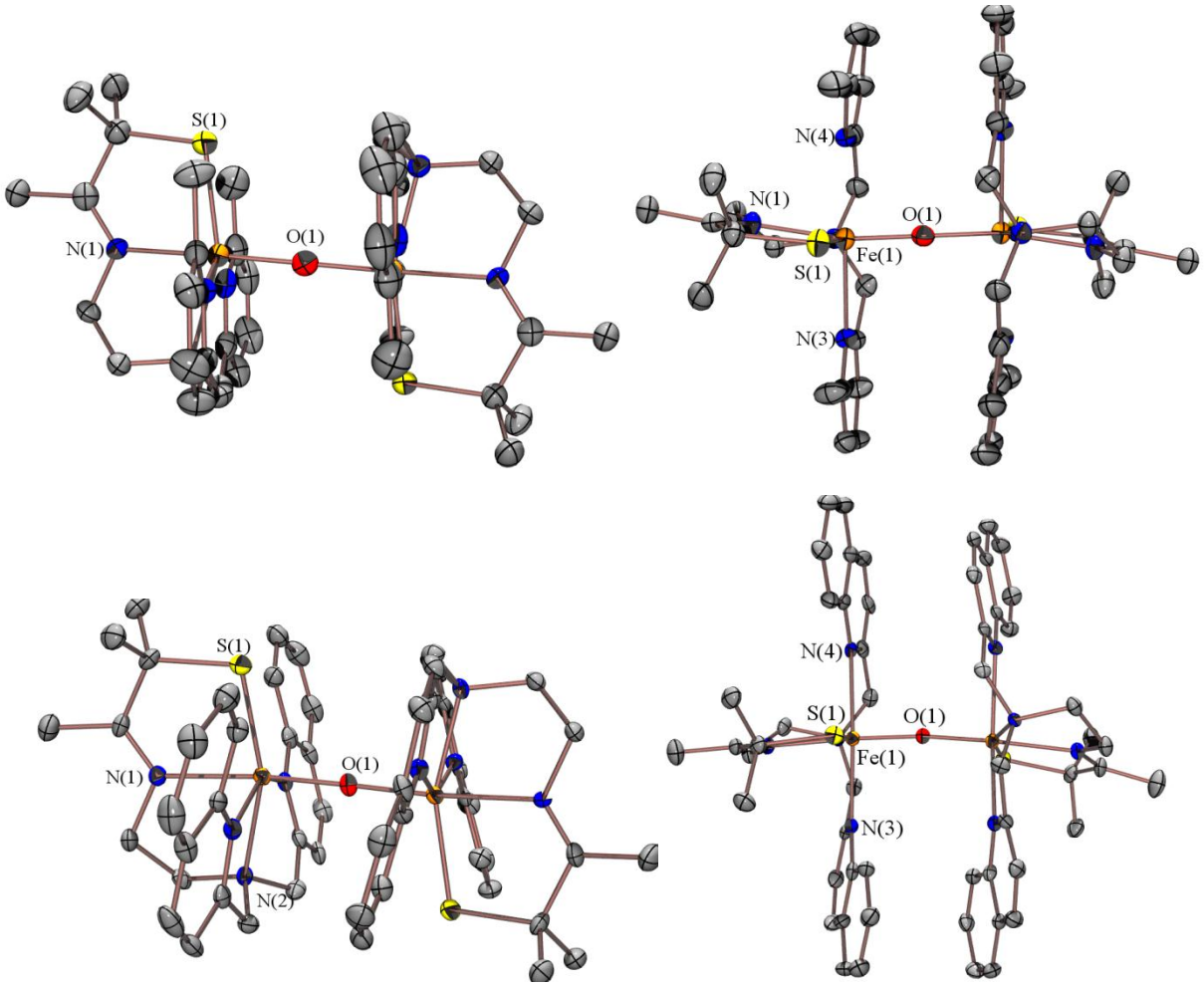

Figure 3.24 ORTEP diagrams (50 % probability) of $\{[Fe^{III}(S^{Me2}N_4(6\text{-Me-DPEN}))]_2(\mu\text{-O})\}^{2+}$ (**32**, top) and $\{[Fe^{III}(S^{Me2}N_4(2\text{-QuinoEN}))]_2(\mu\text{-O})\}^{2+}$ (**33**, bottom) with hydrogen atoms, counterions, and solvents of crystallization omitted for clarity.

Table 3.5 Selected bond distances (Å) and angles (deg) for $[Fe^{III}(S^{Me2}N_4(tren))]_2(\mu\text{-}O)(PF_6)_2\cdot MeCN$ (**29**), $[Fe^{III}(S^{Me2}N_4(6\text{-}H\text{-}DPEN))]_2(\mu\text{-}O)(PF_6)_2\cdot MeCN$ (**30**), $[Fe^{III}(S^{Me2}N_4(6\text{-}H\text{-}DPPN))]_2(\mu\text{-}O)(PF_6)_2\cdot MeCN$ (**31**), $[Fe^{III}(S^{Me2}N_4(6\text{-}Me\text{-}DPEN))]_2(\mu\text{-}O)(BF_4)_2\cdot CH_2Cl_2$ (**32**), and $[Fe^{III}(S^{Me2}N_4(2\text{-}QuinoEN))]_2(\mu\text{-}O)(BF_4)_2\cdot 2MeCN$ (**33**).

	29	**30**	**31**	**32**	**33**
Fe(1)-S(1)	2.317(4)	2.3058(11)	2.2998(19)	2.3049(19)	2.3053(13)
Fe(1)-N(1)	2.239(10)	2.155(3)	2.310(5)	2.186(5)	2.174(3)
Fe(1)-N(2)	2.186(10)	2.222(3)	2.243(5)	2.205(5)	2.175(3)
Fe(1)-N(3)	2.173(10)	2.160(3)	2.136(5)	2.319(5)	2.303(3)
Fe(1)-N(4)	2.208(10)	2.168(4)	2.149(5)	2.364(5)	2.371(3)
Fe(1)-O(1)	1.807(8)	1.787(3)	1.803(4)	1.786(4)	1.778(3)
Fe(2)-S(2)	2.330(4)	2.3243(11)	2.3165(19)	2.3026(19)	2.3089(12)
Fe(2)-N(5)	2.150(10)	2.151(3)	2.297(5)	2.213(6)	2.152(3)
Fe(2)-N(6)	2.216(10)	2.213(3)	2.245(5)	2.189(4)	2.286(3)
Fe(2)-N(7)	2.223(10)	2.171(3)	2.190(6)	2.374(5)	2.179(3)
Fe(2)-N(8)	2.211(11)	2.191(4)	2.139(5)	2.276(5)	2.377(3)
Fe(2)-O(1)	1.809(8)	1.781(3)	1.816(4)	1.789(4)	1.778(3)
S(1)-Fe(1)-N(1)	80.4(3)	81.75(9)	79.40(15)	80.48(15)	80.54(9)
S(1)-Fe(1)-N(2)	157.2(3)	159.17(9)	168.62(15)	158.01(15)	158.48(9)
S(1)-Fe(1)-N(3)	105.3(3)	104.78(9)	104.23(15)	104.55(15)	104.00(9)
S(1)-Fe(1)-N(4)	100.2(3)	101.35(9)	101.61(16)	104.73(14)	104.64(8)
O(1)-Fe(1)-S(1)	99.6(3)	104.61(10)	96.69(15)	101.44(14)	104.15(9)
O(1)-Fe(1)-N(1)	178.6(4)	172.55(13)	175.30(19)	177.52(19)	173.91(12)
O(1)-Fe(1)-N(2)	102.9(4)	95.92(13)	94.3(2)	100.15(19)	97.21(12)
O(1)-Fe(1)-N(3)	102.9(4)	81.84(12)	92.66(19)	96.56(18)	92.00(11)
O(1)-Fe(1)-N(4)	91.4(4)	89.09(12)	89.77(17)	86.97(17)	87.51(11)
S(2)-Fe(2)-N(5)	81.1(3)	80.60(9)	78.08(14)	78.84(15)	80.68(10)
S(2)-Fe(2)-N(6)	158.2(3)	159.56(9)	168.94(16)	155.43(15)	103.76(9)
S(2)-Fe(2)-N(7)	106.1(3)	104.91(9)	103.71(15)	105.20(14)	158.77(9)
S(2)-Fe(2)-N(8)	97.6(3)	102.22(9)	103.93(16)	155.43(15)	104.57(9)
O(1)-Fe(2)-S(2)	98.4(3)	103.22(10)	96.10(15)	102.23(14)	103.95(9)
O(1)-Fe(2)-N(5)	175.4(4)	172.19(13)	173.5(2)	174.35(18)	174.54(13)
O(1)-Fe(2)-N(6)	103.2(4)	97.13(13)	94.9(2)	102.21(19)	92.24(11)
O(1)-Fe(2)-N(7)	94.4(4)	90.40(12)	92.92(18)	88.75(17)	97.09(12)
O(1)-Fe(2)-N(8)	91.7(4)	92.35(12)	90.95(16)	91.73(18)	88.41(11)
Fe(1)··· Fe(2)	3.532	3.566	3.616	3.566	3.551
Fe(1)-O(1)- Fe(2)	155.3(5)	175.95(17)	175.7(2)	172.0(3)	174.02(14)

3.4 Conclusions

This chapter has broadly described the reactivity of the thiolate-ligated Mn(II) complex library described in Chapter 1 with various biological oxidants, including O_2, O_2^-, H_2O_2, PhIO, and *m*CPBA. Despite the relatively wide variety of oxidants used, reactions between each

respective oxidant and thiolate-ligated Mn(II) complex resulted in the formation of an unsupported oxo-bridged Mn(IIII,III) dimer. Most of these dimers were obtained in high yields and found to be extremely robust under ambient conditions, however a few of the dimers were only formed transiently and required low temperature conditions in order for these respective complexes to be observed. Each dimer has been characterized by X-ray crystallography and UV/Vis spectroscopy, while most of the dimers have been characterized by magnetic susceptibility measurements and cyclic voltammetry. Oxo-bridged dimers containing relatively acute Mn-O-Mn bridging angles were found to be reactive with various weak acids in solution, forming the corresponding mononuclear Mn(III)-conjugate base complexes as final products from these reactions. The reactivity of alkoxide- or alcohol-ligated analogues for some of the thiolate-ligated complexes also proved to result in various oxo- or hydroxo-bridged Mn(III,III) dimers as final products. Comparisons between isostructural thiolate-ligated Mn(III,III) and Fe(III,III) dimers revealed that geometrical properties are conserved between dimer pairs containing the same ligand, while metrical differences within each isostructural pair can be attributed to differences in the Lewis acidity and electronic structure of the two metal ions.

3.5 Notes to Chapter 3

1) Vance, C. K.; Miller, A.-F. *Biochemistry* **2001**, *40*, 13079-13087.
2) Jackson, T. A.; Brunold, T. C. *Acc. Chem. Res.* **2004**, *37*, 461-470.
3) Miller, A.-F. *Acc. Chem. Res.* **2008**, *41*, 501-510.
4) Wu, A. J.; Penner-Hahn, J. E.; Pecoraro, V. L. *Chem. Rev.* **2004**, *104*, 903-938.
5) Signorella, S.; Hureau, C. *Coord. Chem. Rev.* **2012**, *256*, 1229-1245.
6) Miller, M. A.; Lipscomb, J. D. *J. Biol. Chem.* **1996**, *271*, 5524-5535.
7) Emerson, J. P.; Kovaleva, E. G.; Farquahar, E. R.; Lipscomb, J. D.; Que, Jr., L. *Proc. Natl. Acad. Sci. USA* **2008**, *105*, 7347-7352.
8) McEvoy, J. P.; Brudvig, G. W. *Chem. Rev.* **2006**, *106*, 4455-4483.

9) Mullins, C. S.; Pecoraro, V. L. *Coord. Chem. Rev.* **2008**, *252*, 416-443.

10) Umena, Y.; Kawakami, K.; Shen, J.-R.; Kamiya, N. *Nature* **2011**, *473*, 903-938.

11) Shook, R. L.; Peterson, S. M.; Greaves, J.; Moore, C.; Rheingold, A. L.; Borovik, A. S. *J. Am. Chem. Soc.* **2011**, *133*, 5810-5817.

12) Shook, R. L.; Gunderson, W. A.; Greaves, J.; Ziller, J. W.; Hendrich, M. P.; Borovik, A. S. *J. Am. Chem. Soc.* **2008**, *130*, 8888-8889.

13) Bossek, U.; Weyhermuller, T.; Wieghardt, K.; Nuber, B.; Weiss, J. *J. Am. Chem. Soc.* **2007**, *129*, 12416-12417.

14) Annaraj, J.; Cho, J.; Lee, Y.-M.; Kim, S. Y.; Latifi, R.; de Visser, S. P.; Nam, W. *Angew. Chem., Int. Ed.* **2009**, *48*, 4150-4153.

15) Kovacs, J. A.; Brines, L. M. *Acc. Chem. Res.* **2007**, *40*, 501-509.

16) Kitagawa, T.; Dey, A.; Lugo-Mas, P.; Benedict, J.; Kaminsky, W.; Solomon, E. I.; Kovacs, J. A. *J. Am. Chem. Soc.* **2006**, *128*, 14448-14449.

17) Venkateswara Rao, P.; Holm, R. H. *Chem. Rev.* **2004**, *104*, 527-559.

18) Theisen, R. M.; Shearer, J.; Kaminsky, W.; Kovacs, J. A. *Inorg. Chem.* **2004**, *43*, 7682-7690.

19) Nam, E.; Alokolaro, P. E.; Swartz, R. D.; Gleaves, M. C.; Pikul, J.; Kovacs, J. A. *Inorg. Chem.* **2011**, *50*, 1592-1602.

20) Villar-Acevedo, G.; Nam, E.; Fitch, S.; Benedict, J.; Freudenthal, J.; Kaminsky, W.; Kovacs, J. A. *J. Am. Chem. Soc.* **2011**, *133*, 1419-1427.

21) Sun, N.; Dey, A.; Villar-Acevedo, G.; Kovacs, J. A.; Darensbourg, M. Y.; Hodgson, K. O.; Hedman, B.; Solomon, E. I. *Inorg. Chem.* **2011**, *50*, 427-436

22) Swartz, R. D.; Coggins, M. K.; Kaminsky, W.; Kovacs, J. A. *J. Am. Chem. Soc.* **2011**, *133*, 3954-3963.

23) http://ewww.mpi-muelheim.mpg.de/bac/logins/bill/julX_en.php.

24) Evans, D. A. *J. Am. Chem. Soc.* **1959**, 2005.

25) Van Geet, A. L. *Anal. Chem.* **1968**, *40*, 2227-2229.

26) Toledo, S. Ph.D. thesis, University of Washington, Seattle, Washington, 2010.

27) Bandlish, B. K.; Shine, H. I. *J. Org. Chem.* **1977**, *42*, 561-563.

28) Sheldrick, G. M. CELL_NOW. University of Goettingen, Germany, 2005.

29) Bruker APEX2 (Version 2.1-2.4), SAINT (Version 7.34A), SADABS (Version 2007/4), BrukerAXS Inc., Madison, Wisconsin, USA.

30) Sheldrick, G. M. TWINABS. University of Goettingen, Germany, 2007.

31) Mackay, S.; Edwards, C.; Henderson, A.; Gilmore, C.; Stewart, N.; Shankland, K.; Donald, A.; MaXus: a Computer Program for the Solution and Refinement of Crystal Structures from Diffraction Data. University of Glasgow, Scotland, 1997.

32) Waasmaier, D.; Kirfel, A. *Acta Crystallogr. A* **1995**, *51*, 416.

33) Jin, N.; Ibrahim, M.; Spiro, T. G.; Groves, J. T. *J. Am. Chem. Soc.* **2007**, *129*, 12416-12417.

34) Connelly, N. G.; Geiger, W. E. *Chem. Rev.* **1996**, *96*, 877-910.

35) Seela, J. L.; Knapp, M. J.; Kolack, K. S.; Chang, H.-R.; Huffman, J. C.; Hendrickson, D. N.; Christou, G. *Inorg. Chem.* **1997**, *37*, 516-525.

36) Costa, T.; Dorfman, J. R.; Hagen, K. S.; Holm, R. H. *Inorg. Chem.* **1983**, *22*, 4091-4099.

37) Cotton, F. A.; Wilkinson, G. *Advanced Inorganic Chemistry*, Interscience: New York, 1972.

38) Mukhopadhyay, S.; Mandal, S. K.; Bhaduri, S.; Armstrong, W. H. **2004**, *104*, 3981-4026.

39) Kahn, O. *Molecular Magnetism;* VCH: New York, 1993.

40) Vogt, Jr., L. H.; Zalkin, A.; Templeton, D. H. *Science* **1996**, *151*, 569-570.

41) Ziolo, R. F.; Stanford, R. H.; Rossman, G. R.; Gray, H. B. *J. Am. Chem. Soc.* **1974**, *96*, 7910-7915.

42) Kipke, C. A.; Scott, M. J.; Gohdes, J. W.; Armstrong, W. H. *Inorg. Chem.* **1990**, *29*, 2193-2194.

43) Horner, O.; Anxolabéhère-Mallart, E.; Charlot, M.-F.; Tchertanov, L.; Guilhem, J.; Mattioli, T. A.; Boussac, A.; Girder, J.-J. *Inorg. Chem.* **1999**, *38*, 1222-1232.

44) Baffert, C.; Collomb, M.-N.; Beronzier, A.; Pécaut, J.; Limburg, J.; Crabtree, R. H.; Brudvig, G. W. *Inorg. Chem.* **2002**, *41*, 1404-1411.

45) Triller, M. U.; Hsieh, W.-Y.; Pecoraro, V. L.; Rompel, A.; Krebs, B. *Inorg. Chem.* **2002**, *41*, 5544-5544.

46) Kitajima, N.; Osawa, M.; Tanaka, M.; Moro-oka, Y. *J. Am. Chem. Soc.* **1991**, *113*, 8952-8953.

47) Blasco, S.; Cano, J.; Paz Clares, M.; García-Granda, S.; Doménech, A.; Jiménez, H. R.; Verdejo, B.; Lloret, F.; Garcí-España, E. *Inorg. Chem.* 2012 ASAP.

48) Ghosh, K.; Eroy-Reveles, A. A.; Olmstead, M. M.; Mascharak, P. K. *Inorg. Chem.* **2005**, *44*, 8469-8475.

49) Nag, S.; Datta, D. *Indian J. Chem.* **2007**, *46*, 1263-1265.

50) Cheng, B.; Cukiernik, F.; Fries, P. H.; Marchon, J.-C.; Scheidt, W. R. *Inorg. Chem.* **1995**, *34*, 4627-4639.

51) Cheng, B.; Fries, P. H.; Marchon, J.-C.; Scheidt, W. R. *Inorg. Chem.* **1996**, *35*, 1024-1032.

Chapter 4

Characterization of Intermediates From Reactions Involving Thiolate-Ligated Manganese(II) Complexes and Dioxygen

4.1 Introduction

Many metalloenzymes activate dioxygen in order to promote a wide variety of biochemical reactions.[1-3] Typically these reactions involve the binding of dioxygen to a low-valent transition metal cofactor, followed by a number of sequential one electron reductive activation steps in which the bond order of O_2 progressively decreases. These events also involve the formation of various metal-O_2 intermediates, such as metal-superoxo, metal-peroxo, and metal-hydroperoxo species.[4-5] The structural, electronic, and reactive properties of these metal-O_2 intermediates have received a considerable amount of attention within the bioinorganic community. Our understanding of such properties in native biological systems is unfortunately limited, as these types of species are often too reactive to observe or characterize.[6]

Towards this end, biomimetic studies with synthetic transition metal complexes have afforded invaluable insights into the properties of metal-O_2 adducts.[6-11] Most of the current knowledge particularly regarding manganese-O_2 species has come by way of synthetic complexes.[12] The properties of synthetic manganese-O_2 complexes are highly relevant to many Mn metalloenzymes proposed to involve Mn-superoxo or Mn-peroxo intermediates, such as the Mn superoxide dismutase, catalase, and oxygen-evolving complex of photosystem II.[13-17] Of the few Mn-O_2 complexes that have been synthesized and characterized, most are monomeric Mn(III)-η^2-peroxo complexes (also referred to as side-on Mn(III)-peroxo complexes) formed with O_2^- or H_2O_2.[18-22] Mn-O_2 complexes which have been derived specifically from dioxygen

are limited to only two Mn(IV)-peroxo species.[23-24] A Mn-superoxo intermediate, which would presumably form prior to a Mn-peroxo intermediate when dioxygen is a substrate, has never been observed. More examples of Mn-O_2 species are clearly needed in order to fully understand the properties of these types of intermediates and how O_2 is transformed by Mn ions in biology.

This chapter will provide a more in depth discussion of the reactivity of $[Mn^{II}(S^{Me2}N_4(6\text{-Me-DPEN}))](BF_4)$ (**1**) and $[Mn^{II}(S^{Me2}N_4(2\text{-QuinoEN}))](BPh_4)\cdot MeCN$ (**2**) with O_2, respectively (Scheme 4.1). The primary focus of this chapter specifically regards low temperature O_2 reactions with each complex and the characterization of O_2-derived intermediates. These studies have resulted in a number of novel observations, including the first observation of a Mn-superoxo species and the first two structurally-characterized peroxo-bridged Mn(III) dimers. Collectively, these intermediates have been characterized by X-ray crystallography, UV/Vis spectroscopy, rapid-scanned stopped-flow spectrophotometry, resonance Raman spectroscopy, X-band EPR spectroscopy, and X-ray absorption spectroscopy. Kinetic data has also been obtained, which has allowed mechanistic proposals for each O_2 reaction to be made.

Scheme 4.1 ChemDraw representation of $[Mn^{II}(S^{Me2}N_4(6\text{-Me-DPEN}))]^+$ (**1**) and $[Mn^{II}(S^{Me2}N_4(2\text{-QuinoEN}))]^+$ (**2**) (revised labeling scheme).

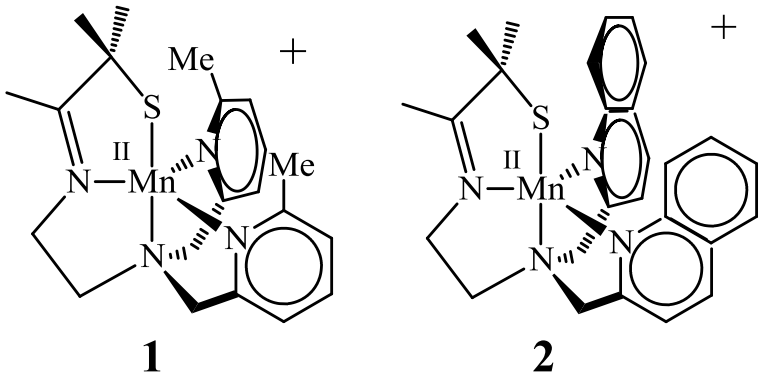

4.2 Experimental Section

4.2.1 General Considerations

All manipulations were performed using Schlenk techniques or under an N_2 atmosphere in a glovebox. Reagents and solvents were purchased from commercial vendors, were of highest available purity, and were used without further purification unless otherwise noted. MeOH (Na), MeCN (CaH_2), and CH_2Cl_2 (CaH_2) were dried and distilled prior to use. Et_2O was rigorously degassed and purified using solvent purification columns housed in a custom stainless steel cabinet and dispensed by a stainless steel schlenk-line (GlassContour). ^1H NMR spectra were recorded on a Bruker AV 300 FT NMR spectrometer at ambient temperature and were referenced to residual deuterated solvent. Chemical shifts are listed in parts per million (ppm). UV/vis spectra were recorded on a Varian Cary 50 spectrophotometer equipped with a fiber optic cable connected to a "dip" ATR probe (C-technologies). A custom-built two-neck solution sample holder equipped with a threaded glass connector was sized specifically to fit the "dip" probe. Electrospray-ionization mass spectrometry (ESI-MS) data were obtained on a Bruker Esquire Liquid Chromatograph-Ion Trap mass spectrometer. Gas chromatography-mass spectrometry (GC/MS) data were obtained using a 5890 gas chromatograph equipped with a 7673A autosampler and interfaced with a 5971A mass spectrometer, all from Hewlett Packard Co. Calibration curves for analytes of interest were made using either *m*-xylene or toluene as an internal reference. EPR spectra were recorded on a Bruker E580 CW-EPR spectrometer operating at X-band frequency and equipped with an Oxford helium cryostat and dual mode cavity. EPR data were fit with EasySpin toolbox for MATLAB.[25-26] Magnetic moments (solid state) were obtained by zero-field cooling experiments from 5 to 300 K with polycrystalline samples in gel-caps using a Quantum Design MPMS S5 SQUID magnetometer. Solid state

magnetic susceptibility data were fit with the julX software program.[27] Pascal's constants were used to correct for diamagnetic contributions to experimental magnetic moments. X-ray crystallography data were recorded on a Bruker APEX II single crystal X-ray diffractometer with Mo Kα radiation. Complexes **1-2** were synthesized as described in Chapter 2 with $NaBPh_4$ used instead of $NaBF_4$ or $NaPF_6$, while complexes **3-4** were synthesized as described in Chapter 3.

4.2.2 Synthetic Protocols for Peroxo-Bridged Dimers 5-6

4.2.2.1 Synthesis of $[Mn^{III}(S^{Me2}N_4(6\text{-Me-DPEN}))]_2(\mu\text{-}1,2\text{-}O_2)(BPh_4)_2\cdot 2CH_3CH_2CN$ (5). A solution of **1** (0.50 g, 0.67 mmol) was prepared in CH_3CH_2CN (0.8 mL) and placed in a capped vial in a dry box. The solution was then removed from the dry box, cooled to 193 K in a freezer for ten minutes, and then allowed to react with atmospheric oxygen. After turning dark green, the reaction solution was then layered with Et_2O (2 mL) and allowed to crystallize at 193 K. After two to three days, dark green needles were harvested by filtering the reaction solution to yield the title compound in 92 % yield (0.47 g, 0.31 mmol). Electronic absorption spectrum: λ_{max} (nm) (ε ($M^{-1}cm^{-1}$)) (MeCN): 390 (1200), 642 (840). Magnetic moment (solid state, 5-275 K): 4.69 μ_B/Mn.

4.2.2.2 Synthesis of $[Mn^{III}(S^{Me2}N_4(2\text{-QuinoEN}))]_2(\mu\text{-}1,2\text{-}O_2)(BPh_4)_2\cdot 2CH_3CH_2CN$ (5). A procedure similar to that described for the synthesis of **5** was performed with the following reagent amounts; **2** (0.20 g, 0.24 mmol). The title compound was obtained as a dark green powder in 37 % yield (0.075 g, 0.044 mmol). Electronic absorption spectrum: λ_{max} (nm) (ε ($M^{-1}cm^{-1}$)) (MeCN): 660.

4.2.3 Hydrogen Peroxide Detection Assay

A concentrated propionitrile solution of **5** (0.1 mL, 5.5 mM) was prepared under an inert atmosphere. After cooling the solution to 193 K (with a dry ice/acetone bath), O_2 was gently bubbled directly from a cylinder into the solution for approximately two minutes. This procedure promoted a color change from light yellow to dark green, indicating the formation of peroxo-bridged **5**. A minimal amount of concentrated H_2SO_4 (3-4 drops) was then added to the dark green solution, causing the solution to turn clear. The resulting reaction mixture was then passed through a small silica plug, collected, and added in a single aliquot to a stirring aqueous solution of $KMnO_4$ (3 mL, 6.15 x 10^{-5} M). The resulting changes in absorbance values were then recorded in one minute intervals until no further changes were observed. The amount of hydrogen peroxide present was calculated based on the decrease in absorbance at 550 nm ($\varepsilon(M^{-1}cm^{-1}$, 293 K) = 2455) caused by the following reaction:

$$2KMnO_4 + 5H_2O_2 + 6H^+ \rightarrow 2Mn^{2+} + 5O_2 + 8H_2O + 2K^+$$

4.2.4 Stopped-Flow Kinetics Experiments

Acetonitrile and propionitrile solutions of each reagent were prepared in an MBraun glovebox filled with high purity argon and placed in Hamilton gas-tight syringes. Time-resolved spectra (400-800 nm) were acquired at low temperatures using a TgK Scientific (U.K.) SF-61DX2 Multi-Mixing CryoStopped-Flow Instrument, a J&M TIDASD-AQ diode array detector, and an MCS UV/NIR lightsource (Spectralytics, DenMark). The stopped-flow instrument was equipped with PEEK tubings fitted inside stainless steel plumbing, a 1.00 cm^3 quartz mixing cell, and an anaerobic kit purged with an inert gas. The temperature in the mixing cell was maintained to 0.1 °C and the mixing time was 2-3 msec. All flow lines of the instrument were

extensively washed with degassed, anhydrous acetonitrile or propionitrile before charging the driving syringes with reactant solutions. The reactions were studied by rapid scanning spectrophotometry under pseudo-first-order conditions with excess dioxygen. Saturated solutions of O_2 were prepared by bubbling dry O_2 gas for 15 minutes into gas-tight syringes containing dry acetonitrile or propionitrile. Dilutions of the O_2 saturated solvent were preformed anaerobically to obtain the desired concentration of O_2. The solubility of O_2 was taken as 8.1 mM in acetonitrile and 8.8 mM in propionitrile at 25 °C.[28] All of the experiments were performed in a single-mixing mode of the instrument with a 1:1 (v/v) mixing ratio. A series of three to four measurements gave an acceptable standard deviation (±10 %). Data analysis was performed with the Kinetic Studio software program from Hi-Tech Scientific and IGOR Pro from Wavemetrics, Inc.

4.2.5 Resonance Raman Experiments

Experiments were conducted on either solid or solution (MeCN) samples with a Coherent 190C-K Kr^+ excitation laser, SPEX model 1877 CP triple monochromator with a filter and blazed holographic gratings of 2400 grooves per millimeter. Scattered signals were measured with a Newton DU940N-BU 2048 x 512 pixel back-illuminated, thermoelectric-cooled CCD array detector. Spectra were taken at 77 K using a 413 nm excitation laser with a power of 5 mw. Samples were continuously rotated in order to minimize photodecomposition.

4.2.6 Mn K-Edge X-ray Absorption Spectroscopic Experiments

XAS data were obtained at the Stanford Synchrotron Radiation Laboratory (SSRL) on beamline 9-3 under ring conditions of 3 GeV and 60-100 mA with a Si(220) double-crystal monochromator and Rh-coated mirror for harmonic injection. Energy calibrations were

performed by assigning the first injection point of the Fe foil spectrum to 7111.2 eV. All samples were maintained between 10-15 K during data collection using an Oxford Instruments CF1208 continuous-flow liquid helium cryostat. Data were collected in fluorescence mode using a Canberra Ge 30-element array detector and measured to k = 13 A^{-1}. Each sample was monitored for photoreduction throughout the course of data collection by comparing individual scans. All data were calibrated and averaged using EXAFSPAK.[29] Normalization was performed by subtracting the spline fit to the data and setting the post-edge absorbance to 1.

4.2.7 X-ray Crystallographic Structure Determination

A green needle of **5** with dimensions 0.20 x 0.15 x 0.05 mm^3 was mounted on a glass capillary with oil. Data was collected at -173 ˚C. The crystal-to-detector distance was set to 40 mm and the exposure time was 30 seconds per degree for all sets of exposure. The scan width was 0.5˚. Data collection was 89.4% complete to 25.0˚ in ϑ. A total of 27,190 partial and complete reflections were collected covering the indices h = -15 to 15, k = -22 to 22, l = -22 to 22. 7,909 reflections were symmetry independent and the R_{int} = 0.0964 indicated that the data was less than average quality (0.07 average quality). Indexing and unit cell refinement indicated a monoclinic P lattice with the space group P 2_1/c (No.14). One highly disordered propionitrile molecule in the structure was modeled over two positions (83/17 ratio), while a second disordered propionitrile was modeled over three positions (66/17/17 ratio). The occupancies of each disorder component were refined freely while restraining the total occupancy sum to one. Disorder in one of the phenyl rings of the tetraphenylborate anion was modeled over two positions (66/34 ratio) without any additional restraints.

A black block of **6** with dimensions 0.03 x 0.03 x 0.01 mm^3 was mounted on a glass capillary with oil. Data was collected at -173 ˚C. The crystal-to-detector distance was set to 40 mm and the exposure time was 100 seconds per degree for all sets of exposure. The scan width was 0.5˚. Data collection was 96.6% complete to 25.0˚ in ϑ. A total of 11,234 partial and complete reflections were collected covering the indices h = -16 to 16, k = -16 to 16, l = -11 to 17. 8,380 reflections were symmetry independent and the R_{int} = 0.2126 indicated that the data was very poor (0.07 average quality). Indexing and unit cell refinement indicated a triclinic P lattice with the space group P $\bar{1}$ (No.2).

All X-ray data sets were integrated and scaled using either hkl-SCALEPACK or SAINT, SADABS within the APEX2 software package by Bruker.[30] Solutions were made by direct methods (SHELXS, SIR97) to produce complete heavy atom phasing models.[31-32] Scattering factors are from Waasmair and Kirfel.[33] Structures were completed by difference Fourier synthesis with either SHELXL97 or SHELXTL 6.10. Hydrogen atoms were placed in geometrically idealized positions and constrained to ride on their parent atoms with C-H distances in the range of 0.95-1.00 Å. Isotropic thermal parameters Ueq were fixed such that they were 1.2Ueq of their parent aom Ueq for C-Hs and 1.5Ueq for methyl groups. All non-hydrogen atoms were refined anisotropically by full-matrix least-squares.

4.2.8 Computational Details

Geometry optimization and single point energy calculations were performed using the Gaussian 08 software package with the spin-unrestricted B3LYP hybrid functional for all complexes.[34] A frequency calculation was performed with each optimized structure to ensure energy minimization. The 6-311G(d) basis set was used for Mn, S, and N atoms, while the 6-

21G(d) basis set was used for C and H atoms. The initial atomic coordinates for the geometry optimization calculations were obtained from the X-ray crystal structures. Single point calculations were performed using the 6-311G(d) basis set for all atoms. Molecular orbitals were plotted using the Gaussview v5.0.8 software.[34] Fragmentation analyses were performed using the QMForge software program.[35]

4.3 Results and Discussion

4.3.1 Low Temperature Dioxygen Reactivity of Thiolate-Ligated Mn(II) Complexes 1 and 2

As was discussed in the previous chapter, coordinatively unsaturated and thiolate-ligated Mn(II) complexes **1** and **2** each react with O_2 at room temperature to form thermally stable unsupported oxo-bridged Mn(III,III) dimers (dimers **3** and **4**, respectively) in quantitative yields. Isotopic labeling studies with $^{18}O_2$ revealed that the oxo-bridging ligands found in these oxo dimers are each derived from O_2, thus demonstrating that an O-O bond activation process is occurring during both reactions. When these reactions were performed at lower temperatures (233 K, MeCN) and monitored by UV/Vis spectroscopy, metastable intermediates were observed. As is shown in Figures 4.1 and 4.2, the intermediates formed in these reactions (intermediate **5** is formed from **1**, intermediate **6** is formed from **2**) are characterized by visible region absorption bands with λ_{max} values of 642 nm (**5**) and 660 nm (**6**). Both intermediates were found to quickly convert to the respective oxo-bridged Mn(III,III) dimers **3** and **4** within minutes at 233 K.

When these reactions were performed with **1** or **2** that had been synthesized with larger counterions (BPh_4^- instead of PF_6^- or BF_4^-), it was found that the relative stability of intermediates **5** and **6**, respectively, increased considerably. Complexes which had specifically

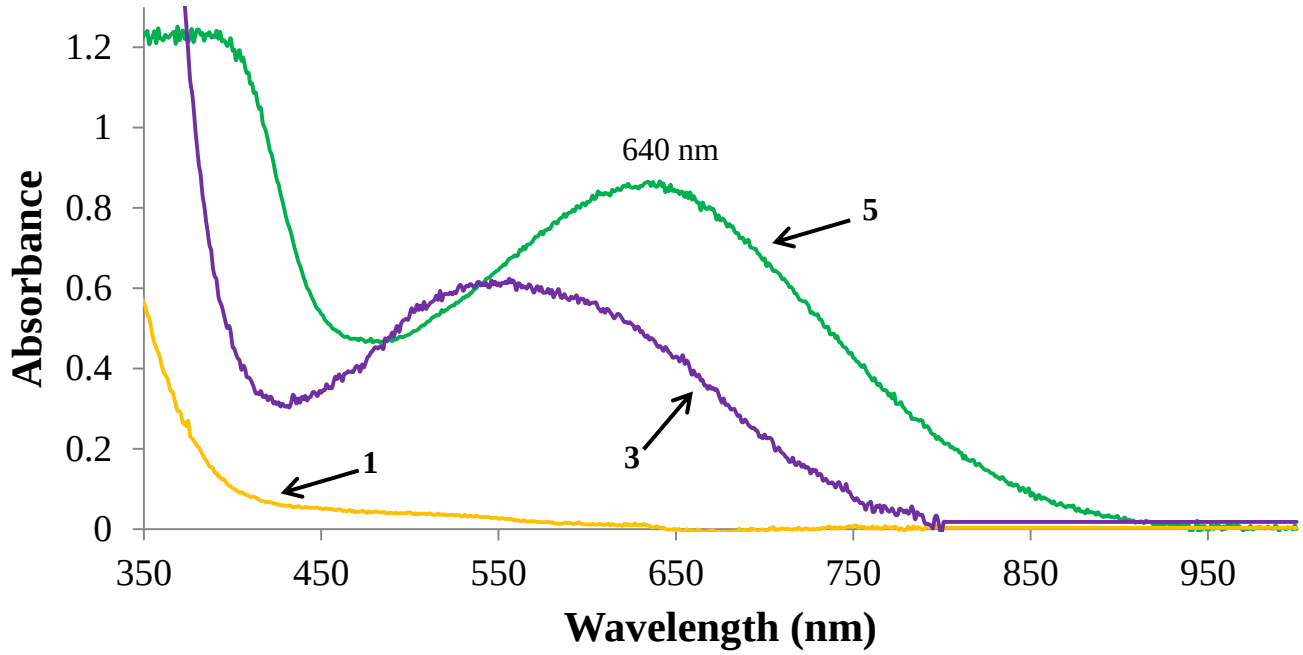

Figure 4.1 UV/Vis spectra of $[Mn^{II}(S^{Me2}N_4(6\text{-Me-DPEN}))]^+$ (**1**, yellow trace), metastable O_2-derived intermediate **5** (green trace), and $\{[Mn^{III}(S^{Me2}N_4(6\text{-Me-DPEN}))]_2(\mu\text{-O})\}^{2+}$ (**3**, purple trace) in MeCN at 233 K.

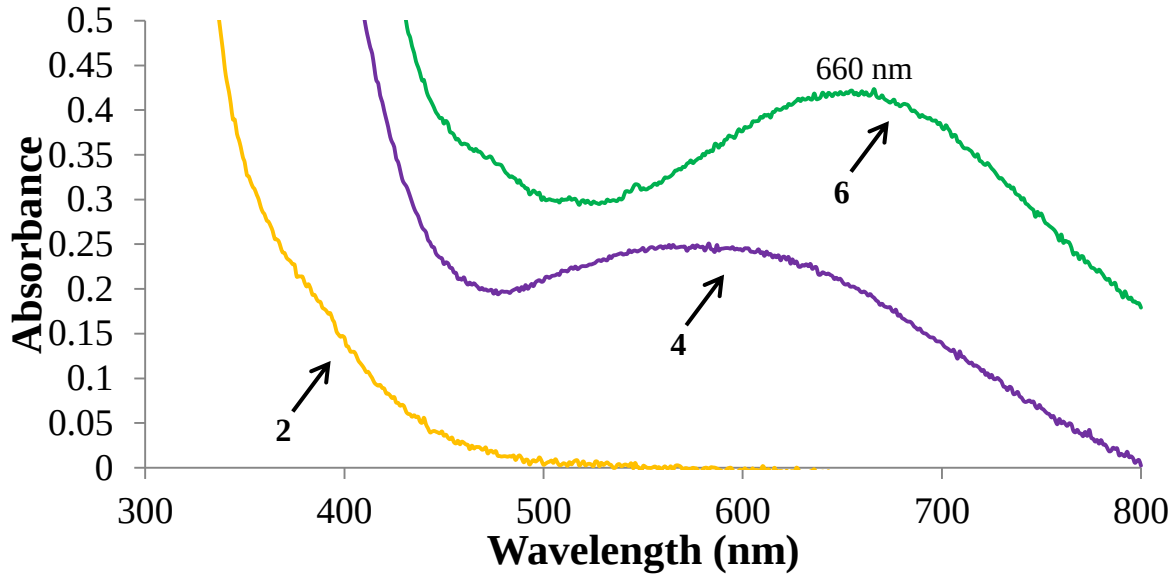

Figure 4.2 UV/Vis spectra of $[Mn^{II}(S^{Me2}N_4(2\text{-QuinoEN}))]^+$ (**2**, yellow trace), metastable O_2-derived intermediate **6** (green trace), and $\{[Mn^{III}(S^{Me2}N_4(2\text{-QuinoEN}))]_2(\mu\text{-O})\}^{2+}$ (**4**, purple trace) in MeCN at 233 K.

been prepared as BPh_4^- salts were found to form O_2-derived intermediates that persisted in solution on the order of tens of minutes instead of minutes (confirmed by stopped-flow kinetics measurements, *vide infra*). Both intermediates have been structurally characterized by X-ray crystallography as unsupported *trans*-μ-1,2-peroxo-bridged Mn(III,III) dimers. ORTEP diagrams of $[Mn^{III}(S^{Me2}N_4(6\text{-Me-DPEN}))]_2(\mu\text{-}O_2)(BPh_4)_2 \cdot 2CH_3CH_2CN$ (**5**) and $[Mn^{III}(S^{Me2}N_4(2\text{-QuinoEN}))]_2(\mu\text{-}O_2)(BPh_4)_2$ (**6**) are provided in Figures 4.3 and 4.4, respectively, while selected metrical parameters and crystal data are compiled in Tables 4.1 and 4.2, respectively. The X-ray structure of **6** was poorly resolved, therefore metrical parameters from this complex are unreliable and not further discussed. Selected metrical parameters for **1**-**4** are also included in Table 4.1 for comparison.

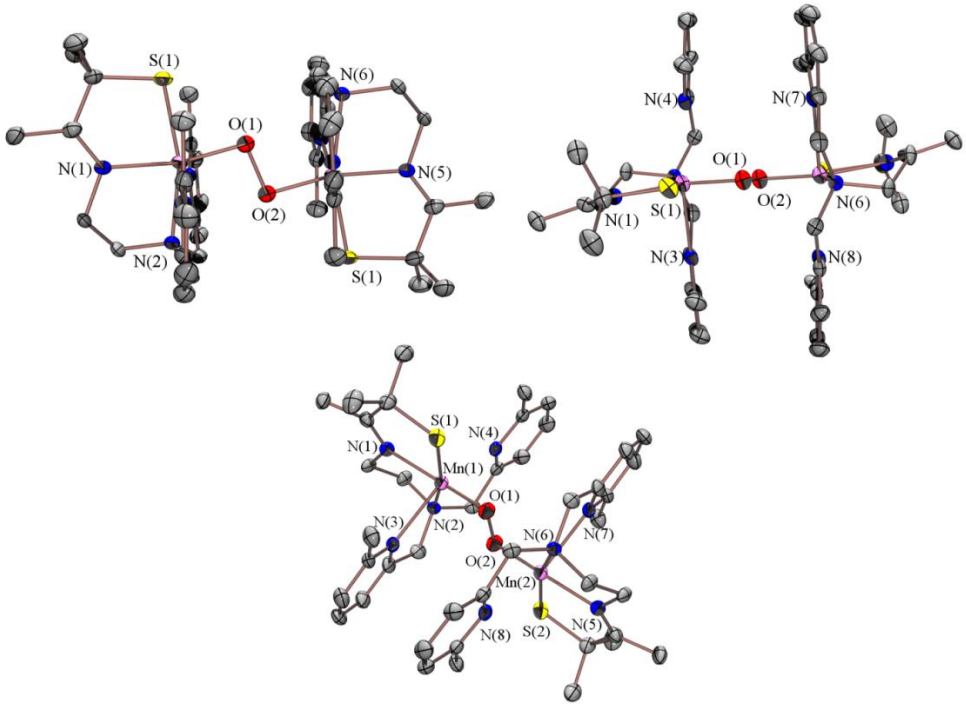

Figure 4.3 ORTEP diagrams (50 % probability) of $\{[Mn^{III}(S^{Me2}N_4(6\text{-Me-DPEN}))]_2(\mu\text{-}O_2)\}^{2+}$ (**5**) with hydrogen atoms, counterions, and solvents of crystallization omitted for clarity.

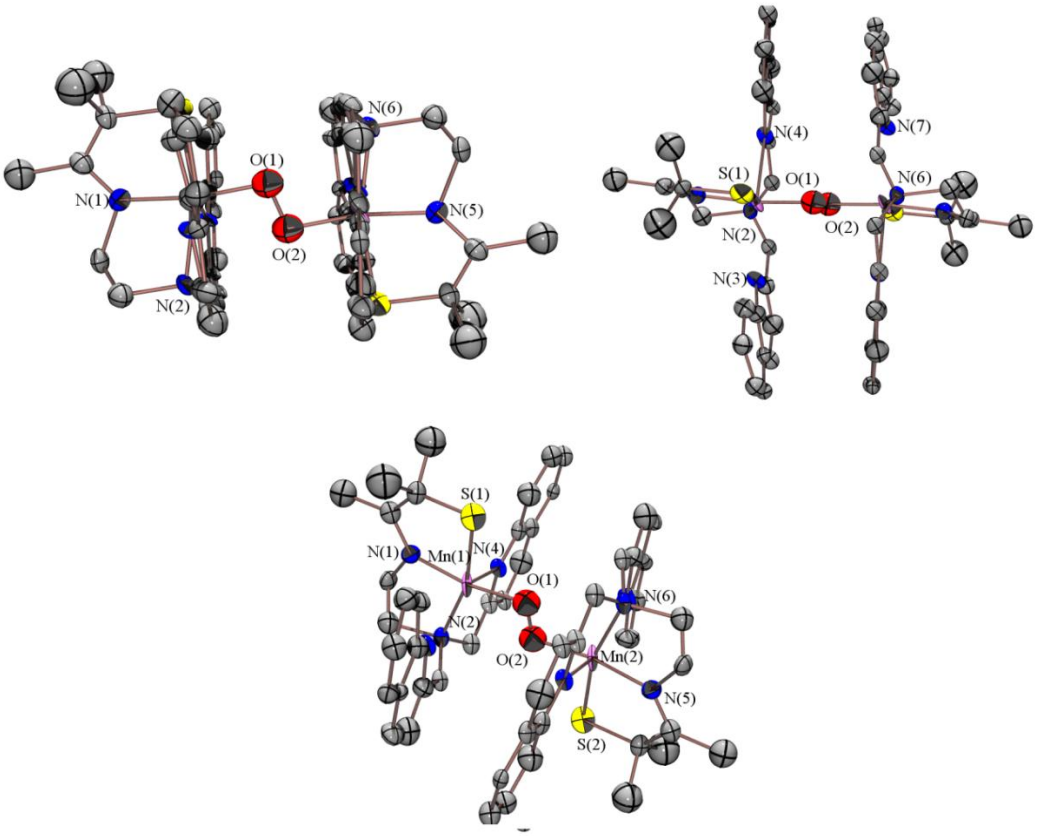

Figure 4.4 ORTEP diagrams (15 % probability) of $\{[Mn^{III}(S^{Me2}N_4(2\text{-QuinoEN}))]_2(\mu\text{-}O_2)\}^{2+}$ (**6**) with hydrogen atoms, counterions, and solvents of crystallization omitted for clarity.

Table 4.1 Selected bond distances (Å) and angles (deg) for $[Mn^{II}(S^{Me2}N_4(6\text{-Me-DPEN}))](BF_4)$ (**1**), $[Mn^{III}(S^{Me2}N_4(6\text{-Me-DPEN}))]_2(\mu\text{-O})(BF_4)_2\cdot(MeOH)_2$ (**3**), $[Mn^{III}(S^{Me2}N_4(6\text{-Me-DPEN}))]_2(\mu\text{-}O_2)(BPh_4)_2\cdot 2CH_3CH_2CN$ (**5**), $[Mn^{II}(S^{Me2}N_4(2\text{-QuinoEN}))](BPh_4)\cdot MeCN$ (**2**), $[Mn^{III}(S^{Me2}N_4(2\text{-QuinoEN}))]_2(\mu\text{-O})(PF_6)_2\cdot(CH_2Cl_2)$ (**4**), and $[Mn^{III}(S^{Me2}N_4(2\text{-QuinoEN}))]_2(\mu\text{-}O_2)(BPh_4)_2\cdot CH_3CH_2CN$ (**6**).

	1	**3**	**5**	**2**	**4**	**6**
Mn(1)-S(1)	2.3710(6)	2.2767(7)	2.2747(12)	2.3835(9)	2.292(1)	2.250(14)
Mn(1)-N(1)	2.186(2)	1.999(3)	2.040(3)	2.170(2)	2.010(3)	1.88(3)
Mn(1)-N(2)	2.297(2)	2.151(2)	2.203(3)	2.274(2)	2.130(3)	2.17(3)
Mn(1)-N(3)	2.222(2)	2.581(2)	2.410(3)	2.225(3)	2.543(3)	2.377(4)
Mn(1)-N(4)	2.239(2)	2.501(2)	2.492(3)	2.200(3)	2.370(3)	2.484(4)
Mn(1)-O(1)	N/A	1.7602(4)	1.832(3)	N/A	1.7599(6)	1.82(5)
O(1)-O(2)	N/A	N/A	1.452(5)	N/A	N/A	1.24(6)
S(1)-Mn(1)-N(1)	81.15(5)	82.08(8)	105.61(9)	82.20(7)	82.60(8)	82.0(12)
S(1)-Mn(1)-N(2)	156.98(5)	164.17(7)	163.3(1)	156.10(7)	163.90(9)	163.4(10)
S(1)-Mn(1)-N(3)	117.36(5)	106.2(1)	109.0(1)	106.98(7)	101.40(8)	118.4(7)
S(1)-Mn(1)-N(4)	117.38(5)	106.84(6)	105.6(1)	123.09(7)	109.23(8)	103.7(5)
O(1)-Mn(1)-S(1)	N/A	95.37(6)	85.12(9)	N/A	99.20(3)	89.2(10)
Mn(1)-O(1)-O(2)	N/A	N/A	97.5(6)	N/A	N/A	103(5)
Mn(1)···Mn(2)	N/A	3.520	4.113	N/A	3.512	4.091

Table 4.2 Crystal data for $[Mn^{III}(S^{Me2}N_4(6\text{-Me-DPEN}))]_2(\mu\text{-}O_2)(BPh_4)_2 \cdot 2CH_3CH_2CN$ (**5**) and $[Mn^{III}(S^{Me2}N_4(2\text{-QuinoEN}))]_2(\mu\text{-}O_2)(BPh_4)_2 \cdot CH_3CH_2CN$ (**6**).

	5	**6**
Formula	$C_{108}H_{128}B_2Mn_2N_{14}O_2S_2$	$C_{110}H_{112}B_2Mn_2N_8O_6S_2$
MW	1849.86	1847.78
T, K	100(2)	100(2)
Unit Cell[a]	Monoclinic	Triclinic
a, Å	14.2799(10)	13.83(2)
b, Å	18.3957(14)	14.142(10)
c, Å	18.5282(13)	14.508(12)
α, deg	90	115.00(3)
β, deg	94.541(2)	98.58(4)
γ, deg	90	105.11(4)
V, $Å^3$	4851.9(6)	2371(4)
Z	2	1
d(calc), g/cm^3	1.266	1.294
Sp. Group	P $2_1/c$	P -1
R[b]	0.0613	0.2527
R_w[c]	0.1614	0.6411
GOF	1.002	1.031

Both Mn ions in peroxo-bridged **5** are coordinated by a thiolate sulfur, imine nitrogen, tertiary amine, two pyridine nitrogens, and a peroxo oxygen. The Mn-S bond lengths in **5** (2.2747(12) Å for each Mn-S bond) are nearly 0.1 Å shorter than the Mn-S bond in reduced **1** (2.3710(6) Å) and within error of the Mn-S bond lengths of oxo-bridged Mn(III,III) dimer **3** (2.2767(7), Table 4.1), indicating the presence of two Mn(III) ions in **5**. The Mn-N(pyridine) (N(3) and N(4)) bond lengths found in **5** (2.410(3) and 2.492(3) Å) are considerably elongated relative to those in **1**, which was also noted in comparing bond lengths between **3** and **1** (Table 4.1, Chapter 2). The peroxo O-O bond length in **5** is 1.452(5) Å, which is much longer than that of O_2 (1.21 Å) but close to that of H_2O_2 (1.49 Å).[1] Long Mn(1)···O(2) and Mn(2)···O(1) distances (2.48 Å) suggest that the peroxo ligand is best described as bridging the two Mn(III) ions in an end-on (η^1:η^1) and a *trans* configuration (*trans*-μ-1,2). This is further supported by the Mn(1)···Mn(2) distance of 4.113 Å (Table 4.1), which is longer than the metal-metal distances

typically found for side-on (μ-η^2:η^2) peroxo-bridged first-row transition metal dimers (~3.5 Å).[36-37] Despite providing unreliable metrical parameters, the X-ray structure of **6** displays a similar bridging geometry to that described for **5** (Figure 4.4). Considering peroxo-bridged **5** was derived from a solution of Mn(II) and O_2, the identification of a peroxo ligand in this structure indicates that O_2 has been reduced via two sequential one electron reductive activation steps involving two equivalents of **1**.

Peroxo-bridged **5** and **6** are two of the very few structurally characterized Mn-peroxo complexes and are novel for a variety of reasons. These two complexes are the only known examples of peroxo-bridged Mn(III,III) dimers and the only structurally characterized Mn(III)-peroxos derived from dioxygen. These complexes are also the only structurally characterized Mn-peroxos containing end-on (η^1) peroxo coordination modes. Although somewhat trivial, **5** and **6** are the only structurally characterized thiolate-ligated transition metal-peroxo complexes. As will be discussed later in this chapter, further reactivity and spectroscopic studies with these complexes have resulted in the first observation of a Mn-superoxo intermediate, as well as the first vibrational data for a Mn-O stretch in a Mn-peroxo species (via resonance Raman spectroscopy, *vide supra*). Selected metrical parameters and vibrational data for all structurally characterized Mn-peroxo complexes are compiled in Table 4.3.

Compared to all other structurally characterized Mn-peroxo complexes, it can be seen that the O-O bond in **5** is within crystallographic error (three estimated standard deviations) of the longest Mn-peroxo O-O bond (1.46(3) Å, Table 4.3).[18-24] Contrarily, the Mn-O bond in **5** is within crystallographic error of the shortest such bond for all Mn-peroxos (1.83(2) Å, Table 4.3).[18-24] Specifically regarding only Mn(III)-peroxos, these two bonds in **5** are indeed the longest and shortest O-O and Mn-O bonds known, respectively.[23-24] These comparisons

suggest that peroxo O-O bond activation is strongly influenced by the coordination mode of the peroxo ligand (η^2 versus μ-1,2), as well as the metal ion oxidation state. It has previously been demonstrated that protonation of a transition metal-peroxo at the distal oxygen promotes longer and more activated O-O bond; if one of the two Mn(III) ions in **5** is viewed simply as a Lewis acid, the same effect should be applicable in this complex.[6,38]

Table 4.3 Selected bond lengths (Å) and vibrational parameters (cm^{-1}) for all structurally characterized Mn-peroxo complexes, including **5**.[18-24]

	Peroxo Coordination Mode	**Mn-O**	**O-O**	ν_{Mn-O}	ν_{O-O}
Mn(III)					
$[K(K222)][MnTTPO_2]$[a]	η^2	1.901(4) 1.888(4)	1.421(5)	N/A	N/A
$Mn(O_2)(3,5\text{-}iPr_2pzH)(HB(3,5\text{-}iPr_2pz)_3)$, A[b]	η^2	1.851(5) 1.850(6)	1.428(7)	N/A	N/A
$Mn(O_2)(3,5\text{-}iPr_2pzH)(HB(3,5\text{-}iPr_2pz)_3)$, B[b]	η^2	1.841(9) 1.878(8)	1.43(1)	N/A	N/A
$Tp^{iPr2}Mn(O_2)(im^{Me}H)$[c]	η^2	1.872(6) 1.838(6)	1.42(1)	N/A	896
$[Mn^{III}(tmc)(O_2)](OTf)$[d]	η^2	1.884(2) 1.884(2)	1.403(4)	N/A	N/A
$[Mn^{III}(13\text{-}tmc)(O_2)](BPh_4)$[e]	η^2	1.863(2) 1.855(2)	1.410(4)	N/A	N/A
5	*trans*-μ-1,2	1.832(3)	1.452(5)	611	819
Mn(IV)					
$[L_2Mn_2(\mu\text{-}O)_2(\mu\text{-}O_2)](ClO_4)$[f]	*cis*-μ-1,2	1.83(2) 1.81(2)	1.46(3)	N/A	N/A
$[Mn(O_2)(P(C_6H_3\text{-}3\text{-}SiMe_3\text{-}2\text{-}S)_3)]^{-}$[g]	η^2	1.883(2) 1.873(2)	1.379(3)	N/A	903

[a]TTP is tetraphenylporphinato. [b]$(HB(3,5\text{-}iPr_2pz)_3)$ is hydrotris(3,5-diisopropyl-1-pyrazolyl)borate, 3,5-Pr_2pzH is 3,5-diiospropylpyrazolyl. [c]Tp^{iPr2} is hydrotris(3,5-diisopropylpyrazolyl)borate. [d]tmc is 1,4,8,11-tetramethyl-1,4,8,11-tetrazazcyclotetradecane. [e]13-tmc is 1,4,7,10-1,4,7,10-tetraazacyclotridecane. [f]L is 1,4,7-trimethyl-1,4,7-triazacyclononane. [g]$(P(C_6H_6\text{-}3\text{-}SiMe_3\text{-}2\text{-}S)_3)$ is (2-thiol-3-trimethylsilyl)triphenylphosphine.

4.3.2 Characterization of Peroxo-Bridged 6 by Density Functional Theory Calculations

In the absence of reliable X-ray crystallographic data for **6**, further insights regarding the structural properties of this complex were explored through DFT calculations. Gas-phase geometry optimization calculations were performed with the spin-unrestricted B3LYP hybrid functional, 6-311G(d) basis set for Mn, S, and N atoms, and 6-21G(d) basis set for C and H atoms on a quintet surface. The energy minimized structure obtained from these calculations was found to contain equivalent bond lengths for each half of the dimer with an O-O length of 1.44 Å, Mn(III)-O lengths of 1.84 Å, Mn(III)-S lengths of 2.27 Å, Mn···Mn distance of 4.44 Å, and Mn-O-O angle of 111° (Figure 4.5). These metrical parameters compare nicely with those from the X-ray structure of **5** (O-O = 1.452(5) Å, Mn-O = 1.832(2) Å, and Mn-S = 2.2767(7)), while the Mn-O-O bond angle and Mn···Mn separation are each considerably larger than those in **5** (97.5(6)° and 4.113 Å, respectively).

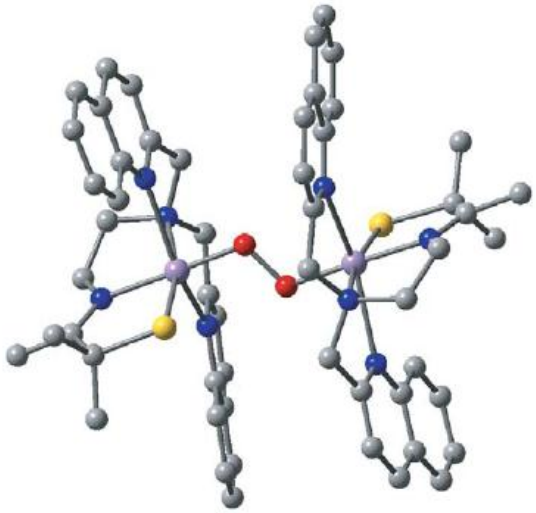

Figure 4.5 DFT (B3LYP/311G(d) for Mn, S, and N/6-21G(d) for C and H) optimized geometry of $\{[Mn^{III}(S^{Me2}N_4(2\text{-QuinoEN}))]_2(\mu\text{-}O_2)\}^{2+}$ (**6**) with hydrogen atoms omitted for clarity.

The geometry optimized structure of **6** was further used for vibrational frequency and time-dependent DFT (TD-DFT) UV/Vis spectra calculations at the B3LYP/311G(d) level of theory. Vibrational frequency calculations yielded theoretical values of $\nu_{Mn\text{-}O}$ = 571 cm^{-1} and $\nu_{O\text{-}O}$ = 839 cm^{-1}, which are each respectively within a reasonable range based upon vibrational data for other first-row transition metal-peroxo complexes.[6-8] These values also agree with resonance Raman data obtained for both **5** and **6** (*vide infra*). The TD-DFT calculated UV/Vis spectrum of **6** was found to contain an intense peroxo (π_{op}*) to Mn (dz^2) charge transfer band centered at 18,790 cm^{-1} (532 nm) (Figure 4.6). The UV/Vis spectrum of **6** in MeCN (Figure 4.2) contains similar spectral features to those observed in this calculated spectrum.

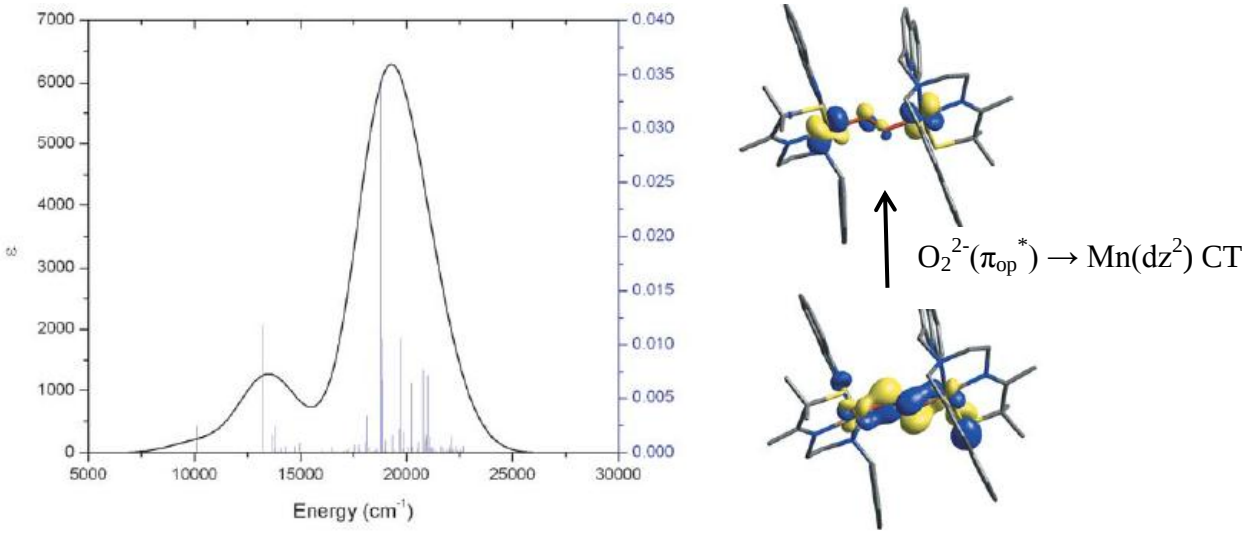

Figure 4.6 TD-DFT calculated $O_2^{2-}(\pi_{op}^*) \rightarrow Mn(dz^2)$ charge transfer band for **6** (left). Isosurface plots of the donor and acceptor orbitals involved in this peroxo-to-Mn(III) charge transfer band (right).

4.3.3 Spectroscopic and Magnetic Characterization of Thiolate-Ligated and Peroxo-Bridged Dimers 5 and 6

4.3.3.1 Resonance Raman Spectroscopy

Resonance Raman (rR) experiments were performed with X-ray quality crystals of **5** at 77 K using a variety of different laser excitation wavelengths (λ_{ex} (nm) = 413, 531, 568, 647, and 676) (Figure 4.7). Spectra obtained from experiments with λ_{ex} = 413 nm contained two distinct isotopically-sensitive bands at 819 cm^{-1} and 611 cm^{-1} that shifted to 772 cm^{-1} and 586 cm^{-1}, respectively, when prepared with $^{18}O_2$ (Figure 4.8). The energy region and isotopic shift

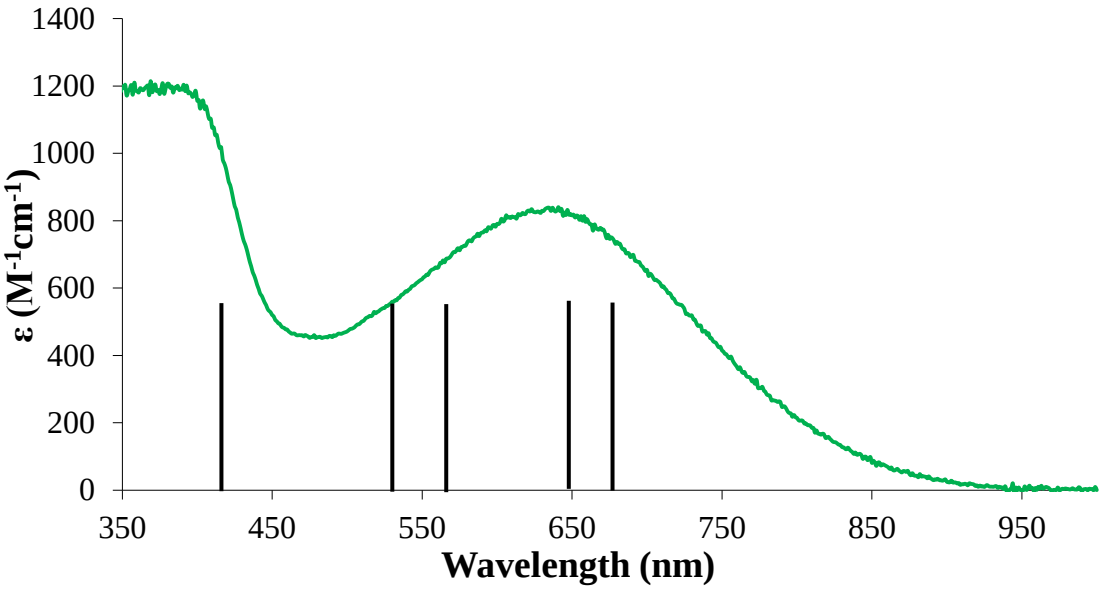

Figure 4.7 Quantitative UV/Vis spectrum (extinction coefficient versus wavelength) and Raman profile of $[Mn^{III}(S^{Me2}N_4(6\text{-Me-DPEN}))]_2(\mu\text{-}O_2)(BPh_4)_2{\cdot}2CH_3CH_2CN$ (**5**) in CH_3CH_2CN at 233 K. Black lines represent the different excitation wavelengths used for resonance Raman experiments.

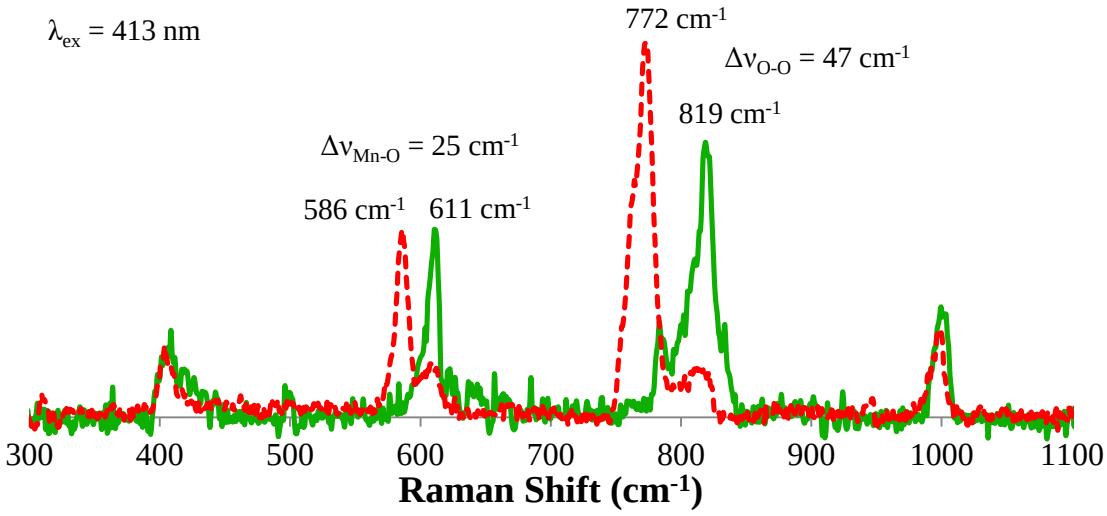

Figure 4.8 Resonance Raman spectra of crystalline $[Mn^{III}(S^{Me2}N_4(6\text{-Me-DPEN}))]_2(\mu\text{-}O_2)(BPh_4)_2 \cdot 2CH_3CH_2CN$ (**5**) generated from $^{16}O_2$ (solid green trace) and $^{18}O_2$ (dashed red trace) (λ_{ex} = 413 nm, 77 K).

observed for the higher energy vibrational features are consistent with those of an O-O stretch ($\Delta\nu(^{16}O\text{-}^{18}O)$ = 47 cm^{-1}), while those for the lower energy features are consistent with a Mn-O stretch ($\Delta\nu(^{16}O\text{-}^{18}O)$ = 25 cm^{-1}). The O-O stretching frequency in **5** (819 cm^{-1}) is much lower in energy than those found in all other Mn-peroxo complexes (887-903 cm^{-1}, all obtained by FT-IR spectroscopy), strongly suggesting the O-O bond is highly activated in this complex.

Assignment of a Mn-O vibrational feature in Figure 4.8 provides the only such data point for any Mn-peroxo. Compared to various Fe-peroxo complexes, the Mn-O stretching frequency is within the range observed for low-spin (S = 1/2) Fe(III)-OOH complexes ($\nu_{Fe\text{-}O}$ ~ 600-630 cm^{-1}), but slightly higher than the range of high-spin (S = 5/2) Fe(III)-OOH and peroxo-bridged Fe(III,III) dimers ($\nu_{Fe\text{-}O}$ ~ 400-580 cm^{-1}).[5,7] It is worthwhile to note that high-spin Mn(III) (S = 2) and low-spin Fe(III) each have an unoccupied d orbital of e_g^* parentage, while both e_g^* d orbitals are half-occupied in a high-spin Fe(III) complex. This fundamental electronic difference

may explain why the Mn-O stretching frequency for **5** is similar to those of low-spin Fe(III)-peroxos and distinct from those of high-spin Fe(III)-peroxos.

The same crystalline samples of **5** used for these experiments were also explored using lower energy laser excitation wavelengths. Spectra obtained from experiments with λ_{ex} = 531 nm and 647 nm are provided in Figure 4.9 and 4.10, respectively. Vibrational features corresponding to a Mn-O stretch are present in both spectra, albeit at much lower intensities than those observed with λ_{ex} = 413 nm (Figures 4.9 and 4.10). Vibrational features corresponding to an O-O stretch are not clearly present in spectra obtained with either λ_{ex} (Figures 4.9 and 4.10). The decreased intensity or absence of peroxo-associated vibrational features with lower energy excitation suggests that a peroxo-to-Mn charge transfer likely exists in the high energy region of the UV/Vis spectra of **5**, hence the resonance enhancement of these features with λ_{ex} = 413 nm. A peroxo-to-Mn charge transfer band was assigned in the TD-DFT calculated UV/Vis spectrum of **6** (*vide supra*, Figure 4.6). These observations are also consistent with previous computational work on a series of side-on Mn(III)-peroxo complexes, where $O_2^{2-}(\pi_{op}^*) \rightarrow Mn(d)$ charge transfer transitions were found at wavelengths ~450 nm.[39-40] The lack of Raman enhancement for vibrational features associated with the peroxo ligand in **5** at lower energy excitation wavelengths also suggests that the broad visible region absorbance band (Figure 4.1) centered at 640 nm does not contain a peroxo-to-Mn charge transfer transition.

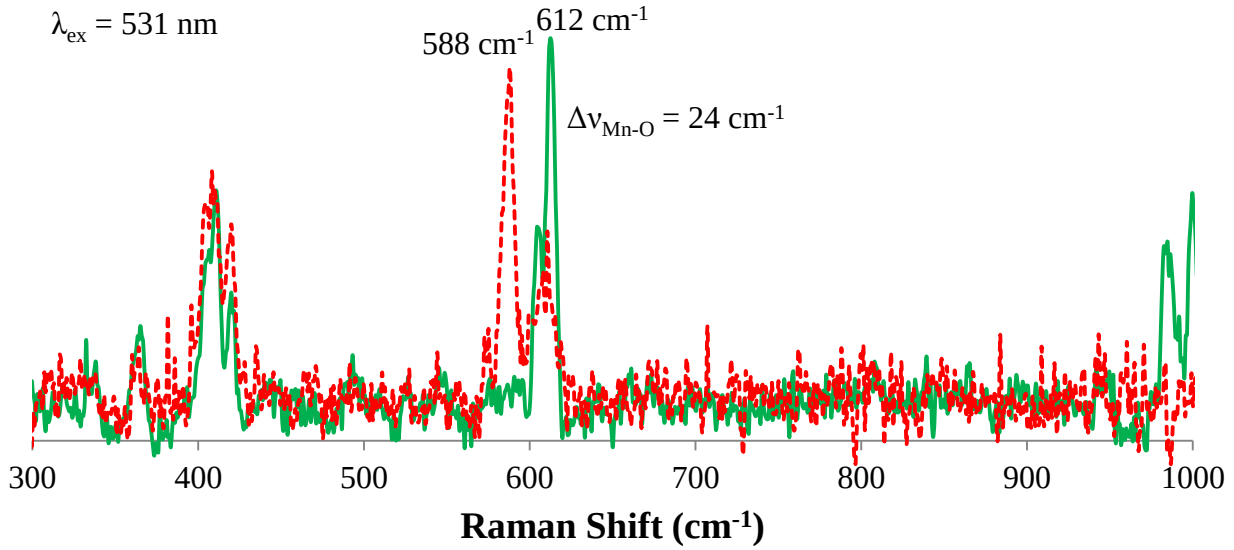

Figure 4.9 Resonance Raman spectra of crystalline $[Mn^{III}(S^{Me2}N_4(6\text{-Me-DPEN}))]_2(\mu\text{-}O_2)(BPh_4)_2{\cdot}2CH_3CH_2CN$ (**5**) generated from $^{16}O_2$ (solid green trace) and $^{18}O_2$ (dashed red trace) obtained with λ_{ex} = 531 nm at 77 K.

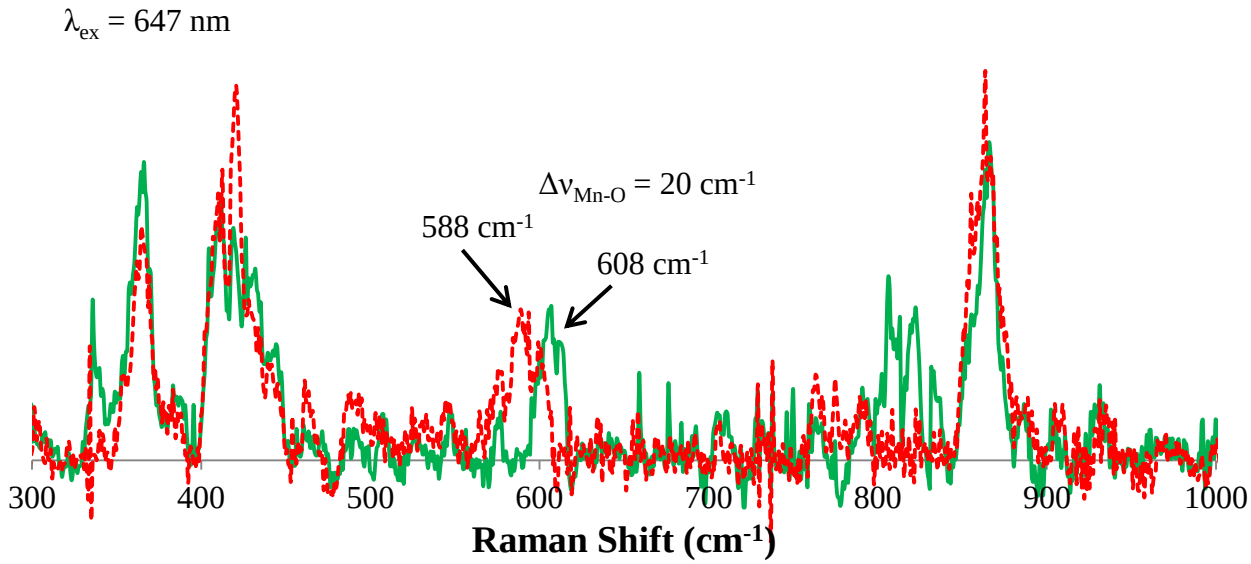

Figure 4.10 Resonance Raman spectra of crystalline $[Mn^{III}(S^{Me2}N_4(6\text{-Me-DPEN}))]_2(\mu\text{-}O_2)(BPh_4)_2{\cdot}2CH_3CH_2CN$ (**5**) generated from $^{16}O_2$ (solid green trace) and $^{18}O_2$ (dashed red trace) obtained with λ_{ex} = 647 nm at 77 K.

Similar experiments were also conducted with solution and solid samples of peroxo-bridged **6** using excitation wavelengths of 413 nm, 514 nm, and 531 nm. Unfortunately, **6** was found to be very unstable when subjected to a laser excitation wavelength of 413 nm, even at low irradiation powers. Isotopically-sensitive features were, however, observed in spectra obtained with λ_{ex} = 514 nm. As shown in Figure 4.11, the resonance Raman spectrum of **6** with λ_{ex} = 514 nm displays a prominent vibrational feature at 622 cm^{-1} that shifts to 593 cm^{-1} ($\Delta\nu$ = 27 cm^{-1}) with samples prepared from $^{18}O_2$. A low intensity Fermi doublet is also observed at 850 cm^{-1} that shifts to 813 cm^{-1} ($\Delta\nu$ = 37 cm^{-1}) in the respective ^{18}O-labeled sample. These two sets of stretches are within the appropriate energy ranges and display the expected isotopic shifts for Mn-O and O-O stretches, respectively, however the intensities of these vibrational features change due to photoirradiation during each experiment at different rates. Plots of normalized signal intensity versus time are provided in Figure 4.12 and shows that the higher energy vibrational feature (850 cm^{-1}) increases at a similar rate that the lower energy features (622 cm^{-1}) decrease. These observations suggest that the two sets of signals cannot be attributed to the same species and that there may be a photoinduced coversion between two different species during these experiments. The ^{16}O- and ^{18}O- resonance Raman spectra of oxo-bridged **4**, which forms following the decay of **6** in solution, do not display any of the isotopically-sensitive features observed in spectra of **6** (Appendix A.36). It can therefore be concluded that **4** is not formed during these resonance Raman experiments, however these observations collectively preclude a confident spectral assignment. Experiments performed with λ_{ex} = 531 yielded similar results to those with λ_{ex} = 513 (Figure 4.13).

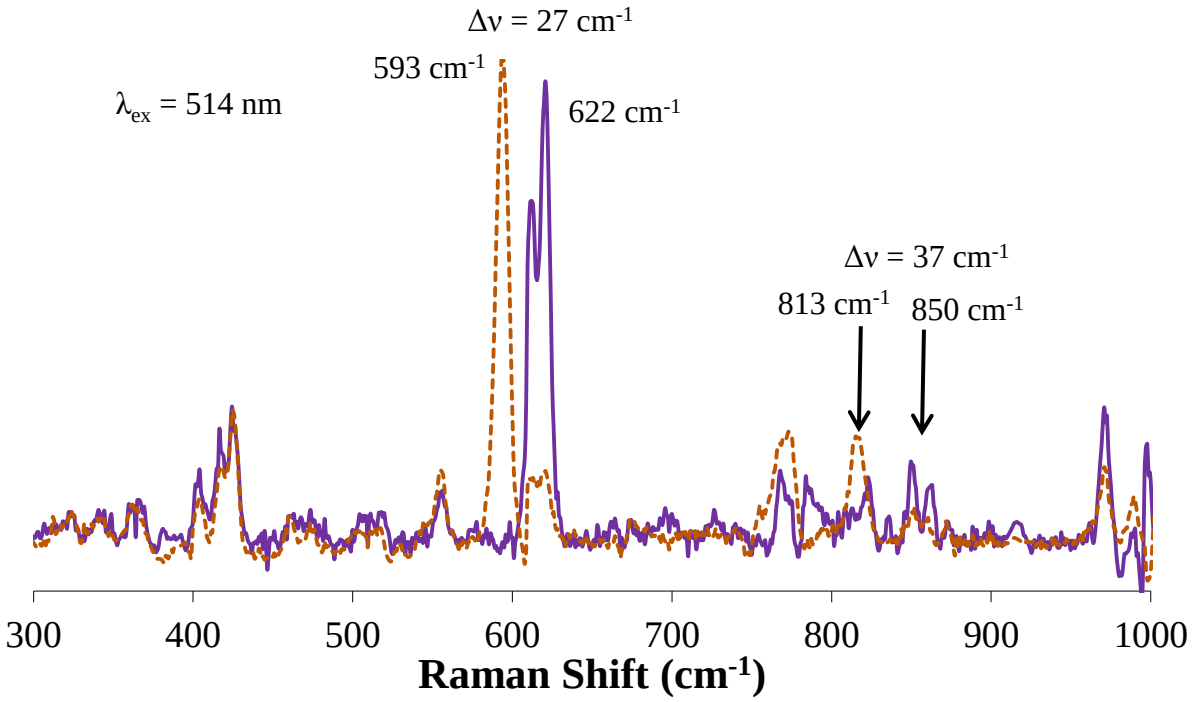

Figure 4.11 Resonance Raman spectra of solid $[Mn^{III}(S^{Me2}N_4(2\text{-QuinoEN}))]_2(\mu\text{-}O_2)(BPh_4)_2{\cdot}CH_3CH_2CN$ (**6**) generated from $^{16}O_2$ (solid purple trace) and $^{18}O_2$ (dashed brown trace) obtained with λ_{ex} = 513 nm at 77 K.

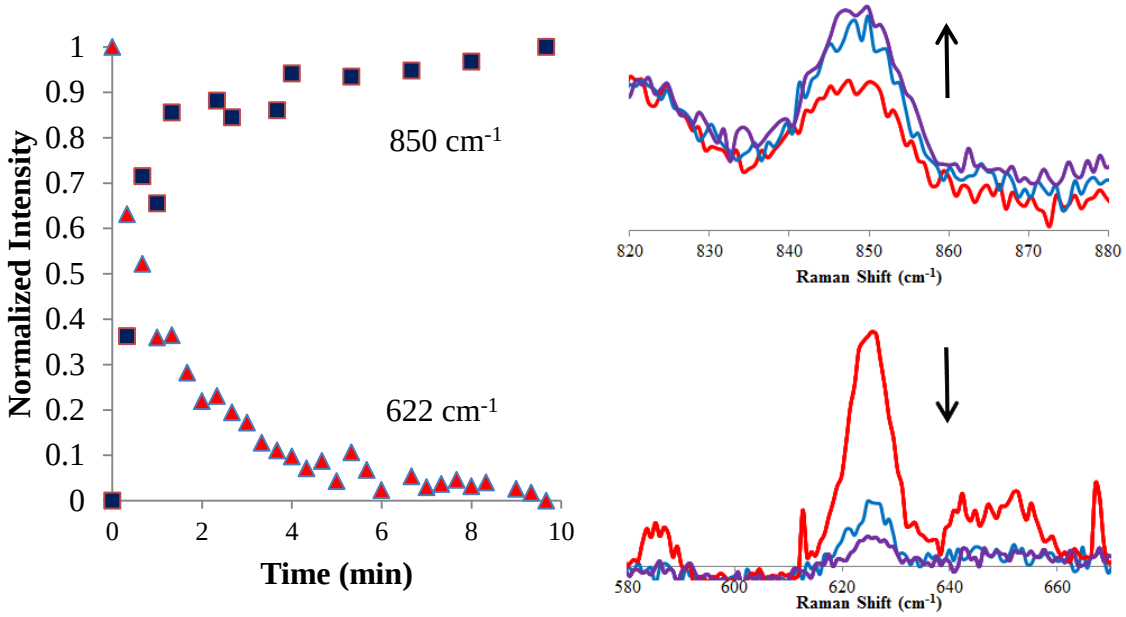

Figure 4.12 Normalized signal intensity versus time for the isotopically-sensitive resonance Raman vibrational features (850 cm^{-1} and 620 cm^{-1}, right) of $[Mn^{III}(S^{Me2}N_4(2\text{-QuinoEN}))]_2(\mu\text{-}O_2)(BPh_4)_2{\cdot}CH_3CH_2CN$ (**6**) generated from $^{16}O_2$ (λ_{ex} = 513 nm at 77 K).

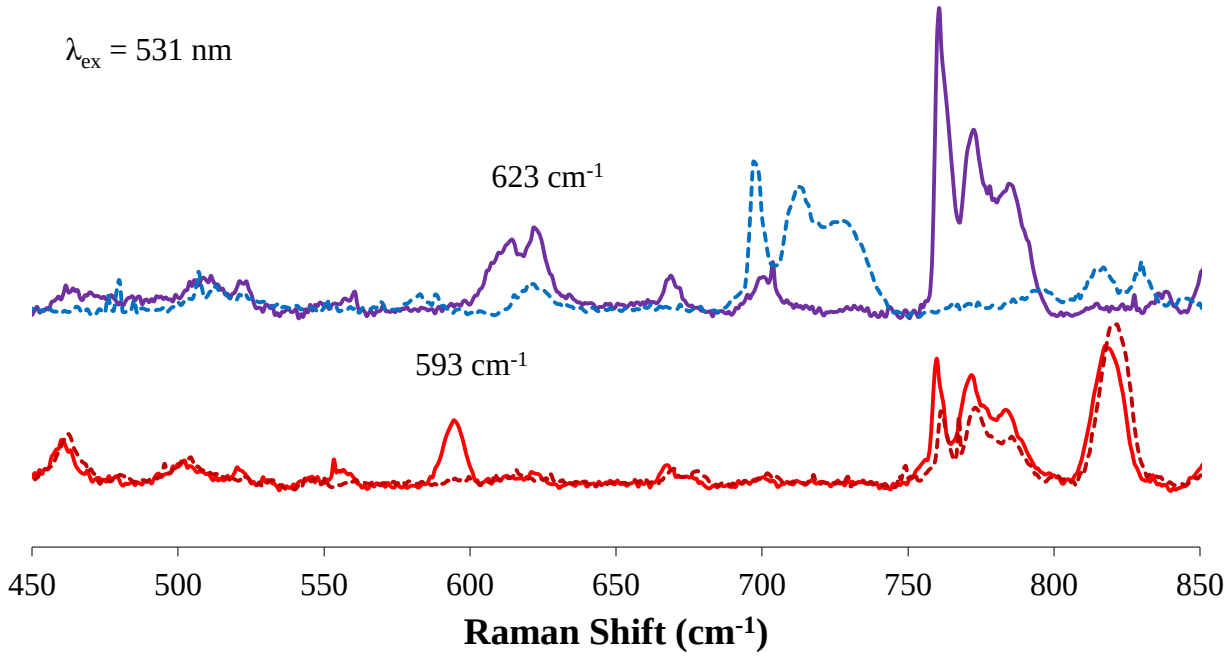

Figure 4.13 Resonance Raman spectra of solid $[Mn^{III}(S^{Me2}N_4(2\text{-QuinoEN}))]_2(\mu\text{-}O_2)(BPh_4)_2 \cdot CH_3CH_2CN$ (**6**) generated from $^{16}O_2$ (top) and $^{18}O_2$ (bottom) obtained with λ_{ex} = 531 nm at 77 K. The final spectrum from each individual experiment is shown as dashed lines.

4.3.3.2 SQUID Magnetometry and EPR Spectroscopy

The magnetic properties of **5** were explored through solid state magnetic susceptibility measurements made by SQUID magnetometry. Plots of inverse molar magnetic susceptibility (χ_M^{-1}) versus temperature (T) and effective magnetic moment (μ_{eff}) versus temperature for **5** are provided in Figure 4.14, while a plot of χ_M versus T is provided along with a best fit (solid trace) to the experimental data in Figure 4.15. As is seen from the two plots in Figure 4.14, peroxo-bridged **5** exhibits Curie-Weiss behavior from 5-275 K, while the μ_{eff} quickly plateaus from 5 K upon increasing temperature to a value of 9.37 B.M. (4.69 B.M. per Mn(III)). This value is consistent with each Mn(III) ion in **5** being high-spin and weakly exchange coupled.

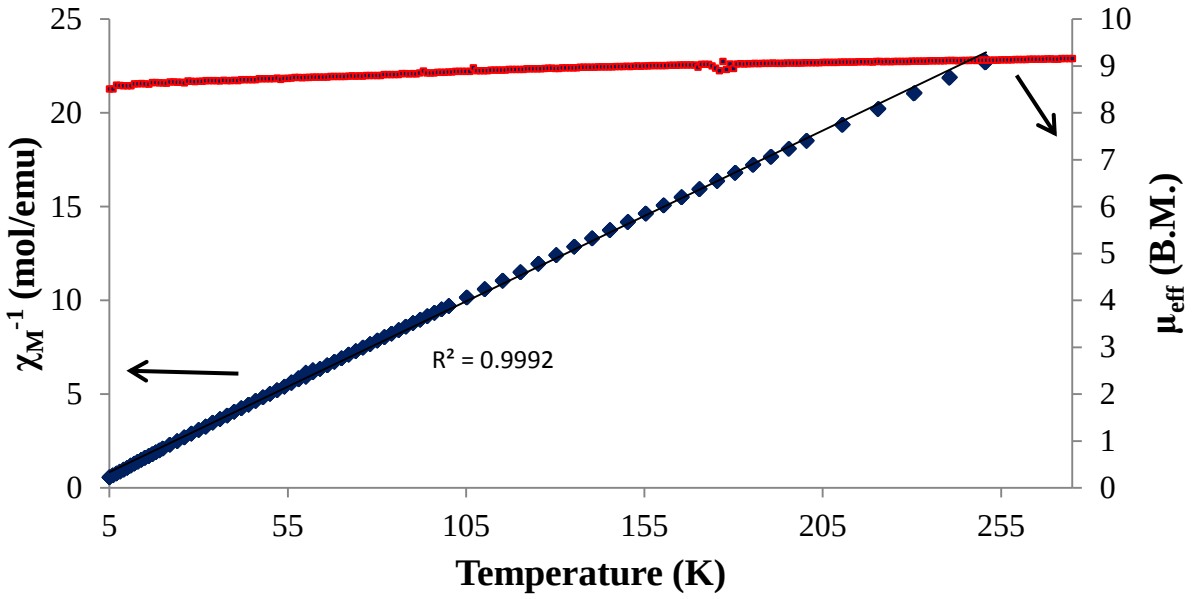

Figure 4.14 Plots of inverse molar magnetic susceptibility (χ_M^{-1}) versus temperature (T) (left) and effective magnetic moment (μ_{eff}) versus temperature (T) (right) for $[Mn^{III}(S^{Me2}N_4(6\text{-Me-DPEN}))]_2(\mu\text{-}O_2)(BPh_4)_2{\cdot}2CH_3CH_2CN$ (**5**) from 5-275 K.

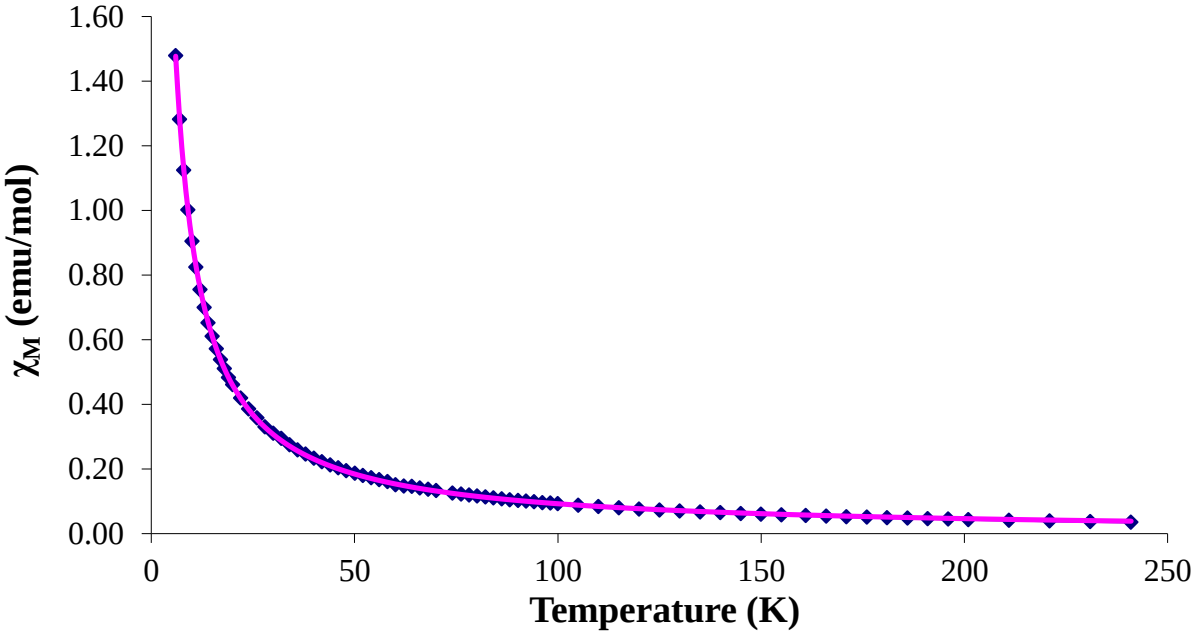

Figure 4.15 Plot of molar magnetic susceptibility (χ_M) versus temperature (T) for $[Mn^{III}(S^{Me2}N_4(6\text{-Me-DPEN}))]_2(\mu\text{-}O_2)(BPh_4)_2{\cdot}2CH_3CH_2CN$ (**5**) from 5-240 K. The best fit to the experimental data (solid pink trace) was made with J = 0 cm^{-1}, g = 2.03, D = -1.6 cm^{-1}, and E/D = 0.

The data in Figure 4.15 was fit using the spin Hamiltonian described in Chapter 3 (Equations 3.1-3.4) with J = 0 cm^{-1}, revealing that the Mn(III) ions in **5** are largely independent of one another. It is important to note that *the claim in not being made* that there is no magnetic coupling present for **5** since dipolar coupling likely exists given the Mn···Mn distance found in the X-ray structure of this dimer is 4.113 Å (Table 4.1). These observations do, however, lend further support to the structural description afforded for this complex regarding the peroxo bridging mode, as transition metal dimers bridged by peroxo ligands in a side-on fashion (μ-η^2:η^2) often display a considerable degree of magnetic coupling.[5-9] The weak to *nearly* non-existing magnetic coupling in **5** cannot be directly attributed to the *trans*-μ-1,2 peroxo bridging configuration preventing operative superexchange pathways, as Karlin has shown that $[(tmpa)_2Cu^{II}(trans\text{-}\mu\text{-}1,2\text{-}O_2)]^{2+}$ (Cu(II)···Cu(II) = 4.36 Å, O-O = 1.43 Å, Cu(II)-O = 1.85 Å) is antiferromagnetically-coupled at 193 K.[41] Satisfactory magnetic susceptibility data has not been obtained thus far for peroxo-bridged **6**.

Although the results from solid state magnetic susceptibility experiments described above strongly suggest the Mn(III) ions in **5** are very weakly coupled ($|J| \approx 0$ cm^{-1}), the magnetic properties of this complex (and **6**) could be considerably different in solution. Towards this end, low temperature X-band EPR experiments were performed with a dual mode resonator in order to further characterize the solution properties of **5** and **6**. The large zero-field splitting values of integer spin systems typically prevent the detection of X-band EPR signals in the conventional perpendicular polarization mode with allowed $\Delta M_s = \pm 1$ transitions ($h\nu \approx 0.3$ cm^{-1} for X-band).[42-43] In these cases EPR signals can be observed in the more non-traditional parallel polarization mode, where transitions formally corresponding to $\Delta M_s = 0$ are allowed (this is somewhat misleading since the z-component of M_s *does* change during an allowed transition).

Parallel polarization mode X-band EPR spectra have been reported for a number of integer spin Mn-containing systems, including the Mn superoxide dismutase, the oxygen evolving complex of photosystem II, and a handful of Mn(III) complexes.[44-48] Spectra from each of these examples contain characteristic signals at low or even zero fields.[44-48] These examples have also illustrated that the two polarization modes are indeed complementary, as similar signals have been observed in both modes for various Mn(III)-containing species.[46-48]

X-band EPR spectra obtained for **5** in both perpendicular and parallel polarization modes are shown in Figure 4.16. Spectra in both modes contain signals at low magnetic fields, which

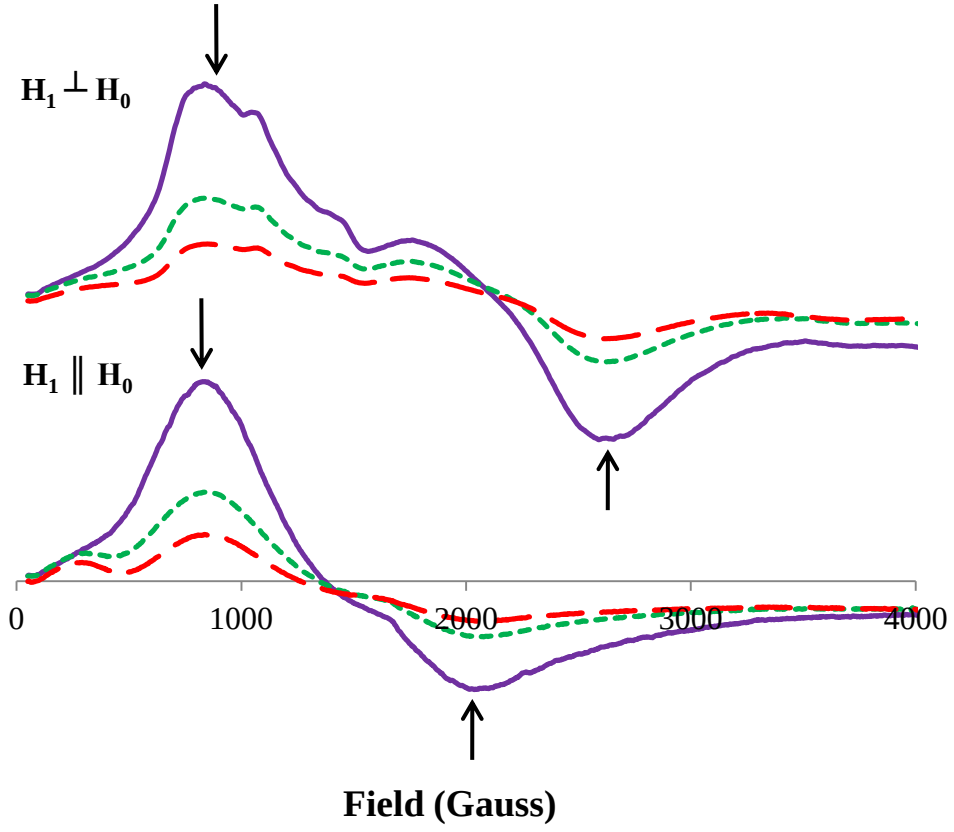

Figure 4.16 Pependicular (top) and parallel (bottom) polarization mode X-band EPR spectra of $[Mn^{III}(S^{Me2}N_4(6\text{-Me-DPEN}))]_2(\mu\text{-}O_2)(BPh_4)_2 \cdot 2CH_3CH_2CN$ **(5**, 5 mM) recorded in MeCN/toluene glass (2:1) at 5 K (solid purple traces), 10 K (dashed green traces), and 15 K (heavy dashed red traces) (23 dB for all spectra, intensities not to scale between the two modes). Arrows indicate spectral changes with increasing temperature.

is typical for even spin systems, particularly Mn(III) containing species (*vide supra*). The absence of signals in the perpendicular polarization mode spectra at 3,300 G ($g_{eff} \approx 2.00$ region) provides evidence that **1** does not contribute to these spectra. A Curie-type temperature dependence is exhibited by all signals, suggesting that the axial zero-field splitting parameter (D) for **5** is negative. This is consistent with D obtained from the best fit to the solid state magnetic susceptibility data in Figure 4.15 ($D = -1.6\ cm^{-1}$). Further interpretation of these spectra is made difficult by the absence of resolved hyperfine structure in the signals and requires detailed spectral simulations.

Unlike the EPR spectra of **5**, parallel polarization mode EPR spectra of peroxo-bridged **6** were found to contain ^{55}Mn hyperfine features in signals at low fields (Figure 4.17, perpendicular

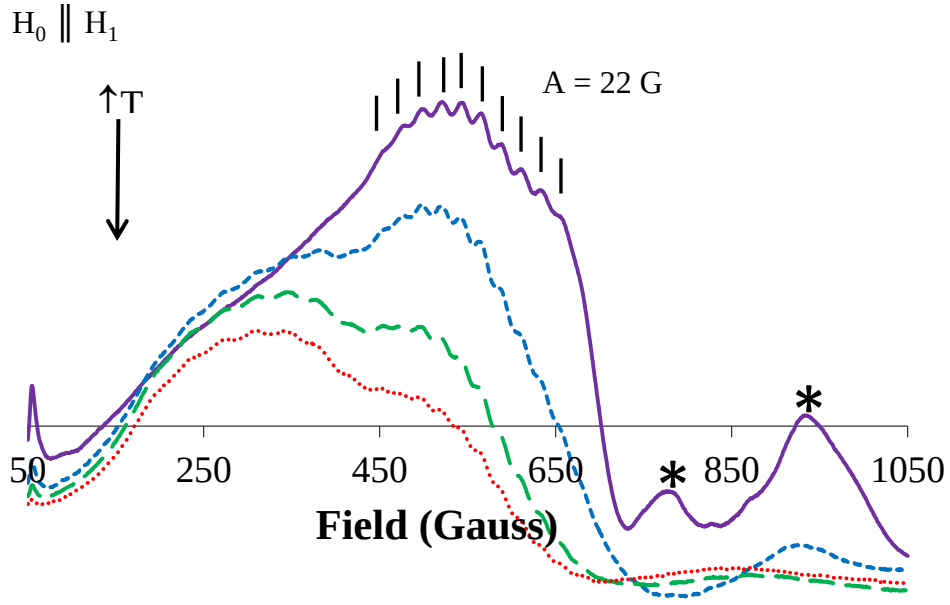

Figure 4.17 Parallel polarization mode X-band EPR spectra of $[Mn^{III}(S^{Me2}N_4(2\text{-QuinoEN}))]_2(\mu\text{-}O_2)(BPh_4)_2 \cdot CH_3CH_2CN$ **(6**, 3 mM) recorded in MeCN/toluene glass (2:1) at 5 K (solid purple trace), 10 K (dashed blue trace), and 15 K (heavy dashed green trace), and 20 K (dotted red trace) (13 dB for all spectra). Signals designated with an asterisk (*) are signals from frozen O_2.

polarization mode spectra of **6** are shown in Appendix A.37). The 5 K spectrum of **6** contains at least ten clearly visible hyperfine lines equally spaced by 22 G, signifying that that the species responsible for this particular signal contains more than one Mn ion (2nI + 1) and the ions are magnetically-coupled (signals for uncoupled Mn ions would only contain six equally separated hyperfine lines). An inverse relationship between signal intensity and temperature is again observed, suggesting D < 0 for **6**. Simulations of the signal position and hyperfine splittings in this spectrum have been performed using the spin Hamiltonian provided in Equation 4.1 and with the following fitting parameters; $S_1 = S_2 = 2.00$, $J = 2\ cm^{-1}$, $D_1 = D_2 = -1\ cm^{-1}$, and $g_1 = g_2 = 2.00$. In Equation 4.1, β_e is the Bohr magneton, B_0 is the static magnetic field vector, g is the electron g tensor, S is the electron spin operator, and D is the axial zero-field splitting parameter. The simulated 5 K spectrum for **6** is shown in Figure 4.18 along with the experimental spectrum.

$$H = \beta_e B_0 g_1 S_1 + \beta_e B_0 g_2 S_2 + S_1 D_1 S_1 + S_2 D_2 S_2 + J S_1 S_2 \quad (4.1)$$

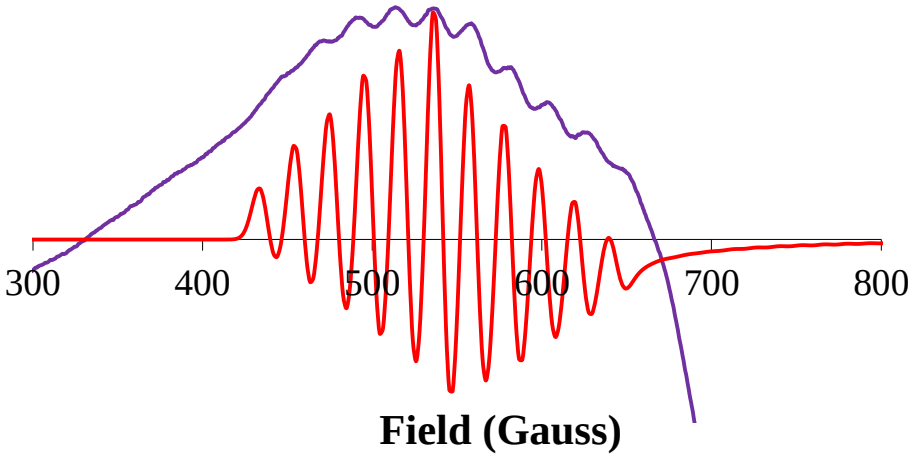

Figure 4.18 Parallel polarization mode X-band EPR spectra of **6** (3 mM) recorded in MeCN/toluene glass (2:1) at 5 K (solid purple trace) and simulated spectrum (solid red trace).

A detailed simulation of the temperature-dependence for this particular signal has thus far been difficult to obtain, however the fitting parameters used are consistent with those of **5** and suggest the two Mn(III) ions in **6** being weakly antiferromagnetically-coupled. This is a particularly unusual spin system, as D and J are on the same order of magnitude. This certainly complicates further analysis of these spectra due to the presence of 900 spin levels (two S = 2 Mn ions each with I = 5/2 ^{55}Mn nuclei). It is also worth noting that the hyperfine coupling constant (A) for **6** is very small, as Mn(III) ions typically exhibit A values on the order of 60-80 G.[47-48] Unusually small hyperfine coupling constants have been observed in the EPR spectra of many thiolate-ligated transition metal ions (blue copper proteins, for example), which results due to highly covalent metal-thiolate bonding.[49]

4.3.3.3 Mn K-edge X-ray Absorption Spectroscopy

In the absence of high-resolution X-ray data for **6**, XAS experiments were conducted to further characterize this particular intermediate. The Mn K-edge XANES spectra were of particular interest, as the rising edge energy in each spectra provides insight regarding the oxidation state(s) of the Mn ions in the respective sample. Plots of normalized absorption versus energy for complexes **2**, **4**, and **6** (Mn(II), oxo-bridged Mn(III,III), and peroxo-bridged Mn(III,III), respectively) are provided in Figure 4.19, while the second derivatives of these three individual spectra of provided in Figure 4.20. As is seen in both figures, the rising edge energies for **2**, **4**, and **6** are 6547.1 eV, 6548.6 eV, and 6548.7 eV, respectively. The rising edge energy for **4** is approximately 1 eV blue shifted relative to that of **2**, which is consistent with a difference in Mn oxidation state of 1 between the two complexes (Mn(III) versus Mn(II)). Edge energies for **4** and **6** are within experimental error of one another (experimental error is ±0.1 eV), suggesting the Mn ions in **6** are indeed in the +3 oxidation state. The edge energy for **6** is also

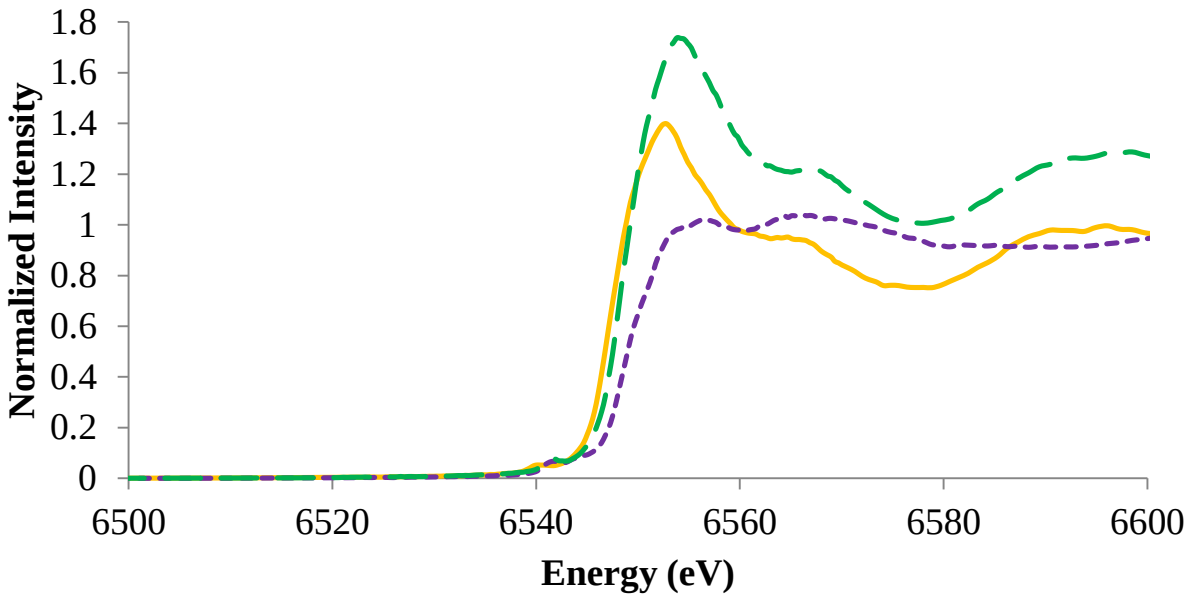

Figure 4.19 Normalized Mn K-edge XANES of solid $[Mn^{II}(S^{Me2}N_4(2\text{-QuinoEN}))](BPh_4)\cdot MeCN$ (**2**, solid yellow trace), $[Mn^{III}(S^{Me2}N_4(2\text{-QuinoEN}))]_2(\mu\text{-}O)(PF_6)_2\cdot(CH_2Cl_2)$ (**4**, purple dotted trace), and $[Mn^{III}(S^{Me2}N_4(2\text{-QuinoEN}))]_2(\mu\text{-}O_2)(BPh_4)_2\cdot CH_3CH_2CN$ (**6**, green dashed trace) (10 K).

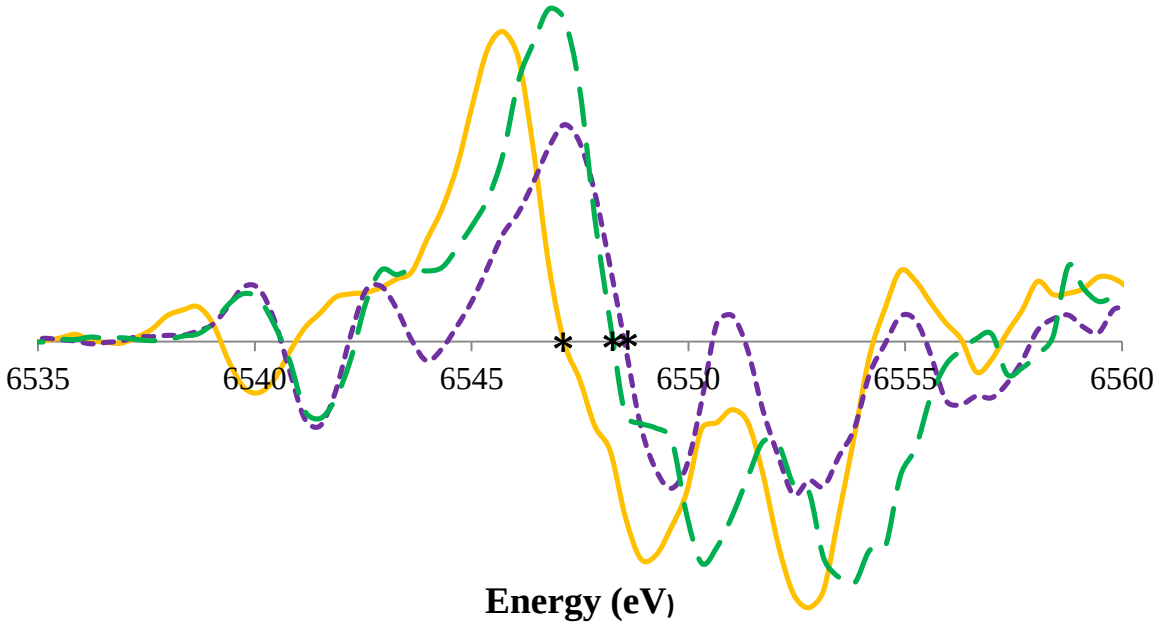

Figure 4.20 Second derivative Mn K-edge XANES of solid $[Mn^{II}(S^{Me2}N_4(2\text{-QuinoEN}))](BPh_4)\cdot MeCN$ (**2**, solid yellow trace), $[Mn^{III}(S^{Me2}N_4(2\text{-QuinoEN}))]_2(\mu\text{-}O)(PF_6)_2\cdot(CH_2Cl_2)$ (**4**, purple dotted trace), and $[Mn^{III}(S^{Me2}N_4(2\text{-QuinoEN}))]_2(\mu\text{-}O_2)(BPh_4)_2\cdot CH_3CH_2CN$ (**6**, green dashed trace) (10 K). The edge energy in each spectrum is designated with an asterisk (*).

very close to that of **5** (6548.1 eV, Figure 4.21). This may seem somewhat expected from the similarities between the respective UV/Vis spectra and X-ray structures of **5** and **6**, however it has previously been found that X-ray crystallography data for peroxo-bridged transition metal dimers can exist with a small amount of the respective high-valent bis(μ-oxo) isomer.[50] These results clearly reveal that a Mn(IV)-containing species is not present in the solid state sample of **6**.

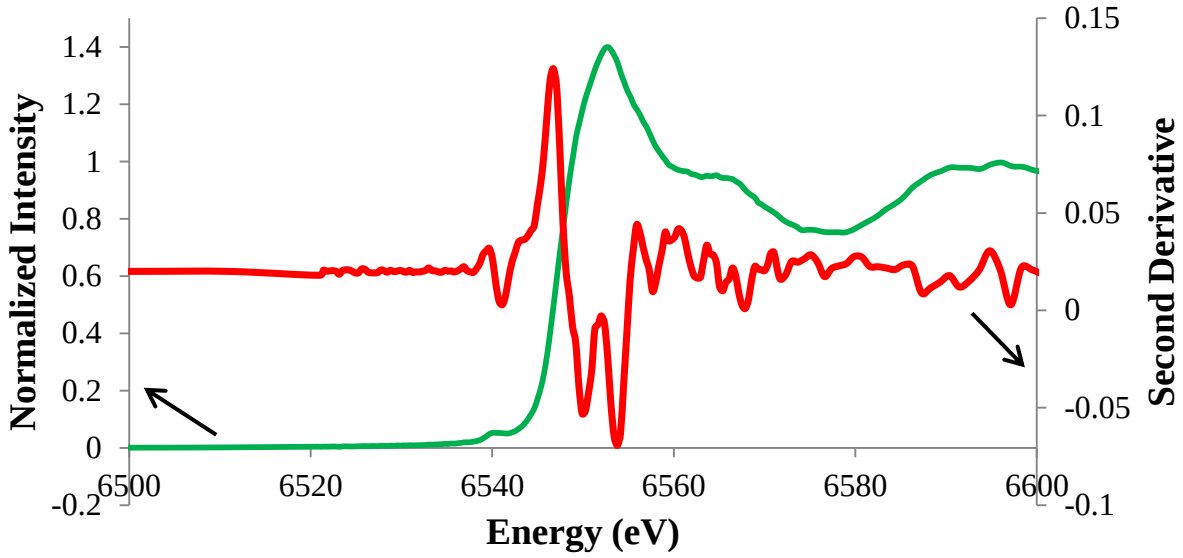

Figure 4.21 Normalized absorption (green trace) and second derivative (red trace) Mn K-edge XANES of crystalline $[Mn^{III}(S^{Me2}N_4(6\text{-MeDPEN}))]_2(\mu\text{-}O_2)(BPh_4)_2{\cdot}2CH_3CH_2CN$ (**5**) at 10 K.

4.3.4 Dioxygen Reaction Kinetics

4.3.4.1 $[Mn^{II}(S^{Me2}N_4(6\text{-Me-DPEN}))](BPh_4)$ (**1·BPh$_4$**)

The kinetics of low temperature reactions between thiolate-ligated **1·BPh$_4$** and O_2 were explored by UV/Vis spectroscopy and rapid-scanning stopped-flow spectrophotometry in MeCN. These studies resulted in the observation of yet another intermediate (**7**) that forms prior to peroxo-bridged intermediate **5**, as was indicated by the appearance of a new visible region

absorption band at λ_{max} = 515 nm (Figure 4.22). Intermediate **7** forms within seconds at low temperatures, and then rapidly converts to **5**. The accumulation of **7** and subsequent decay of **7** to **5** were each monitored by time-dependent absorbance changes at 515 nm under pseudo first-order reaction conditions with excess O_2. All kinetic traces were fit to a two term rate law

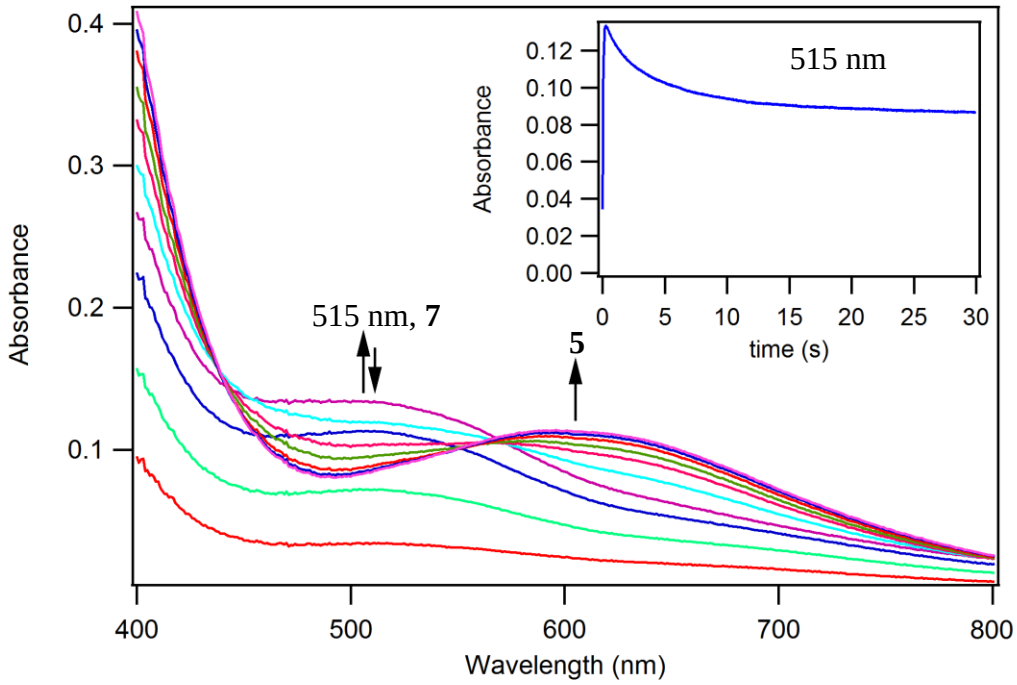

Figure 4.22 Time resolved spectral changes from reactions between [$Mn^{II}(S^{Me2}N_4$(6-Me-DPEN))](BPh_4) (**1·BPh$_4$**) (1.5 mM) and O_2 (4.05 mM) in MeCN at 263 K. Inset illustrates a typical kinetic trace (λ = 515 nm) showing the formation of **7** and subsequent decay of **7** to **5**.

(Equation 4.2) to yield pseudo first-order rate constants ($k_{1,obs}$ and $k_{2,obs}$) corresponding to each of

$$rate = ae^{-k_{1,obs}t} + be^{-k_{2,obs}t} \quad (4.2)$$

the two respective processes. Observed rate constants corresponding to the formation of intermediate **7**, $k_{1,obs}$, were found to increase linearly with increasing dioxygen concentrations, [O_2], at four different temperatures (233 K, 243 K, 253 K, and 263 K), revealing that the

formation of **7** is first-order with respect to O_2 (Figure 4.23). It is worthwhile to note that the y-intercept of each plot in Figure 4.21 is close to zero, suggesting that the formation of **7** is essentially irreversible. Observed rate constants corresponding to the decay of **7** to peroxo-bridged **5**, $k_{2,obs}$, were found to be independent of $[O_2]$ at all temperatures studies, therefore the conversion of **7** to **5** is zero order with respect to $[O_2]$ (Figure 4.23). Second order rate constants

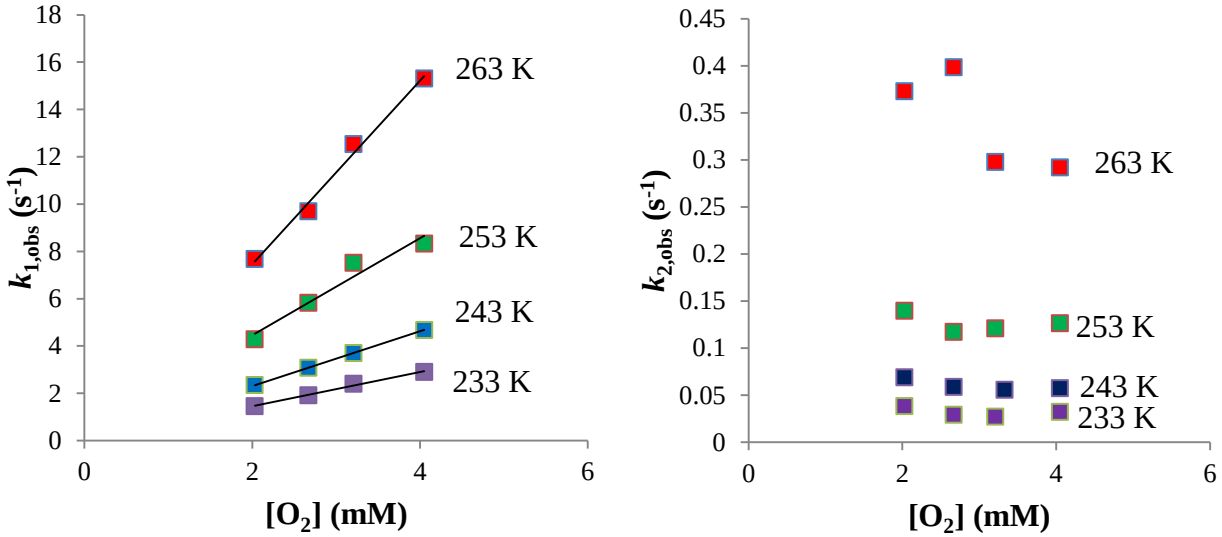

Figure 4.23 Plots of observed rate constants for the formation of intermediate **7** from ($k_{1,obs}$) versus O_2 concentration ($[O_2]$) (left) and observed rate constants for the conversion of **7** to **5** ($k_{2,obs}$) versus O_2 concentration ($[O_2]$) (right). Each plot contains k_{obs} values determined at 233 K, 243 K, 253 K, and 263 K in MeCN with excess O_2 and [**1**·**BPh$_4$**] = 1 mM.

for the formation of **7** (k_1) were determined from the slope of each individual $k_{1,obs}$ versus $[O_2]$ plot. Eyring ($\ln(k_1/T)$ versus T^{-1}) and Arrhenius ($\ln(k_1)$ versus T^{-1}) plots were constructed using the k_1 values determined at all four temperatures to afford activation parameters ($\Delta H^{\ddagger}$ = 6.30 kcal/mol , $\Delta S^{\ddagger}$ = -18.06 cal/mol·K, E_a = 6.78 kcal/mol) for the formation of **7** (Figure 4.24).

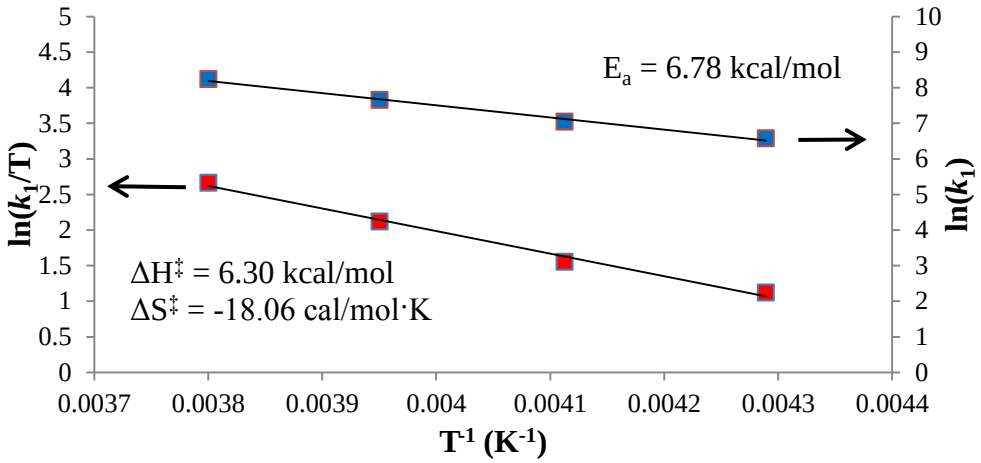

Figure 4.24 Eyring (ln(k_1/T) versus T^{-1}) (left y-axis) and Arrhenius (ln(k_1) versus T^{-1}) (right y-axis) plots for the formation of **7** from **1·BPh$_4$** in MeCN.

Experiments were also conducted with a fixed concentration of excess O_2 ([O_2] = 4.1 mM after mixing) and with varying amounts of [**1·BPh$_4$**] in MeCN at 243 K. Kinetic traces were obtained by monitoring time-dependent absorbance changes at 515 nm and fit to Equation 4.2. These measurements yielded pseudo first-order rate constants $k'_{1,obs}$ and $k'_{2,obs}$ corresponding again to the formation of **7** and subsequent conversion of **7** to **5**. Under these reaction conditions, $k'_{1,obs}$ was found to be independent of [**1·BPh$_4$**], which agrees with the formation of **7** being first-order with respect to **1·BPh$_4$** (Figure 4.25). The $k'_{2,obs}$ values obtained for the conversion of **7** to **5** were found to display a linear dependence upon **1·BPh$_4$** at four different temperatures (233 K, 243 K, 253 K, 263 K), thus supporting the formation of **5** as a second-order process overall with respect to **1·BPh$_4$** (Figure 4.25). Second order rate constants (k_2) for the conversion of **7** to **5** were obtained by refitting kinetic traces at 515 nm to the second-order expression provided in Equation 4.3. These k_2 values were then used to obtain activation parameters for this conversion ($\Delta H^{‡}$ = 11.25 kcal/mol , $\Delta S^{‡}$ = -3.58 cal/mol·K, E_a = 10.06 kcal/mol) (Figure 4.26).

$$rate = Abs_{final} - [\frac{(Abs_{final} - Abs_0)}{(1 + k_2[\mathbf{1}]_0 t)}] \quad (4.3)$$

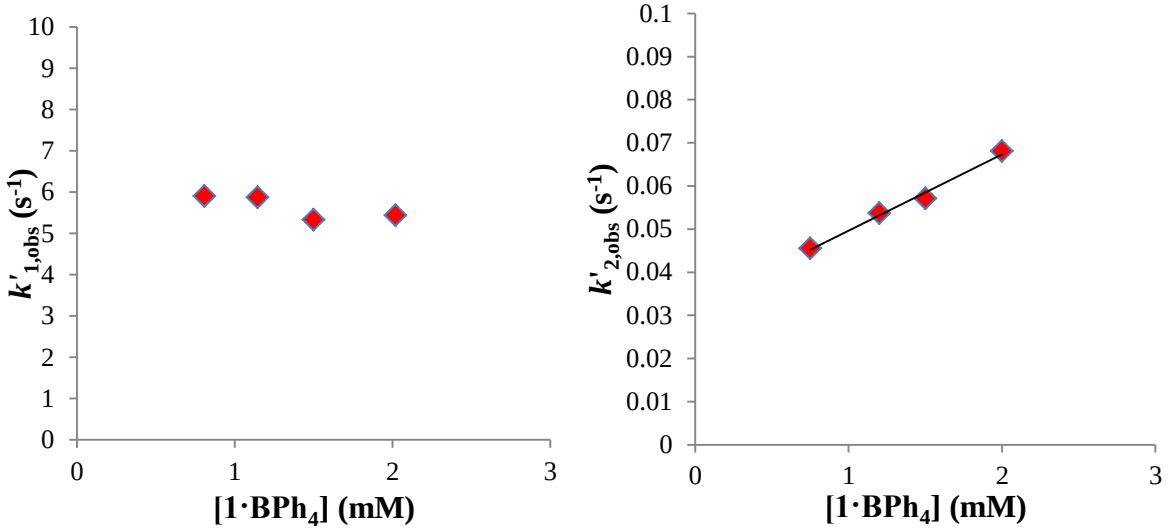

Figure 4.25 Plots of observed first-order rate constants for the formation of **7** ($k'_{1,obs}$) versus the concentration of **1·BPh$_4$** ([**1·BPh$_4$**]) (left) and observed first-order rate constants for the conversion of **7** to **5** ($k'_{2,obs}$) versus the concentration of **1·BPh$_4$** ([**1·BPh$_4$**]) (right). Experiments were performed at 243 K in MeCN and with [O_2] = 4.1 mM.

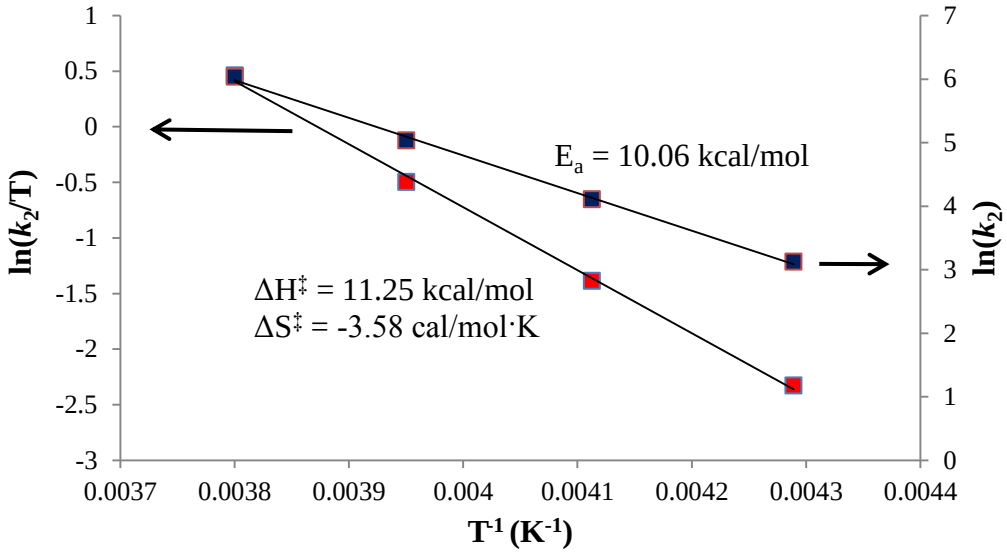

Figure 4.26 Eyring (ln(k_1/T) versus T^{-1}) (left y-axis) and Arrhenius (ln(k_1) versus T^{-1}) (right y-axis) plots for the conversion of **7** to **5** in MeCN.

In sum, the kinetic data obtained for the two observable steps during the conversion of **1·BPh$_4$** to **5** are best described by the rate laws provided in Equations 4.4-4.5. The first reaction

$$rate_1 = k_1[\mathbf{1}\cdot\boldsymbol{BPh_4}][O_2] \quad (4.4)$$

$$rate_2 = k_2[\mathbf{7}][\mathbf{1}] \quad (4.5)$$

step appears to involve O_2 binding to **1·BPh$_4$**, forming a mononuclear Mn-O_2 intermediate (**7**). The second reaction step involves the binding of a second equivalent of **1·BPh$_4$** to intermediate **7**, resulting in the formation of peroxo-bridged intermediate **5**. Based upon the presence of two Mn(III) ions in peroxo-bridged **5**, intermediate **7** is formulated as a Mn(III)-superoxo species. This kinetic scheme illustrated in Scheme 4.2. Kinetics data from experiments monitoring the conversion of **5** to oxo-bridged **3** have been difficult to fit and therefore are not discussed here. However, experiments exploring this particular conversion using the PF_6^- salt of **1** have yielded data that could be reproducibly fit and are discussed below.

Scheme 4.2 Kinetic scheme for the formation of peroxo-bridged **5** from **1·BPh$_4$** and O_2.

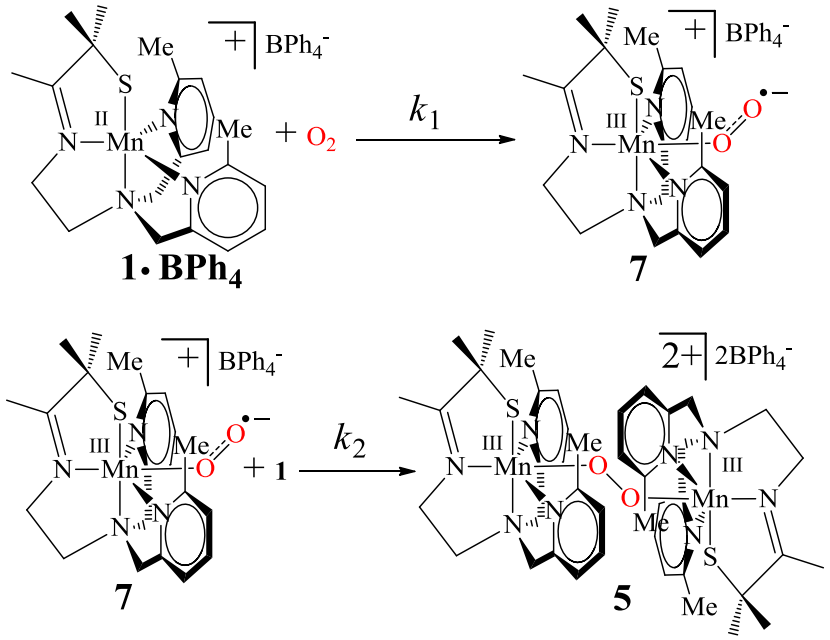

4.3.4.2 [$Mn^{II}(S^{Me2}N_4$(6-Me-DPEN))](PF_6) (**1·PF_6**)

As was noted previously in this chapter, the stability of peroxo-bridged **5** was found to increase when formed from the BPh_4^- salt of **1** compared to the PF_6^- or BF_4^- salts of **1**. In order to explore (and further validate) these observations, similar kinetics experiments to those described for **1·BPh_4** (*vide supra*) were conducted with the PF_6^- salt of complex **1** (**1·PF_6**) in CH_3CH_2CN (EtCN) or MeCN at low temperatures. It should be noted that **1·BPh_4** was the only salt of complex **1** that was used for any other experiment discussed in this chapter. Unlike the O_2 reactions with **1·BPh_4**, a Mn-O_2 intermediate was not observed during the conversion of **1·PF_6** to **5**. Instead, the rapid accumulation of **5** was followed by a direct conversion of this intermediate to oxo-bridged **3** (Figure 4.27). The formation of **5** and subsequent conversion of **5** to **3** were monitored by time-dependent absorbance changes at 749 nm under pseudo first-

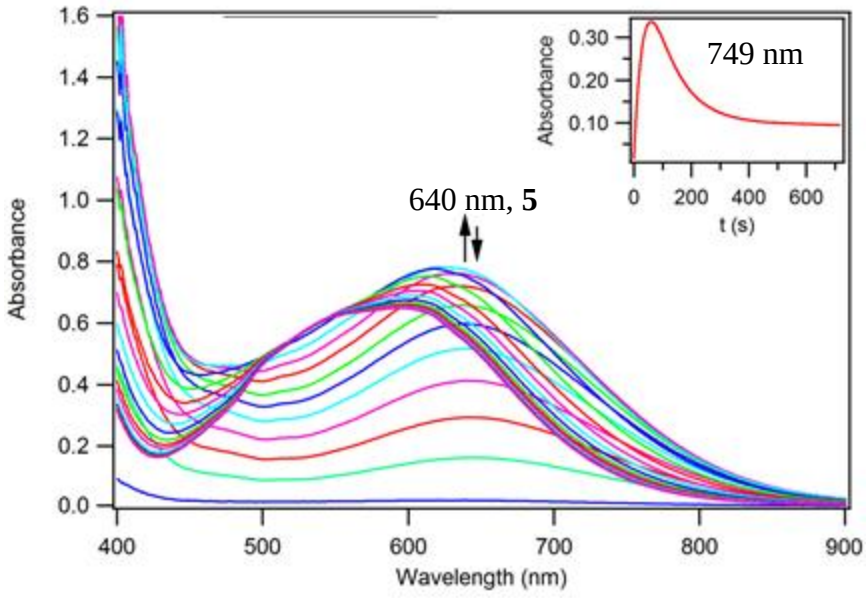

Figure 4.27 Time resolved spectral changes from reactions between [$Mn^{II}(S^{Me2}N_4$(6-Me-DPEN))](PF_6) (**1·PF_6**) (1.0 mM) and O_2 (3.97 mM) in EtCN at 213 K. The inset illustrates a typical kinetic trace (λ = 645 nm) showing the formation of **5** and subsequent decay of **5** to **3**.

order reaction conditions with excess O_2 at 233 K, 223 K, 213 K, and 203 K. All kinetic traces were fit using Equation 4.2 to yield pseudo first-order rate constant for the formation of peroxo-bridged **5** ($k_{3,obs}$) and the conversion of **5** to oxo-bridged **3** ($k_{4,obs}$). The $k_{3,obs}$ values were found to display a linear dependence on [O_2], which is consistent with the formation of **5** being first-order with respect to O_2 (Figure 4.28). Values of $k_{4,obs}$ were found to be independent of [O_2] over the measured temperature range, indicating the conversion of **5** to **3** is zero order with respect to [O_2] (Figure 4.28). Interestingly, the $k_{4,obs}$ values were also found to be independent of temperature, which likely results due to cancellation of the activation energies for all individual reaction steps involved in the decay of **5** to **3** (Figure 4.28). Second order rate constants for the formation of **5** (k_3) were obtained from the data in Figure 4.28 and used to obtain activation parameters for this process with ($\Delta H^{\ddagger}$ = 5.95 kcal/mol , $\Delta S^{\ddagger}$ = -26.76 cal/mol·K, E_a = 6.33 kcal/mol) (Figure 4.29).

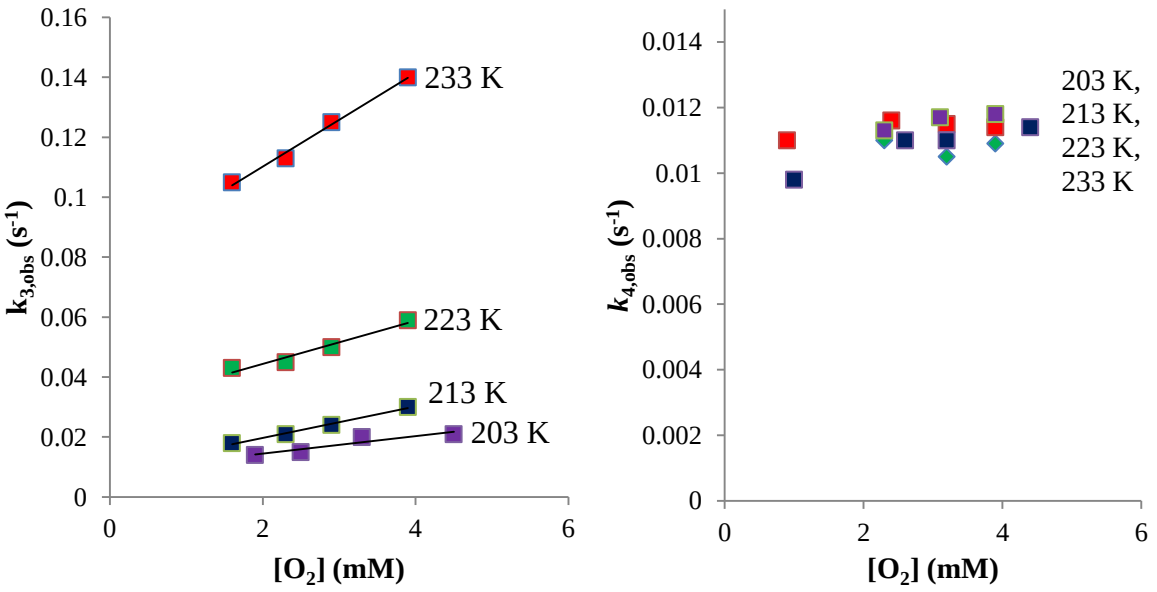

Figure 4.28 Plots of observed rate constants for the formation of **5** ($k_{3,obs}$) versus O_2 concentration ([O_2]) (left) and observed rate constants for the conversion of **5** to **3** ($k_{4,obs}$) versus O_2 concentration ([O_2]) (right). Each plot contains k_{obs} values determined at 203 K, 213 K, 223 K, and 233 K in EtCN with excess O_2 and [**1·PF$_6$**] = 1 mM.

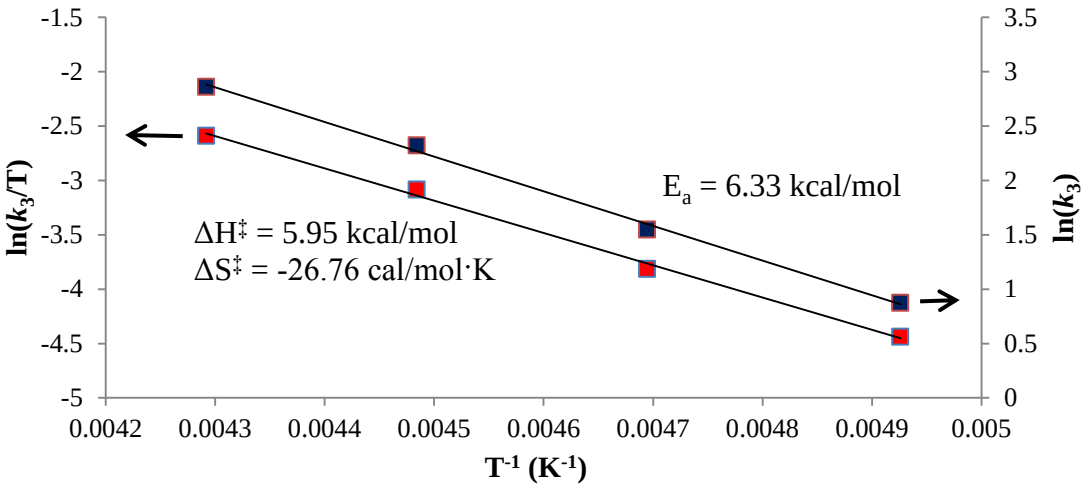

Figure 4.29 Eyring (ln(k_1/T) versus T^{-1}) (left y-axis) and Arrhenius (ln(k_1) versus T^{-1}) (right y-axis) plots for the formation of **5** from **1·PF$_6$** in EtCN.

The dependence of each reaction step on **1·PF$_6$** was explored through experiments in MeCN at 233 K with a constant amount of O_2 (4.1 mM) and varying concentrations of **1·PF$_6$**. The formation of **5** and subsequent conversion of **5** to **3** again monitored by time-dependent absorbance changes at 749 nm. All kinetic traces from these experiments were fit with Equation 4.2 to afford pseudo first-order rate constants ($k'_{3,obs}$ and $k'_{4,obs}$) for each respective reaction step. The $k'_{3,obs}$ and $k'_{4,obs}$ values were each found to be independent of [**1·PF$_6$**], which suggests the formation of **5** is a first-order process with respect to **1·PF$_6$** and the decay of **5** to **3** is independent of **1·PF$_6$** (Figure 4.30).

The kinetic data obtained from O_2 reactions with **1·PF$_6$** are consistent with the rate laws shown in Equations 4.6 – 4.7 and kinetic scheme provided in Scheme 4.3. The formation of peroxo-bridged **5** is found to be first-order with respect to both **1·PF$_6$** and O_2 (second order overall), which suggests that formation of a mononuclear Mn-O_2 adduct is rate-limiting. The

$$rate_3 = k_3[\mathbf{1{\cdot}PF_6}][O_2] \quad (4.6)$$

$$rate_4 = k_4[\mathbf{5}] \quad (4.7)$$

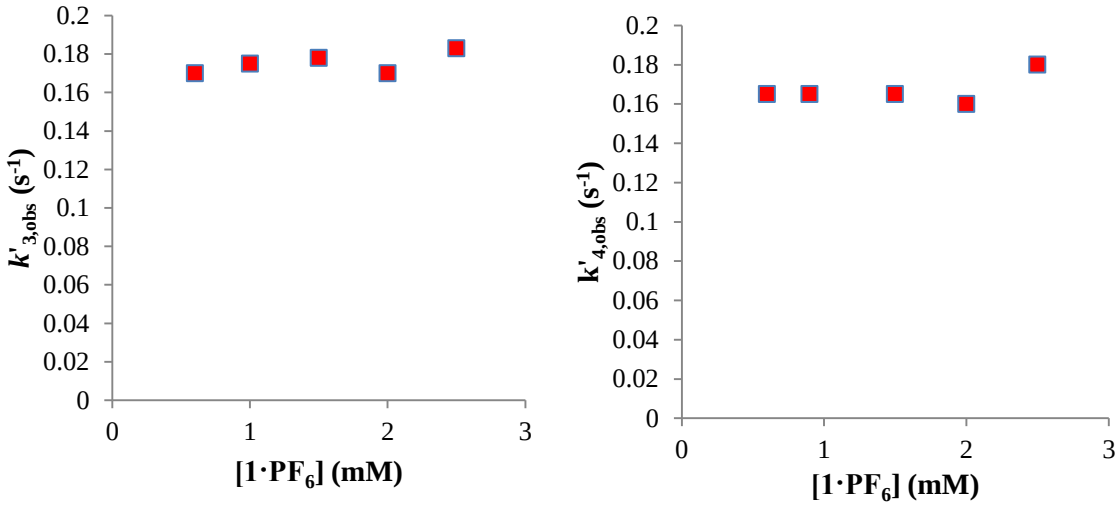

Figure 4.30 Plots of observed first-order rate constants for the formation of **5** ($k'_{3,obs}$) versus the concentration of **1·PF$_6$** ([**1·PF$_6$**]) (left) and observed first-order rate constants for the conversion of **5** to **3** ($k'_{4,obs}$) versus the concentration of **1·PF$_6$** ([**1·PF$_6$**]) (right). Experiments were performed at 233 K in MeCN and with [O_2] = 4.1 mM.

Scheme 4.3 Kinetic scheme for the O_2 reaction with **1·PF$_6$**.

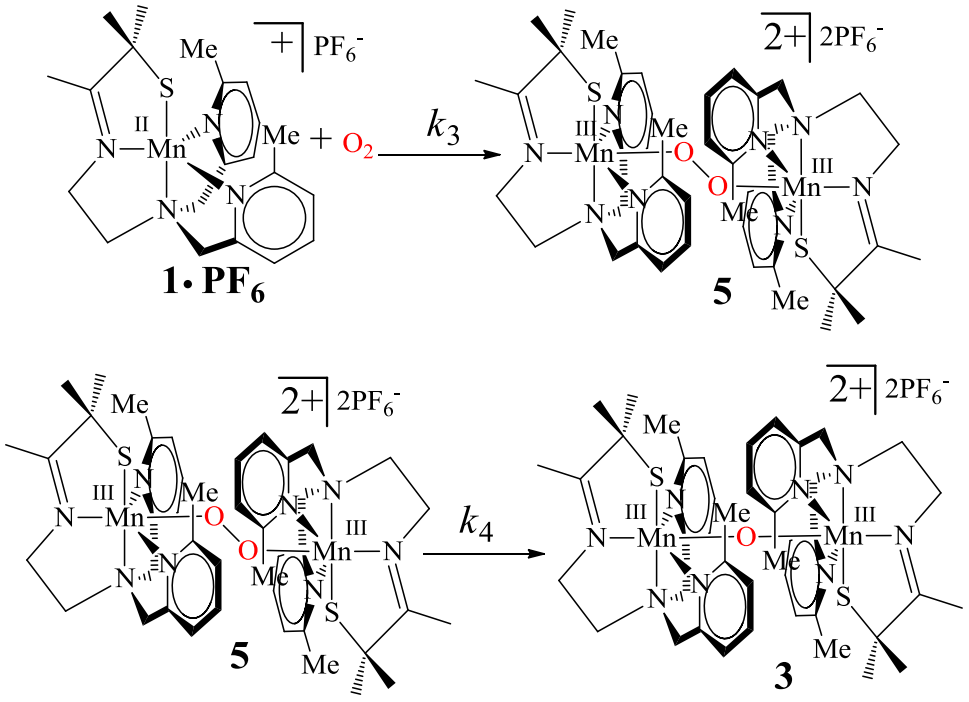

decay of **5** to oxo-bridged **3** is independent of both **1·PF$_6$** and O_2, and is consistent with this process essentially being a first-order overall process with respect to peroxo-bridged **5**.

4.3.4.3 [Mn^{II}(S^{Me2}N$_4$(2-QuinoEN))](BPh$_4$)·MeCN (2)

Kinetic experiments similar to those conducted with **1·BPh$_4$** and **1·PF$_6$** were also performed with **2** in EtCN. Much like reactions with **1·PF$_6$**, these reactions were also found to occur in two steps; the rapid formation of peroxo-bridged **6** followed by a slow decay of **6** to oxo-bridged **4**. These two processes were monitored by time-dependent absorbance changes at 645 nm under pseudo first-order reaction conditions with excess O_2. Kinetic traces from these experiments were fit to Equation 4.2 to yield pseudo first-order rate constants for the growth of **6** ($k_{5,obs}$) and decay of **6** to **4** ($k_{6,obs}$). As is shown in Figure 4.31, a linear relationship exists between $k_{5,obs}$ and [O_2], which is consistent with the formation of **6** being a first-order process with respect to O_2. The $k_{6,obs}$ values are independent of [O_2] and suggest that the conversion of **6** to **4** is zero order with respect to O_2 (Figure 4.31) These values are found to be independent of temperature, which was also noted in the conversion of **5** to **3** (*vide supra*). Second order rate constants (k_5) for the formation of **6** were obtained from the slope each $k_{5,obs}$ versus [O_2] plot and used to obtain activation parameters for this process with Eyring and Arrhenius plots ($\Delta H^{\ddagger}$ = 2.08 kcal/mol , $\Delta S^{\ddagger}$ = -42.4 cal/mol·K, E_a = 2.59 kcal/mol) (Figure 4.32). Due to the low solubility of complex **2** in MeCN and EtCN (maximum solubility ~1.5 mM), kinetic experiments with varying amounts of **2** were not performed.

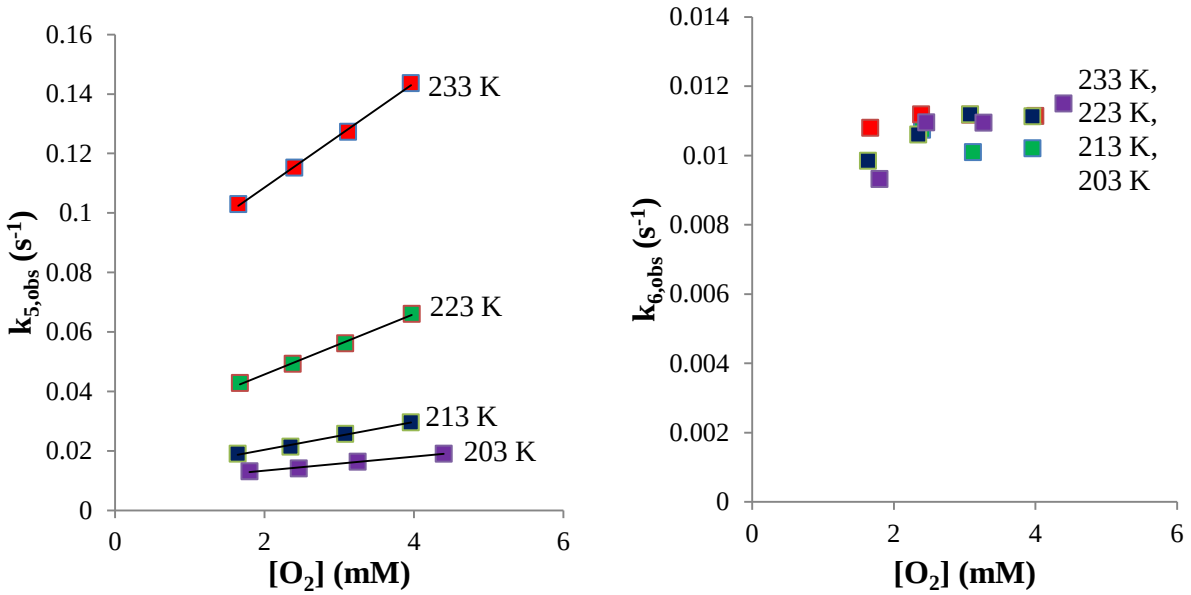

Figure 4.31 Plots of observed rate constants for the formation of **6** ($k_{5,obs}$) versus O_2 concentration ($[O_2]$) (left) and observed rate constants for the conversion of **6** to **4** ($k_{6,obs}$) versus O_2 concentration ($[O_2]$) (right). Each plot contains k_{obs} values determined at 203 K, 213 K, 223 K, and 233 K in EtCN with excess O_2 and [**2**] = 0.5 mM.

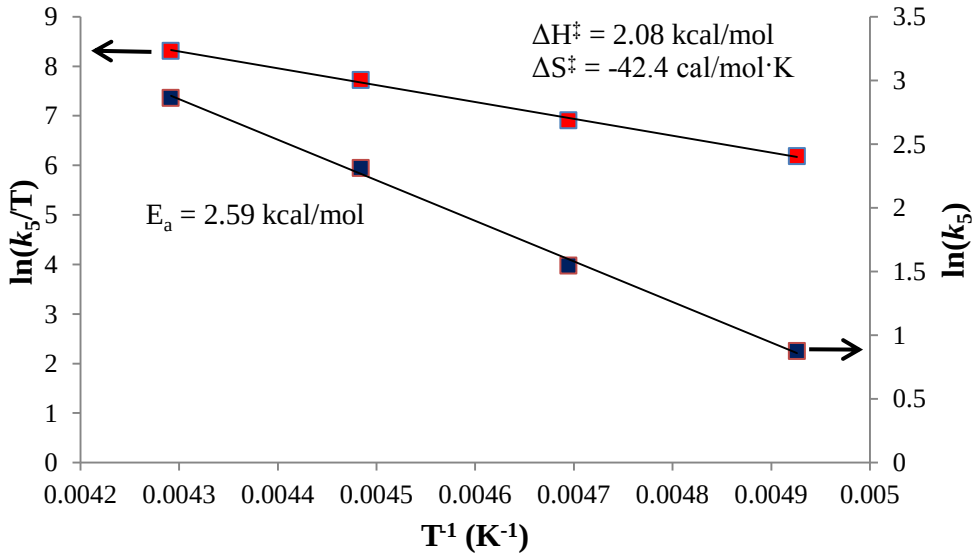

Figure 4.32 Eyring ($\ln(k_5/T)$ versus T^{-1}) (left y-axis) and Arrhenius ($\ln(k_5)$ versus T^{-1}) (right y-axis) plots for the formation of **6** from **2** in EtCN.

The somewhat limited amount of kinetic data obtained for the reaction between **2** O_2 reaction is consistent with that of **1·PF$_6$** (*vide supra*). Both **1·PF$_6$** and **2** react with O_2 to form a peroxo-bridged Mn(III,III) intermediate (**5** and **6**, respectively), and both intermediates decay in a single observable step to the respective oxo-bridged Mn(III,III) dimer **3** and **4**. The formation of each peroxo-bridged intermediate is a second-order overall process with a first order dependence upon O_2 and presumably a first-order dependence upon the respective Mn(II) complex. The conversion of each peroxo-bridged intermediate to the respective oxo-bridged dimer is also independent of O_2. These similarties suggest that the rate laws for the conversion of **2** to **6** and subsequently **6** to **4** could possibly be the same as those in Equations 4.6-4.7.

4.3.4.4 Further Mechanistic Insights Provided by Kinetics Measurements

The kinetics data obtained for **1·BPh$_4$** are distinct from those of **1·PF$_6$** and **2** due to the observation of a putative Mn(III)-superoxo intermediate, which is highly unanticipated given that **1·BPh$_4$** and **1·PF$_6$** contain the same Mn(II) complex. There are reported examples of peroxo-bridged Cu complexes where the counterion has a significant influence upon the stabilities and reactivity of these complexes, however these observations have been attributed to the ability of smaller counterions to actually coordinate to each respective Cu ion.[8,37] Such an effect seems highly unlikely in complexes **1** and **2** given the sterically-congested primary coordination sphere of each complex, as well as the fact that BPh_4^- and PF_6^- are both typically considered non-coordinating anions. To ensure that these findings are indeed due to difference in counterion and not trace impurities, kinetic measurements have been made with **1·PF$_6$** that was intentionally "contaminated" with $NaBPh_4$. These experiments resulted in the observation of the Mn(III)-superoxo intermediate (**7**) and similar rate constants as those obtained with **1·BPh$_4$**. Such results

have been highly reproducible and are therefore considered legitimate; however, a reasonable explanation for these observations is still needed.

Activation parameters associated with the initial binding of O_2 to **1·BPh$_4$** and **1·PF$_6$** ($\Delta H^{\ddagger}$ = 6.30 kcal/mol, $\Delta S^{\ddagger}$ = -18.06 cal/mol·K for (**1·BPh$_4$**), $\Delta H^{\ddagger}$ = 5.95 kcal/mol, $\Delta S^{\ddagger}$ = -26.76 cal/mol·K for (**1·PF$_6$**)) are very close to one another. This observation is consistent with the fact that O_2 is presumably binding to the same Mn(II) complex in each case. The activation parameters for O_2 binding to complex **2** are, however, starkly different, as is represented by the activation enthalpy for this process ($\Delta H^{\ddagger}$ = 2.08 kcal/mol) being 2-3 times smaller than are these values for **1·BPh$_4$** and **1·PF$_6$**. Activation enthalpies for O_2 binding to coordinatively unsaturated transition metal complexes are typically found with a range of 2-5 kcal/mol, which is well within the range of **2**, but slightly lower than those of **1·BPh$_4$** and **1·PF$_6$**.[28] It is also worth noting that the activation parameters associated with the conversion of superoxo-bound **7** to peroxo-bridged **5** are the highest of any kinetic step observed from these reactions. Considering that a mononuclear Mn-O_2 adduct is not observed with **1·PF$_6$** or **2**, it can be assumed that the activation parameters associated with the conversion of **7** to **5** are large for this particular type of process.

4.3.5 Reactivity of Peroxo-Bridged 5 and 6 with External Substrates

Biological and synthetic transition metal-peroxo species are known to promote a wide range of oxidative transformations. Synthetic Mn-peroxo and Fe-peroxo complexes have each been shown to perform aldehyde deformylation reactions.[1,3,5-8] There are also a few reported cases where various transition metal-hydroperoxo species have been proposed to epoxidize olefins, although direct observations have yet to be made.[52-53] Ni and Cu complexes containing μ-η^2:η^2 peroxo bridging ligands have been shown to promote PCET reactions, as well as oxygen

atom transfer reactions to phosphines and thioethers.[5,54] The reactive properties of peroxo-bridged **5** and **6** were therefore each explored with a wide range of organic substrates commonly used to probe each of these types of reactions.

4.3.5.1 Electrophilic Aldehyde, Acyl Chloride, Acid Anhydride, and Alkene Substrates

The ability of **5** or **6** to react with cyclohexane carboxaldehyde, benzoyl chloride, acetic anhydride, or tetracyanoethyelene was explored by UV/Vis spectroscopy. Each substrate was added in high excess amounts (~1000 equivalents) to 233 K MeCN solutions of **5** or **6**, respectively, generated from *in situ* reactions between the requisite Mn(II) complex and O_2. None of these substrates elicited a considerable change in the kinetics for the conversion of **5** to **3** or **6** to **4**, respectively, indicating that neither intermediate was reactive with these substrates. The final reaction mixtures were also analyzed by GC/MS and found to contain no oxidized organic products from these reactions, suggesting that neither the respective peroxo-bridged intermediate nor any unobservable intermediate formed after the decay of these species are capable of promoting aldehyde deformylation reactions.

4.3.5.2 Acidic Substrates

Although **5** and **6** did not react with electrophilic aldehydes, acid chlorides, anhydrides, or alkenes, the peroxo bridging ligand in each of these complexes were found to be relatively basic, as both intermediates reacted almost immediately with acids. As is shown in Figure 4.33, **6** reacts with trifluoroacetic acid (TFA, pK_a in MeCN = 12.65) at 233 K in MeCN to form a new species characterized by an absorbance band with λ_{max} = 468 nm.[55] Nearly identical spectra were

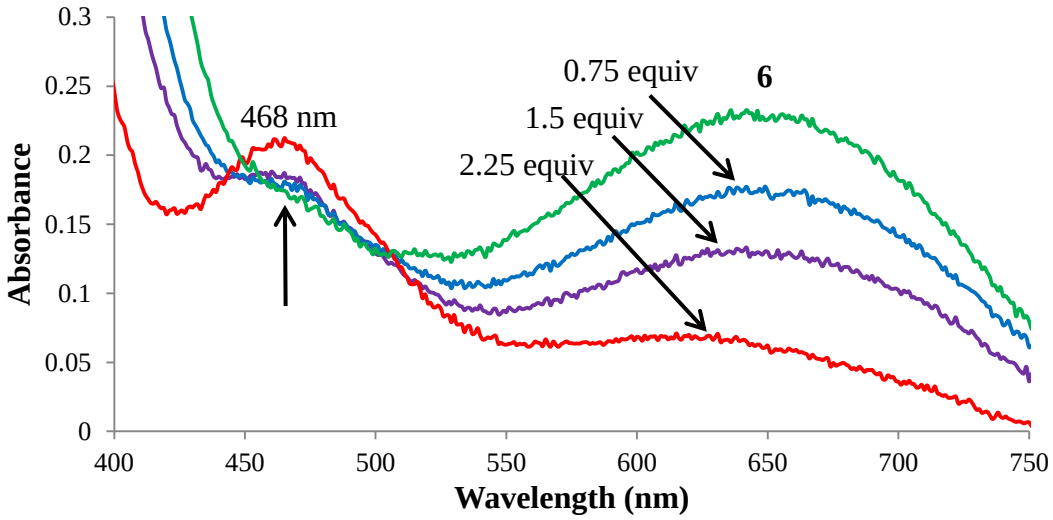

Figure 4.33 Anaerobic UV/Vis titration experiment displaying the reaction between $[Mn^{III}(S^{Me2}N_4(2\text{-QuinoEN}))]_2(\mu\text{-}O_2)(BPh_4)_2{\cdot}CH_3CH_2CN$ (**6**, 0.9 mM) and trifluoroacetic acid (each trace represents a 0.75 equivalent aliquot from a 100 mM stock solution in MeCN) in MeCN at 233 K. Aliquots were added in 1 minute intervals.

obtained from reactions between TFA and **5** (Appendix A.38). Both reactions were found to require 2-3 equivalents of TFA to fully maximize the absorbance features of the respective reaction product(s). It is worthwhile to note that the absorbance features representative of these reaction products are very similar to those observed from the acid-promoted bridge-cleavage reactions involving the N-heterocyclic-ligated oxo-bridged Mn(III,III) dimers discussed in Chapter 3, as well as the products from outer-sphere oxidation of the thiolate-ligated Mn(II) complexes (also discussed in Chapter 3). Hydrogen peroxide detection assays were also performed with the products from each reaction between **5** or **6** and TFA (as described in the experimental section), which resulted in the detection of 0.86(8) and 0.78(16) equivalents of H_2O_2 per equivalent of **5** and **6**, respectively (Appendix A.38). These results suggest that reactions between each peroxo-bridged Mn(III,III) dimer and acid involve the protonation and subsequent dissociation of H_2O_2, as well as the formation of a mononuclear Mn(III) species.

The tentatively-assigned Mn(III) species formed from these reactions were able to be reduced back to the respective Mn(II) complex (**1** and **2**, respectively) with one equivalent of cobaltacene (Cp_2Co, E° = -920 mV vs. SCE) per Mn(III) (Figure 4.34).[51] Exposure of each

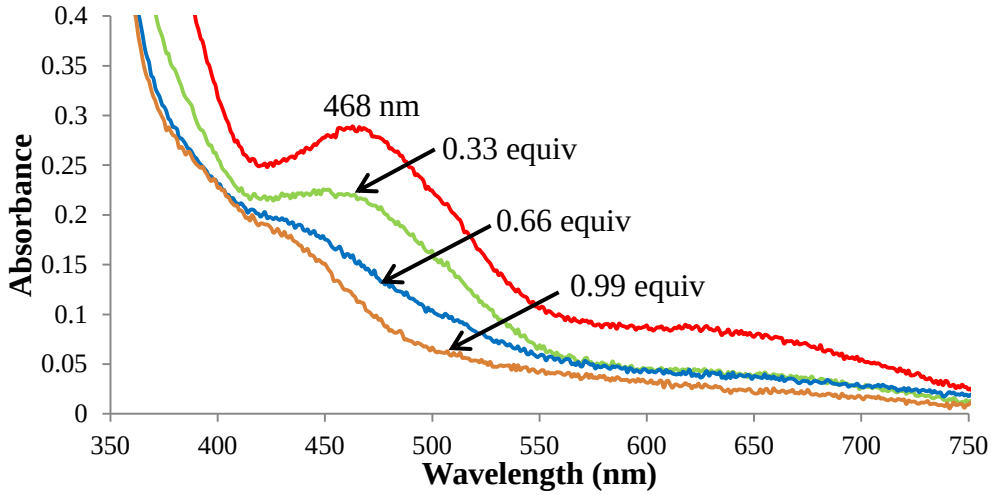

Figure 4.34 Anaerobic UV/Vis titration experiment displaying the reaction between the tentatively-assigned Mn(III) product from Figure 4.33 and cobaltacene (each trace represents a 0.33 equivalent aliquot from a 7 mM stock solution in MeCN) in MeCN at 233 K. Aliquots were added in 2 minute intervals.

reduced product to excess O_2 at 233 K resulted in the reformation of peroxo-bridged **5** or **6**, respectively, which is consistent with the reduced products indeed being complexes **1** and **2**, respectively. All Mn-containing species (reduced Mn(II) complexes, peroxo-bridged Mn(III,III) dimers, and the putative mononuclear Mn(III) intermediates) involved in this reaction cycle (Scheme 4.4) have been found to be very unstable in the presence of relatively high concentrations of acid, which has unfortunately precluded these systems from being explored for the ability to catalytically reduce O_2 to H_2O_2.

Scheme 4.4 Reaction cycle demonstrating the two electron reduction of O_2 to H_2O_2 with **1** at 233 K in MeCN. This cycle also applies to complex **2** with the involvement of peroxo-bridged **6**.

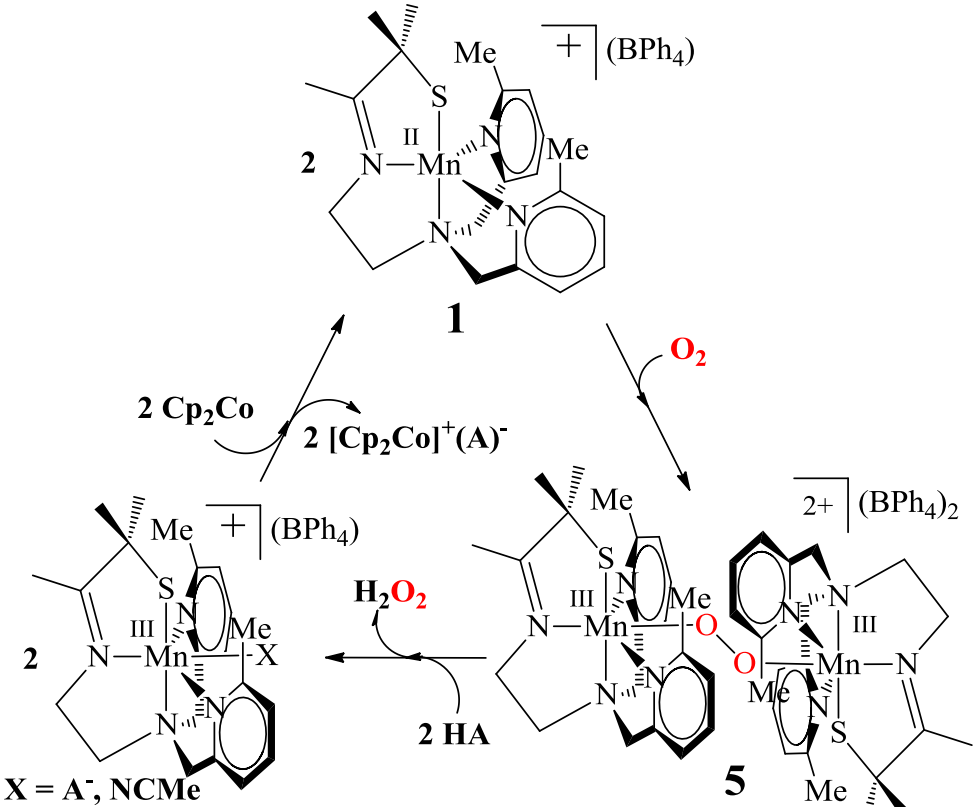

4.3.5.3 Nucleophilic Phosphine Substrates

Reactions between **5** or **6** and triphenylphosphine and tributylphosphine were attempted at low temperatures (233 K and 253 K) in MeCN and monitored by either UV/Vis spectroscopy or rapid-scanning stopped flow spectrophotometry. Kinetic measurements were also made for the conversion of **6** to **4** both in the presence and absence of PPh_3 with excess O_2 at 253 K in MeCN by monitoring time-dependent absorbance changes at 645 nm. Under these conditions, an observed rate constant for the quantitative conversion of **6** to **4** while in the absence of PPh_3 ($k_{6,obs}$) was determined to be 0.0235 s^{-1}. In the presence of 1.5 equivalents of PPh_3, this observed rate constant increased to a value of 0.072 s^{-1}, suggesting PPh_3 is involved in the conversion of **6** to **4**. However, $k_{6,obs}$ was found to be independent of the concentration of PPh_3 present in the

reaction, further suggesting that although PPh_3 does influence the decay of **6** to **4**, it does not directly react with **6** (Figure 4.35). The final products from these reactions were analyzed

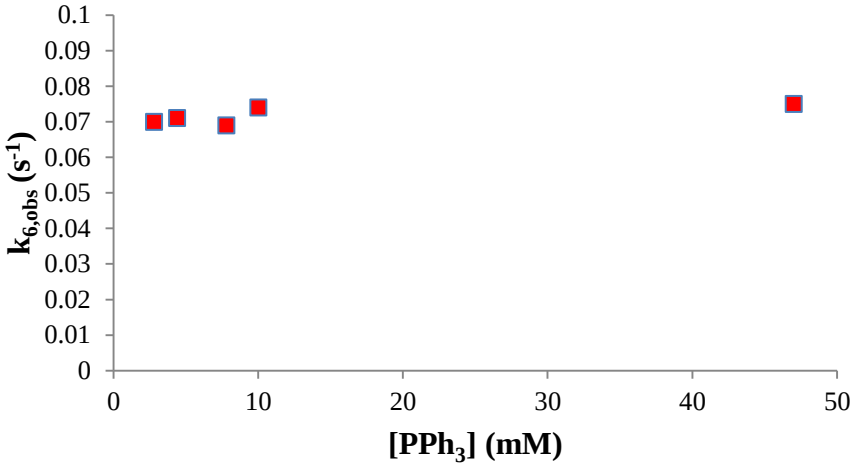

Figure 4.35 Plot of observed rate constants for the conversion of **6** to **4** ($k_{6,obs}$) versus PPh_3 concentration ([PPh_3]) determined at 253 K in MeCN with [O_2] = 2.025 mM and [**2**] = 0.15 mM.

GC/MS and found to contain $Ph_3P{=}O$, which provides the strongest evidence that PPh_3 does indeed react with a unobserved Mn-containing species present during the conversion of **6** to **4**. $Ph_3P{=}O$ was also detected as a product from aerobic reactions between peroxo-bridged **5** and PPh_3, therefore a similar process is likely to be operative during the conversion of **5** to **3**.

Further evidence that phosphine oxidation was being promoted by an unobserved Mn-containing intermediate was obtained through reactions with PBu_3. These reactions were performed by slowly bubbling O_2 directly from a tank into 243 K MeCN solutions of **1** or **2** and a high excess of PBu_3 (200 equivalents). The final reaction products were then analyzed by GC/MS after 30 minutes in order to quantify any $Bu_3P{=}O$ formed during these reactions. Two important control experiments were also conducted; first, the amount of $Bu_3P{=}O$ formed from aerobic autooxidation under these conditions was determined and subtracted from the total yield of $Bu_3P{=}O$ in each Mn-containing experiment. Second, reactions were performed in which

concentrated HCl was added to reaction solutions following the complete formation of each respective peroxo-bridged intermediate. The final reaction mixtures from these experiments were also analyzed by GC/MS and yielded little to no $Bu_3P{=}O$ formation. This particular control experiment was performed in order to determine whether or not an intermediate formed during the conversion of each Mn(II) complex (**1** or **2**) to the respective peroxo-bridged intermediate (**5** or **6**) was capable of oxidizing PBu_3. After accounting for these controls, it was determined that the total yield of $Bu_3P{=}O$ from reactions with each Mn complex was directly proportional the total concentration of Mn in each reaction solution (Figure 4.36). These results agree with the general conclusion reached from the PPh_3 experiments in that an unobserved intermediate present during the decay of each peroxo-bridged intermediate to the respective oxo-bridged dimer is capable of oxidizing phosphines to phosphine oxides.

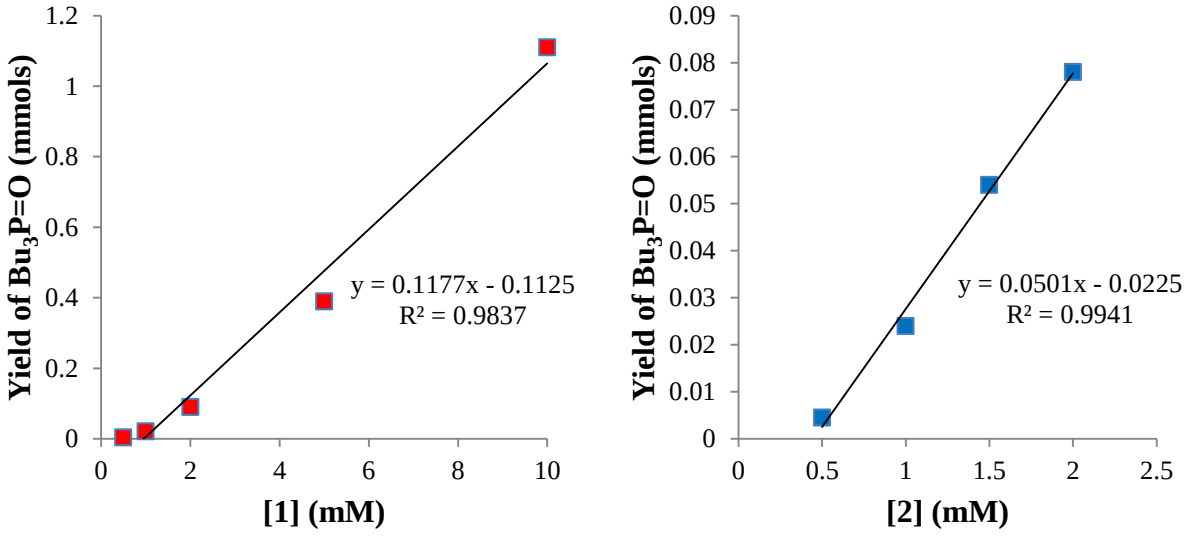

Figure 4.36 Plots of $Bu_3P{=}O$ formed (mmols) as a function of the starting concentration of complexes **1** (left plot) and **2** (right plot). All reactions were performed in 3 mL of MeCN at 243 K with excess O_2.

4.3.5.4 Substrates with Weak O-H or C-H Bonds

The reactivity of peroxo-bridged **5** and **6** with 2,4-di-*tert*-butylphenol (DBP, O-H BDFE = 80.5 kcal/mol) and dihydroanthracene (DHA, C-H BDFE 76.0 = kcal/mol) were explored at 253 K in MeCN and monitored by UV/Vis spectroscopy.[56] Complexes **5** and **6** each appeared to exhibit similar lifetimes in the presence and absence of these substrates, suggesting that no direct reactions were occurring. Kinetics measurements are still needed to further validate these observations. Analysis of the final products from these reactions did, however, yield oxidized phenol products (50-55% yield of 2,2'-dihydroxy-3,3',5,5'-tetra-*tert*-butylbiphenyl based on total [Mn]), again suggesting that an unobserved intermediate formed during the peroxo-dimer to oxo-dimer conversions is capable of removing a hydrogen atom from DBP. If a Mn(IV)=O is responsible for the oxidation of DBP, this reaction would lead to a transient Mn(III)-OH intermediate prior to conversion to the respective oxo-bridged dimer final product. It is worthwhile to note that evidence was provided in Chapter 3 to support the conversion of a transient Mn(III)-OH intermediate to each respective oxo-bridged dimer. No oxidized products from DHA were formed from these reactions.

4.3.5.4 $H_2{}^{18}O$ and Low-Valent Fe(II) Complexes

High-valent Mn(IV)- and Mn(V)-oxo complexes have been shown to promote both the oxidation of phosphines to phosphine oxides and phenols to the corresponding phenoxides and biphenyls.[56-60] Given that both types of oxidation processes appear to be occurring during the conversion of each peroxo-bridged dimer to the corresponding oxo-bridged final product, experiments were designed to gain further indirect evidence that high-valent Mn-oxo species may exist during each of these reactions. Initial evidence that high-valent Mn-oxo intermediates

may be participating in these reactions was provided in Chapter 3 (section 3.3.1), as it was found that an intermediate formed during these O_2 reactions could exchange with H_2O in solution. Similar experiments were performed by adding a small amount of $H_2{}^{18}O$ (50-75 equivalents per equivalent of Mn) to solutions of **5** or **6** at 253 K in MeCN. After warming these solutions to room temperature, each reaction mixture was analyzed by ESI-MS and found to contain a significant amount of ^{18}O-labeled **3** and **4**. These results again support the existence of a high-valent Mn-oxo intermediate in these reactions.

The formation of phosphine oxides during the peroxo-dimer to oxo-dimer conversions demonstrated that the Mn-based intermediates responsible for these reactions were specifically capable of performing oxygen atom transfer reactions. Along this vein, experiments were performed in MeCN solutions between peroxo-bridged **5** and $[Fe^{II}(S^{Me2}N_4$(2-QuinoEN))$](PF_6)\cdot$MeOH (**8**). If a Mn(IV)-oxo is formed following the decay of **5**, it would be expected that this intermediate should react with low-valent **8** to yield a Mn(III)-O-Fe(III) product. These reactions were performed specifically by adding two equivalents of **8** to anaerobic solutions of **5** (before any significant decay to **3** occurred) at 233 K and monitoring the UV/Vis spectra until no changes were observed. A representative ESI mass spectrum from these reactions is provided in Figure 4.37 and contains peaks corresponding to the homobinuclear Mn(III,III) (**3**) and Fe(III,III) dimers at *m/z* = 432.3 and 505.2, respectively. A prominent peak at *m/z* = 468.3 is also observed in this mass spectrum and is consistent with the mass of a dicationic heterobinuclear Mn(III)-O-Fe(III) product.

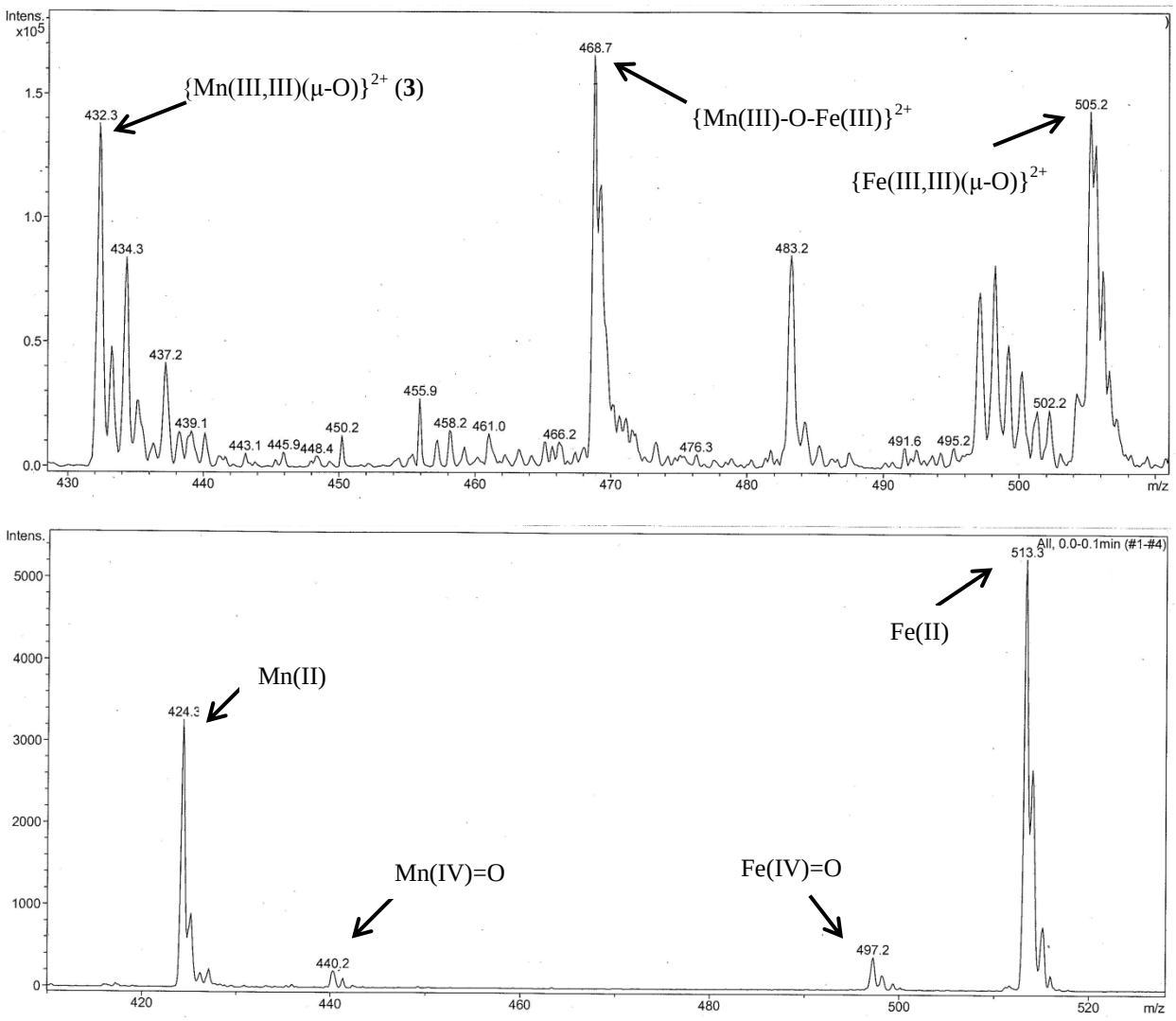

Figure 4.37 ESI mass spectrum of products from a reaction between **5** and **8** at 233 K in MeCN (top). ESI mass spectrum obtained from fragmentation of *m/z* = 468.7 (bottom)

4.4 Summary and Proposed Mechanism for Reactions Between Complexes 1 or 2 and O_2

Considering all of the data provided in this Chapter, a mechanism consistent with these findings has been formulated and is provided in Scheme 4.5. Dioxygen binding to a coordinatively unsaturated Mn(II) complex (**1** or **2**) results in the formation of a transient Mn(III-superoxo intermediate. A second equivalent of Mn(II) then binds to the distal superoxo oxygen and forms a peroxo-bridged Mn(III,III) dimer. Protonation of the peroxo bridging ligand

Scheme 4.5 Proposed mechanism for the dioxygen reactivity of **1** and **2**.

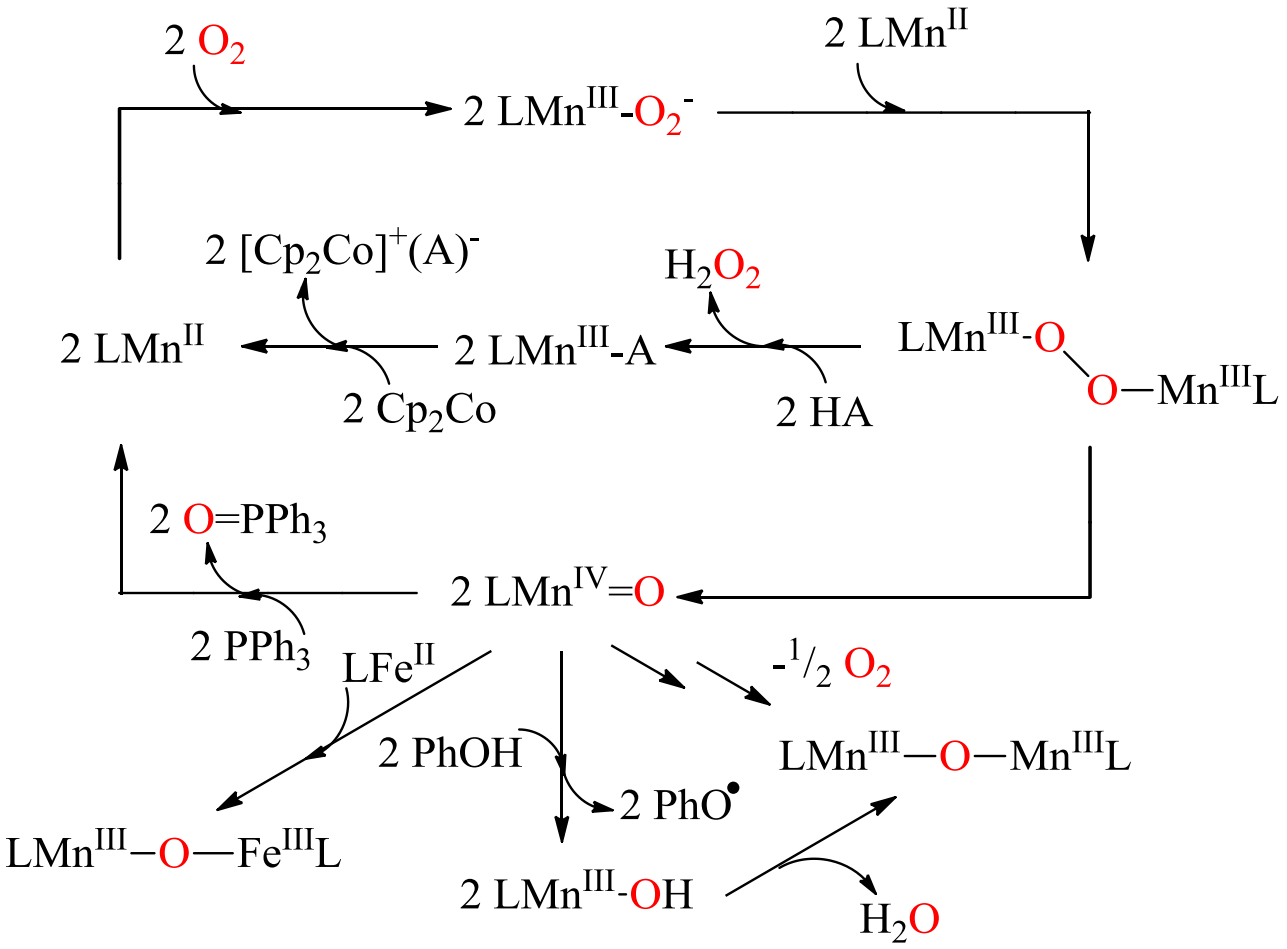

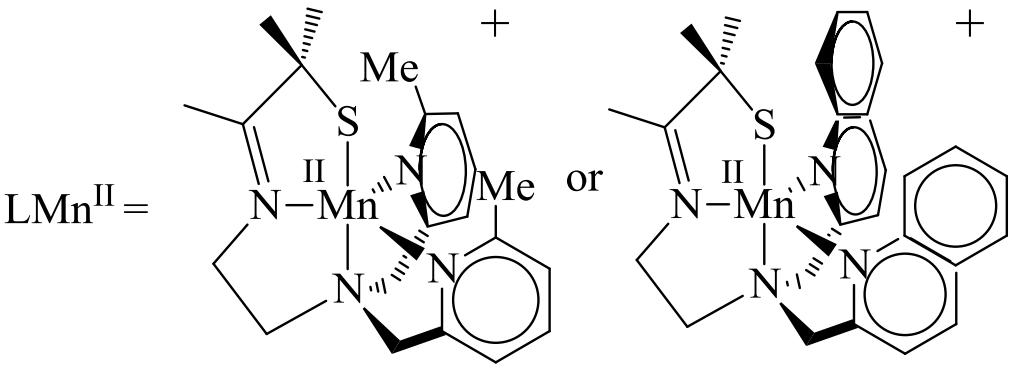

followed by the one electron reduction of the transient mononuclear Mn(III) species reforms the starting Mn(II) complex, representing a full turnover for a potentially catalytic O_2 reduction cycle. In the absence of any external substrates, the peroxo-bridged Mn(III,III) dimer converts to an oxo-bridged Mn(III,III) dimer in quantitative yield. Specific mechanistic aspects regarding the peroxo dimer to oxo dimer conversion are still unclear. However, indirect evidence has been obtained to suggest that a high-valent Mn(IV)=O is involved in this process. Reactions with substrates that can participate in both one electron (phenols) and two electron (phosphines) reactions were found to alter the kinetics of the peroxo dimer to oxo dimer conversion. The expected products from oxidation of these substrates were also detected in these reactions, illustrating that a Mn-based oxidant is indeed present during these conversions. The proposed Mn(IV)=O was also found to exchange with ^{18}O-labeled water in solution, as well as trapped with a low-valent Fe(II) complex. These observations are consistent with the decay of the peroxo-bridged intermediates involving a homolytic O-O bond cleavage step as the rate determining step in the peroxo dimer to oxo dimer conversion.

Mechanistic details regarding the conversion of each peroxo-bridged dimer to the respective oxo-bridged final product in the absence of external substrates are still unclear. Two extra electrons are necessary to for these conversions to occur quantitatively, however the source of these reducing equivalents are still unknown. The one detail that is clear is that these reactions do not involve sacrificial Mn complexes as sources of these necessary reducing equivalents given that ~100 % yield of each oxo-bridged final product. It has been proposed in the literature that high-valent metal-oxo complexes can activate the strong C-H bonds found in organonitrile solvents (or trace impurities in these solvents) by PCET pathways, suggesting that the solvent used in these reactions could, in principle, serve as the necessary electron source.[61-62]

In the absence of direct or indirect evidence for an oxidized organonitrile-derived product, these statements are purely speculative.

4.5 Notes to Chapter 4

1) Borovik, A. S.; Zart, M. K.; Zinn, P. J. In *Activation of Small Molecules: Organometallic and Bioinorganic Perspectives*, Tolman, W. B., Ed.; Wiley-VCH: Weinheim, Germany, 2006.

2) Decker, A.; Chow, M. S.; Kemsley, J. N.; Lehnert, N.; Solomon, E. I. *J. Am. Chem. Soc.* **2006**, *128*, 4719-4733.

3) Groves, J. T.; Han, Y.-Z. In *Cytochrome P-450. Structure, Mechanism, and Biochemistry*; Ortiz de Montellano, P. R., Ed.; Plenum Press: New York, 1995.

4) Que, Jr., L.; Watanabe, Y. *Science* **2001**, *292*, 651-653.

5) Mirica, L. M.; Ottenwaelder, X.; Stack, T. D. P. *Chem. Rev.* **2004**, *104*, 1013-1045.

6) Solmon, E. I.; Brunold, T. C.; Davis, M. I.; Kemsley, J. N.; Lee, S.-K.; Lehnert, N.; Neese, F.; Skulan, A. J.; Yang, Y.-S.; Zhou, J. *Chem. Rev.* **2001**, *100*, 235-349.

7) Costas, M.; Mehn, M. P.; Jensen, M. P.; Que, L., Jr. *Chem. Rev.* **2004**, *104*, 939-986.

8) Kim, E.; Chufán, E. E.; Kamaraj, K.; Karlin, K. D. *Chem. Rev.* **2004**, *104*, 1077-1133.

9) Cramer, C. J.; Tolman, W. B. *Acc. Chem. Res.* **2007**, *40*, 601-608.

10) Suzuki, M. *Acc. Chem. Res.* **2007**, *40*, 609-617.

11) Himes, R. A.; Karlin, K. D. *Curr. Opin. Chem. Biol.* **2009**, *13*, 119-131.

12) Cho, J.; Sarangi, R.; Nam, W. *Acc. Chem. Res.* **2012**, 45, 1321-1330.

13) Jackson, T. A.; Brunold, T. C. *Acc. Chem. Res.***2004**, *37*, 461-470.

14) Wu, A. J.; Penner-Hahn, J. E.; Pecoraro, V. L. *Chem. Rev.* **2004**, *104*, 903-938.

15) Mullins, C. S.; Pecoraro, V. L. *Coord. Chem. Rev.* **2008**,252*0*, 416-443.

16) McEvoy, J. P.; Brudvig, G. W. *Chem. Rev.* **2001**, *106*, 4455-4483.

17) Mukhopadhyay, S.; Mandal, S. K.; Bhaduri, S.; Armstrong, W. H. *Chem. Rev.* **2004**, *104*, 3981-4026.

18) VanAtta, R. B.; Strouse, C. E.; Hanson, L. K.; Valentine, J. S. *J. Am. Chem. Soc.* **1987**, *109*, 1425-1434.

19) Kitajima, N.; Komatsuzaki, H.; Hikichi, S.; Osawa, M.; Moro-oka, Y. *J. Am. Chem. Soc.* **1994**, *116*, 11596-11597.

20) Singh, U. P.; Sharma, A. K.; Hikichi, S.; Komatsuzaki, H.; Moro-oka, Y.; Akita, M. *Inorg. Chim. Acta* **2006**, *359*, 4407-4411.

21) Seo, M. S.; Kim, J. Y.; Annaraj, J.; Kim, Y.; Lee, Y.-M.; Kim, S.-J.; Kim, J.; Nam, W. *Angew. Chem. Int. Ed.* **2007**, *46*, 377-380.

22) Annaraj, J.; Cho, J.; Lee, Y.-M.; Kim, S. Y.; Latifi, R.; De Visser, S. P.; Nam, W. *Angew. Chem. Int. Ed.* **2009**, *48*, 4150-4153.

23) Bossek, U.; Weyhermüller, T.; Wieghardt, K.; Nuber, B.; Weiss, J. *J. Am. Chem. Soc.* **1990**, *112*, 6387-6388.

24) Lee, C.-M.; Chuo, C.-H.; Chen, C.-H.; Hu, C.-C.; Chiang, M.-H.; Tseng, Y.-J.; Hu, C.-H.; Lee, G.-H. *Angew. Chem. Int. Ed.* **2012**, *51*, 5427-5430.

25) Stoll, S.; Schweiger, A. *J. Magn. Reson.* **2006**, *178*, 42-55.

26) MATLAB version 7.10.0. Natick, Massachusetts: The MathWorks Inc., 2010.

27) http://eww.mpi-muelheim.mpg.de/bac/logins/bill/julX_en.php

28) Kryatov, S. V.; Rybak-Akimova, E. V.; Schindler, S. *Chem. Rev.* **2005**, *105*, 2175-2226.

29) George, G. N.; *EDG_FIT*; Stanford Synchrotron Radiation Laboratory, Stanford Linear Accelerator Center, Stanford University: Stanford, CA, 2000.

30) (a) Altomare, A.; Burla, C.; Camalli, M.; Cascarano, L.; Giacovazzo, c.; Guagliardi, A.; Moliterni, A. G. G.; Polidori, G.; Spanga, R. *J. Appl. Cryst.* **1999**, *32*, 115-119. (b) Altomare, A.; Cascarano, G.; Giacovazzo, C.; Guagliardi, A. *J. Appl. Cryst.* **1993**, *26*, 343.

31) Sheldrick, G. M. SHELXL-97: Program for the Refinement of Crystal Structures **1997**, University of Gottingen, Germany.

32) Mackay, S.; Edwards, C.; Henderson, A.; Gilmore, C.; Stewart, N.; Shankland, K.; Donald, A.; MaXus: a Computer Program for the Solution and Refinement of Crystal Structures from Diffraction Data. University of Glasgow, Scotland, 1997.

33) Waasmaier, D.; Kirfel, A. *Acta Crystallogr. A* **1995**, *51*, 416.

34) Frisch, M. J.; Trucks, G. W.; Schlegel, H. B.; Scuseria, G. E.; Robb, M. A.; Cheeseman, J. R.; Montgomery, J. A., Jr.; Vreven, T.; Kudin,K. N.; Burant, J. C.; Millam, J. M.; Lyengar, S. S.; Tomasi, J.; Barone, V.; Mennucci, B.; Cossi, M.; Scalmani, G.; Rega, N.; Petersson, G.A.; Nakatsuji, H.; Hada, M.; Ehara, M.; Toyota, K.; Fukuda, R.; Hasegawa, J.; Ishida, M.; Nakajima, T.; Honda, Y.; Kitao, O.; Nakai,H.; Klene, M.; Li, X.; Knox, J. E.; Hratchian, H. P.; Cross, J. B.; Adamo, C.; Jaramillo, J.; Gomperts, R.; Stratmann, R.

E.; Yazyev, O.; Austin, A. J.; Cammi, R.; Pomelli, C.; Ochterski, J. W.; Ayala, P. Y.; Morokuma, K.; Voth, G. A.; Salvador, P.; Dannenberg, J. J.; Zakrzewski, V. G.; Dapprich, S.; Daniels, A. D.; Strain, M. C.; Farkas, O.; Malick, D. K.; Rabuck, A. D.; Raghavachari, K.; Foresman, J. B.; Ortiz, J. V.; Cui, Q.; Baboul, A. G.; Clifford, S.; Cioslowski, J.; Stefanov, B. B.; Liu, G.; Liashenko, A.; Piskorz, P.; Komaromi, I.; Martin, R. L.; Fox, D. J.; Keith, T.; Al-Laham, M. A.; Peng, C. Y.; Nanayakkara, A.; Challacombe, M.; Gill, P. M. W.; Johnson, B.; Chen, W.; Wong, M. W.; Gonzalez, C.; Pople, J. A. Gaussian 03, revision C.01; Gaussian, Inc.: Wallingford, CT, 2004.

35) Tenderholt, A. L. *QMForge*, Version 2.1, http://qmforge.sourceforge.net

36) Que, L., Jr.; Tolman, W. B. *Nature* **2008**, *455*, 333-340.

37) Tolman, W. B. *Acc. Chem. Res.* **1997**, *30*, 227-237.

38) Roelfes, G.; Vrajmasu, V.; Chen, K.; Ho, R. Y. N.; Rohde, J.-U.; Zondervan, C.; la Crois, R. M.; Schudde, E. P.; Lutz, M.; Spek, A. L.; hage, R.; Feringa, B. L.; Münck, E.; Que, L., Jr. *Inorg. Chem.* **2003**, *42*, 2639-2653.

39) Geiger, R. A.; Leto, D. F.; Chattopadhyay, S.; Dorlet, P.; Anxolabèhére-Mallart, E.; Jackson, T. A. *Inorg. Chem.* **2011**, *50*, 10190-10203.

40) Geiger, R. A.; Chattopadhyay, S.; Day, V. W.; Jackson, T. A. *J. Am. Chem. Soc.* **2010**, *132*, 2821-2831.

41) Jacobson, R. R.; Tyeklár, Z.; Farooq, A.; Karlin, K. D.; Liu, s.; Zubieta, J. *J. Am. Chem. Soc.* **1988**, *110*, 3635-3638.

42) Abragam, A.; Bleany, B. *Electron Paramagnetic Resonance of Transition Ions*; Oxford University Press: London, 1970.

43) Peterson, J.; Fee, J. A.; Day, E. P. *Biochem. Biophys. Acta* **1991**, *1079*, 161-168.

44) Campbell, K. A.; Yikilmaz, e.; Grant, C. V.; Gregor, W.; Miller, A.-F.; Britt, R. D. *J. Am. Chem. Soc.* **1999**, *121*, 4714-4715.

45) Britt, R. D.; Campbell, K. A.; Peloquin, J. M.; Gilchrist, M. L.; Aznar, C. P.; Dicus, M. M.; Robblee, J.; Messinger, J.; *Biochem. Biophys. Acta* **2004**, *1655*, 158-171.

46) Dexheimer, S. L.; Gohdes, J. W.; Chan, M. K.; Hagen, K. S.; Armstrong, W. H.; Klein, M. P. *J. Am. Chem. Soc.* **1989**, *111*, 8923-8925.

47) Groni, S.; Blain, G.; Guillot, R.; Policar, C.; Anxolabèhére-Mallart, E. *Inorg. Chem.* **2007**, *46*, 1951-1953.

48) Shook, R. L.; Gunderson, W. A.; Greaves, J.; Ziller, J. W.; Hendrich, M. P.; Borovik, A. S. *J. Am. Chem. Soc.* **2008**, *130*, 8888-8889.

49) Solomon, E. I.; Gorelsky, S. I.; Dey, A. *J. Comp. Chem.* **2006**, *27*, 1415-1428.

50) Park, G. Y.; Qayyum, M. F.; Woertink, J.; Hodgson, K. O.; Hedman, B.; Narducci Sarjeant, A. A.; Solomon, E. I.; Karlin, K. D. *J. Am. Chem. Soc.* **2012**, *134*, 8513-8524.

51) Connelly, N. G.; Geiger, W. E. *Chem. Rev.* **1996**, *96*, 877-910.

52) Strukul, G.; Michelin, R. A. *J. Am. Chem. Soc.* **1985**, *107*, 7563-7569.

53) Wenzel, T. T. In *Dioxygen Activation and Homogeneous Catalytic Oxidations*; Simandi, L. I., Ed.; Elseiver Science Publishers; Amsterdamn, 1991.

54) Kieber-Emmons, M. T.; Riordan, C. G. *Acc. Chem. Res.* **2007**, *40*, 618-625.

55) Eckert, F.; Leito, I.; Kaljurand, I.; Kütt, A.; Klamt, A.; Kiedenhofen, M. *J. Comp. Chem.* **2009**, *30*, 799-810.

56) Collins, T. J.; Gordon-Wylie, S. W. *J. Am. Chem. Soc.* **1989**, *111*, 4511-4513.

57) Collins, T. J.; Powell, R. D.; Slebodnick, C.; Uffelman, E. S. *J. Am. Chem. Soc.* **1990**, *112*, 899-901.

58) Parsell, T. H.; Behan, R. K.; Green, M. T.; Hendirch, M. P.; Borovik, A. S. *J. Am. Chem. Soc.* **2006**, *128*, 8728-8729.

59) Woon, J. S.; Mi, S. S.; George, S. D.; Ohta, T.; Song, R.; Kang, M.-J.; Tosha, T.; Kitagawa, T.; Solomon, E. I.; Nam, W. *J. Am. Chem. Soc.* **2007**, *129*, 1269-1277.

60) Tahuchi, T.; Gupta, R.; Lassalle-Kaiser, B.; Boyce, D. W.; Yachandra, V. K.; Tolman, W. B.; Yang, J.; Hendrich, M. P.; Borovik, A. S. *J. Am. Chem. Soc.* **2012**, *134*, 1996-1999.

61) Shirin, Z.; Young, V. G., Jr.; Borovik, A. S. *Chem. Comm.* **1997**, 1967-1968.

62) Goldsmith, C. R.; Jonas, R. T.; Stack, T. D. P. *J. Am. Chem. Soc.* **2001**, *124*, 83-96.

Chapter 5

Correlations Between Structural, Spectroscopic, and Reactivity Properties Within a Series of Manganese(III)-Alkylperoxo Complexes

5.1 Introduction

Manganese-containing metalloenzymes promote a number of important biochemical transformations involving dioxygen and reduced dioxygen derivatives.[1-14] Mn-peroxo and Mn-hydroperoxo species are commonly invoked as key intermediates in these reactions, particularly regarding those which cleave or form O-O bonds.[1,7,15] The Mn lipoxygenase and homoprotocatechuate 2,3-dioxygenase are two of the few Mn metalloenzymes that are proposed to form Mn-alkylperoxo intermediates, although neither have never been directly observed in the native enzyme.[3,16-20] Towards this end, synthetic Mn-peroxo, -hydroperoxo, and -alkylperoxo complexes have been explored to better understand the fundamental properties of these types of intermediates.[21-31] Unfortunately, very few examples of synthetic Mn-peroxos of any type have been observed or characterized. Prior to the work described in this chapter, only one Mn-alkylperoxo (a Mn(II)-alkylperoxo complex) had ever been reported.[32] More examples of Mn-alkylperoxos are therefore needed in order to further understand the structural, electronic, and reactive properties of these types of intermediates.

This chapter describes the structural and spectroscopic properties of a series of Mn(III)-alkylperoxo complexes, thus providing the first benchmark parameters for this particular type of species. Subtle structural differences in the supporting ligands in these complexes are found to modulate the alkylperoxo O-O bond length, which ultimately influences reactivity. These observations are supported by both variable temperature kinetics measurements and theoretical computational insights. Correlations between various metrical, spectroscopic, and kinetic

parameters provide strong evidence that the decay pathway of each complex involves homolytic O-O bond cleavage, which has previously been unobserved for any Mn-O_2 species. The Mn(II) complexes used in this study are most of the same complexes described in Chapter 2; $[Mn^{II}(S^{Me2}N_4(6\text{-Me-DPEN}))](BF_4)$ (**1**), $[Mn^{II}(S^{Me2}N_4(2\text{-QuinoEN}))](BPh_4)\cdot MeCN$ (**2**), $[Mn^{II}(S^{Me2}N_4(6\text{-Me-DPPN}))](BPh_4)$ (**3**), $[Mn^{II}(S^{Me2}N_4(2\text{-QuinoPN}))](PF_6)$ (**4**), $[Mn^{II}(S^{Me2}N_4(tren))](PF_6)$ (**5**), $[Mn^{II}(S^{Me2}N_4(6\text{-H-DPEN}))(MeOH)](PF_6)\cdot MeOH$ (**6**), $[Mn^{II}(S^{Me2}N_4(6\text{-H-DPPN}))]_2(BF_4)_2$ (**7**), $[(Mn^{II}(S^{Me2}N_4(4\text{-OMe-3,5-Me-DPEN})))(Mn^{II}(S^{Me2}N_4(4\text{-OMe-3,4-Me-DPEN}))(Cl))(BF_4)\cdot Et_2O$ (**8**), $[Mn^{II}(HO^{Me2}N_4(6\text{-Me-DPEN})(CHO_2))](BPh_4)\cdot MeCN\cdot Et_2O$ (**9**), $[Mn^{II}(O^{Me2}N_4(6\text{-Me-DPPN}))](BPh_4)$ (**10**) (with revised labeling scheme, Scheme 5.1 – 5.2).

Scheme 5.1 ChemDraw representations of $[Mn^{II}(S^{Me2}N_4(6\text{-Me-DPEN}))]+$ (**1**), $[Mn^{II}(S^{Me2}N_4(2\text{-QuinoEN}))]^+$ (**2**), $[Mn^{II}(S^{Me2}N_4(6\text{-Me-DPPN}))]^+$ (**3**), $[Mn^{II}(S^{Me2}N_4(2\text{-QuinoPN}))]^+$ (**4**), $[Mn^{II}(S^{Me2}N_4(tren))]^+$ (**5**), and $[Mn^{II}(S^{Me2}N_4(6\text{-H-DPEN}))(MeOH)]+$ (**6**).

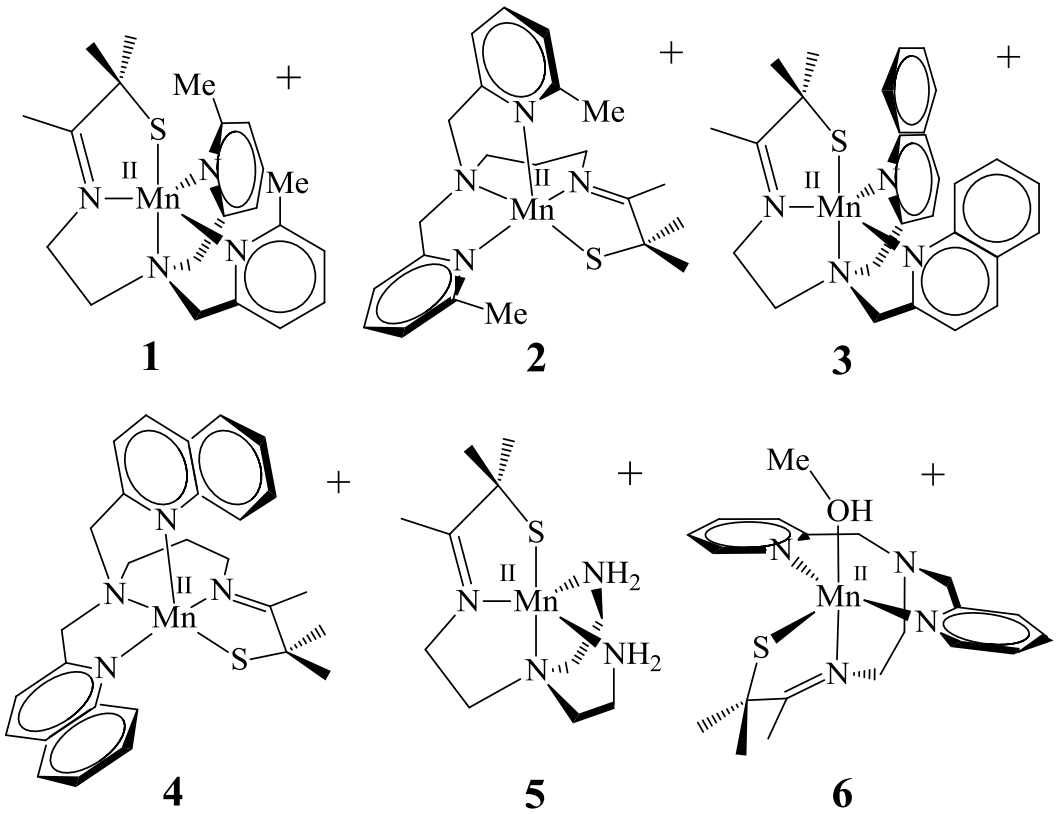

Scheme 5.2 ChemDraw representations of $\{[Mn^{II}(S^{Me2}N_4(6\text{-H-DPPN}))]_2\}^{2+}$ (**7**), $[(Mn^{II}(S^{Me2}N_4(4\text{-OMe-3,5-Me-DPEN})))(Mn^{II}(S^{Me2}N_4(4\text{-OMe-3,4-Me-DPEN}))(Cl))]^{+}$ (**8**), $[Mn^{II}(HO^{Me2}N_4(6\text{-Me-DPEN})(CHO_2))]^{+}$ (**9**), and $[Mn^{II}(O^{Me2}N_4(6\text{-Me-DPPN}))]^{+}$ (**10**).

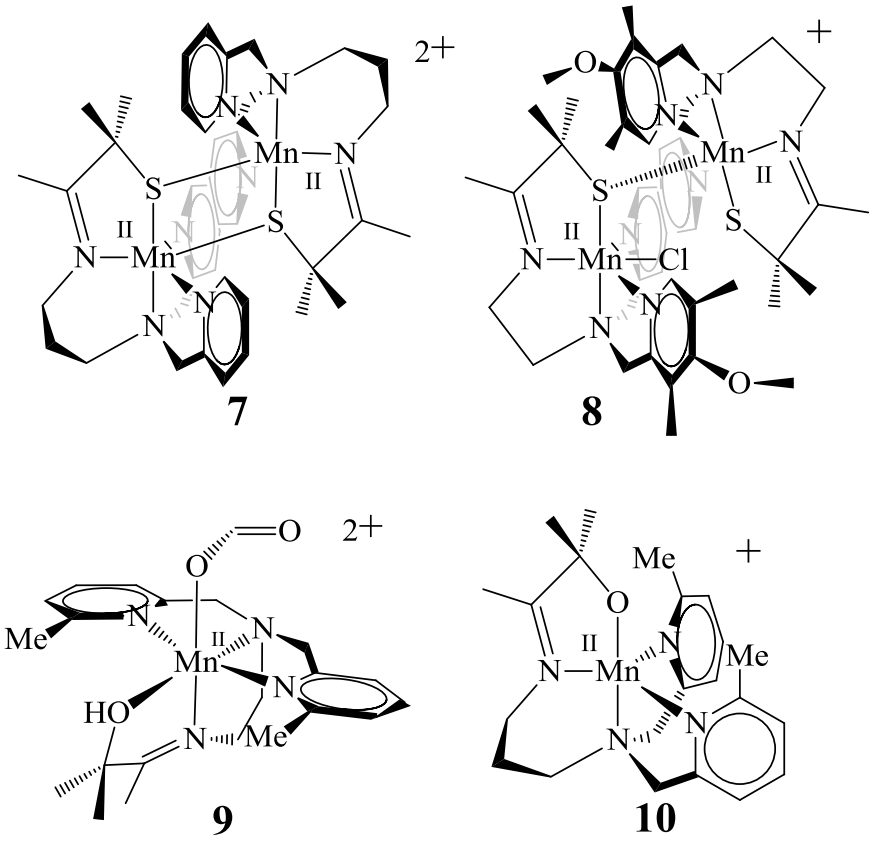

5.2 Experimental Section

5.2.1 General Considerations

All manipulations were performed using Schlenk techniques or under an N_2 atmosphere in a glovebox. Reagents and solvents were purchased from commercial vendors, were of highest available purity, and were used without further purification unless otherwise noted. MeOH (Na), MeCN (CaH_2), and CH_2Cl_2 (CaH_2) were dried and distilled prior to use. Et_2O was rigorously degassed and purified using solvent purification columns housed in a custom stainless steel cabinet and dispensed by a stainless steel schlenk-line (GlassContour). ^1H NMR spectra were

recorded on a Bruker AV 300 FT NMR spectrometer at ambient temperature and were referenced to residual deuterated solvent. UV/Vis spectra were recorded on a Varian Cary 50 spectrophotometer equipped with a fiber optic cable connected to a "dip" ATR probe (C-technologies). A custom-built two-neck solution sample holder equipped with a threaded glass connector was sized specifically to fit the "dip" probe. Electrospray-ionization mass spectrometry (ESI-MS) data were obtained on a Bruker Esquire Liquid Chromatograph-Ion Trap mass spectrometer. Gas chromatography-mass spectrometry (GC/MS) data were obtained using a 5890 gas chromatograph equipped with a 7673A autosampler and interfaced with a 5971A mass spectrometer, all from Hewlett Packard Co. Calibration curves for analytes of interest were made using either *m*-xylene or toluene as an internal reference. FT-IR spectra were recorded on a Perkin-Elmer 1700 FT-IR spectrometer as nujol mulls of NaCl salt plate. EPR spectra were recorded on a Bruker E580 CW-EPR spectrometer operating at X-band frequency and equipped with an Oxford helium cryostat and dual mode cavity. EPR data were fit with EasySpin toolbox for MATLAB.[33] Solid state magnetic susceptibility data were fit with the julX software program.[34] Pascal's constants were used to correct for diamagnetic contributions to experimental magnetic moments. Solution magnetic moments were determined by the Evans method.[35] X-ray crystallography data were recorded on a Bruker APEX II single crystal X-ray diffractometer with Mo Kα radiation. Complexes **1**-**10** were synthesized as described in Chapter 2 with $NaBPh_4$ used instead of $NaBF_4$ or $NaPF_6$, while $^{t}Bu^{18}O^{18}OH$ and $Et_2PO^{t}Bu$ were each synthesized as previously described.[36-37]

5.2.2 Preparation of $[Mn^{III}(S^{Me2}N_4(6\text{-Me-DPEN}))(OO^{t}Bu)](BPh_4)$ (1·OO^{t}Bu), $[Mn^{III}(S^{Me2}N_4(6\text{-Me-DPEN}))(OOCm)](BPh_4)$ (1·OOCm), $[Mn^{III}(S^{Me2}N_4(2\text{-QuinoEN}))(OO^{t}Bu)](BPh_4)$ (2·OO^{t}Bu), $[Mn^{III}(S^{Me2}N_4(2\text{-QuinoEN}))(OOCm)](BPh_4)$

(2·OOCm), [Mn^{III}($S^{Me2}N_4$(6-Me-DPPN))(OO^tBu)](BPh_4)·Et_2O (3·OO^tBu), [Mn^{III}($S^{Me2}N_4$(2-QuinoPN))(OO^tBu)](PF_6)·pentane (4·OO^tBu), and [Mn^{III}($O^{Me2}N_4$(6-Me-DPEN))(OO^tBu)](BPh_4)·Et_2O (5·OO^tBu) for UV/Vis Spectroscopic Characterization

In a typical reaction, a 1-2 mM solution of the requisite Mn(II) precursor was prepared in CH_2Cl_2 (3-4 mL) inside a glovebox. The resulting solution was transferred by a gas-tight syringe to a custom-made two-neck vial equipped with a stir bar, septrum cap, and threated dip-probe feed-through adaptor that had previously been purged with argon. The solution was then cooled to 258 K using an ethylene glycol/dry ice bath. Tert-butyl hydroperoxide (^tBuOOH, 1.5 equivalents from a 0.1 M anaerobic stock solution in CH_2Cl_2) was added via syringe to a stirring Mn(II) solution along with 2.0 equivalents of triethylamine. Scans were recorded from 300-1000 nm in one minute intervals until observable changes in each respective absorption spectrum ceased for approximately 10 minutes.

5.2.3 Preparation of [Mn^{III}($S^{Me2}N_4$(6-Me-DPEN))(OO^tBu)](BPh_4) (1·OO^tBu), [Mn^{III}($S^{Me2}N_4$(2-QuinoEN))(OO^tBu)](BPh_4) (2·OO^tBu), [Mn^{III}($S^{Me2}N_4$(6-Me-DPPN))(OO^tBu)](BPh_4)·Et_2O (3·OO^tBu), [Mn^{III}($S^{Me2}N_4$(2-QuinoPN))(OO^tBu)](PF_6)·pentane (4·OO^tBu), and [Mn^{III}($O^{Me2}N_4$(6-Me-DPEN))(OO^tBu)](BPh_4)·Et_2O (5·OO^tBu) for FT-IR Spectroscopic Characterization

Solid samples of **1·OO^tBu - 5·OO^tBu** were obtained immediately following *in situ* generation of each respective intermediate via precipitation from a concentrated reaction mixture. In a typical experiment, a 20-35 mM supersaturated solution of the appropriate Mn(II) precursor was prepared in MeCN (2-3 mL) in a glovebox. The resulting solution was then transferred to an anaerobic vial (as was described for the for the UV/Vis experiments above) and

was cooled to 233 K for 10 minutes. ^{t}BuOOH (2.0 equivalents) was then added from an anaerobic 1 M stock solution (CH_2Cl_2). The resulting reaction mixture was allowed to stir for 5-7 minutes. Cold Et_2O (10-15 mL) was quickly added to the reaction mixture to promote the rapid precipitation of solid material. The resulting solid was isolated via filtration, mixed with cold nujol, and immediately analyzed by FT-IR. The identity of the sample was verified by redissolving the solid material in cold CH_2Cl_2 and recorded a UV/Vis spectrum, which revealed spectral features identical to those observed from the *in situ* generation and characterization of each intermediate.

5.2.4 Variable-Temperature Kinetics and Reactivity Studies With $[Mn^{III}(S^{Me2}N_4$(6-Me-DPEN))$(OO^tBu)](BPh_4)$ (1·OO^{t}Bu), $[Mn^{III}(S^{Me2}N_4$(6-Me-DPEN))(OOCm)$](BPh_4)$ (1·OOCm), $[Mn^{III}(S^{Me2}N_4$(2-QuinoEN))$(OO^tBu)](BPh_4)$ (2·OO^{t}Bu), $[Mn^{III}(S^{Me2}N_4$(6-Me-DPPN))$(OO^tBu)](BPh_4)\cdot Et_2O$ (3·OO^{t}Bu), and $[Mn^{III}(S^{Me2}N_4$(2-QuinoPN))$(OO^tBu)](PF_6)\cdot$pentane (4·OO^{t}Bu)

In a typical experiment, a 1-2 mM solution of each requisite Mn(II) complex (4 mL in CH_2Cl_2) was prepared under an inert atmosphere in a glovebox. The resulting solution was then transferred via gas-tight syringe to a custom-made two-neck vial equipped with a stir bar, septum cap, and threaded dip-probe feed-through adaptor that had previously been purged with argon. Each respective solution was brought to the desired temperature using low temperature baths (258 K, ethylene glycol/dry ice; 268 K, NaCl/ice water; 273 K, ice water). Gentle stirring was maintained throughout the course of each experiment in order to maintain solution homogeneity. ^{t}BuOOH (1.5 equivalents) was added in a single aliquot to the Mn(II) solution, causing an immediate production of the corresponding Mn(III)-OO^{t}Bu intermediate as indicated by changes in the respective UV/Vis absorption spectrum. Decay of each respective intermediate was

monitored at the low energy visible region λ_{max} once formation was complete. UV/Vis scans were recorded at 1 minute intervals until no further change in absorbance intensity occurred for at least 10 minutes. First-order rate constants were calculated by plotting $\ln[(A_x-A_\infty)/(A_0-A_\infty)]$ versus time. Experiments were conducted in at least triplicate under any given set of reaction conditions.

Reactions between each Mn(III)-OO^{t}Bu intermediate and various substrates were performed in an analogous fashion by adding the substrate to the fully-formed intermediate in a single aliquot at either 273 K or 298 K. Concentrated stock solutions of each substrate were prepared under an inert atmosphere in a glovebox and transferred to the reaction solution with a gas-tight syringe. After changes in absorbance values ceased for at least 10 minutes, insoluble were removed from the crude reaction mixtures by filtration through a fine-fritted filter. Soluble organics were diluted with an appropriate amount of CH_2Cl_2 and analyzed by GC/MS. Products were identified by comparison with authentic standards and product yields were determined using calibration curves referenced to 1,4-dioxane as an internal standard.

5.2.5 General Work-Up Procedure for Analysis of the Thermal Decomposition Products From $[Mn^{III}(S^{Me2}N_4$(6-Me-DPEN))$(OO^tBu)](BPh_4)$ (1·OO^{t}Bu), $[Mn^{III}(S^{Me2}N_4$(6-Me-DPEN))$(OOCm)](BPh_4)$ (1·OOCm), $[Mn^{III}(S^{Me2}N_4$(2-QuinoEN))$(OO^tBu)](BPh_4)$ (2·OO^{t}Bu), $[Mn^{III}(S^{Me2}N_4$(2-QuinoEN))$(OOCm)](BPh_4)$ (2·OOCm), $[Mn^{III}(S^{Me2}N_4$(6-Me-DPPN))$(OO^tBu)](BPh_4)\cdot Et_2O$ (3·OO^{t}Bu), $[Mn^{III}(S^{Me2}N_4$(2-QuinoPN))$(OO^tBu)](PF_6)$·pentane (4·OO^{t}Bu), and $[Mn^{III}(O^{Me2}N_4$(6-Me-DPEN))$(OO^tBu)](BPh_4)$ (5·OO^{t}Bu)

In a typical reaction, a 1-2 mM solution of the desired intermediate was prepared in a fashion identical to that described above at 273 K in CH_2Cl_2. Reactions were allowed to progress until the absorption features of the respective Mn(III)-OOR intermediate bleached and no further changes to the absorption spectrum were observed for at least 1 hour. The final reaction mixtures were found to contain white insoluble solids, black insoluble solids, and components soluble in CH_2Cl_2. Insolubles were removed by filtering each reaction through a fine-fritted filter. In order to identify the CH_2Cl_2 soluble reaction mixture components, all volatiles were distilled *in vacuo* to a separate container. Non-volatile components remaining in the initial sample container were then analyzed by ^{1}H NMR spectroscopy and ESI-MS, while volatile components were analyzed by ^{1}H NMR spectroscopy and GC/MS. The clear and black insoluble reaction mixture components were separated by suspending these products in $CHCl_3$, which caused the white solid product to dissolve and leaving the insoluble black precipitate. After filtration to separate the black insoluble precipitate, the resulting $CHCl_3$ solution was dried in vacuo, redissolved in $CDCl_3$, and analyzed by ^{1}H NMR spectroscopy, ESI-MS, and GC/MS.

5.2.6 *Ab Initio* Density Functional Theory Calculations

All calculations were performed using the ORCA program package.[38] Geometries were optimized based on coordinated from X-ray crystal structures and with a high-spin state using the TPSS functional and the def3-TZVP(-f) basis set in combination with the def2-TZV/J auxiliary basis set for the Coulomb density fitting approximation.[39-46] Scalar relativistic effects were accounted for using the ZORA approximation and a conductor-like screening model was applied using CH_2Cl_2 as the solvent (COSMO, ε = 9.08). Minimum deviations from the crystallographically-determined geometries, bond angles, and bond distances were obtained when intramolecular Van der Waals interactions were accounted for using the vdw10 keyword.

All calculations were performed using an integration grid of 5 (Grid5) for the complex and a grid of 7 for the Mn(III) ion. Relaxed surface scans were performed on the O-O bond length from 1.1 to 1.6 Å to explore the impact the alkylperoxo bond length has on the coordination sphere of the Mn ion.

5.2.7 X-ray Crystallographic Structure Determination

A blue prism of **1·OO^{t}Bu** with dimensions 0.15 x 0.10 x 0.05 mm^3 was mounted on a glass capillary with oil. Data was collected at -173 ˚C. The crystal-to-detector distance was set to 40 mm and the exposure time was 120 seconds per degree for all sets of exposure. The scan width was 0.5˚. Data collection was 98.9% complete to 25.0˚ in ϑ. A total of 76,962 partial and complete reflections were collected covering the indices h = -20 to 20, k = -30 to 30, l = -13 to 13. 4,716 reflections were symmetry independent and the R_{int} = 0.4200 indicated that the data was poor (0.07 average quality). Indexing and unit cell refinement indicated an orthorhombic P lattice with the space group P n a 2_1 (No.33).

A blue plate of **1·OOCm** with dimensions 0.10 x 0.05 x 0.05 mm^3 was mounted on a glass capillary with oil. Data was collected at -173 ˚C. The crystal-to-detector distance was set to 40 mm and the exposure time was 20 seconds per degree for all sets of exposure. The scan width was 0.5˚. Data collection was 98.8% complete to 25.0˚ in ϑ. The raw data was twinned. A 4.3° rotation twin operation about (0 0 1) was found with CELL_NOW, which would have caused considerable overlap with diffraction peak intensities from different domains of the sample if left unresolved. A total of 66,667 partial and complete reflections were collected covering the indices h = -15 to 15, k = -16 to 11, l = 0 to 18. 9,356 reflections were symmetry independent and the R_{int} = 0.2165 indicated that the twin-refined data was acceptable (0.07

average quality). Indexing and unit cell refinement indicated a triclinic P lattice with the space group P $\bar{1}$ (No.2). The asymmetric unit was found to contain a CH_2Cl_2 and Et_2O molecule occupying the same space.

A blue plate of **2·OO^{t}Bu** with dimensions 0.10 x 0.10 x 0.10 mm^3 was mounted on a glass capillary with oil. Data was collected at -173 ˚C. The crystal-to-detector distance was set to 40 mm and the exposure time was 60 seconds per degree for all sets of exposure. The scan width was 0.5˚. Data collection was 97.3% complete to 25.0˚ in ϑ. A total of 37,037 partial and complete reflections were collected covering the indices h = -15 to 16, k = -15 to 16, l = -17 to 18. 9,786 reflections were symmetry independent and the R_{int} = 0.3890 indicated that the data was poor (0.07 average quality). Indexing and unit cell refinement indicated a triclinic P lattice with the space group P $\bar{1}$ (No.2).

A green needle of **2·OOCm** with dimensions 0.25 x 0.10 x 0.05 mm^3 was mounted on a glass capillary with oil. Data was collected at -173 ˚C. The crystal-to-detector distance was set to 40 mm and the exposure time was 50 seconds per degree for all sets of exposure. The scan width was 0.5˚. Data collection was 90.9% complete to 25.0˚ in ϑ. The raw data was twinned with the transformation matrix (-1 0 0, 0 -1 0, -0.135 -0.683 1). Although a similar twin law was found with CELL_NOW, the overlap of diffraction peak intensities was not resolved with multi-domain integration or absorption correction.[47] Instead, the twin law was applied within the refinement, which led to a considerable reduction of the R1 value, but not a complete removal of intensity overlap. A total of 52,214 partial and complete reflections were collected covering the indices h = -18 to 18, k = -24 to 24, l = -25 to 52. 19,485 reflections were symmetry independent and the R_{int} = 0.4497 indicated that the twinned data was very poor (0.07 average quality).

Indexing and unit cell refinement indicated a triclinic P lattice with the space group P $\bar{1}$ (No.2). The asymmetric unit consists of two Mn(III)-OOR complexes, two Et_2O molecules, two BPh_4^- counterions, and two acetonitrile molecules. Each Mn complex was symmetry-independent of the other and found to contain unique metrical parameters; these two complexes are referred to as **2·OOCm-A** and **2·OOCm-B**.

A blue block of **3·OO^{t}Bu** with dimensions 0.25 x 0.20 x 0.10 mm^3 was mounted on a glass capillary with oil. Data was collected at -173 ˚C. The crystal-to-detector distance was set to 40 mm and the exposure time was 10 seconds per degree for all sets of exposure. The scan width was 0.5˚. Data collection was 98.0% complete to 25.0˚ in ϑ. A total of 32,127 partial and complete reflections were collected covering the indices h = -11 to 11, k = -14 to 17, l = -19 to 19. 7,856 reflections were symmetry independent and the R_{int} = 0.0766 indicated that the data was acceptable (0.07 average quality). Indexing and unit cell refinement indicated a triclinic P lattice with the space group P $\bar{1}$ (No.2).

A blue block of **4·OO^{t}Bu** with dimensions 0.15 x 0.15 x 0.05 mm^3 was mounted on a glass capillary with oil. Data was collected at -173 ˚C. The crystal-to-detector distance was set to 40 mm and the exposure time was 10 seconds per degree for all sets of exposure. The scan width was 0.5˚. Data collection was 100% complete to 25.0˚ in ϑ. A total of 49,617 partial and complete reflections were collected covering the indices h = -12 to 12, k = -17 to 17, l = -28 to 28. 6,557 reflections were symmetry independent and the R_{int} = 0.0875 indicated that the data was less than average quality (0.07 average quality). Indexing and unit cell refinement indicated a monoclinic P lattice with the space group P $2_1/n$ (No.14). The asymmetric unit contains one

disordered pentane molecule that likely contributes to some disorder in one quinoline moiety in the Mn complex.

A blue plate of **5·OO^{t}Bu** with dimensions 0.60 x 0.10 x 0.05 mm^3 was mounted on a glass capillary with oil. Data was collected at -173 ˚C. The crystal-to-detector distance was set to 40 mm and the exposure time was 10 seconds per degree for all sets of exposure. The scan width was 0.5˚. Data collection was 100% complete to 25.0˚ in ϑ. A total of 160,795 partial and complete reflections were collected covering the indices h = -22 to 22, k = -33 to 33, l = -15 to 15. 12,081 reflections were symmetry independent and the R_{int} = 0.0408 indicated that the data was good (0.07 average quality). Indexing and unit cell refinement indicated an orthorhombic P lattice with the space group P n a 2 (No.33).

A black block of **11** with dimensions 0.25 x 0.20 x 0.10 mm^3 was mounted on a glass capillary with oil. Data was collected at -173 ˚C. The crystal-to-detector distance was set to 40 mm and the exposure time was 10 seconds per degree for all sets of exposure. The scan width was 0.5˚. Data collection was 100% complete to 25.0˚ in ϑ. A total of 61,494 partial and complete reflections were collected covering the indices h = -10 to 13, k = -38 to 34, l = -16 to 18. 9,475 reflections were symmetry independent and the R_{int} = 0.0693 indicated that the data was good (0.07 average quality). Indexing and unit cell refinement indicated a monoclinic P lattice with the space group P 2_1/c (No.14).

A colorless plate of **12** with dimensions 0.10 x 0.05 x 0.05 mm^3 was mounted on a glass capillary with oil. Data was collected at -173 ˚C. The crystal-to-detector distance was set to 40 mm and the exposure time was 20 seconds per degree for all sets of exposure. The scan width was 0.5˚. Data collection was 99.9% complete to 25.0˚ in ϑ. A total of 138,191 partial and

complete reflections were collected covering the indices h = -21 to 21, k = -18 to 18, l = -23 to 23. 9,679 reflections were symmetry independent and the R_{int} = 0.0675 indicated that the data was good (0.07 average quality). Indexing and unit cell refinement indicated a monoclinic P lattice with the space group P $\bar{1}$ (No.33).

A yellow prism of **13** with dimensions 0.15 x 0.05 x 0.05 mm^3 was mounted on a glass capillary with oil. Data was collected at -173 ˚C. The crystal-to-detector distance was set to 40 mm and the exposure time was 20 seconds per degree for all sets of exposure. The scan width was 0.5˚. Data collection was 96.5% complete to 25.0˚ in ϑ. A total of 22,505 partial and complete reflections were collected covering the indices h = -16 to 16, k = -16 to 16, l = -18 to 18. 8,374 reflections were symmetry independent and the R_{int} = 0.0994 indicated that the data was good (0.07 average quality). Indexing and unit cell refinement indicated a monoclinic P lattice with the space group P $2_1/n$ (No.14).

A colorless plate of N,N-bis(6-methyl-2-pyridilmethyl)ethane-1,2-diamine with dimensions 0.20 x 0.20 x 0.15 mm^3 was mounted on a glass capillary with oil. Data was collected at -173 ˚C. The crystal-to-detector distance was set to 40 mm and the exposure time was 10 seconds per degree for all sets of exposure. The scan width was 0.5˚. Data collection was 99.4% complete to 25.0˚ in ϑ. A total of 63,341 partial and complete reflections were collected covering the indices h = -13 to 13, k = -17 to 17, l = -18 to 18. 8,954 reflections were symmetry independent and the R_{int} = 0.0519 indicated that the data was good (0.07 average quality). Indexing and unit cell refinement indicated a triclinic P lattice with the space group P $\bar{1}$ (No.2).

A colorless plate of N,N-bis(2-quinolinemethyl)propane-1,3-diamine with dimensions 0.10 x 0.10 x 0.15 mm^3 was mounted on a glass capillary with oil. Data was collected at -173 ˚C. The crystal-to-detector distance was set to 40 mm and the exposure time was 20 seconds per degree for all sets of exposure. The scan width was 0.5˚. Data collection was 95.5% complete to 25.0˚ in ϑ. A total of 178,295 partial and complete reflections were collected covering the indices h = -24 to 24, k = -19 to 19, l = -27 to 27. 12,558 reflections were symmetry independent and the R_{int} = 0.1201 indicated that the data was less than good (0.07 average quality). Indexing and unit cell refinement indicated a monoclinic P lattice with the space group P $2_1/n$ (No.2).

All X-ray data sets were integrated and scaled using SAINT, SADABS within the APEX2 software package by Bruker.[48] Solutions were made by direct methods (SHELXS, SIR97) to produce complete heavy atom phasing models. Scattering factors are from Waasmair and Kirfel.[49] Structures were completed by difference Fourier synthesis with either SHELXL97 or SHELXTL 6.10.[50] Hydrogen atoms were placed in geometrically idealized positions and constrained to ride on their parent atoms with C-H distances in the range of 0.95-1.00 Å. Isotropic thermal parameters Ueq were fixed such that they were 1.2Ueq of their parent aom Ueq for C-Hs and 1.5Ueq for methyl groups. All non-hydrogen atoms were refined anisotropically by full-matrix least-squares.

5.3 Results and Discussion

5.3.1 Reactivity of Thiolate-Ligated Complexes 1-8 With *tert*-Butyl Hydroperoxide

5.3.1.1 General Observations From Reactions With Complexes 1-4

Anaerobic reactions between five-coordinate complexes **1-4** and *tert*-butyl hydroperoxide (^{t}BuOOH) were performed with 2.0 equivalents of triethylamine in CH_2Cl_2 solutions and

monitored by UV/Vis spectroscopy. Addition of ^{t}BuOOH into clear solutions of each respective Mn(II) complex promoted the formation of new blue species characterized by distinct visible region absorption bands centered between 560-605 nm. The intensity of each absorption band maximized following the addition of 1.5-1.8 equivalents of ^{t}BuOOH per equivalent of Mn(II) (Figure 5.1 and Appendix A.40-A.42). Spectral features of these products rapidly bleached over 10-30 minutes, even at low temperatures (258 K), suggesting that these are intermediate species.

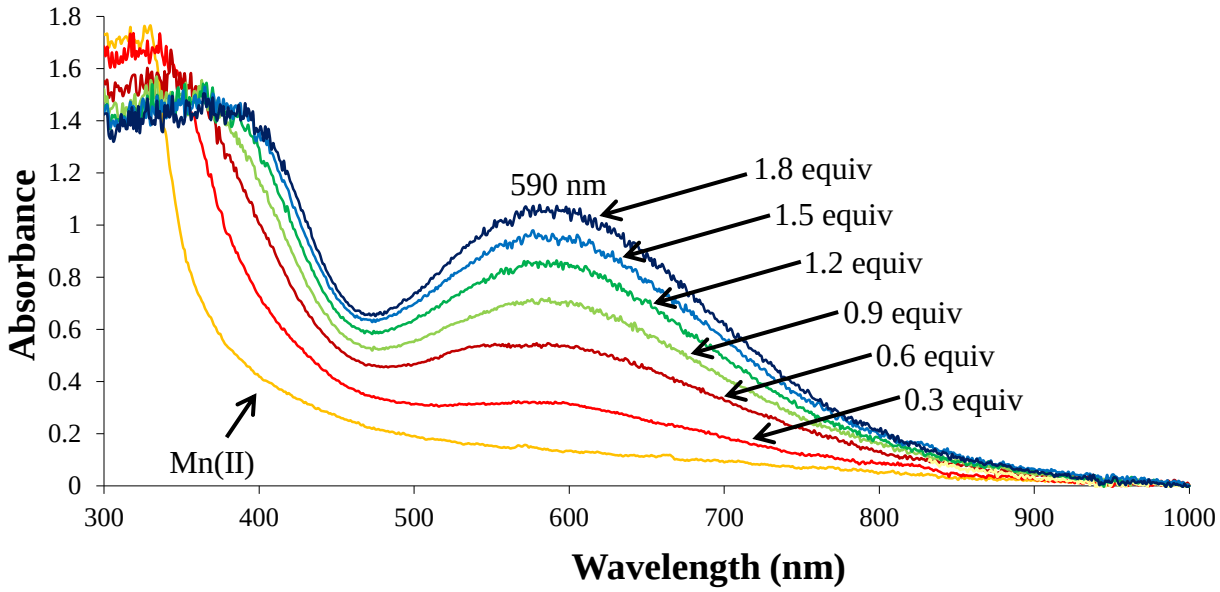

Figure 5.1 Anaerobic UV/Vis titration experiment displaying the reaction between [$Mn^{II}(S^{Me2}N_4$(2-QuinoEN))](BPh$_4$)·MeCN (**2**, 2.4 mM) and 0.3 equivalent aliquots of ^{t}BuOOH (0.1 M stock solution in CH_2Cl_2) with 2.0 equivalents of triethylamine in CH_2Cl_2 at 258 K.

Initial attempts to identify these transient complexes were made by analyzing freshly prepared solutions of each respective intermediate by ESI mass spectrometry. Prominent peaks in the mass spectra of these intermediates were observed at *m/z* = 513.0 (**1**), 585.2 (**2**), 526.9 (**3**), and 598.8 (**4**); each peak is very close to the theoretical mass of the respective [Mn(III)-OO^{t}Bu]$^{+}$ species (*m/z* = 513.6 (**1**, calc), 585.1 (**2**, calc), 526.6 (**3**, calc), 598.6 (**4**, calc). Each of these peaks were also found to shift by approximately 4 mass units when prepared from ^{t}Bu^{18}O^{18}OH to *m/z* =

516.9 (**1**-^{18}O), 589.1 (**2**-^{18}O), 530.8 (**3**-^{18}O), 602.7 (**4**-^{18}O), further supporting the identification of these species as Mn(III)-OO^{t}Bu intermediates (Figure 5.2 and Appendix A.43-A.45). Further structural and spectroscopic data for these intermediates have also been obtained and are discussed in the proceeding sections below.

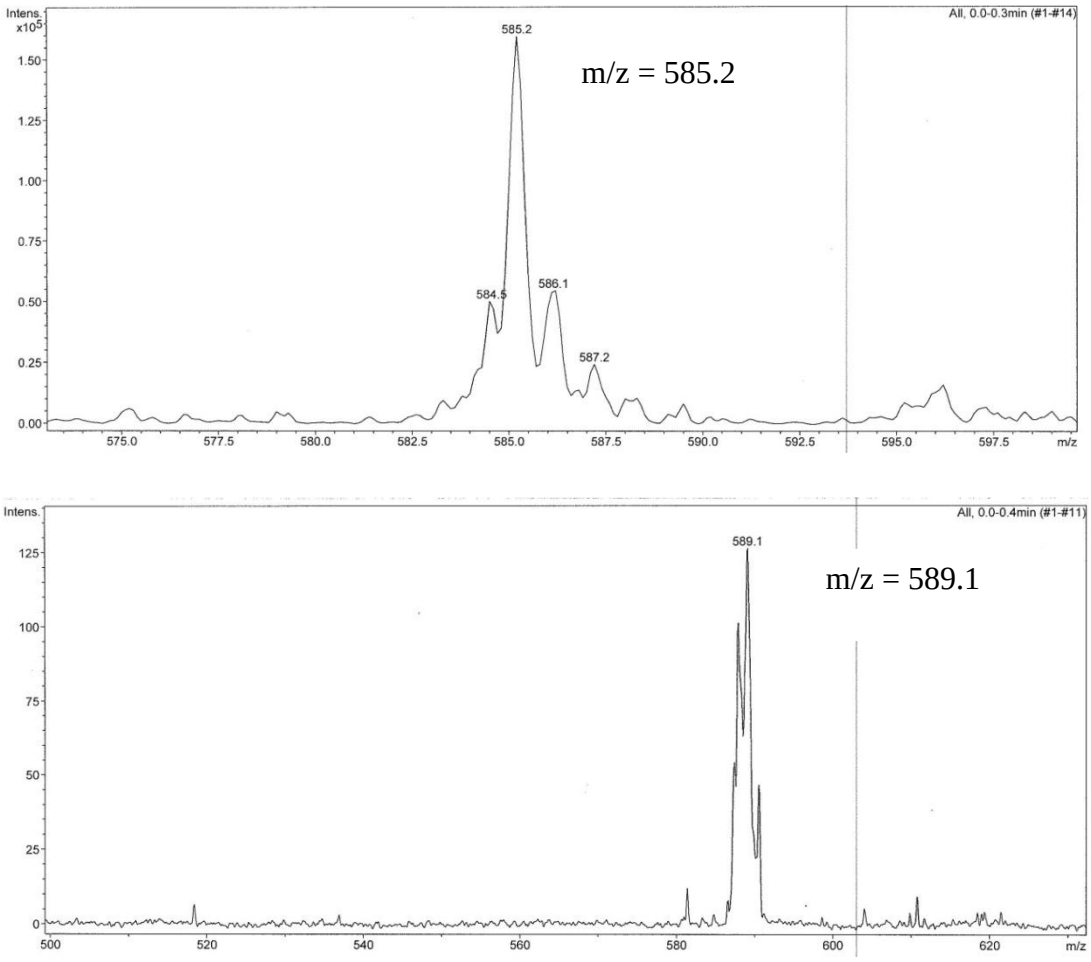

Figure 5.2 ESI mass spectra obtained from solutions containing the intermediate formed between [Mn^{II}(S^{Me2}N$_4$(2-QuinoEN))](BPh$_4$)·MeCN (**2**, 1 mM) and either ^{t}Bu^{16}O^{16}OH (top) or ^{t}Bu^{18}O^{18}OH (bottom).

5.3.1.2 General Observations From Reactions With Complexes 5-8

Reactions between complexes **5-8** and ^{t}BuOOH (along with 2.0 equivalents of triethylamine) were also explored in anaerobic CH_2Cl_2 solutions and monitored by UV/Vis

spectroscopy. Under these conditions, each reaction was found to result in quantitative formation of the respective oxo-bridged Mn(III,III) dimer (which were described in Chapter 3). These transformations were found to require roughly 0.5 equivalents of ^{t}BuOOH per equivalent of Mn(II) for complete formation of the respective oxo-bridged dimer product. In the absence of triethylamine, each of these reactions yielded multiple products, many of which have thus far been unidentified. A few small X-ray quality crystals of a product from reactions involving complex **8** were obtained and analyzed to reveal this product is a six-coordinate 3-methyl-3-thiolate-2-butanone-ligated Mn(III) species (**11**). An ORTEP diagram of [Mn^{III}($S^{Me2}N_4$(4-OMe-3,5-Me-DPEN))(3-methyl-3-thiolate-2-butanone)](PF6)·MeCN (**11**) is provided in Figure 5.3, while crystal data is compiled in Table 5.1. No intermediates were observed during any of these reactions by low temperature UV/Vis spectroscopy, therefore further reactions between **5**-**8** and ^{t}BuOOH were not pursued.

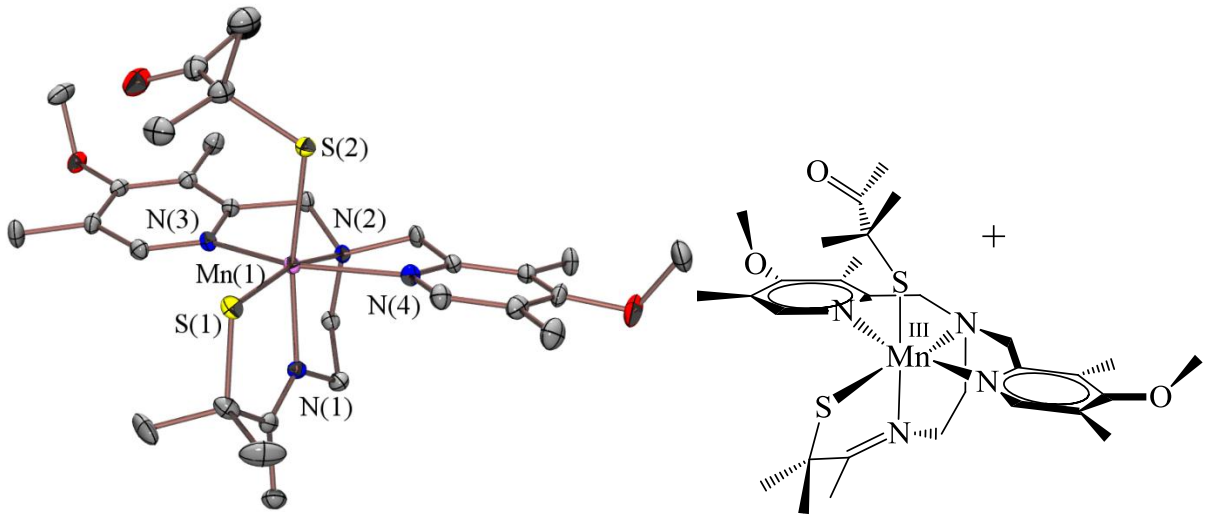

Figure 5.3 ORTEP diagram (50 % probability, left) and ChemDraw representation (right) of [Mn^{III}($S^{Me2}N_4$(4-OMe-3,5-Me-DPEN))(3-methyl-3-thiolate-2-butanone)]$^{+}$ (**11**) with hydrogen atoms, counterion, and solvent of crystallization omitted for clarity. Selected bond distances (Å) and angles (deg); Mn(1)-S(1), 2.2671(9); Mn(1)-N(1), 2.024(2); Mn(1)-N(2), 2.235(3); Mn(1)-N(3), 2.254(3); Mn(1)-N(4), 2.235(3); Mn(1)-S(2), 2.2956(9); S(1)-Mn(1)-N(1), 82.91(7); S(1)-Mn(1)-N(2), 165.84(7); S(1)-Mn(1)-N(3), 105.90(7); S(1)-Mn(1)-N(4), 105.73(7); S(1)-Mn(1)-S(2), 95.87(3); N(3)-Mn(1)-N(4), 148.12(9); N(1)-Mn(1)-S(2), 169.35(8).

5.3.2 Structural Characterization of Mn(III)-OOR Intermediates 1·OO^{t}Bu - 4·OO^{t}Bu

The blue intermediate formed in each respective reaction between complexes **1-4** and ^{t}BuOOH were conclusively identified as Mn(III)-OO^{t}Bu species by X-ray crystallography. X-ray quality crystals of each intermediate were obtained by layering either pentane or Et_2O onto concentrated CH_2Cl_2 solutions of each respective intermediate (**1·OO^{t}Bu - 4·OO^{t}Bu**) at 193 K. ORTEP diagrams of [Mn^{III}($S^{Me2}N_4$(6-Me-DPEN))(OO^{t}Bu)](BPh$_4$) (**1·OO^{t}Bu**), [Mn^{III}($S^{Me2}N_4$(2-QuinoEN))(OO^{t}Bu)](BPh$_4$) (**2·OO^{t}Bu**), [Mn^{III}($S^{Me2}N_4$(6-Me-DPPN))(OO^{t}Bu)](BPh$_4$)·Et_2O (**3·OO^{t}Bu**), and [Mn^{III}($S^{Me2}N_4$(2-QuinoPN))(OO^{t}Bu)](PF_6)·pentane (**4·OO^{t}Bu**) are provided in Figure 5.4, while crystal data and selected metrical parameters are provided in Tables 5.1 and 5.2, respectively. Molecular representations of **1·OO^{t}Bu - 4·OO^{t}Bu** are also shown in Scheme 5.3. The presence of a single anionic counterion per Mn complex reveals that **1·OO^{t}Bu - 4·OO^{t}Bu** are each monocationic. The +3 oxidation state of each Mn ion in **1·OO^{t}Bu - 4·OO^{t}Bu** is evident from the Mn(1)-S(1) bond distances (2.241(3)-2.270(3) Å), which are each ~0.1 Å shorter than those found in complexes **1**-**4**, but similar to those in the oxo- and peroxo-bridged Mn(III,III) dimers discussed in Chapters 3 and 4, respectively (Table 5.2). The only other Mn-OOR species reported is that by Moro-oka, [Tp^{tBu,iPr}Mn(OO^{t}Bu)], which was found to contain a Mn(II) ion; these complexes, therefore, constitute the first examples of Mn(III)-OOR species.[32]

The Mn(III) ion in each Mn-OOR complex is coordinated by an alkylperoxo oxygen (O(1)), thiolate sulfur (S(1)), imine nitrogen (N(1)), and tertiary amine (N(2)) (Figure 5.4). The distances between each of the two N-heterocyclic nitrogens (N(3) and N(4)) and respective Mn(III) ion in each complex are considerably elongated (2.349(7)-2.527(14) Å, Table 5.2) to the

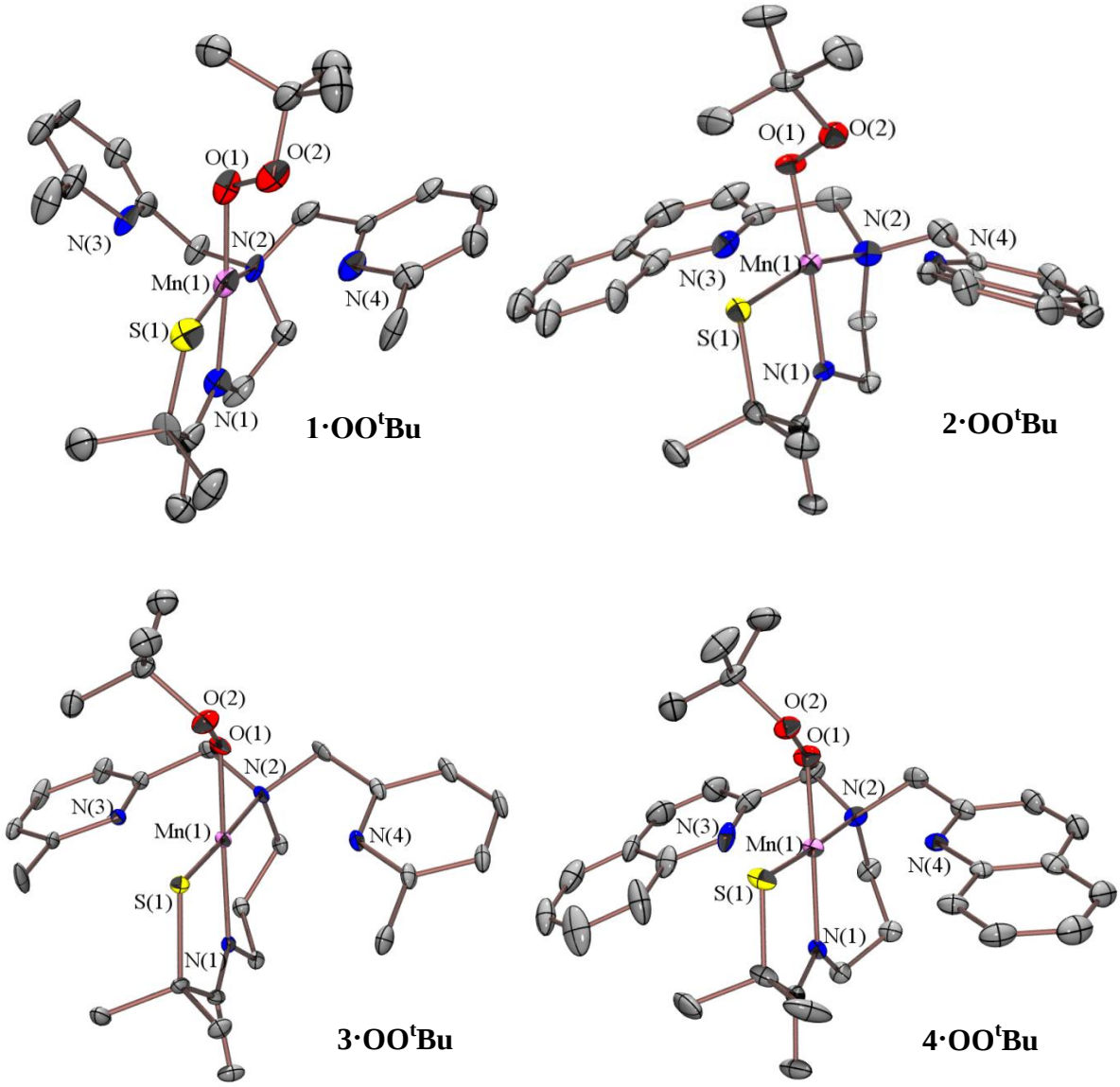

Figure 5.4 ORTEP diagrams (50 % probability) of $[Mn^{III}(S^{Me2}N_4(6\text{-Me-DPEN}))(OO^tBu)]^+$ (**1·OO^{t}Bu**, top left), $[Mn^{III}(S^{Me2}N_4(2\text{-QuinoEN}))(OO^tBu)]^+$ (**2·OO^{t}Bu**, top right), $[Mn^{III}(S^{Me2}N_4(6\text{-Me-DPPN}))(OO^tBu)]^+$ (**3·OO^{t}Bu**, bottom left), and $[Mn^{III}(S^{Me2}N_4(2\text{-QuinoPN}))(OO^tBu)]^+$ (**4·OO^{t}Bu**, bottom right) with hydrogen atoms, counterions, and solvents of crystallization omitted for clarity.

Scheme 5.3 ChemDraw representations of $[Mn^{III}(S^{Me2}N_4(6\text{-Me-DPEN}))(OO^tBu)]^+$ (**1·OO^{t}Bu**, top left), $[Mn^{III}(S^{Me2}N_4(2\text{-QuinoEN}))(OO^tBu)]^+$ (**2·OO^{t}Bu**, top right), $[Mn^{III}(S^{Me2}N_4(6\text{-Me-DPPN}))(OO^tBu)]^+$ (**3·OO^{t}Bu**, bottom left), and $[Mn^{III}(S^{Me2}N_4(2\text{-QuinoPN}))(OO^tBu)]^+$ (**4·OO^{t}Bu**, bottom right)

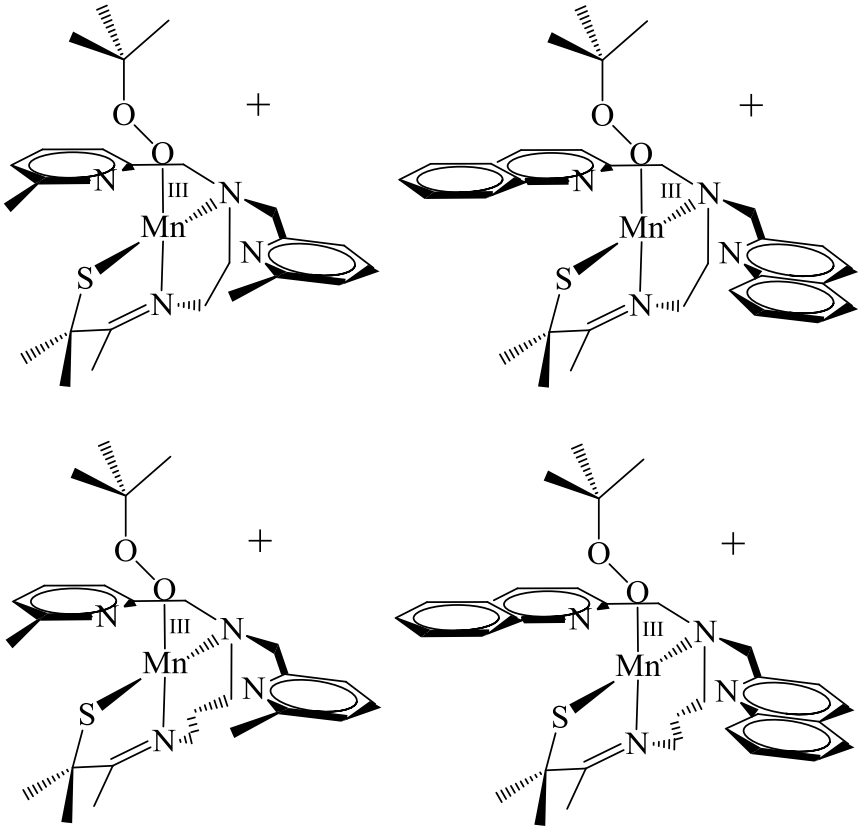

point that it calls into question whether or not these are formal bonding distances or simply ionic interactions. Given the sum of the ionic and covalent radii for a high-spin Mn(III) ion and sp^2-hybridized nitrogen is 2.105 Å, the X-ray structures of **1·OO^{t}Bu** - **4·OO^{t}Bu** are *best described* as being four-coordinate Mn(III) complexes with long range Mn-N(pyridine) or Mn-N(quinoline) interactions. Similar bond distances were also observed in the oxo- and peroxo-bridged Mn(III,III) dimers discussed in Chapters 3 and 4.[51] The Mn(III)···N(3,4) distances represent by far the largest structural variable (± 0.17 Å) within this series of complexes, as the Mn(III)-O(1), Mn(III)-N(1), Mn(III)-N(2), and Mn(III)-S(1) distances are well within

Table 5.1 Crystal data for **1·OO^{t}Bu** - **5·OO^{t}Bu**, **1·OOCm** - **2·OOCm**, and **9-11**.

	1·OO^{t}Bu	**1·OOCm**	**2·OO^{t}Bu**	**2·OOCm**	**3·OO^{t}Bu**
Formula	$C_{53}H_{68}BMnN_4O_3S$	$C_{56}H_{64.65}BCl_{1.34}MnN_4O_{2.33}S$	$C_{59}H_{68}BMnN_4O_3S$	$C_{66}H_{73}BMnN_5O_3S$	$C_{50}H_{60}BMnN_4O_2S$
MW	906.92	976.36	978.99	1082.10	846.83
T, K	100(2)	100(2)	100(2)	110(2)	100(2)
Unit Cell[a]	Orthorhombic	Triclinic	Triclinic	Triclinic	Triclinic
a, Å	17.265(2)	12.8928(18)	13.541(3)	15.098(5)	9.5420(7)
b, Å	25.499(3)	14.433(2)	13.757(4)	20.289(7)	14.5846(11)
c, Å	11.2048(14)	15.069(3)	14.826(4)	20.645(7)	16.4547(13)
α, deg	90	71.085(10)	73.397(14)	69.84(2)	77.689(4)
β, deg	90	77.463(10)	82.728(13)	83.47(2)	83.682(4)
γ, deg	90	82.463(9)	76.658(14)	78.29(2)	78.144(4)
V, Å^3	4932.7(11)	2583.7(7)	2569.9(11)	5806(3)	2184.3(3)
Z	4	2	2	4	2
d(calc), g/cm^3	1.221	1.255	1.265	1.238	1.288
Sp. Group	P n a 2_1	P -1	P $\bar{1}$	P -1	P $\bar{1}$
R[b]	0.0696	0.1004	0.0964	0.1620	0.0667
R_w[c]	0.1246	0.2391	0.1914	0.4441	0.1786
GOF	1.000	0.952	0.944	0.976	1.008
	4·OO^{t}Bu	**5·OO^{t}Bu**	**9**	**10**	**11**
Formula	$C_{69}H_{92}F_{12}Mn_2N_8O_2P_2S$	$C_{53}H_{68}BMnN_4O_4$	$C_{31}H48Cl_2F_6MnN_4O_3PS_2$	$C_{80}H_{86.29}B_2Mn_2N_8O_4$	$C_{90}H108B_2Mn_2N_8O_4$
MW	1561.45	890.86	859.66	1355.36	1497.34
T, K	100(2)	100(2)	100(2)	100(2)	100(2)
Unit Cell[a]	Monoclinic	Orthorhombic	Monoclinic	Triclinic	Monoclinic
a, Å	10.5559(8)	17.1020(17)	10.2310(6)	12.169(3)	15.926(2)
b, Å	14.0937(10)	25.273(3)	29.0291(19)	12.404(4)	13.8629(18)
c, Å	23.9583(16)	11.2735(10)	13.5288(9)	13.845(4)	17.620(3)
α, deg	90	90	90	69.752(7)	90
β, deg	94.560(4)	90	109.484(3)	67.355(8)	90.814(10)
γ, deg	90	90	90	68.725(7)	90
V, Å^3	3553.0(4)	4872.6(8)	3787.9(4)	1744.7(8)	3889.8(9)
Z	2	4	4	1	2
d(calc), g/cm^3	1.460	1.214	1.507	1.290	1.278
Sp. Group	P 2_1/n	P n a 2_1	P 2_1/c	P $\bar{1}$	P 2_1/n
R[b]	0.0688	0.0283	0.0514	0.0720	0.0846
R_w[c]	0.2088	0.669	0.1242	0.1577	0.2405
GOF	1.013	1.027	1.036	0.963	1.016

[a]In all cases: Mo Kα(λ = 0.7170 Å) radiation. [b]$R = \Sigma||F_0| - |F_c||/ \Sigma|F_0|$. [c]$R_w = [\Sigma w(|F_0| - |F_c|)^2/ \Sigma wF_0^{1/2}$, where $w^{-1} = [\sigma_{count}^2 + (0.05F^2)^2]4F^2$.

Table 5.2 Selected bond lengths (Å) and angles (deg) for $[Mn^{III}(S^{Me2}N_4(6\text{-Me-DPEN}))(OO^tBu)](BPh_4)$ (**1·OO^{t}Bu**), $[Mn^{III}(S^{Me2}N_4(6\text{-Me-DPEN}))(OOCm)](BPh_4)$ (**1·OOCm**), $[Mn^{III}(S^{Me2}N_4(2\text{-QuinoEN}))(OO^tBu)](BPh_4)$ (**2·OO^{t}Bu**), $[Mn^{III}(S^{Me2}N_4(2\text{-QuinoEN}))(OOCm)](BPh_4)$ isomer A (**2·OOCm-A**), $[Mn^{III}(S^{Me2}N_4(2\text{-QuinoEN}))(OOCm)](BPh_4)$ isomer B (**2·OOCm-B**), $[Mn^{III}(S^{Me2}N_4(6\text{-Me-DPPN}))(OO^tBu)](BPh_4)\cdot Et_2O$ (**3·OO^{t}Bu**), and $[Mn^{III}(S^{Me2}N_4(2\text{-QuinoPN}))(OO^tBu)](PF_6)\cdot$pentane (**4·OO^{t}Bu**).

	1·OO^{t}Bu	**1·OOCm**	**2·OO^{t}Bu**	**2·OOCm-A**	**2·OOCm-B**	**3·OO^{t}Bu**	**4·OO^{t}Bu**
Mn(1)-S(1)	2.241(3)	2.268(2)	2.270(3)	2.276(5)	2.267(5)	2.2603(13)	2.2693(15)
Mn(1)-N(1)	2.015(8)	2.018(5)	2.034(7)	2.008(13)	1.984(14)	2.061(4)	2.046(4)
Mn(1)-N(2)	2.163(7)	2.145(5)	2.173(7)	2.168(14)	2.144(14)	2.178(4)	2.182(4)
Mn(1)-N(3)	2.354(8)	2.499(6)	2.349(7)	2.480(15)	2.527(14)	2.517(4)	2.450(5)
Mn(1)-N(4)	2.471(7)	2.389(5)	2.522(8)	2.446(14)	2.449(14)	2.504(4)	2.518(5)
Mn(1)-O(1)	1.853(6)	1.848(4)	1.861(5)	1.844(11)	1.845(12)	1.843(3)	1.840(4)
O(1)-O(2)	1.468(7)	1.457(5)	1.457(7)	1.430(16)	1.507(17)	1.431(5)	1.438(5)
Mn(1)···O(2)	2.769	2.756	2.714	2.689	2.803	2.901	2.861
Mn(1)-O(1)-O(2)	112.4(4)	112.4(3)	109.2(4)	117.3(9)	106.2(8)	124.2(3)	121.1(3)
S(1)-Mn(1)-N(1)	83.6(2)	83.11(16)	82.3(2)	83.4(4)	84.1(4)	83.32(11)	82.44(12)
S(1)-Mn(1)-N(2)	162.6(2)	164.95(14)	163.1(2)	163.5(4)	165.6(4)	176.78(11)	177.62(13)
S(1)-Mn(1)-N(3)	112.4(2)	103.28(15)	107.6(2)	105.0(4)	99.0(5)	105.87(9)	107.36(11)
S(1)-Mn(1)-N(4)	109.13(18)	107.23(16)	105.6(3)	108.8(4)	106.8(4)	108.32(10)	108.98(14)
N(1)-Mn(1)-N(3)	101.1(3)	99.25(18)	87.0(2)	97.6(5)	80.9(5)	74.60(13)	73.70(16)
N(1)-Mn(1)-N(4)	103.7(3)	83.59(18)	94.2(3)	83.3(5)	98.8(5)	71.43(14)	91.41(16)
N(3)-Mn(1)-N(4)	133.3(3)	149.5(2)	146.7(3)	146.1(5)	147.4(5)	145.67(13)	143.61(16)
O(1)-Mn(1)-S(1)	94.9(2)	99.92(14)	97.5(2)	99.0(4)	95.2(4)	91.79(11)	93.69(12)
O(1)-Mn(1)-N(1)	175.7(3)	176.9(2)	175.4(3)	169.5(6)	179.3(5)	174.27(15)	176.12(16)
O(1)-Mn(1)-N(2)	102.2(3)	94.23(19)	97.9(3)	97.3(5)	98.9(5)	85.02(14)	84.16(17)
O(1)-Mn(1)-N(3)	83.2(3)	80.87(18)	97.4(2)	91.7(5)	99.0(5)	90.11(14)	89.54(17)
O(1)-Mn(1)-N(4)	72.9(2)	94.71(18)	81.5(2)	86.3(5)	81.7(5)	91.71(14)	84.16(17)

acceptable bonding ranges and display little overall variation throughout this series (± 0.02 Å, ± 0.03 Å, ± 0.04 Å, and ± 0.03 Å, respectively).

Metrical parameters associated with the ^{t}BuOO$^-$ ligands in **1·OO^{t}Bu - 4·OO^{t}Bu** are all within the anticipated ranges for metal-alkylperoxos. The long distances between each Mn(III) ion and respective ^{t}BuOO$^-$ distal oxygen (O(2)) in all four complexes (2.714-2.901 Å) suggest that each ^{t}BuOO$^-$ ligand is bound in an end-on (η^1) fashion (Table 5.2). This is further supported by the Mn(1)-O(1)-O(2) angles (106.2(8)-124.2(3)°), which are much larger than those found in other Mn(III)(η^2-O_2) complexes (60-80°) but similar to that of $[Tp^{tBu,iPr}Mn(II)(OO^tBu)]$ (105.1(2)°).[31] The Mn(III)-O(1) bond lengths range from 1.840(4)-1.861(5) Å within this series,

which falls at the short end of other Mn(III)-O_{peroxo} bonds reported (1.85-1.90 Å), but are longer that that found in $[Mn^{III}(S^{Me2}N_4(6\text{-Me-DPEN}))]_2(\textit{trans}\text{-}\mu\text{-}1,2\text{-}O_2)(BPh_4)_2\cdot 2CH_3CH_2CN$ (Mn(1)-O(1) = 1.832(3) Å, Chapter 4).[27-32] It is worthwhile to note that all other reported Mn(III)-peroxos outside of this thesis exhibit side-on (η^2) peroxo coordination modes, suggesting that shorter Mn-O bonds may be promoted by an end-on coordination mode. This is a tentative conclusion, however, given that none of the other structurally characterized Mn(III)-peroxo complexes display bond elongations (Mn(1)-N(3,4)) to the same extent as are found in this series of Mn-OOR complexes. If **1·OO^{t}Bu - 4·OO^{t}Bu** are indeed coordinatively unsaturated (less than six coordinate), it would stand to reason that the Mn(III)-O(1) bond lengths in these complexes should be especially short relative to other coordinatively saturated Mn(III)-peroxos.

The O(1)-O(2) bond lengths found in **1·OO^{t}Bu - 4·OO^{t}Bu** range from 1.431(5)-1.468(7) Å and are longer than those found in all other structurally characterized Mn(III)-peroxos (1.403(4)-1.428(7) Å) and in $[Tp^{tBu,iPr}Mn(II)(OO^tBu)]$ (1.411(4) Å). These lengths are also similar to that found in $[Mn^{III}(S^{Me2}N_4(6\text{-Me-DPEN}))]_2(\textit{trans}\text{-}\mu\text{-}1,2\text{-}O_2)(BPh_4)_2\cdot 2CH_3CH_2CN$ (O(1)-O(2) = 1.452(5) Å, Chapter 4). These comparisons would suggest that longer and more activated O-O bonds are promoted by the end-on versus side-on peroxo coordination mode, however the elongated Mn(1)-N(3,4) distances observed within this series of complexes again preclude these observations from being assessed confidently. Comparisons within this series, however, can afford insights regarding how the coordination sphere influences the metrical parameters associated with the $^tBuOO^-$ ligand in each complex. These comparisons are discussed below in section 5.3.5.

5.3.3 Spectroscopic and Magnetic Characterization of 1·OO^{t}Bu - 4·OO^{t}Bu

The relative ease at which X-ray quality crystals of **1·OO^{t}Bu** - **4·OO^{t}Bu** were obtained greatly facilitated further spectroscopic characterization of these species. UV/Vis extinction coefficients for all four complexes were determined in CH_2Cl_2 (258 K) solutions (Figure 5.5). These spectra are each identical to those observed during reactions between complexes **1-4** and

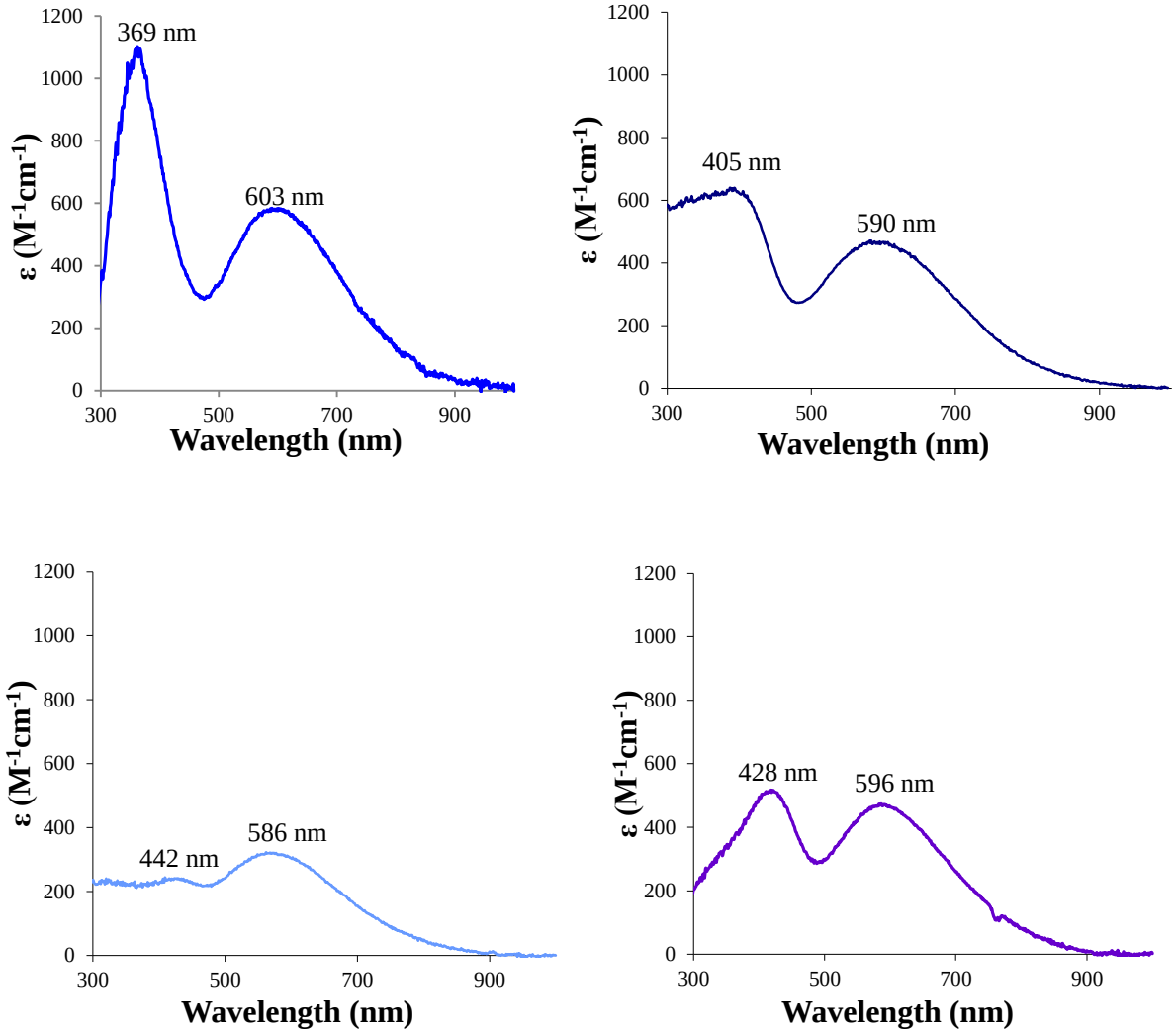

Figure 5.5 Quantitative UV/Vis spectra (extinction coefficient versus wavelength) for [Mn^{III}(S^{Me2}N$_4$(6-Me-DPEN))(OO^{t}Bu)](BPh$_4$) (**1·OO^{t}Bu**), [Mn^{III}(S^{Me2}N$_4$(2-QuinoEN))(OO^{t}Bu)](BPh$_4$) (**2·OO^{t}Bu**), [Mn^{III}(S^{Me2}N$_4$(6-Me-DPPN))(OO^{t}Bu)](BPh$_4$)·Et$_2$O (**3·OO^{t}Bu**), and [Mn^{III}(S^{Me2}N$_4$(2-QuinoPN))(OO^{t}Bu)](PF$_6$)·pentane (**4·OO^{t}Bu**) (CH_2Cl_2, 258 K).

^{t}BuOOH under the same conditions (*vide supra*), thus revealing that intermediates **1·OO^{t}Bu** - **4·OO^{t}Bu** indeed represent the major species formed in each of these respective reactions. The UV/Vis spectrum of each Mn(III)-OO^{t}Bu complex contains two broad absorption bands of moderate intensity (Figure 5.5). The relative intensities and energies of these absorption features compare well with that observed for $[Mn^{III}(S^{Me2}N_4(6\text{-Me-DPEN}))]_2$(*trans*-μ-1,2-$O_2$)$(BPh_4)_2$·$2CH_3CH_2CN$ (λ_{max} = 390 nm and 640 nm) and $[Mn^{III}(S^{Me2}N_4(2\text{-QuinoEN}))]_2$(*trans*-μ-1,2-$O_2$)$(BPh_4)_2$·$CH_3CH_2CN$ in MeCN (λ_{max} = 416 nm and 660 nm) (Chapter 4). These spectra are also similar with those found in all other Mn(III)-peroxo complexes (with or without structural characterization), which have exclusively been shown to exhibit low intensity visible region absorption features.[25-32]

Extinction coefficients for **1·OO^{t}Bu** - **4·OO^{t}Bu** were used to reevaluate the titration experiments in which substoichiometric amounts of ^{t}BuOOH were added to low temperature solutions of complexes **1**-**4**, respectively, along with 2.0 equivalents of triethylamine (*vide supra*). Based upon these experimentally-determined ε values, it was found that ~100% of each starting Mn(II) complex was transformed into the corresponding Mn(III)-OO^{t}Bu intermediate during each titration experiment. These observations confirm that 1.5-1.8 equivalents of ^{t}BuOOH are sufficient for the nearly quantitative conversion of each five-coordinate Mn(II) complex to the Mn(III)-OO^{t}Bu species. This stoichiometry would be consistent with a mechanism involving initial oxidation of Mn(II) by 0.5 equivalents of ^{t}BuOOH to afford an unobserved Mn(III) intermediate (possibly a Mn(III)-OH), followed by an immediate reaction between this unobserved intermediate with the remaining ~1.0 equivalent of ^{t}BuOOH to afford the observed Mn(III)-OO^{t}Bu species (Equations 5.1-5.3). Similar mechanisms have been afforded to explain the conversion of various Fe(II) complexes to the corresponding Fe(III)-OOR

intermediates with excess ROOH.[52] Support for this mechanistic proposal has been demonstrated by Que with $[(6\text{-}Me_3\text{-}TPA)Fe(II)(O_2CPh)]^+$ (6-Me_3-TPA = *tris*(6-methyl-2-pyridylmethyl)amine), where the addition of 0.5 and 5 equivalents of ^{t}BuOOH yielded $[(6\text{-}Me_3\text{-}TPA)Fe(III)(O_2CPh)(OH)]^+$ and $[(6\text{-}Me_3\text{-}TPA)Fe(III)(O_2CPh)(OO^tBu)]^+$, respectively.[53]

$$2Mn(II) + ROOH \rightarrow Mn(III)\text{-}OH + Mn(III)\text{-}OR \quad (5.1)$$

$$Mn(III)\text{-}OH + ROOH \rightarrow Mn(III)\text{-}OOR + H_2O \quad (5.2)$$

$$Mn(III)\text{-}OR + ROOH \rightarrow Mn(III)\text{-}OOR + ROH \quad (5.3)$$

Crystalline samples of **1·OO^{t}Bu** - **4·OO^{t}Bu** were also characterized by FT-IR spectroscopy as Nujol mulls at 293 K. In order to ensure that the counterion did not dominate the spectral region of interest (400-1000 cm^{-1}), the BPh_4^- salt of each complex was prepared and used for these experiments. As shown in Figure 5.6, isotopically-sensitive features are observed at 875 cm^{-1} ($\Delta\nu(^{16}O\text{-}^{18}O)$ = 59 cm^{-1}, **1·OO^{t}Bu**), 888 cm^{-1} ($\Delta\nu(^{16}O\text{-}^{18}O)$ = 52 cm^{-1}, **2·OO^{t}Bu**), 893 cm^{-1} ($\Delta\nu(^{16}O\text{-}^{18}O)$ = 64 cm^{-1}, **3·OO^{t}Bu**), and 895 cm^{-1} ($\Delta\nu(^{16}O\text{-}^{18}O)$ = 58 cm^{-1}, **4·OO^{t}Bu**) in the respective IR spectra. Each of these vibrational features are within the expected energy range for a metal-peroxo ν(O-O) stretch and very close to the range of other reported Mn(III)-peroxos which have been characterized by FT-IR spectroscopy (885-896 cm^{-1}).[23-27] The one outlier within this small number of examples is the ν(O-O) stretch of $[Mn^{III}(S^{Me2}N_4(6\text{-Me-DPEN}))]_2(\textit{trans}\text{-}\mu\text{-}1,2\text{-}O_2)(BPh_4)_2\cdot 2CH_3CH_2CN$ (819 cm^{-1}), as was discussed in Chapter 4. The isotopic shifts ($\Delta\nu(^{16}O\text{-}^{18}O)$) for **1·OO^{t}Bu** - **4·OO^{t}Bu** vary by as much as 20 cm^{-1} from the predicted shift based upon a harmonic oscillator model, which could result due to varying degrees of coupling between the *tert*-butyl alkyl group and the O-O stretching modes.

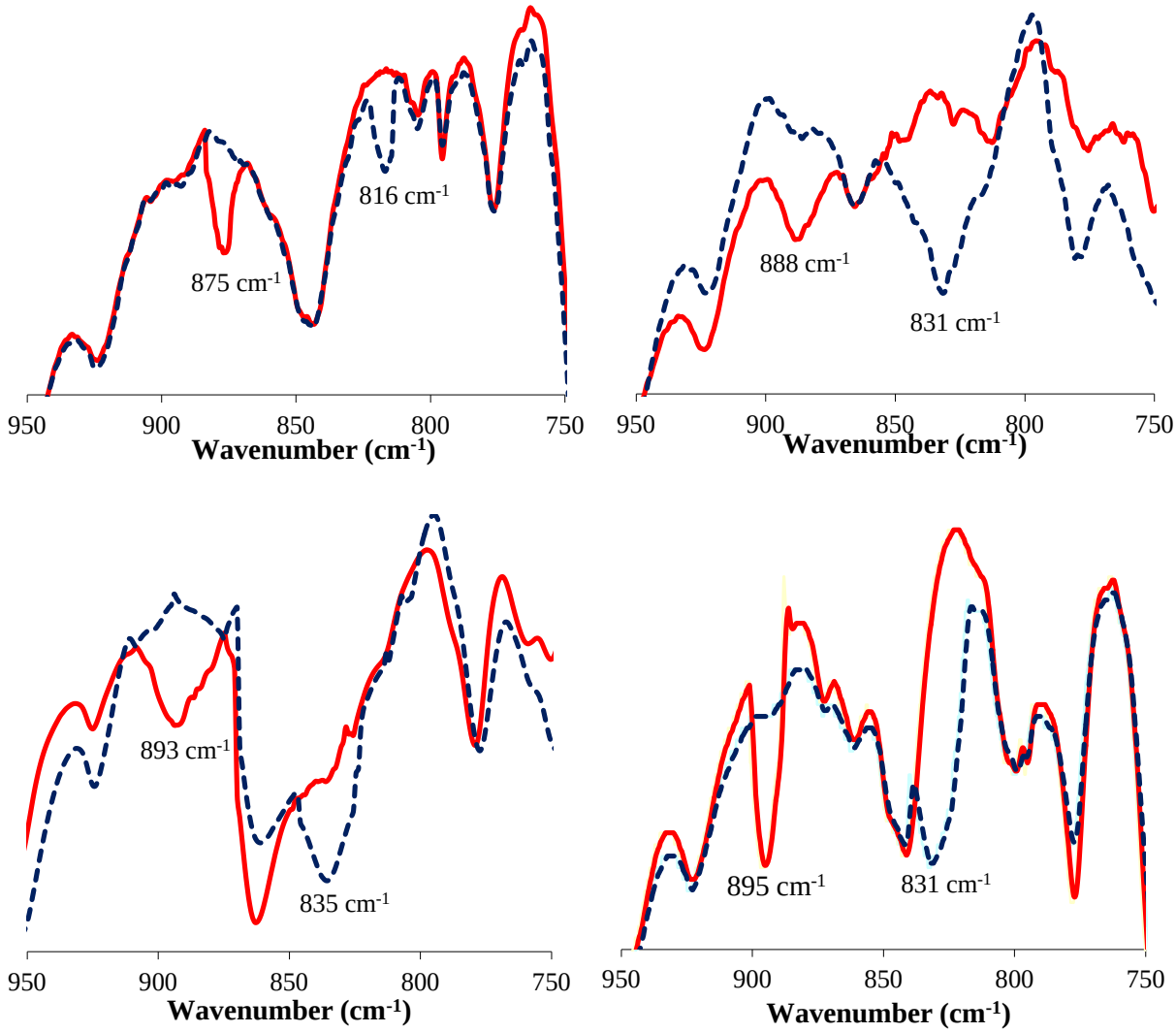

Figure 5.6 FT-IR spectra of ^{16}O- (red solid traces) and ^{18}O-labeled (blue dotted traces) $[Mn^{III}(S^{Me2}N_4(6\text{-Me-DPEN}))(OO^tBu)](BPh_4)$ (**1·OO^{t}Bu**, top right), $[Mn^{III}(S^{Me2}N_4(2\text{-QuinoEN}))(OO^tBu)](BPh_4)$ (**2·OO^{t}Bu**, top left), $[Mn^{III}(S^{Me2}N_4(6\text{-Me-DPPN}))(OO^tBu)](BPh_4)\cdot Et_2O$ (**3·OO^{t}Bu**, bottom left), and $[Mn^{III}(S^{Me2}N_4(2\text{-QuinoPN}))(OO^tBu)](PF_6)\cdot$pentane (**4·OO^{t}Bu**, bottom right) (Nujol mull, NaCl plates, 293 K).

The magnetic properties of **1·OO^{t}Bu** - **4·OO^{t}Bu** were explored in CD_2Cl_2 solutions by the Evans method. Data from these experiments yielded effective magnetic moments (μ_{eff}) of 4.79 B.M. (**1·OO^{t}Bu**), 4.84 B.M. (**2·OO^{t}Bu**), 4.89 B.M. (**3·OO^{t}Bu**), and 4.78 B.M (**4·OO^{t}Bu**). Each of these values are close to the spin-only value of 4.90 B.M. for an S = 2 spin state.

Complex **2·OO^{t}Bu** was also characterized by parallel polarization mode X-band EPR spectroscopy at 7 K. The resulting EPR spectrum is shown in Figure 5.7 and contains a distinct low field resonance that is characteristic of S = 2 spin systems. No signals were observed at slightly elevated temperatures (15 K), indicating D < 0. It is worthwhile to note that the parallel polarization mode X-band EPR spectra of $[Mn^{III}(S^{Me2}N_4(6\text{-Me-DPEN}))]_2(\textit{trans}\text{-}\mu\text{-}1,2\text{-}O_2)(BPh_4)_2\cdot 2CH_3CH_2CN$ and $[Mn^{III}(S^{Me2}N_4(2\text{-QuinoEN}))]_2(\textit{trans}\text{-}\mu\text{-}1,2\text{-}O_2)(BPh_4)_2\cdot CH_3CH_2CN$ recorded at low temperatures and in MeCN/toluene glasses also displayed similar low field signals that exhibited inverse relationships between relative signal intensity and temperature (Chapter 4). All spectroscopic data for **1·OO^{t}Bu - 4·OO^{t}Bu**, as well as a few relevant metrical parameters, are compiled in Table 5.3.

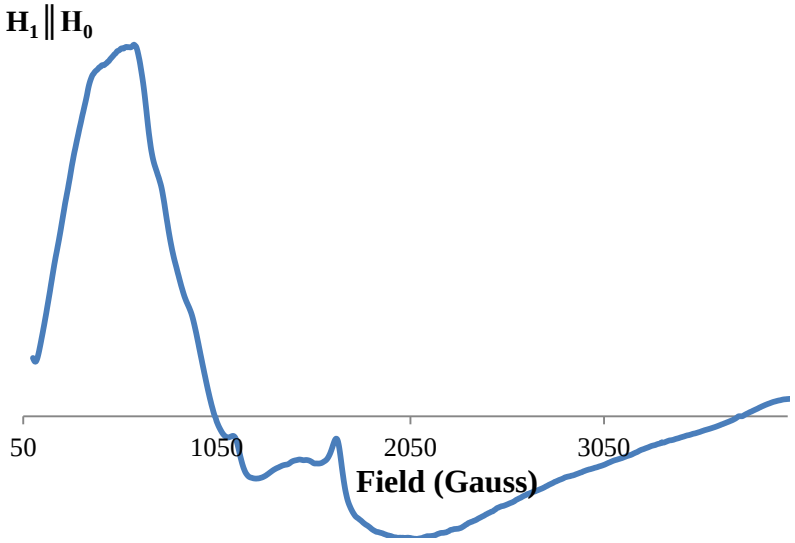

Figure 5.7 X-band EPR spectrum (parallel polarization mode) of $[Mn^{III}(S^{Me2}N_4(2\text{-QuinoEN}))(OO^{t}Bu)](BPh_4)$ (**2·OO^{t}Bu**) in MeCN/toluene glass (1:1) at 7 K.

Table 5.3 UV/vis absorption band maxima (nm), extinction coefficients ($M^{-1}cm^{-1}$), ν(O-O) frequencies (cm^{-1}), effective magnetic moments (B.M.), bond lengths (Å), and bond angles (deg) for $[Mn^{III}(S^{Me2}N_4$(6-Me-DPEN))$(OO^tBu)](BPh_4)$ (**1·OO^{t}Bu**), $[Mn^{III}(S^{Me2}N_4$(2-QuinoEN))$(OO^tBu)](BPh_4)$ (**2·OO^{t}Bu**), $[Mn^{III}(S^{Me2}N_4$(6-Me-DPPN))$(OO^tBu)](BPh_4)\cdot Et_2O$ (**3·OO^{t}Bu**), and $[Mn^{III}(S^{Me2}N_4$(2-QuinoPN))$(OO^tBu)](PF_6)$·pentane (**4·OO^{t}Bu**).

	1·OO^{t}Bu	**2·OO^{t}Bu**	**3·OO^{t}Bu**	**4·OO^{t}Bu**
λ_{max} (ε)[a]	369 (1070)	405 (620)	442 (230)	428 (490)
	603 (580)	591 (470)	586 (320)	596 (48)
ν(O-O)[b]	875	888	893	895
μ_{eff} [c]	4.79	4.84	4.89	4.78
Mn(1)-O(1)	1.853(6)	1.861(5)	1.843(3)	1.840(4)
O(1)-O(2)	1.468(7)	1.457(7)	1.431(3)	1.438(5)
Mn(1)-S(1)	2.241(3)	2.270(3)	2.2603(13)	2.2693(15)
Mn(1)-O(1)-O(2)	112.4(4)	109.2(4)	124.2(3)	121.1(3)

[a]CH_2Cl_2 solutions, 258 K. [b]FT-IR, Nujol mull, NaCl salt plates. [c]Evans method, CD_2Cl_2, 273 K.

5.3.4 Isolation and Characterization of Mn(III)-OOCm Intermediates 1·OOCm - 2·OOCm

In order determine how the alkyl substituent (R) of the ROO^- ligand may influence the properties of these Mn(III)-OOR complexes, reactions were performed between complexes **1**-**4** and cumene hydroperoxide (CmOOH) under the same conditions used for the synthesis of **1·OO^{t}Bu** - **4·OO^{t}Bu**. X-ray quality crystals of two Mn(III)-OOCm intermediates were successfully isolated from these reactions and structurally characterized by X-ray crystallography, yielding $[Mn^{III}(S^{Me2}N_4$(6-Me-DPEN))(OOCm)$](BPh_4)$ (**1·OOCm**) and $[Mn^{III}(S^{Me2}N_4$(2-QuinoEN))(OOCm)$](BPh_4)$ (**2·OOCm**). ORTEP diagrams of **1·OOCm** - **2·OOCm** are shown in Figure 5.8, while crystal data and selected metrical parameters are provided in Tables 5.1 and 5.2, respectively. The asymmetric unit from the X-ray structure of **2·OOCm** was found to contain two Mn(III)-OOCm complexes with distinct metrical parameters relative to one another (isomers **2·OOCm-A** and **2·OOCm-B**, Figure 5.9). Unfortunately this structure was solved at a relatively low resolution (R = 16%), therefore the metrical parameters from these two isomers have been considered unreliable and are not further discussed.

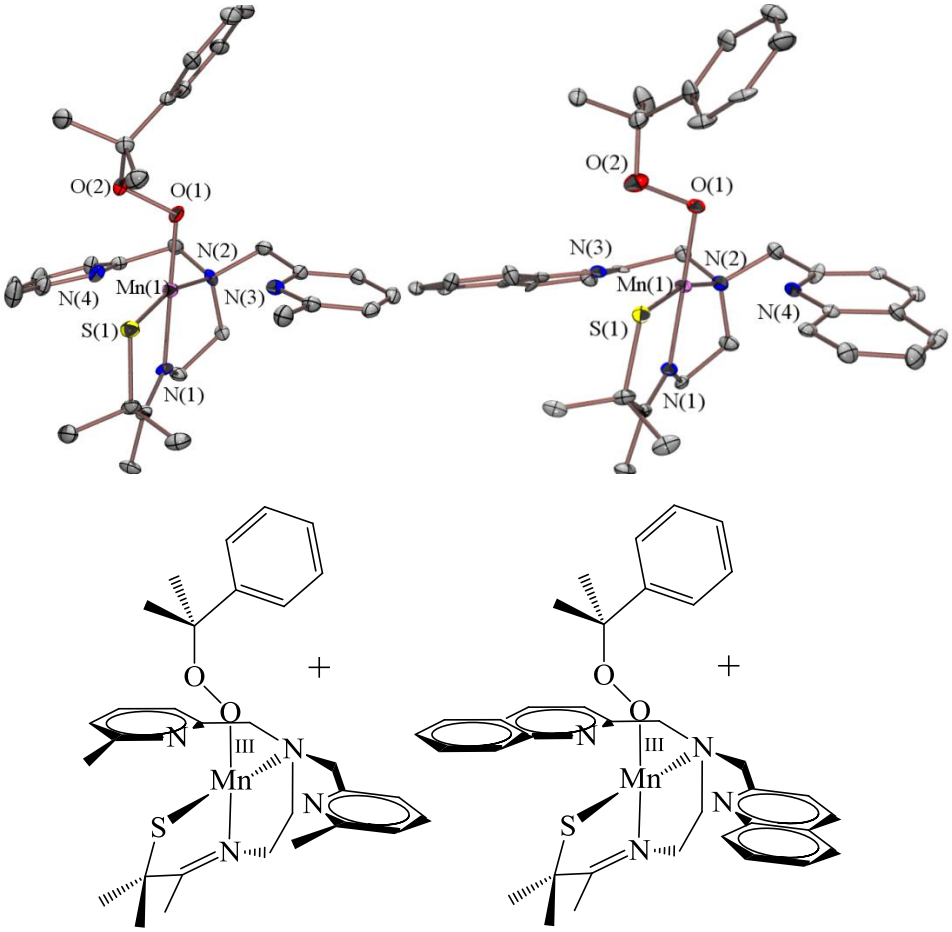

Figure 5.8 ORTEP diagrams (50 % probability) of $[Mn^{III}(S^{Me2}N_4(6\text{-Me-DPEN}))(OOCm)](BPh_4)$ (**1·OOCm**) and $[Mn^{III}(S^{Me2}N_4(2\text{-QuinoEN}))(OOCm)](BPh_4)$ (**2·OOCm**, isomer A) with hydrogen atoms, counterions, and solvents of crystallization omitted for clarity

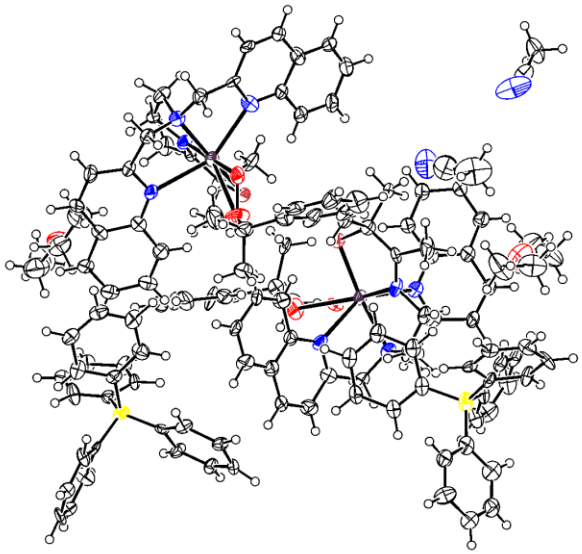

Figure 5.9 ORTEP diagram (50 % probability) displaying the asymmetric unit of **2·OOCm**.

Structural comparisons between intermediates **1·OO^{t}Bu** and **1·OOCm**, which are both formed from complex **1**, reveal only small differences between the two regarding bond lengths and angles (Table 5.2). The Mn(1)-O(1) bond lengths for these two complexes (1.853(6) Å and 1.848(4) Å, respectively), as well as the O(1)-O(2) bond lengths (1.468(7) Å and 1.457(5) Å, respectively), are within crystallographic error of one another, suggesting that replacement of the alkylperoxo R-group from -^{t}Bu to -Cumene has little effect upon these particular metrical parameters. Also, the Mn(1)-O(1)-O(2) bond angles, which reflect the relative hybridization of the proximal oxygen (O(1)), for these two complexes are 112.4(4)° and 112.4(3)° (Table 5.2), respectively, again demonstrating that the alkyl substituent has little effect upon metrics associated the Mn(III)-O-O-R unit. The X-ray structures of both intermediates also contain elongated Mn(1)-N(3,4) distances (2.354(8) Å and 2.471(7) Å for **1·OO^{t}Bu**, 2.499(6) and 2.389(5) for **1·OOCm**, respectively, Table 5.2). The only metrical parameters that are unique between the two complexes are the Mn(1)-S(1) bond lengths, which are 2.241(3) Å in **1·OO^{t}Bu** and 2.268(2) Å in **1·OOCm**, although there does not appear to be a clear rationale for this difference.

Crystalline samples of **1·OOCm** were also used to determine UV/Vis extinction coefficients. The UV/Vis spectrum of **1·OOCm** at 258 K in CH_2Cl_2 is provided in Figure 5.10 and contains two broad visible region absorption bands centered at 378 nm (520 $M^{-1}cm^{-1}$) and 615 nm (200 $M^{-1}cm^{-1}$). The UV/Vis spectrum of **2·OOCm** is also provided in Appendix A.46). The energies and extinction coefficients for these two bands compare well with those observed in the UV/Vis spectra of **1·OO^{t}Bu** - **4·OO^{t}Bu** (Figure 5.5). These extinction coefficients were again used to analyze titration experiments where substoichiometric amounts of CmOOH were added to anaerobic low temperature CH_2Cl_2 solutions of **1** and monitored by UV/Vis

spectroscoopy. Results from these experiments were identical to those described for **1·OO^{t}Bu** - **4·OO^{t}Bu** (vide supra), as 1.5-1.8 equivalents of CmOOH per equivalent of 1 promoted the nearly quantitative formation of **1·OOCm**.

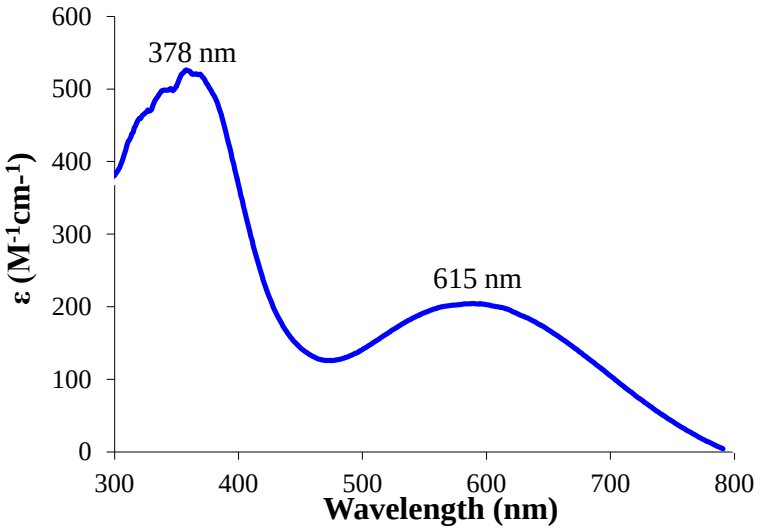

Figure 5.10 Quantitative UV/Vis spectrum (extinction coefficient versus wavelength) of [Mn^{III}(S^{Me2}N$_4$(6-Me-DPEN))(OOCm)](BPh$_4$) (**1·OOCm**) in CH_2Cl_2 at 258 K.

5.3.5 Structural and Spectroscopic Trends Within the Mn(III)-OOR Series 1·OO^{t}Bu - 4·OO^{t}Bu and 1·OOCm

Further inspection of the structural and spectroscopic data described for **1·OO^{t}Bu** - **4·OO^{t}Bu** and **1·OOCm** reveal a number of systematic trends, some of which provide insights regarding the degree of O-O bond activation exhibited by each complex. As is shown in Figure 5.11, the Mn(1)-O(1) bond lengths in each complex decrease as the Mn(1)-O(1)-O(2) bond angles increase. An increase in Mn(1)-O(1)-O(2) bond angle would suggest that the proximal oxygen (O(1)) undergoes a change in relative hybridization from sp^3 to sp^2, and thus an increase in s-character would result in stronger (i.e shorter) Mn(1)-O(1) bonds. This is also consistent with the fact that the O(1)-O(2) bond lengths decrease as the Mn(1)-O(1)-O(2) bond angle

increases (Figure 5.11). These trends contrast with those of side-on Mn(III)(η^2-O_2) complexes, where shorter Mn-O bond lengths have been found to be correlated with longer O-O bonds.

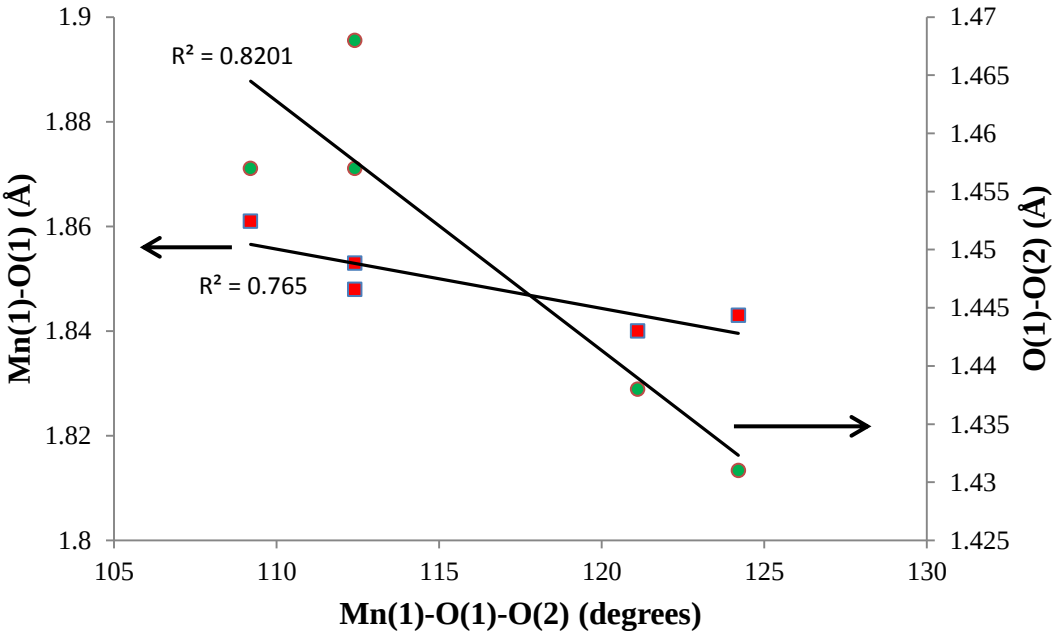

Figure 5.11 Plots of Mn(1)-O(1) bond length (Å) versus Mn(1)-O(1)-O(2) bond angle (deg) (left y-axis, red data points) and O(1)-O(2) bond length (Å) versus Mn(1)-O(1)-O(2) bond angle (deg) (right y-axis, green data points) for **1·OO^{t}Bu** - **4·OO^{t}Bu** and **1·OOCm**. Individual values are provided in Table 5.2.

Experimental and computational data has been provided for a number of metal-peroxo complexes that suggests electron-donating ligands promote longer and more activated peroxo O-O bonds. The structural data obtained for this series of Mn(III)-OOR complexes are consistent with this general observation, as an inverse correlation exists between the average Mn(1)-N(3) and Mn(1)-N(4) distances (Mn(1)-N(3,4)$_{ave}$) and O(1)-O(2) bond lengths (Figure 5.12). As was previously mentioned in Section 5.3.2, the Mn(1)-N(3) and Mn(1)-N(4) distances represent the largest structural variables within this series of complexes; the exceptionally strong correlation shown in Figure 5.12 indicates that longer (more activated) O-O bonds are promoted in complexes with shorter (stronger) Mn(1)-N(3) and Mn(1)-N(4) interactions. It is worthwhile to

note that the O(1)-O(2) bond length from the X-ray structures complexes **2·OO^{t}Bu** and **1·OOCm** are identical to one another (1.457 Å), while the Mn(1)-N(3,4)$_{ave}$ distances are also extremely close to one another (2.436 Å and 2.419 Å, respectively). Given that these two complexes have different thiolate-containing and alkylperoxo ligands, these observations substantiate the correlation made in Figure 5.12 and suggest the N-heterocyclic moieties have the largest influence upon the degree of O-O bond activation with this series.

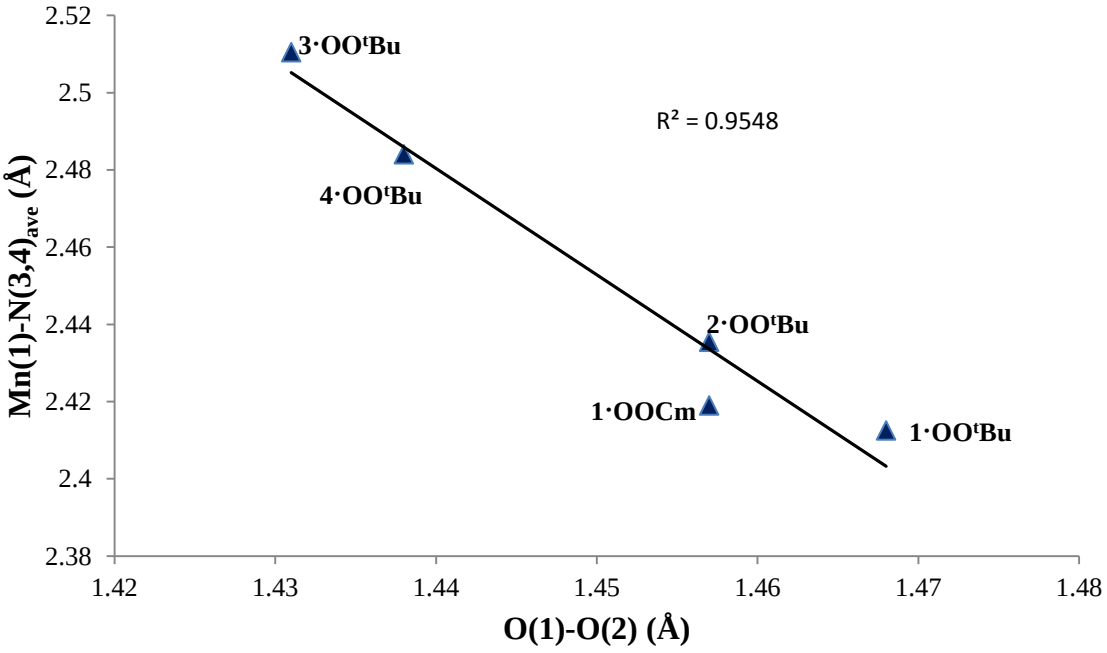

Figure 5.12 Plot of average Mn(1)-N(3,4) distance (Å) versus O(1)-O(2) bond length (Å) for **1·OO^{t}Bu - 4·OO^{t}Bu** and **1·OOCm**. Individual values are provided in Table 5.2. Individual data are provided in Table 5.2.

An inversely proportional trend is found to exist between the O(1)-O(2) bond lengths of **1·OO^{t}Bu - 4·OO^{t}Bu** and the corresponding ν(O-O) stretching frequencies determined by FT-IR studies (Figure 5.13). Although not particularly tight, this correlation provides spectroscopic evidence that the O-O bonds within this series weaken as they become longer. When considering the statistical differences between these four O-O bonds (Table 5.2), it would appear

that the O-O bonds in **1·OO^{t}Bu** and **2·OO^{t}Bu** are within crystallographic error of one another. Likewise, the O-O bonds in **3·OO^{t}Bu** and **4·OO^{t}Bu** are also indistinguishable when considering crystallographic error. The correlation in Figure 5.13 thus allows for each individual complex within these pairs to be differentiated and shows that varying degrees of O-O bond activation are exhibited by each member within this series.

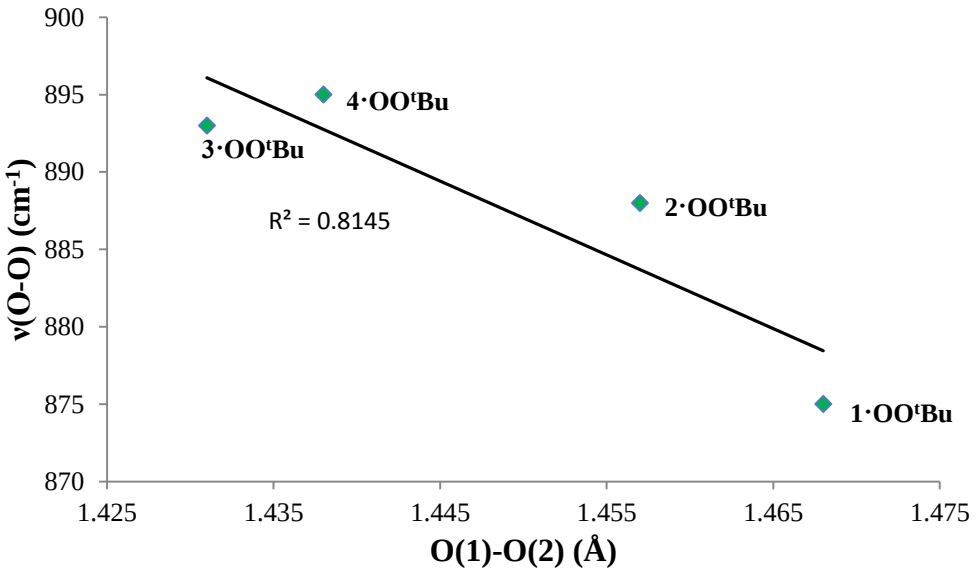

Figure 5.13 Plot of ν(O-O) stretching frequency (cm^{-1}) versus O(1)-O(2) bond length (Å) for **1·OO^{t}Bu - 4·OO^{t}Bu**.

5.3.6 Density Functional Theory (DFT) Calculations

5.3.6.1 Geometry Optimization, Single Point Energy, and Vibrational Spectra Calculations

DFT calculations were performed for **1·OO^{t}Bu - 4·OO^{t}Bu** in order to further assess how the O-O bonds in these complexes may be influenced by the N-heterocyclic moieties. Geometry optimizations for these four complexes were made starting from the respective X-ray crystal structure atomic coordinates on a high-spin surface (S = 2) with the TPSS functional and def2-

TZVP(-f) basis set. The def2-TZV/J auxillary basis set was used for Coulomb density fitting approximations, which afforded Mulliken charge densities for all coordinating atoms. These calculations were also performed with intramolecular Van der Waal interactions accounted for and a conductor-like screening model (as opposed to gas-phase calculation) to reproduce the dielectric environment promoted by CH_2Cl_2 (COSMO, CH_2Cl_2 ε = 9.08). The geometry optimized structures of all four Mn(III)-OO^{t}Bu complexes (**1·OO^{t}Bu-DFT** - **4·OO^{t}Bu-DFT**) are provided in Figure 5.14, while selected metrical parameters from these models are compiled in Table 5.4.

The metrical parameters from **1·OO^{t}Bu-DFT** - **4·OO^{t}Bu-DFT** each compare well with those from the respective X-ray crystal structure (Tables 5.2 and 5.4), as all bond lengths and angles deviate by less than 3% when comparing experimental to computational values. These calculations also reproduce most of the structural trends discussed above in Section 5.3.5. The O(1)-O(2) bond lengths from **1·OO^{t}Bu-DFT** and **2·OO^{t}Bu-DFT** are nearly the same (1.479 Å and 1.475 Å, respectively), while those for **3·OO^{t}Bu-DFT** and **4·OO^{t}Bu-DFT** are exactly the same (1.466 Å for both). These observations are consistent with those from the respective X-ray structures, where O(1)-O(2) bond lengths from these two distinct sets of complexes were found to be within crystallographic error of one another. However, vibrational spectra calculations performed on **1·OO^{t}Bu-DFT** - **4·OO^{t}Bu-DFT** reveal that there are slight energetic differences between the four O-O bonds, as the calculated ν(O-O) stretching frequencies were found to be 903 cm^{-1}, 902 cm^{-1}, 897 cm^{-1}, and 899 cm^{-1}, respectively. This is again consistent with experimental data and supports the claim that there are energetic differences in the O-O bonds of these complexes. It is also worth mentioning that the calculated ν(Mn-O) stretching frequencies were found to be 656 cm^{-1}, 659 cm^{-1}, 643 cm^{-1}, and 638 cm^{-1} for **1·OO^{t}Bu-DFT**-**4·OO^{t}Bu-DFT**,

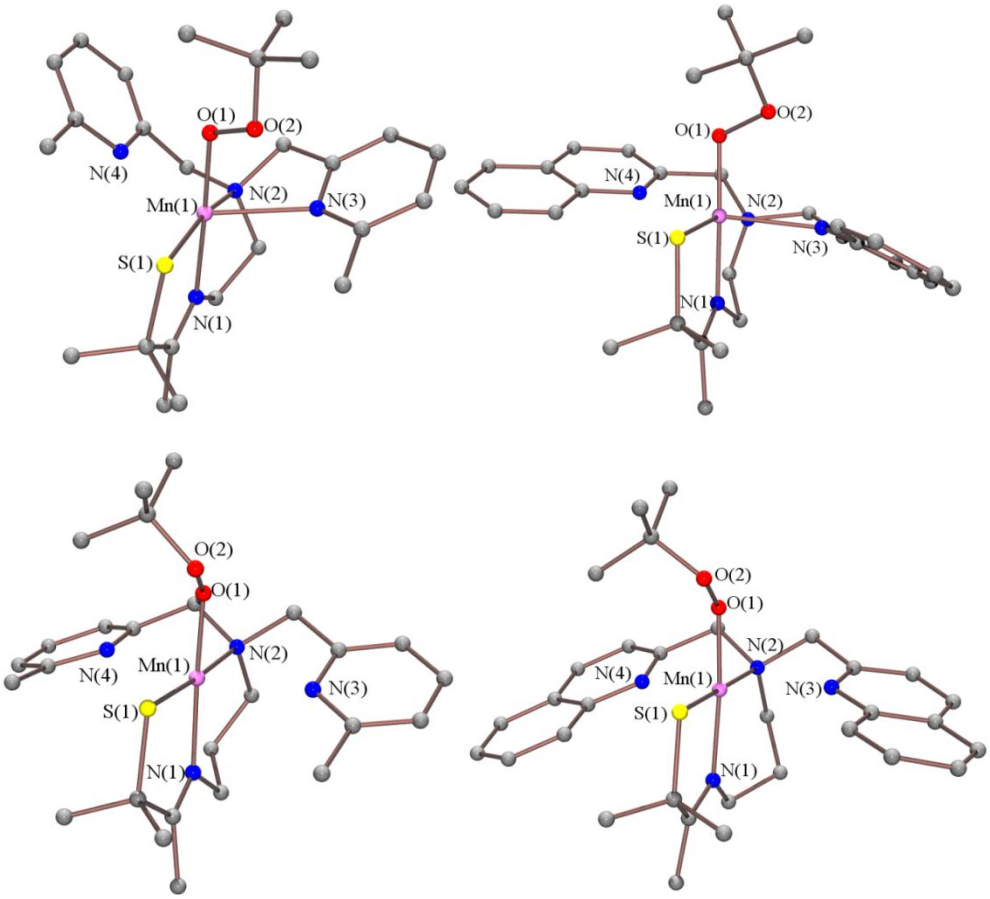

Figure 5.14 Models of $[Mn^{III}(S^{Me2}N_4(6\text{-Me-DPEN}))(OO^tBu)]^+$ (**1·OO^{t}Bu-DFT**, top left), $[Mn^{III}(S^{Me2}N_4(2\text{-QuinoEN}))(OO^tBu)]^+$ (**2·OO^{t}Bu-DFT**, top right), $[Mn^{III}(S^{Me2}N_4(6\text{-Me-DPPN}))(OO^tBu)]^+$ (**3·OO^{t}Bu-DFT**, bottom left), and $[Mn^{III}(S^{Me2}N_4(2\text{-QuinoPN}))(OO^tBu)]^+$ (**4·OO^{t}Bu-DFT**, bottom right) from DFT (TPSS/def3-TZVP(-f)/def2-TZV/J/van der Waals corrected) geometry optimization calculations.

respectively. These values were not experimentally determined, but they do compare well with the ν(Mn-O) frequency of $[Mn^{III}(S^{Me2}N_4(6\text{-Me-DPEN}))]_2(\textit{trans}\text{-}\mu\text{-}1,2\text{-}O_2)(BPh_4)_2\cdot 2CH_3CH_2CN$ (611 cm^{-1}, Chapter 4) and are similar to the ν(Fe-O) frequencies found in low-spin Fe(III)-(η^1-OOH) and Fe(III)-(η^1-OOR) complexes (600-630 cm^{-1}, high-spin Mn(III) and low-spin Fe(III) both have an empty d orbital of e_g^* parentage).

Table 5.4 Selected bond lengths (Å) and angles (deg) from DFT (TPSS/def3-TZVP(-f)/def2-TZV/J/van der Waals corrected) optimized geometries of $[Mn^{III}(S^{Me2}N_4(6\text{-Me-DPEN}))(OO^tBu)]^+$ (**1·OO^{t}Bu-DFT**), $[Mn^{III}(S^{Me2}N_4(2\text{-QuinoEN}))(OO^tBu)]^+$ (**2·OO^{t}Bu-DFT**), $[Mn^{III}(S^{Me2}N_4(6\text{-Me-DPPN}))(OO^tBu)]^+$ (**3·OO^{t}Bu-DFT**), and $[Mn^{III}(S^{Me2}N_4(2\text{-QuinoPN}))(OO^tBu)]^+$ (**4·OO^{t}Bu-DFT**).

	1·OO^{t}Bu-DFT	**2·OO^{t}Bu-DFT**	**3·OO^{t}Bu-DFT**	**4·OO^{t}Bu-DFT**
Mn(1)-S(1)	2.247	2.267	2.260	2.266
Mn(1)-N(1)	2.022	2.031	2.066	2.070
Mn(1)-N(2)	2.179	2.177	2.202	2.214
Mn(1)-N(3)	2.457	2.367	2.458	2.510
Mn(1)-N(4)	2.375	2.466	2.582	2.450
Mn(1)-O(1)	1.842	1.835	1.837	1.840
O(1)-O(2)	1.479	1.475	1.466	1.466
Mn(1)···O(2)	2.777	2.742	2.879	2.870
Mn(1)-O(1)-O(2)	113.02	111.42	126.94	120.07
S(1)-Mn(1)-N(1)	84.06	83.42	83.14	82.88
S(1)-Mn(1)-N(2)	164.60	164.62	176.90	177.65
S(1)-Mn(1)-N(3)	111.59	107.16	110.67	104.09
S(1)-Mn(1)-N(4)	107.96	105.59	103.88	110.30
N(1)-Mn(1)-N(3)	97.76	71.74	87.39	96.16
N(1)-Mn(1)-N(4)	104.26	85.30	95.19	86.45
N(3)-Mn(1)-N(4)	136.20	147.25	145.40	145.56
O(1)-Mn(1)-S(1)	95.85	99.53	94.44	94.98
O(1)-Mn(1)-N(1)	177.95	175.94	175.94	175.34
O(1)-Mn(1)-N(2)	99.44	94.82	83.49	83.69
O(1)-Mn(1)-N(3)	88.05	78.76	90.44	88.37
O(1)-Mn(1)-N(4)	73.71	96.43	88.54	90.43

Models **1·OO^{t}Bu-DFT** - **4·OO^{t}Bu-DFT** were also found to reproduce they long Mn(1)-N(3) and Mn(1)-N(4) distances that were observed in the X-ray crystal structures of **1·OO^{t}Bu** - **4·OO^{t}Bu** (Figure 5.15). Although this correlation is not as strong as that found in the X-ray data (Table 5.2, Figure 5.12), there does appear to be an inversely proportional relationship between the Mn(1)-N(3,4)$_{ave}$ distances and O(1)-O(2) bond lengths. Further insight into this relationship was provided by the Mulliken charge densities of the Mn ion and coordinating atoms of **1·OO^{t}Bu-DFT** - **4·OO^{t}Bu-DFT** (Table 5.5); complexes with the longest O-O bonds (**3·OO^{t}Bu-DFT** and **4·OO^{t}Bu-DFT**) have the most positive Mn ion charges, while the two complexes with the shortest O-O bonds (**1·OO^{t}Bu-DFT** and **2·OO^{t}Bu-DFT**) have less positive Mn ion charges. This suggests that the N-heterocyclic moieties may be indirectly influencing the degree

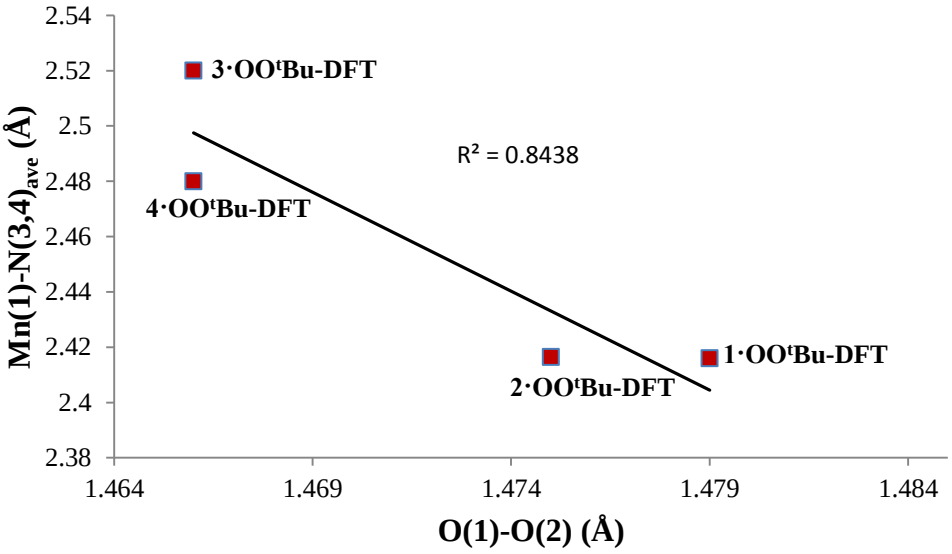

Figure 5.15 Plot of average Mn(1)-N(3) and Mn(1)-N(4) distances ($Mn(1)\text{-}N(3,4)_{ave}$) versus O(1)-O(2) bond lengths from **1·OO^{t}Bu-DFT** - **4·OO^{t}Bu-DFT**.

Table 5.5 Selected Mulliken charge densities from DFT (TPSS/def3-TZVP(-f)/def2-TZV/J/van der Waals corrected) optimized geometries of $[Mn^{III}(S^{Me2}N_4(6\text{-Me-DPEN}))(OO^tBu)]^+$ (**1·OO^{t}Bu-DFT**), $[Mn^{III}(S^{Me2}N_4(2\text{-QuinoEN}))(OO^tBu)]^+$ (**2·OO^{t}Bu-DFT**), $[Mn^{III}(S^{Me2}N_4(6\text{-Me-DPPN}))(OO^tBu)]^+$ (**3·OO^{t}Bu-DFT**), and $[Mn^{III}(S^{Me2}N_4(2\text{-QuinoPN}))(OO^tBu)]^+$ (**4·OO^{t}Bu-DFT**).

	1·OO^{t}Bu	**2·OO^{t}Bu**	**3·OO^{t}Bu**	**4·OO^{t}Bu**
Mn(1)	+0.42	+0.49	+0.50	+0.48
N(1)	-0.26	-0.29	-0.37	-0.37
N(2)	-0.40	-0.33	-0.41	-0.39
N(3)	-0.54	-0.58	-0.58	-0.57
N(4)	-0.59	-0.52	-0.52	-0.58
O(1)	-0.38	-0.39	-0.39	-0.38
O(2)	-0.20	-0.19	-0.21	-0.20
S(1)	-0.28	-0.30	-0.19	-0.22

of O-O bond activation in these complexes by modulating the relative Lewis acidity of the respective Mn ions. The Mulliken charge densities in Table 5.5 also reveal that the sulfur atom displays the largest degree of variation through this series of models (-0.19 to -0.30); as is shown in Figure 5.16, more positive sulfur atom charge densities are found in complexes with shorter

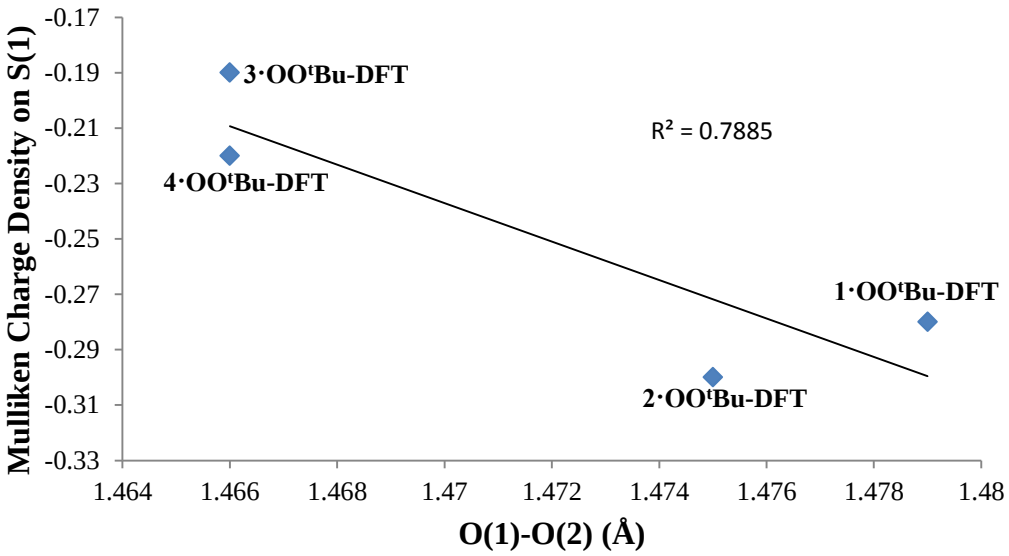

Figure 5.16 Plot of Mulliken charge density on S(1) versus O(1)-O(2) bond length from **1·OO^{t}Bu-DFT - 4·OO^{t}Bu-DFT**.

O-O bonds. This correlation again indirectly suggests that the degree of O-O bond activation exhibited by these complexes is directly related to the partitioning of electron density through the Mn ion and coordinating atoms in each complex, particularly involving of the thiolate and two N-heterocyclic moieties.

5.3.6.2 Electronic Structure Calculations Probing the Influence of Electron Density on O-O Bond Length for 1·OO^{t}Bu-DFT

In order to understand how changes in O-O bond length are reflected in the electronic structure of these Mn(III)-OO^{t}Bu complexes, relaxed surface scans were performed with **3·OO^{t}Bu-DFT** in which the O-O bond length was systematically varied from 1.1 Å to 1.6 Å while all other coordinates were optimized accordingly. Changes in O-O bond length were most reflected in the alpha spin π-bonding interaction between the alkylperoxo π_v^* and Mn d_{xz} orbtials (Mn-O π-bonding molecular orbital), which are shown in Figure 5.17 at the 1.2 Å and

1.5 Å O-O bond limits. These calculations demonstrate that as the O-O bond lengthens from 1.2 Å to 1.5 Å, the Mn(III) ion contributes less to this MO (33% to 27%), while a slight rise in alkylperoxo contribution (9.4% to 10.3%) occurs along with a considerable increase in sulfur contribution (5.7% to 11%). These results could be interpreted as suggesting that O-O bond lengthening is a direct result of increased amounts of electron density being localized into this metal-alkylperoxo bonding ortibal, which is formally antibonding with respect to the alkylperoxo O-O bond.

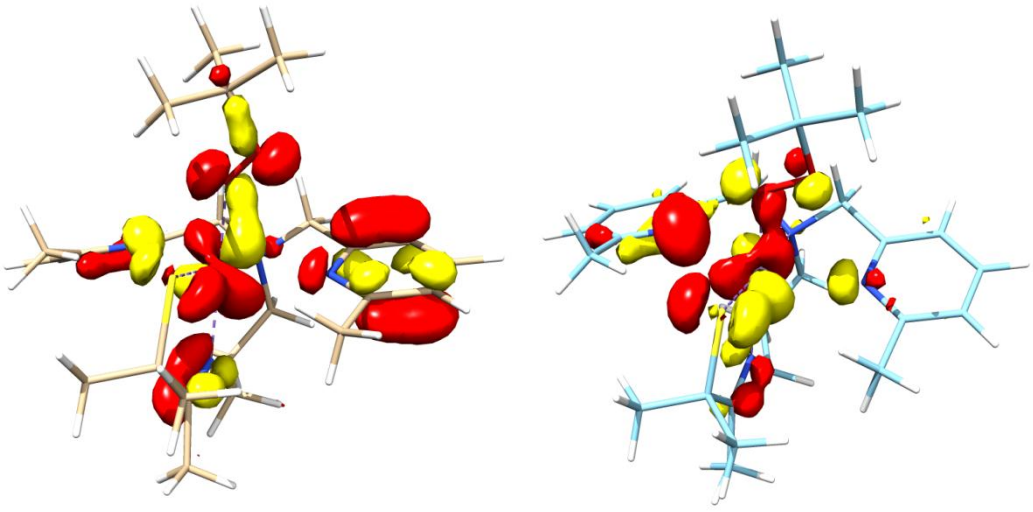

Figure 5.17 Isosurface plots (isovalue = 0.035) for the π-bonding interaction between the peroxo π_v*(O-O) and Mn d_{xz} orbitals of $[Mn^{III}(S^{Me2}N_4(6\text{-Me-DPPN}))(OO^tBu)]^+$ (**3·OO^{t}Bu-DFT**) generated from relaxed surface scans with an O-O bond of 1.2 Å (left) and 1.5 Å (right).

Further evidence to suggest that localization of electron density onto the alkylperoxo oxygen atoms promotes longer O-O bonds was provided by fluorinated analogues **1·OO^{t}Bu-DFT** generated *in silico*. These models were made by replacing hydrogen atoms with fluorine substituents in five different regions of **1·OO^{t}Bu-DFT**; the six hydrogens on the two pyridine methyl substituents (model **B**), two hydrogens adjacent to the imine nitrogen (model **C**), six hydrogens on the gem-dimethyls adjacent to the sulfur (model **D**), nine hydrogens on the *tert*-

butyl group of the ROO- ligand (model **E**), and two hydrogens adjacent to the tertiary amine (model **F**). These models are provided in Figure 5.18, while selected metrical parameters and Mulliken charge populations are provided in Tables 5.6 and 5.7, respectively. As is seen from

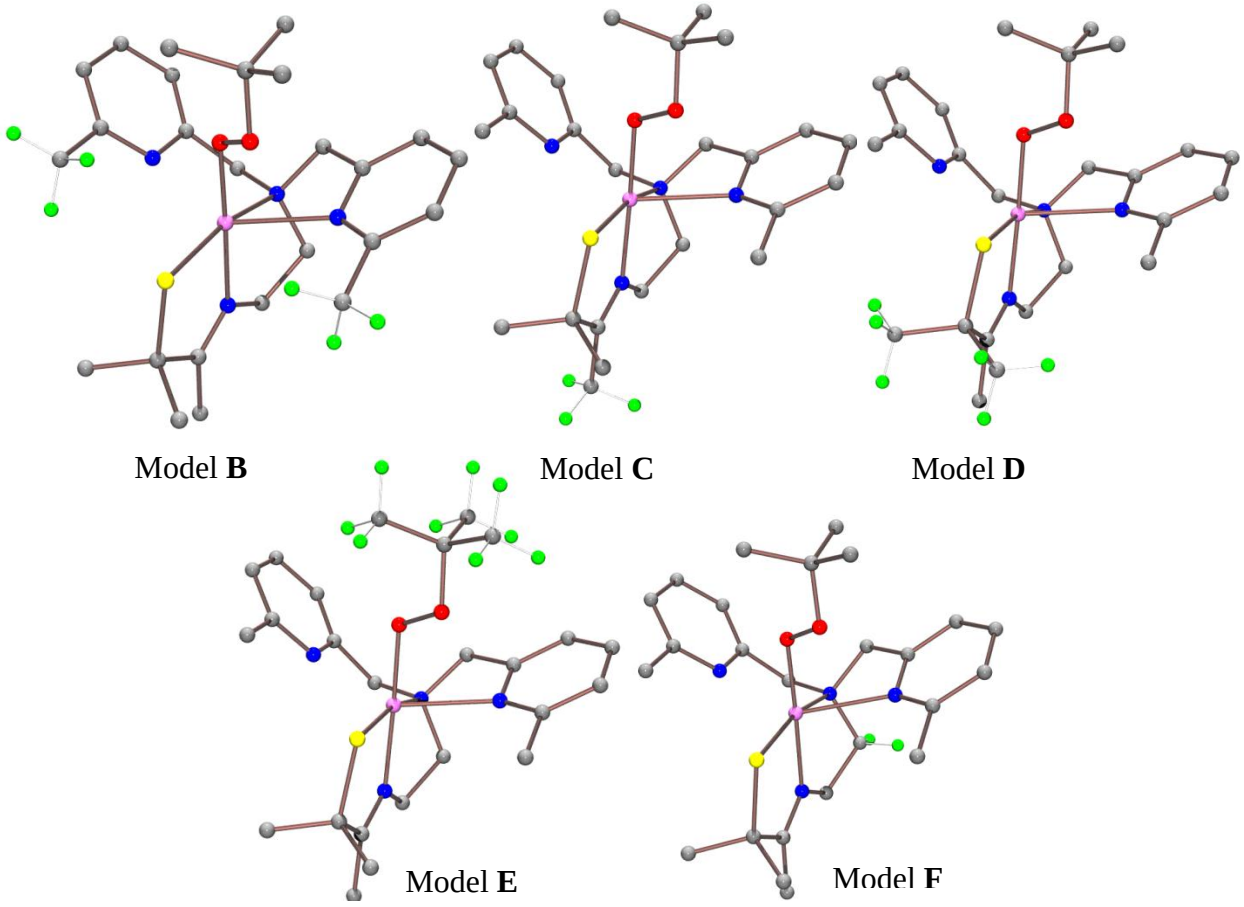

Figure 5.18 Fluorinated models of $[Mn^{III}(S^{Me2}N_4(6\text{-Me-DPEN}))(OO^tBu)]^+$ (**1·OO^{t}Bu-DFT**, models **B**-**F**) generated by DFT calculations (TPSS/def3-TZVP(-f)/def2-TZV/J/van der Waals corrected).

Table 5.6 Selected bond distances (Å) and angles (deg) for $[Mn^{III}(S^{Me2}N_4$(6-Me-DPEN))$(OO^tBu)]^+$ (**1·OO^{t}Bu**) and DFT (TPSS/def3-TZVP(-f)/def2-TZV/J/van der Waals corrected) optimized geometries for non-fluorinated (**A**) and fluorinated (**B**-**F**) DFT-optimized models of **1·OO^{t}Bu-DFT**.

	1·OO^{t}Bu	**A**	**B**	**C**	**D**	**E**	**F**
Mn(1)-S(1)	2.241(3)	2.247	2.23	2.25	2.27	2.25	2.25
Mn(1)-N(1)	2.015(8)	2.022	2.03	2.06	2.04	2.02	2.05
Mn(1)-N(2)	2.163(7)	2.179	2.17	2.17	2.18	2.17	2.26
Mn(1)-N(3)	2.354(8)	2.457	2.97	2.48	2.48	2.47	2.49
Mn(1)-N(4)	2.471(7)	2.375	2.46	2.44	2.42	2.44	2.40
Mn(1)-O(1)	1.853(6)	1.842	1.84	1.84	1.84	1.88	1.84
O(1)-O(2)	1.468(7)	1.479	1.48	1.48	1.48	1.49	1.48
Mn(1)-O(1)-O(2)	112.4(4)	113.02	113.40	114.10	112.90	112.80	115.20

Table 5.7 Selected Mulliken charge densities from DFT (TPSS/def3-TZVP(-f)/def2-TZV/J/van der Waals corrected) optimized geometries of non-fluorinated (**A**) and fluorinated (**B**-**F**) DFT-optimized models of **1·OO^{t}Bu-DFT**.

	A	**B**	**C**	**D**	**E**	**F**
Mn(1)	+0.42	+0.48	+0.47	+0.44	+0.44	+0.47
N(1)	-0.26	-0.33	-0.28	-0.27	-0.27	-0.27
N(2)	-0.40	-0.41	-0.37	-0.40	-0.38	-0.39
N(3)	-0.54	-0.58	-0.55	-0.54	-0.55	-0.56
N(4)	-0.59	-0.63	-0.58	-0.59	-0.59	-0.57
O(1)	-0.38	-0.41	-0.26	-0.36	-0.39	-0.36
O(2)	-0.20	-0.19	-0.37	-0.20	-0.24	-0.19
S(1)	-0.28	-0.22	-0.26	-0.27	-0.26	-0.29

values in Table 5.6, placing electron-withdrawing fluorine substituents at each of the five positions shown in Figure 5.18 causes the O(1)-O(2) bond to slightly lengthen from 1.479 Å (non-fluorinated mode **A**) to between 1.480-1.490 Å (models **B**-**F**). This is accompanied in each case by an increase in positive charge at the respective Mn(III) ion from +0.42 to between +0.44 and +0.48 (Table 5.7). Fluorination of the two pyridine methyl substituents causes the largest changes regarding bond lengths and Mulliken charge densities (mode **B**, Tables 5.6 and 5.7), as this model has the most positive Mn(III) charge (+0.48), least negative sulfur charge (-0.22), and most importantly the most negative charge localized on the proximal alkylperoxo oxygen (O(1), -0.41) within this series. A decrease in charge on the sulfur atom appears to result due to a

stronger Mn(1)-S(1) bond, as model **B** has the shortest such bond within this series (2.23 Å, Table 5.6). An increase in negative charge at O(1) is consistent with the MO description afforded above, as this model has a longer O(1)-O(2) bond (1.48 Å) than does non-fluorinated model **A**.

Model **B** also demonstrates that the N-heterocyclic moieties and thiolate are influenced by one another due to changes in electronics at the metal. As the pyridines are projected further from the metal, the charge on the thiolate sulfur decreases as the Mn(1)-S(1) bond shortens (strengthens). As the pyridines move in closer to the metal, the negative charge on the thiolate increases as the Mn-S bond lengthens. The sulfur atom responds to these changes by larger fluctuations in charge density relative to the pyridine nitrogens (N(3) and N(4), Table 5.7) since sulfur is a larger and more polarizable atom. Despite these compensating effects, slight differences in electronics at the Mn ion ultimately results in modulation of the O-O bond length by the relative strength of the bonding interaction between the alkylperoxo and Mn ion. These calculations suggest that more Lewis acidic Mn ions result in stronger Mn-OOR bonding interactions, which in turn promotes shorter O-O bonds. Conversely, as the Mn ion becomes less Lewis acidic, the Mn-OOR bonding interactions are not as strong and the O-O bond becomes progressively more activated.

A considerable amount of literature precedent exists which supports the observation that less Lewis acidic transition metal centers promote longer peroxo O-O bonds. For example, electron donating ligands *trans* to the peroxo of $[Mn^{III}(13\text{-TMC})(\eta^2\text{-}O_2)]^+$ have been shown to promote longer Mn-O and O-O bonds, as well as larger Mn-O-O angles.[24] Similar influences have been observed when modulating ligands *cis* to the peroxo moiety in $[Mn^{III}(O_2)(L_7py_2^{Me})]^+$ and $[Mn^{III}(O_2)(L_7py_2^{H})]^+$.[25,26] Electron donating ligands have also been shown to promote longer

O-O bonds in peroxo-bridged Cu dimers due to localization of electron density in antibonding peroxo π*(O-O) orbitals, similar to what was proposed within this series.[54-57] Precedent specifically regarding the effect of Lewis acidity upon O-O bond length has been established by Que with a series of Fe(III)-OOH complexes, where stronger O-O bonds were observed in complexes containing more Lewis acidic Fe(III) centers.[58] Finally, Mascharak has described a series of structurally analogous Co(III)-OOR complexes where more electron donating supporting ligands were found in complexes with longer O-O bonds.[59]

5.3.7 Variable-Temperature Decay Kinetics for Mn(III)-OOR Intermediates 1·OO^{t}Bu - 4·OO^{t}Bu and 1·OOCm

The decay kinetics of **1·OO^{t}Bu - 4·OO^{t}Bu** and **1·OOCm** in CH_2Cl_2 solutions were explored by variable-temperature UV/Vis measurements in order to determine if differences in O-O bond length were reflected in the relative lifetimes of these intermediates. Kinetic traces were obtained by monitoring absorption changes at 594 nm (**1·OO^{t}Bu**), 592 nm (**2·OO^{t}Bu**), 450 nm (**3·OO^{t}Bu**), 590 nm (**4·OO^{t}Bu**), and 615 nm (**1·OOCm**) at four different temperatures in CH_2Cl_2 along with 2.0 equivalents of triethylamine (Figure 5.19 and Appendix A.47-A50x). Linear fits to $\ln[(A_x-A_\infty)/(A_0-A_\infty)]$ versus time plots indicated that each decay process was first-order with respect to the Mn(III)-OOR intermediate (Figure 5.19). Half-lives were found to be independent of the initial concentrations of each Mn(III)-OOR intermediate, providing additional support for a first-order decay process. The rate law that describes each of these decay processes is provided in Equation 5.4. Activation parameters for the decay of these five intermediates were obtained

$$\text{rate} = k_1[\text{Mn(III)-OOR}] \quad (5.4)$$

from linear fits to Eyring plots (Figure 5.20 and Table 5.8). The $\Delta H^{\ddagger}$ and $\Delta S^{\ddagger}$ values for the decay of these five complexes each fall within a relatively narrow range of one another and display an enthalpy-entropy compensation relationship (Figure 5.21), which again suggests these intermediates decay by similar mechanisms (Table 5.8).

Strong correlations are found between each of the activation parameters, $\Delta H^{\ddagger}$ and $\Delta S^{\ddagger}$, and O(1)-O(2) bond lengths from the X-ray structures of **1·OO^{t}Bu - 4·OO^{t}Bu** and **1·OOCm**, while only weak correlations exist between these parameters and Mn(1)-O(1) bonds (Figures 5.22 and 5.23). These observations are supported by plots of $\Delta G^{\ddagger}$ versus O(1)-O(2) and Mn(1) O(1) bond lengths (Figure 5.24). Both plots (Figure 5.22 and 5.24) reveal that complexes with longer O-O bonds decay at progressively faster rates. Collectively, these observations are most consistent with a common decay mechanism involving rate-determinng O-O bond cleavage (as opposed to Mn-O bond cleavage). It is worthwhile to note that this mechanism would be expected to display a positive activation entropy, which is contrary to these experimental results

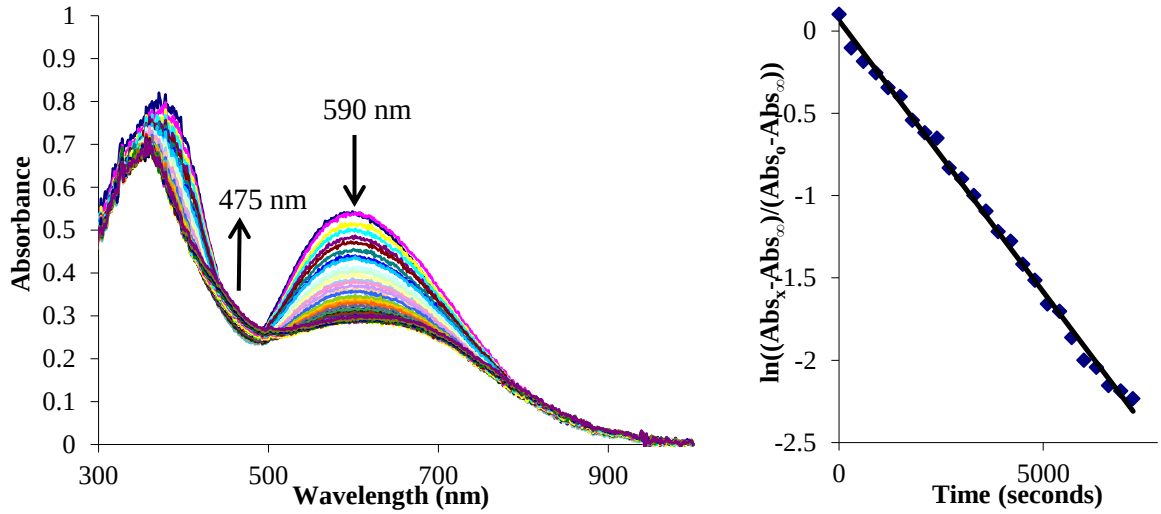

Figure 5.19 UV/Vis spectra (recorded in five minute intervals) displaying the decay of [Mn^{III}(S^{Me2}N$_4$(2-QuinoPN))(OO^{t}Bu)](PF$_6$)·pentane (**4·OO^{t}Bu**) with 2.0 equivalents of triethylamine in CH_2Cl_2 at 258 K (left). Plot of ln[(A_x-A_∞)/(A_0-A_∞)] versus time (λ = 590) (right).

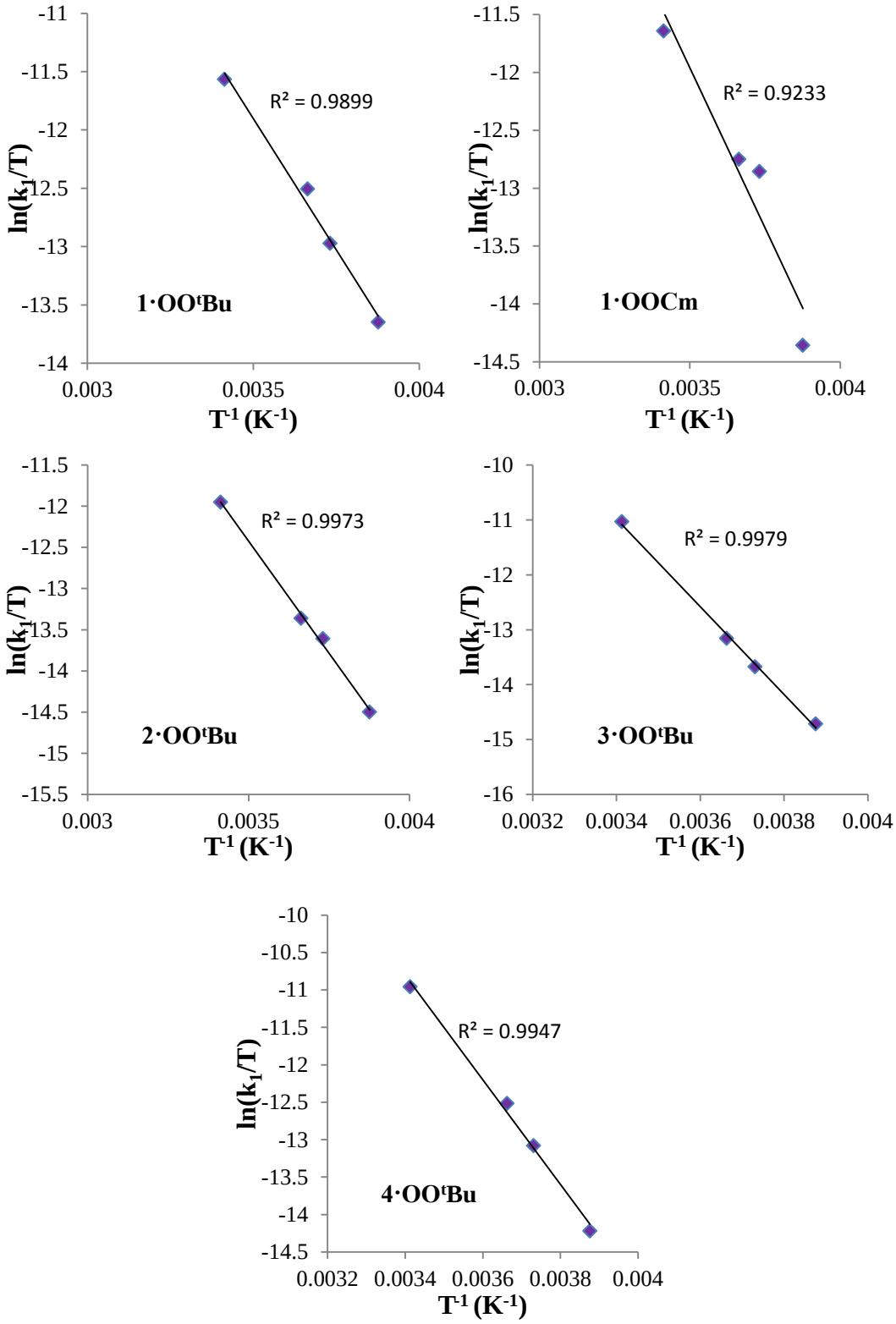

Figure 5.20 Eyring plots from variable-temperature kinetics measurements for the decay of **1·OO^{t}Bu** – **4·OO^{t}Bu** and **1·OOCm** in CH_2Cl_2.

Table 5.8 Activation enthalpies (kcal/mol), activation entropies (cal/mol·K), and activation free energies (273 K, kcal/mol) for the decay of $[Mn^{III}(S^{Me2}N_4(6\text{-Me-DPEN}))(OO^tBu)](BPh_4)$ (**1·OO^{t}Bu**), $[Mn^{III}(S^{Me2}N_4(6\text{-Me-DPEN}))(OOCm)](BPh_4)$ (**1·OOCm**), $[Mn^{III}(S^{Me2}N_4(2\text{-QuinoEN}))(OO^tBu)](BPh_4)$ (**2·OO^{t}Bu**), $[Mn^{III}(S^{Me2}N_4(6\text{-Me-DPPN}))(OO^tBu)](BPh_4)\cdot Et_2O$ (**3·OO^{t}Bu**), and $[Mn^{III}(S^{Me2}N_4(2\text{-QuinoPN}))(OO^tBu)](PF_6)\cdot$pentane (**4·OO^{t}Bu**) in CH_2Cl_2.

	1·OO^{t}Bu	**1·OOCm**	**2·OO^{t}Bu**	**3·OO^{t}Bu**	**4·OO^{t}Bu**
$\Delta H^{\ddagger}$	10.4	11.0	10.8	15.9	13.9
$\Delta S^{\ddagger}$	-34	-32	-34	-15	-21
$\Delta G^{\ddagger}$ (at 273 K)	11.3	11.9	11.7	16.3	14.5

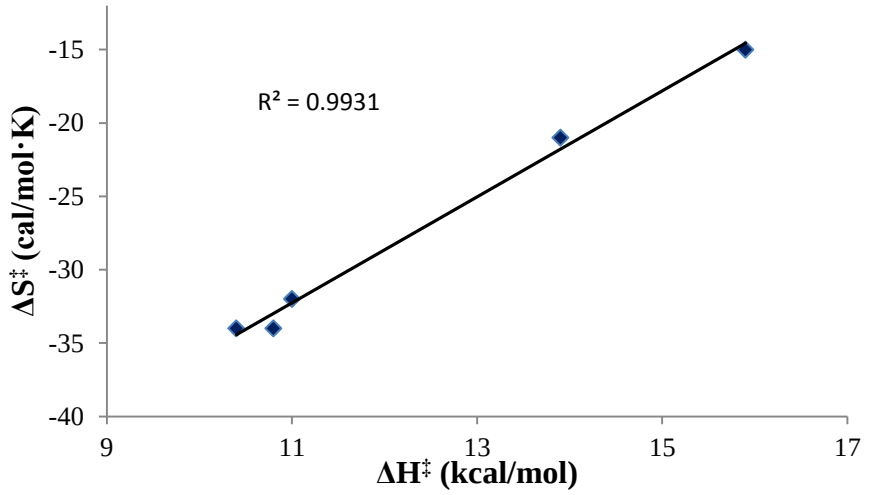

Figure 5.21 Isokinetic plot ($\Delta S^{\ddagger}$ versus $\Delta H^{\ddagger}$) for **1·OO^{t}Bu** – **4·OO^{t}Bu** and **1·OOCm** (individual data provided in Table 5.7).

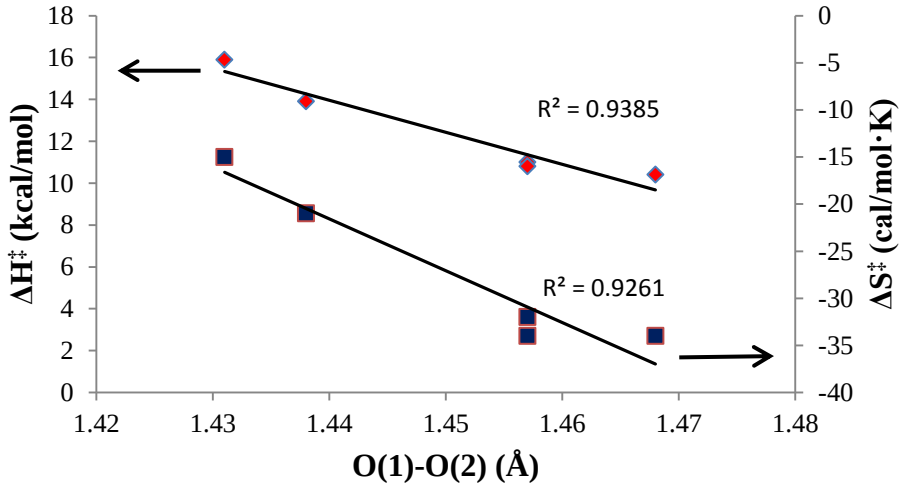

Figure 5.22 Plots of activation enthalpy ($\Delta H^{\ddagger}$, left y-axis) and activation entropy ($\Delta S^{\ddagger}$, right y-axis) versus O(1)-O(2) bond length for **1·OO^{t}Bu** – **4·OO^{t}Bu** and **1·OOCm**.

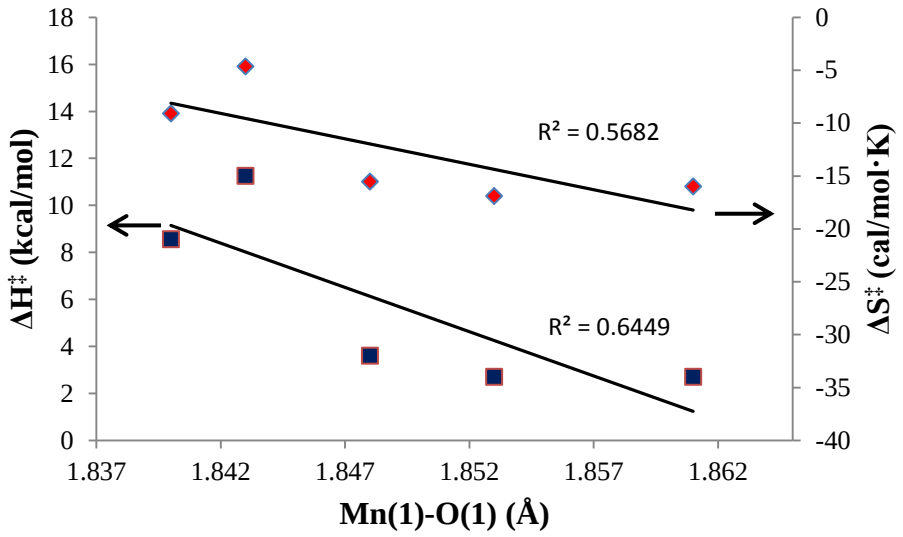

Figure 5.23 Plots of activation enthalpy ($\Delta H^{\ddagger}$, left y-axis) and activation entropy ($\Delta S^{\ddagger}$, right y-axis) versus Mn(1)-O(1) bond length for **1·OO^{t}Bu** – **4·OO^{t}Bu** and **1·OOCm**.

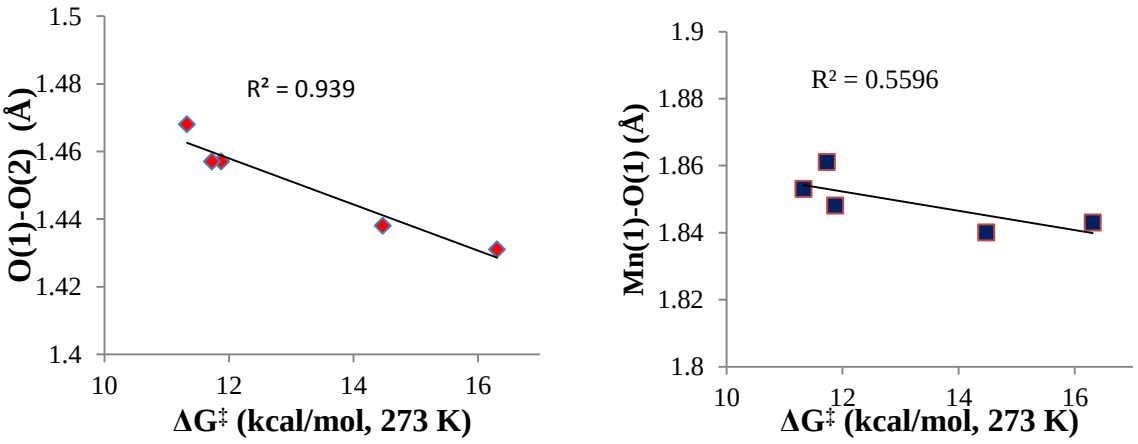

Figure 5.24 Plots of O(1)-O(2) bond length (left) and Mn(1)-O(1) bond length versus activation free energy ($\Delta G^{\ddagger}$, at 273 K) for the decay of intermediates **1·OO^{t}Bu** – **4·OO^{t}Bu** and **1·OOCm**.

(Table 5.7). Given that longer O-O bonds are found in complexes with shorter Mn(1)-N(3,4)$_{ave}$ distances (Table 5.2), one possible explanation for this discrepancy is that the transition state that leads to successful O-O bond cleavage has a more ordered geometry with respect to these particular metrics. This observation has been noted in other first-row transition metal-

alkylperoxo systems; Que has reported a series of high-spin Fe(III)-OO^{t}Bu complexes that decay via rate-determining Fe-O cleavage with negative activation entropy values.[60-61] Likewise, Balch has reported a negative activation entropy value for the homolytic O-O cleavage of the peroxo ligand in (TMP)Fe(III)-O-O-Fe(III)(TMP).[62]

5.3.8 Identification of Final Reaction Products

5.3.8.1 Final Products From the Decay of Isolated Intermediates

The final products formed following the decay of intermediates **1·OO^{t}Bu** – **4·OO^{t}Bu** and **1·OOCm - 2·OOCm** were identified using a combination of various methods. Each respective final reaction mixture was found to contain white solids, black solids, and materials which were soluble in CH_2Cl_2. The white solids were identified as the X^- (X- = BPh_4^- for **1·OO^{t}Bu** – **3·OO^{t}Bu** and **1·OOCm - 2·OOCm**, or PF_6^- for **3·OO^{t}Bu**) salts of either protonated N,N-bis(6-methyl-2-pyridilmethyl)ethane-1,2-diamine (**1·OO^{t}Bu** and **1·OOCm**), N,N-bis(2-quinoline)ethane-1,2-diamine (**2·OO^{t}Bu** and **2·OOCm**), N,N-bis(6-methyl-2-pyridilmethyl)propane-1,3-diamine (**3·OO^{t}Bu**), or N,N-bis(2-quinoline)propane-1,3-diamine (**4·OO^{t}Bu**) by ^{1}H NMR spectroscopy, ESI-MS, and X-ray crystallography, each of which were obtained in 70-85% yields (Figure 5.25). The products soluble in CH_2Cl_2 were identified as 3-methyl-2-butanone-3-disulfide (80-90 % yield, Figure 5.26), as well as either *tert*-butanol (70-80 % from **1·OO^{t}Bu** – **4·OO^{t}Bu**) or acetophenone (68-75 % from **1·OOCm - 2·OOCm**). The disulfide product may form from a reaction between a highly-oxidizing tert-butoxy radical (which would form following homolytic O-O bond cleavage) and the thiolate ligand moiety, thus suggesting the pentadentate ligands in these complexes may be serving as internal "trapping"

reagents. Identification of the insoluble black precipitate was less conclusive, however it is suspected that this product is likely a manganese oxide of some sort.

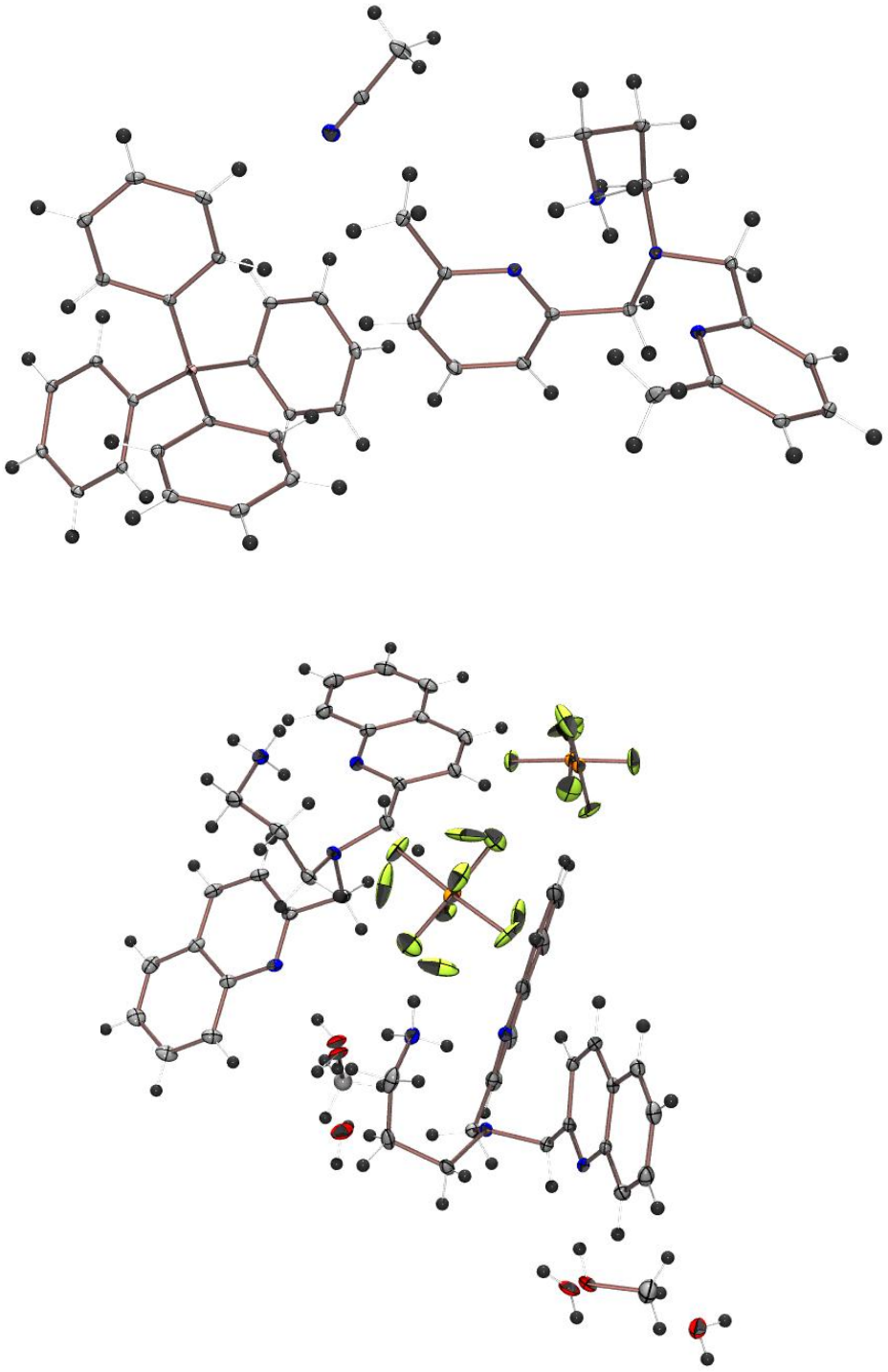

Figure 5.25 ORTEP diagrams (50 % probability) of ligand fragments and counterions from the decay of intermediates **1·OO^{t}Bu** (top) and **4·OO^{t}Bu** (bottom).

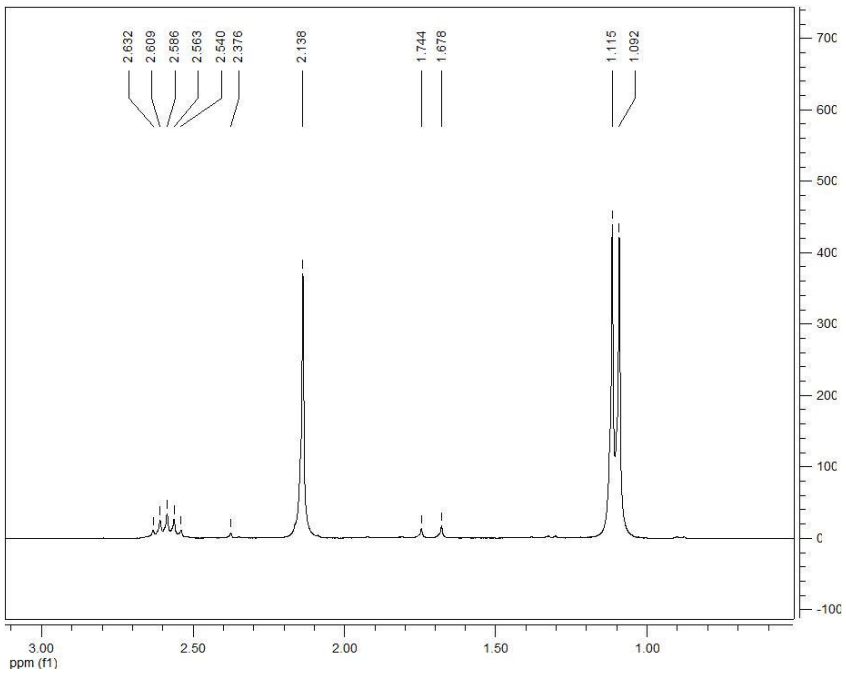

Figure 5.26 ^{1}H NMR spectrum of 3-methyl-2-butanone-3-disulfide ($CDCl_3$, 300 MHz, 293 K).

Analysis of the final products formed from **1·OOCm** - **2·OOCm** was of particular interest, as cumene hydroperoxide is well-recognized as a mechanistic probe for homolytic versus heterolytic O-O bond cleavage pathways. As stated above, these two complexes decay to afford acetophenone (the product formed from homolytic O-O bond scission) in 68-72 % yield. Cumenol, which is the product formed from heterolyic O-O bond cleavage of cumene hydroperoxide, was unobserved in both reaction mixtures. These results provide direct evidence that O-O bond homolysis is the predominant reaction pathways for the decay of **1·OOCm** - **2·OOCm**. In light of the trends established between **1·OOCm** and **1·OO^{t}Bu** – **4·OO^{t}Bu**, it can be reasoned that the decay of the four Mn(III)-OO^{t}Bu intermediates also involves rate-determining O-O bond homolysis.

5.3.8.2 Final Products From Reactions With External Substrates

In order to determine if **1·OOCm** and **1·OO^{t}Bu** – **4·OO^{t}Bu** were reactive with exogenous substrates, various organic molecules were added to solutions of each respective intermediate at 268 K and the resulting mixtures were monitored by UV/Vis spectroscopy. Substrates screened include cyclohexane, cyclohexane carboxaldehyde, tetracyanoethylene, styrene, triethylphosphine, thioaniosle, 2,2,6,6-tetramethyl-piperidine-1-ol (TEMPO-H), dihydroanthracene, and 2,4-di-*tert*-butylphenol. The decay of each intermediate displayed a zero-order dependence on the concentration of these substrates (even at 500-fold excess amounts), suggesting **1·OOCm** and **1·OO^{t}Bu** – **4·OO^{t}Bu** do not undergo a direct reaction with these substrates. Analysis of the final reaction mixtures did, however, reveal the presence of oxidized organic substrates. These observations suggest that the oxidant (or oxidants) responsible for reacting with these substrates is (or are) formed following rate-limiting O-O bond cleavage.

Reactions involving triethylphosphine (Et_3P) afforded yet another line of evidence to support a homolytic O-O cleavage mechanism for the decay of these intermediates. The highly oxidizing *tert*-butoxide radical has been shown to react with Et_3P to form the corresponding *tert*-butyl-phosphonite (Et_2PO^tBu); analysis of the final products from the decay of **1·OO^{t}Bu** – **4·OO^{t}Bu** yielded both Et_2PO^tBu (31 %) and Et_3PO.[37] Identification of these products signifies the formation of the *tert*-butoxide radical and further supports O-O bond homolysis as the rate-determining step in the decay of these intermediates.

Finally, reactions were explored between **1·OO^{t}Bu** – **4·OO^{t}Bu** and **1·OOCm** and acids in order to gauge the relatively basicity of the alkylperoxo ligands in these complexes. Addition

of acetic acid (2 equivalents per equivalent of Mn(III)-OOR) to CH_2Cl_2 solutions of each respective intermediate at 258 K in a single aliquot resulted in an immediate reaction as was determined by the growth of a new absorbance bands centered between 475-494 nm (Figure 5.27). The absorbance band shape and energy of each respective product resemble those observed from chemical oxidation of each Mn(II) complex, as well as proton-assisted oxo-bridged cleavage of the oxo-bridged Mn(III,III) dimers discussed in Chapter 3. These experiments suggest that the proximal alkylperoxo oxygen in each intermediate is sufficiently basic enough to be protonated, presumably affording ROOH and the respective mononuclear Mn(III) complex.

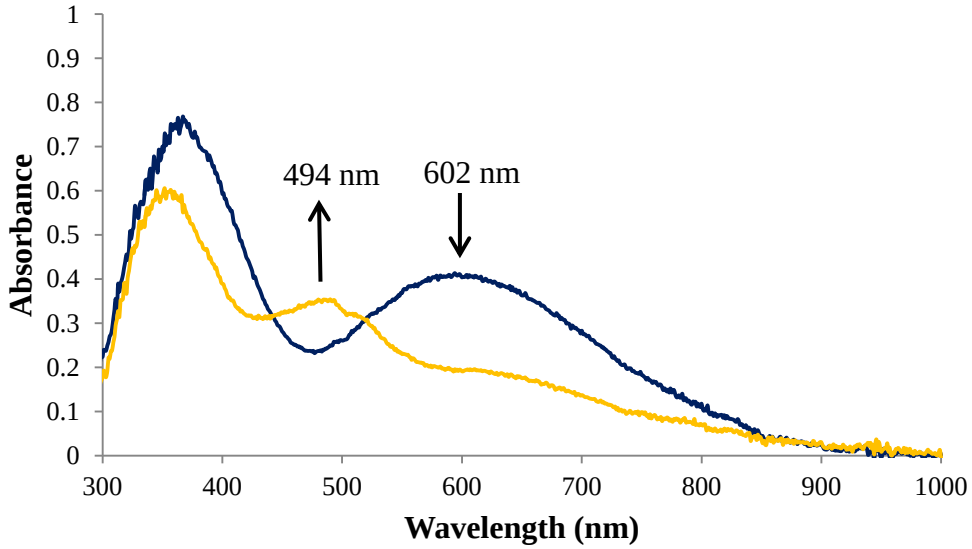

Figure 5.27 UV/Vis spectra displaying the reaction between $[Mn^{III}(S^{Me2}N_4(2\text{-QuinoEN}))(OO^tBu)](BPh_4)$ (**2·OO^{t}Bu**, 1.5 mM) and AcOH (2 equivalents) in CH_2Cl_2 at 258 K.

5.3.9 Reactivity of Alcohol- and Alkoxide-Ligated Complexes 9 and 10 with *tert*-Butyl Hydroperoxide

5.3.9.1 Complex 9

Reactions between complexes **9** and ^{t}BuOOH were pursued in order to obtain an alkoxide analogue of one of the thiolate-ligated Mn(III)-OO^{t}Bu complexes. An alkoxide analogue of **1·OO^{t}Bu**, complex **5·OO^{t}Bu**, was successfully isolated and characterized from reactions between complex **9** and ^{t}BuOOH in CH_2Cl_2. X-ray quality crystals of [Mn^{III}($O^{Me2}N_4$(6-Me-DPEN))(OO^{t}Bu)](BPh_4) (**5·OO^{t}Bu**) were obtained from concentrated CH_2Cl_2 solutions layered with Et_2O at 193 K. An ORTEP diagram of **5·OO^{t}Bu** is provided in Figure 5.28, while crystal data is compiled in Table 5.1. Similar to **1·OO^{t}Bu** - **4·OO^{t}Bu**, the Mn ion in **5·OO^{t}Bu** is coordinated by an imine nitrogen (N(1), tertiary amine (N(2)), and a ^{t}BuOO oxygen (O(1)). An

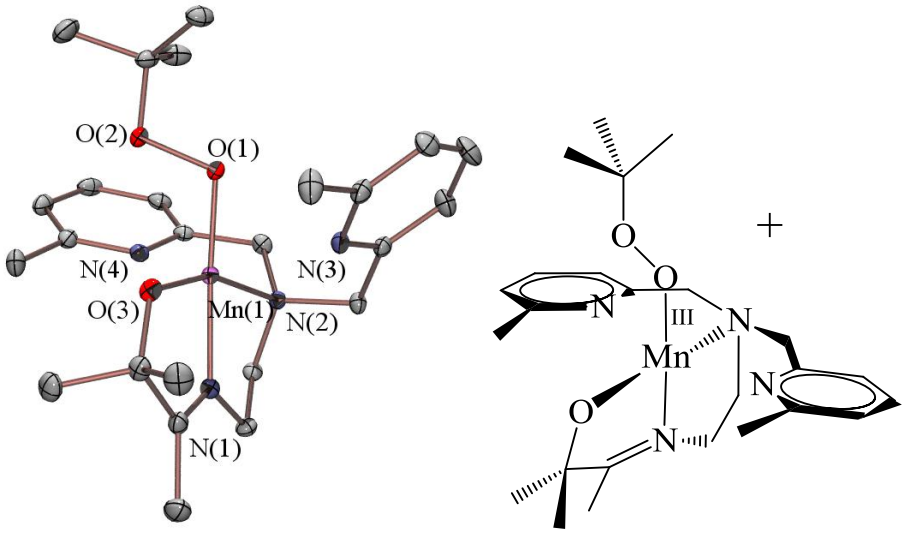

Figure 5.28 ORTEP diagram (50 % probability) of [Mn^{III}($O^{Me2}N_4$(6-Me-DPEN))(OO^{t}Bu)]$^{+}$ (**5·OO^{t}Bu**) with hydrogen atoms, counterion, and solvent of crystallization omitted for clarity. Selected bond distances (Å) and angles (deg); Mn(1)-O(1), 1.8563(10); Mn(1)-O(3), 1.8535(9); Mn(1)-N(1), 2.0042(12); Mn(1)-N(2), 2.1608(11); Mn(1)-N(3), 2.3547(11); Mn(1)-N(4), 2.4314(12); O(1)-O(2), 1.4732(13); Mn(1)-O(1)-O(2), 110.41(7); O(1)-Mn(1)-O(3), 98.26(4); O(1)-Mn(1)-N(1), 81.20(5); O(1)-Mn(1)-N(2), 101.77(4); O(1)-Mn(1)-N(3), 83.03(4); O(1)-Mn(1)-N(4), 73.13(4); O(3)-Mn(1)-N(2), 113.08(4); N(3)-Mn(1)-N(4), 134.84(4).

alkoxide oxygen (O(3)) has replaced the thiolate sulfur (S(1)) which was present in the **1·OO^{t}Bu** - **4·OO^{t}Bu** . The Mn(1)-N(6-methylpyridine) (N(3) and N(4)) distances are also fairly elongated, therefore (in the solid state) this structure is best described as containing a four coordinate Mn ion. The presence of a single BPh_4^- counterion per Mn complex confirms the Mn ion oxidation state in this complex is indeed +3.

On average, the metal-ligand bonds in alkoxide-ligated **5·OO^{t}Bu** are shorter than those in thiolate-ligated **1·OO^{t}Bu** (Table 5.2 and Figure 5.28). This is, of course, not considering the Mn(1)-O(3) and Mn(1)-S(1) distances in **5·OO^{t}Bu** and **1·OO^{t}Bu**, respectively. The longer-range Mn(1)-N(3) and Mn(1)-N(4) interactions are also only slightly shorter in **5·OO^{t}Bu** relative to **1·OO^{t}Bu**. Contrary to these observations, the alkylperoxo O(1)-O(2) bond length in **5·OO^{t}Bu** (1.4732(13) Å) is longer than those found in all of the thiolate-ligated Mn(III)-OOR complexes (1.431(5)-1.468(7) Å). These metrical parameters fit nicely within the trends previously established for the thiolate-ligated Mn(III)-OOR series; as is shown in Figure 5.29, replacement of the thiolate moiety with an alkoxide does not appear to influence the empirical relationship between Mn(1)-N(3,4)$_{ave}$ distance and O(1)-O(2) bond length.

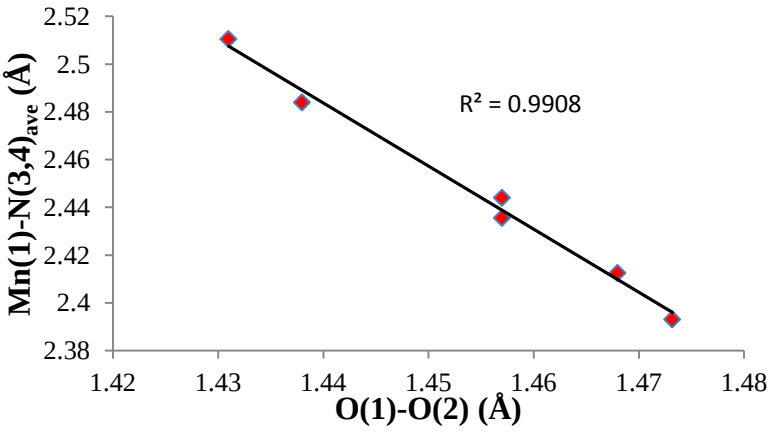

Figure 5.29 Plot of Mn(1)-N(3,4)$_{ave}$ distance versus O(1)-O(2) bond length for **1·OO^{t}Bu** - **5·OO^{t}Bu** and **1·OOCm**.

Despite being structurally similar to **1·OO^{t}Bu** - **5·OO^{t}Bu** and **1·OOCm** , alkoxide-ligated **5·OO^{t}Bu** was found to be considerably more stable compared to the thiolate-ligated Mn(III)-OOR complexes. Room temperature CH_2Cl_2 solutions of **5·OO^{t}Bu** were found to be stable for days, while low temperature CH_2Cl_2 solutions of **1·OO^{t}Bu** - **4·OO^{t}Bu** and **1·OOCm** each completely decayed in no more than a few hours. The X-ray quality crystals obtained for **5·OO^{t}Bu** were found to be fairly stable at room temperature, as positive elemental analysis results were obtained from crystals which had been aged on the benchtop for months.[63]

The incredible stability exhibited by this complex permitted further spectroscopic studies to be conducted. UV/Vis titration experiments (similar to those described with complexes **1**-**4**) were performed in which substoichiometric amounts of ^{t}BuOOH were added to anaerobic CH_2Cl_2 of complex **9** at 293 K. These experiments revealed that ~1.7 equivalents of ^{t}BuOOH resulted in the nearly quantitative formation of **5·OO^{t}Bu** (Figure 5.30). The yield of **5·OO^{t}Bu** determined from these experiments was calculated using experimentally-determined extinction

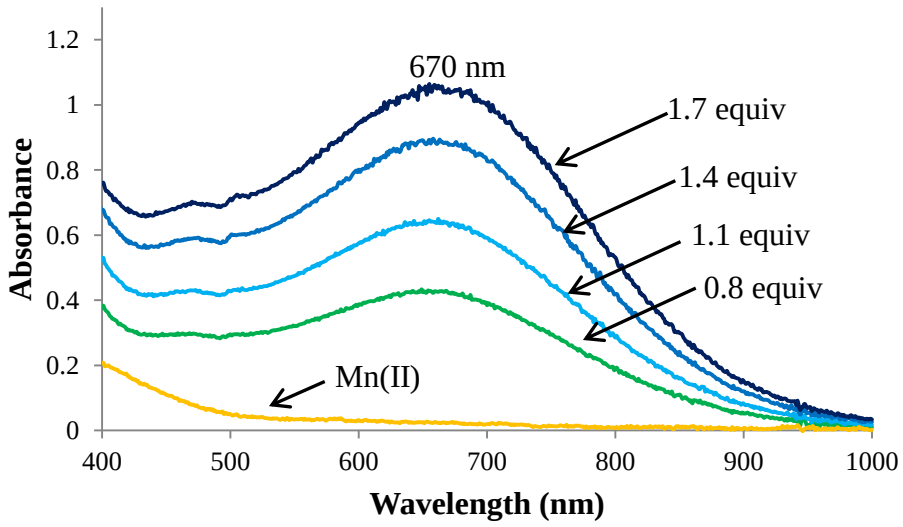

Figure 5.30 Anaerobic UV/Vis titration experiment displaying the reaction between [Mn^{II}(OH^{Me2}N$_4$(6-Me-DPEN))(CHO$_2$)](BPh$_4$) (**9**, 1.05 mM) and subquantitative aliquots of ^{t}BuOOH (0.1 M stock solution in CH_2Cl_2) in CH_2Cl_2 at 293 K.

coefficients for this complex (Appendix A.51). It is worthwhile to note that these unlike UV/Vis titration experiments with thiolate-ligated **1-4**, these experiments were not conducted with triethylamine. UV/Vis spectra displaying the slow decay of **5·OO^{t}Bu** in CH_2Cl_2 at room temperature is provided in the Appendix (A.52).

Intermediate **5·OO^{t}Bu** was also characterized by IR and parallel polarization mode X-band EPR spectroscopies. The FT-IR spectra of **5·OO^{t}Bu** prepared from $^{t}Bu^{16}O^{16}OH$ and $^{t}Bu^{18}O^{18}OH$ are shown in Figure 5.31. An isotopically-sensitive stretch at 850 cm^{-1} (^{16}O-) shifts to 816 cm^{-1} (^{18}O-); the isotopic shift (34 cm^{-1}) and energies for these vibrational features are each in the correct respective ranges for an ν(O-O) stretch. Aside from the ν(O-O) stretch of $[Mn^{III}(S^{Me2}N_4(6\text{-Me-DPEN}))]_2(\textit{trans}\text{-}\mu\text{-}1,2\text{-}O_2)(BPh_4)_2\cdot 2CH_3CH_2CN$ (819 cm^{-1}, Chapter 4), the ν(O-O) stretch for **5·OO^{t}Bu** is the lowest for any Mn-peroxo complex reported or discussed in this thesis.

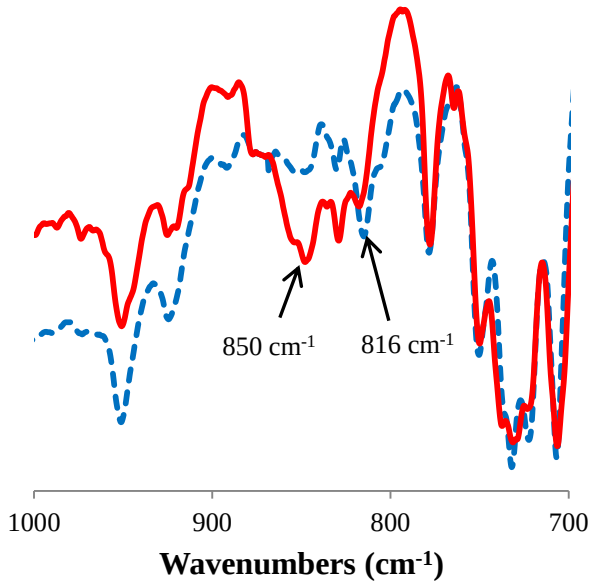

Figure 5.31 FT-IR spectra of **5·OO^{t}Bu** prepared from $^{t}Bu^{16}O^{16}OH$ (solid red trace) and $^{t}Bu^{18}O^{18}OH$ (dashed blue trace) (Nujol mull, NaCl salt plates, 293 K).

The parallel polarization mode X-band EPR spectrum of **5·OO^{t}Bu** at 32 K in MeCN/toluene glass (1:1) is provided in Figure 5.32 and displays a single broad signal at low fields, which is similar to the spectra obtained for **2·OO^{t}Bu** (*vide supra*) and the peroxo-bridged Mn(III,III) dimers discussed in Chapter 4. The spectrum in Figure 5.32 was fit (dashed blue trace) with S = 2, g_{iso} = 2.00, D = -2.00 cm^{-1}, and E/D = 0.23. The sign and magnitude of D are close to those from fits to both the solid state magnetic susceptibility data and EPR spectra of the peroxo-bridged Mn(III,III) dimers discussed in Chapter 4. Consistent with these measurements is the solution effective magnetic moment for **5·OO^{t}Bu**, which was determined to be 4.55 B.M. in CD_2Cl_2.

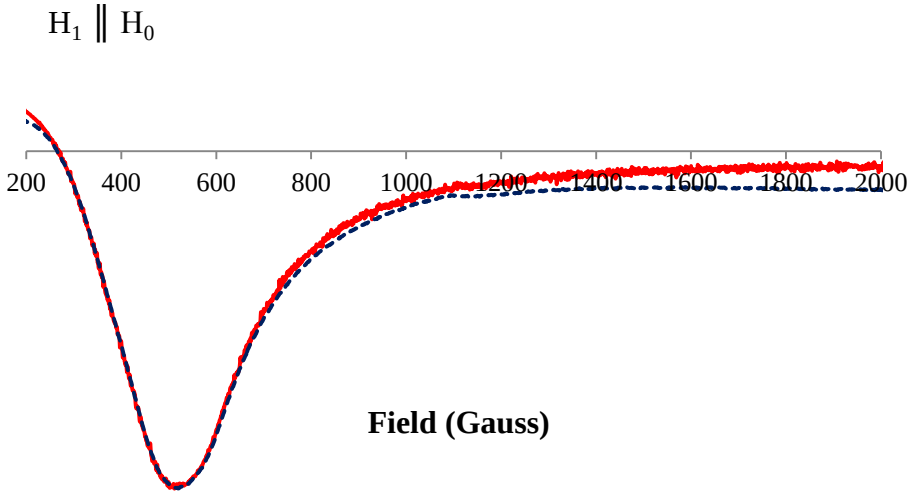

Figure 5.32 Parallel polarization mode X-band EPR spectrum of [Mn^{III}(O^{Me2}N$_4$(6-Me-DPEN))(OO^{t}Bu)](BPh$_4$) (**5·OO^{t}Bu**) in MeCN/toluene glass (1:1) at 32 K (solid red trace), along with a best fit to the experimental data (dashed blue trace).

Complex **5·OO^{t}Bu** was found to eventually decay in solution over a period of a few days, but the final products formed during this process have largely gone unidentified. One Mn-

containing product has, however, been structurally characterized by X-ray crystallography as a bis(μ-oxo)Mn_2^{IV} dimer (complex **12**), which was recovered in ~40% yield (Figure 5.33). Crystal data for **12** is provided in Table 5.1. It is worthwhile to note that the Schiff base has been lost from each half of dimer **12**, although this ligand fragment has yet to be detected from final reaction mixtures containing this particular product.

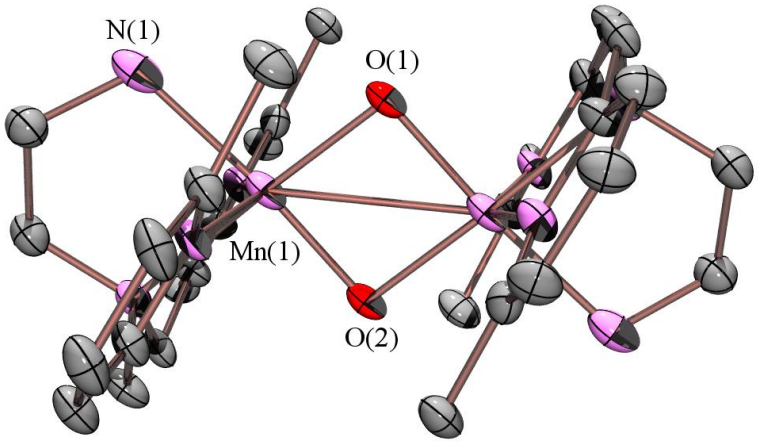

Figure 5.33 ORTEP diagram of $\{[Mn^{IV}(N_4(6\text{-Me-DPEN}))]_2(\mu\text{-}O)_2\}^{2+}$ (**12**) with hydrogen atoms and counterions omitted for clarity. Selected bond distances (Å) and angles (deg) for **12**: Mn(1)-O(1), 1.8324(15); Mn(1)-N(1), 1.96(3); Mn(1)-N(2), 2.133(6); Mn(1)-N(3), 2.3522(18) Mn(1)-N(4), 2.3251(18); Mn(1)-O(2), 1.8349(15); O(1)-Mn(1)-N(1), 89.10(13); O(1)-Mn(1)-N(2), 174.90(7); O(1)-Mn(1)-N(3), 106.39(6); O(1)-Mn(1)-N(4), 94.31(6); O(1)-Mn(1)-O(2), 85.98(7), Mn(1)-O(2)-Mn(2), 94.02(7).

5.3.9.3 Complex 10

Reactions between alkoxide-ligated complex **10** and ^{t}BuOOH were explored in anaerobic CH_2Cl_2 solutions at low temperatures. Unfortunately, no metastable intermediates were detected during these reactions. Final reaction solutions were analyzed and found to contain a bis(μ-oxo)Mn_2^{IV} product (**13**) analogous to **12** (Figure 5.34, crystal data is found in Table 5.1). No further reactions between **10** and any alkyl hydroperoxide reagent have been explored.

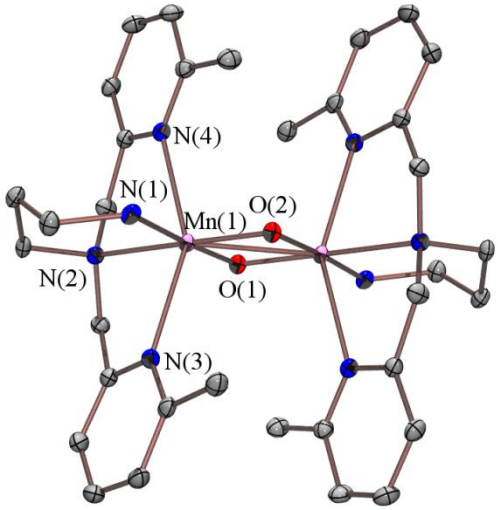

Figure 5.34 ORTEP diagram of $\{[Mn^{IV}(N_4(6\text{-Me-DPPN}))]_2(\mu\text{-}O)_2\}^{2+}$ (**13**) with hydrogen atoms and counterions omitted for clarity.

5.4 Summary

This chapter has described the synthesis of seven new Mn(III)-alkylperoxo complexes. Characterization of these species was performed via UV/Vis spectroscopy, ESI mass spectrometry, FT-IR spectroscopy, X-band EPR spectroscopy, and X-ray crystallography. Systematic trends were established from the structural, spectroscopic, and reactivity data obtained, which have afforded insights regarding correlations between the geometric and electronic structures of these species. These correlations ultimately were conveyed to help rationalize the reactivity of these complexes. From the structural trends, it has been concluded that the electron-donating ability of the N-heterocyclic moieties located *cis* to the alkylperoxo ligand play a key role in determining the degree of O-O bond activation in each complex. Computational studies show that the relatively Lewis acidity of the metal ion directly influences the extent of O-O bond activation, with longer O-O bonds occurring in less Lewis acidity metal

complexes. The identity of the alkyl group in the ROO^- ligand was found to have no considerable effect upon these trends. Variable-temperature decay kinetics were evaluated for each complex, affording activation parameters for the thermal decay of each intermediate. Correlations between the metrical and activation parameters of decay provide evidence to suggest each complex decays via a similar mechanism involving homolytic O-O bond cleavage.

5.5 Notes to Chapter 5

1) Cotruvo, J. A., Jr.; Stubbe, J. *Biochemistry* **2010**, *49*, 1297-1309.

2) Umena, Y.; Kawakami, K.; Shen, J.-R.; Kamiya, N. *Nature* **2011**, *473*, 55-60.

3) Oliw, E. H.; Jerneren, F.; Hoffmann, I.; Sahlin, M.; Garscha, U. *Biochimica Biophysica Acta* **2011**, *1811*, 138-147.

4) Perry, J. J. P.; Hearn, A. S.; Cabelli, D. E.; Nick, H. S.; Tainer, J. A.; Silverman, D. N. *Biochemistry* **2009**, *48*, 3417-3424.

5) Boal, A. K.; Cotruvo, J. A., Jr.; Stubbe, J.; Rosenzweig, A. C. *Science* **2010**, *329*, 1526-1530.

6) Barnese, K.; Sheng, Y.; Stich, T.; Gralla, E. B.; Britt, R. D.; Cabelli, D.; Valentine, J. S. *J. Am. Chem. Soc.* **2010**, *132*, 12525-12527.

7) Armstrong, F. A. *Phil. Trans. R. Soc. B* **2008**, *363*, 1263-1270.

8) Emerson, J. P.; Kovaleva, E. G.; Farquhar, E. R.; Lipscomb, J. D.; Que, L., Jr. *Proc. Natl. Acad. Sci, USA* **2008**, *105*, 7347-7352.

9) McEvoy, J. P.; Brudvig, G. W. *Chem. Rev.* **2006**, *106*, 4455-4483.

10) Hearn, A. S.; Stroupe, M. E.; Cabelli, D. E.; Lepock, J. R.; Tainer, J. A.; Nick, H. S.; Silverman, D. N. *Biochemistry* **2001**, *40*, 12051-12058.

11) Jackson, T. A.; Karapetian, A.; Miller, A.-F.; Brunold, T. C., *Biochemistry* **2005**, *44*, 1504-1520.

12) Miller, A.-F. *Curr. Op. Chem. Biol.* **2004**, *8*, 162-168.

13) Yachandra, V. K.; Sauer, K.; Klein, M. P. *Chem. Rev.* **1996**, *96*, 2927-2950.

14) Bull, C.; Niederhoffer, E. C.; Yoshida, T.; Fee, J. A. *J. Am. Chem. Soc.* **1991**, *113*, 4069-4076.

15) Lewis, N. S.; Nocera, D. G. *Proc. Natl. Acad. Sci, USA* **2006**, *103*, 15729-15735.

16) Goldsmith, C. R.; Cole, A. P.; Stack, T. D. P. *J. Am. Chem. Soc.* **2005**, *127*, 9904-9912.

17) Hamberg, M.; Su, C.; Oliw, E. *J. Biol. Chem.* **1998**, *273*, 13080-13088.

18) Skrzypczak-Jankun, E.; Bross, R. A.; Carroll, R. T.; Dunham, W. R.; Funk, M. O. *J. Am. Chem. Soc.* **2001**, *123*, 10814-10820.

19) Kovaleva, E. G.; Lipscomb, J. D. *Science* **2007**, *316*, 453-456.

20) Emerson, J. P.; Kovaleva, E. G.; Farquhar, e. R.; Lipscomb, J. D.; Que, L., Jr. *Proc. Natl. Acad. Sci, USA* **2008**, *105*, 7347-7352.

21) Geiger, R. A.; Wijeratne, G.; Day, V. W.; Jackson, T. A. *Eur. J. Inorg. Chem.* **2012**, *10*, 1598-1608.

22) Annaraj, J.; Cho, J.; Lee, Y.-M.; Kim, S. Y.; Latifi, R.; de Visser, S. P.; Nam, W. *Angew. Chem. lnt. Ed. Engl*. **2009**, *48*, 4150-4153.

23) Geiger, R. A.; Chattopadhyay, S.; Day, V. W.; Jackson, T. A. *J. Am. Chem. Soc.* **2010**, *132*, 2821-2831.

24) Geiger, R. A.; Leto, D. F.; Chattopadhyay, S.; Dorlet, P.; Anxolabéhère-Mallart; E.; Jackson, T. A. *Inorg. Chem.* **2011**, *50*, 10190-10203.

25) Hearn, A. S.; Tu, C. K.; Nick, H. S.; Silverman, D. N. *J. Biol. Chem.* **1999**, *274*, 24457-24460.

26) Seo, M. S.; Kim, J. Y.; Annaraj, J.; Kim, Y.; Lee, Y.-M.; Kim, S.-J.; Nam, W. *Angew. Chem lnt. Ed. Engl.* **2007**, *46*, 377-380.

27) Bossek, U.; Weyhermuller, T.; Wieghardt, K.; Nuber, B.; Weiss, J. *J. Am. Chem. Soc.* **1990**, *112*, 6387-6388.

28) Groni, S.; Dorlet, P.; Blain, G.; Bourcier, S.; Guillot, R.; Anxolabéhère-Mallart, E. *Inorg. Chem.* **2008**, *47*, 3166-3172.

29) VanAtta, R. B.; Strouse, C. E.; Hanson, L. K.; Valentine, J. S. *J. Am. Chem. Soc.* **1987**, *109*, 1425-1434.

30) Kitajima, N.; Komatsuzaki, H.; Hikichi, S.; Osawa, M.; Moro-oka, Y. *J. Am. Chem. Soc.* **1994**, *116*, 11596-11597.

31) Singh, U. P.; Sharma, A. K.; Hikichi, S.; Komatsuzaki, H.; Moro-oka, Y.; Akita, M. *Inorg. Chim. Acta.* **2006**, *359*, 4407-4411.

32) Komatsuzaki, H.; Sakamoto, N.; Satoh, M.; Hikichi, S.; Akita, M.; Moro-oka, Y. *Inorg. Chem.* **1998**, *37*, 6554-6555.

33) Stoll, S.; Schweiger, A. *J. Magn. Reson.* **2006**, *178*, 42-55.

34) http://eww.mpi-muelheim.mpg.de/bac/logins/bill/julX_en.php

35) Live, D. H.; Chan, S. I. *Anal. Chem.* **1970**, *42*, 791.

36) Walling, C.; Buckler, S. A. *J. Am. Chem. Soc.* **1955**, *77*, 6032-6038.

37) DiPasquale, A. G.; Hrovat, D. A.; Mayer, J. M. *Organometallics* **2006**, *25*, 915-924.

38) Neese, F. ORCA-an ab initio, density functional and semi-empirical program package, Version 2.7; University of Bonn: Bonn, Germany, 2010.

39) Roemelt, M.; Beckwith, M. A.; Duboc, C.; Collomb, M.-N.; Neese, F.; DeBeer, S. *Inorg. Chem.* **2012**, *51*, 680-687.

40) Buhl, M.; Kabrede, H. *J. Chem. Theory Comput.* **2006**, *2*, 1282-1290.

41) Lenthe, E. V.; Baerends, E. J.; Snijders, J. G. *J. Chem. Phys.* **1993**, *99*, 4597.

42) van Wullen, C. *J. Chem. Phys.* **1998**, *109*, 392.

43) Weigend, F.; Ahlrichs, R. *Phys. Chem. Chem. Phys.* **2005**, *7*, 3297.

44) Klamt, A.; Schüürmann, G. *J. Chem. Soc., Perkin Trans.* **1993**, *799*.

45) Tao, J.; Perdew, J. P.; Staroverov, V. N.; Scuseria, G. E. *Phys. Rev. Lett.* **2003**, *91*, 146401.

46) Tao, J.; Perdew, J. P.; Staroverov, V. N.; Scuseria, G. E. *Phys. Rev. Lett.* **2004**, *120*, 6898–6911.

47) Sheldrick, G. M. CELL_NOW. 2005, University of Goettingen, Germany.

48) Bruker APEX2 (Version 2.1-.4), SAINT (Version 7.34A), SADABS. 2007.

49) Waasmair, D.; Kirfel, A. *Acta Cryst.* **1997**, *30*, 565.

50) Sheldrick, G. M. SHELXL-97: Program for the Refinement of Crystal Structures. 1997, University of Goettingen, Germany.

51) Shannon, R. D. *Acta. Cryst.* **1976**, *A32*, 751-767.

52) Namuswe, F.; Kasper, G. D.; Narducci Sarjeant, A. A.; Hayashi, T.; Krest, C. M.; Green, M. T.; Moenne-Loccoz, P.; Goldberg, D. P. *J. Am. Chem. Soc.* **2008**, *130*, 14189-14200.

53) Kim, J.; Zang, Y.; Costas, M.; Harrison, R. G.; Wilkinson, E. C.; Que, L., Jr. J. *Biol. Inorg. Chem.* **2001**, *6*, 275-284.

54) Henson, M. J.; Vance, M. A.; Zhang, C. X.; Liang, H.-C.; Karlin, K. D.; Solomon, E. I. *J. Am. Chem. Soc.* **2003**, *125*, 5186-5192.

55) Hatcher, L. Q.; Vance, M. A.; Narducci Sarjeant, A. A.; Solomon, E. I.; Karlin, K. D. *Inorg. Chem.* **2006**, *42*, 3004-3013.

56) Hatcher, L. Q.; Lee, D.-H.; Vance, M. A.; Milligan, A. E.; Sarangi, R.; Hodgson, K. O.; Hedman, B.; Solomon, E. I.; Karlin, K. D. *Inorg. Chem.* **2006**, *45*, 10055-10057.

57) Lee, Y.; Park, G. Y.; Lucas, H. R.; Vajda, P. L.; Kamaraj, K.; Vance, M. A.; Milligan, A. E.; Woertink, J. S.; Siegler, M. A.; Narducci Sarjeant, A. A.; Zakharov, L. N.; Rheingold, A. L.; Solomon, E. I.; Karlin, K. D. *Inorg. Chem.* **2009**, *48*, 11297-11309.

58) Roelfes, G.; Vrajmasu, V.; chen, K.; Ho, R. Y. N.; Rohde, J.-U.; Zondervan, C.; Crois, R. M.; Schudde, E. P.; Lutz, M.; Spek, A. L.; Hage, R.; Feringa, B. L.; Munck, E.; Que, L., Jr. *Inorg. Chem.* **2003**, *42*, 2639-2653.

59) Dawson, J. H.; Holm, R. H.; Trudell, J. R.; Barth, G.; Linder, R. E.; Bunneberg, E.; Djerassi, C.; Tang, S. C. *J. Am. Chem. Soc.* **1976**, *98*, 3707-3709.

60) Jensen, M. P.; Mairata i Payeras, A.; Fielder, A. T.; Costas, M.; Kaizer, J.; Stubna, A.; Münck, E.; Que, L., Jr. *Inorg. Chem.* **2007**, *46*, 2398-2408.

61) Liu, S.-Y.; Soper, J. D.; Yang, J. Y.; Rybak-Akimova, E. V.; Nocera, D. G. *Inorg. Chem.* **2006**, *45*, 7572-7574.

62) Chin, D.-H.; La Mar, G. N.; Balch, A. L. *J. Am. Chem. Soc.* **1980**, *102*, 4344-4350.

63) Elemental analysis for $C_{50}H_{58}BN_4O_3Mn$; Calculated: C, 72.06; H, 7.16 N, 6.86. Found: C, 71.11; H, 7.60; N, 6.40.

Chapter 6

Proton-Coupled Electron Transfer Reactions Promoted by Manganese and Iron Lipoxygenase Model Complexes

6.1 Introduction

Lipoxygenases are a family of mononuclear non-heme iron (FeLO) or manganese (MnLO) enzymes which catalyze the regiospecific and stereospecific oxidation of *cis,cis*-1,4-pentadiene-containing fatty acids to alkyl hydroperoxides.[1-3] FeLOs have been discovered for a number of different organisms, including animals, plants, and fungi, while MnLOs have been isolated exclusively from fungi. X-ray crystal structures have been obtained for three FeLOs and display a considerable amount of structural homology between these three examples. X-ray structures of soybean lipoxygenase-1and soybean lipoxygenase-3, two plant FeLOs, each reveal a single Fe cofactor coordinated by three histidine imidazole nitrogens, an asparagine amide oxygen, and the carboxylate oxygen of the C-terminus.[4-6] The X-ray structure of rabbit 15-lipoxygenase contains a similar primary coordination sphere, except that the asparagine amide oxygen is replaced by a histidine imidazole residue.[7-8] Although not observed in any of these three X-ray structures, an exogenous water ligand is presumed to also be coordinated to the Fe cofactor in each respective enzyme. Genomic sequencing of MnLO from *Gaeumannomyces graminis* revealed a large amount of homology with the two soybean lipoxygenases, suggesting that the active site of this enzyme is likely similar to the two soybean LOs.[9]

The generally accepted mechanism for fatty acid peroxidation by LOs has received a large amount of interest, as these are rare examples of enzymes believed to activate the substrate

rather than O_2. Kinetic isotope effects have been observed for both soybean lipoxygenases (k_H/k_D > 50) and the MnLO (k_H/k_D = 21-24), suggesting that the rate determining step in each catalytic cycle involves C-H bond activation.[10-12] This step is believed to involve proton-coupled electron transfer (PCET) from the respective fatty acid substrate to a M(III)-OH LO active site, resulting in transient M(II)-OH_2 and fatty acid radical intermediates (where M = Mn or Fe). The fatty acid radical is then believed to isomerize and subsequently be trapped by O_2 to form an alkylperoxy radical intermediate. The catalytic cycle is then completed by a second PCET step in which the alkylperoxy radical abstracts an electron and proton from the M(II)-OH_2 enzyme intermediate (see Chapter 1 for a scheme of the proposed catalytic cycle).[13] None of these proposed enzyme intermediates in this catalytic cycle have been directly observed in any LO enzyme.

LOs are unique in that they promote C-H bond cleavage with a relatively low-valent M(III)-OH oxidant, as opposed to most other heme and non-heme iron enzymes which rely upon high-valent metal-oxos for such reactions.[13-15] Given that the strength of an oxidant is typically reflected in a relatively high reduction potential, it is surprising that these enzymes function with such a low-valent transition metal oxidant. Thermochemical cycles have been used to evaluate reactions in which metal-based oxidants cleave X-H bonds (X = O, C), which have revealed that the strength of a transition metal-based oxidant is depedent not only upon reduction potential, but also upon the relative basicity of the oxidant when electron transfer is coupled to proton transfer.[16-18] These two thermodynamic parameters are each "tunable" properties which can be manipulated to influence the oxidizing capability of a transition metal species. The interplay between reduction potential and pK_a in influencing the strength of a transition metal-based oxidant has been invoked to explain how many enzymes, including cytochrome P450 and

chloroperoxidase, can activate the strong C-H bonds in various substrates without activating amino acids located in the enzyme active site.[19-22]

This chapter discusses the synthesis, characterization, and reactivity of various model complexes of MnLO and FeLOs. Mononuclear Mn(III)-OH and Mn(III)-OCH_3 complexes have been isolated from bridge-cleaving reactions involving $[Mn^{III}(S^{Me2}N_4(tren))]_2(\mu\text{-}O)(PF_6)_2$ and either H_2O or CH_3OH, respectively, (these reactions were briefly introduced and discussed in Chapter 3). Both model complexes have proven capable of oxidizing organic substrates via PCET reactions, thus mimicking the proposed rate determining step of MnLO. A mononuclear Fe(II)-OH_2 complex has also been independently synthesized and characterized, and was found to be oxidized in a PCET reaction. Oxidation of this Fe complex can thus be considered as mimicking the microscopic reverse of the rate determining step of the FeLO, or as mimicking the final step in the proposed FeLO catalytic cycle in which the enzyme is oxidized by the alkylperoxy radical via a PCET reaction. Each of these reactions are analyzed with thermochemical cycles in order to determine how reduction potential and pK_a influence the oxidizing capability of each species. This chapter ends with a brief discussion of preliminary work aimed towards modulating the reduction potential and relative pK_a of the aforementioned Fe(II)-OH_2 complex.

6.2 Experimental Section

6.2.1 General Considerations

All manipulations were performed using Schlenk techniques or under an N_2 atmosphere in a glovebox. Reagents and solvents were purchased from commercial vendors, were of highest available purity, and were used without further purification unless otherwise noted. MeOH (Na),

MeCN (CaH_2), and CH_2Cl_2 (CaH_2) were dried and distilled prior to use. Et_2O was rigorously degassed and purified using solvent purification columns housed in a custom stainless steel cabinet and dispensed by a stainless steel schlenk-line (GlassContour). ^1H NMR spectra were recorded on a Bruker AV 300 FT NMR spectrometer at ambient temperature and were referenced to residual deuterated solvent. Cyclic voltammograms were recorded in either MeCN (100 mM $^nBu_4N(PF_6)$ supporting electrolyte) or H_2O (100 mM KClO4 supporting electrolyte) with a PAR 263A potentiostat, glassy carbon working electrode, platinum auxillary electrode, and Ag^+/Ag reference electrode. pH measurements were made using a Beckman Coulter 400 series handheld meter. UV/Vis spectra were recorded on a Varian Cary 50 spectrophotometer equipped with a fiber optic cable connected to a "dip" ATR probe (C-technologies). A custom-built two-neck solution sample holder equipped with a threaded glass connector was sized specifically to fit the "dip" probe. Electrospray-ionization mass spectrometry (ESI-MS) data were obtained on a Bruker Esquire Liquid Chromatograph-Ion Trap mass spectrometer. Gas chromatography-mass spectrometry (GC/MS) data were obtained using a 5890 gas chromatograph equipped with a 7673A autosampler and interfaced with a 5971A mass spectrometer, all from Hewlett Packard Co. Calibration curves for analytes of interest were made using either *m*-xylene or toluene as an internal reference. FT-IR spectra were recorded on a Perkin-Elmer 1700 FT-IR spectrometer as nujol mulls on NaCl salt plates or KCl pellets. EPR spectra were recorded on a Bruker E580 CW-EPR spectrometer operating at X-band frequency. Solution magnetic moments were determined by the Evans method.[23] X-ray crystallography data were recorded on a Bruker APEX II single crystal X-ray diffractometer with Mo Kα radiation. Complexes **1** and **7** were synthesized as described in Chapter 2, while complexes **8-9** were

synthesized as described in Chapter 3. Complexes **15-16**, **18**, and 2,2,6,6-tetramethylpiperidine-1-ol (TEMPO-H) and TEMPO-D were synthesized as previously described.[24-25]

6.2.2 Synthetic Protocols for Complexes 3-6, 10-14, 17, and 19-21

6.2.2.1 Synthesis of $[Mn^{III}(S^{Me2}N_4(tren))(OH)](PF_6)\cdot H_2O$ (3). An anaerobic aqueous solution of **1** (3 mL, 0.50 g, 1.1 mmol) was prepared in H_2O in a drybox. The resulting was then removed from the drybox, opened to air, and allowed to stir at room temperature for 2-3 minutes. Removal of volatiles *in vacuo* afforded in the title compound as a red solid in quantitative yield (0.52 g, 1.1 mmol). Single crystals of **3** were grown from a 1/6 mixture of MeCN/Et_2O at 0 °C overnight. Solid **3** was stored at -80 °C due to signs of decomposition at room temperature over ~24 hours. Electronic absorption spectrum: λ_{max} (nm) (ε ($M^{-1}cm^{-1}$)) (MeCN): 299 (2221), 386 (260), 500 (233); (H_2O): 287 (3720), 405 (230), 489 (290). IR spectrum (Nujol): ν_{O-H} = 3367 cm^{-1}, ν_{O-D} = 2457 cm^{-1}, $\nu_{C=N}$ = 1585 cm^{-1}. Redox potential (MeCN vs. $Fc^{+/0}$, 298 K): $E_{1/2}$ ($Mn^{III/II}$) = -350 mV. Magnetic moment (299 K, solution state, CD_3CN): 4.89 μ_B/Mn. Elemental analysis for $C_{11}H_{26}N_4OF_6PSMn$; Calculated: C, 28.58; H, 5.67; N, 12.12. Found: C, 28.43; H, 5.43; N, 11.37.

6.2.2.2 Synthesis of $[Mn^{III}(S^{Me2}N_4(tren))(OCH_3)](PF_6)$ (4). An anaerobic MeOH solution (1 mL) of **1** (0.10 g, 0.22 mmol) was prepared in a drybox. The solution was removed from the drybox, opened to air, and allowed to stir for five minutes. Removal of all volatiles *in vacuo* afforded the title compound as a red solid in nearly quantitative yield (0.11 g, 0.22 mmol). Electronic absorption spectrum: λ_{max} (nm) (ε ($M^{-1}cm^{-1}$)) (MeCN): 340 (410), 430 (330), 520 (250). Redox potential (MeCN vs. $Fc^{+/0}$, 298 K): $E_{1/2}$ ($Mn^{III/II}$) = -197 mV. Magnetic moment (299 K,

solution state, CD_3CN): 4.99 μ_B/Mn. Elemental analysis for $C_{12}H_{28}N_4OF_6PSMn$; Calculated: C, 30.26; H, 5.92; N, 11.76. Found: C, 30.29; H, 5.56; N, 11.61.

6.2.2.3 Synthesis of $[Mn^{III}(S^{Me2}N_4(tren))(OPh)](PF_6)\cdot MeCN\cdot Et_2O$ (5). An anaerobic MeCN solution (2 mL) of **2** (0.10 g, 0.11 mmol) was prepared in a drybox. An excess amount of PhOH (1.04 g, 11.0 mmol) as added was a solid directly to the reaction solution. After allowing the resulting solution to stir at room temperature for ten minutes, all volatiles were removed *in vacuo* to afford a dark red solid. The crude solid was recrystallized twice from MeCN/Et_2O to afford the title compound as a red solid in 89 % yield (0.11 g, 0.20 mmol). Electronic absorption spectrum: λ_{max} (nm) (ε ($M^{-1}cm^{-1}$)) (MeCN): 495 (370). Redox potential (MeCN vs. $Fc^{+/0}$, 298 K): $E_{1/2}$ ($Mn^{III/II}$) = -184 mV. Magnetic moment (299 K, solution state, CD_3CN): 4.88 μ_B/Mn. Elemental analysis for $C_{17}H_{30}N_4OF_6PSMn$; Calculated: C, 37.92; H, 5.62; N, 10.41. Found: C, 38.00 H; 5.70; N; 10.49.

6.2.2.4 Synthesis of $[Mn^{III}(S^{Me2}N_4(tren))(OPh\text{-}^pNO_2)](PF_6)\cdot MeCN$ (6). An anaerobic MeCN solution (2 mL) of **2** (0.10 g, 0.11 mmol) was prepared in a drybox. An excess of para-NO_2-PhOH (0.77 g, 5.0 mmol) was added as a solid to this solution. After allowing the resulting solution to stir at room temperature for ten minutes, all volatiles were removed *in vacuo* to afford a black solid. The resulting crude solid was recrystallized three times from MeCN/Et_2O (1/5) to afford the title compound as a dark red solid in 95 % yield (0.12 g, 0.21 mmol). Electronic absorption spectrum: λ_{max} (nm) (ε ($M^{-1}cm^{-1}$)) (MeCN): 395 (1180), 460 (820). Redox potential (MeCN vs. $Fc^{+/0}$, 298 K): $E_{1/2}$ ($Mn^{III/II}$) = -137 mV. Magnetic moment (299 K, solution state, CD_3CN): 4.80 μ_B/Mn. Elemental analysis for $C_{17}H_{29}N_5O_3F_6PSMn$; Calculated: C, 35.00; H, 5.01. Found: C, 35.49; H, 5.21.

6.2.2.5 Synthesis of [$Fe^{II}(O^{Me2}N_4$(tren))(H_2O)](OTf) (10). Sodium methoxide (0.22 g, 4.0 mmol), 3-hydroxy-3-methyl-2-butanone (0.41 g, 4.0 mmol), tris(2-aminoethyl)amine (0.59 g, 4.0 mmol), and $Fe(MeCN)_2(OTf)_2$ (1.74 g, 4.0 mmol) were stirred together in MeOH (15 mL) in a drybox for approximately one day. All volatiles were then removed *in vacuo* to afford a bright yellow solid. The resulting solid was washed with Et_2O (3 x 15 mL) and dried again under vacuum. Recrystallization of the crude yellow solid from MeCN/Et_2O (1/2) afforded the title compound in 50 % yield (0.91 g, 2.0 mmol). Electronic absorption spectrum: λ_{max} (nm) (ε ($M^{-1}cm^{-1}$)) (MeCN): 368 (680). Magnetic moment (solid state, 5-300 K): 4.99 B.M. Magnetic moment (300 K, solution state, CD_3OD): 5.00 μ_B/Mn. ESI-MS; Calculated for $[C_{11}H_{25}N_4OFe]^+$: 285.2; Found: 284.1. Elemental analysis for $C_{12}H_{27}N_4O_5SF_3Fe$; Calculated: C, 31.87; H, 6.02; N, 12.39. Found: C, 30.67; H, 5.81; N, 12.52.

6.2.2.6 Synthesis of [$Fe^{III}(O^{Me2}N_4$(tren))]$_2$(μ-O)($OTf)_2$·MeOH (11). A solution of **10** (0.30 g, 0.65 mmol) was prepared in MeOH (15 mL) in a drybox, then removed and stirred while exposed to air at room temperature for six hours. Volatiles were then removed *in vacuo* to afford a dark yellow solid. The crude solid was recrystallized from MeOH/Et_2O at room temperature to afford the title compound as a dark yellow solid in 31 % yield (0.092 g, 0.10 mmol). Electronic absorption spectrum: λ_{max} (nm) (ε ($M^{-1}cm^{-1}$)) (MeCN): 231 (13200), 332 (10100), 464 (910), 494 (820). Magnetic moment (298 K, solution state, CD_3CN): 1.72 μ_B/Mn. Elemental analysis for $C_{24}H_{50}N_8O_9S_2F_6Fe_2$; Calculated: C, 32.59; H, 5.70; N, 12.67. Found: C, 32.50; H, 5.74; N, 12.57.

6.2.2.7 Synthesis of [$Fe^{III}(O^{Me2}N_4$(tren))]$_2$(μ-OH)($OTf)_3$ (12). A solution of **10** (0.22 g, 0.50 mmol) was prepared in MeCN (15 mL) in a drybox. Ferrocenium triflate (0.17 g, 0.5 mmol) was then added to this solution and allowed to stir overnight at room temperature. Volatiles were then

removed *in vacuo* to afford a dark yellow solid. The solid was then recrystallized twice from MeOH/Et_2O to afford the title compound a dark yellow solid in 70 % yield (0.18 g, 0.18 mmol). Electronic absorption spectrum: λ_{max} (nm) (ε ($M^{-1}cm^{-1}$)) (MeCN): 238 (10200), 313 (5540). IR spectrum (KBr): $\nu_{O\text{-}H}$ = 3462 cm^{-1}, $\nu_{O\text{-}D}$ = 2526 cm^{-1}. Magnetic moment (298 K, solution state, CD_3OD): 3.78 μ_B/Mn. Elemental analysis for $C_{27}H_{59}N_8O_{13}S_3F_9Fe_2$; Calculated: C, 32.59; H, 5.70; N, 12.67. Found: C, 32.50; H, 5.74; N, 12.57.

6.2.2.8 Synthesis of [$Fe^{II}(O^{Me2}N_4$(6-Me-DPEN))](PF_6) (13). $FeCl_2$ (0.094 g, 0.74 mmol), N,N-bis(6-methyl-2-pyridilmethyl)ethane-1,2-diamine (0.20 g, 0.74 mmol), 3-hydroy-3-methyl-2-butanone (0.09 g, 0.86 mmol), $NaOCH_3$ (0.40 g, 0.74 mmol) and $NaPF_6$ (0.12 g, 0.74 mmol) were stirred together in MeOH (10 mL) in a drybox for two days. Removal of all volatiles *in vacuo* resulted in an orange solid. The crude solid was recrystallized from MeCN/Et_2O at 258 K to afford the title compound as an orange solid in 47 % yield (0.20 g, 0.35 mmol). Electronic absorption spectrum: λ_{max} (nm) (ε ($M^{-1}cm^{-1}$)) (MeCN): 410 (490). Redox potential (MeCN vs. $Fc^{+/0}$, 298 K): $E_{1/2}$ ($Fe^{III/II}$) = +120 mV. Magnetic moment (299 K, solution state, CD_3OD): 4.72 μ_B/Mn.

6.2.2.9 Synthesis of [$Fe^{III}(O^{Me2}N_4$(6-Me-DPEN))]$_2$(μ-OH)$_2$(PF_6)$_2$ (14). Complex **13** (0.20 g, 0.36 mmol) was dissolved in MeCN (5 mL) in a drybox, then removed from the drybox and exposed to air. After stirring at room temperature for thirty minutes, all volatiles were removed *in vacuo* to afford a bright yellow solid. The resulting crude solid was recrystallized from MeCN/Et_2O (1/6) at 243 K to afford the title compound as a yellow solid in 96 % yield (0.19 g, 0.17 mmol). Electronic absorption spectrum: λ_{max} (nm) (ε ($M^{-1}cm^{-1}$)) (MeCN): 410 (490). Magnetic moment (299 K, solution state, CD_3OD): 4.72 μ_B/Mn.

6.2.3 Reactions with TEMPO-H(D)

In a typical reaction, a 0.5 mM solution of a Mn(III)-OR complex was prepared in 4 mL of either H_2O or MeCN under an inert atmosphere in a drybox. The solution was then transferred with a gas-tight syringe to a custom-made two-neck vial. The vial was equipped with a septum cap and threated dip-probe feed-through adaptor that had previously been purged with argon and contained a stir bar. The anaerobic solution was continuously stirred while 0.2 equivalent aliquots of TEMPO-H(D) solution (0.1 M stock solution) prepared in the appropriate solvent were added to the reaction mixture.

6.2.4 Kinetics Measurements

In a typical experiment, a ~0.5 mM solution of a Mn(III)-OR complex was prepared in a drybox and injected with a gas-tight syringe into a custom-made two-neck vial. The vial was equipped with a septum cap and threaded dip-probe feed-through adaptor that had previously been purged with argon and contained a stirbar. A known excess amount of TEMPO-H(D) (0.1 M stock solution in MeCN) was then injected into reaction solution. Reaction progress was monitored by time-dependent absorption changes at 507 nm (**3**) or 520 nm (**4**) until no further changes were observed for at least one minute. First-order rate constants were calculated by plotting $\ln[(A_x-A_f)/(A_0-A_f)]$ versus time. Experiments were repeated at least four times at each concentration of TEMPO-H(D). Gentle stirring was maintained throughout each experiment in order to maintain solution homogeneity. Variable-temperature measurements were made by cooling each reaction solution to a desired temperature with a cryogenic bath. Temperatures were monitored and maintained throughout the duration of each experiment.

6.2.5 X-ray Crystallographic Structure Determination

A colorless plate of **3** with dimensions 0.50 x 0.40 x 0.15 mm^3 was mounted on a glass capillary with oil. Data was collected at -173 ˚C. The crystal-to-detector distance was set to 40 mm and the exposure time was 10 seconds per degree for all sets of exposure. The scan width was 0.5˚. Data collection was 99.5% complete to 25.0˚ in ϑ. A total of 67,058 partial and complete reflections were collected covering the indices h = -11 to 11, k = -22 to 22, l = -18 to 18. 4,905 reflections were symmetry independent and the R_{int} = 0.0195 indicated that the data was good (0.07 average quality). Indexing and unit cell refinement indicated a monoclinic P lattice with the space group P 2_1/c (No.14). A water molecule was found to be disordered with two different hydrogen geometries; one with hydrogen bonds to the hydroxide ligand of the Mn complex and a fluoride of PF_6^-, and a second with hydrogen bonds to the sulfur atom in the Mn complex and a fluoride of PF_6^-.

A red needle of **4** with dimensions 0.15 x 0.05 x 0.5 mm^3 was mounted on a glass capillary with oil. Data was collected at -173 ˚C. The crystal-to-detector distance was set to 40 mm and the exposure time was 10 seconds per degree for all sets of exposure. The scan width was 0.5˚. Data collection was 96.6% complete to 25.35˚ in ϑ. A total of 26,870 partial and complete reflections were collected covering the indices h = -16 to 16, k = -9 to 10, l = -19 to 19. 1,868 reflections were symmetry independent and the R_{int} = 0.0792 indicated that the data was of average quality (0.07 average quality). Indexing and unit cell refinement indicated an orthorhombic P lattice with the space group P n m a (No.62). The structure exhibits disorder across a mirror symmetry plane through the Mn ion, sulfur atom, and imine nitrogen. The PF_6^- molecule is heavily disordered with two superimposed geometries at 0.66:0.34 occupancies.

A colorless plate of **5** with dimensions 0.25 x 0.10 x 0.05 mm^3 was mounted on a glass capillary with oil. Data was collected at -173 ˚C. The crystal-to-detector distance was set to 40 mm and the exposure time was 10 seconds per degree for all sets of exposure. The scan width was 0.5˚. Data collection was 100% complete to 25.0˚ in ϑ. A total of 106,880 partial and complete reflections were collected covering the indices h = -11 to 11, k = -22 to 22, l = -29 to 29. 7,668 reflections were symmetry independent and the R_{int} = 0.0313 indicated that the data was good (0.07 average quality). Indexing and unit cell refinement indicated a monoclinic P lattice with the space group P $2_1/n$ (No.14). The PF_6^- and MeCN molecules are each slightly disordered in the structure.

A colorless plate of **6** with dimensions 0.15 x 0.10 x 0.10 mm^3 was mounted on a glass capillary with oil. Data was collected at -173 ˚C. The crystal-to-detector distance was set to 40 mm and the exposure time was 10 seconds per degree for all sets of exposure. The scan width was 0.5˚. Data collection was 99.1% complete to 25.0˚ in ϑ. A total of 85,796 partial and complete reflections were collected covering the indices h = -41 to 41, k = -18 to 18, l = -16 to 16. 6,622 reflections were symmetry independent and the R_{int} = 0.0361 indicated that the data was good (0.07 average quality). Indexing and unit cell refinement indicated a monoclinic C lattice with the space group C 2/c (No.15). One PF_6^- molecule was found in two positions, each with 50% occupancy.

A clear plate of **10** with dimensions 0.36 x 0.34 x 0.31 mm^3 was mounted on a glass capillary with oil. Data was collected at -143 ˚C. The crystal-to-detector distance was set to 40 mm and the exposure time was 10 seconds per degree for all sets of exposure. The scan width was 2˚. Data collection was 98.7% complete to 25.0˚ in ϑ. A total of 37,364 partial and complete reflections were collected covering the indices h = -10 to 12, k = -13 to 11, l = -13 to

14. 4,603 reflections were symmetry independent and the R_{int} = 0.0819 indicated that the data was slightly less than average quality (0.07 average quality). Indexing and unit cell refinement indicated a monoclinic P lattice with the space group P $\bar{1}$ (No.2).

A black plate of **11** with dimensions 0.41 x 0.30 x 0.26 mm^3 was mounted on a glass capillary with oil. Data was collected at -143 ˚C. The crystal-to-detector distance was set to 30 mm and the exposure time was 30 seconds per degree for all sets of exposure. The scan width was 2˚. Data collection was 99.0% complete to 25.0˚ in ϑ. A total of 36,608 partial and complete reflections were collected covering the indices h = -31 to 31, k = -31 to 31, l = -31 to 31. 4,752 reflections were symmetry independent and the R_{int} = 0.0690 indicated that the data was good (0.07 average quality). Indexing and unit cell refinement indicated a cubic I lattice with the space group I 2_1 3 (No.199). The dimer is accompanied by only two OTf^- anions, with one disordered over two positions

A yellow prism of **12** with dimensions 0.52 x 0.31 x 0.14 mm^3 was mounted on a glass capillary with oil. Data was collected at -143 ˚C. The crystal-to-detector distance was set to 30 mm and the exposure time was 15 seconds per degree for all sets of exposure. The scan width was 2˚. Data collection was 98.7% complete to 25.0˚ in ϑ. A total of 116,886 partial and complete reflections were collected covering the indices h = -26 to 25, k = -15 to 17, l = -24 to 24. 10,375 reflections were symmetry independent and the R_{int} = 0.0919 indicated that the data was slightly less than average quality (0.07 average quality). Indexing and unit cell refinement indicated a monoclinic P lattice with the space group P 2_1/c (No.14). Slight disorder was found in one of the OTf^- and Et_2O molecules.

A yellow prism of **13** with dimensions 0.40 x 0.05 x 0.04 mm^3 was mounted on a glass capillary with oil. Data was collected at -143 ˚C. The crystal-to-detector distance was set to 30 mm and the exposure time was 60 seconds per degree for all sets of exposure. The scan width was 2˚. Data collection was 99.4% complete to 25.0˚ in ϑ. A total of 56,116 partial and complete reflections were collected covering the indices h = -21 to 21, k = -19 to 19, l = -32 to 32. 69,506 reflections were symmetry independent and the R_{int} = 0.1250 indicated that the data was poor (0.07 average quality). Indexing and unit cell refinement indicated an orthorhombic P lattice with the space group P b c a (No.61).

A colorless plate of **14** with dimensions 0.20 x 0.10 x 0.10 mm^3 was mounted on a glass capillary with oil. Data was collected at -173 ˚C. The crystal-to-detector distance was set to 40 mm and the exposure time was 30 seconds per degree for all sets of exposure. The scan width was 0.5˚. Data collection was 99.9% complete to 25.0˚ in ϑ. A total of 51,770 partial and complete reflections were collected covering the indices h = -15 to 14, k = -15 to 15, l = -17 to 17. 7,264 reflections were symmetry independent and the R_{int} = 0.0512 indicated that the data was slightly less than average quality (0.07 average quality). Indexing and unit cell refinement indicated a triclinic P lattice with the space group P $\bar{1}$ (No.2).

All X-ray data sets were integrated and scaled using SAINT, SADABS within the APEX2 software package by Bruker. Solutions were made by direct methods (SHELXS, SIR97) to produce complete heavy atom phasing models.[26] Scattering factors are from Waasmair and Kirfel.[27] Structures were completed by difference Fourier synthesis with either SHELXL97 or SHELXTL 6.10. Hydrogen atoms were placed in geometrically idealized positions and constrained to ride on their parent atoms with C-H distances in the range of 0.95-1.00 Å. Isotropic thermal parameters Ueq were fixed such that they were 1.2Ueq of their parent aom Ueq

for C-Hs and 1.5Ueq for methyl groups. All non-hydrogen atoms were refined anisotropically by full-matrix least-squares.

6.3 Results and Discussion

6.3.1 Manganese Lipoxygenase Model Complexes

6.3.1.1 Synthesis and Structural Characterization of Thiolate-Ligated Mn(III)-OR (-R = -H, -CH_3, -Ph, -Ph-$^pNO_2$) Complexes 3-6

As discussed in Chapter 3, reactions between five-coordinate $[Mn^{II}(S^{Me2}N_4(tren))](PF_6)$ (**1**) and O_2 were found to result in quantitative formation of the oxo-bridged Mn(III,III) dimer $[Mn^{III}(S^{Me2}N_4(tren))]_2(\mu\text{-}O)(PF_6)_2$ (**2**). The presence of a thiolate ligand coordinated to each Mn(III) ion in this dimer, as well as the fairly acute Mn(III)-O-Mn(III) bridging angle (158.8(3)°, Table 3.1, Chapter 3), collectively suggested that the oxo bridging ligand in **2** may be considerably basic. In order to gauge the relative basicity of this bridging oxo ligand, reactions between dimer **2** and various weak acids (H_2O, CH_3OH, PhOH, $^pNO_2$-PhOH) were performed in anhydrous MeCN solutions under anaerobic conditions at room temperature and monitored by UV/Vis spectroscopy. Solutions of **2** rapidly converted from purple to dark red upon introduction of excess amounts of each respective acid (5-30 equivalents), indicating that reactions were indeed occurring (Figure 6.1). The final product formed in reactions between **2** and each respective acid have been isolated and structurally-characterized by X-ray crystallography as mononuclear Mn(III)-OR complexes, where -R is -H (H_2O, **3**), -CH_3 (CH_3OH, **4**), -Ph (PhOH, **5**), and -Ph-$^pNO_2$ ($^pNO_2$-PhOH, **6**). ORTEP diagrams of complexes **3-6** are provided in Figures 6.2-6.3, while selected metrical parameters and crystal data are provided in Tables 6.1 and 6.2, respectively. ChemDraw illustrations of 3-6 are shown in Scheme 6.1.

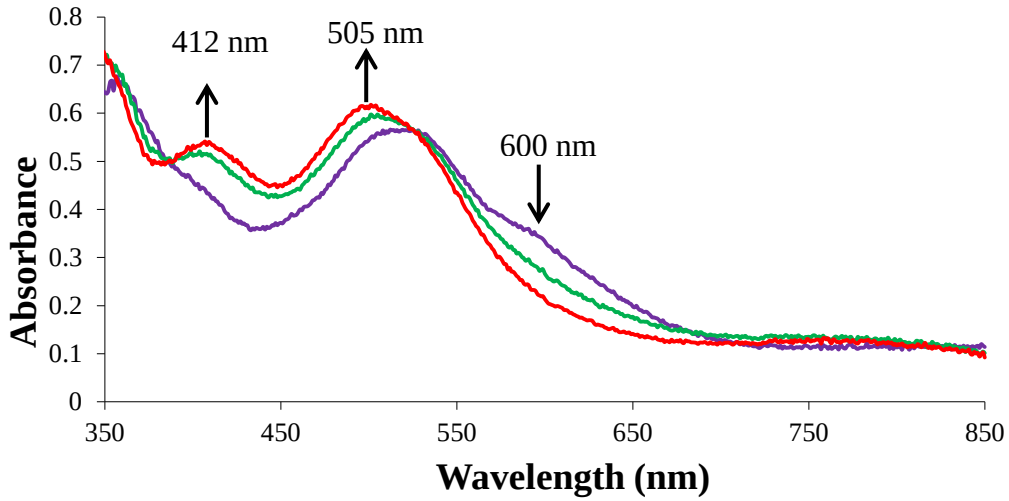

Figure 6.1 UV/Vis spectra displaying the reaction between $[Mn^{III}(S^{Me2}N_4(tren))]_2(\mu\text{-}O)(PF_6)_2$ (**2**) and H_2O (15 equivalent aliquots) in MeCN at 293 K.

Table 6.1 Selected bond distances (Å) and angles (deg) for $[Mn^{II}(S^{Me2}N_4(tren))](PF_6)$ (**1**), $[Mn^{III}(S^{Me2}N_4(tren))]_2(\mu\text{-}O)(PF_6)_2$ (**2**), $[Mn^{III}(S^{Me2}N_4(tren))(OH)](PF_6)\cdot H_2O$ (**3**), $[Mn^{III}(S^{Me2}N_4(tren))(OCH_3)](PF_6)$ (**4**), $[Mn^{III}(S^{Me2}N_4(tren))(OPh)](PF_6)\cdot MeCN\cdot Et_2O$ (**5**), $[Mn^{III}(S^{Me2}N_4(tren))(OPh\text{-}^pNO_2)](PF_6)\cdot MeCN$ (**6**), and $[Mn^{III}(S^{Me2}N_4(2\text{-}QuinoPN))(OCH_3)](PF_6)$ (**7**).

	1	**2**	**3**	**4**	**5**	**6**	**7**
Mn(1)-S(1)	2.4033(3)	2.286(2)	2.2840(4)	2.2937(14)	2.2675(3)	2.2578(8)	2.2650(9)
Mn(1)-N(1)	2.1738(8)	2.017(6)	2.0133(9)	2.018(4)	2.0043(10)	1.999(2)	2.084(3)
Mn(1)-N(2)	2.3193(8)	2.172(7)	2.1634(9)	2.176(5)	2.1474(10)	2.148(2)	2.180(3)
Mn(1)-N(3)	2.1938(8)	2.351(8)	2.2747(10)	2.295(4)	2.3152(11)	2.288(2)	2.411(2)
Mn(1)-N(4)	2.1956(9)	2.280(6)	2.3222(9)	2.295(4)	2.3173(10)	2.300(2)	2.483(2)
Mn(1)-O(1)[a]	N/A	1.783(5)	1.8540(8)	1.836(5)	1.8678(8)	1.9013(19)	1.837(2)
Mn(2)-O(1)	N/A	1.799(5)	N/A	N/A	N/A	N/A	N/A
S(1)-Mn(1)-N(1)	81.75(2)	83.1(2)	83.48(3)	83.53(12)	82.36(3)	83.94(7)	83.00(7)
S(1)-Mn(1)-N(2)	158.71(2)	164.58(19)	165.40(3)	166.05(13)	165.65(3)	166.11(7)	178.93(8)
S(1)-Mn(1)-N(3)	114.15(2)	104.6(2)	98.85(3)	103.42(9)	98.47(3)	104.36(7)	106.27(6)
S(1)-Mn(1)-N(4)	109.339(2)	102.3(2)	106.63(3)	103.42(9)	107.23(3)	103.45(8)	105.43(7)
N(1)-Mn(1)-N(3)	125.48(3)	87.1(3)	96.12(4)	90.92(9)	95.36(4)	104.36(7)	93.00(10)
N(1)-Mn(1)-N(4)	109.64(3)	89.7(3)	89.19(3)	90.92(9)	87.89(4)	97.35(9)	94.34(9)
N(3)-Mn(1)-N(4)	112.28(3)	152.3(3)	154.41(3)	153.13(18)	154.30(4)	151.61(10)	148.09(9)
O(1)-Mn(1)-S(1)	N/A	96.65(17)	96.88(3)	98.78(15)	99.20(3)	98.38(7)	91.41(7)
O(1)-Mn(1)-N(1)	N/A	177.7(3)	177.30(4)	173.2(7)	171.55(4)	173.15(9)	173.53(10)
O(1)-Mn(1)-N(2)	N/A	98.9(2)	97.04(4)	95.07(15)	94.63(4)	95.50(9)	88.10(10)
O(1)-Mn(1)-N(3)	N/A	90.7(2)	86.47(4)	82.3(7)	92.28(4)	81.99(9)	85.82(10)
O(1)-Mn(1)-N(4)	N/A	92.6(2)	88.15(3)	82.3(7)	83.66(4)	88.41(8)	89.97(10)
Mn(1)-O(1)-C	N/A	N/A	N/A	124.0(9)	134.25(7)	136.77(18)	127.4(2)
Mn(1)-O(1)-Mn(2)	N/A	158.8(3)	N/A	N/A	N/A	N/A	N/A

[a]O(1) = -μ-O (**2**), -OH (**3**), $-OCH_3$ (**4**, **7**), -OPh (**5**), and -OPh-para-NO_2 (**6**).

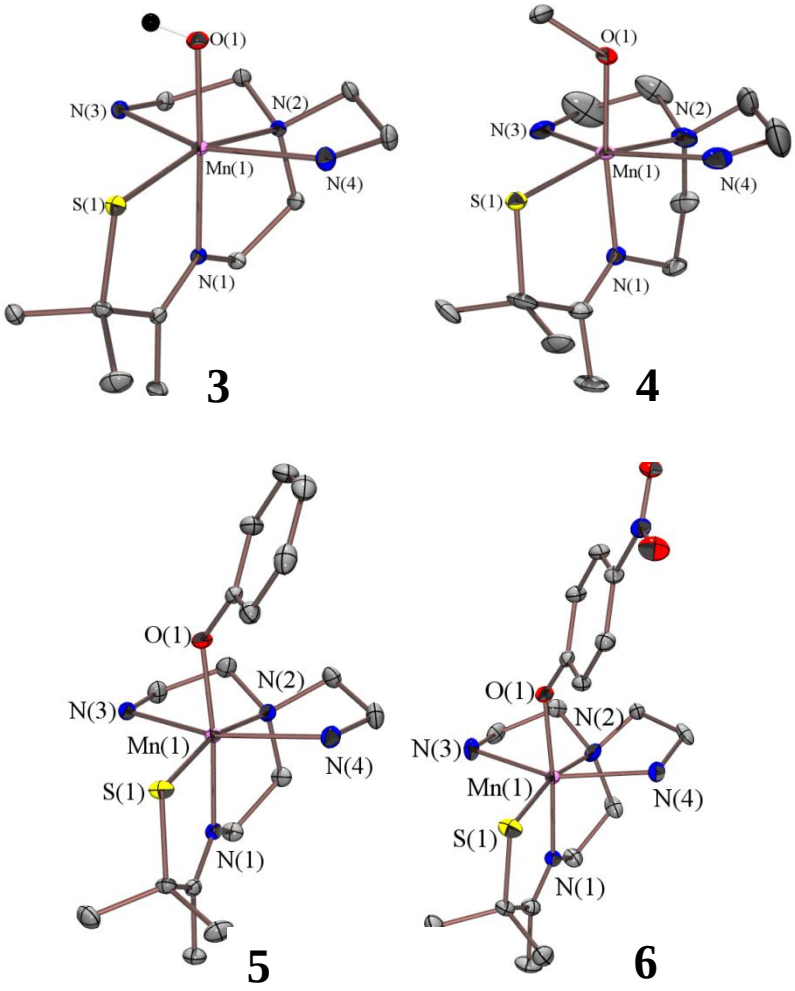

Figure 6.2 ORTEP diagrams (50 % probability) of $[Mn^{III}(S^{Me2}N_4(tren))(OH)]^+$ (**3**), $[Mn^{III}(S^{Me2}N_4(tren))(OCH_3)]^+$ (**4**), $[Mn^{III}(S^{Me2}N_4(tren))(OPh)]^+$ (**5**), and $[Mn^{III}(S^{Me2}N_4(tren))(OPh\text{-}^pNO_2)]^+$ (**6**) with most hydrogen atoms, counterions, and solvents of crystallization omitted for clarity

Table 6.2 Crystal data for $[Mn^{III}(S^{Me2}N_4(tren))(OH)](PF_6)\cdot H_2O$ (**3**), $[Mn^{III}(S^{Me2}N_4(tren))(OCH_3)](PF_6)$ (**4**), $[Mn^{III}(S^{Me2}N_4(tren))(OPh)](PF_6)\cdot MeCN\cdot Et_2O$ (**5**), $[Mn^{III}(S^{Me2}N_4(tren))(OPh\text{-}^{p}NO_2)](PF_6)\cdot MeCN$ (**6**), $[Fe^{II}(O^{Me2}N_4(tren))(H_2O)](OTf)$ (**10**), $[Fe^{III}(O^{Me2}N_4(tren))]_2(\mu\text{-}O)(OTf)_2\cdot MeOH$ (**11**), $[Fe^{III}(O^{Me2}N_4(tren))]_2(\mu\text{-}OH)(OTf)_3$ (**12**), $[Fe^{II}(O^{Me2}N_4(6\text{-}Me\text{-}DPEN))](PF_6)$ (**13**), and $[Fe^{III}(O^{Me2}N_4(6\text{-}Me\text{-}DPEN))]_2(\mu\text{-}OH)_2(PF_6)_2$ (**14**).

	3	**4**	**5**	**6**	**10**
Formula	$C_{11}H_{28}F_6MnN_4O_2PS$	$C_{12}H_{28}F_6MnN_4O_2PS$	$C_{23}H_{43}F_6MnN_5O_2PS$	$C_{19}H_{32}F_6MnN_6O_3PS$	$C_{11}H_{27}F_3FeO_5N_4S$
MW	480.35	476.35	653.59	624.48	452.29
T, K	100(2)	100(2)	110(2)	100(2)	130(2)
Unit Cell[a]	Monoclinic	Orthorhombic	Monoclinic	Monoclinic	Triclinic
a, Å	8.5318(6)	13.5710(19)	8.4834(3)	31.099(2)	9.4900(2)
b, Å	16.6962(13)	8.8115(12)	16.4970(7)	14.0709(8)	9.9290(3)
c, Å	13.7039(10)	16.452(2)	22.0354(2)	12.1715(7)	10.8760(3)
α, deg	90	90	90	90	100.5110(11)
β, deg	94.552(3)	90	97.872(2)	91.213(4)	98.0540(11)
γ, deg	90	90	90	90	99.3920(15)
V, $Å^3$	1945.9(2)	1967.4(5)	3054.8(2)	5324.9(6)	978.74(5)
Z	4	4	4	8	2
d(calc), g/cm^3	1.640	1.608	1.421	1.558	1.535
Sp. Group	P $2_1/c$	P n m a	P $2_1/n$	C 2/c	P $\bar{1}$
R[b]	0.0211	0.0494	0.0265	0.0506	0.0550
R_w[c]	0.0559	0.1339	0.0668	0.1099	0.1250
GOF	1.042	1.077	1.041	1.169	1.137

	11	**12**	**13**	**14**
Formula	$C_{24}H_{50}F_6Fe_2O_9N_8S_2$	$C_{52}H_{112}F_{18}Fe_4O_{25}N_{16}S_{12}$	$C_{21}H_{29}F_6FeON_4P$	$C_{48}H_{70}F_{12}Fe_2O_4N_{10}P_2$
MW	884.54	2143.42	553.40	1252.78
T, K	130(2)	130(2)	130(2)	100(2)
Unit Cell[a]	Cubic	Monoclinic	Orthorhombic	Triclinic
a, Å	22.6101(5)	20.5640(5)	15.9090(11)	11.237(2)
b, Å	22.6101(5)	13.0420(4)	17.1316(12)	11.403(2)
c, Å	22.6101(5)	18.4360(7)	17.6610(13)	13.33492)
α, deg	90	90	90	70.554(9)
β, deg	90	111.1170(10)	90	66.281(9)
γ, deg	90	90	90	87.391(10)
V, $Å^3$	11558.7(4)	4612.4(3)	4813.3(6)	1467.3(5)
Z	12	2	9	1
d(calc), g/cm^3	1.525	1.543	1.530	1.418
Sp. Group	I 2_1 3	P $2_1/c$	P b c a	P $\bar{1}$
R[b]	0.0913	0.0655	0.0592	0.0366
R_w[c]	0.1162	0.1418	0.1154	0.0796
GOF	1.046	0.982	0.928	1.007

[a]In all cases: Mo Kα(λ = 0.7170 Å) radiation. [b]$R = \Sigma||F_0| - |F_c||/ \Sigma|F_0|$. [c]$R_w = [\Sigma w(|F_0| - |F_c|)^2/ \Sigma wF_0^{1/2}$, where $w^{-1} = [\sigma_{count}^2 + (0.05F^2)^2]4F^2$.

Scheme 6.1 ChemDraw representations of $[Mn^{III}(S^{Me2}N_4(tren))(OH)]^+$ (**3**), $[Mn^{III}(S^{Me2}N_4(tren))(OCH_3)]^+$ (**4**), $[Mn^{III}(S^{Me2}N_4(tren))(OPh)]^+$ (**5**), and $[Mn^{III}(S^{Me2}N_4(tren))(OPh\text{-}^pNO_2)]^+$ (**6**).

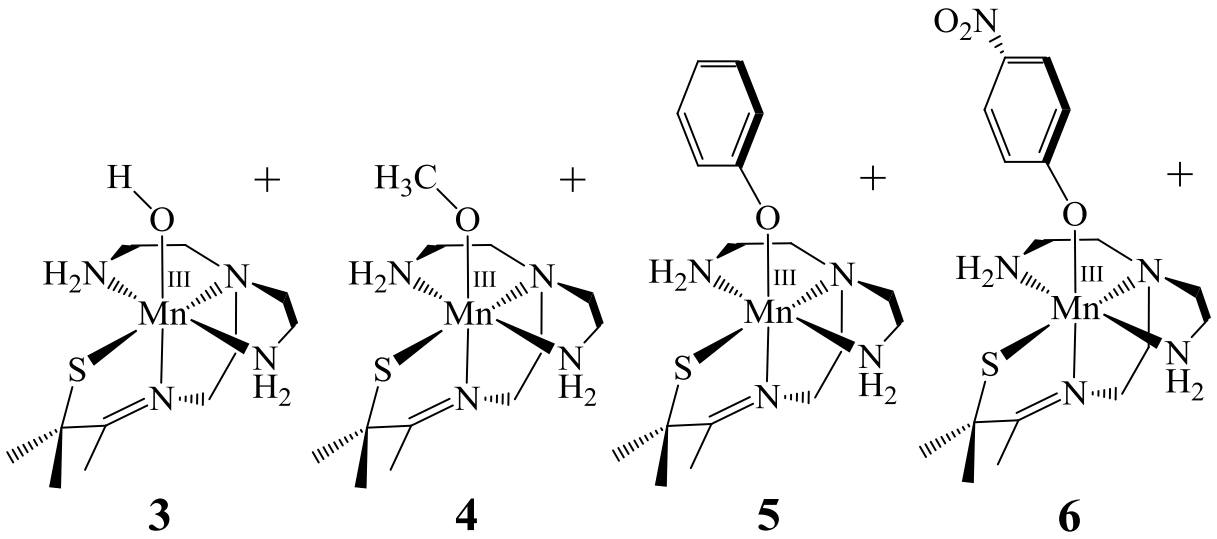

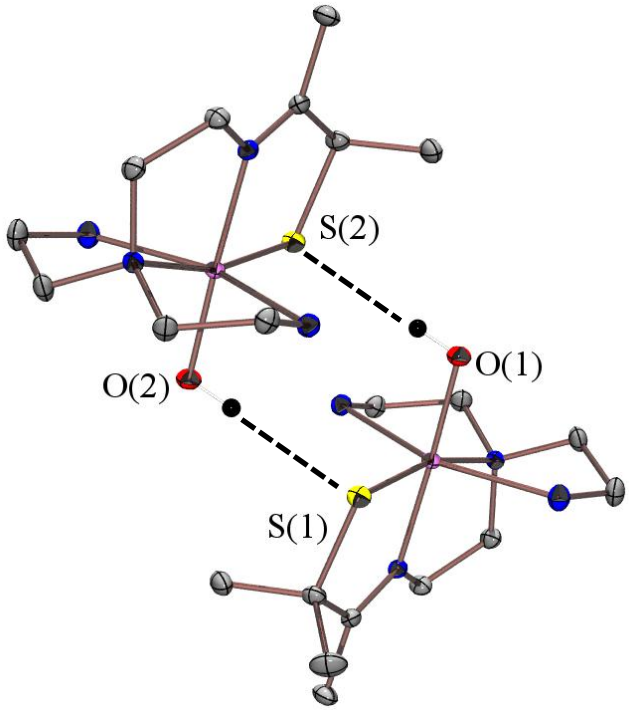

Figure 6.3 ORTEP diagram (50 % probability) displaying the hydrogen bonding interactions in the X-ray crystal structure of $[Mn^{III}(S^{Me2}N_4(tren))(OH)]^+$ (**3**); O(1)-H···S(2) = O(2)-H···S(1) = 1.097(3) Å.

Identification of these products reveals that the oxo bridge in **2** is cleaved upon reacting with weak acids to afford two conjugate base-ligated mononuclear Mn(III) complexes. Given that excess amounts of acid are necessary to fully promote the conversion of **2** to each respective Mn(III)-OR complex, each of these reactions are presumably reversible. A proposed mechanism for these transformations is provided in Scheme 6.2. Protonation of **2** and subsequent bridge cleavage would result in two mononuclear Mn(III) complexes; a Mn(III)-OR and Mn(III)-OH species. A reaction between the Mn(III)-OH intermrediate and acid then results in formation of a second equivalent of the respective Mn(III)-OR species and water. Similar reactions between oxo-bridged $[Mn^{III}(S^{Me2}N_4(2\text{-QuinoPN}))]_2(\mu\text{-O})(PF_6)_2$ and CH_3OH were discussed in Chapter 3

Scheme 6.2 Proposed mechanism for the acid-promoted bridge cleaving reactions involving dimer **2** and various weak acids, yielding complexes **3**-**6**. All reactions were performed with excess ROH.

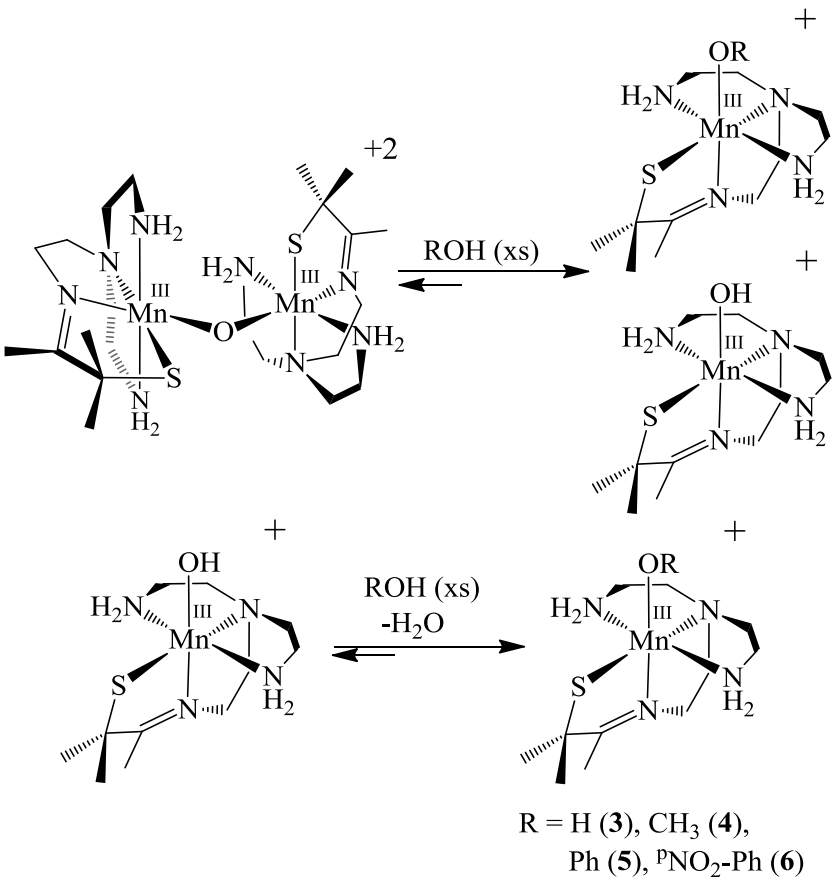

and found to yield the corresponding mononuclear Mn(III)-OCH_3 complex, [Mn^{III}($S^{Me2}N_4$(2-QuinoPN))(OCH_3)](PF6) (**7**), quantitatively. Conversion of **2** to **3**-**6**, respectively, were also found to be clean reactions, as each Mn(III)-OR species was isolated in nearly quantitative yields.

In further support of the proposed mechanism described in Scheme 6.2, it was found that each of the four Mn(III)-OR complexes could be interconverted between one another through reactions with excess amounts of each respective acid (Scheme 6.3). These transformations are illustrated by the UV/Vis spectra in Figure 6.4, which display reactions in MeCN between hydroxide-bound **3** and MeOH, PhOH, and $^{p}NO_2$-PhOH (forming **4**, **5**, and **6**, respectively).

Scheme 6.3 Interconversions between Mn(III)-OR complexes **3**-**6** in MeCN. Each acid is represented in excess amounts.

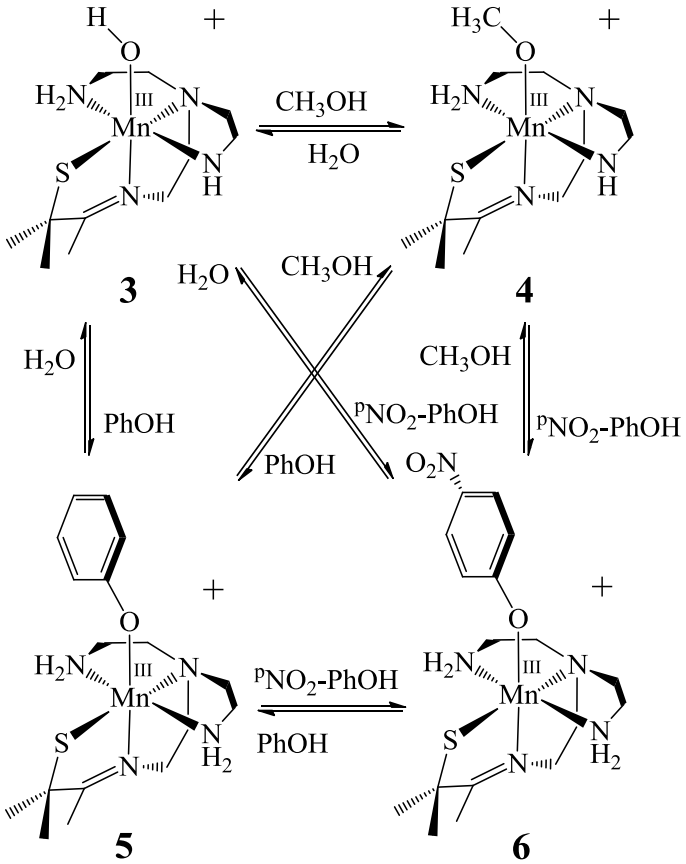

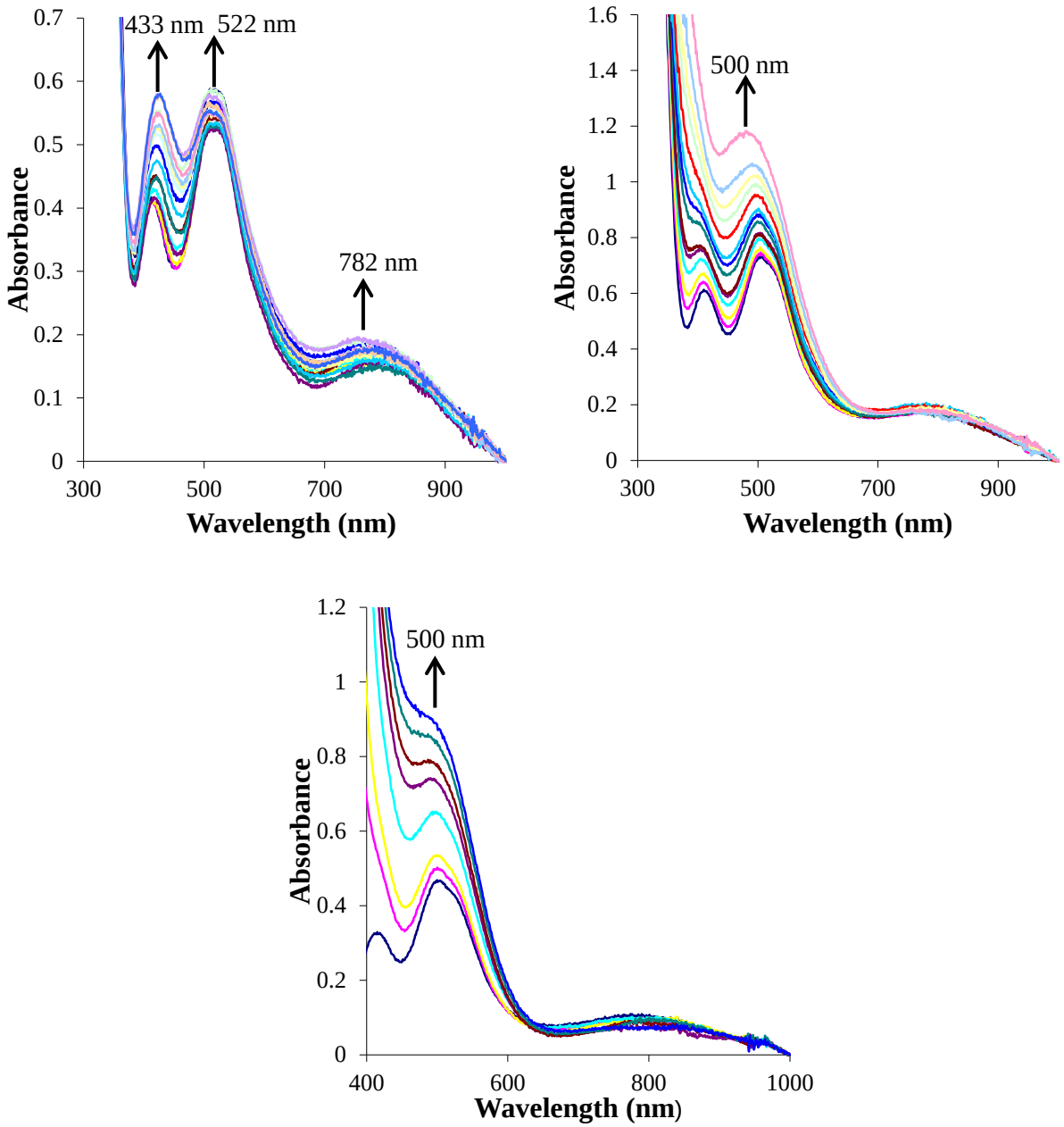

Figure 6.4 UV/Vis spectra displaying reactions between $[Mn^{III}(S^{Me2}N_4(tren))(OH)](PF_6)\cdot H_2O$ (**3**) and CH_3OH (top left, each trace represents 8 equivalent aliquots), PhOH (top right, each trace represents 2 equivalent aliquots), and $^{p}NO_2$-PhOH (bottom, each trace represents 2 equivalent aliquots) in anaerobic MeCN at 293 K.

The final spectrum observed in each UV/Vis titration experiment is identical to that of analytically-pure samples of **4**-**6**, respectively. These experiments also show quantitative

formation of each Mn(III)-OR species (using experimentally-determined extinction coefficients, Appendix A.53-A.56).

The X-ray structures of **3**-**6** each contain a single Mn ion coordinated by a thiolate sulfur (S(1)), imine nitrogen (N(1)), tertiary amine (N(2)), and two primary amines (N(3) and N(4)) (Figure 6.2), but are differentiated by the identity of the -O(1)R ligand (-OH (**3**), -OCH_3 (**4**), -OPh (**5**), and –OPh-$^{p}NO_2$ (**6**)). The Mn(1)-S(1) distances for **3**-**6** are 2.2840(4) Å (**3**), 2.2937(14) Å (**4**), 2.2675(3) Å (**5**), and 2.2937(9) Å (**6**), which are over 0.1 Å shorter than that of complex **1** (2.4033(3) Å), but close to that of oxo-bridged **2** (2.286(2) Å) and methoxide-bound **7** (2.2650(9) Å) (Table 6.1). The Mn(1)-N(3) and Mn(1)-N(4) distances in **3**-**6** are longer (2.2747(10)-2.3222(9) Å) than those in **1** (2.1938(8) Å and 2.1956(9) Å, respectively) by over 0.1 Å. Collectively, these observations and comparisons are consistent with a +3 oxidation state for each Mn ion in complexes **3**-**6**.

Further inspection of the metrical parameters for **4**-**6** reveals that the electronic properties of each -OR ligand R group influences a number of structural properties within this series. The Mn(1)-S(1) bond lengths become shorter along the series **4** > **5** > **6**, which parallels the relative electron-donating ability of each respective -OR ligand (CH_3O- > PhO- > $^{p}NO_2$-PhO-, more to less electron-donating). Similar observations can be made when comparing the Mn(1)-O(1) distances within this series, which become longer (1.836(5) Å (**4**), 1.8678(8) Å (**5**), 1.9013(19) Å (**6**)) in the same order (Table 6.1). The Mn(1)-O(1)-C bond angles, which reflect the relative hybridization of O(1), also become larger in the same order within this series (124.0(9)° (**4**), 134.25(7)° (**5**), and 136.77(18)° (**6**), Table 6.1). The metrical parameters of hydroxide-bound **3** do not fit into any of these trends, which is likely due to the presence of hydrogen bonding interactions between the thiolate and hydroxide ligands between neighboring complexes in the

X-ray structure of this complex (Figure 6.3). These observations reveal that as the RO- ligand in each complex becomes more electron-donating, the Mn(1)-O(1) bond strengthens (becomes shorter and more sp^2-hybridized). In response to these changes, the Mn(1)-S(1) bond becomes weaker (i.e. longer) as the RO- ligand becomes more electron donating.

6.3.1.2. Magnetic and Electrochemical Characterization of Complexes 3-7

The magnetic properties of complexes **3**-**7** were each explored by the Evans method in either CD_2Cl_2 or CD_3CN solutions at room temperature. Solution effective magnetic moments were determined to be 4.89 B.M. (**3**), 4.99 B.M. (**4**), 4.88 B.M. (**5**), 4.80 B.M. (**6**), and 4.61 B.M. (**7**). Each of these values are close to the spin-only value of 4.90 B.M. for an S = 2 spin-state. Solid state magnetic susceptibility measurements were made using crystalline samples of **3** by SQUID magnetometry. Plots of inverse molar magnetic susceptibility (χ_M^{-1}) versus temperature (T) and effective magnetic moments (μ_{eff}) versus temperature (T) are provided in Figure 6.5. These measurements afforded an effective magnetic moment of 4.81 B.M. for **3**, which is again consistent with an S = 2 spin state.

The electrochemical properties of **3**-**6** were explored by cyclic voltammetry experiments in MeCN at 293 K. Representative cyclic voltammograms are shown in Figure 6.6. Each complex exhibits either a quasi-reversible or irreversible $Mn^{III/II}$ couple with $E_{1/2}$ values of -350 mV (**3**), -197 mV (**4**), -184 mV (**5**), and -137 mV (**6**) (each versus $Fc^{+/0}$) (Figure 6.6). These $E_{1/2}$ values become more positive as the electron withdrawing ability of the RO- ligand increases. Hydroxide-bound **3** has the lowest $Mn^{III/II}$ couple within this series.

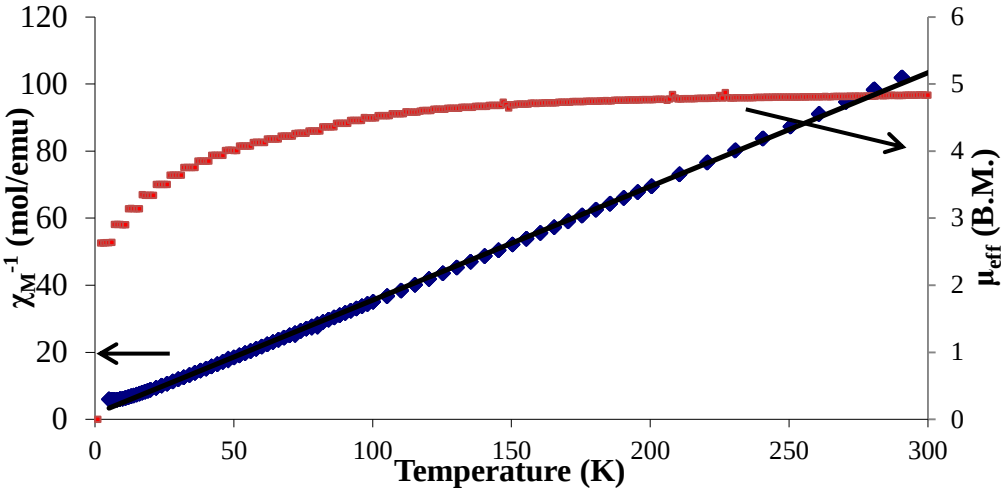

Figure 6.5 Plots of inverse molar magnetic susceptibility (χ_M^{-1}) versus temperature (T) (left y-axis) and effective magnetic moment (μ_{eff}) versus temperature (T) (right y-axis) for [Mn^{III}($S^{Me2}N_4$(tren))(OH)](PF_6)·H_2O (**3**).

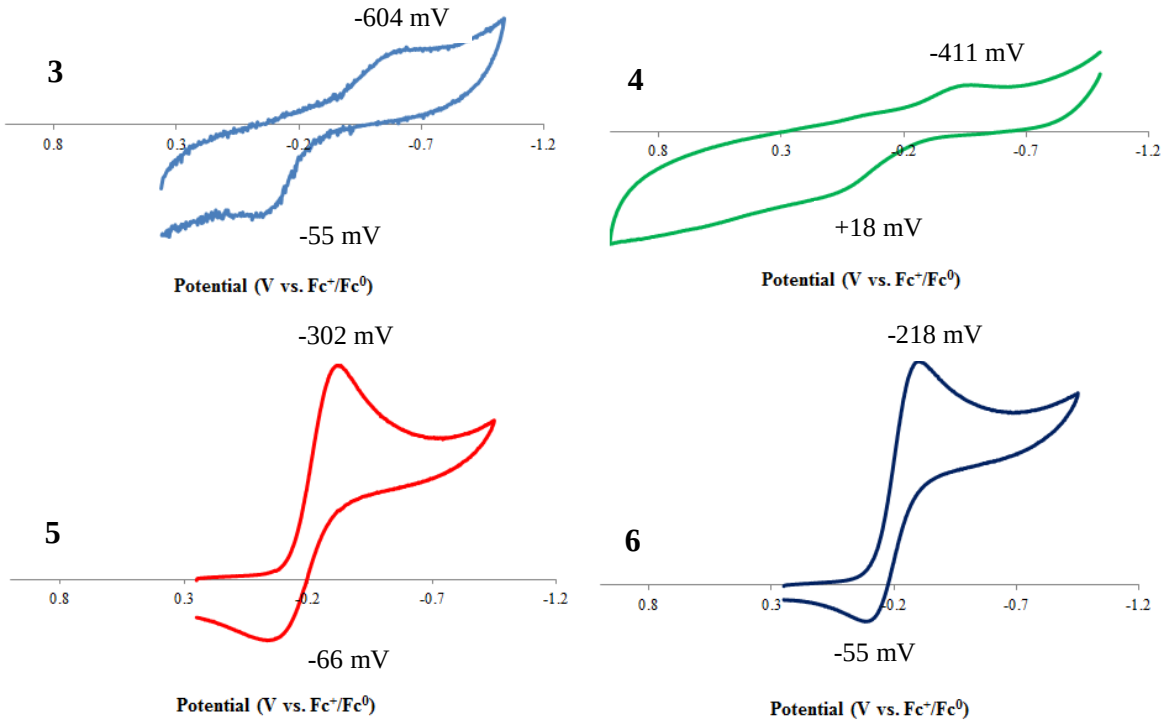

Figure 6.6 Cyclic voltammograms for complexes [Mn^{III}($S^{Me2}N_4$(tren))(OH)](PF_6)·H_2O (**3**, top left), [Mn^{III}($S^{Me2}N_4$(tren))(OCH_3)](PF_6) (**4**, top right), [Mn^{III}($S^{Me2}N_4$(tren))(OPh)](PF_6)·MeCN·Et_2O (**5**, bottom left), [Mn^{III}($S^{Me2}N_4$(tren))(OPh-$^pNO_2$)](PF_6)·MeCN (**6**, bottom right), in MeCN and referenced versus the $Fc^{+/0}$ couple. Each experiment was performed using a 0.1 M $^nBu_4PF_6$ supporting electrolyte and with scan rates of 120-150 mV·s^{-1} at room temperature. Anodic (E_{pa}) and catholic (E_{pc}) peak potentials are labeled in each voltammogram.

Hydroxide-bound **3** was found to be water-soluble and stable within a pH range of ~5-10, therefore the electrochemical properties of this complex were also explored in aqueous solution. A pH-dependent and irreversible $Mn^{III/II}$ couple was observed in the cyclic voltammograms from these experiments (Appendix A.57). This redox couple was further determined to be a one electron/one proton process (PCET) as indicated by the slope of the Pourbaix diagram shown in Figure 6.8 (52 mV/pH, close to 59 mV/pH for ideal Nernstian behavior, Figure 6.7). The Pourbaix diagram in Figure 6.7 also allows for a direct calculation of the O-H bond dissociation free energy (BDFE) in the reduced Mn(II)-OH_2 product via Equation 6.1. In Equation 6.1, E_{pH} is the redox potential at a given pH and $C_{G,sol}$ is the free energy of solvation for $H^{\cdot}$ (57.6 kcal/mol in H_2O).[28] Using Equation 6.1, the O-H BDFE of the reduced Mn(II)-OH_2

$$BDFE = 23.06(E_{pH}) + 1.37(pH) + C_{G,sol} \quad (6.1)^{29}$$

species formed from **3** is found to be 74.8 ± 0.5 kcal/mol. This value, along with a Mn(III)-OH_2 pK_a value of 5.3 (determined by titration experiments with HOTf), can be used to calculate the formal potential of the Mn(III)-OH_2/Mn(II)-OH_2 couple using

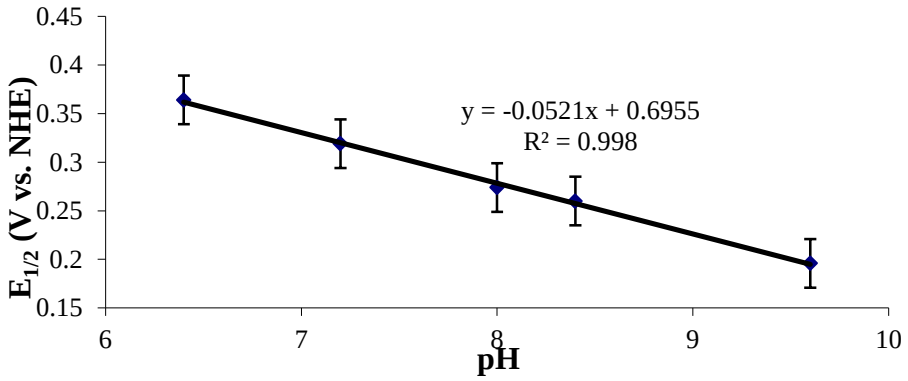

Figure 6.7 Pourbaix diagram displaying pH-dependent changes in the $Mn^{III/II}$ redox couple of **3**. pH was adjusted using either dilute aqueous HBF_4 or NH_4OH. $E_{1/2}$ values were measured at 293 K with 0.1 M $KClO_4$ supporting electrolyte, glassy carbon working electrode, Ag/AgCl reference electrode, Pt wire counter electrode, and at a 50 mV/sec scan rate.

Bordwell's equation as modified by Mayer, yielding a value of +431 mV vs. NHE (Equation 6.2, HOTf titration curve is provided in Appendix A.58).[29] The end of the Pourbaix diagram in

$$\text{BDFE (X-H)} = 23.06(E^0) + 1.37(pK_a) + C_{G,H} \qquad (6.2)$$

Figure 6.7 also affords a lower limit for the pK_a of the reduced Mn(II)-OH_2 complex in this cycle ($pK_a \geq 9.6$), which can be used along with the O-H BDFE to calculate an upper limit to the $Mn^{III/II}$-OH formal potential ($E^0 \leq +176$ mV vs. NHE, Equation 6.2). Collectively, these experimentally-determined and calculated values form a complete thermodynamic 'square scheme' for the proton-coupled reduction of **3**, as is illustrated in Scheme 6.4.

Scheme 6.4 Thermochemistry of complex **3** in aqueous solution.

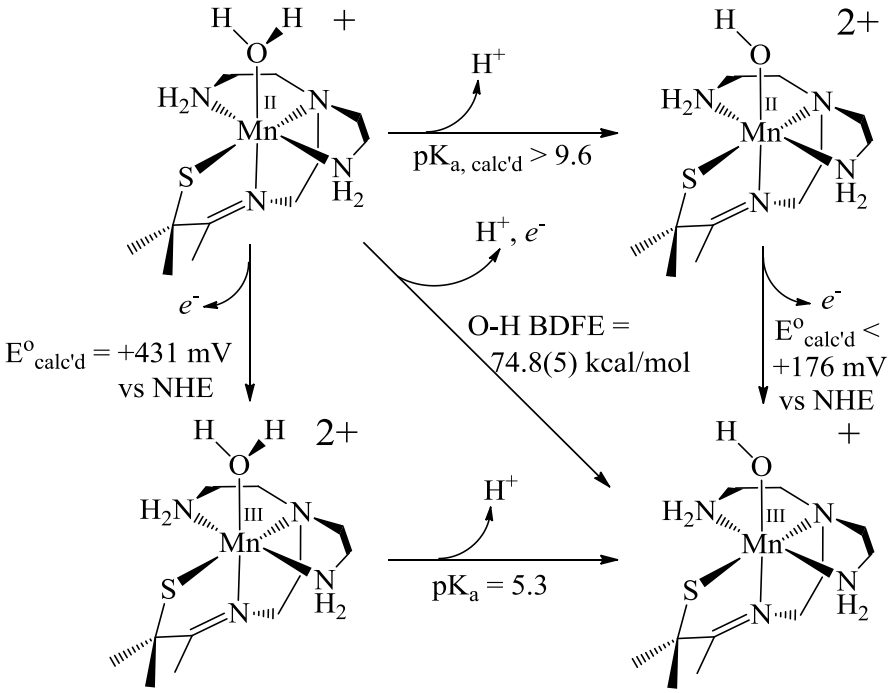

Complex **3** is the only Mn(III)-OH complex with thermodynamic data reported in aqueous solution, which unfortunately precludes a comparison between the O-H BDFE of the reduced complex and other similar systems. Comparisons can be made if thermodynamic data for **3** is obtained in organic solvents. The pK_a of protonated **3** (Mn(III)-OH_2) could not be

determined experimentally in MeCN, as the hydroxide ligand is displaced upon reacting with acids. This ultimately prevented an experimental determination of the O-H BDFE for the reduced Mn(II)-OH_2 complex. A crude approximation of the O-H BDFE for the reduced and protonated form of **3** (Mn(II)-OH_2) can be made, however, if it is assumed that the solvation energy of **3** and Mn(II)-OH_2 are the same (ΔG^0_{sol}(**3**) ≈ ΔG^0_{sol}(Mn(II)-OH_2)). This assumption results in the difference between O-H BDFE values in water and MeCN being equal to the difference between the free energy of solvation for H· in water (8.98 kcal/mol) versus MeCN (5.12 kcal/mol), affording an approximated O-H BDFE value of 70.9 kcal/mol in MeCN.[30] This value, along with the experimentally-determined $Mn^{III/II}$-OH $E_{1/2}$ of -350 mV vs. $Fc^{+/0}$ (Figure 6.6), permits a calculated Mn(II)-OH_2 pK_a value of 17.2 (Equation 6.2). These three values represent half of a thermodynamic cycle for the proton-coupled reduction of **3** in MeCN, which is illustrated in Scheme 6.5.

Scheme 6.5 Thermochemistry of complex **3** in MeCN.

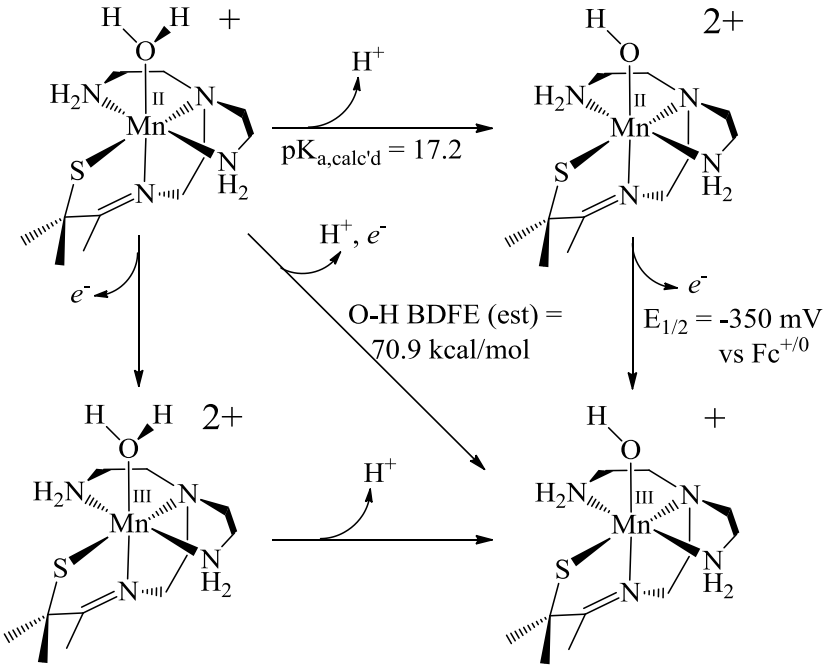

6.3.1.3. Reactivity of Complexes 3-7 with TEMPO-H

In order to determine whether complexes **3-7** were capable of oxidizing organic substrates in a proton-coupled process, reactions between each individual complex and 2,2,6,6-tetramethylpiperidine-1-ol (TEMPO-H) were performed and monitored by UV/Vis spectroscopy. These reactions were each performed in anaerobic MeCN solutions at room temperature. Complexes **3** and **4** were both found to be reduced with a stoichiometric amount of TEMPO-H under these conditions, reforming the corresponding Mn(II) complex (complex **1**) in each case. No reactions between **5-7** and TEMPO-H were observed (even with an excess of TEMPO-H, ~500 equivalents). Representative UV/Vis spectra from a titration experiment in which substoichiometric amounts of TEMPO-H were added to a solution of **3** in MeCN are provided in Figure 6.8. As is shown in these spectra, 1 equivalent of TEMPO-H completely reduces **3** to complex **1**. Exposure of this resulting reaction solution to atmospheric O_2 resulted in the formation of oxo-bridged dimer **2**, confirming that **1** was indeed reformed during the reaction between **3** and TEMPO-H. Identical observations have been made from reactions between **4** and TEMPO-H.

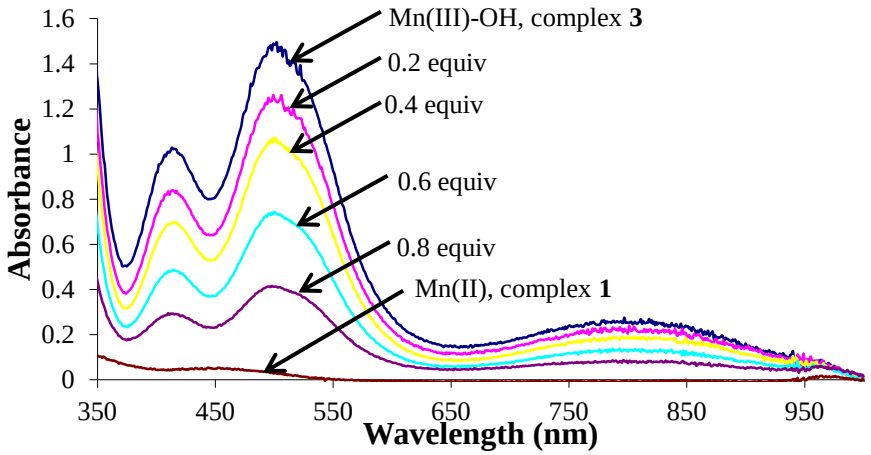

Figure 6.8 UV/Vis spectra displaying the titration of TEMPO-H (0.2 equivalent aliquots) to $[Mn^{III}(S^{Me2}N_4(tren))(OH)](PF_6)\cdot H_2O$ (**3**, 1.7 mM) in anaerobic MeCN at 293 K.

Kinetics measurements were also made for reactions between TEMPO-H (and TEMPO-D) and complexes **3** and **4** in MeCN by monitoring absorbance changes at 507 nm (**3**) or 520 nm (**4**). These experiments were performed under pseudo first-order conditions with excess TEMPO-H or TEMPO-D and 1 mM Mn(III)-OR. Plots of $\ln[(A_x-A_\infty)/(A_0-A_\infty)]$ versus time were constructed in order to obtain observed rate constants ($k_{1,obs}$ and $k_{2,obs}$ for **3** and **4**, respectively) for each reaction at four different concentrations of TEMPO-H(D). Plots of $k_{1,obs}$ and $k_{2,obs}$ versus TEMPO-H(D) concentration are provided in Figures 6.9 and 6.10 for reactions with **3** and **4**, respectively. The slope of each plot in Figures 6.9 and 6.10 affords the second order rate constant for the reduction of **3** and **4** by TEMPO-H (k_1 and k_2). A kinetic isotope effect is also evident by comparing each of these rate constants with those obtained from reactions with TEMPO-D (k_H/k_D = 2.55 for **3** and 2.07 for **4**, Figures 6.9 and 6.10). Variable temperature kinetics measurements were also made for both reactions; Eyring plots from these measurements afford the activation parameters $\Delta H^{\ddagger}$ = 8.2 kcal/mol and $\Delta S^{\ddagger}$ = -26 cal/mol·K for **3**, and 8.3 kcal/mol and -29 cal/mol·K for **4** (Figures 6.11 and 6.12). Collectively, these kinetics data are consistent with the second order rate laws provided in Equations 6.3-6.4 and are consistent with a PCET process occurring during reactions between **3** and **4** with TEMPO-H, respectively.

$$rate_1 = k_1[\mathbf{3}][TEMPO-H] \quad (6.3)$$

$$rate_2 = k_2[\mathbf{4}][TEMPO-H] \quad (6.4)$$

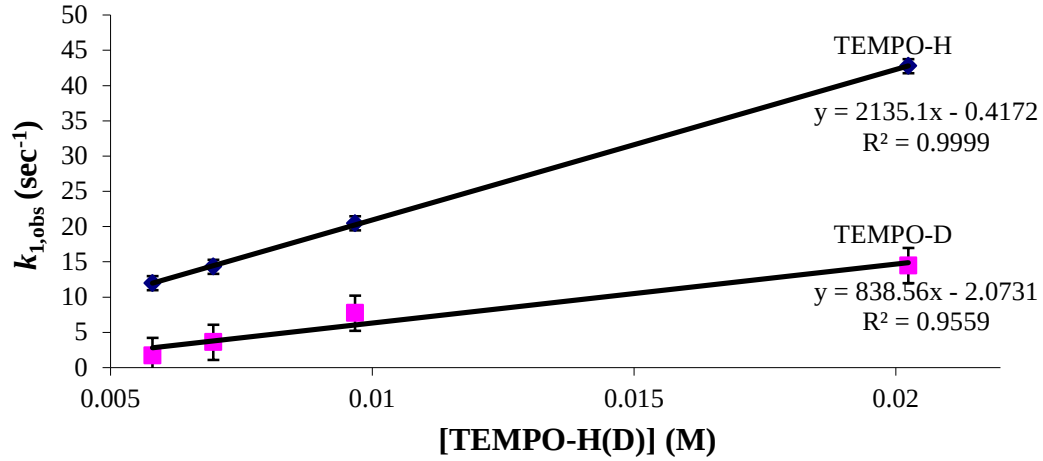

Figure 6.9 Plots of observed rate constant ($k_{1,obs}$) versus TEMPO-H or TEMPO-D concentration ([TEMPO-H(D)]) for reactions involving complex **3** (1 mM) in MeCN at 293 K.

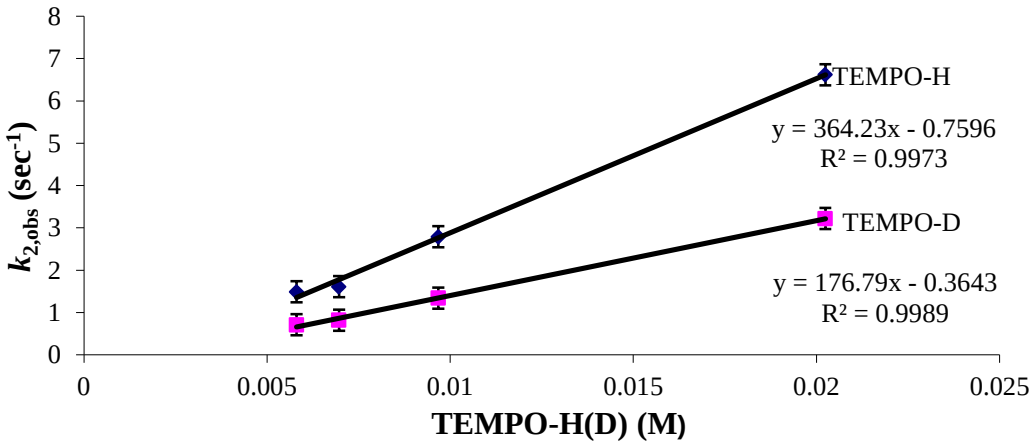

Figure 6.10 Plots of observed rate constant ($k_{2,obs}$) versus TEMPO-H or TEMPO-D concentration ([TEMPO-H(D)]) for reactions involving complex **4** (1 mM) in MeCN at 293 K.

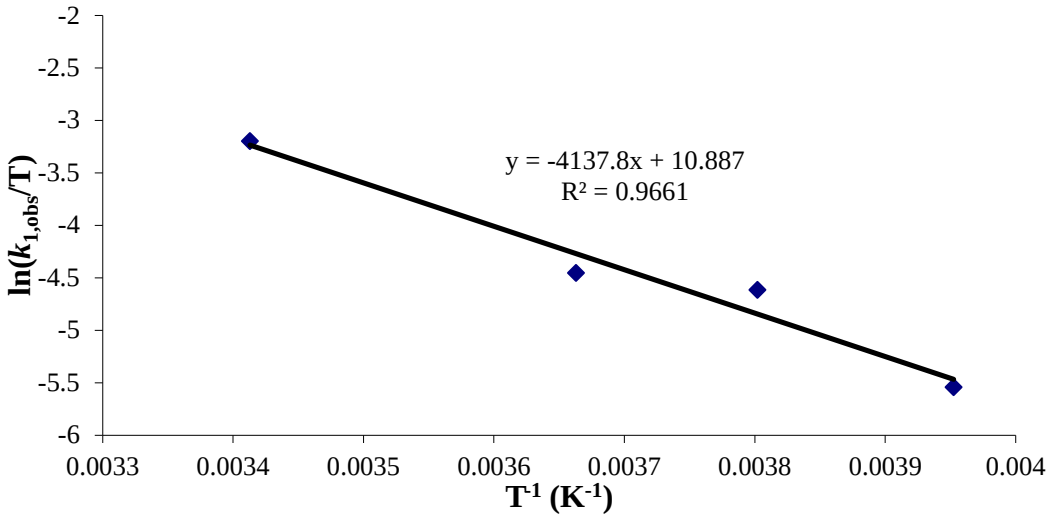

Figure 6.11 Eyring plot with variable temperature $k_{1,obs}$ values for the second order reaction between complex **3** and TEMPO-H in MeCN.

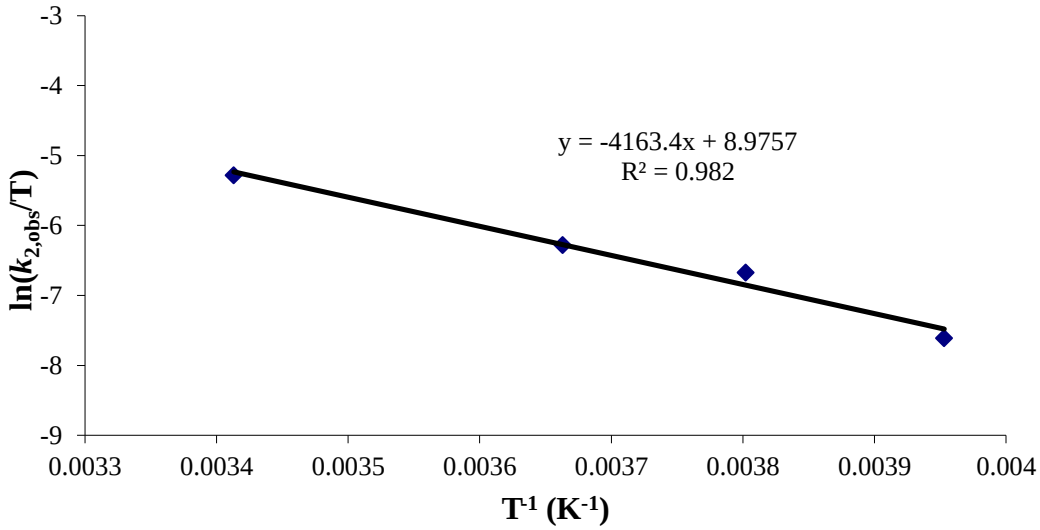

Figure 6.12 Eyring plot with variable temperature $k_{2,obs}$ values for the second order reaction between **4** and TEMPO-H in MeCN.

Although these results show that TEMPO-H can reduce both **3** and **4** to form **1**, there are various mechanisms by which each reaction could occur. Three plausible scenarios include initial electron transfer followed by proton transfer (ET-PT), proton transfer followed by electron transfer (PT-ET), or a concerted process in which both the electron and proton are transferred in the same kinetic step and originate from the same orbital in the reactant (hydrogen atom transfer, HAT) (Scheme 6.6).[30] Unfortunately, there is an insufficient amount of data in MeCN to allow these three mechanistic possibilities to be distinguished. The relatively low acidity of TEMPO-H and high TEMPO-$H^{+\cdot/0}$ redox couple does, however, suggest that a HAT process is likely operative in each case.[29] This is further supported by comparing the O-H BDFE values for TEMPO-H in H_2O (74.8 kcal/mol) and MeCN (70.9 kcal/mol) to those determined (or estimated) for **3** (71.0 kcal/mol (H_2O) and 66.5 kcal/mol (MeCN)), which reveals that the HAT pathway is thermodynamically favored by 3.8 kcal/mol in H_2O and 4.4 kcal/mol in MeCN.[28] It is also worth noting that neither **3** nor **4** were found to react with substrates containing O-H or C-H bonds containing BDFE values greater than 75 kcal/mol, which is consistent with this assessment. A complete reaction cycle for the oxidation of reduced complex **1** to oxo-bridged **2**, conversion of **2** to either hydroxo-bound **3** or methoxide-bound **4**, and reaction between **3** or **4** with TEMPO-H to regenerate **1** is provided in Scheme 6.7.

Scheme 6.6 Mechanistic possibilities for the reaction between complex **3** and TEMPO-H, including proton transfer-electron transfer (PT-ET, mechanism A), electron transfer-proton transfer (ET-PT, mechanism B), and hydrogen atom transfer (HAT, mechanism C).

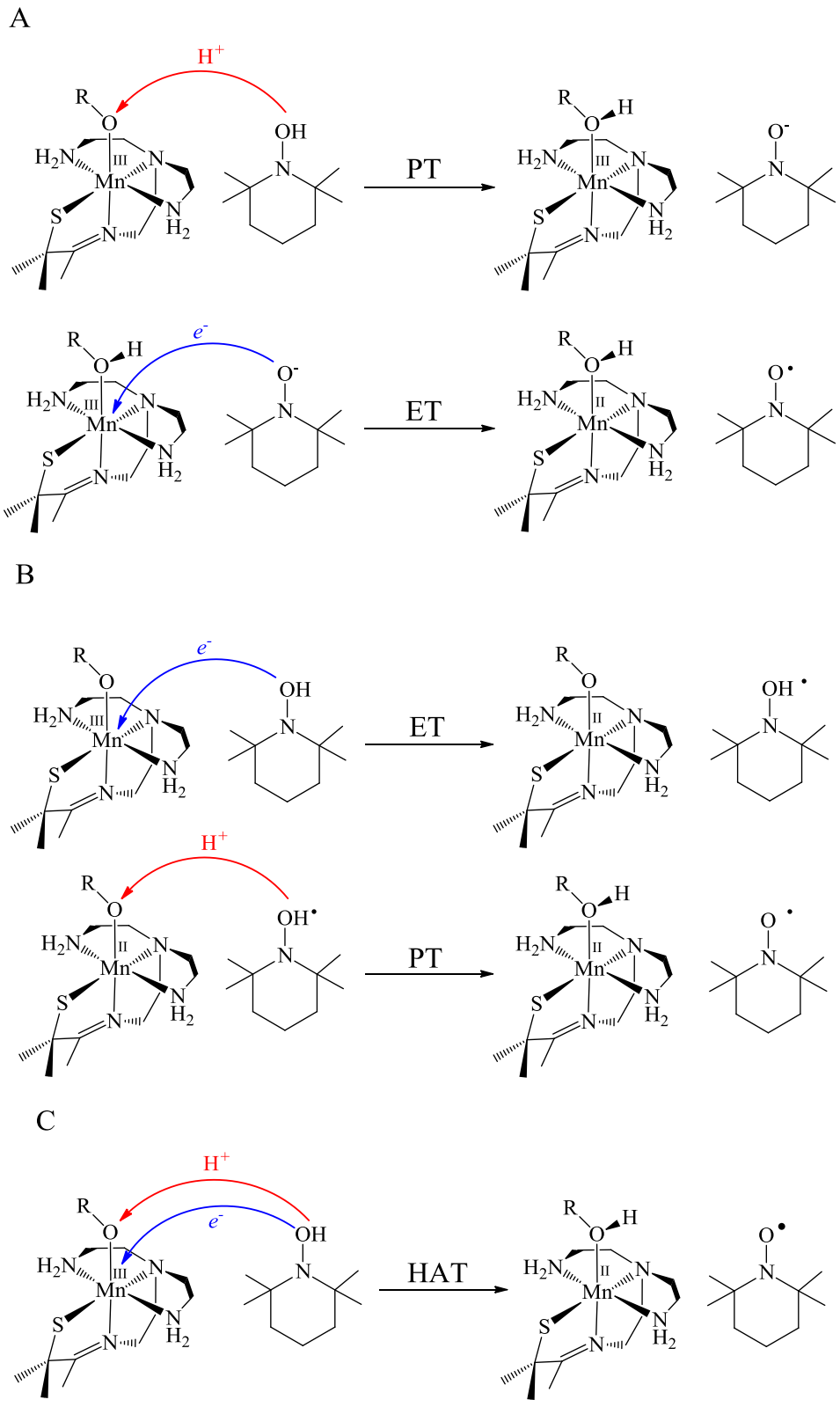

Scheme 6.7 Oxidation and subsequent reformation of complex **1** in MeCN at 293 K.

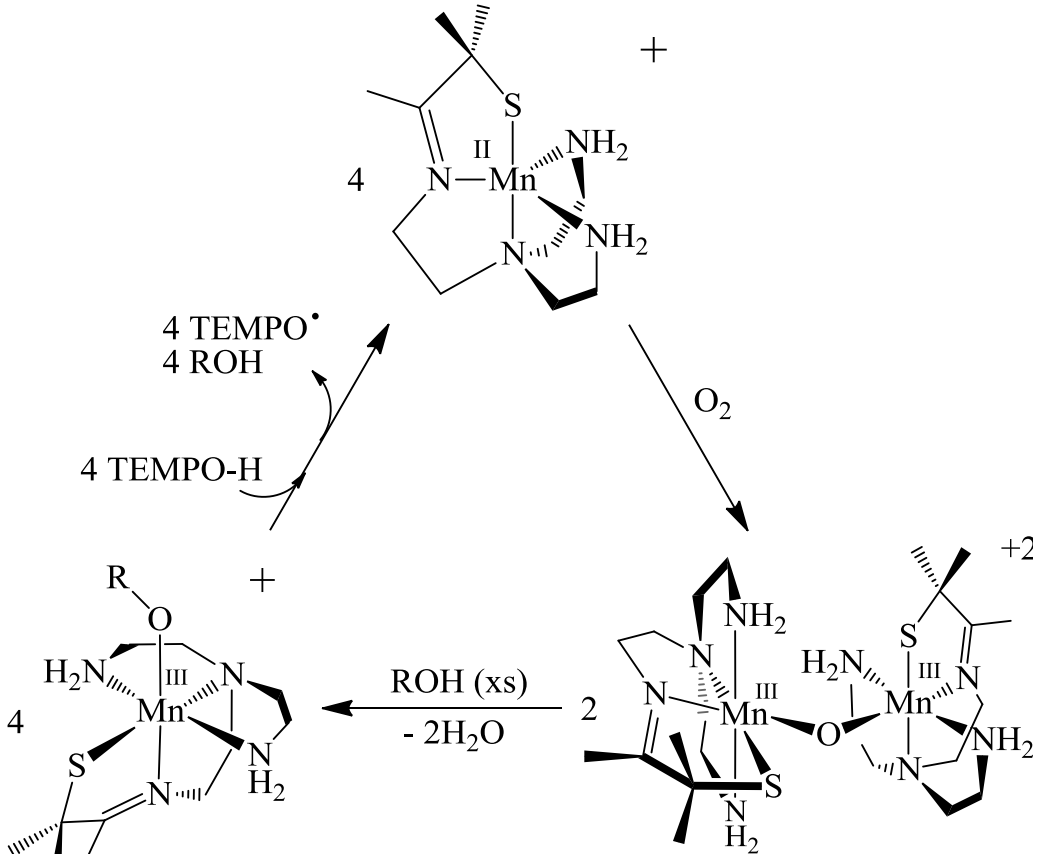

6.3.1.6 Comments on the Influence of Thiolate Ligation Upon the Reactivity of Complexes 3 and 4

In order to gain insight how the presence of a thiolate ligand in complexes **3** and **4** influences the reactivity of these complexes, one would typically compare their thermodynamic properties to other synthetic Mn(III)-OR complexes which have demonstrated the ability to oxidize substrates in a proton-coupled fashion. Unfortunately, only one other synthetic Mn(III)-OH complex ($[Mn^{III}(PY5)(OH)](CF_3SO_3)_2$ (PY5 = 2,6-bis(bis(2-pyridyl)methoxymethane)-

pyridine)) has demonstrated this type of reactivity.[31] Complex **4** is also the only Mn(III)-OCH_3 complex known which can oxidize organic substrates in such fashion. Comparisons between the properties and reactivity of **3**-**4** and $[Mn^{III}(PY5)(OH)](CF_3SO_3)_2$ could be made, however differences in charge between these three complexes (+1 for **3** and **4**, +2 for $[Mn^{III}(PY5)(OH)]$) prevent strong comparisons to be made.[30]

It can be reasonably stated that the reduction potentials of **3** and **4** (-350 mV (**3**) and -197 mV (**4**) vs $Fc^{+/0}$ in MeCN, Figure 6.6) are particularly low for metal-based oxidants, which can be at least partially attributed to the presence of a thiolate ligand in each complex. There is a growing body of literature which has shown that the strength of a metal-based oxidant involved in a PCET reaction is related to both reduction potential and pK_a.[16,19-22] This effect can be inferred from Equations 6.1 and 6.2, which relate BDFE to both of these thermodynamic values. Thiolate ligands are known to increase the relative basicity of transition metal complexes, as well as metal cofactors in metalloenzyme active sites. It stands to reason that the ability of **3** and **4** to each oxidize TEMPO-H is highly influenced by the thiolate in each complex, as an increase in basicity offsets the relatively low $Mn^{III/II}$ couples for these species, however these are purely speculative conclusions.

Synthetic attempts have also been made towards isolating alkoxide-ligated derivatives of complexes **3** and **4**, as these derivatives should allow for indirect insights into the effect of thiolate ligation to be obtained. Unfortunately, these analogues were not successfully obtained despite many synthetic attempts using a wide variety of proposed synthetic routes. The alkoxide-ligated Mn(III) complex with the most similarities to **3** and **4** was obtained through reactions between $[Mn^{II}(O^{Me2}N_4(tren))]_2(PF_6)_2$ (**8**) and O_2, which yielded the hydroxide-bridged Mn(III,III) dimer $[Mn^{III}(O^{Me2}N_4(tren))]_2(\mu\text{-}OH)(PF_6)_2$ (**9**, Scheme 6.8). The X-ray crystal

structures of complexes **8** and **9** were provided in Chapters 2 and 3, respectively. Preliminary studies have shown that dimer **9** is unreactive with TEMPO-H. Without these analogues, a strong argument regarding the influence of the thiolate ligation upon the properties and reactivity of **3** and **4** cannot be made.

Scheme 6.8 ChemDraw representation of $[Mn^{III}(O^{Me2}N_4(tren))]_2(\mu\text{-}OH)(PF_6)_2$ (**9**).

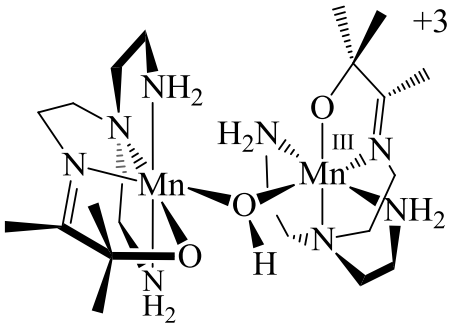

6.3.2 Iron Lipoxygenase Model Complexes

6.3.2.1 Synthesis, Characterization, and Reactivity of a Model Complex of the Reduced FeLO, Complex 10

Synthetic attempts towards a model complex of the reduced FeLO (as described in the experimental section) successfully resulted in the isolation of $[Fe^{II}(O^{Me2}N_4(tren)(H_2O))](OTf)$ (**10**). X-ray quality crystals of **10** were obtained from $MeOH/Et_2O$ at room temperature; an ORTEP diagram of **10** is provided in Figure 6.13, while crystal data and selected metrical parameters are provided in Tables 6.2 and 6.3, respectively. The X-ray structure of **10** contains a

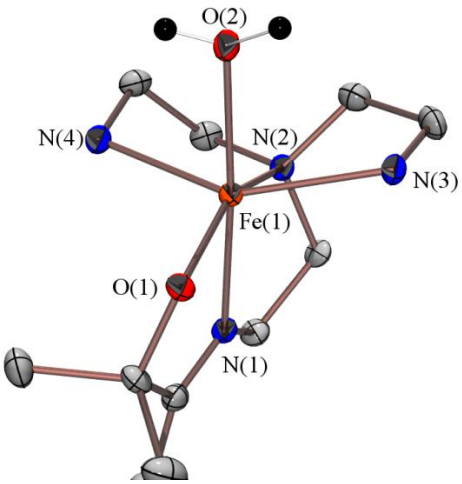

Figure 6.13 ORTEP diagram (50 % probability) of $[Fe^{II}(O^{Me2}N_4(tren)(H_2O))]^+$ (**10**) with most hydrogen atoms and counterion omitted for clarity.

six-coordinate Fe(II) ion coordinated by an alkoxide oxygen (O(1)), tertiary amine (N(2)), and two primary amines (N(3) and N(4)) in the equatorial plane, while a water ligand (O(2)) and imine nitrogen (N(1)) are found in the axial positions (Figure 6.13). Solid and solution magnetic susceptibility measurements are consistent with the Fe(II) ion in **10** being high-spin (μ_{eff} = 4.99 (solid, 5-300 K), 5.00 (CD_3OD, 298 K)).

Aerobic oxidation of **10** in MeCN solution yielded the oxo-bridged Fe(III,III) dimer $[Fe^{III}(O^{Me2}N_4(tren))]_2(\mu\text{-}O)(OTf)_2 \cdot MeOH$ (**11**). X-ray quality crystals of dimer **11** were obtained for MeOH/Et_2O; and ORTEP diagram of this complex is provided in Figure 6.14, while crystal data and selected metrical parameters are provided in Tables 6.2 and 6.3, respectively. The Fe(1)-O(1) and Fe(2)-O(2) bond lengths in **11** are each 1.917(3) Å, which are nearly ~0.1 Å shorter than that in **10** and consistent with both Fe ions being oxidized to the +3 oxidation state. It is also worthwhile to note that the Fe(1)-O(2)-Fe(2) bridging angle is 132.47(12)°, which is particularly acute for ferric dimers containing a single bridging oxo ligand (Table 6.3). The Fe···Fe distance found in **11** is 3.315 Å.

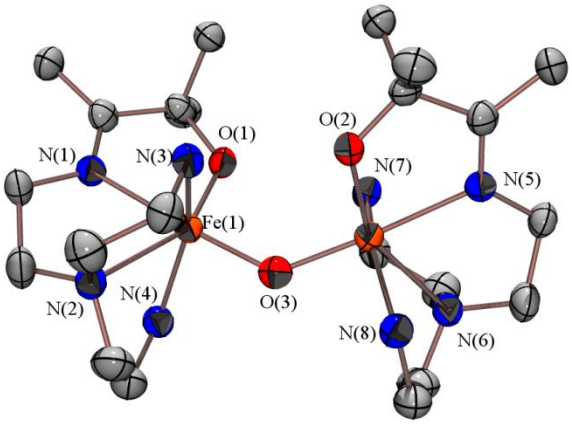

Figure 6.14 ORTEP diagram (50 % probability) of $\{[Fe^{III}(O^{Me2}N_4(tren))]_2(\mu\text{-}O)\}^{2+}$ (**11**) with hydrogen atoms, counterions, and solvent of crystallization omitted for clarity.

(Table 6.3). Solid state magnetic susceptibility measurements reveal that the Fe ions in **11** exhibit moderate exchange coupling with J = -174 cm^{-1}.

The relatively acute Fe(1)-O(2)-Fe(2) bridging angle in **11** suggested that the oxo bridge may be relatively basic (similar to observations made for oxo-bridged **2**, *vide supra*), therefore reactions were performed between **11** and HBF_4 in MeCN. These experiments revealed HBF_4 could indeed protonate the oxo-bridge of **11**, forming the corresponding hydroxide-bridged Fe(III,III) dimer $[Fe^{III}(O^{Me2}N_4(tren))]_2(\mu\text{-}OH)(OTf)_3$ (**12**). X-ray quality crystals of **12** were grown from MeOH/Et_2O; an ORTEP diagram of **12** is provided in Figure 6.15, while crystal data and selected metrical parameters are provided in Tables 6.2 and 6.3, respectively. The Fe(1)-O(2) and Fe(2)-O(2) bonds in **12** are each 1.869(3) Å, which is even shorter than those found in **11** and consistent with an increase in overall charge between **11** and **12** (+2 versus +3). Interestingly, the Fe(1)-O(2)-Fe(2) bond angle does not change considerably between **11** (132.47(12)°) and **12** (132.11°). Protonation of the oxo bridge does, however, increase the intermetallic distance to 3.695 Å, as well as decrease the magnitude of exchange coupling between the two Fe(III) ions (J = -9.7 cm^{-1}). Dimer **12** was also able to be obtained via chemical

oxidation of complex **10** with a stoichiometric amount of FcOTf. X-band EPR spectra of **12** obtained in MeOH/EtOH (9:1) glasses at 7 K were reproducibly found to contain a rhombic EPR signal (g_z = 8.82, g_y = 5.12, g_x = 3.23), which is inconsistent with an antiferromagnetically-coupled dimer. These results suggest that while **12** was crystallized and structurally characterized as a dimer, this species likely exists as a high-spin Fe(III) monomer in protic solvents. A reaction scheme demonstrating the oxidation of **10** to **11** and **12**, as well as the protonation of **11** to form **12**, is provided in Scheme 6.9.

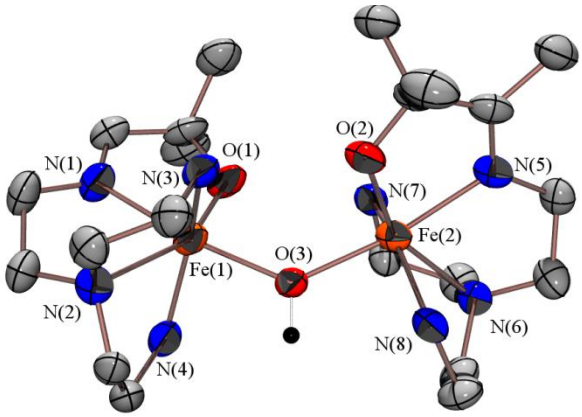

Figure 6.15 ORTEP diagram (50 % probability) of $\{[Fe^{III}(O^{Me2}N_4(tren))]_2(\mu\text{-}OH)\}^{3+}$ with most hydrogen atoms and counterions omitted for clarity.

Table 6.3 Selected bond distances (Å) and angles (degrees) for $[Fe^{II}(O^{Me2}N_4(tren))(H_2O)](OTf)$ (**10**), $[Fe^{III}(O^{Me2}N_4(tren))]_2(\mu\text{-}O)(OTf)_2\cdot MeOH$ (**11**), $[Fe^{III}(O^{Me2}N_4(tren))]_2(\mu\text{-}OH)(OTf)_3$ (**12**), $[Fe^{II}(O^{Me2}N_4(6\text{-}Me\text{-}DPEN))](PF_6)$ (**13**), and $[Fe^{III}(O^{Me2}N_4(6\text{-}Me\text{-}DPEN))]_2(\mu\text{-}OH)_2(PF_6)_2$ (**14**).

	10	**11**	**12**	**13**	**14**
Fe(1)-O(1)	2.0010(15)	1.917(3)	1.869(3)	1.925(3)	1.8721(13)
Fe(1)-N(1)	2.1294(17)	2.164(3)	2.114(5)	2.086(4)	2.1121(15)
Fe(1)-N(2)	2.2571(18)	2.305(3)	2.244(4)	2.274(5)	2.2556(15)
Fe(1)-N(3)	2.2488(17)	2.178(3)	2.125(5)	2.139(4)	2.2144(16)
Fe(1)-N(4)	2.2221(17)	2.158(3)	2.134(5)	2.121(4)	5.253
Fe(1)-O(2)	2.1494(15)	1.8108(17)	2.023(3)	N/A	1.9715(13)
Fe(1)-O(4)	N/A	N/A	N/A	N/A	2.0037(14)
Fe(2)-O(3)	N/A	1.917(3)	1.875(4)	N/A	1.8721(13)
Fe(2)-N(5)	N/A	2.164(3)	2.108(4)	N/A	2.1121(15)
Fe(2)-N(6)	N/A	2.305(3)	2.252(4)	N/A	2.2556(15)
Fe(2)-N(7)	N/A	2.178(3)	2.110(4)	N/A	2.2144(16)
Fe(2)-N(8)	N/A	2.158(3)	2.114(4)	N/A	5.253
Fe(2)-O(2)	N/A	1.8108(17)	2.019(3)	N/A	1.9715(13)
Fe(2)-O(4)	N/A	N/A	N/A	N/A	2.0037(14)
O(1)-Fe(1)-N(1)	76.49(6)	76.83(12)	77.62(17)	78.96(16)	78.34(6)
O(1)-Fe(1)-N(2)	153.14(6)	151.31(12)	152.77(16)	154.83(14)	148.61(5)
O(1)-Fe(1)-N(3)	105.45(6)	103.84(13)	104.56(17)	117.96(16)	98.17(6)
O(1)-Fe(1)-N(4)	108.00(6)	105.02(13)	106.00(17)	116.24(16)	N/A
O(1)-Fe(1)-O(2)	103.44(6)	100.54(12)	93.56(14)	N/A	106.24(5)
O(1)-Fe(1)-O(4)	N/A	N/A	N/A	N/A	104.88(6)
O(2)-Fe(1)-N(1)	175.84(6)	176.85(15)	170.90(16)	N/A	163.94(6)
O(2)-Fe(1)-N(2)	103.42(6)	108.14(12)	113.66(14)	N/A	89.99(5)
O(2)-Fe(1)-N(3)	81.22(6)	90.95(11)	87.27(15)	N/A	87.17(6)
O(2)-Fe(1)-N(4)	80.51(6)	90.09(14)	87.61(16)	N/A	N/A
O(2)-Fe(2)-N(5)	N/A	176.85(15)	171.13(15)	N/A	163.94(6)
O(2)-Fe(2)-N(6)	N/A	108.14(12)	112.36(15)	N/A	89.99(5)
O(2)-Fe(2)-N(7)	N/A	90.95(11)	86.27(15)	N/A	87.17(6)
O(2)-Fe(2)-N(8)	N/A	90.09(14)	88.64(15)	N/A	N/A
O(3)-Fe(2)-O(2)	N/A	100.54(12)	94.35(15)	N/A	106.24(5)
O(3)-Fe(2)-N(5)	N/A	76.83(12)	77.34(16)	N/A	78.34(6)
O(3)-Fe(2)-N(6)	N/A	151.31(12)	153.13(16)	N/A	148.61(5)
O(3)-Fe(2)-N(7)	N/A	103.84(13)	107.19(16)	N/A	98.17(6)
O(3)-Fe(2)-N(8)	N/A	105.02(13)	102.54(16)	N/A	N/A
Fe(1)···Fe(2)	N/A	3.315	3.695	N/A	3.172
Fe(1)-O(2)-Fe(2)	N/A	132.47(12)	132.11(16)	N/A	105.88(6)
Fe(1)-O(4)-Fe(2)	N/A	N/A	N/A	N/A	105.88(6)

Scheme 6.9 Reaction scheme for oxidation of **10** to **11** and **12**, respectively, as well as protonation of **11** to form **12**. All reactions are in MeCN at 293 K.

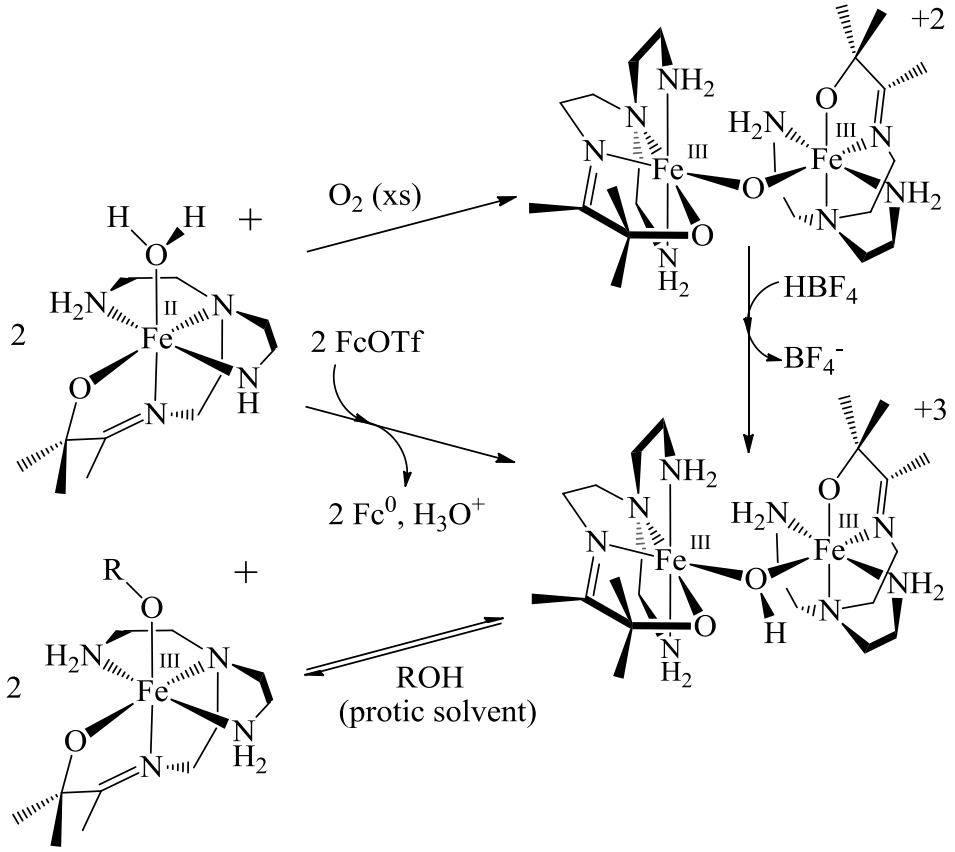

6.3.2.2 Thermochemistry of Complex 10

Complex **10** was found to be water-soluble and thus permitted variable-pH electrochemical experiments to be performed. Cyclic voltammograms of **10** in aqueous solution displayed a pH-dependent and irreversible $Fe^{III/II}$ couple, as is illustrated by the Pourbaix diagram in Figure 6.16 (a representative cyclic voltammogram of **10** in aqueous solution is provided in Appendix A.59). The slope of the plot in Figure 6.16 (41 mV/pH) is close to that for an ideal Nernstian $1e^-/1H^+$ process (59 mV/pH), suggesting that the oxidation of **10** is a proton-coupled process. Using Equation 6.1, this affords an O-H BDFE of 64.7 kcal/mol for **10**. The pK_a of **10** was experimentally-determined to be 12.3 through pH titration experiments in aqueous

solution with NaOH (titration data in Appendix A.60). These two experimental values were then used to calculate the formal potential of the $Fe^{III/II}$-OH couple for **10**, which is -422 mV vs. NHE. Given that evidence was provided to suggest that **12** existed as a monomeric Fe(III)-OR species in protic solvent, pH titration experiments were conducted with this compound in order to obtain an experimental pK_a value for the Fe(III)-OH_2 complex associated with **10**. These experiments yielded a pK_a of 4.4 for this species, which was used along with the O-H BDFE of **10** to calculated the formal potential of the $Fe^{III/II}$-OH_2 couple (+46 mV vs. NHE). These values collectively represent a complete thermochemical cycle for the proton-coupled oxidation of **10** to the corresponding Fe(III)-OH species, as is represented in Scheme 6.10.

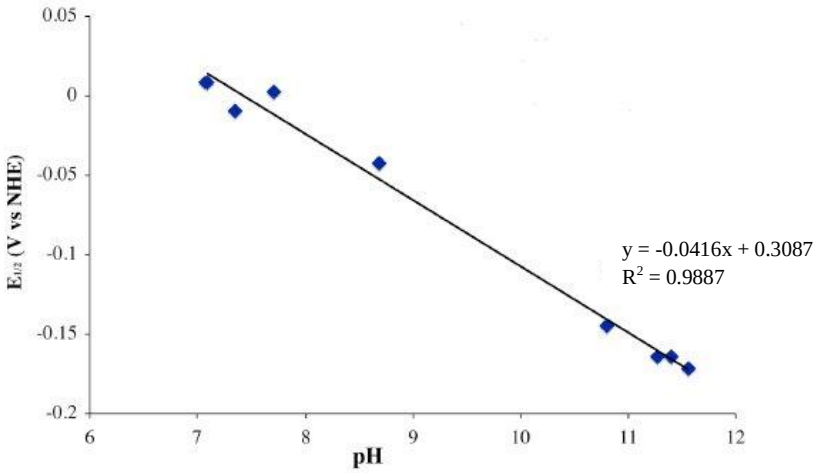

Figure 6.16 Pourbaix diagram displaying pH-dependent changes in the $Fe^{III/II}$ redox couple of **10**. pH was adjusted using either dilute aqueous HBF_4 or NH_4OH. $E_{1/2}$ values were measured at 293 K with 0.1 M $KClO_4$ supporting electrolyte, glassy carbon working electrode, Ag/AgCl reference electrode, Pt wire counter electrode, and at a 50 mV/sec scan rate.

Scheme 6.10 Thermochemistry of complex **10** in aqueous solution.

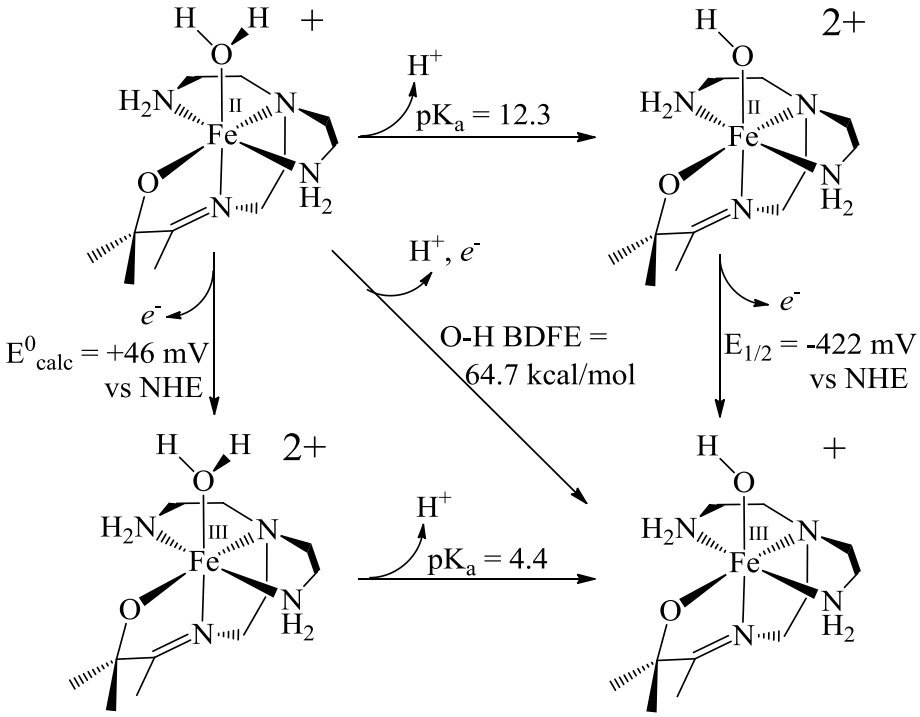

6.3.2.3 Reactivity of Complex 10 with TEMPO·

The relatively weak O-H bond found in **10** (64.7 kcal/mol) suggested that this complex could possibly be oxidized in a proton-coupled fashion. Reactions were therefore performed in anaerobic aqueous solution between complex **10** and TEMPO·. Given the O-H BDFE of TEMPO-H in H_2O is 71.0 kcal/mol, HAT from **10** to TEMPO· should be thermodynamically favorable by 6.3 kcal/mol. It was indeed found that a stoichiometric amount of TEMPO· promoted the oxidation of **10** to **12**, as was determined by UV/Vis spectroscopy and ESI-MS. Titration experiments were also performed in MeCN solution in which 0.25 equivalents of **10** were added to solution of TEMPO· and subsequently analyzed by X-band EPR spectroscopy. These experiments revealed that the EPR signal of TEMPO· was absent following the complete addition of one equivalent of **10**, which is consistent with a redox process occurring between the

two reagents (Figure 6.17). It is also worth noting that these EPR spectra do not contain a signal attributable to a mononuclear Fe(III) complex (as was previously noted for complex **12** in MeOH, *vide supra*), which is consistent with complex **12** only existing as a monomeric species in protic solvents.

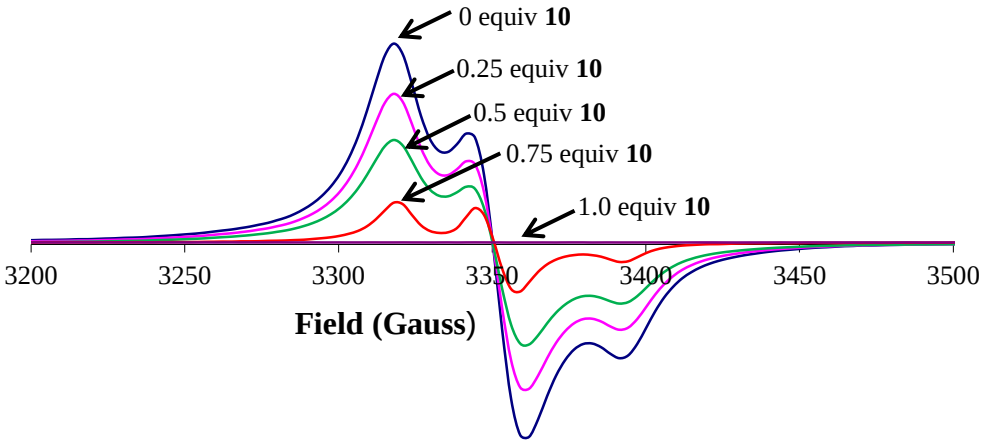

Figure 6.17 X-band EPR spectra displaying the titration of $[Fe^{II}(O^{Me2}N_4(tren)(H_2O))](OTf)$ (**10**, 0.25 equivalent aliquots) into a solution of $TEMPO^{\cdot}$ in MeCN/toluene (4.6 K).

Just as was discussed for the reaction between complex **3** and TEMPO-H, the proton-coupled oxidation of **10** by $TEMPO^{\cdot}$ could potentially occur via an ET-PT, PT-ET, or concerted process in which the electron and proton originate from different orbitals in the reactant (electron-proton transfer, EPT). Fortunately, there is a sufficient amount of thermochemical data to allow the most thermodynamically favorable pathway to be determined. A lower limit to the activation energy for each mechanistic pathway can be calculated by the change in ground state energy, which can be calculated via Equations 6.5-6.7, respectively. Using the values provided in Scheme 6.11, along with $E^0(TEMPO^{0/-})$ = -175 mV vs. NHE and the pK_a (TEMPO-H) = 12.9,

$$\Delta G_{ET}{}^0 = -FE^0 = (-23.06 \text{ kcal/mol}\cdot\text{V}) \times (E_{1/2}(Fe^{III/II}\text{-}OH_2) - E^0(TEMPO^{0/-}) \qquad (6.5)$$

$$\Delta G_{PT}^{0} = -RT\ln(K_{eq}) = (-1.37 \text{ kcal/mol}) \times (pK_a(\text{TEMPO-H}) - pK_a(Fe^{III/II}\text{-}OH_2)) \quad (6.6)$$

$$\Delta G_{EPT}^{0} = [BDFE(\text{O-H}, Fe^{II}\text{-}OH_2) - BDFE(\text{O-H, TEMPO-H})] \quad (6.7)$$

these ground state free energy changes are calculated to be ΔG_{ET}^{0} = -5.09 kcal/mol, ΔG_{PT}^{0} = -0.82 kcal/mol, and ΔG_{EPT}^{0} = -6.3 kcal/mol, which support an EPT mechanism as being the most thermodynamically favorable for this reaction (Scheme 6.11).[28]

Scheme 6.11 Electron-proton transfer from complex **10** to TEMPO$^{\cdot}$, followed by equilibration with dimer **12** in H_2O.

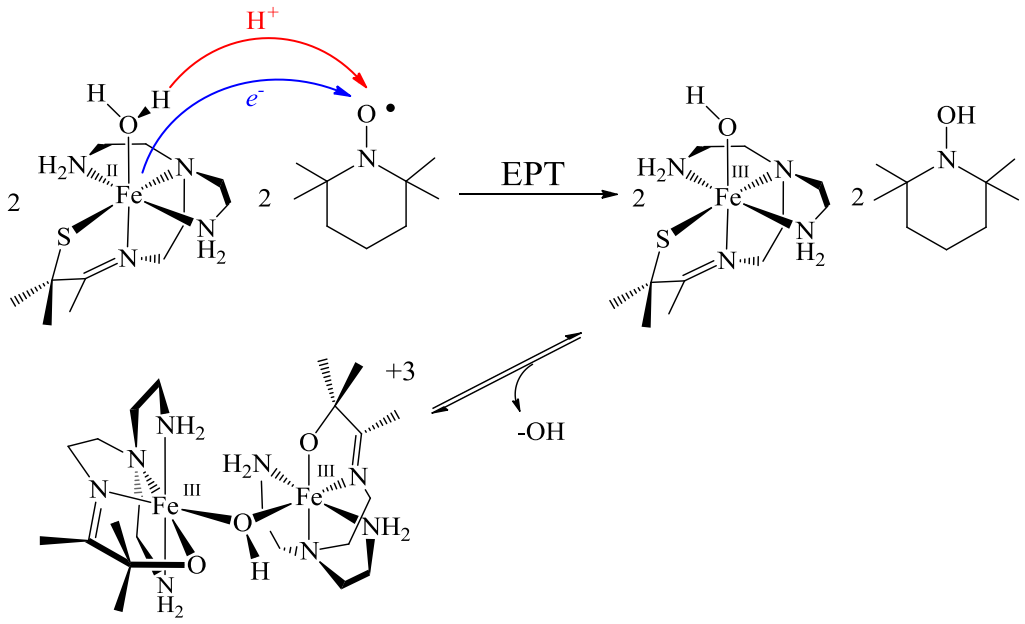

6.3.2.4 Synthesis, Characterization, and Reactivity of Five-Coorindate Complex 13 and Hydroxide-Bridged Dimer 14

Synthetic attempts towards a more electrophilic analogue of complex **10** were made using N,N-bis(6-methyl-2-pyridilmethyl)ethane-1,2-diamine, which resulted in the isolation of $[Fe^{II}(O^{Me2}N_4(6\text{-Me-DPEN}))](PF_6)$ (**13**). X-ray quality crystals of **13** were obtained from

MeCN/Et_2O; an ORTEP diagram of 13 is provided in Figure 6.18, while selected metrical parameters and crystal data are provided in Tables 6.3 and 6.2, respectively. Unlike alkoxide-

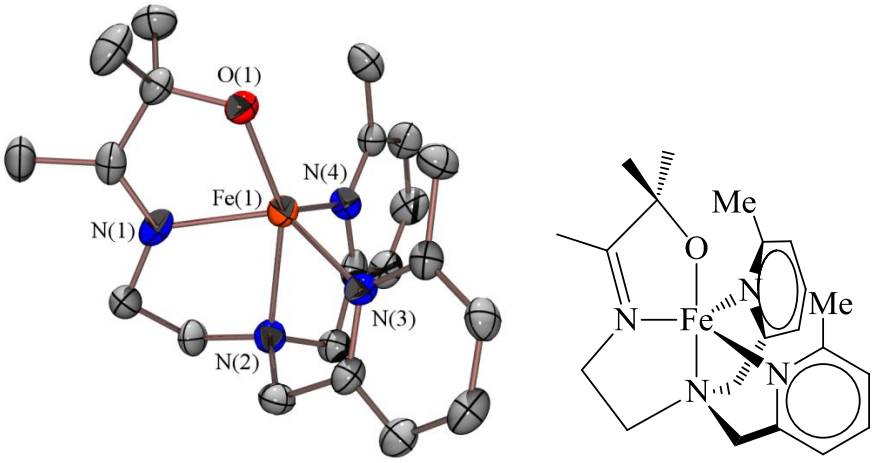

Figure 6.18 ORTEP diagram (50 % probability) of $[Fe^{II}(O^{Me2}N_4(6\text{-Me-DPEN}))]^+$ (**13**) with hydrogen atoms and counterion omitted for clarity (left). A ChemDraw representation of **13** is provided on the right.

ligated **10**, complex **13** was characterized as a coordinatively unsaturated complex (Figure 6.18). Metrical comparisons between these two Fe(II) complexes are not strictly considered given the difference in coordination numbers, however it is worthwhile to note that the Fe-pyridine bond lengths in **13** (Fe(1)-N(3) and Fe(1)-N(4) are 2.139(4) Å and 2.121(4) Å, respectively) are much shorter than the Fe-primary amine bond lengths in **10** (Fe(1)-N(3) and Fe(1)-N(4) are 2.2488(17) Å and 2.2221(17) Å, respectively), which would be consistent with **13** being more electrophilic than **10** (Table 6.x). Solution magnetic susceptibility measurements made in CD_3OD at room temperature afforded an effective magnetic moment of 4.72 B.M. for **13**, which is suggests that complex 13 contains a high-spin (S = 2) Fe^{II} ion. The electrochemical properties of **13** were also explored via cyclic voltammetry in MeCN, which revealed a quasi-reverisble $Fe^{III/II}$ couple ($E_{1/2}$ = +120 mV vs. $Fc^{+/0}$, ΔE = 212 mV, Figure 6.19).

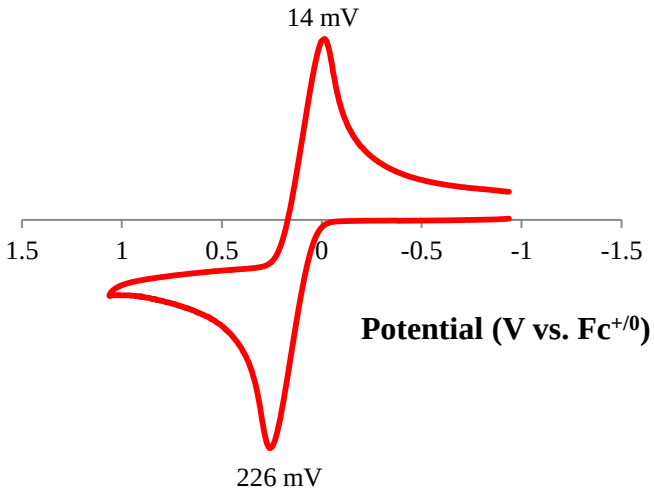

Figure 6.19 Cyclic voltammogram of $[Fe^{II}(O^{Me2}N_4(6\text{-Me-DPEN}))](PF_6)$ (**13**) in MeCN and referenced versus the $Fc^{+/0}$ couple (0.1 M $^nBu_4PF_6$ supporting electrolyte, glassy carbon working electrode, Ag/AgCl reference electrode, Pt wire counter electrode, 150 mV/sec scan rate, 293 K). Anodic and cathodic peak potentials are labeled in the voltammogram.

The reactivity of **13** towards a wide variety of oxidants (O_2, KO_2, PhIO) was surveyed in CH_3CH_2CN (EtCN) solutions at various temperatures (293 K and 193 K) and monitored by UV/Vis spectroscopy. Each of these oxidants were found to react with **13** to afford the same final product; X-ray quality crystals of this product were obtained from EtCN and analyzed to reveal a bis(μ-hydroxo)-Fe(III,III) dimer, $[Fe^{III}(O^{Me2}N_4(6\text{-Me-DPEN}))]_2(\mu\text{-}OH)_2(PF_6)_2$ (**14**). Two ORTEP diagrams of **14** are provided in Figure 6.20, while selected metrical parameters and crystal data are provided in Tables 6.3 and 6.2, respectively. The intermetallic distance (Fe(1)···Fe(2)) of **14** is 3.172 Å, which is slightly longer than those found in other complexes containing a dihydroxide core (3.078-3.155 Å). As shown by the ORTEP diagrams of **14** in Figure 6.20, a pyridine moiety in each half of the dimer is projected away from each respective Fe(III) ion, presumably due to an increase in steric congestion around each Fe ion upon

formation the dihydroxide bridging motif. A quantitative UV/Vis spectrum of **14** in MeCN is provided in Figure 6.21.

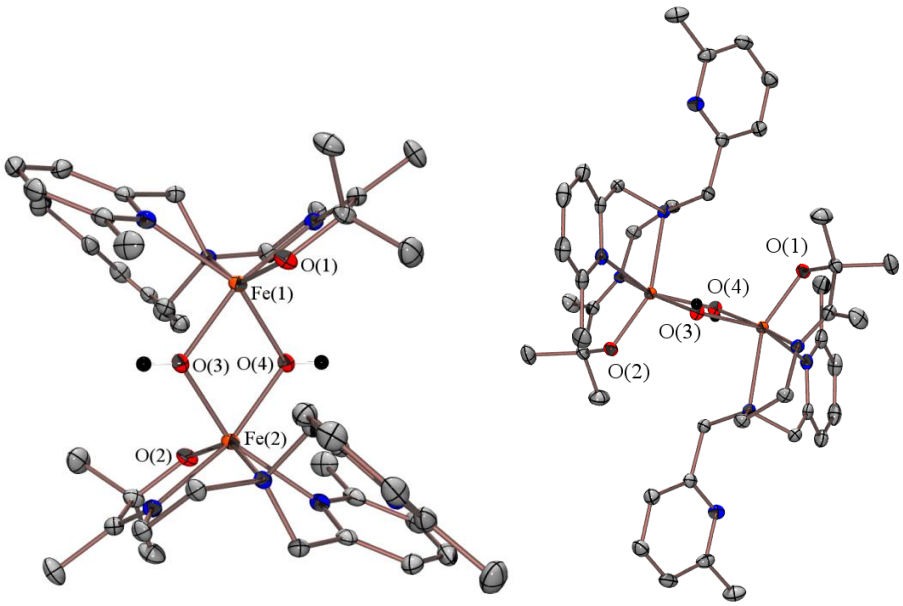

Figure 6.20 ORTEP diagrams (50 % probability) of $\{[Fe^{III}(O^{Me2}N_4(6\text{-Me-DPEN}))]_2(\mu\text{-}OH)_2\}^{2+}$ (**14**) with most hydrogen atoms and counterions omitted for clarity.

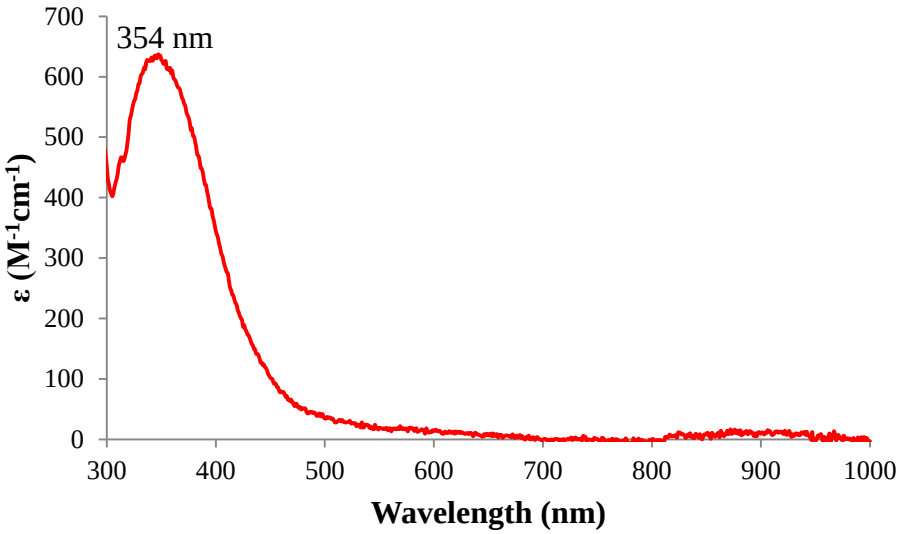

Figure 6.21 Quantitative UV/Vis spectrum (extinction coefficient versus wavelength) of $[Fe^{III}(O^{Me2}N_4(6\text{-Me-DPEN}))]_2(\mu\text{-}OH)_2(PF_6)_2$ (**14**) in MeCN at 293 K.

The 5 K X-band EPR spectrum of **14** in MeOH/EtOH (9:1) glass was found to display signals consistent with a rhombic high-spin Fe(III) ion (g_z = 8.32, g_y = 4.17, g_x = 3.18, Appendix A.61), suggesting that **14** may exist predominantly as a monomeric Fe(III)-OH species in solution. Solution magnetic susceptibility measurements for **14** were made in CD_3CN, which yielded an effective magnetic moment of 4.72 B.M. per Fe(III) ion. This measurement further suggests that **14** likely exists as a monomer in solution, as all other Fe(III,III) dimers with dihydroxide bridging motifs exhibit considerable degrees of antiferromagnetic coupling.[31]

The electrochemical properties of **14** were explored by cyclic voltammetry in MeCN at room temperature. Assuming **14** is indeed a monomeric Fe(III)-OH species in solution, this species was found to exhibit a quasi-reversible $Fe^{III/II}$ couple ($E_{1/2}$ = -1.52 V vs. $Fc^{+/0}$, ΔE = 180 mV). Complex **14** was also found to be irreversibly oxidized, presumably to an Fe(IV) species, at a potential of +520 mV vs. $Fc^{+/0}$.

Given that **14** was formed in high yields from reactions between **13** and O_2 or PhIO in anhydrous MeCN solutions, the presence of two hydroxide bridging ligands in the X-ray structure of **14** was an unexpected structural feature. This observation could be explained if the solvent was serving as a hydrogen atom source, which has been suggested in a number of other iron and manganese system which react with O_2 and result in hydroxide-bound oxidized products. In order to determine whether or not MeCN was directly participating in these reactions, **14** was isolated from reactions between **13** and O_2 performed in CH_3CN or CD_3CN solutions, respectively. Since **14** was found to be formed in nearly quantitative yield under these conditions, solid products formed from reactions in each solvent were isolated simply by removing all volatiles. The isolated solid product from each reaction was then analyzed by FT-IR spectroscopy. An isotopically-sensitive feature in the IR spectrum of **14** formed in CH_3CN

was found at 3614 cm^{-1}, which shifted by 880 cm^{-1} to 2734 cm^{-1} when prepared in CD_3CN (Figure 6.22). The observed isotopic shift is close to that predicted based upon a harmonic oscillator approximation for an O-H stretch (ν_{O-H}/ν_{O-D} = 1.322 (exp), 1.374 (theoretical)), and is within the expected energy region for an O-H stretch. This data supports MeCN serving as the source of hydrogens in the hydroxide bridges of **14**.

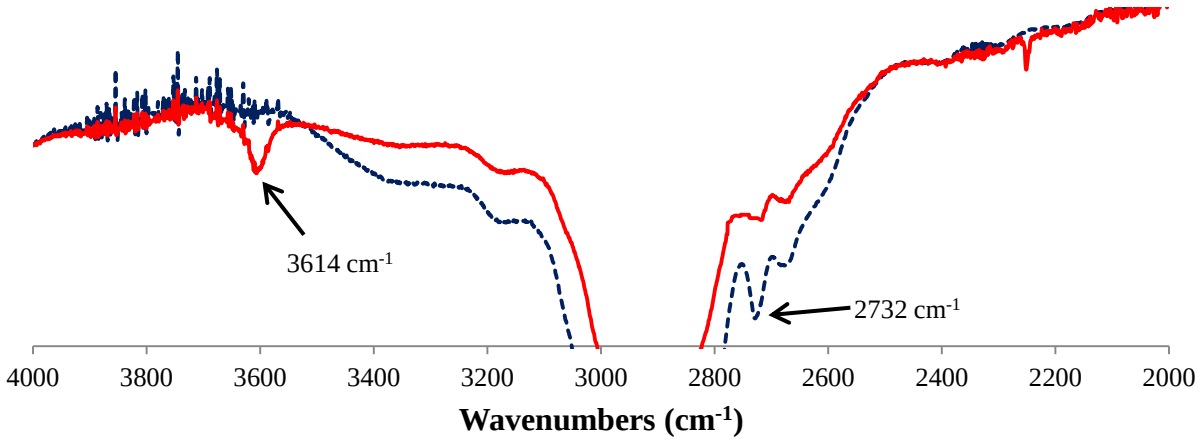

Figure 6.22 FT-IR spectra of $[Fe^{III}(O^{Me2}N_4(6\text{-Me-DPEN}))]_2(\mu\text{-}OH)_2(PF_6)_2$ (**14**) formed from reactions between $[Fe^{II}(O^{Me2}N_4(6\text{-Me-DPEN}))](PF_6)$ (**13**) and O_2 in CH_3CN (solid red trace) and CD_3CN (dashed blue trace).

Preliminary reactivity have been performed between **14** and dihydroanthracene (C-H BDFE = 76 kcal/mol in DMSO) or 2,4,6-tri-*tert*-butylphenol (O-H BDFE = 77.1 kcal/mol in MeCN) in MeCN solution at room temperature.[29] These reactions have resulted in the observation of oxidized organic products (anthracene and 2,4,6-tri-*tert*-butylphenoxy radical, respectively), as well as the reformation of **13**, each in nearly stoichiometric yields. Further investigations into the reactive properties of **14** are currently underway.

6.4 Notes to Chapter 6

1) Nelson, M. J.; Seitz, S. P. In *Active Oxygen in Biochemistry*; Valentine, J. S.; Foote, C. S.; Greenberg, A.; Liebman, J. F.; Eds.; Blackie Academic & Professional: London, 1995; Vol. 3.

2) Su, C.; Oliw, E. *J. Biol. Chem.* **1998**, *273*, 13072-13079.

3) Hamberg, M.; Su, C.; Oliw, E. *J. Biol. Chem.* **1998**, *273*, 13080-13088.

4) Skrzypczak-Jankun, E.; Amzel, L. M.; Kroa, B. A.; Funk, M. O., Jr. *Proteins: Struct., Funct. Genet.* **1997**, *29*, 15-31.

5) Minor, W.; Steczko, J.; Stec, B.; Otwinowski, Z.; Bolin, J. T.; Walter, R.; Axelrod, B. *Biochemistry* **1996**, *35*, 10687-10701.

6) Boyington, J. C.; Gaffney, B. J.; Amzel, L. M. *Science* **1993**, *260*, 1482-1486.

7) Fleming, J.; Thiele, B. J.; Chester, J.; O'Prey, J.; Janetzki, S.; Aitken, A.; Anton, I. A.; Rapoport, S. M.; Harrison, P. R. *Gene* **1989**, *79*, 181-188.

8) Sigal, E.; Craik, C. S.; Highland, E.; Grunberger, D.; Costello, L. L.; Dioxon, R. A.; Nadel, J. A. *Biochem. Biophys. Res. Commun.* **1988**, *157*, 457-464.

9) Hörnsten, L.; Su, C.; Osbourn, A. E.; Hellman, U.; Oliw, E. H. *Eur. J. Biochem.* **2002**, *269*, 2690-2697.

10) Su, C.; Sahlin, M.; Oliw, E. H. *J. Biol. Chem.* **2000**, *275*, 18830-18835.

11) Glickman, M. H.; Klinman, J. P. *Biochemistry* **1995**, *34*, 14077-14092.

12) Segraves, E. N.; Holman, T. R. *Biochemistry* **2003**, *42*, 5236-5243.

13) Que, L., Jr.; Ho, R. Y. N. *Chem. Rev.* **1996**, *96*, 2607-2624.

14) Que, L., Jr.; Watanabe, Y. *Science* **2001**, *292*, 651-653.

15) Solomon, E. I.; Brunold, T. C.; Davis, M. I.; Kemsley, J. N.; Lee, S.-K.; Lehnert, N.; Neese, F.; Skulan, A. J.; Yang, Y.-S.; Zhou, J. *Chem. Rev.* **2000**, *100*, 235-349.

16) Mayer, J. M. *Acc. Chem. Res.* **1998**, *31*, 441-450.

17) Stone, K. L. Borovik, A. S. *Curr. Opin. Chem. Bio.* **2009**, *13*, 114-118.

18) Borovik, A. S. *Chem. Soc. Rev.* **2011**, *40*, 1870-1874.

19) Green, M. T.; Dawson, J. H.; Gray, H. B. *Science* **2004**, *304*, 1653-1656.

20) Stone, K. L.; Behan, R. K.; Green, M. T. *Proc. Natl. Acad. Sci. U.S.A.* **2006**, *103*, 12307-12310.

21) Green, M. T. *Curr. Opin. Chem. Biol.* **2009**, *13*, 84-88.

22) Rittle, J.; Green, M. T. *Science* **2010**, *330*, 933-937.

23) Evans, D. L. *J. Am. Chem. Soc.* **1959**, 2005.

24) Brines, L. M. Ph.D. thesis, University of Washington, Seattle, Washington, 2007.

25) Ozinskas, A. J.; Bobst, A. M. *Helv. Chim. Acta* **1980**, *63*, 1407-1411.

26) Bruker APEX2 (Version 2.1-2.4), SAINT (Version 7.34A), SADABS (Version 2007/4), BrukerAXS Inc., Madison, Wisconsin, USA.

27) Waasmair, D.; Kirfel, A. *Acta Crystallogr. A* **1995**, *51*, 416.

28) Warren, J. J.; Tronic, T. A.; Mayer, J. M. *Chem. Rev.* **2010**, *110*, 6961-7001 and references therein.

29) Weinberg, D. R.; Gagliardi, C. J.; Hull, J. F.; Murphy, C. F.; Kent, C. A.; Westlake, B. C.; Paul, A.; Ess, D. H.; McCafferty, D. G.; Meyer, T. J. *Chem. Rev.* **2012**, *112*, 4015-4093.

30) Goldsmith, C. R.; Cole, A. P.; Stack, T. D. P. *J. Am. Chem. Soc.* **2005**, *127*, 9904-9912.

31) Que, L., Jr.; Tolman, W. B. *Angew. Chem. Int. Ed.* **2002**, *41*, 1114-1137 and references therein.

A1. Electronic absorption spectrum of $[Mn^{II}(S^{Me2}N_4(tren))](PF_6)$ (**1**) (MeCN, 298 K).

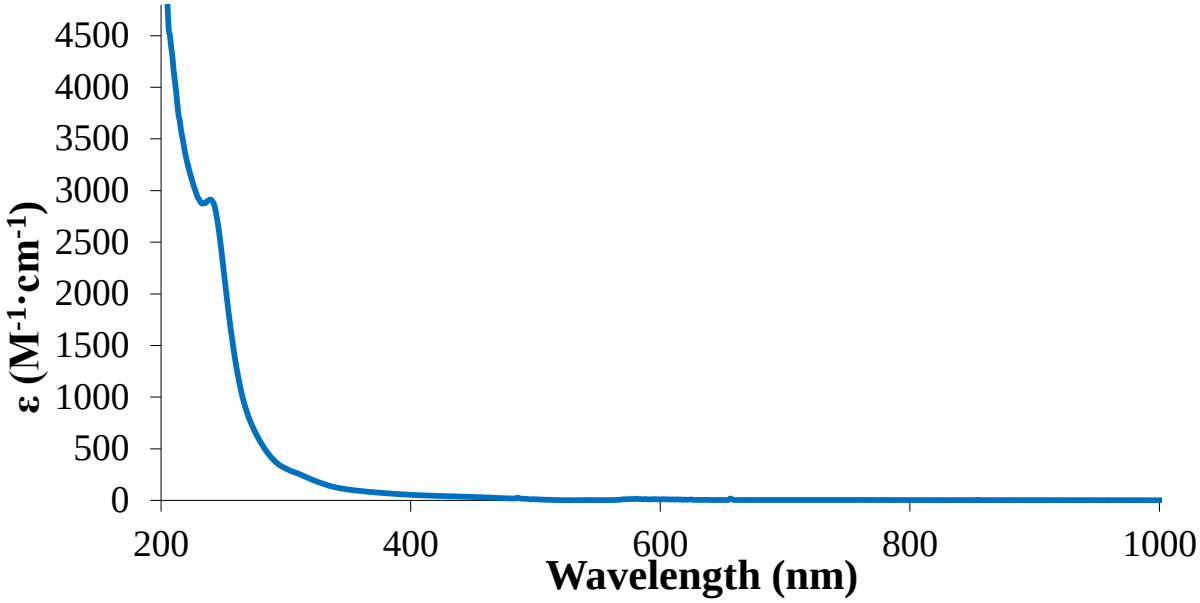

A2. Electronic absorption spectrum of $[Mn^{II}(S^{Me2}N_4(6\text{-H-DPEN}))(MeOH)](PF_6)\cdot MeOH$ (**2**) (MeCN, 298 K).

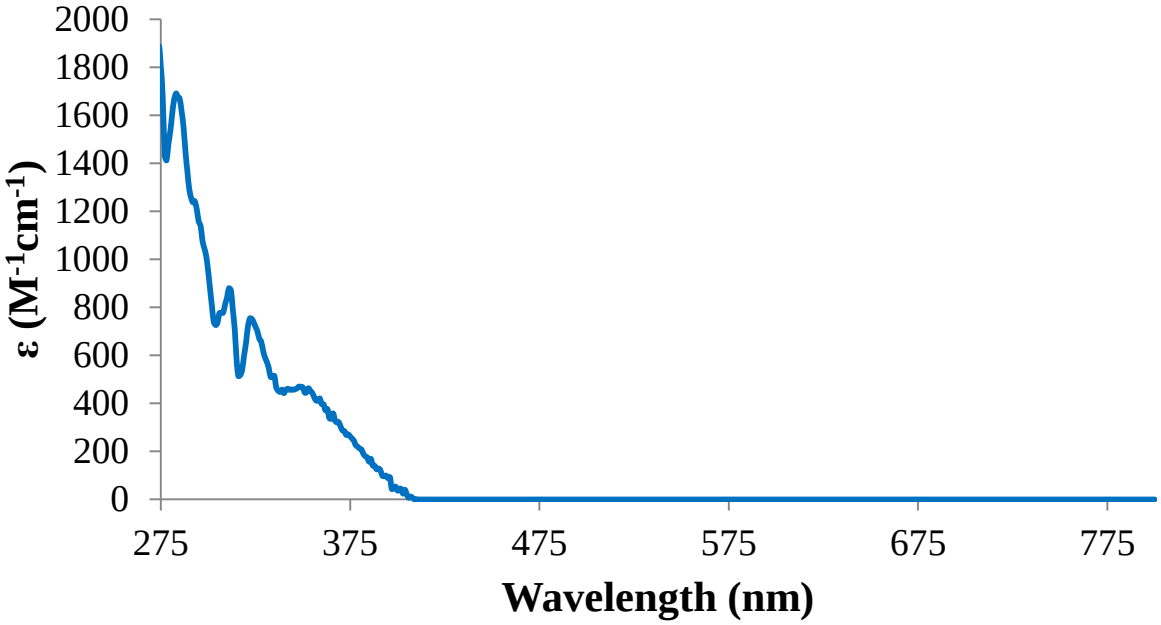

A3. Electronic absorption spectrum of $[Mn^{II}(S^{Me2}N_4(6\text{-H-DPPN}))]_2(BF_4)_2$ (**3**) (MeCN, 298 K).

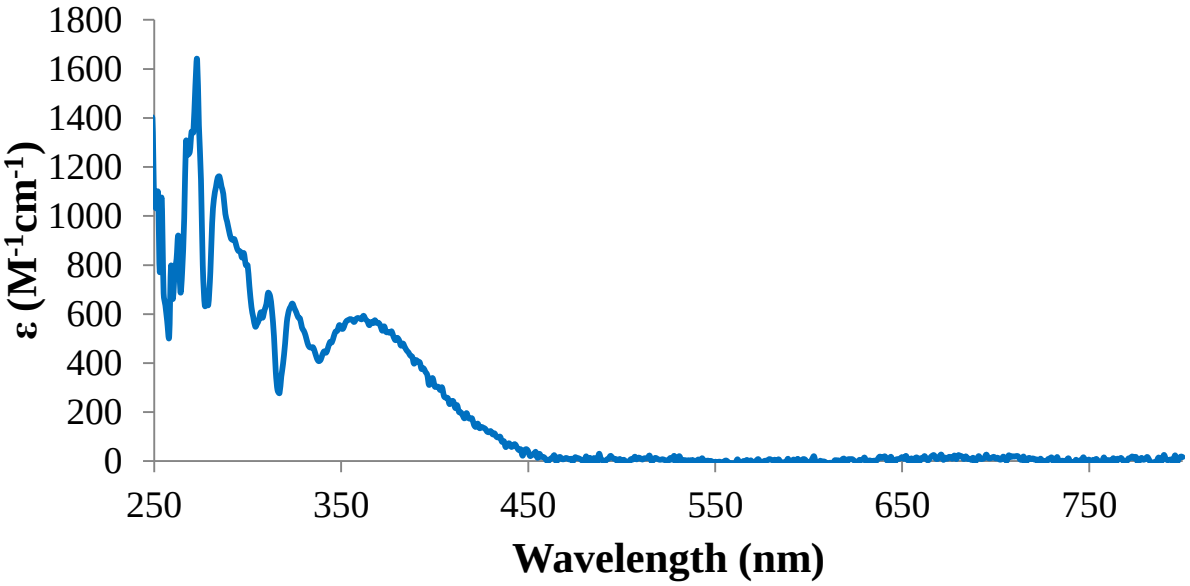

A4. Electronic absorption spectrum of $[Mn^{II}(S^{Me2}N_4(6\text{-Me-DPEN}))](BF_4)$ (**4**) (MeCN, 298 K).

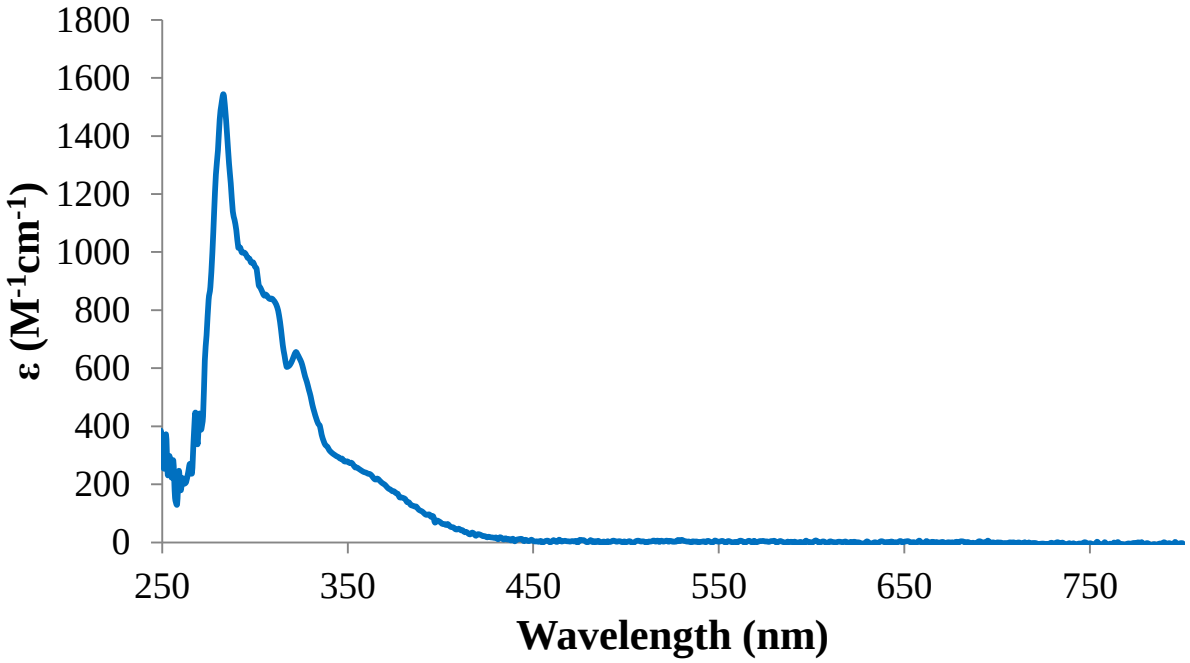

A5. Electronic absorption spectrum of [$Mn^{II}(S^{Me2}N_4$(6-Me-DPPN))](BPh_4) (**5**) (MeCN, 298 K).

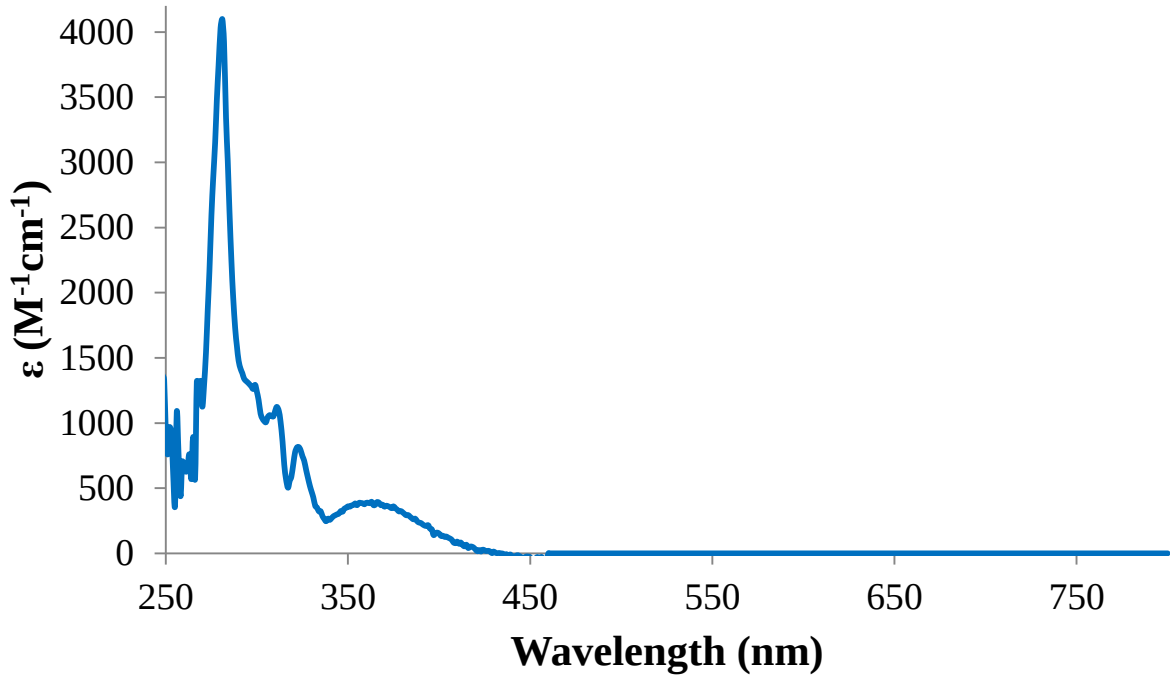

A6. Electronic absorption spectrum of [$Mn^{II}(S^{Me2}N_4$(2-QuinoEN))](BPh_4)·MeCN (**8**) (MeCN, 298 K).

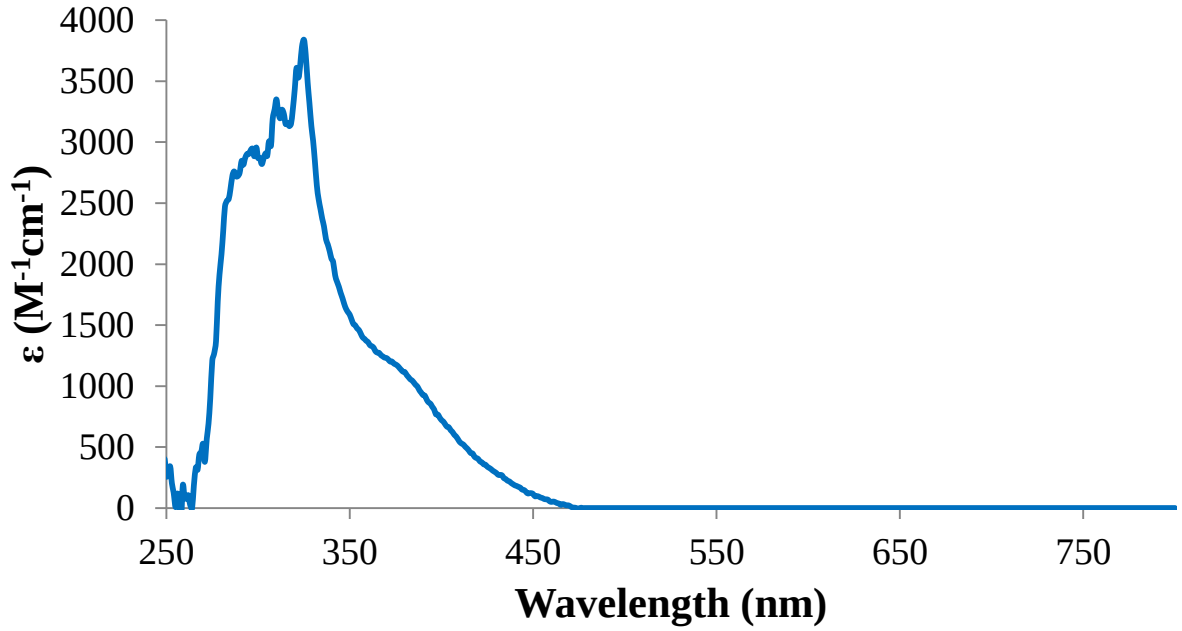

A7. Electronic absorption spectrum of [Mn^{II}($S^{Me2}N_4$(2-QuinoPN))](PF_6) (**9**) (MeCN, 298 K).

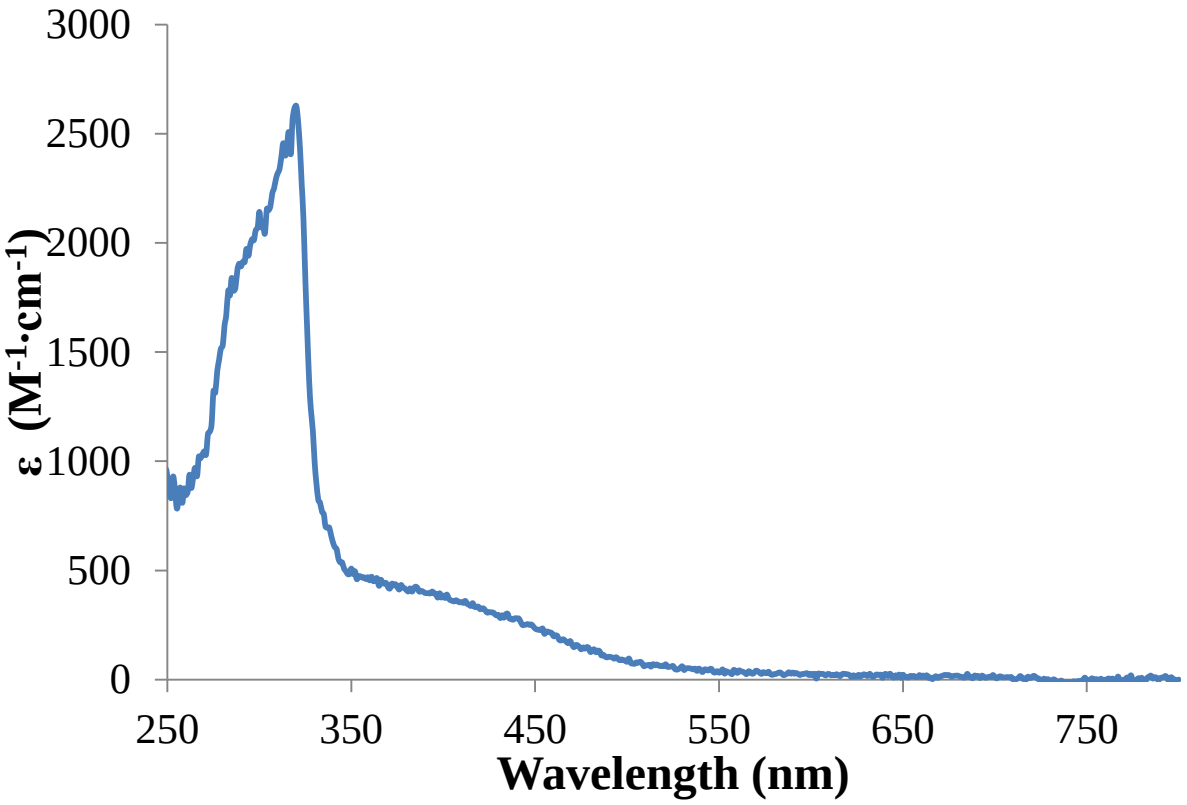

A8. Cyclic voltammogram of [Fe^{II}($S^{Me2}N_4$(6-H-DPEN))(MeOH)](PF_6) (**17**) (MeCN, 298 K, vs. SCE). See Chapter 2 Section 2.2.1 for experimental considerations.

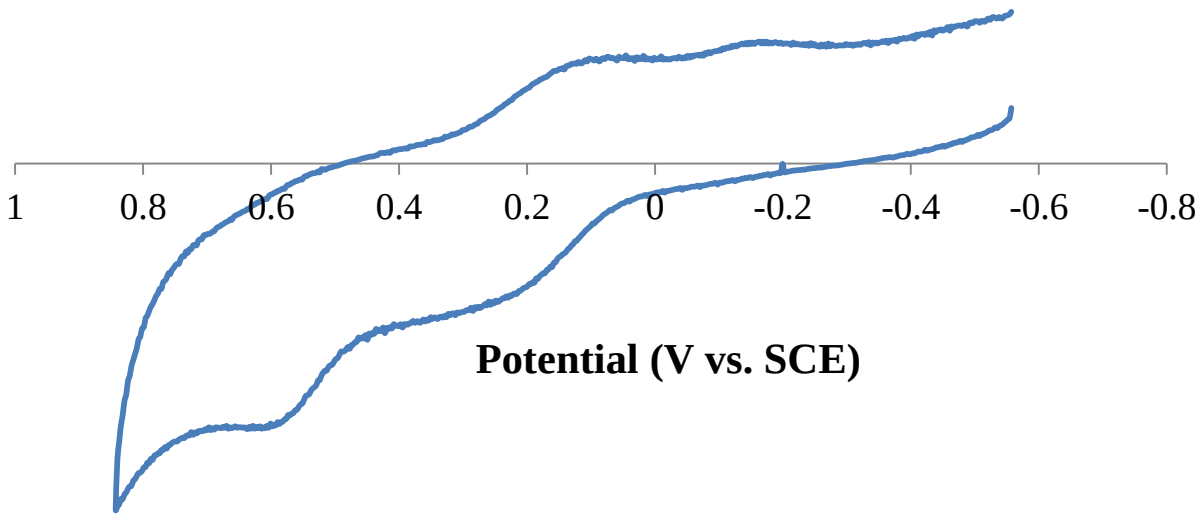

A9. Crystal data for [$Zn^{II}(S^{Me2}N_4$(6-Me-DPEN))](BPh_4) (**23**) and [$Zn^{II}(S^{Me2}N_4$(6-Me-DPPN))](BPh_4)·MeCN (**24**).

	23	**24**
Formula	$C_{45}H_{49}BN_4SZn$	$C_{48}H_{54}BN_5SZn$
MW	754.12	809.20
T, K	100(2)	100(2)
Unit Cell[a]	Triclinic	Monoclinic
a, Å	9.5542(3)	17.1976(10)
b, Å	12.3475(4)	11.6284(7)
c, Å	17.6481(6)	22.1746(13)
α, deg	106.9870(10)	90
β, deg	100.545(2)	106.423(3)
γ, deg	95.829(2)	90
V, $Å^3$	1930.70(11)	4253.6(4)
Z	2	4
d(calc), g/cm^3	1.297	1.264
Sp. Group	P -1	P $2_1/c$
R[b]	0.0450	0.0482
R_w[c]	0.0961	0.1414
GOF	1.009	1.082

A.10. Fit to the normalized S K-edge XAS spectrum for [$Mn^{II}(S^{Me2}N_4$(6-Me-DPEN))](BF_4) (**4**).

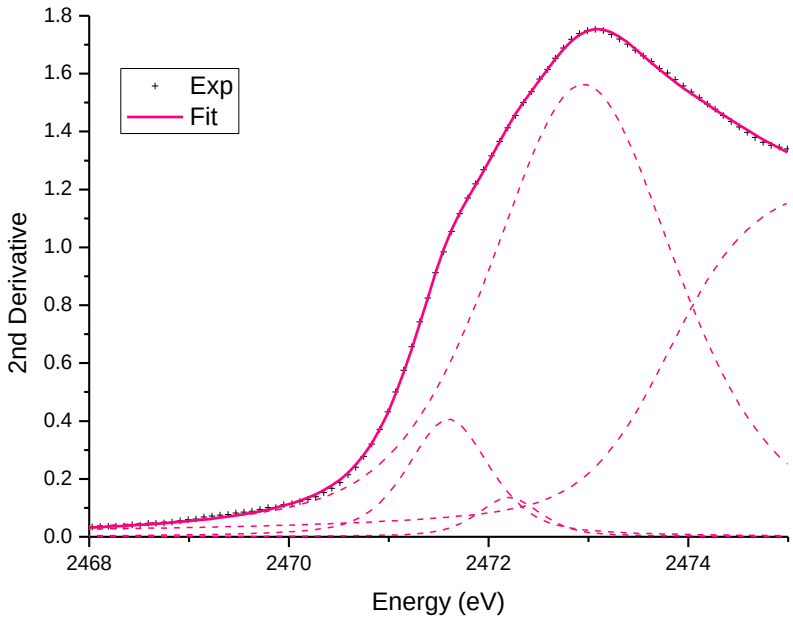

A.11. Fit to the second derivative of the S K-edge XAS spectrum for [$Mn^{II}(S^{Me2}N_4$(6-Me-DPEN))](BF_4) (**4**).

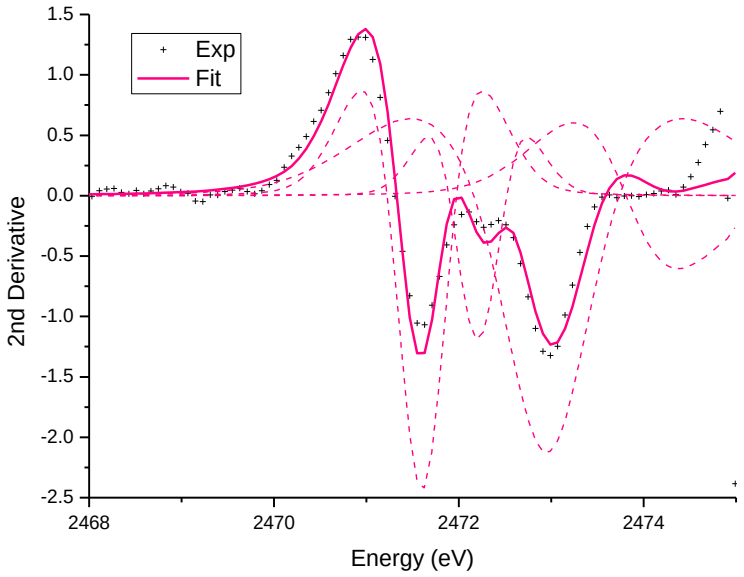

A.12. Fit to the normalized S K-edge XAS spectrum for [$Fe^{II}(S^{Me2}N_4$(6-Me-DPEN))](PF_6) (**19**).

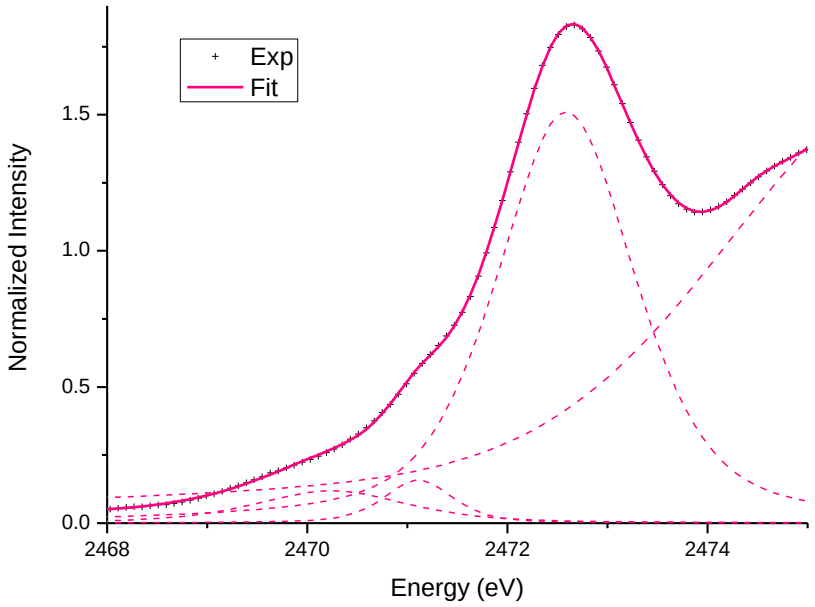

A.13. Fit to the second derivative of the S K-edge XAS spectrum for [Fe^{II}($S^{Me2}N_4$(6-Me-DPEN))](PF_6) (**19**).

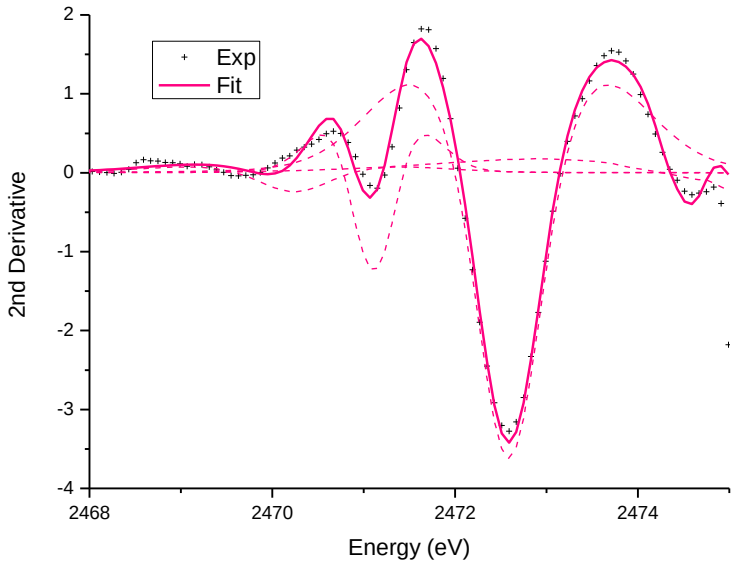

A.14. Fit to the normalized S K-edge XAS spectrum for [Mn^{II}($S^{Me2}N_4$(2-QuinoEN))](BPh_4)·MeCN (**8**).

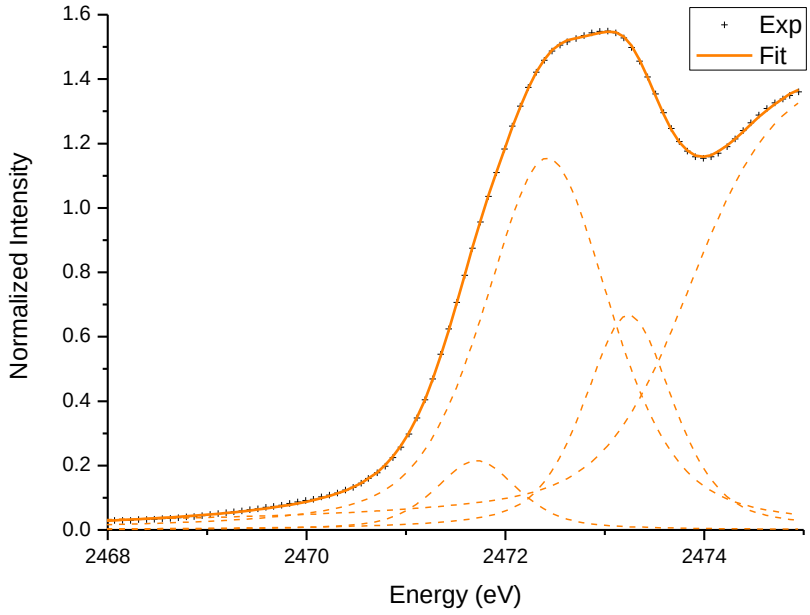

A.15. Fit to the second derivative of the S K-edge XAS spectrum for [$Mn^{II}(S^{Me2}N_4$(2-QuinoEN))](BPh_4)·MeCN (**8**).

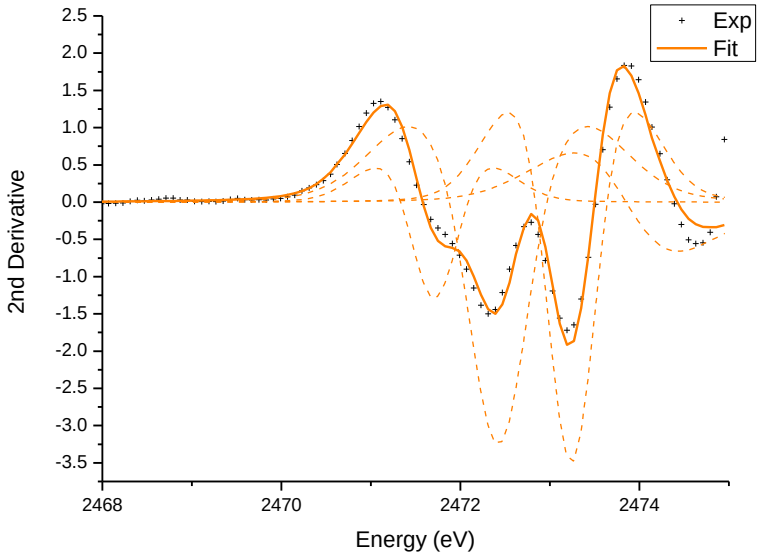

A.16. Fit to the normalized S K-edge XAS spectrum for [$Fe^{II}(S^{Me2}N_4$(2-QuinoEN))](PF_6)·MeOH (**21**).

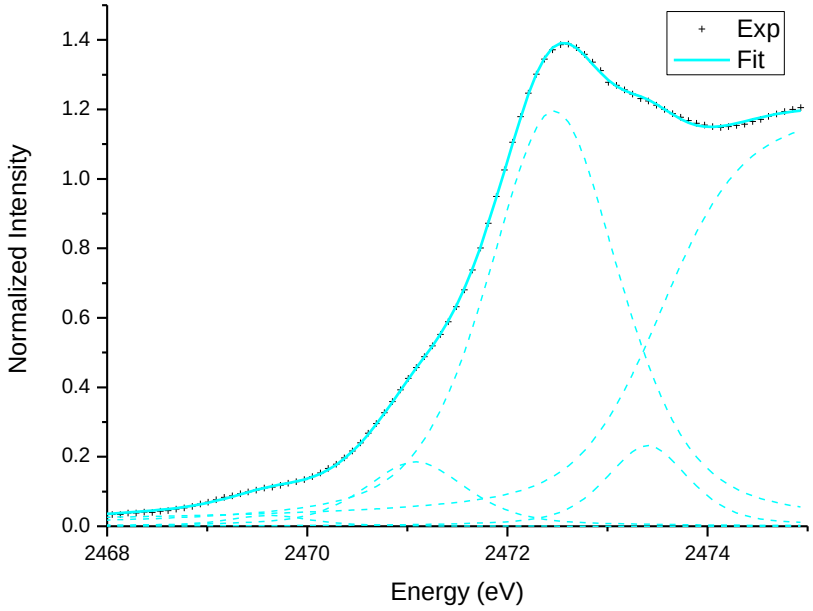

A.17. Fit to the second derivative of the S K-edge XAS spectrum for [Fe^{II}($S^{Me2}N_4$(2-QuinoEN))](PF_6)·MeOH (**21**).

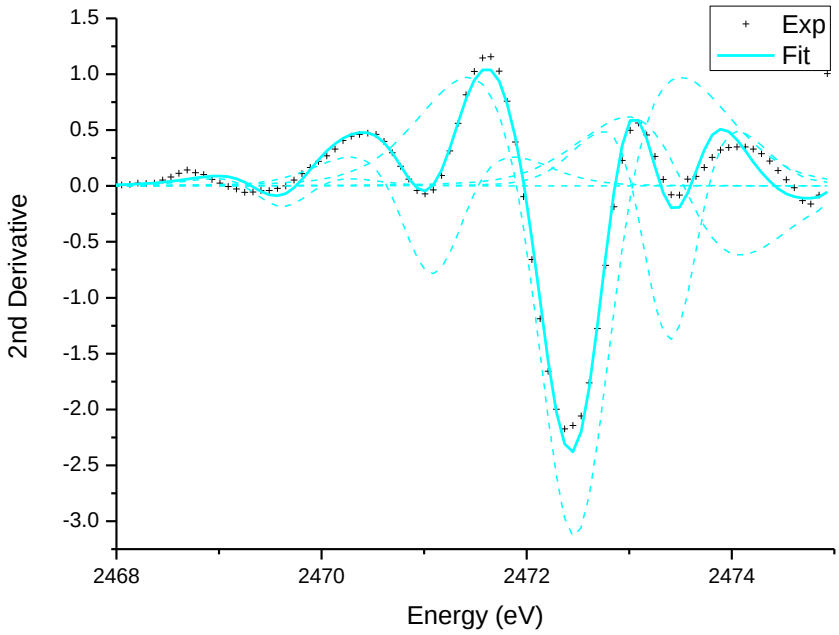

A.18. Selected bond lengths (Å) and angles (deg) for DFT geometry optimized structures of [Mn^{II}($S^{Me2}N_4$(6-Me-DPEN))]$^+$ (**4**), [Fe^{II}($S^{Me2}N_4$(6-Me-DPEN))]$^+$ (**19**), [Mn^{II}($S^{Me2}N_4$(2-QuinoEN))]$^+$ (**8**), and [Fe^{II}($S^{Me2}N_4$(2-QuinoEN))]$^+$ (**21**).

	4	**19**	**8**	**21**
Mn-S(1)	2.364	2.300	2.367	2.308
Mn-N(1)	2.223	2.136	2.212	2.128
Mn-N(2)	2.319	2.257	2.319	2.256
Mn-N(3)	2.272	2.212	2.255	2.195
Mn-N(4)	2.261	2.209	2.261	2.206
S(1)-Mn-N(1)	81.51	84.20	82.01	84.37
S(1)-Mn-N(2)	156.61	159.93	156.47	159.15
S(1)-Mn-N(3)	119.90	118.41	122.28	120.64
S(1)-Mn-N(4)	113.52	108.41	111.49	106.02
N(1)-Mn-N(3)	117.66	117.57	114.21	114.38
N(1)-Mn-N(4)	119.78	122.19	121.81	123.58
N(3)-Mn-N(4)	104.24	105.24	104.97	106.47
τ	0.61	0.63	0.58	0.59

A.19. Quantitative electronic absorption spectrum (extinction coefficient versus wavelength) of $[Mn^{III}(S^{Me2}N_4(tren))]_2(\mu\text{-}O)(PF_6)_2$ (**12**) in MeCN at 298 K.

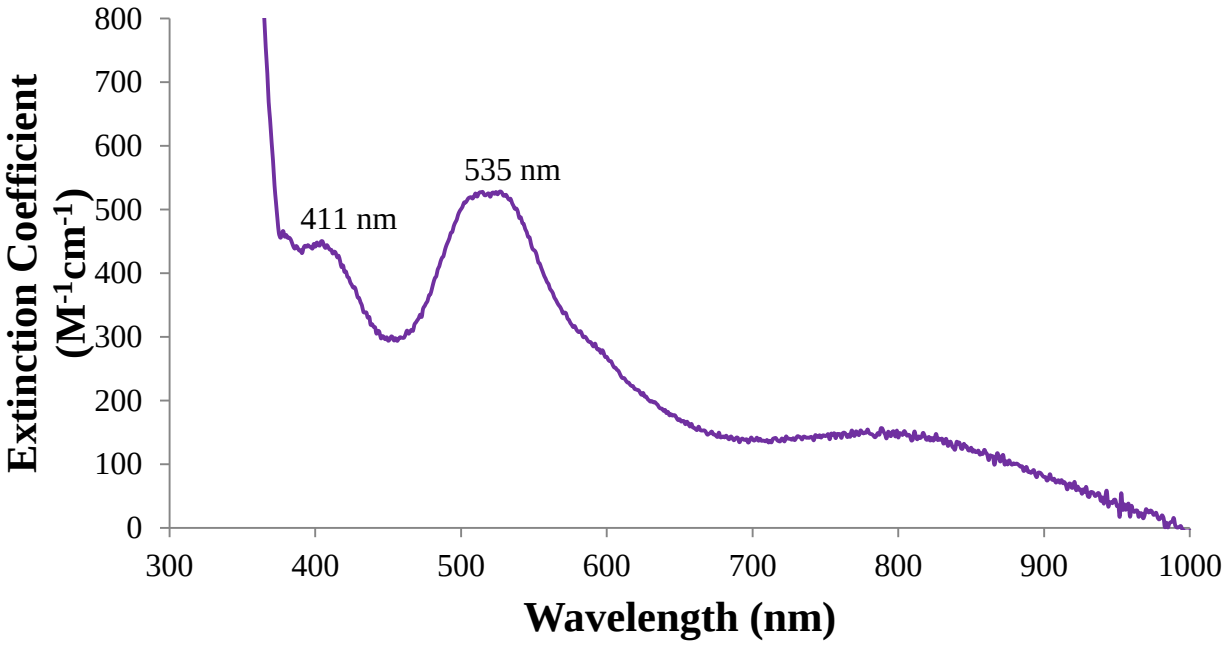

A.20. Quantitative electronic absorption spectrum (extinction coefficient versus wavelength) of $[Mn^{III}(S^{Me2}N_4(6\text{-H-DPEN}))]_2(\mu\text{-}O)(PF_6)_2\cdot(MeCN)_2$ (**13**) in MeCN at 298 K.

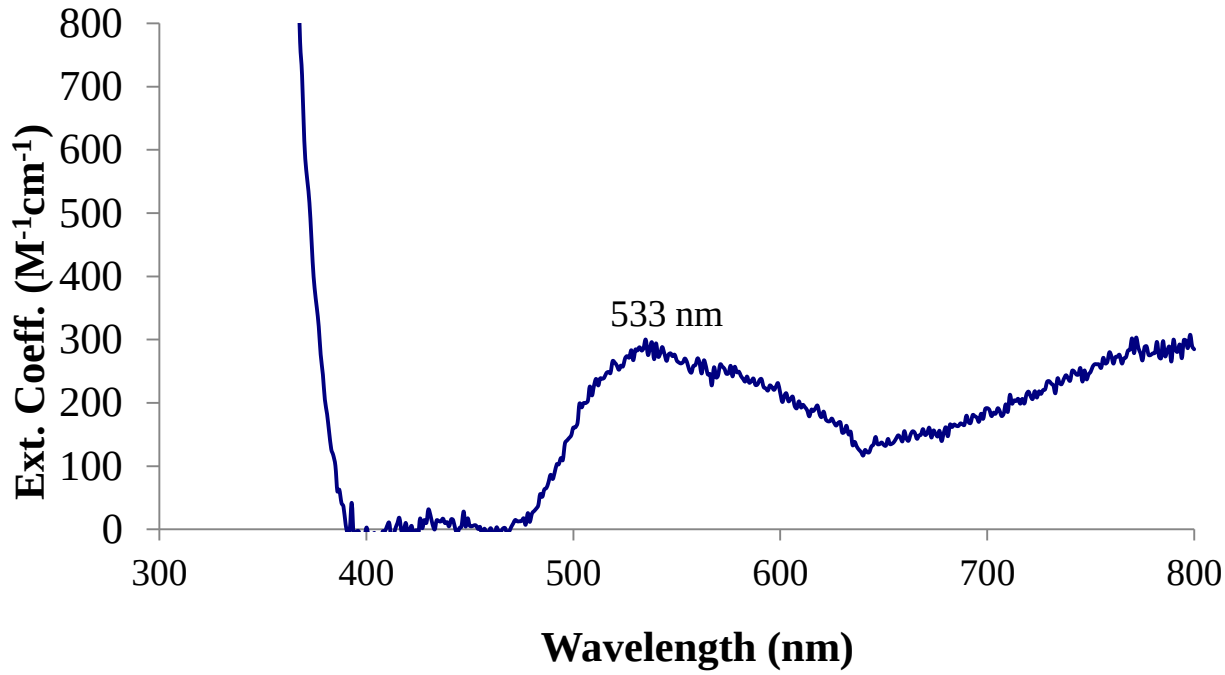

A.21. Quantitative electronic absorption spectrum (extinction coefficient versus wavelength) of $[Mn^{III}(S^{Me2}N_4(6\text{-H-DPPN}))]_2(\mu\text{-O})(PF_6)_2\cdot(MeCN)_2$ (**14**) in MeCN at 298 K.

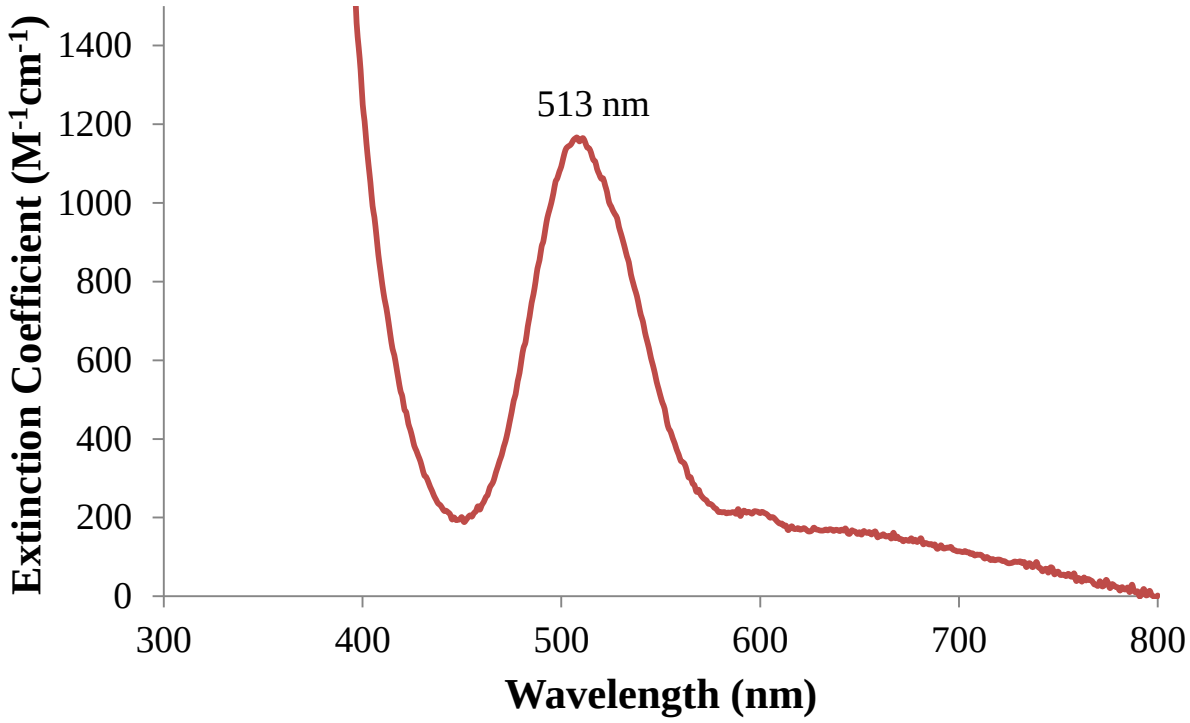

A.22. Quantitative electronic absorption spectrum (extinction coefficient versus wavelength) of $[Mn^{III}(S^{Me2}N_4(6\text{-Me-DPEN}))]_2(\mu\text{-O})(BF_4)_2\cdot(MeOH)_2$ (**15**) in MeCN at 298 K.

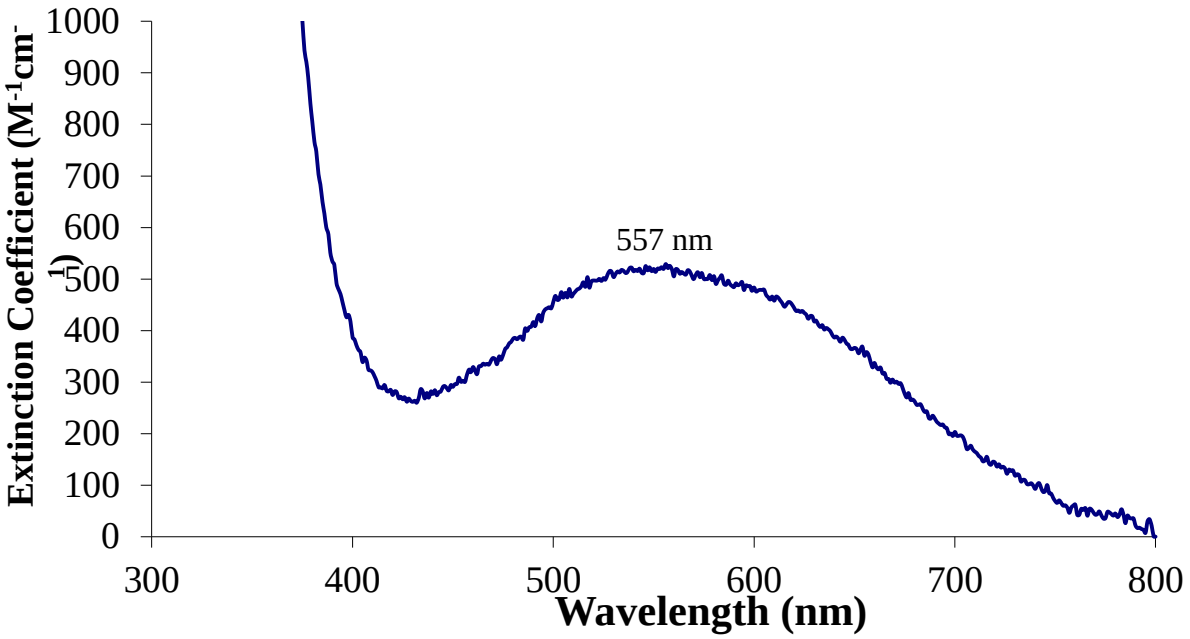

A.23. Quantitative electronic absorption spectrum (extinction coefficient versus wavelength) of $[Mn^{III}(S^{Me2}N_4(4\text{-MeO-3,5-Me-DPEN}))]_2(\mu\text{-O})(PF_6)_2\cdot(MeCN)_2$ (**17**) in MeCN at 298 K.

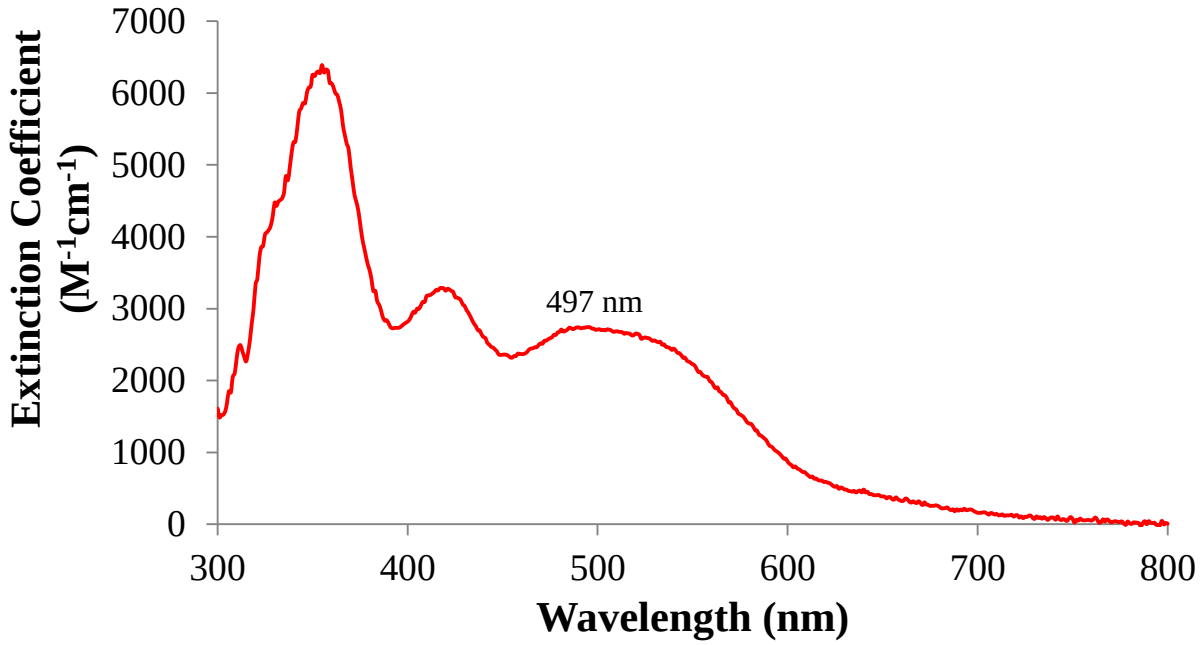

A.24. Quantitative electronic absorption spectrum (extinction coefficient versus wavelength) of $[Mn^{III}(S^{Me2}N_4(2\text{-QuinoEN}))]_2(\mu\text{-O})(PF_6)_2\cdot(CH_2Cl_2)$ (**18**) in MeCN at 298 K.

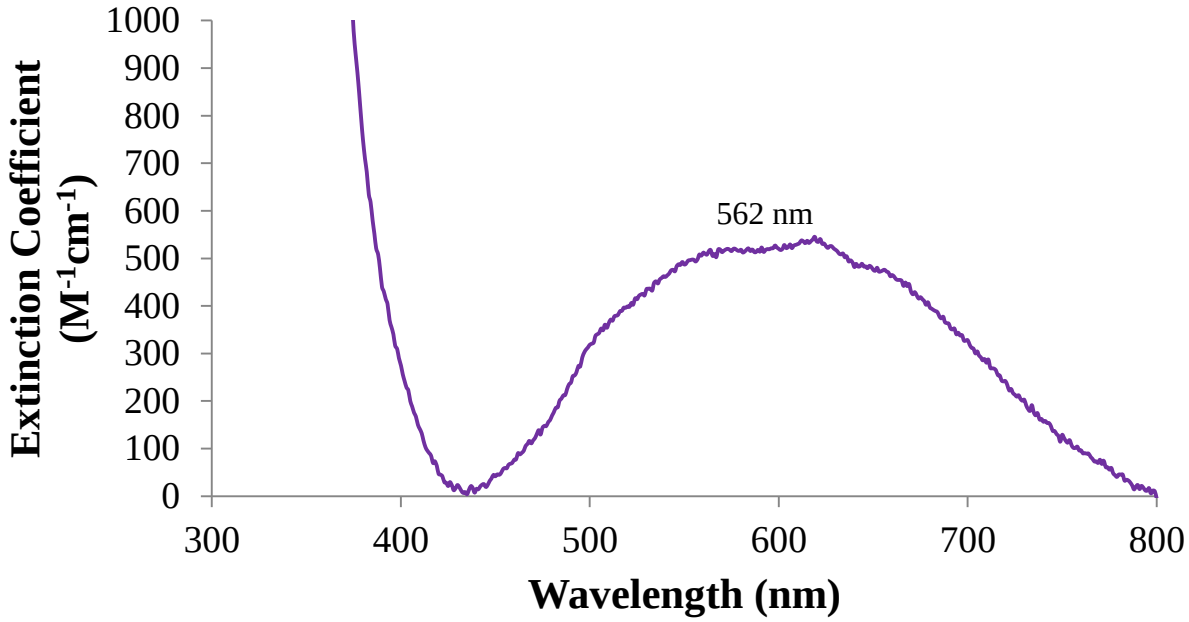

A.25. UV/Vis spectrum of the product from a reaction between [$Mn^{II}(S^{Me2}N_4(tren))](PF_6)$ (**1**, 1 mM) and 1 equivalent of tri(para-tolyl)aminium hexafluorophosphate in MeCN at 0 °C.

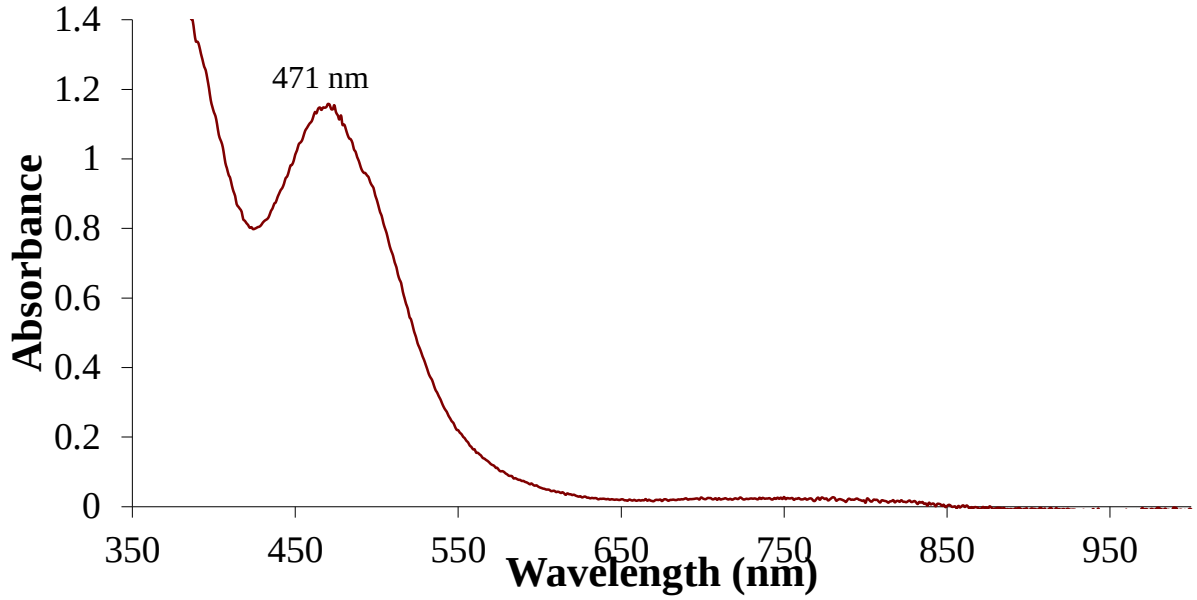

A.26 UV/Vis spectrum of the product from a reaction between [$Mn^{II}(S^{Me2}N_4$(6-H-DPEN))(MeOH)](PF_6)·MeOH (**2**, 1.7 mM) and 1 equivalent of tri(para-tolyl)aminium hexafluorophosphate in MeCN at 0 °C.

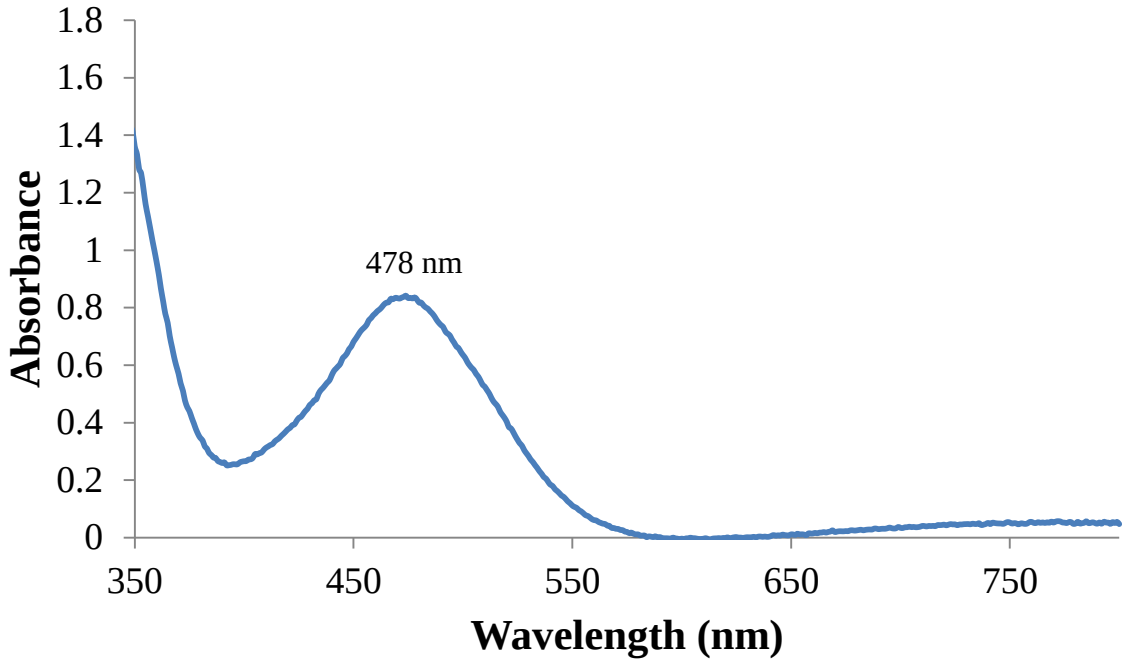

A.27 UV/Vis spectrum of the product from a reaction between $[Mn^{II}(S^{Me2}N_4(6\text{-H-DPPN}))]_2(BF_4)_2$ (**3**, 1.2 mM) and 1 equivalent of tri(para-tolyl)aminium hexafluorophosphate in MeCN at 0 °C.

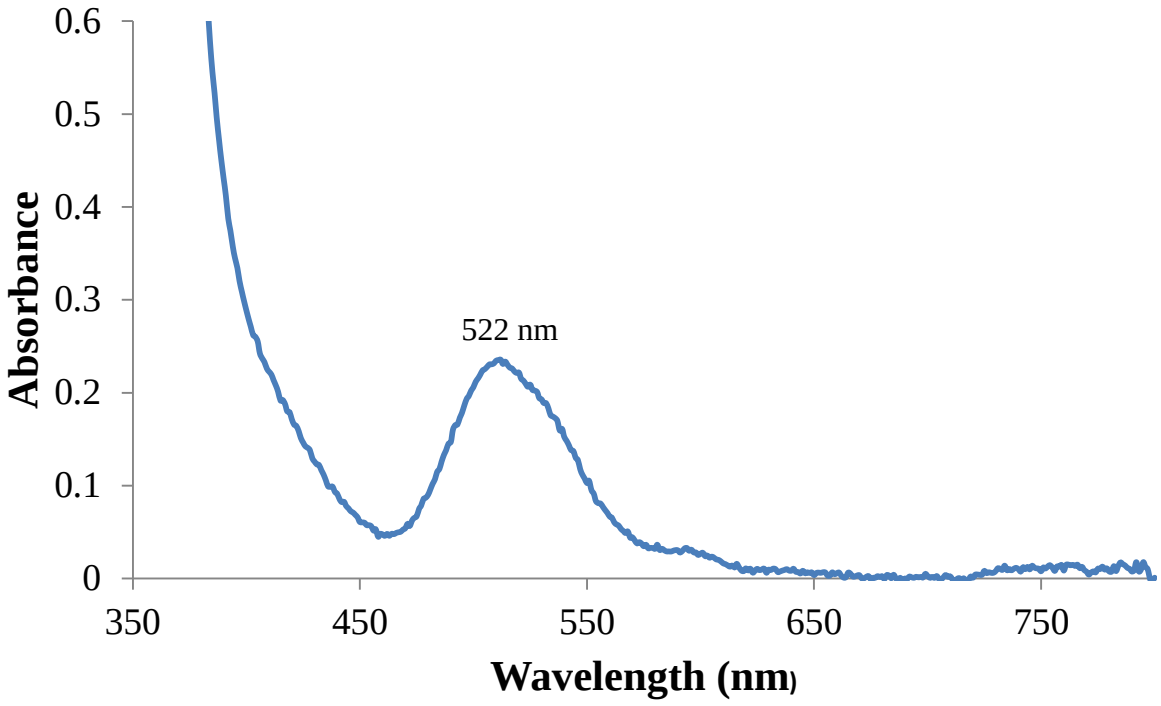

A.28 UV/Vis spectrum of the product from a reaction between $[Mn^{II}(S^{Me2}N_4(6\text{-Me-DPPN}))](BPh_4)$ (**5**, 1.5 mM) and 1 equivalent of tri(para-tolyl)aminium hexafluorophosphate in MeCN at 0 °C.

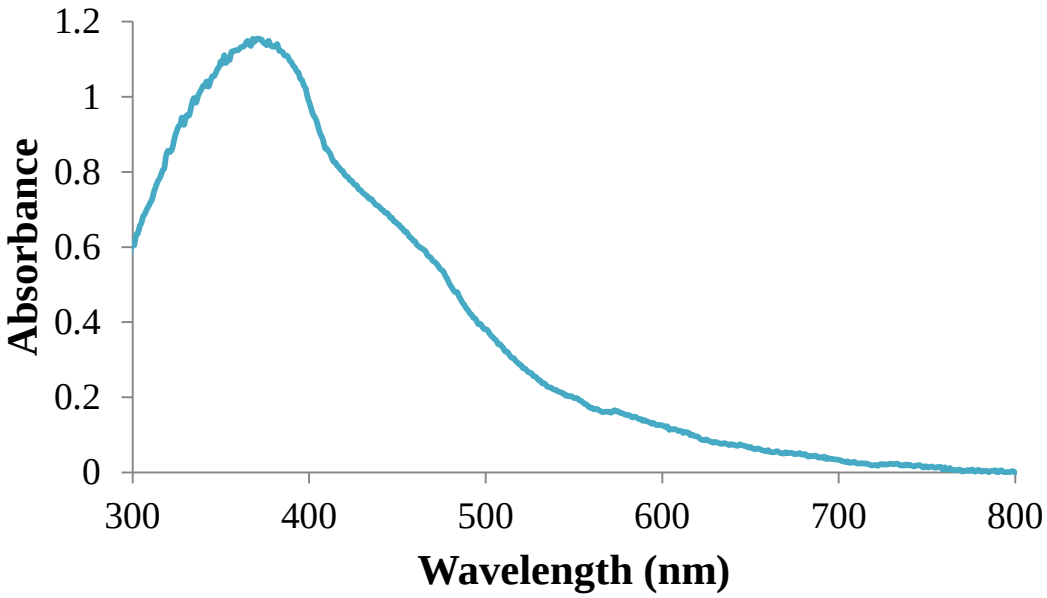

A.29 UV/Vis spectrum of the product from a reaction between [(Mn^{II}($S^{Me2}N_4$(4-OMe-3,5-Me-DPEN)))(Mn^{II}($S^{Me2}N_4$(4-OMe-3,4-Me-DPEN))(Cl))](BF $_4$)·Et_2O (**6**, 0.9 mM) and 1 equivalent of tri(para-tolyl)aminium hexafluorophosphate in MeCN at 0 °C.

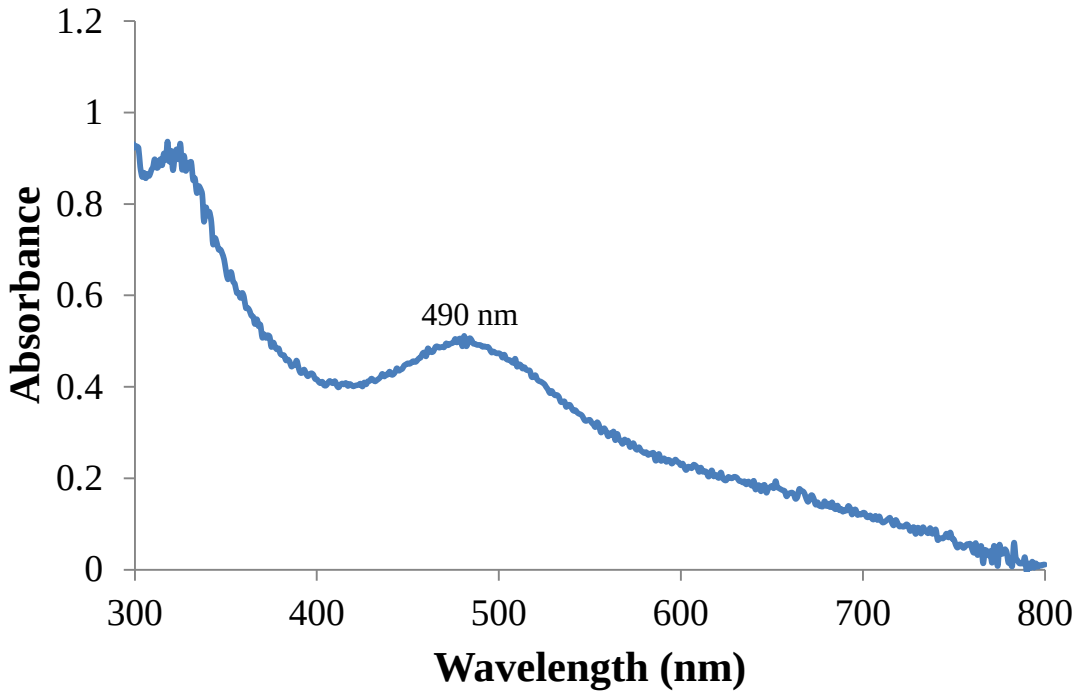

A.30 UV/Vis spectrum of the product from a reaction between [Mn^{II}($S^{Me2}N_4$(2-QuinoEN))](BPh$_4$)·MeCN (**7**, 1.3 mM) and 1 equivalent of tri(para-tolyl)aminium hexafluorophosphate in MeCN at 0 °C.

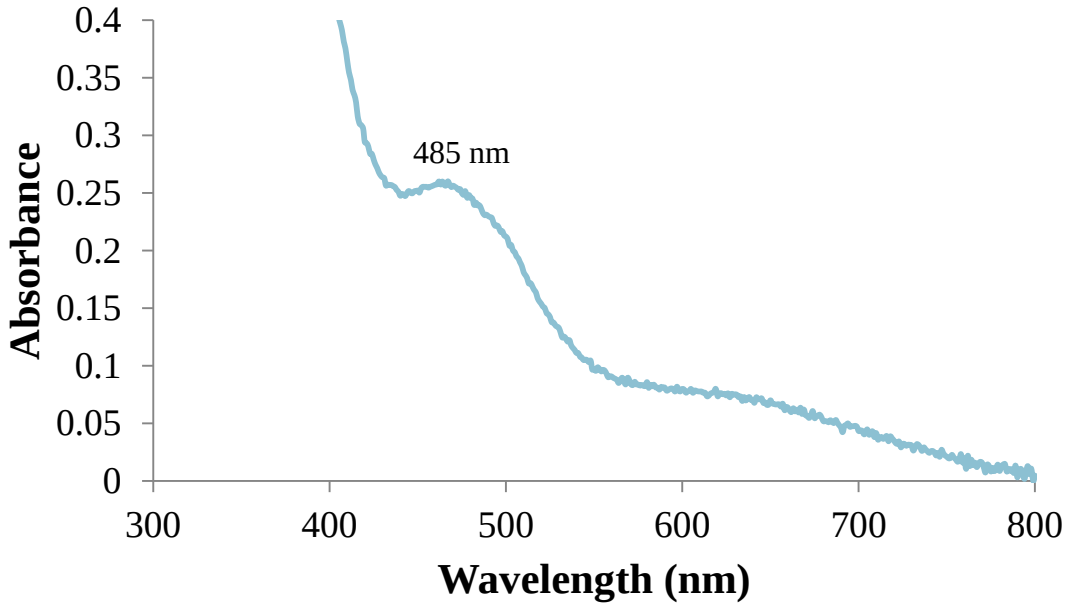

A.31 UV/Vis spectrum of the product from a reaction between $[Mn^{II}(S^{Me2}N_4(2\text{-QuinoPN}))](PF_6)$ (**8**, 1.5 mM) and 1 equivalent of tri(para-tolyl)aminium hexafluorophosphate in MeCN at 0 °C.

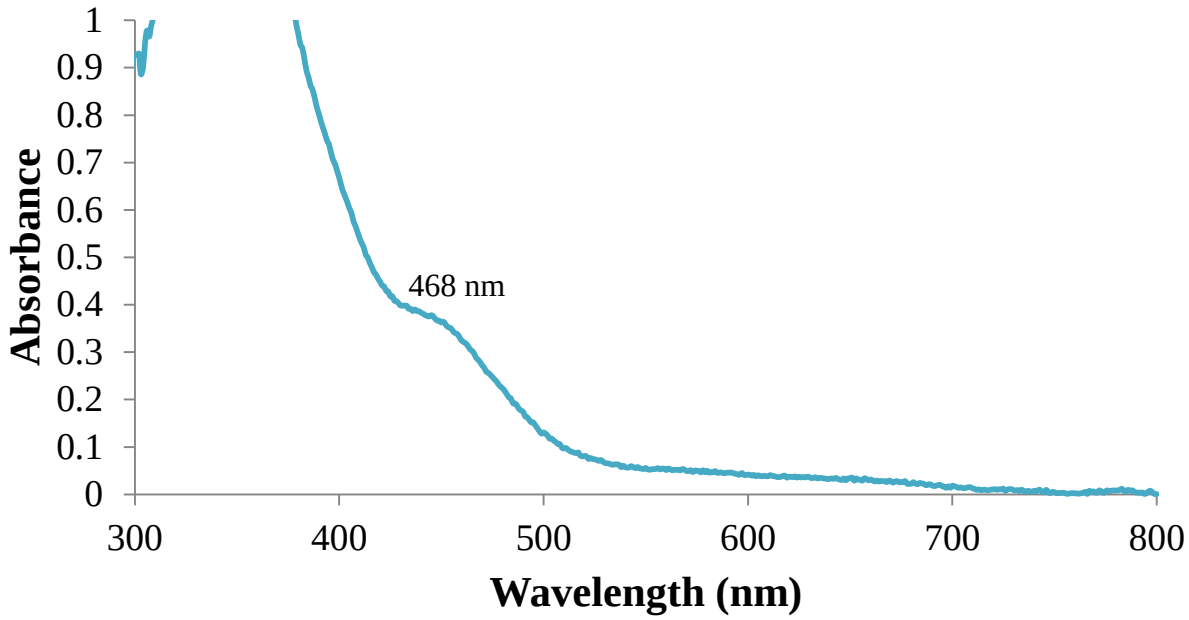

A.32 Molar magnetic susceptibility (χ_M) versus temperature (K) for $[Mn^{III}(S^{Me2}N_4(6\text{-H-DPEN}))]_2(\mu\text{-O})(PF_6)_2\cdot(MeCN)_2$ (**13**). The best fit line to the experimental data is represented by the solid line.

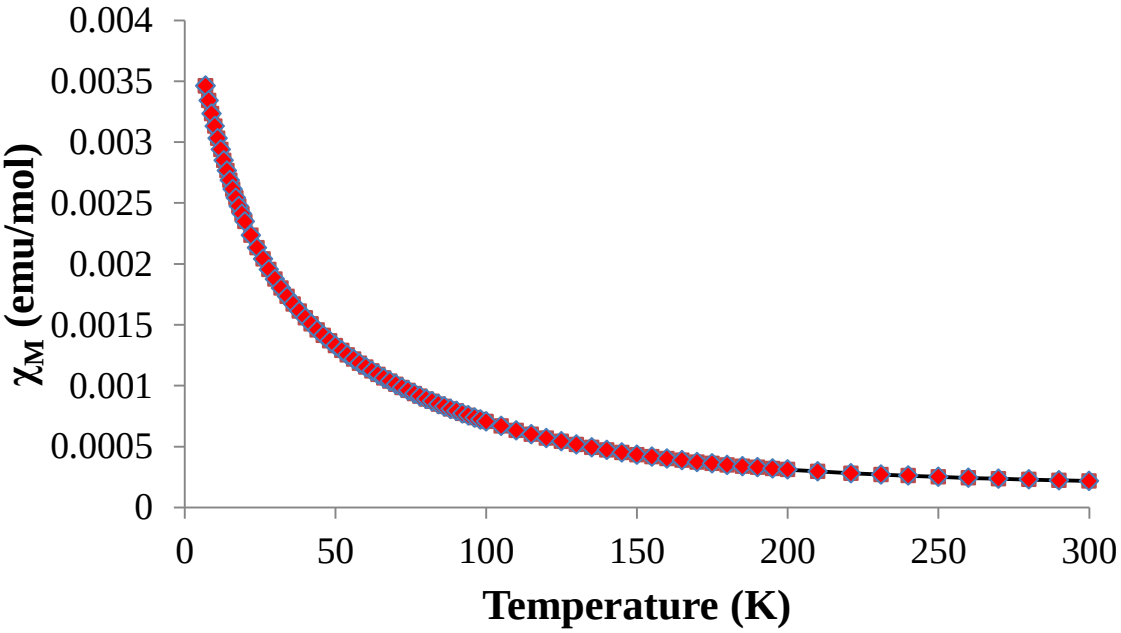

A.33 Inverse molar magnetic susceptibility (χ_M^{-1}) versus temperature (K) for $[Mn^{III}(S^{Me2}N_4(6\text{-H-DPPN}))]_2(\mu\text{-O})(PF_6)_2\cdot(MeCN)_2$ (**14**).

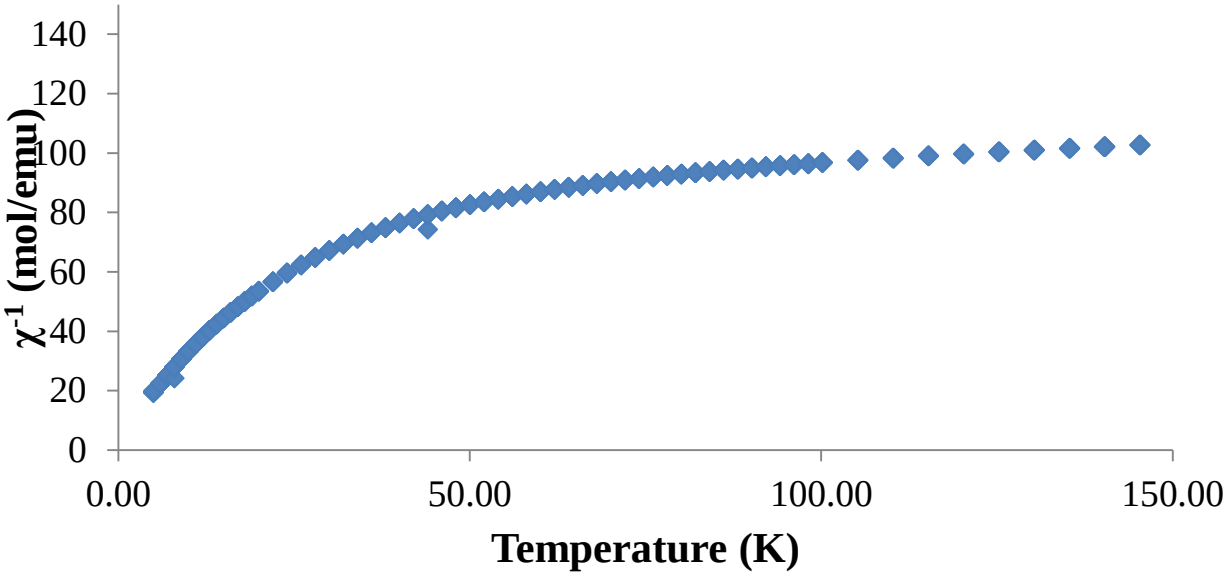

A.34 Molar magnetic susceptibility (χ_M) versus temperature (K) for $[Mn^{III}(S^{Me2}N_4(4\text{-MeO-3,5-Me-DPEN}))]_2(\mu\text{-O})(PF_6)_2\cdot(MeCN)_2$ (**17**). The best fit line to the experimental data is represented by the solid line.

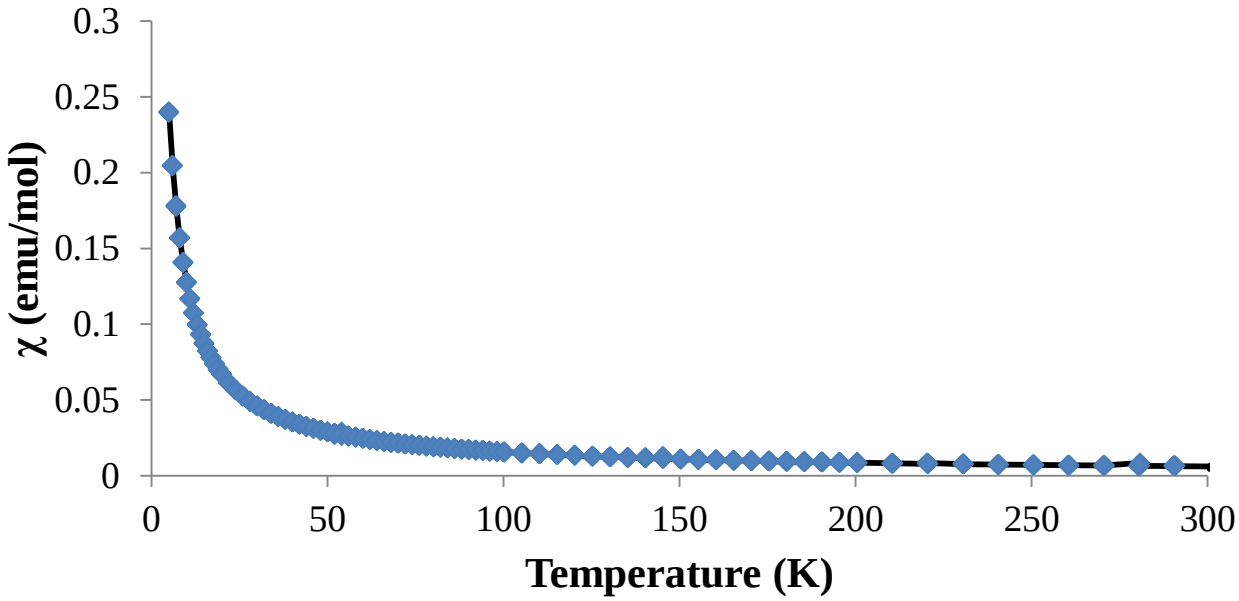

A.35 Molar magnetic susceptibility (χ_M) versus temperature (K) for $[Mn^{III}(S^{Me2}N_4(2\text{-QuinoEN}))]_2(\mu\text{-O})(PF_6)_2\cdot(CH_2Cl_2)$ (**18**). The best fit line to the experimental data is represented by the solid line.

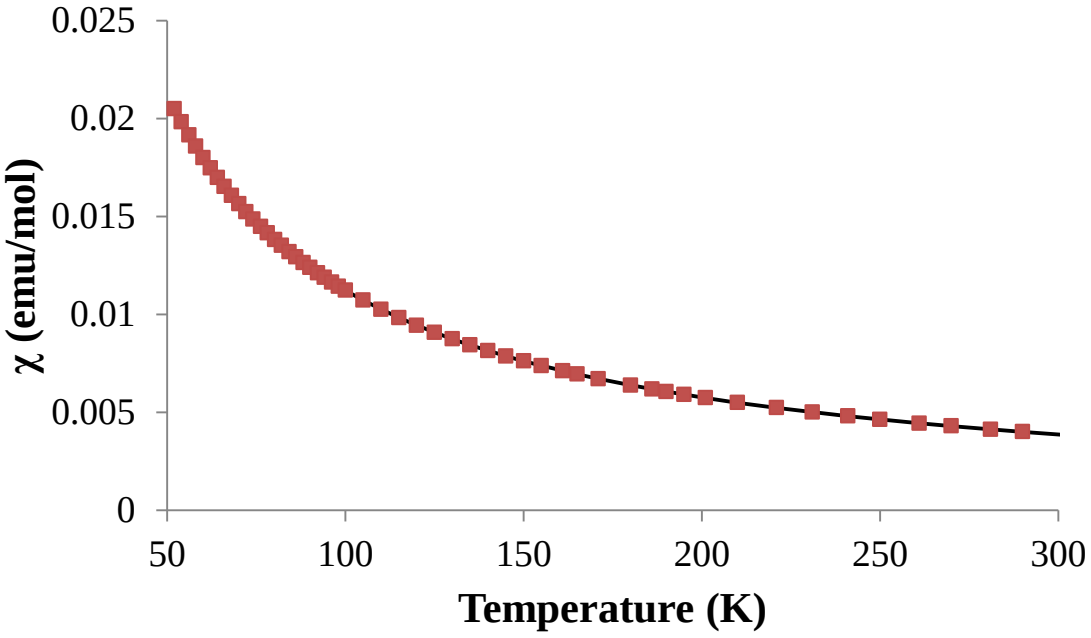

A.36 Resonance Raman spectra of $[Mn^{III}(S^{Me2}N_4(2\text{-QuinoEN}))]_2(\mu\text{-O})(PF_6)_2\cdot(CH_2Cl_2)$ (**4**) prepared with generated from $^{16}O_2$ (solid purple trace) and $^{18}O_2$ (dashed green trace) obtained with λ_{ex} = 513 nm at 77 K.

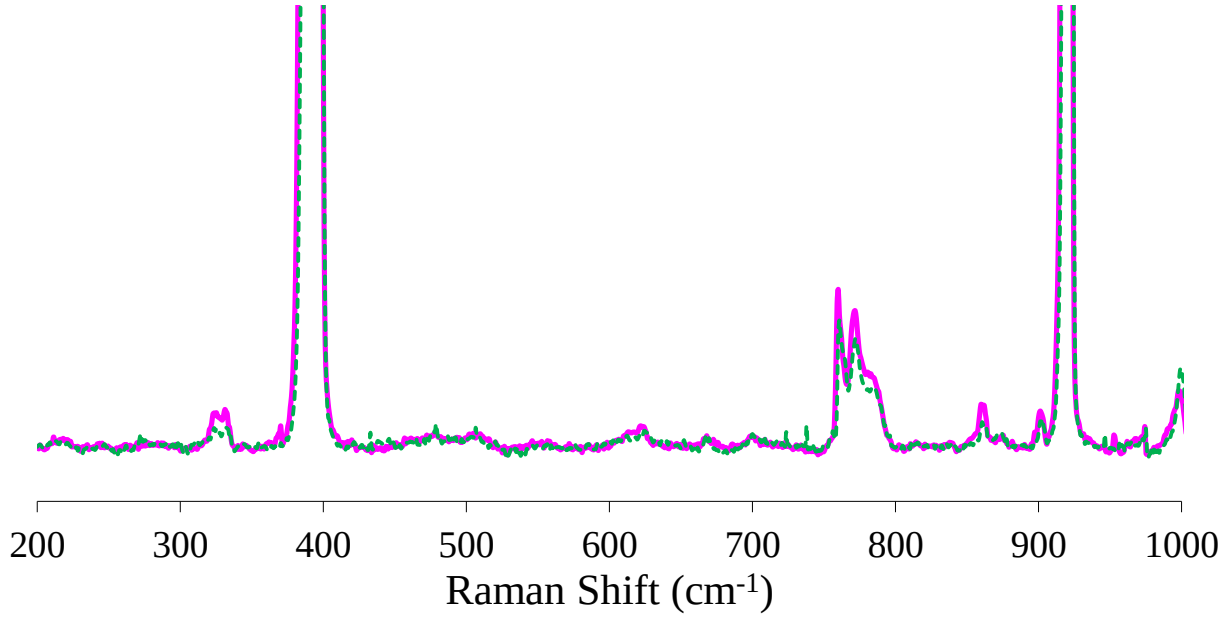

A.37 Perpendicular polarization mode X-band EPR spectra of $[Mn^{III}(S^{Me2}N_4(2\text{-QuinoEN}))]_2(\mu\text{-}O_2)(BPh4)_2{\cdot}CH_3CH_2CN$ (**6**, 3 mM) recorded in MeCN/toluene glass (2:1) at variable temperatures.

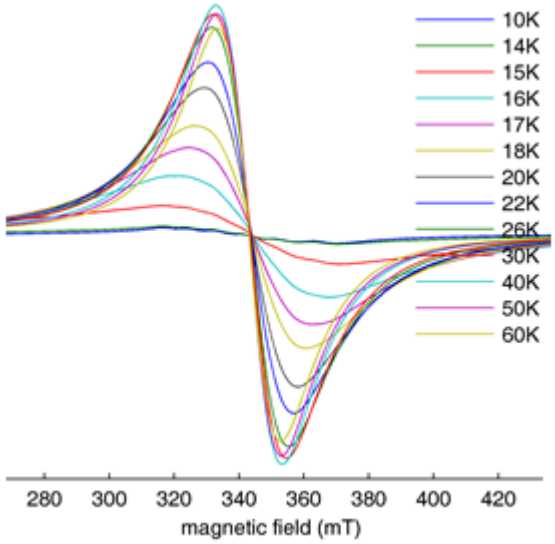

A.38 Anaerobic UV/Vis titration experiment displaying the reaction between $[Mn^{III}(S^{Me2}N_4(6\text{-Me-DPEN}))]_2(\mu\text{-}O_2)(BPh_4)_2{\cdot}2CH_3CH_2CN$ (**5**, 1.1 mM) and trifluoroacetic acid (3 equivalents from a 100 mM stock solution in MeCN) in MeCN at 233 K, followed by the addition of cobaltacene (0.2 equivalent aliquots (based upon total [Mn] from a 15 mM stock solution).

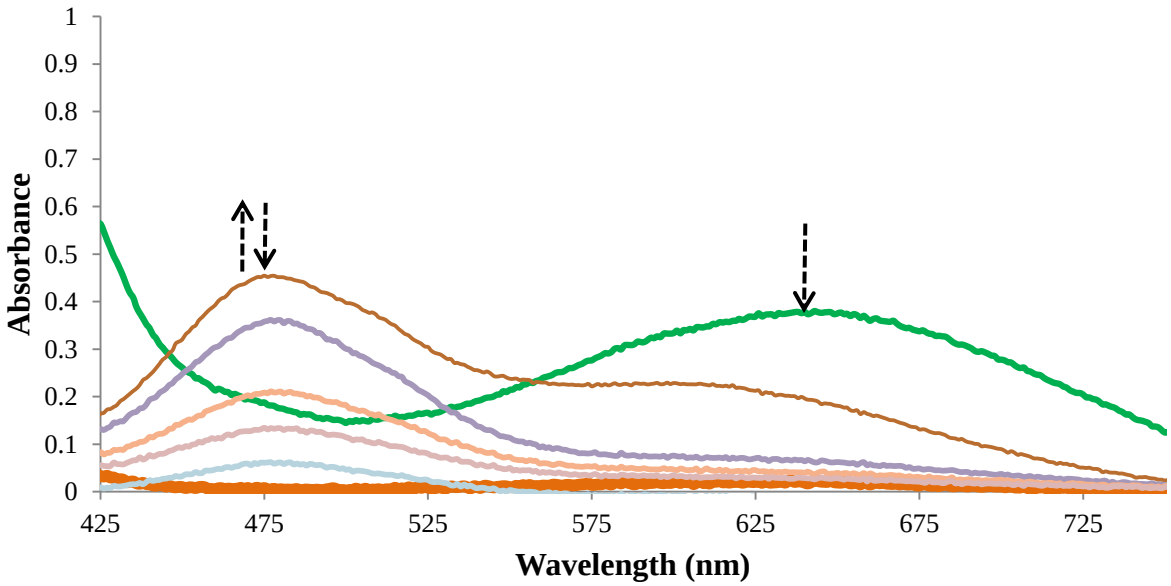

A.39 UV/vis spectra showing the change in absorption of $KMnO_4$ (3 mL of a 6.15 x 10^{-5} M aqueous solution; purple spectrum) which occurs upon the addition of H_2O_2 (orange spectrum) that is released in the reaction between concentrated H_2SO_4 (3-4 drops) and **5** (0.1 mL of 5.5 mM in propionitrile).

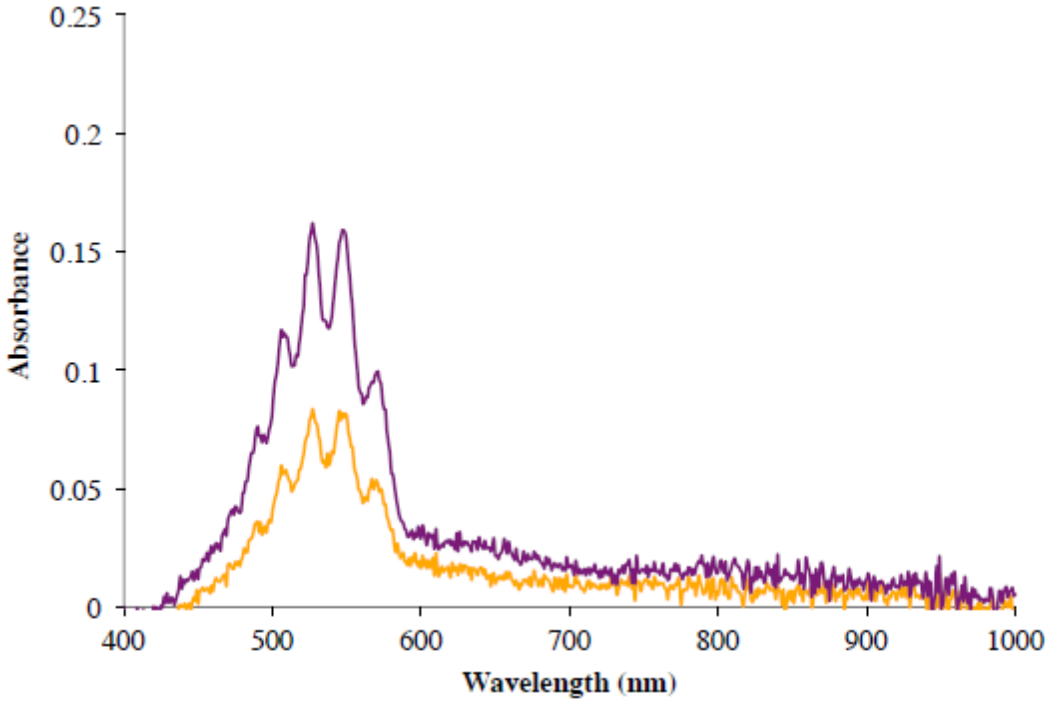

A.40 Anaerobic UV/Vis titration experiment displaying the reaction between [$Mn^{II}(S^{Me2}N_4$(6-Me-DPEN))](BPh_4) (**1**, 1.1 mM) and 0.3 equivalent aliquots of ^tBuOOH (0.1 M stock solution in CH_2Cl_2) with 2.0 equivalents of triethylamine in CH_2Cl_2 at 258 K.

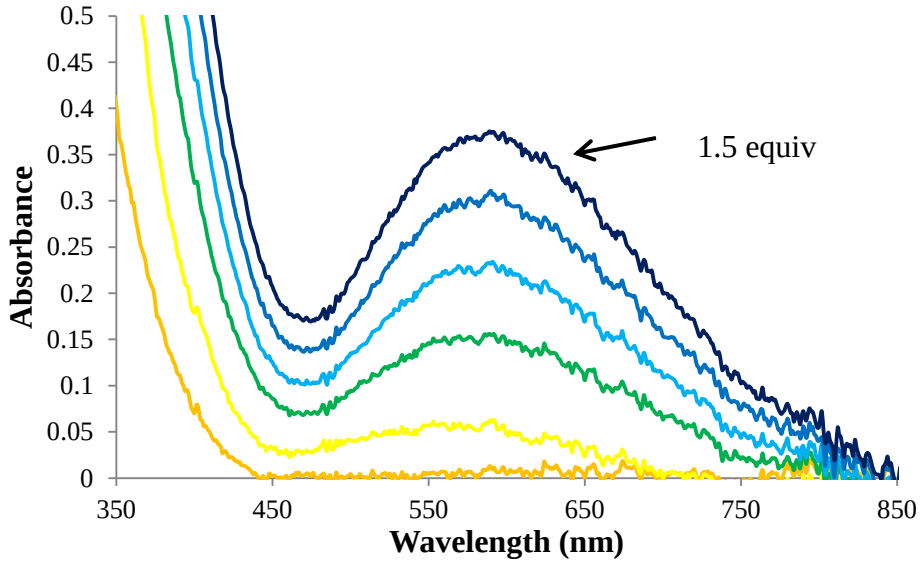

A.41 Anaerobic UV/Vis titration experiment displaying the reaction between [$Mn^{II}(S^{Me2}N_4$(6-Me-DPPN))](BPh$_4$) (**3**, 1.4 mM) and 0.3 equivalent aliquots of ^{t}BuOOH (0.1 M stock solution in CH_2Cl_2) with 2.0 equivalents of triethylamine in CH_2Cl_2 at 258 K.

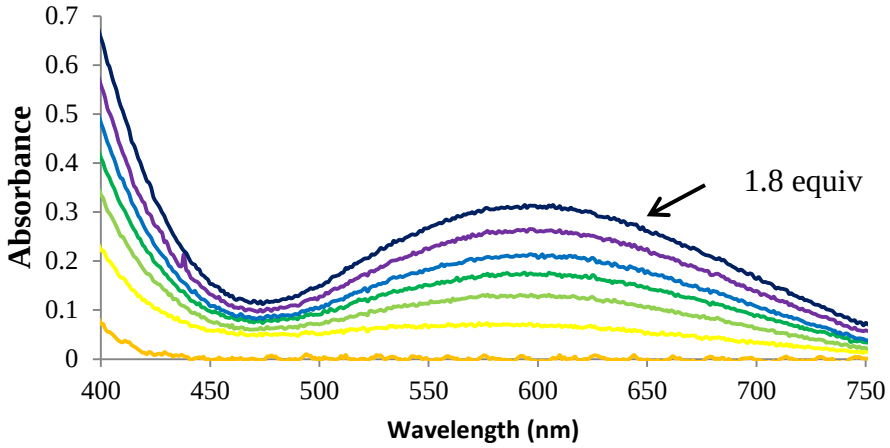

A.42 Anaerobic UV/Vis titration experiment displaying the reaction between [$Mn^{II}(S^{Me2}N_4$(2-QuinoPN))](BPh$_4$) (**4**, 1.5 mM) and 0.4 equivalent aliquots of ^{t}BuOOH (0.1 M stock solution in CH_2Cl_2) with 2.0 equivalents of triethylamine in CH_2Cl_2 at 258 K.

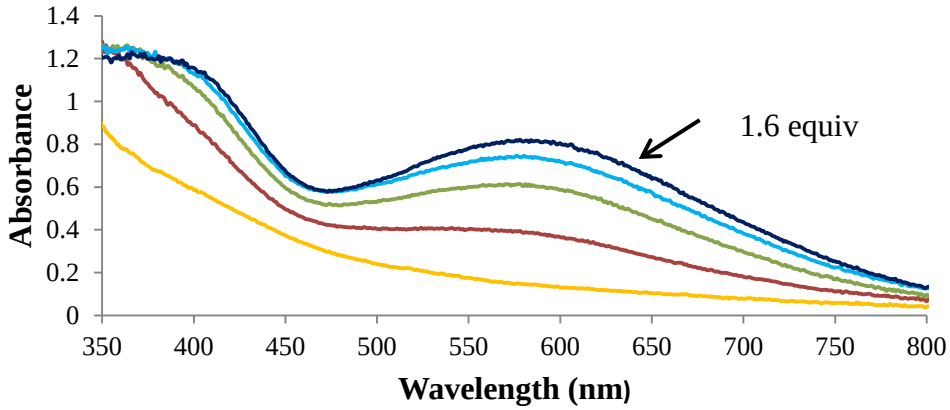

A.43 ESI-MS of ^{16}O- (top) and ^{18}O-labeled $[Mn^{III}(S^{Me2}N_4(6\text{-Me-DPEN})(OO^tBu)]^+$ (**1·OO^{t}Bu**).

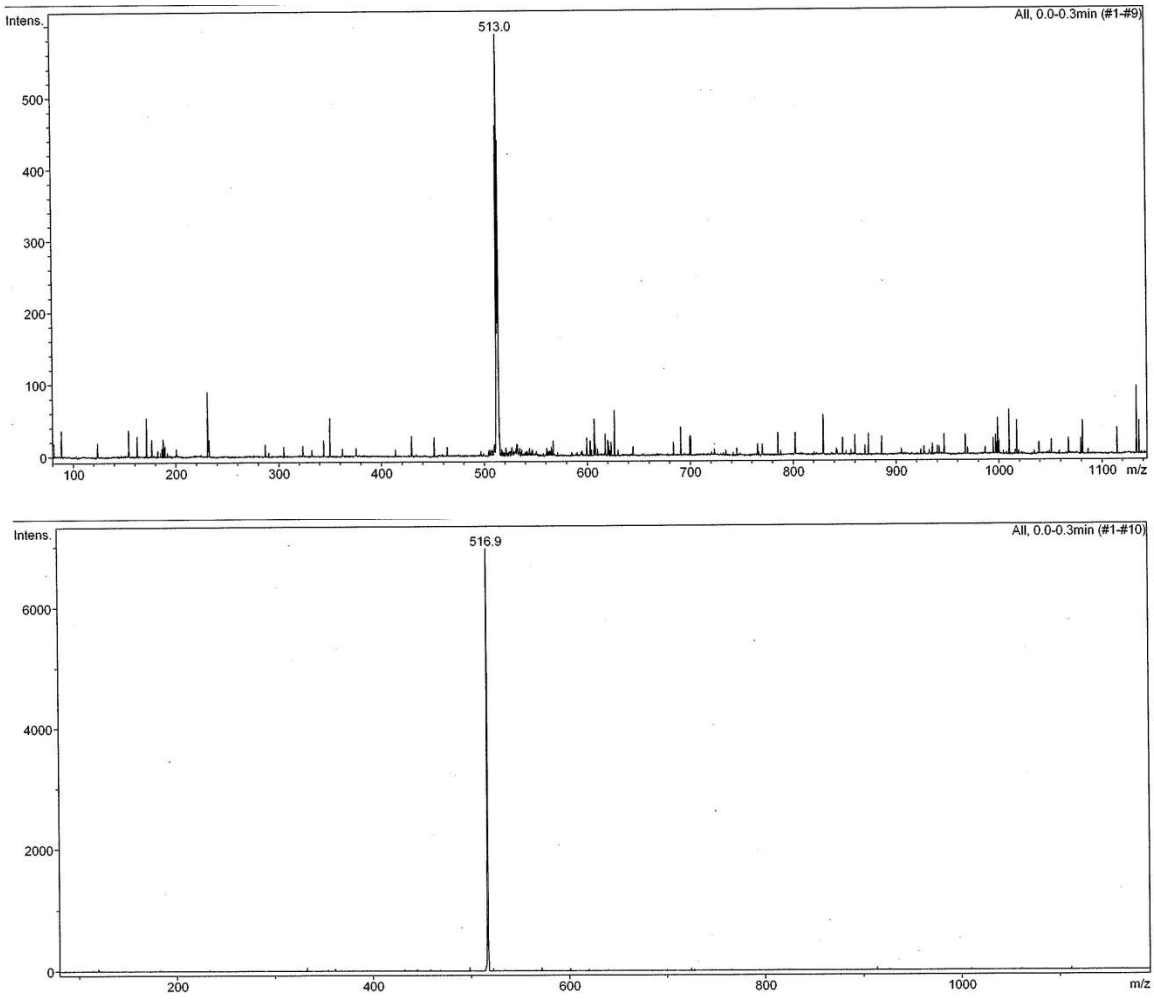

A.44 ESI-MS of ^{16}O- (top) and ^{18}O-labeled $[Mn^{III}(S^{Me2}N_4(6\text{-Me-DPPN})(OO^tBu)]^+$ (**3·OO^{t}Bu**).

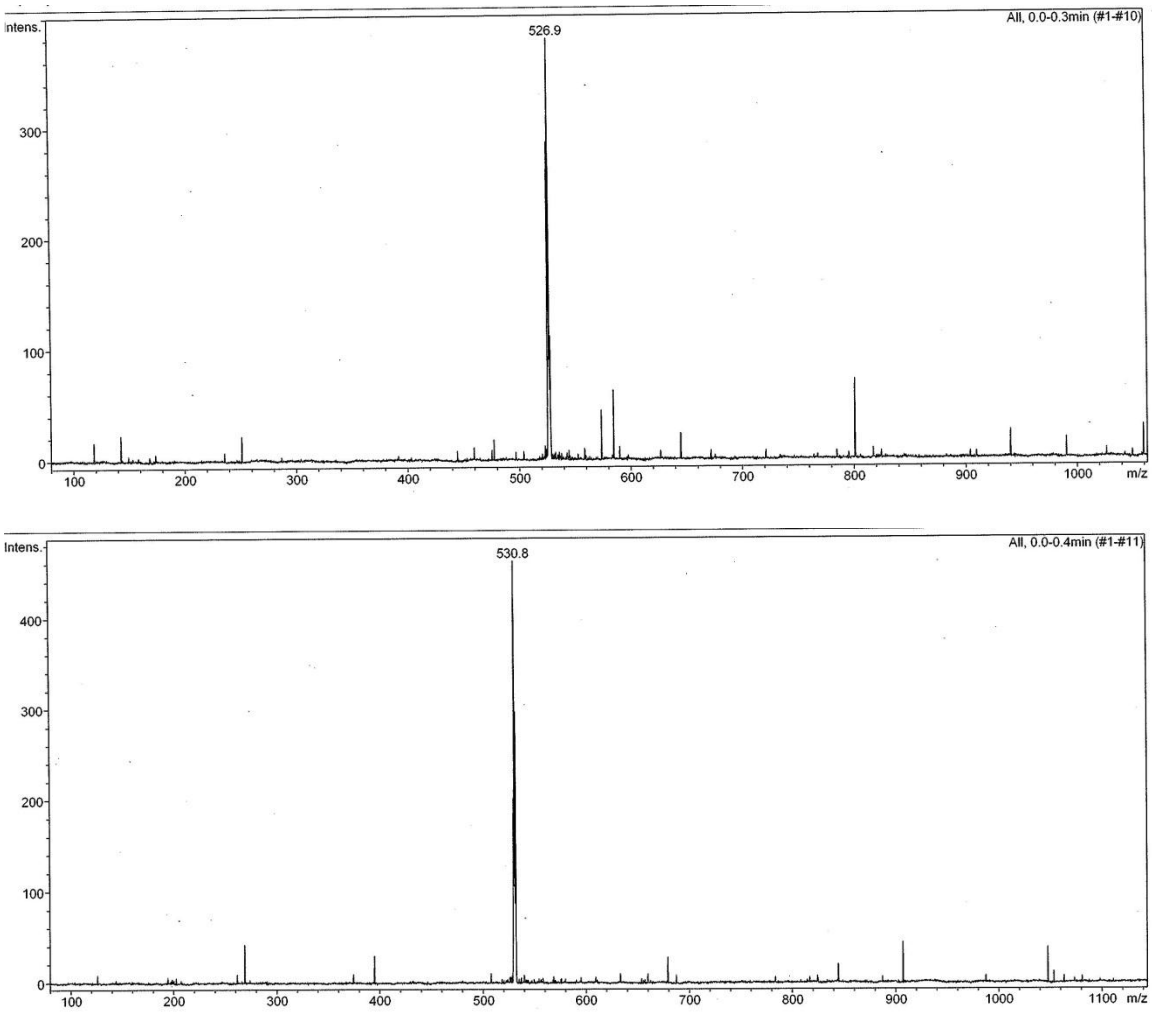

A.45 ESI-MS of ^{16}O- (top) and ^{18}O-labeled $[Mn^{III}(S^{Me2}N_4(2\text{-QuinoPN})(OO^tBu)]^+$ (**4·OO^{t}Bu**).

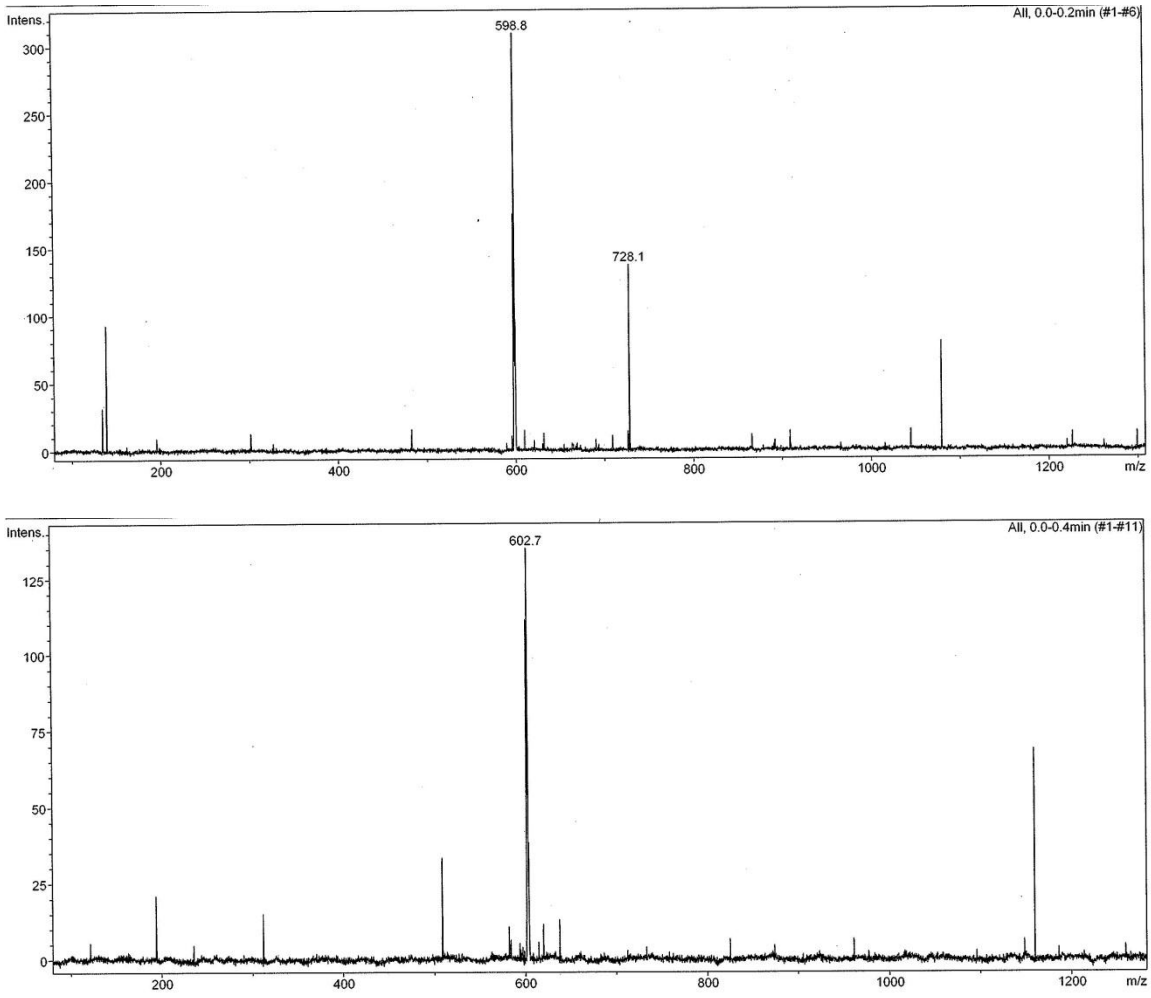

A.46 Quantitative electronic absorption spectrum (extinction coefficient versus wavelength) of $[Mn^{III}(S^{Me2}N_4(2\text{-QuinoEN})(OOCm))](BPh_4)$ (**2·OOCm**) in CH_2Cl_2 at 258 K.

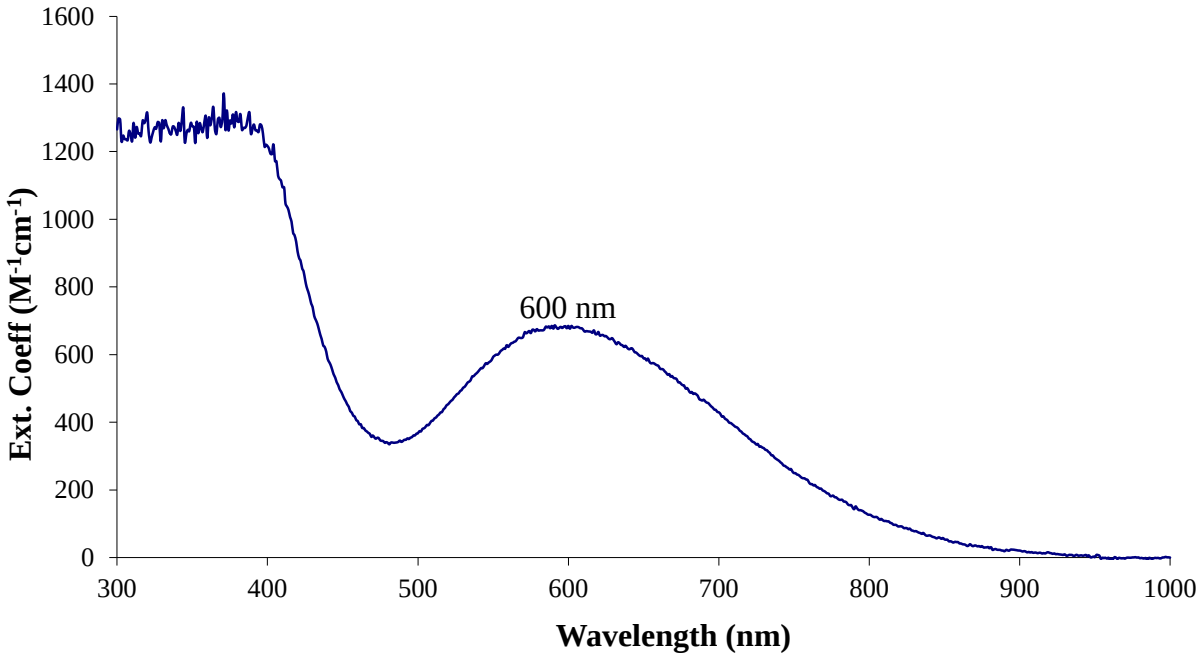

A.47 UV/Vis spectra displaying the decay of $[Mn^{III}(S^{Me2}N_4(6\text{-Me-DPEN}))(OO^tBu)](BPh_4)$ (**1·OO^{t}Bu**) with 2.0 equivalents of triethylamine in CH_2Cl_2 at 258 K (30 minute intervals).

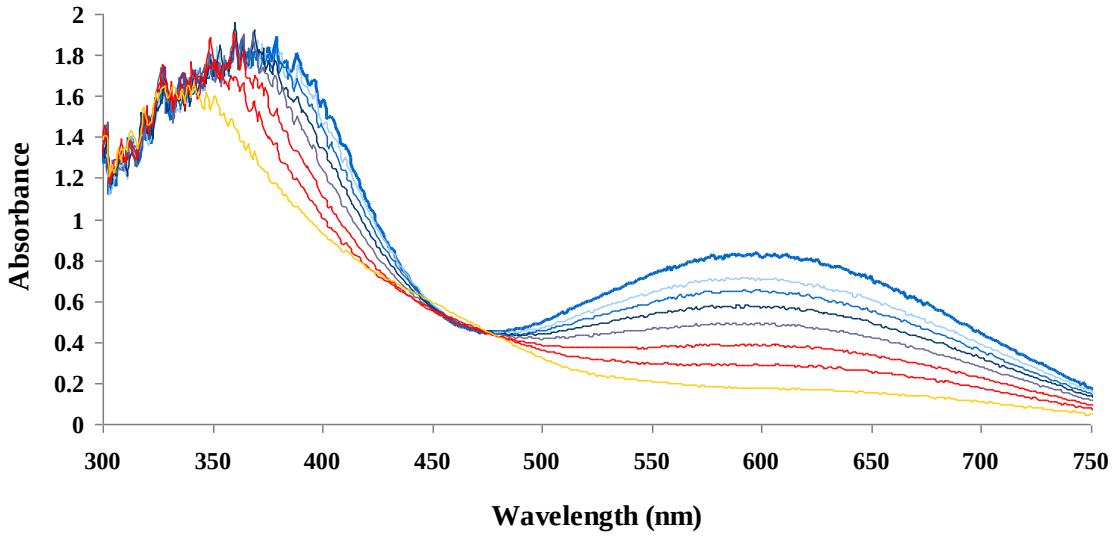

A.48 UV/Vis spectra displaying the decay of $[Mn^{III}(S^{Me2}N_4(6\text{-Me-DPEN}))(OOCm)](BPh_4)$ (**1·OOCm**) with 2.0 equivalents of triethylamine in CH_2Cl_2 at 258 K (30 minute intervals).

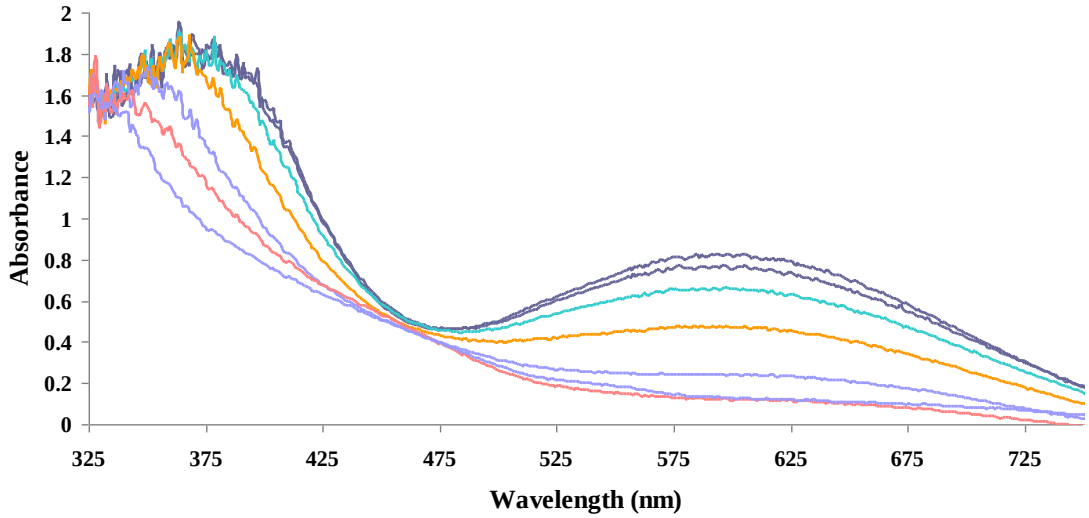

A.49 UV/Vis spectra displaying the decay of $[Mn^{III}(S^{Me2}N_4(2\text{-QuinoEN}))(OO^tBu)](BPh_4)$ (**2·OO^{t}Bu**) with 2.0 equivalents of triethylamine in CH_2Cl_2 at 258 K (30 minute intervals).

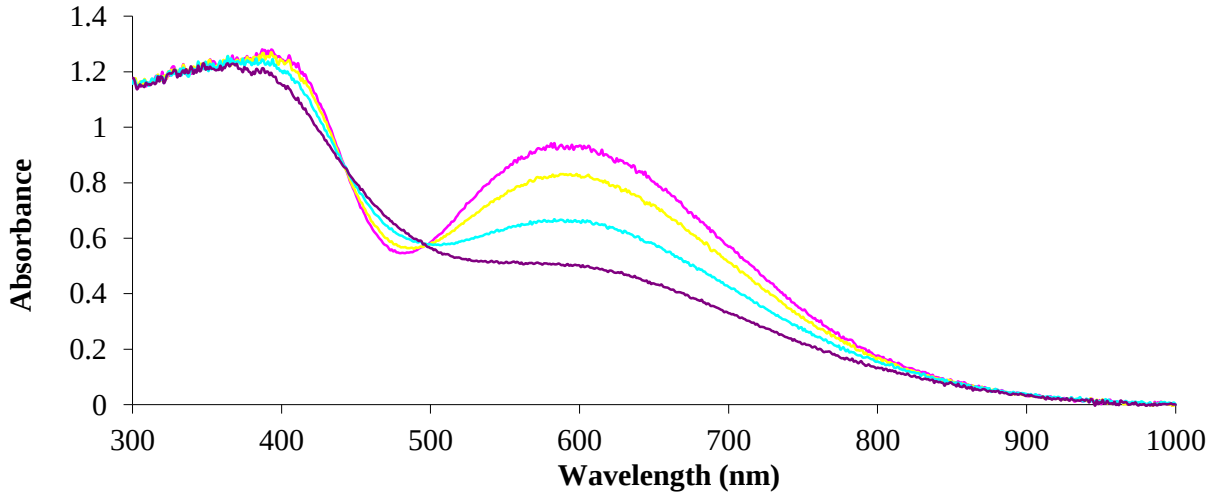

A.50 UV/Vis spectra displaying the decay of $[Mn^{III}(S^{Me2}N_4(6\text{-Me-DPPN}))(OO^tBu)](BPh_4)$ (**3·OO^{t}Bu**) with 2.0 equivalents of triethylamine in CH_2Cl_2 at 258 K (30 minute intervals).

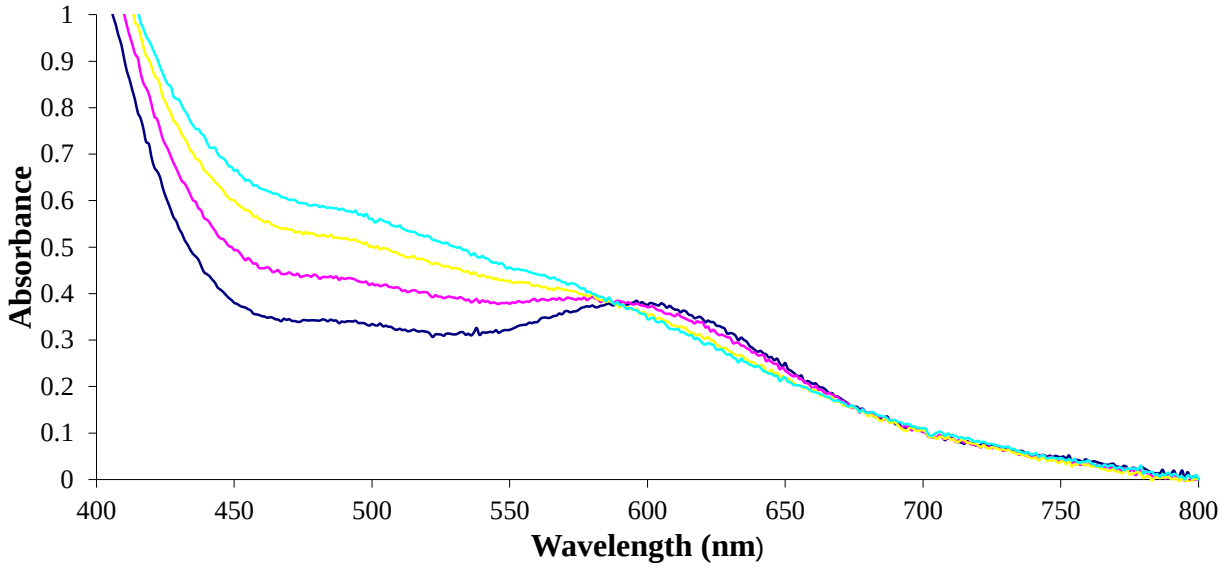

A.51 Quantitative electronic absorption spectrum (extinction coefficient versus wavelength) of $[Mn^{III}(O^{Me2}N_4(6\text{-Me-DPEN})(OO^tBu))](BPh)_4$ (**5·OO^{t}Bu**) in CH_2Cl_2 at 293 K.

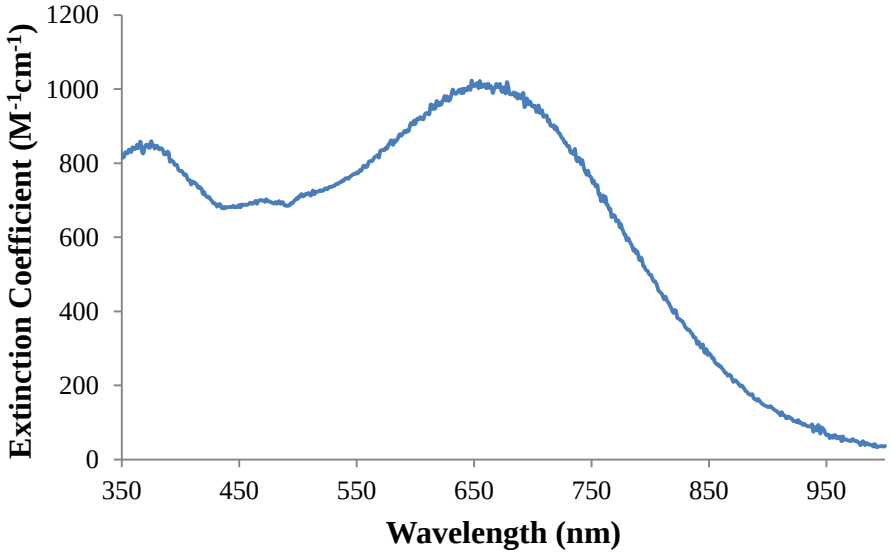

A.52 UV/Vis spectra displaying the decay of [Mn^{III}($O^{Me2}N_4$(6-Me-DPEN))(OO^tBu)](BPh_4) (**5·OO^{t}Bu**) in CH_2Cl_2 at 293 K (2 hour intervals).

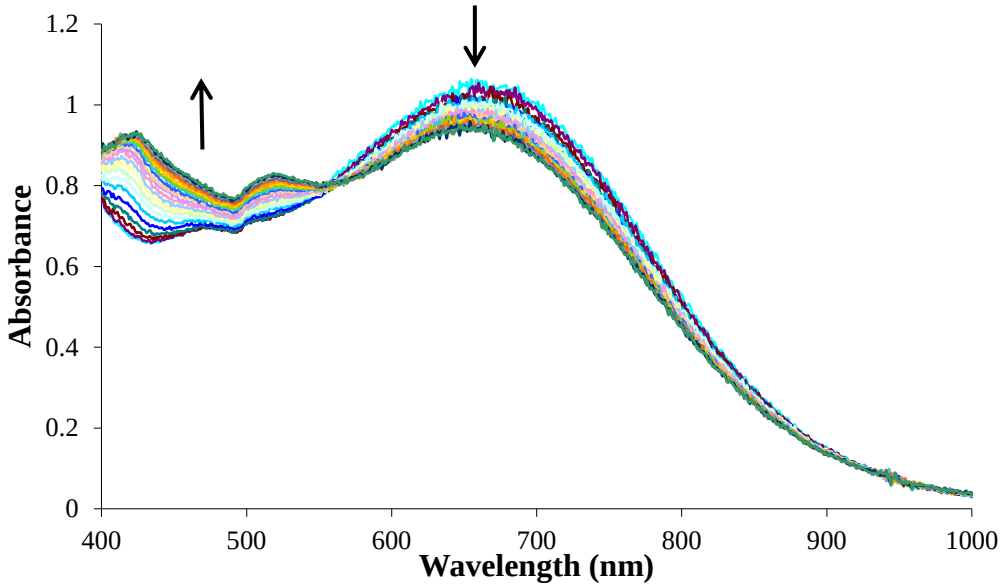

A.53 Quantitative UV/Vis spectrum of [Mn^{III}($S^{Me2}N_4$(tren))(OH)](PF_6)·H_2O (**3**) in MeCN at 293 K.

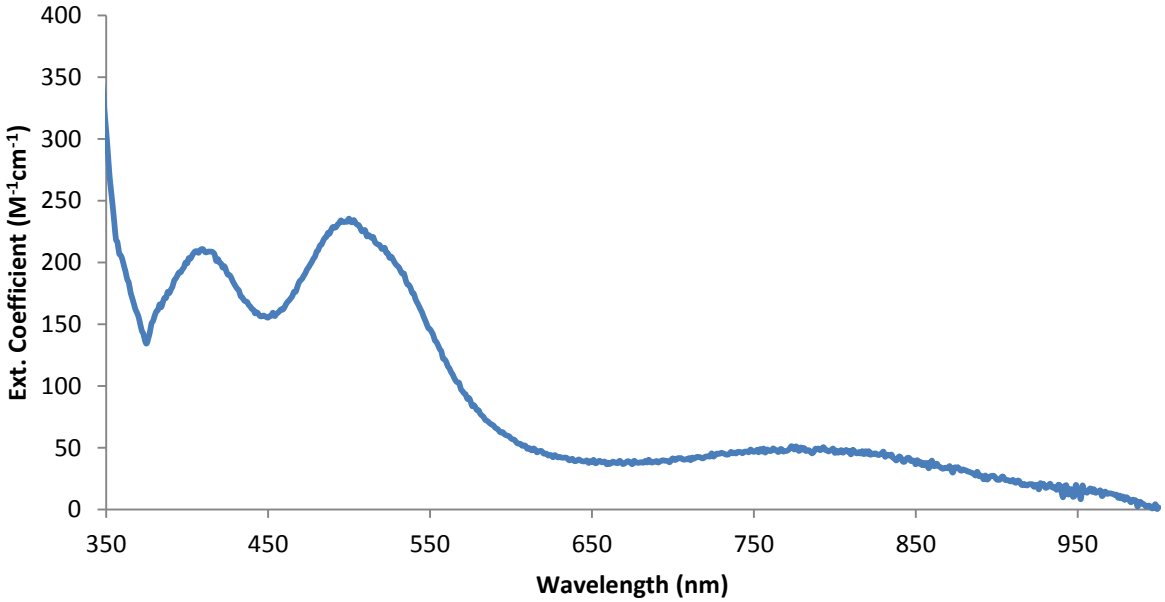

A.54 Quanitative UV/Vis spectrum of $[Mn^{III}(S^{Me2}N_4(tren))(OCH_3)](PF_6)$ (**4**) in MeCN at 293 K.

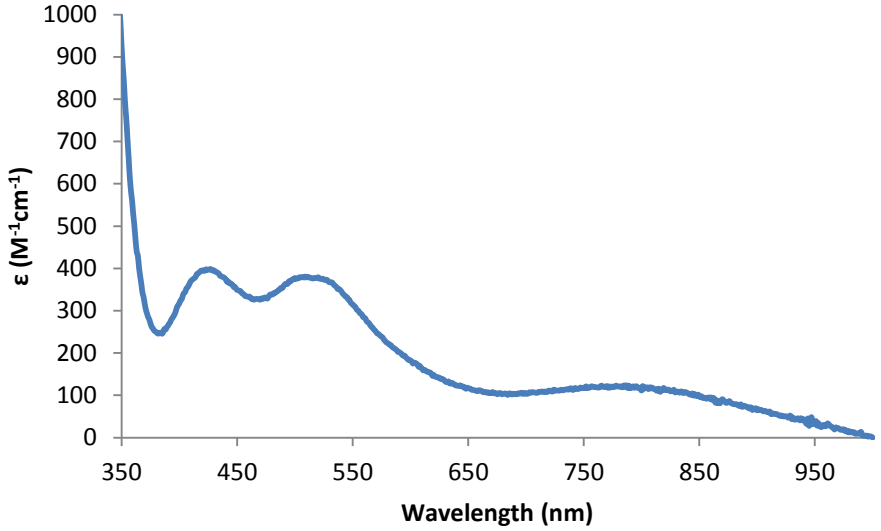

A.55 Quanitative UV/Vis spectrum of $[Mn^{III}(S^{Me2}N_4(tren))(OPh)](PF_6)$ (**5**) in MeCN at 293 K.

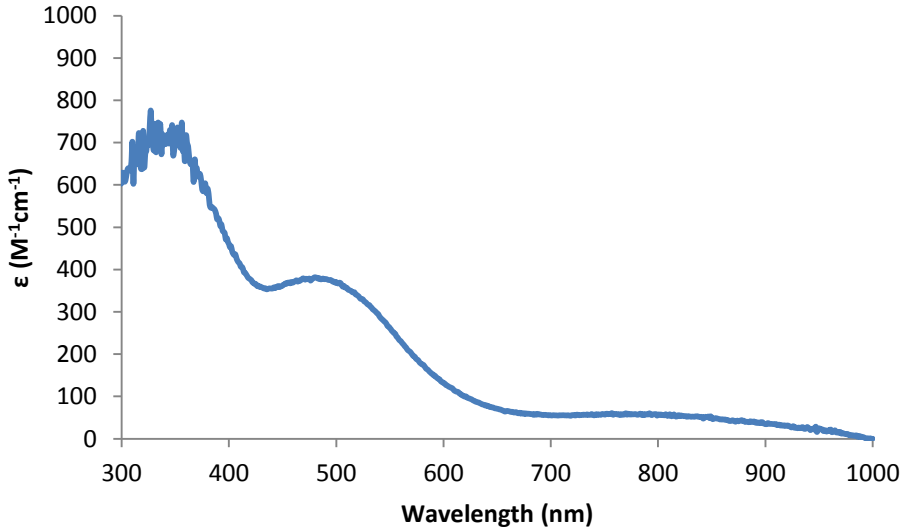

A.56 Quanitative UV/Vis spectrum of $[Mn^{III}(S^{Me2}N_4(tren))(OPh\text{-}^{p}NO_2)](PF_6)$ (6) in MeCN at 293 K.

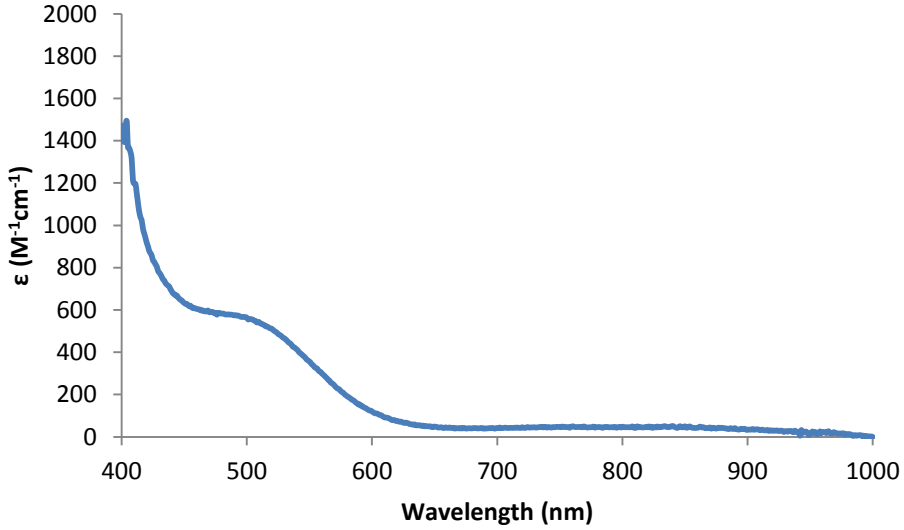

A.57 Representative cyclic voltammograms of $[Mn^{III}(S^{Me2}N_4(tren))(OH)](PF_6)\cdot H_2O$ (**3**) in aqueous solution at room temperature. See Chapter 6 for experimental details.

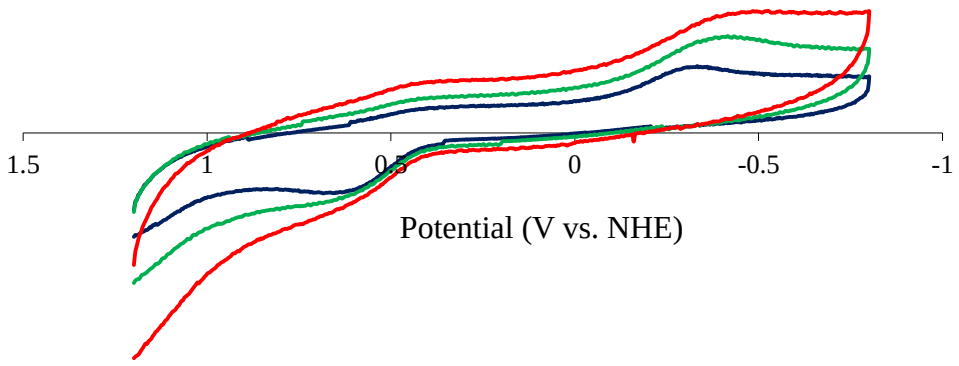

A.58 Titration curve for the protonation of $[Mn^{III}(S^{Me2}N_4(tren))(OH)](PF_6)$ (**3**).

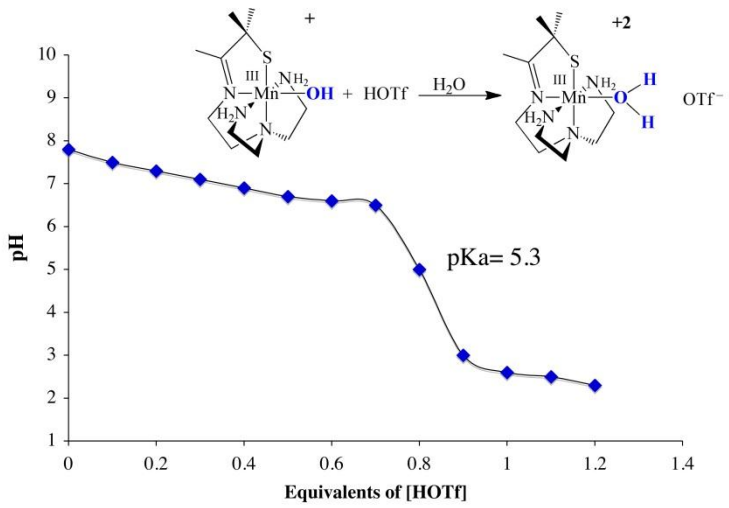

A.59 Representative cyclic voltammogram for $[Fe^{II}(O^{Me2}N_4(tren)(H_2O))](OTf)$ (**10**) in aqueous solution. See Chapter 6 for experimental details.

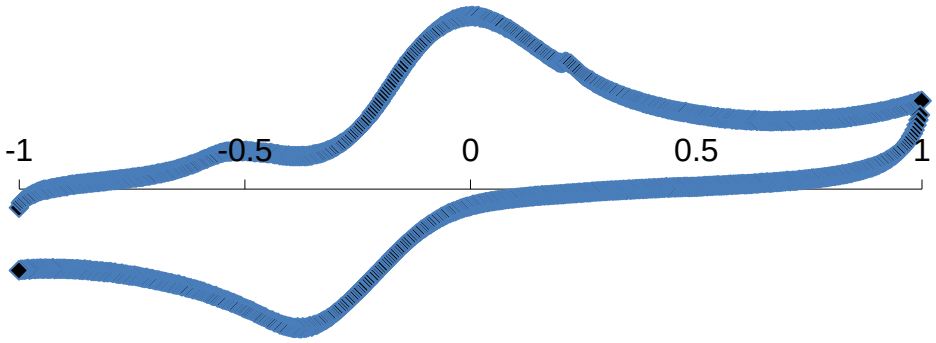

A.60 Titration curve for the deprotonation of $[Fe^{II}(O^{Me2}N_4(tren))(H_2O)](OTf)$ (**10**).

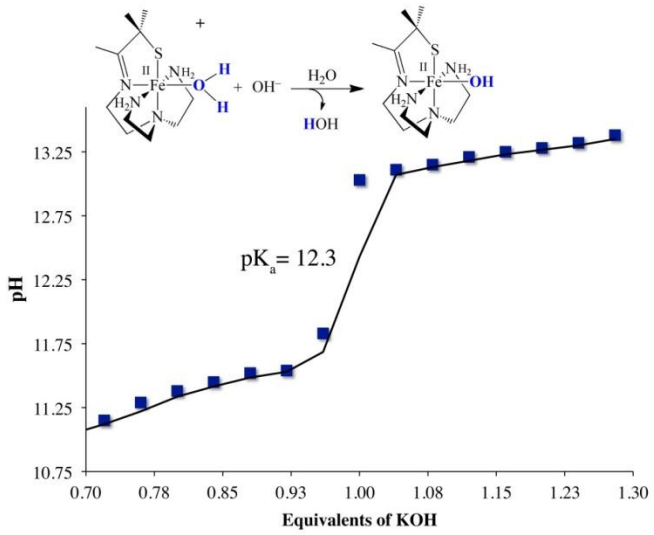

A.61 X-band EPR spectrum of $[Fe^{III}(O^{Me2}N_4(6\text{-Me-DPEN}))]_2(\mu\text{-}OH)_2(PF_6)_2$ (**14**) in MeOH/EtOH glass (9/1) at 5 K.

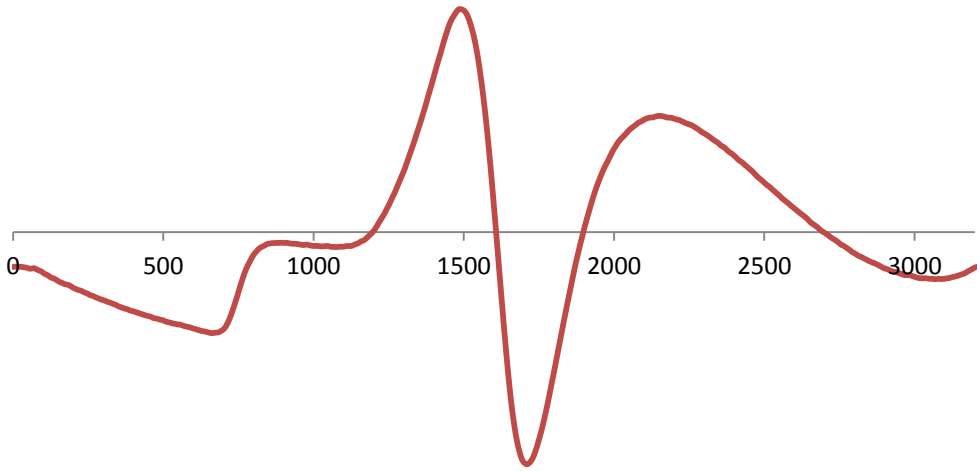

Vita

Michael K. Coggins was born and raised in Travelers Rest, South Carolina. He graduated summa cum laude from the University of South Carolina with a dual degree in chemistry and biology in 2007. While at the University of South Carolina, he worked in the laboratory of Professor John H. Dawson performing mechanistic studies on various heme-containing metalloenzymes. After a brief stint working in the laboratory of Professor Rhett C. Smith at Clemson University on zinc metalloenzymes model complexes, he joined the research group of Professor Julie A. Kovacs at the University of Washington in the fall of 2008. After completing his Ph.D. at the University of Washington in the fall of 2012, he will remain a member of the Kovacs research group as a postdoctoral research associate until June of 2013, when he will join Professor Thomas J. Meyer's research group at the University of North Carolina at Chapel Hill. In his free time, Michael enjoys spending time with his lovely lady and his two golden retrievers.